NOTE TO USERS

BOND CHARACTERIZATION OF REINFORCING BARS AND PRESTRESSING STRANDS IN HIGH PERFORMANCE FIBER REINFORCED CEMENTITIOUS COMPOSITES UNDER MONOTONIC AND CYCLIC LOADING

by

Shih-Ho Chao

A dissertation submitted in partial fulfillment
of the requirements for the degree of
Doctor of Philosophy
(Civil and Environmental Engineering)
in The University of Michigan
2005

Doctoral Committee:

Professor Antoine E. Naaman, Co-Chair
Assistant Professor Gustavo J. Parra-Montesinos, Co-Chair
Professor Subhash C. Goel
Professor Richard E. Robertson

To my wife, Chen-Ying and my family for
their encouragement, supporting, and understanding

ACKNOWLEDGMENTS

The author wishes to express his profound gratitude and sincere appreciation to Professor Antoine E. Naaman, co-chairman of his doctoral committee, for introducing him to the area of HPFRCCs and suggesting this challenging research topic for his dissertation. His continuous guidance, support, and patience have been extremely valuable without which his doctoral study and this dissertation could not have been completed. Special thanks are due to Assistant Professor Gustavo J. Parra-Montesinos, co-chairman of his doctoral committee, who gave the author many opportunities to conduct precious research studies. His numerous suggestions and efforts of reviewing the manuscript have been invaluable to this dissertation. The author also would like to thank Professor Subhash C. Goel, member of the doctoral committee, for his valuable comments and advices on this dissertation, as well as on research works that the author has cooperated with him. It has been a real pleasure and privilege to work with all of them. Appreciation is also extended to member of the dissertation committee, Professor Richard E. Robertson, for his participation in the author's doctoral committee and valuable comments.

Many special people have helped the author along the way. To them the author will always be indebted. The author wishes to thank all his colleagues, in particular Visit Likitruangsilp, for his tremendous help in the lab. Heartfelt thanks also go to Dr. Prabuddha Dasgupta and Dr. Luis Fargier-Gabaldón, former officemates of the author, for their friendship along the way. Thanks also to the technicians at G.G. Brown Structural Engineering Laboratory, Robert Fischer, Robert Spence, and Jan Pantolin, for their competence and professionalism, which the author could always count on. A very

special thank you to the structural and materials engineering faculty at the University of Michigan, from them the author starts to realize the beauty of knowledge.

The author would like to acknowledge the sponsorship of the U.S. National Science Foundation, who provided support for this research under Grant No. CMS-0408623.

The author is deeply grateful to his parents for their encouragement and support, which was crucial to the author's decision in pursuing his doctoral study.

And finally, these five years in Michigan would not have been possible if not for the author's lovely companion, his wife, Chen-Ying. She has been by his side every step of the way. The author would like to thank her for all that she means to him, friend, companion, lab assistant, confidant, wife, and God's blessing.

TABLE OF CONTENTS

LIST OF TABLES

Table

LIST OF FIGURES

Figure

CHAPTER 1

INTRODUCTION

1.1 The Importance of Bond

The bond characteristics of reinforcing steel bars and/or prestressing tendons embedded in concrete matrices play a major role in the behavior of reinforced concrete and prestressed concrete structural members whether subjected to static and dynamic loads. Aspects of this behavior include strength development, development length, transfer length, anchorage of reinforcement, and bar splicing. Bond is often described by an average bond strength (a stress unit), which represents the average shear strength that can be counted on along the interface between the reinforcing steel and the concrete matrix.

Composite action between concrete and reinforcing bars cannot occur without bond. When a reinforced concrete beam, for instance, is subjected to a static load, compressive force (in the concrete) and tensile force (in the reinforcing steel) exist simultaneously. To prevent the reinforcing bars from slipping out, bond between the steel and the surrounding concrete must exist, as illustrated in Figure 1.1. If bond is destroyed, the reinforcing bars will pull out of the concrete, which in turn results in sudden failure of the beam.

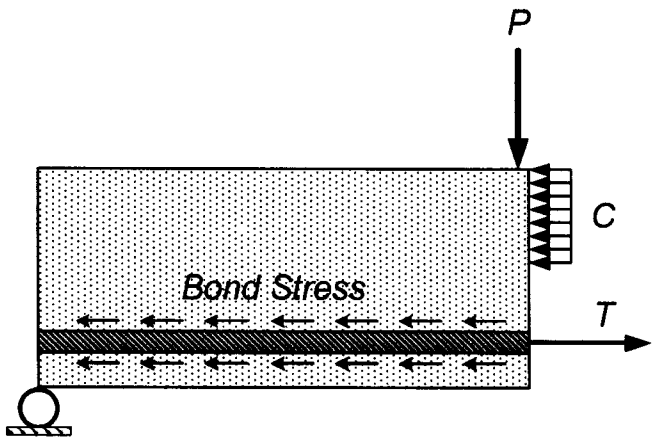

Figure 1.1 Structural safety by means of bond

Not only can poor bond lead to complete loss of strength of a structural element, but also it can reduce its maximum load carrying capacity. It suffices, for example, to consider the case of bonded versus unbonded tendons in a prestressed beam. Assume a prestressing tendon is only bonded at both ends of a beam by mechanical anchorage without any bond throughout the whole length of the steel, as shown in Figure 1.2. When the load P is increased, the first crack will occur in the vicinity of the mid-span section of the beam, where the concrete tensile strength is exceeded. Accordingly, the tensile stress in the steel increases suddenly. This increase of stress extends over the entire length of the steel, from anchorage to anchorage, thereby resulting in significant elongation which in turn leads to a wider crack in the middle of the beam. The neutral axis quickly rises and reduces the area of compression zone. Therefore, the load-carry capacity of the beam diminishes. That is, in the absence of bond, only a lower ultimate strength can be achieved, while the strength of the steel may not be fully utilized. Indeed, in an unbonded prestressing beam, it is very likely that concrete failure at ultimate occurs before yielding of the tendon. Everything else being the same, the stress at ultimate in unbonded tendons

can be 30% less than that in bonded tendons, leading to a similar decrease in nominal bending resistance. (Naaman, 2004; Naaman, Burns, French, Gamble, and Mattock, 2002).

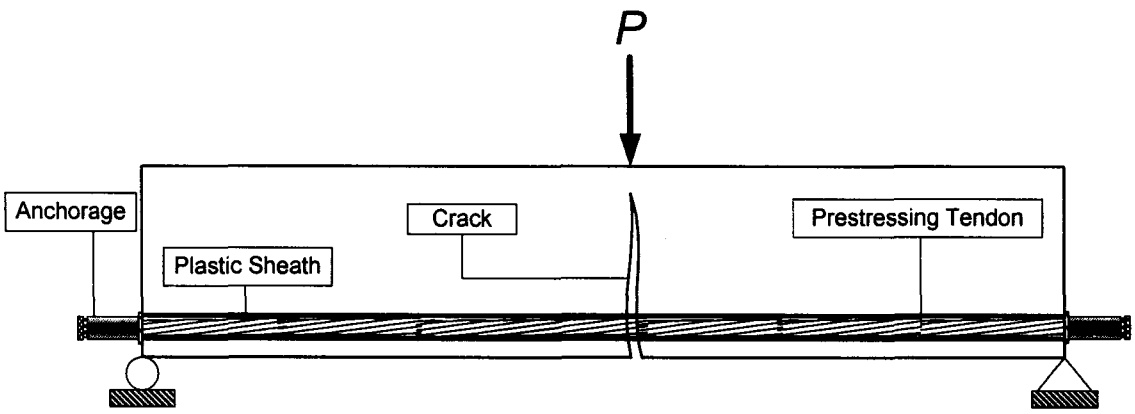

Figure 1.2 Beam with unbonded tendon

On the other hand, if bond is present throughout the entire steel length, the stress increment in the steel at the location of the first crack is reduced in the vicinity of the crack due to bond stresses, as shown in Figure 1.3 (Leonhardt, 1964). If sufficient bond is maintained, the increased steel stress will remain limited to a short length and produces only a slight local elongation of the steel, thus keeping the crack narrow. As a result of tensile force transmitted to the concrete by bond, additional closely spaced cracks near the first crack continue to form. The cracks will gradually extend upwards, along with a gradual rise of neutral axis. If the compressive zone is sufficiently large, the steel stress in the cracked section would increase up to yielding. It follows that the strength of steel can be fully utilized and a higher beam ultimate strength can be achieved.

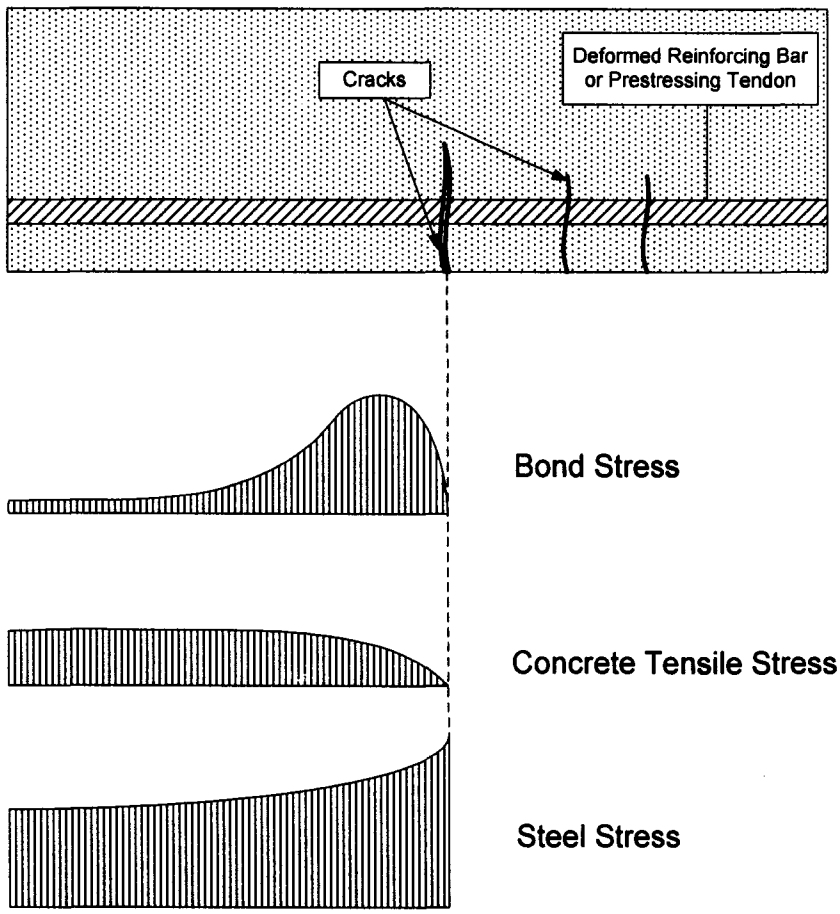

Figure 1.3 Distribution of bond stress, concrete tensile stress, and steel stress beside a crack

Bond properties of reinforcing bars are not expected to deteriorate significantly in common well-designed reinforced concrete and prestressed concrete structures subjected to static and repetitive live loads. However, bond deterioration can be significant in structures subjected to load reversals, such as those induced by earthquakes, or equivalently to high deformation demands. In such cases, bond loss in reinforcing bars can lead to a significant decrease in load resistance, stiffness, and thus collapse of the structure. The progressive deterioration of bond due to cyclic loading may lead to pullout

of reinforcing bars, which in turn results in member or structure failure. In reinforced concrete framed structure subjected to earthquake ground motions, plastic hinges are expected to develop at beam ends, the tensile stresses in the longitudinal beam bars could be significantly higher than the nominal yield strength of the steel due to material overstrength and strain-hardening. Moreover, in an interior beam-column joint, the longitudinal beam bars could be subjected to simultaneous pull-push forces on the opposite sides as illustrated in Figure 1.4 (a). This combination of forces tends to pull the bars out of the joint, and is much more severe than for the case of simply supported beams. As a result, very high bond stress demand can occur, which could lead to damage of bond and thus, excessive slip of beam bars. Slippage of reinforcing bars through the joint leads to concentrated rotations at the column faces with significant stiffness decay and "pinching" in the hysteretic response of the structure. Besides, analysis has shown that the energy dissipation capacity of a beam-column joint would decrease by 30% if a 15% reduction in bond strength along a bar occurs (Filippou, Popov, and Bertero, 1983).

The bond forces developed in the beam and column bars of a beam-column joint are shown in Figure 1.4 (a). Bond deterioration may occur due to the high shear forces and pull-push action results from severe cyclic loading. If the bond deterioration is minor, the tensile stress on the right side of the top bar cannot penetrate through the entire joint core and the bar on the left side of the joint will remain in compression, thus maintaining the flexural strength and the ductility of the beam (Figure 1.4 (b)). However, as shown in Figure 1.4 (c), if the bond is destroyed, in order to maintain equilibrium, the tensile stress will penetrate through the entire joint core, putting the compression steel on the left side in tension. This can lead to a reduction in flexural strength and ductility of the beam

(Paulay and Priestley, 1992; Hakuto, Park, and Tanaka, 1999).

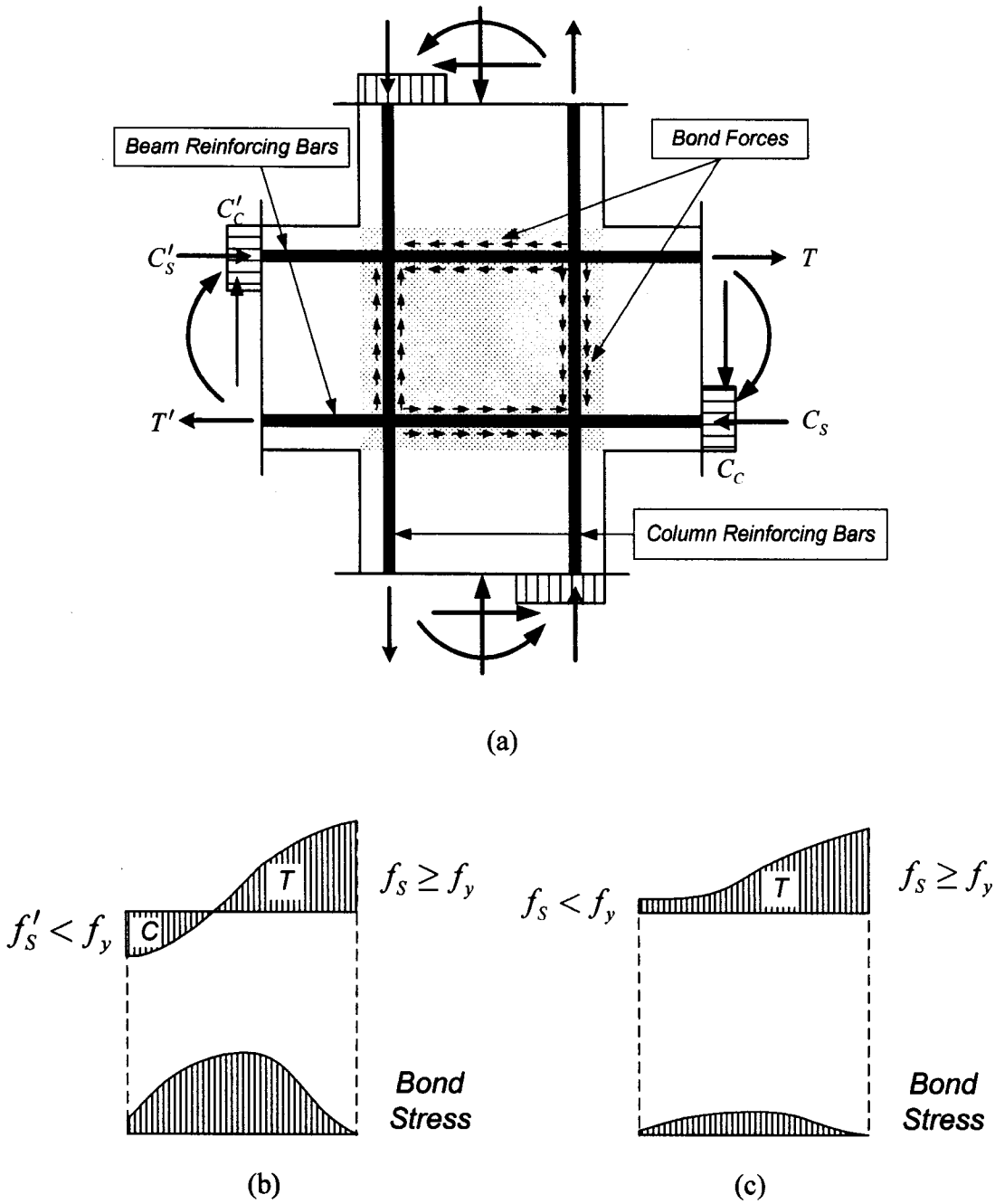

Figure 1.4 Bond forces in an interior beam-column joint subjected to lateral loads : (a) Internal forces in concrete and reinforcing bars; (b) Stress in top bars and bond stress distribution at minor bond deterioration; (c) Stress in top bars and bond stress distribution at significant bond deterioration

From this discussion, it can be concluded that bond stress-slip characteristics of reinforcing bars significantly influence the stiffness, strength, ductility, and the safety of structural members. Besides, the development length needed for a reinforcing bar to develop its strength in a concrete element, and/or the transfer length of a prestressing strand to fully transfer the effective prestressing force to the concrete, also depend on the quality of bond.

1.2 Improvement of Bond

1.2.1 Bond Failure in Conventional Reinforced or Prestressed Concrete Elements

The bond resistance of reinforcing bars or prestressing tendons embedded in concrete depends primarily on frictional resistance and mechanical interlock. The chemical adhesion bond, if any, fails at very small slips. Frictional bond provides initial resistance against loading and further loading mobilizes the mechanical interlock between the concrete and bar ribs or strands. While the protruding lugs offer the mechanical interlock in a reinforcing bar, the helical outer wires around a straight center wire are responsible for the mechanical action in a prestressing tendon (den Uijl, 1998).

Mechanical interlock creates inclined forces which in turn lead to internal inclined cracks in a reinforced concrete element (Figures 1.5 (b)). These cracks, commonly referred to as "Goto Cracks" (Goto , 1971), reduce the bond strength and, should their opening become too large, bond deteriorates progressively. A direct cone-shaped fracture

could result due to the propagation of these inclined cracks. When reinforcing bars are subjected to reversed cyclic loading, the opened inclined cracks lead to significant deterioration in bond stiffness and strength when bar force is reversed due to the presence of gaps between the steel and concrete (Viwathanatepa, Popov, and Bertero, 1979). The radial component of the inclined forces (Figure 1.5 (a)), acting like bursting pressure (Kemp, 1986), cause splitting of surrounding concrete (Figures 1.6 (a) and 1.6 (b)). When the tensile cracks reach the concrete surface, bond resistance drops significantly. It is evident that, for a splitting type failure, the tensile strength of concrete is a major factor affecting the bond behavior and development of reinforcement.

Lateral confinement is an effective way to restrain the expansion and extension of cracks, which in turn increases bond strength (Figure 1.6 (c)). However, a relatively large amount of transverse confinement is needed to prevent the opening and propagation of splitting cracks in regions of members/structures where bond demand is high, such as in beam-column joints of framed structures subjected to lateral loading, and anchorage zones of prestressed concrete beams. This leads to congestion of reinforcement and thus, construction-manufacturing of such regions of members becomes difficult, costly, and requires close quality control.

1.2.2. Proposed Remedy

Considerable attention has been paid in recent years to high performance fiber reinforced cementitious composites (HPFRCCs). HPFRC composites exhibit a quasi strain-hardening behavior with multiple cracking when subjected to direct tension

(Naaman and Reinhard, HPFRCC 1-4, Sujivorakul, C., 2002; Chandrangsu, K., 2003). Such behavior is illustrated in Figure 1.7 in comparison to conventional fiber reinforced concrete (FRC). As can be seen, the tensile strength of plain concrete drops very quickly after cracks occur. In contrast, HPFRC composites show no degradation in post-cracking tensile strength up to very large strains. Furthermore, fibers in HPFRC composites can effectively bridge the tensile cracks and hinder the opening and propagation of cracks, thus redistributing the internal tensile stresses and leading to the formation of multiple fine cracks. It is believed that the unique characteristics of HPFRCCs can significantly enhance the bond characteristics of reinforcing bars and prestressing strands embedded in concrete matrices. A host of additional benefits may be offered by using HPFRC composites, such as reducing reinforcement congestion problems in beam-column joints of earthquake resistant framed structures and anchorage zones of prestressed concrete beams.

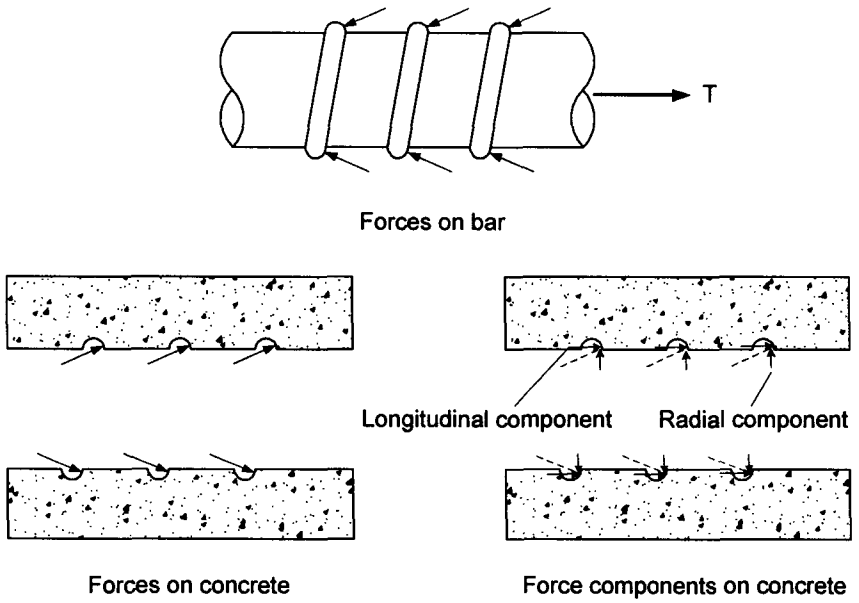

Figure 1.5 (a) Forces between reinforcing bar and concrete

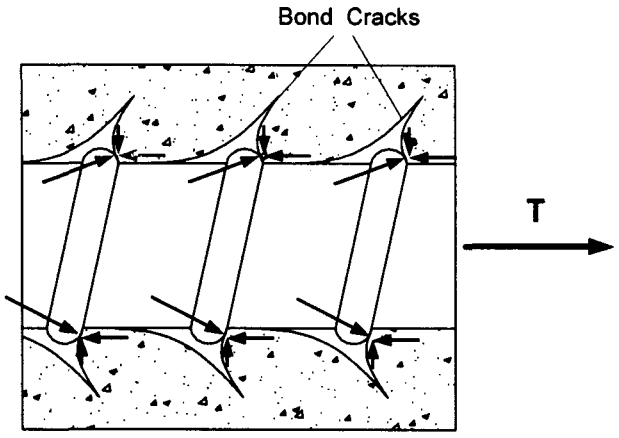

Figure 1.5 (b) Bond cracks and forces acting on concrete

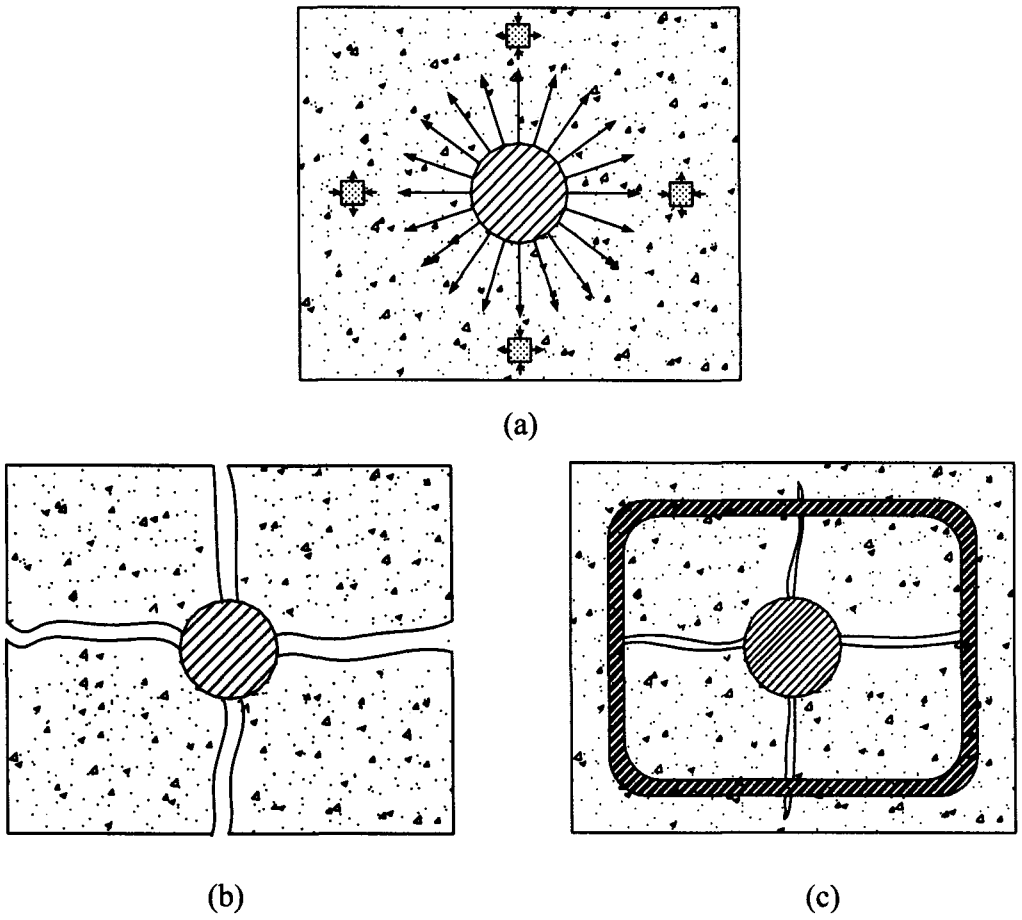

Figure 1.6 Splitting cracks created by radial pressure: (a) Radial pressure; (b) Splitting cracks extend to edges with no confinement present; (c) Splitting cracks confined by transverse confinement

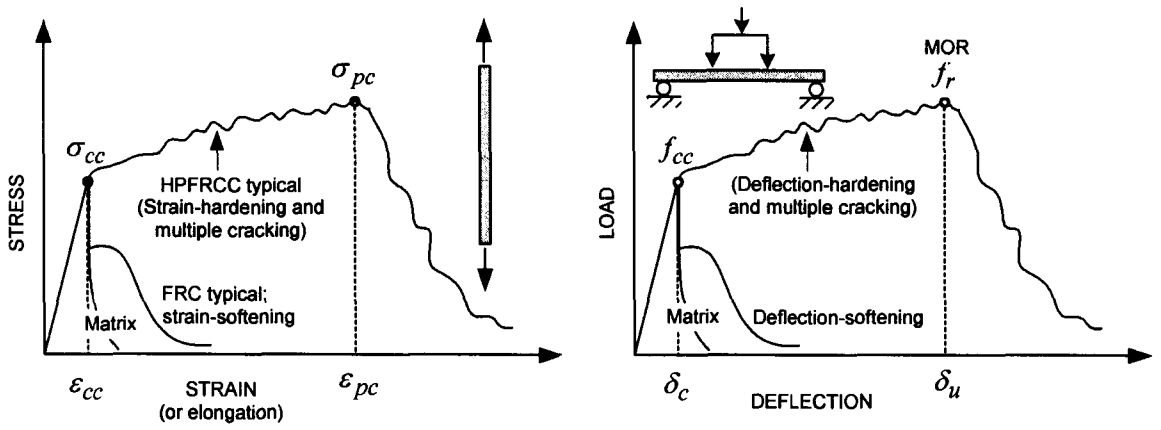

Figure 1.7 Typical responses of strain-hardening and deflection-hardening FRC composites (Naaman, 2003)

1.3 Objectives and Scope

Although the value of average or maximum bond strength developed by a reinforcing bar or a prestressing strand remains a measure of evaluation of bond, it is believed that the main signature of bond behavior can be best described by the bond stress versus slip relationship of the interface between a reinforcing steel bar or strand and the surrounding matrix. Such a relationship can be considered the "constitutive" property of the interface. It gives an entire description of the bond resistance at any given slip, thus allowing the measurement of maximum bond stress, the bond modulus, the average bond stress over a given slip, and the shear-friction energy (thus pull-out work) absorbed up to any given slip. As a consequence, the main objective of this research is to study the bond stress-slip characteristics of deformed reinforcing steel bars and prestressing strands embedded in high-performance fiber reinforced cementitious composites (HPFRCCs). In addition, for comparison purposes, bond behavior of FRC composites showing tensile strain-softening responses was also evaluated.

It is the intent of this study to impose two key constraints on the HPFRC composites used:

1. The fiber reinforced concrete composite should have a "strain-hardening" response in tension.

2. The amount of fibers needed to achieve composite strain-hardening response should be amenable to premixing with the concrete matrix such as in a ready-mix concrete truck or with common field mixers. The current experience suggests a volume fraction of fibers less than about 2% for proper mixing.

The second constraint should allow the wider use of high-performance fiber reinforced cement composites in common structural applications. In summary, the matrix will be a strain-hardening fiber reinforced cement composite containing less than 2% fibers by volume. Various types of fibers were employed in this study although it is believed that steel fibers will provide the more cost effective solution; however, there is need to provide a solution with at least one polymeric fiber to address particular applications where the magnetic properties of steel can be detrimental, such as in structures for maglev trains, radar stations, and x-ray rooms. In order to achieve the research objectives, an experimental and an analytical program were undertaken.

The experimental program consists primarily of pull-out type bond stress-slip tests and large-scale beam-column tests.

In the experimental phase, the following parameters were investigated:

1. Reinforcing steel bars: Grade 60 No. 8, No. 5 and No. 4 deformed bars. No. 4 bars were tested in order to compare the bond behavior of reinforcing bars with that of prestressing strands (both of them have a 0.5 in. nominal diameter).
2. Prestressing steel strands: 0.5 in. diameter; Grade 270.
3. Fiber type: Dramix® steel hooked fiber, PVA 13 fiber, PVA K-II fiber, Torex steel fibers (square, rectangular), Helix® fiber, and Spectra® fiber (see below for additional details on fibers).
4. Fiber volume fraction: 0%, 1%, and 2%. The 0% fiber content represents the control specimens. The 1% and 2% contents cover the range of both deflection-hardening and strain-hardening FRC composites.
5. Confinement: to supplement the control tests (with no fibers) in Item 4, tests using confinement in the form of spirals were also conducted to provide a fair range of results for comparison.
6. Matrix compressive strength: Three strengths were tested, a normal strength of about 5.9 ksi and high strengths of 7.6 and 11 ksi.
7. Loading type for pull-out load tests: a) monotonic; b) unidirectional cyclic with displacement control; c) unidirectional cyclic with force control; d) fully reversed cyclic loading with displacement control; and e) fully reversed cyclic loading with force control.

The following test results were evaluated:

1. Bond stress versus slip relationship; bond modulus; bond strength and

corresponding slip.

2. Cracking pattern and fiber bridging effect.
3. Bond deterioration under cyclic loading and bond deterioration mechanisms.
4. Pull-out energy up to given slip levels.
5. Development length of reinforcing bars and flexural bond length of prestressing strands.
6. Bond stress distribution and efficiency in HPFRCC beam-column connections subjected to displacement reversals.

Bond stress-slip models for both deformed reinforcing bars and prestressing strands were formulated, which account for the most important phenomena observed in the experiments.

Figures 1.8, 1.9, and 1.10 present overall flowcharts of this study.

1.4 Research Significance

The global building industry faces a growing need for advanced materials to address increasing complexity, more stringent code requirements, demand for longer service life, needs to reduce repair-rehabilitation-maintenance cost, and escalating security and protection requirements (Naaman and Parra-Montesinos, 2003). This research represents a major step in addressing the above needs by investigating the bond mechanisms and bond behavior of reinforcing bars and prestressing strands embedded in HPFRC

composites under a variety of loading conditions; this will allow the development of new structural concepts, and offers the means to improve the performance of existing designs. Applications of HPFRCC materials include: blast and impact resistant structures; anchorage zones of prestressed beams where congestion of reinforcement can be a problem; members subjected to large inelastic deformation demands in earthquake resistant structures where congestion of reinforcement renders difficult construction; generally all design involving development, splices, and anchorage lengths; bridge decks; all precast/prestressed concrete products where the transverse reinforcement can be replaced by fibers; all connectors such as for headed studs in precast elements.

1.5 Dissertation Organization

This dissertation is organized into eight chapters. Details of each chapter are described as follows.

Chapter1— Introduction: A general overview of the bond importance and current problems encountered in conventional reinforced concrete design are presented. Research significance, as well as objectives, are described. The overall research work is explained through the use of flowcharts.

Chapter 2— Literature Review: This chapter gives a general review of previous work on bond mechanisms, bond strength, bond stress distribution, bond stress-slip relationship and models, bond test types, development length of reinforcement, parameters affecting bond strength, bond performance in conventional fiber reinforced

concrete, and characteristics of HPFRCCs.

Chapter 3— First phase experimental program on bond stress-slip response: The pull-out type tests on reinforcing bars and untensioned prestressing strands embedded in FRC composite prisms are described. Material properties of matrices, reinforcement, and fibers are elaborated. Specimen preparation and mixing procedure, as well as test setup and instrumentation, are described. Testing procedure and loading protocols are also discussed.

Chapter 4— Experimental results for specimens with reinforcing bars: This chapter provides information on bond performance of reinforcing bars embedded in FRCCs. Bond strength, bond stiffness, pullout work, and cracking patterns under monotonic as well as various cyclic loading regimes are reported. Influence of fiber or reinforcement types, matrix compressive strengths, fiber volume fractions, and bar diameters on bond response is discussed. Predicted development lengths based on test results are also given. Bond mechanisms for reinforcing bars embedded in HPFRCCs are described.

Chapter 5—Experimental results for specimens with prestressing strands: Bond resistance mechanisms for prestressing strands embedded in conventional concrete elements are explained. Test results on bond strength, bond stiffness, pullout work, and cracking patterns under monotonic as well as various cyclic loading regimes are reported. Influence of fiber or reinforcement types, matrix compressive strengths, and fiber volume fractions on bond response is discussed. Average bond strengths obtained from tests are compared with the bond strength values given in current design codes. Bond mechanisms

for prestressing strands embedded in HPFRCCs are described. Potential applications using the test results are discussed.

Chapter 6—Second phase experimental program and results of large-Scale HPFRCC beam-column joints subjected to displacement reversals: Results from the lateral load tests of two 3/4-scale beam-column subassemblies constructed with HPFRCC materials in the joint and beam plastic hinging regions are reported. Emphasis was placed on the bond performance of longitudinal beam bars in the joint region under displacement reversals. Steel stress and bond stress distributions were obtained through the measured strains and the use of the Menegotto-Pinto constitutive model for steel. Overall bond performance was evaluated through a bond efficiency parameter and calculated bond strengths.

Chapter 7—Bond modeling and design recommendations: Bond stress-slip models for reinforcing bars and prestressing strands embedded in HPFRC composites under monotonic as well as various cyclic loading regimes are proposed based on fundamental composite tensile stress-strain responses. A global bond-slip model is also proposed for bars passing through HPFRCC beam-column joints.

Chapter 8—Summary, Conclusions, and Future Research: This chapter presents a summary of the overall research study. Main conclusions from each phase are given based on experimental and analytical results. Some future research work, based on the findings from this study, is advised.

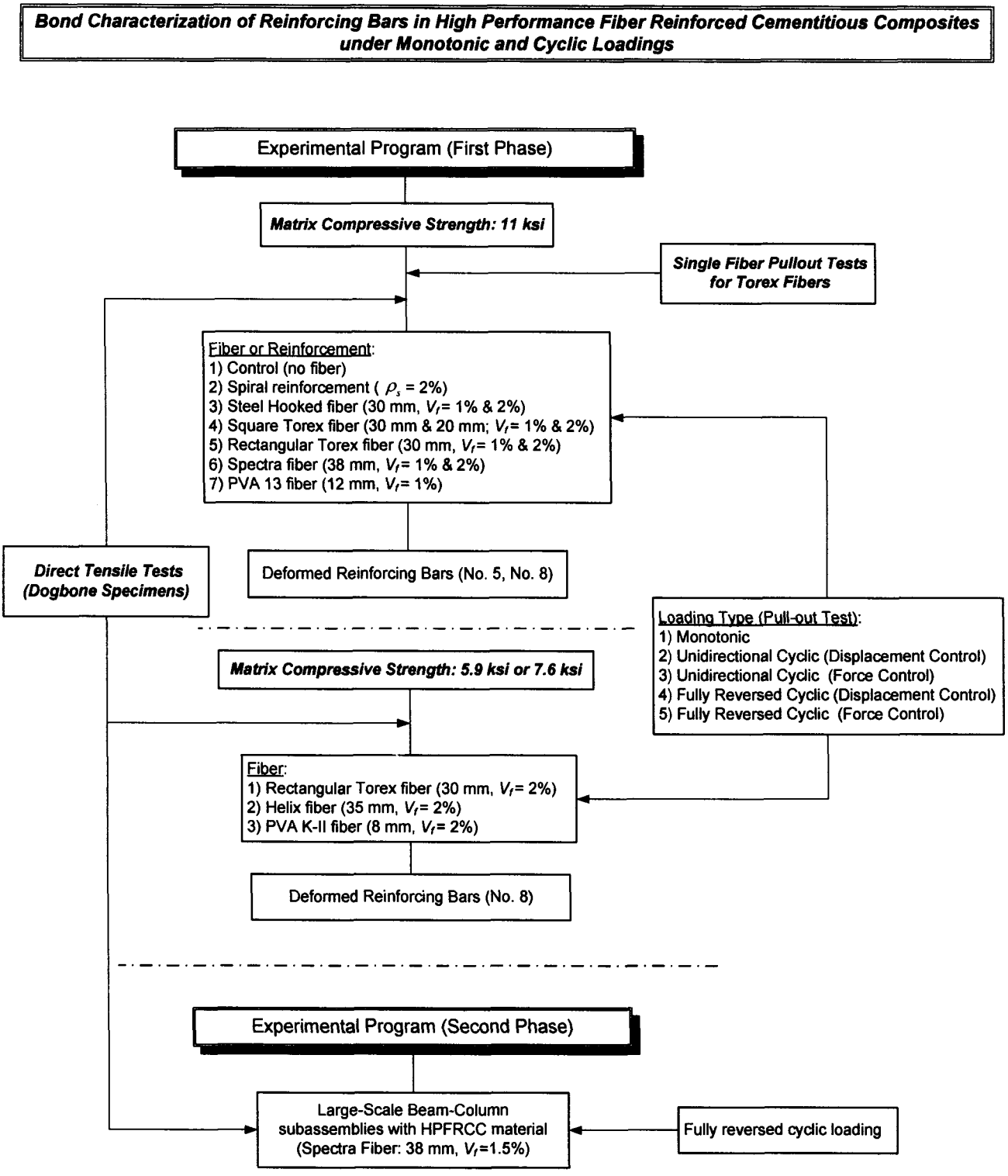

Figure 1.8 Flowchart of experimental program for specimens with reinforcing bars

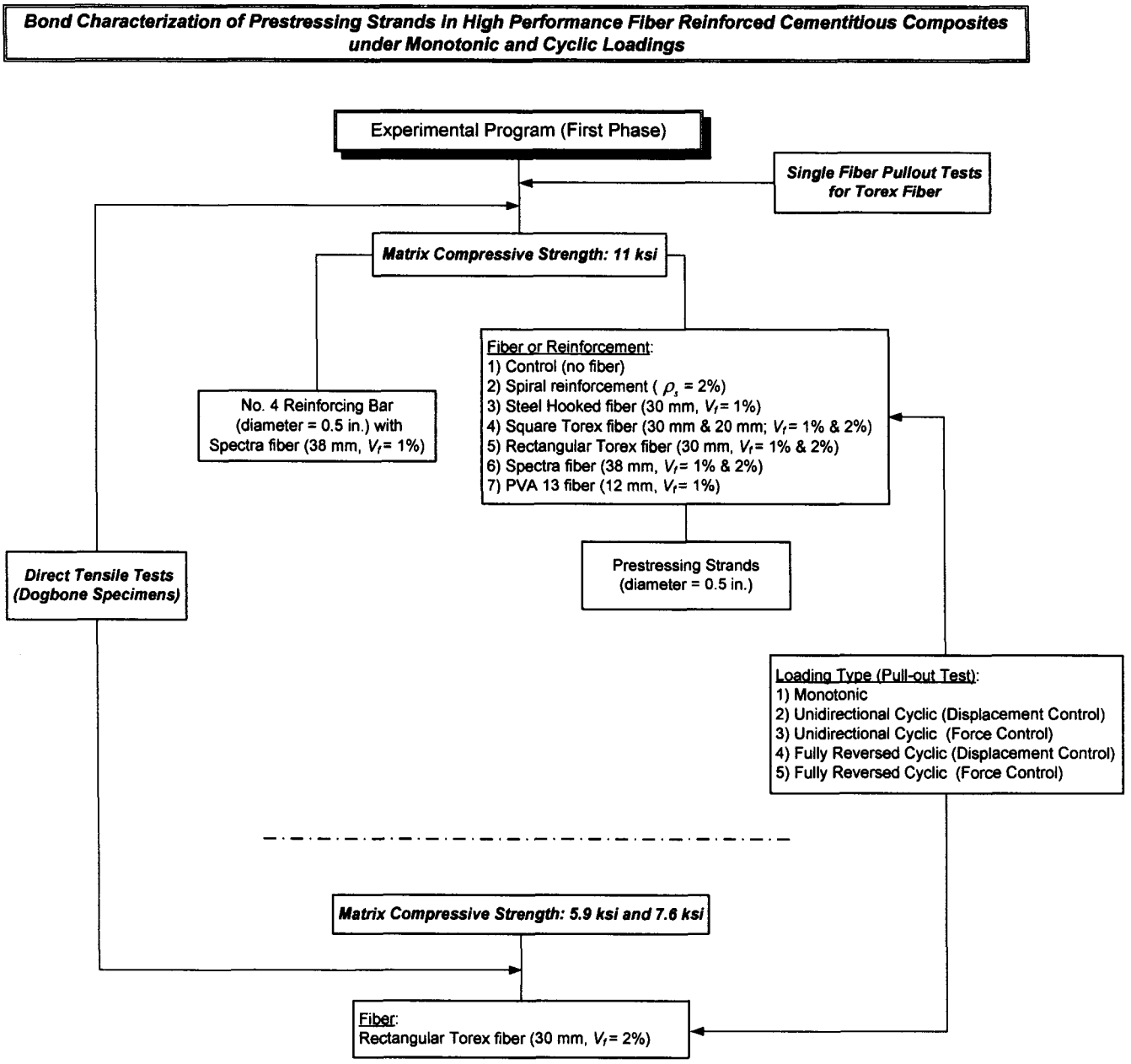

Figure 1.9 Flowchart of experimental program for specimens with prestressing strands

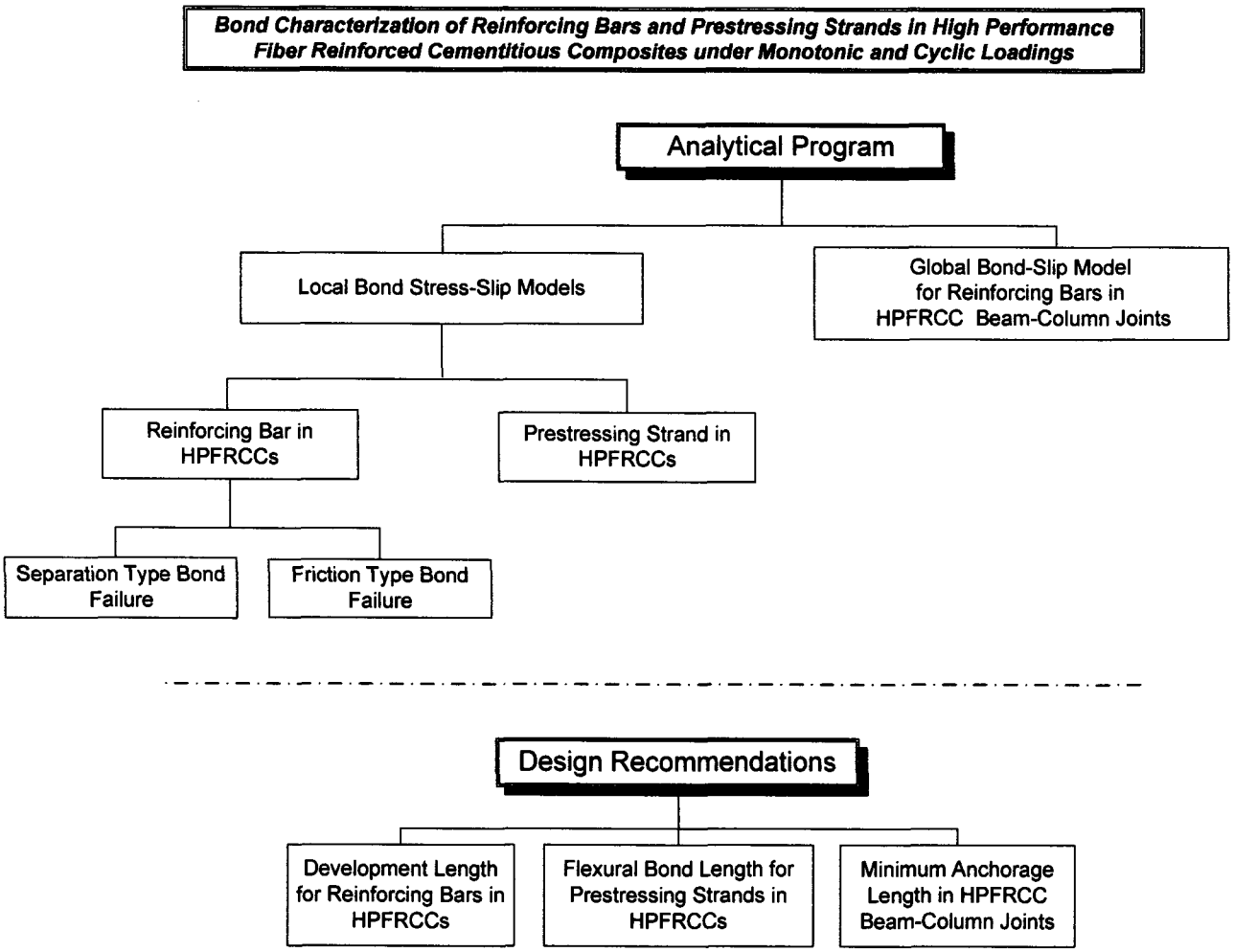

Figure 1.10 Flowchart of analytical program

CHAPTER 2

LITERATURE REVIEW

2.1 History of Research on Bond of Reinforcing Bars

2.1.1 Research Studies on Bond Strength

The nature of research studies on bond has changed drastically during its 90-years history. Early studies concentrated on average bond strength, to determine acceptable values for allowable stress design. These studies also provided information about factors that have an effect on the quality of bond, but they did little to quantify the characteristics of bond strength.

In 1887, Hyatt demonstrated that deformed reinforcing bars can provide superior performance in terms of bond. This is the earliest published tests on bond between concrete and reinforcement. Bond was intensively studied by means of pull-out and beam tests by Abrams in 1913 and 1925. Plain and deformed reinforcing bars were tested to study the effect of various parameters on bond. The results of these two studies provided the principal source of information on bond. It was suggested that improvement of bond could be obtained by improving the deformation geometry of the bars. It was also found that the bond strength may be proportional to the compressive strength of concrete.

Some other parameters influencing bond of reinforcing bars in pull-out tests were reported by Menzel (1939). The bond resistance developed by bars with longitudinal ribs showed less than half that of bars with transverse ribs. Bond resistance was maximum when pulling of the bars was done in the opposite direction to casting.

Mylrea (1948) emphasized the concept of a minimum development length of the bar rather than the unit bond stress based mainly on Abram's (1913 and 1925) test results. He observed that the bond stress varied greatly from point to point along the bar, and that the bond stress distribution was not proportional to the applied load.

A "basic law of bond" was proposed by Rehm in 1957. This law was based on pull-out tests results of a single rib bars with short embedment length; therefore, the bond stress-slip relationship obtained was localized in nature. Rehm's test results showed that rib height and bar diameter affect the bond strength. Additionally, the bar loaded opposite to the direction of concrete casting gave the highest bond resistance as notice by Menzel (1939).

2.1.2 Research Studies on Bond Stress Distribution

The bond stress distribution is one of the important aspects of the study of the bond mechanisms of reinforcing bars. It is presented usually in the form of diagrams that gives an indication of the rate of force transferred from the bars to the concrete. Several researchers developed methods for measuring the steel strain to understand the force transfer mechanism between a reinforcing bar and concrete (i.e., bond mechanism), and

to calculate the shear stress at the interface which was termed as the bond stress.

The bond stress distribution was first studied by Watstein (1947). Pull-out tests were conducted on five different types of deformed bars. The steel strains were measured using mechanical strain gauges. It was found that the bond stress was maximum at the loaded end of the bar and decreased in magnitude towards the free end of the bar. The difference between the magnitude of the bond stress at the loaded end and that at the free end became smaller as the load was increased. It was also shown that bond stresses along a short embedment length varied considerably less than those along a longer embedment length.

The accuracy of the computed bond stress distribution depends on the accuracy of the measured steel strain along the reinforcing bar. A method was devised by Mains (1951) for measuring the steel strain along the bar without disturbing the bonding property of the bar. In this method, the bar was simply split longitudinally, a groove was made in one of the slices, the strain gauges were placed inside the groove, and the two slices were then back-welded together. Mains showed a difference in bond stress distribution between pull-out and beam tests with plain and deformed bars. For the plain bars, the maximum local bond stress occurred near the unloaded end and was not reached until the maximum total load was applied. For the deformed bars, on the other hand, the maximum local bond stress occurred near the loaded end. For all beam tests, the magnitude and distribution of bond stresses was controlled by the location of cracks. Mains also showed that very high local bond stress frequently exceeded twice the average bond stress.

Viwathanatepa, Popov, and Bertero (1979) conducted pull-out test to study the bond strength characteristics of reinforcing bars inside beam-column joints. It was found that the peak bond stress occurred near the loaded end. They pointed out that the bond stress could have a variation of 0.85 to 1.1 between grooved bars (for installation of strain gages) and ungrooved bars. The discrepancy became smaller if larger bar size was used.

Dorr (1978) modified Mains technique of mounting the strain gauges in symmetrically opposed longitudinal grooves. The gauges were connected in series in a Wheatstone bridge to avoid disturbing the axial force information. The grooves in this configuration were external and had to be filled with epoxy, the advantage of this modification are that it is considerably less expensive, and the strain gages can be replaced without repeating the costly machine and welding procedures.

Care must be taken in interpretation of bond stress distribution, mainly because the accuracy of the computed bond stress depends on the steel strain data obtained from the test. Because of the high contact stress occurring at the bar rib, the true local bond stress is usually much higher than the average bond stress. Also, the value of the computed bond stress is affected by the spacing between the strain gages and the type of bond test.

2.1.3 Research Studies on Bond Stress-Slip Relationship

With the introduction of the finite element (FE) method, research studies on bond turned to bond stress vs. slip measurements. The general bond stress-slip relationship was constructed from different values of bar slip and the corresponding tension force in the

bar. It is noted that bond stress-slip curves, like bond strength, are structural properties that depend on both the geometry of the bar and details of the concrete member, including the cover, transverse reinforcement, confinement, and state of stress in the concrete surrounding the reinforcement.

Nilson (1971 and 1972) carried out tension test to study the local bond stress-slip relationship of reinforcing steel bars in concrete. All test specimens were subjected to concentric tension forces acting on both ends of the bar. The Main's technique was used to measure the steel strain along the reinforcing bar. The displacements or both concrete and steel were obtained by integration of the strains. The slip at the location of the gage was the difference between the two displacements of concrete and steel at that point; thus bond stress-slip curves could be obtained at any point along the bar. It was concluded that the bond stress-slip relationship varies along the bar embedment length. Nilson developed the following equation for the bond stress τ_b at a particular value of slip Δ.

$$\tau_b = \left[3100(1.43c + 1.5)\sqrt{f_c'}\right]\Delta \qquad [2.1]$$

$$\text{with } \tau_b \leq (1.43c + 1.5)\sqrt{f_c'} \qquad [2.2]$$

where c represents the distance from the point considered to the loaded face in inches, and f_c' is the compressive strength of concrete in psi.

Mirza and Houde (1979) derived an expression for the bond stress-slip relationship based on experimental results from tension and beam tests. Bond stresses were derived in

the manner of Mains' technique, and slip was calculated from measured end slips and an assumed concrete strain distribution. In contrast to the earlier finding by Nilson (1971 and 1972), they reported that the bond stress-slip relationship at any point was independent of the location of this point from the loaded end. They reported the following equation for the bond stress-slip relationship at any point.

$$\tau_b = 1.95\times10^6\Delta - 2.35\times10^9\Delta^2 + 1.39\times10^{12}\Delta^3 - 0.33\times10^{15}\Delta^4 \qquad [2.3]$$

where Δ is the slip in inches and τ_b is the bond stress in psi, normalized to $\sqrt{f_c'}$ (f_c' = 5,000 psi). Concrete strengths over 5,000 psi can be accounted for by multiplying the right hand side of the above equation by $\sqrt{\frac{f_c'}{5000}}$.

An extensive study was conducted by Eligehausen, Popov, and Bertero (1983) for determining the bond stress-slip relationship of bars embedded in confined concrete. Pull-out concrete specimens with small bar embedment lengths, $L_e = 5d_b$, were tested. Their bond stress-slip relationship differed remarkably from those obtained from previous investigations (Figure 2.1). The difference may come from the testing method, the stress paths, or the confining conditions. It was observed that confinement helps in restraining the propagation of internal tensile cracks around the bar ribs, leading to significant increases in bond strength. It was also found that the bar diameter has little influence on the maximum bond strength, and for a given slip, the bond strength increases linearly with $\sqrt{f_c'}$. The following expression was suggested for the ascending portion of the local

bond stress-slip curve (Figure 2.2):

$$\tau = \tau_{max}(\frac{s}{s_1})^{0.4} \qquad [2.4]$$

where τ is the local bond stress; τ_{max} is the average bond stress at peak, s is the average slip and s_1 is the average slip corresponding to τ_{max}. The average observed values of τ_{max} and s_1 were 1,960 psi and 0.004 in. respectively, for 4,350 psi concrete compressive strength.

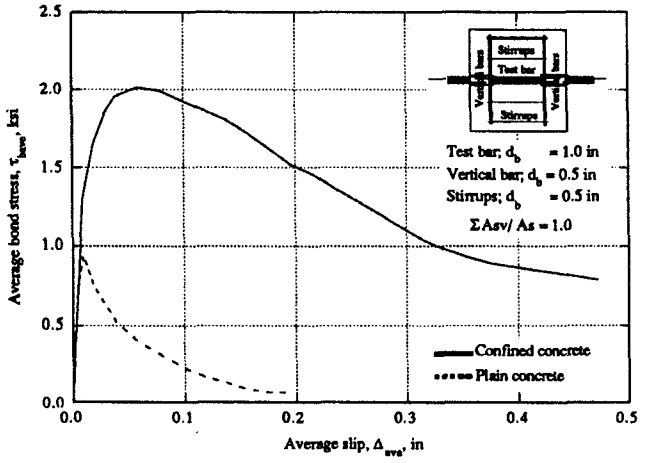

Figure 2.1 Average bond stress versus average slip of short embedment bar (Eligehausen, Popov, and Bertero, 1983)

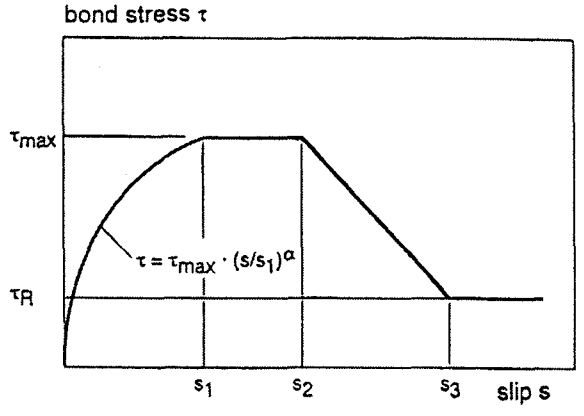

Figure 2.2 Local bond stress-slip curve suggested by Eligehausen et al. (1983)

The above model was further modified by Eligehausen, Ozbolt, and Mayer (1998) to account for the decreasing bond strength close to cracks. Parameters of this model were determined based on results of special pull-out tests, which took into account the influence of splitting cracks on the bond stress-slip relationships and inelastic steel strains. The bond stress-slip models and related parameters are shown in Figure 2.3.

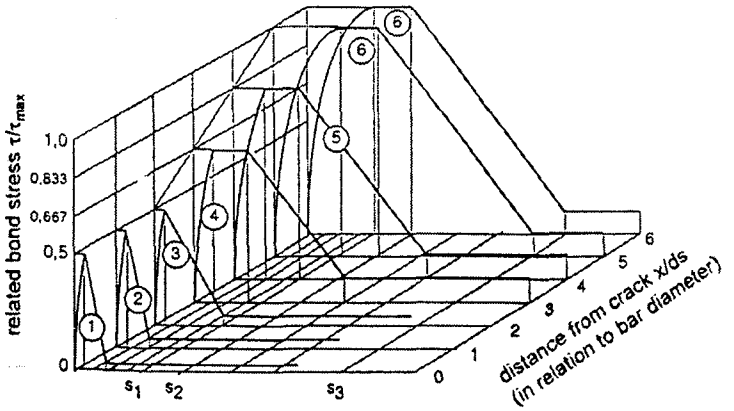

Parameter		good bond area acc. to CEB-FIP Model Code 1990	all other bars (top bar effect)	remarks
τ_{max}	=	$a \cdot \sqrt{f_c}$		f_c [MPa]
		$a = 0.36 \cdot \frac{c}{d_s} + 1.28$		usual concrete cover and no stirrups
		$a = 0.36 \cdot \frac{c}{d_s} + 2.00$		narrowly spaced stirrups
τ_R	=	$0.15 \cdot \tau_{max}$		
α	=	$0.0030 \cdot f_c + 0.1625$		f_c [MPa]
s_1	=	0.25 mm	0.40 mm	
s_2	=	0.35 mm	0.60 mm	
s_3	=	1.00 mm	2.50 mm	usual concrete cover and no stirrups
s_2	=	2.00 mm	-	narrowly spaced stirrups

bond law no.	good bond area acc. to CEB-FIP Model Code 1990				all other bars (top bar effect)			
-	s_1 [mm]	s_2 [mm]	s_3 [mm]	τ_R/τ_{max}	s_1 [mm]	s_2 [mm]	s_3 [mm]	τ_R/τ_{max}
1	0.014	0.014	0.05	0.001	0.022	0.022	0.05	0.001
2	0.014	0.014	0.15	0.025	0.022	0.022	0.30	0.025
3	0.014	0.014	0.30	0.050	0.022	0.022	0.60	0.050
4	0.045	0.145	0.55	0.150	0.074	0.174	1.45	0.150
5	0.116	0.215	0.75	0.150	0.185	0.385	1.95	0.150

[1] for f_c = 25 MPa

Figure 2.3 Modified local bond stress-slip curve suggested by Eligehausen et al. (1998)

The bond stress-slip model of CEB-FIP Model Code 90 (1993) for ribbed reinforcing bar is shown in Figure 2.4, which is composed of four branches:

$$\tau = \tau_{max}(\frac{s}{s_1})^{\alpha} \quad \text{if } 0 \le s \le s_1 \quad [2.5a]$$

$$\tau = \tau_{max} \quad \text{if } s_1 < s \le s_2 \quad [2.5b]$$

$$\tau = \tau_{max} - (\tau_{max} - \tau_f)\frac{(s - s_2)}{(s_3 - s_2)} \quad \text{if } s_2 < s \le s_3 \quad [2.5c]$$

$$\tau = \tau_f \quad \text{if } s > s_3 \quad [2.5d]$$

Once a suitable bond stress-slip model has been selected for an "interface bond element", a finite element analysis for RC members can be performed using this element in between reinforcing bar and concrete matrix (Tajima, Mishima, and Shirai, 2004; Lowes, Moehle, and Govindjee, 2004)), as schematically shown in Figure 2.5.

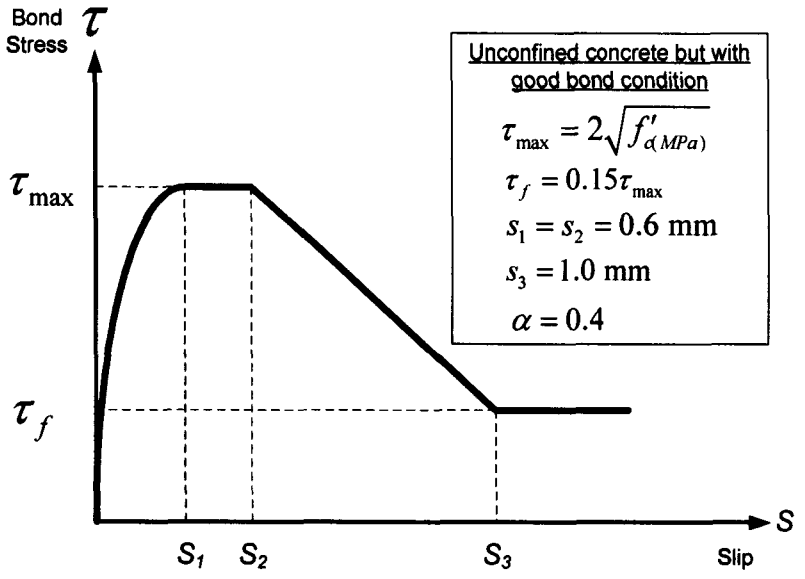

Figure 2.4 Bond stress-slip relationship for RC structures (CEB-FIP Model Code 90, 1993)

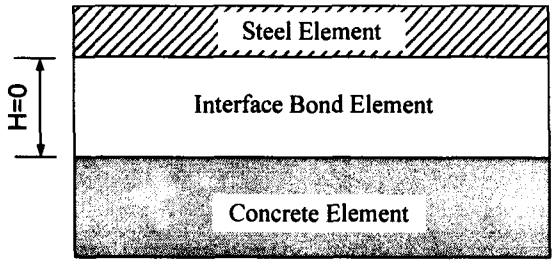

Figure 2.5 Finite element analysis implementation of bond element in RC members

2.1.4 Types on Bond Test

Numerous types of bond tests were used to evaluate the manner in which stresses are transferred from reinforcing bars to their surrounding concrete, as shown in Figure 2.6 (Chapman and Shah, 1987). The aim of these tests is to allow for the modeling of the true behavior of the interaction between reinforcing bars and concrete in real structures. This is difficult to achieve because the bond problem is complicated by other structural actions, e.g. the flexural bond, lateral pressure, dowel forces, and crack pattern. The type of bond test should be carefully selected to reflect the real condition of the structure.

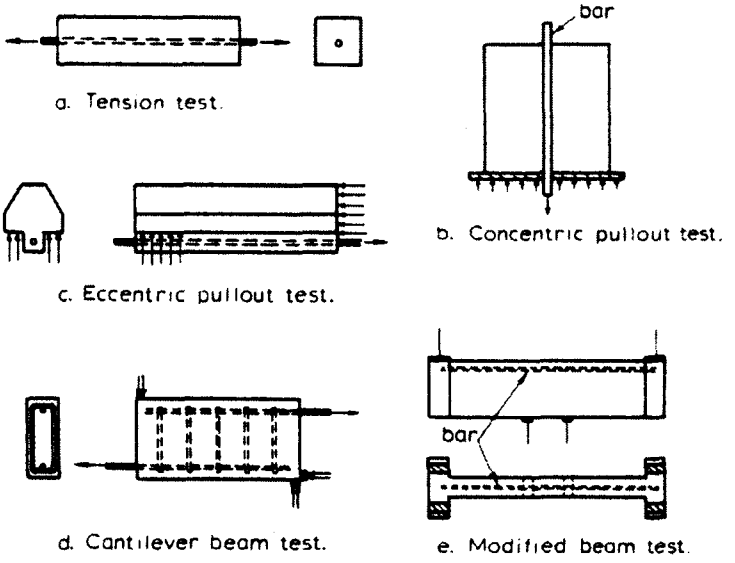

Figure 2.6 Types of tests for evaluating bond strength (Chapman and Shah, 1987)

2.1.4.1 Pull-out Test

The pull-out test (Figure 2.6b) is the oldest, simplest, least expensive, and least time consuming method for bond testing. In the pull-out test, the bar is embedded in a cylinder or prism of concrete. While the concrete is held by reaction pressure on the end using a bearing plate, the bar is pulled out from the same end. Since the bar is in tension and the concrete is in compression, differential strains will result in a relative slip. This test can provide a good comparison of the bond strength of reinforcing bars and the corresponding embedment lengths. However, it gives an upper value of the actual bond stress developed in a structural beam because of the longitudinal compression in concrete and the frictional restraint provided by the base plate. These would provide confinement against splitting of the concrete. It is noted that, in a reinforced concrete member, such as a beam, both the bar and the surrounding concrete are in tension; however, the concrete surrounding the bar is in compression in the pull-out test (ACI Committee 408 Report, 2003). Moreover, the shear stresses in a beam combine with the splitting stresses (from bar ribs) to give larger principal tension stresses, this cannot be simulated by pull-out test (Ferguson, Turpin, and Thompson, 1954).

2.1.4.2 Tension Test

The tension test (Figure 2.6a) is conducted by subjecting embedded reinforcing bar in concrete prism or cylinder to tensile force at both ends, In this test, both bar and concrete are subjected to tensile loads. The tension test simulates the behavior of reinforced concrete members between two primary cracks (Mirza and Houde, 1979;

Kankam, 1997). The bond stress developed in this type of test may be called "Compatibility Bond" because it arises from the compatibility conditions. The equilibrium of the specimen is always satisfied, even after the bond has been completely destroyed.

2.1.4.3 Stub-Cantilever Beam Test

The stub-cantilever beam test (Figure 2.6d) was developed by Kemp, Brezny, and Unterspan (1968) to overcome some objections raised regarding the pull-out test. This type of test represents the bond situation existing between a flexural crack and the end of a simple beam; it produces the same type of strain gradient. The stub-cantilever beam test has the advantage of being smaller and cheaper than the beam test. It generally duplicates the stress state obtained in reinforced concrete members; the reinforcing steel and the surrounding concrete are simultaneously placed in tension. Moreover, in order to achieve the desired stress state, the compressive force must be located away from the reinforcing bar by a distance approximately equal to the embedded or bonded length of the bar within the concrete. However, the disadvantage of this type of bond test lies in the confining pressure exerted on the bar by the support reaction. Also, there is a greater length of concrete subjected to splitting for a given bar test length than will exist in the actual member, making the apparent bond strength too large (Clark and Johnson, 1983).

2.1.4.4 Beam Test

The beam test is considered more reliable than the pull-out test because it reflects

the influence of flexural cracks. However, it is more expensive and time consuming to undertake. Also, the interpretation of the beam test results is more difficult than those obtained from pull-out tests (Ferguson, Turpin, and Thompson, 1954). Mathey and Watstein (1961) modified the beam specimen for which the supported ends were "Hammer-Head" shaped, in order to avoid the support reaction effect on bond. ACI Committee 408 (1964) recommended this type of test for further research on bond in beams. The bond strength value observed depends on the type of bond test. Clark (1949) showed that results from pull-out tests and beam tests did not differ significantly. Ferguson, Turpin, and Thompson (1954) reported that bond strength obtained from eccentric pull-out tests (Figure 2.6c) were 10% higher than those obtained from beam tests. Test results from Mathey and Watstein (1961) indicated that the ultimate bond stress in the pull-out specimens agrees in general with the values obtained from beams with small reinforcing bars (No. 4) rather than large reinforcing bars (No. 8).

Two beam tests, i.e. beam anchorage specimen test and splice specimen test, are recognized by ACI Committee 408 (2003).

2.1.5 Requirements of Development Length

Instead of dealing with the bond stress directly, the design codes usually use the development length for the purposes of design. Orangun, Jirsa, and Breen (1975, 1977) proposed an expression for the average bond stress at failure based on a nonlinear regression analysis of test results of 62 beams:

$$\frac{u_c}{\sqrt{f_c'}} = 1.2 + 3\frac{c_{\min}}{d_b} + 50\frac{d_b}{l_d} \qquad [2.6]$$

where $c_{\min}$ = smaller of minimum concrete cover or 1/2 of the clear spacing between bars; l_d = development or splice length; d_b = bar diameter.

The bond strength of a bar confined by transverse reinforcement was represented by:

$$\frac{u_b}{\sqrt{f_c'}} = \frac{u_c}{\sqrt{f_c'}} + \frac{u_s}{\sqrt{f_c'}} = \left(1.2 + 3\frac{c_{\min}}{d_b} + 50\frac{d_b}{l_d}\right) + \left(\frac{A_{tr} f_{yt}}{500 s n d_b}\right) \qquad [2.7]$$

where A_{tr} is the area of transverse reinforcement normal to the plane of splitting through the anchored bars; s is the spacing of transverse reinforcement; f_{yt} is the nominal yield strength of the transverse reinforcement; and n is the number of bars developed or spliced at the same location.

In terms of total bond force, Equation [2.7] can be written as:

$$\frac{T_b}{\sqrt{f_c'}} = \frac{T_c}{\sqrt{f_c'}} + \frac{T_s}{\sqrt{f_c'}} = \frac{A_b f_s}{\sqrt{f_c'}} = \left(3\pi l_d \left(c_{\min} + 0.4 d_b\right) + 200 A_b\right) + \left(\frac{\pi l_d A_{tr} f_{yt}}{500 s n}\right) \qquad [2.8]$$

where A_b is the area of developed or spliced bar.

This equation served as the basis of the development length provisions in the ACI Code. Equation [2.8] was further simplified in the ACI Code by replacing $(c_{\min} + 0.4d_b)$ with $c = (c_{\min} + 0.5d_b)$ and solving for the ratio of the development length l_d to the bar diameter d_b:

$$\frac{l_d}{d_b} = \frac{\frac{f_y}{\sqrt{f_c'}} - 200}{12\left(\frac{c + K_{tr}}{d_b}\right)} \qquad [2.9]$$

where $K_{tr} = \frac{A_{tr} f_{yt}}{1500sn}$

At nominal capacity, $f_s = f_y$, and Equation [2.9] is further simplified by removing the 200 from the numerator and changing the constant multiplying the expression from 1/12 (=0.083) to 3/40 (0.075):

$$l_d = \left(\frac{3}{40}\frac{f_y}{\sqrt{f_c'}}\frac{1}{\left(\frac{c_b + K_{tr}}{d_b}\right)}\right) d_b \qquad [2.10]$$

To limit the probability of a pullout failure, ACI 318 (ACI 2005) requires that:

$$\frac{c_b + K_{tr}}{d_b} \leq 2.5 \qquad [2.11]$$

The effects of bar location, epoxy coating, reinforcement size, and lightweight concrete on bond are included by multiplying l_d by the factors Ψ_t, Ψ_e, Ψ_s, and λ.

where,

Ψ_t = reinforcement location factor = 1.0 for bottom bars condition
Ψ_e = coating factor = 1.0 for uncoated reinforcement
Ψ_s = reinforcement size factor = 1 for No. 7 (No. 22)] and larger bars; 0.8 for No. 6 (No. 19) and smaller bars
λ = lightweight aggregate concrete factor = 1.0 for normal weight concrete; =1.3 for lightweight concrete
c_b = spacing or cover dimension: the smallest of the side cover, the cover over the bar (measured to the center of the bar), or one-half the center-to-center spacing of the bars
K_{tr} = transverse reinforcement index = $\frac{A_{tr} f_{yt}}{1500sn}$; n is the number of bars being developed along the plane of splitting
f_y = nominal yield stress
f_c' = compressive strength of concrete
d_b = bar diameter

For the anchorage of a straight bar in an interior beam-column joint, Leon (1989) suggested a length of 28 bar diameters to insure that bond can maintain its efficiency during severe seismic loading. This would however require large joint dimensions, which is usually not economical. Therefore the ACI-ASCE Committee 352 (2002) as well as ACI Code (2005) suggest the following minimum anchorage length for beam bars passing through a beam-column joint:

$$l_d \geq 20 d_b \qquad [2.12]$$

2.2 History of Research on Bond of Prestressing Strands

2.2.1 Functions of Bond

For a post-tensioning member the prestressing force is transferred from the strands to the concrete through permanent end anchorages rather than through bond; therefore, there is no development length for a post-tensioned member (FHWA, 1998). A bond between the strand and surrounding concrete must exist if concrete is to be prestressed by the pre-tensioning method whereby the strands are tensioned before the concrete is poured and are released after the concrete has developed sufficient strength. The tension in the strands is transferred to the concrete entirely by bond.

The transferred bond is present from the ends of the prestressed member to the beginning of a region in which the strands tension becomes constant. The length over which this transfer is made is termed prestress *transfer length* (l_t), and depends mainly on the amount of prestress, surface condition of the strand, the strength of concrete, and the method of steel stress release, i.e., slow or fast (Hanson and Kaar, 1959). Three factors which contribute to bond are adhesion, friction, and mechanical interlock. In general the contribution of adhesion is little because it is broken after very small slips. While the mechanical interlock can be a significant factor of bond in the seven-wire tendon, friction is also considered to be the major contributor causing stress transfer from pre-tensioning strands to concrete due to the *Hoyer's effect*. As illustrated in Figure 2.7, on the release of the strands, the end of the strand swells as a result of the recovery of the lateral contraction and develops a wedge effect because the prestressing force must

diminish to zero at the end of strand. The swelling of the strand is only a few thousandths of a millimeter; the produced radial pressure on the concrete may be as high as 11 ksi (Leonhardt, 1964). The confinement is therefore quite considerable and gives rise to large friction forces if sliding movement occurs.

Mechanical interlocking results from the helical winding shape of the seven-wire strands. However, the importance of this contribution has received opposing viewpoints between researchers (Stocker and Sozen, 1971; Russell, 1992; den Uijl, 1998). Unlike reinforcing bars, when a strand is pulled out of concrete, it tends to move helically along the path formed by the surrounding concrete. If constraint against rotation is present along the path, then concrete and the outside wires stay intimate, which in turn provides mechanical interlocking. Pullout tests conducted by Stocker and Sozen showed that no significant difference exists in the bond of strands with and without twist restraint. This observation leads to discounting the contribution of mechanical interlocking to bond in the current ACI and AASHTO codes. However, Russell pointed out that the low mechanical interlocking observed by Stocker and Sozen can be attributed to their test setup. He further suggested that the Hoyer's effect in the end zone can offer sufficient resistance against twisting by friction, and mechanical interlocking should be the largest contributor to flexural bond.

The prestressing strands in the tension zone will further develop bond stresses as a direct consequence of flexural action, which in turn lead to increase of strand stress. If cracks occur, the bond between strand and concrete in the flexural region plays an important role in governing the subsequent performance of the member. This bond is

referred as flexural bond. Opposite to the transfer bond, the stress increase in the strand due to flexural loading results in a contraction of the strand, thereby reducing the frictional bond resistance. Following loss of frictional resistance, mechanical interlock remains the only factor which can contribute to bond between concrete and strand. The *flexural bond length* (l_f) is the length needed beyond the transfer length to achieve bonding between the prestressing strand and the concrete to attain the stress in the strand at the ultimate load of the member; the transfer length l_t added to the flexural bond length l_f leads to a value called *development length* l_d (FHWA, 1998; Naaman, 2004).

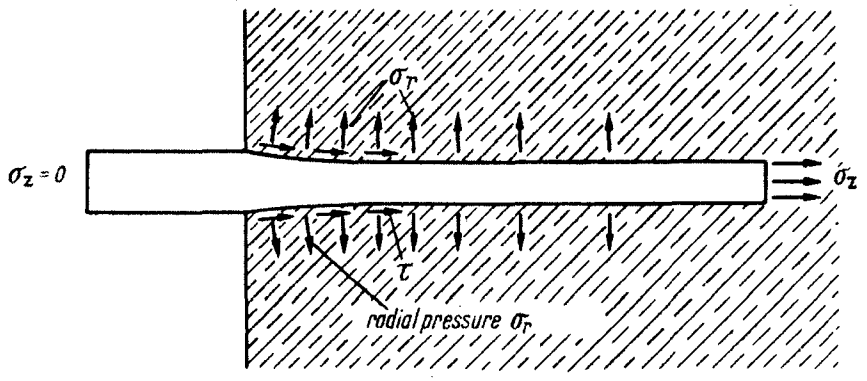

Figure 2.7 The Hoyer's effect in a released pre-tensioned strand (Leonhardt, 1964)

2.2.2 Requirements of Development Length

Based on test results by Kaar, LaFraugh, and Mass (1963) for transfer length, and Hanson and Kaar (1959) for flexural bond length, the ACI and AASHTO recommend an empirical equation for development length l_d, as follows:

$$l_d = l_t + l_f = \left(\frac{f_{pe}}{3}\right) d_b + \left(f_{ps} - f_{pe}\right) d_b = \left(f_{ps} - \frac{2}{3} f_{pe}\right) d_b \qquad [2.13]$$

where f_{pe} is the effective stress in prestressing steel after losses; d_b is the nominal diameter of prestressing strand; f_{ps} is the nominal strength of prestressing steel. The above equation is schematically illustrated in Figure 2.8 For a Grade 270 strand, f_{ps}=270 ksi, and assuming the effective stress f_{pe} is 150 ksi, then:

$$l_d = l_t + l_f = \left(\frac{150}{3}\right) d_b + (270 - 150) d_b = 50 d_b + 120 d_b = 170 d_b \qquad [2.14]$$

It is seen that the transfer length is about $50\,d_b$ and the flexural bond length is $120\,d_b$. This indicates a lower bond strength along the flexural bond length than along the transfer length, which can be attributed to the loss of frictional bond in the flexural bond length (den Uijl, 1998). The Federal Highway Administration (FHWA) proposed a new equation for development length l_d based on FHWA full-size beam data and available new research results:

$$l_d = l_t + l_f = \left(\frac{4 f_{pt} d}{f_c'} - 5\right) + \left(\frac{6.4\left(f_{ps} - f_{pe}\right) d}{f_c'} + 15\right) \qquad [2.15]$$

where f_{pt} is the stress in prestressing strand prior to transfer of prestress. Note this new equation accounts for the influence of concrete strength.

Russell and Burns (1996) conducted a series of beam tests and concluded that the Code specified the transfer length is not conservative. They suggested a transfer length of $\left(\frac{f_{pe}}{2}\right)d_b$.

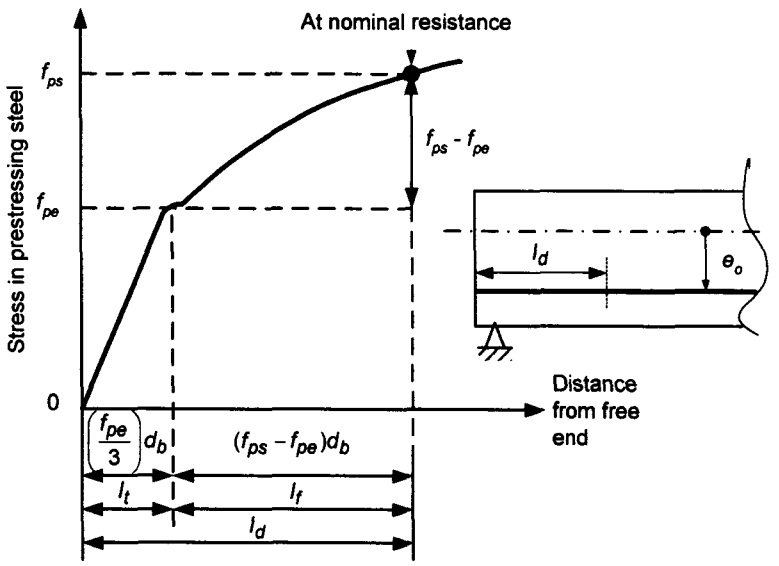

Figure 2.8 Codes assumed variation of steel stress with distance from free end for pretensioned strands (Naaman, 2004)

2.3 Parameters Affecting Bond Strength

The parameters affecting bond strength in reinforced concrete (and prestressed concrete) are numerous and far from being fully understood; this is even more so for the case of fiber reinforced concrete. These parameters may be divided into four groups related to the structural characteristics, reinforcing steel properties, concrete properties, and the type of bond test:

1. Structural characteristics group: This group includes: concrete cover and steel spacing, the embedment (anchorage) and splice length of the steel, amount and position of transverse steel, steel casting position, noncontact lap splices,

2. Reinforcing steel properties group: This group includes: steel size, steel stress and yield strength, bar rib geometry, and steel surface condition (cleanliness and epoxy coatings).

3. Concrete properties group: This group includes: concrete compressive strength, aggregate type and quantity, tensile strength and fracture energy, lightweight concrete, concrete slump and workability admixtures, mineral admixtures, fiber reinforcement, consolidation (vibration), and direction of concrete casting.

4. Type of bond test group: This group includes: method of testing, rate of loading, strain (or stress range) direction of loading, confining pressure, and modes of bond failure.

Brief discussions are given below for the parameters related to this study and the detailed discussion can be found elsewhere (ACI Committee 408, 2003):

- Tensile strength and fracture energy: When transverse steel is absent, thus no confinement is provided, the bond failure usually exhibits splitting of concrete. The peak bond strength depends on both the tensile capacity and fracture energy G_f of

concrete. Concrete having higher fracture energies provide improved bond capacities, even if the concrete has similar tensile strengths. This is particularly relevant when fibers are used.

- Transverse reinforcement: Transverse steel serves as confinement by means of limiting the progression of splitting cracks and, thus, increasing the bond force required to cause failure. Bond failure mode is able to be converted from a splitting failure to a pullout type failure by increasing transverse reinforcement amount. However, additional transverse reinforcement, above that needed to cause the transition from splitting to pullout, becomes progressively less effective, eventually providing no increase in bond strength (Orangun, Jirsa, and Breen, 1977). It has been observed that, transverse reinforcement rarely yields during bond failure (Maeda, Otani, and Aoyama, 1991; Sakurada, Morohashi, and Tanaka, 1993; Azizinamini, Chisala, and Ghosh, 1995). As a result, the yield strength of the transverse reinforcement f_{yt} does not play a role in the steel contribution to bond force (ACI Committee 408, 2003).

- Reinforcing bar size: The influences of reinforcing bar size on bond strength can be summarized as follows: (1) While a larger size bar requires a larger force to cause either a splitting or pullout failure, the bond forces at failure, however, increase more slowly than the bar area. This indicates that a longer embedment length is needed for a larger bar to fully develop a given bar stress. In this regard, it is desirable to use larger number of smaller bars rather than a smaller number of larger bars; this is true

until bar spacing is reduced to the point that bond strength is decreased; (2) Larger size bar tends to mobilize higher transverse reinforcement confining effect, which in turn enhances bond strength. This is because as a larger bar slips, higher strains and, thus, higher stresses, are mobilized in the transverse reinforcement, providing better confinement.

- Reinforcing bar rib geometry: It has been observed that bond strength could be enhanced through the use of high-relative-rib-area bars (defined as $0.10 \le R_r \approx \frac{h_r}{s_r} \le 0.14$; where h_r is the average height of bar ribs and s_r is the average spacing of bar ribs). Note that conventionally deformed reinforcing bars have relative rib areas of 0.06 to 0.085 (ACI Committee 408, 2001). Research has shown that, compared with conventional deformed bars, the increase in bond strength was as high as 25% when a high rib area bar was used in either pull-out type or beam type specimens (Darwin and Graham, 1993; Hamad, 1995; Zuo and Darwin, 1997).

- Concrete compressive strength: Traditionally, such as ACI 318 and AASHTO, the effect of concrete influence on bond strength is represented using the square root of the compressive strength $\sqrt{f_c'}$. However, investigations conducted by Darwin et al. (Darwin, Tholen, Idun, and Zuo, 1996; Zuo and Darwin, 1998; Zuo and Darwin, 2000) on a large international database show that a best fit with existing data (compressive strength from 3000 psi to 16,000 psi) was obtained using $f_c'^{1/4}$ to represent the effect of concrete compressive strength on development and splice

strength. For bars confined by transverse reinforcement, they found $f_c'^{3/4}$ is more suitable to represent the influence of compressive strength on bond strength. Based on these observations, ACI Committee 408 (2003) recommends the following equation for development length of reinforcing bars:

$$l_d = \left(\frac{\frac{f_y}{f_c'^{1/4}} - 1970\omega}{62\left(\frac{c\omega + K_{tr}}{d_b}\right)} \right) d_b \qquad [2.16]$$

where K_{tr} = transverse reinforcement index = $\left(\frac{0.5 t_d A_{tr}}{sn}\right) f_c'^{1/2}$, $t_d = 0.78 d_b + 0.22$, ω is a coefficient related to concrete cover and bar spacing.

It is noted that both the $f_c'^{1/4}$ and $f_c'^{3/4}$ effects have been accounted for in Eq. [2.16] (Note: $f_c'^{1/2} = f_c'^{3/4} / f_c'^{1/4}$). Also, the influence of transverse reinforcement yield strength (f_{yt}) was removed.

Generally, as concrete compressive strength increases, bond strength increases at a progressively slower rate, while the failure mode becomes more ductile.

2.4 Bond in Fiber Reinforced Cementitious Composite Systems

In general, adding fibers into concrete is able to increase the post-cracking resistance

of concrete. Fibers bridge across cracks and allow some tensile stress to be transferred; as a consequence, fiber reinforced concrete provides higher fracture energy and higher confinement, which in turn enhance the bond strength of reinforcement.

2.4.1 Fiber-Matrix Interaction

Two types of bond between fiber and matrix are identified, depending on type of stress transferred across the interface, namely, tensile bond and shear bond (Swamy, 1975). The tensile bond resists displacement caused by forces acting perpendicular to the interface. The shear bond controls the transfer of stresses parallel to the longitudinal axis of the fiber.

In an uncracked composite, the shear bond transfers stresses from the matrix back into the reinforcement. When the matrix cracks and the load is carried by the fibers bridging the crack, the shear bond enables the load to be transferred back into the uncracked parts of the matrix. Shear bond also resists the pull-out of the fibers from the matrix and is, therefore, one of the main factors influencing the mode of failure of a composite.

In FRC composites, the major role played by the fibers occurs in the post-cracking mode, in which the fibers bridge across the cracked matrix (Shah and Rangan, 1971). The fibers may increase the strength of the composite over that of the matrix. However, more importantly, they increase the toughness of the composite by the debonding and pull-out process of the fibers bridging the cracks. As cracking occurs in the brittle matrix, the load

is transferred to the fiber; if the load bearing capacity of the fibers is greater than the load on the composite at first crack, then failure is prevented and redistribution of the load between the matrix and the fibers occurs. Additional loading will lead to additional cracks, until the matrix is divided into a number of segments, separated by cracks. This process is known as multiple cracking. When there is no further cracking, any additional tensile load will cause pull-out failure of the fibers.

2.4.2 Steel-Concrete Interaction

The bond strength between reinforcing steel and concrete depends on the properties of the concrete. In a typical bond test, failure occurs by concrete splitting along the steel length before full anchorage strength of the steel is reached. When deformed bars are used, the breakdown of bond may occur by bursting of the concrete under very high local stresses in the vicinity of bar ribs. The bond strength of steel in concrete drops rapidly when tensile cracks develop, unless lateral reinforcement is provided to restrain these cracks. The load at which a splitting failure develops is mainly a function of the tensile strength of the concrete. The tensile strength of concrete may be substantially increased by addition of fibers. Thus, it is believed that the addition of fibers to concrete will enhance the bond behavior of reinforcing bars because the fibers will bridge the concrete tensile cracks.

2.4.3 Literature Review of Bond in FRC Composites

Swamy and Al-Noori (1974) conducted pull-out test ($6\times6\times20$ in.) on FRC to study

the effect of fibers on the bond strength of reinforcing bars. Five bar sizes with different bar diameters were used. The embedment length was 4 in. for 0.4 and 0.5 in. bar diameters and 6 in. for the 0.8 and 1.0 in. bar diameters. The fiber weight fraction was 7% of (2×0.02 in.) straight steel fibers (approximately 2% by volume), and 3.5% of (1×0.015 in.) deformed steel fiber (approximately 1% by volume). Test results showed that bars embedded in FRC have bond strength 35~45% greater than embedded in concrete. The bond stress-slip curves show that, for the same bond strength, the slip in plain concrete was greater than that in FRC.

The bond between deformed reinforcing bars and FRC under monotonic and reversed cyclic loading was examined by Spencer, Panda, and Mindess (1982). The tension test specimens (Section 2.1.4.2) with the dimension of $40\times20\times10$ in. reinforced with No. 8 bar were used. Two types of steel fibers (0.5×0.022 in. and 1×0.022 in.) with two fiber volume friction (0.75% and 1.5%) were used. The steel strain along the reinforcing bars was measured by Dorr's technique (1978). The results indicated that fiber addition increased the load level at which visible cracking first appeared, and tended to make crack growth more gradual. However, changing fiber volume fractions had no significant effect on the strain distribution in the reinforcing bar, bond stress, or bar slippage. There was some evidence that fibers improved the bond effectiveness, but the data were not conclusive.

Yerex, Wenzel, and Davies (1985) conducted experimental tests to determine the effects of polypropylene fibers on the bond strength of reinforcing bars. Pull-out specimens reinforced by one single bar (No. 4 or No. 6) with two embedment lengths (6.0

and 30.0 in.) were tested. Two fiber lengths (2.25 and 3.5 in.) and four fiber contents (from 0 to $0.086 lb/ft^3$) were used. It was observed that the addition of polypropylene fibers to the concrete does not affect the bond strength. The results did not indicate improved performance in bond strength for either longer length fibers, or higher fiber content.

The bond strength of reinforcing bar in FRC was also studied by Rostásy and Hartwich (1988). They conducted pull-out tests with short embedment lengths equal to 5 times the bar diameter of 0.65 in. Two types of steel fibers were used, namely 1.0 in. straight and 1.2 in. hooked fibers. The fiber volume fractions were varied from 0% to 2.25%. The tests showed that fiber content does not have a significant influence on bond strength of reinforcing bars embedded in FRC.

More experimental test results on the bond of reinforcing bars in FRC are reported by Ezeldin and Balaguru (1989). The main variables were fiber length and fiber content. A modified pull-out test was used in which the concrete surrounding the bar was in uniform tension. The embedment lengths were varied from 2.0 to 7.0 in. depending on the bar diameter used, which were either No. 3 or No. 8 bars. No significant effect on the maximum bond stress was observed. However, the post-cracking behavior was improved by increasing the fiber volume fraction.

Hamza and Naaman (1992, 1996), conducted a series of stub-cantilever beam tests to investigate the bond behavior with various reinforcing bars sizes (No. 6, No. 8, and No. 10), as well as with various embedment length (No. 8 bar with 4, 8, 12, and 16 in.

embedded length); these lengths corresponding to about 25% to 100% the development length given by ACI 318-89 for reinforcing bars embedded in conventional concrete) in the slurry-infiltrated fiber concrete (SIFCON) using 5% volume fraction of hooked steel fiber (Dramix: 2.0 in. long, 0.5 mm diameter, tensile strength = 170 ksi, aspect ratio = 100). They concluded that SIFCON leads to a significant increase in the bond strength of deformed reinforcing bars. Specimen with 50% to 100% code-specified embedded length failed by bar yielding instead of bar pullout. This indicated that SIFCON is able to have only 50% the development length as that of conventional reinforced concrete. Specimen with 25% of the ACI development length exhibited pullout type of failure. Average peak bond stresses ranging from 2000 to 4000 psi were observed in SIFCON specimens. Everything else being equal (Bar embedment length = 4 in., No. 8 bar, concrete cover = 1.5 in., and concrete strength = 6200 psi), it was observed that SIFCON specimen had an increase in the average bond stress of 150% and 40% in comparing to plain and heavily confined concrete (about 2% transverse reinforcement by volume), respectively. The maximum bond stresses recorded for SIFCON, confined concrete, and plain concrete were 3.44 ksi, 2.44 ksi, and 1.35 ksi, respectively. Multiple fine cracks were observed in SIFCON specimens while plain concrete specimens showed a few large cracks. It was also found that average bond stress increased with an increase in the compressive strength of SIFCON and concrete cover, and decreased with an increase in the bar diameter.

Harajli (1994) analyzed the previous test results and concluded that the presence of steel fibers improves the ductility of splitting bond failure. The development/splice

strengths vary linearly with fiber reinforcing index $V_f L / d_f$.

Hota and Naaman (1995, 1997) conducted pull-out tests using a specially design setup which can easily perform different types of loading (monotonic, unidirectional cyclic, and fully reversed cyclic loadings). They tested SIFCON (V_f =9.7%), FRC (V_f =2%), confined concrete without fibers, and plain concrete specimens with an embedded length of 4 in. (No. 8 bar) The fiber used was steel hooked fiber with a length 30 mm and 0.5 mm diameter. It was observed that SIFCON specimens failed by frictional pullout, while the plain concrete and FRC failed by splitting even though 2% steel fiber was added in the FRC specimens. The confined concrete specimens failed by pullout of a cone-shaped chunk of concrete attached to the reinforcing bar. It was also observed that the use of fiber can slow down degradation of the specimen's bond strength by delaying the onset of cracks and slowing down the opening of existing cracks, especially for the SIFCON specimens.

Balaguru et al. (1996) summarized some test results of reinforcing steel embedded in steel fiber reinforced concrete and concluded that the main contribution of steel fiber to concrete subjected to reversed cyclic loading is in the enhancement of ductility. The formation of cracks is slower and their propagation and growth are much more stable than in normal concrete, thus delaying the deterioration of bond.

Parra-Montesinos (2000) tested a RCS exterior beam-column using ECC (Engineered Cement Composite) material reinforced with 1.5% volume fraction of

polyethylene (Spectra) fibers (1 in. long). The bond behavior of longitudinal column bars was observed and no bond deterioration was found. This excellent bond behavior occurred even though no transverse reinforcement was placed in the beam-column joint.

Fischer and Li (2002) conducted a tension test on ECC prisms with the dimension of $500\times175\times175$ mm and embedded with No. 8 bar. 1.5% volume fraction polyethylene (Spectra) fibers were used. Due to the pseudo strain-hardening behavior of the ECC material, the matrix and steel deformed compatibly in both postcracking and postyielding process. This resulted in more uniform strain distribution in the reinforcement and matrix, thus reducing the interfacial bond stress. They concluded that the bond strength in R/ECC members is not as significant as in RC members.

Harajli and Mabsout (2002), proposed a development length equation that accounts for the effect of steel fiber with a similar form with ACI Committee 408 equation (Equation [2.16]):

$$l_d = \left(\frac{\frac{f_y}{(f_c')^{1/4}} - 2100}{68\left(\frac{c + K_{tr}}{d_b}\right)} \right) d_b \qquad [2.17]$$

The expression K_{tr} takes into account the effect of both transverse reinforcement and fiber reinforcement:

$$K_{tr} = 0.52\frac{t_r t_d A_{tr}}{sn}(f_c')^{1/2} + 0.16\left(\frac{V_f L}{d_f}\right)c(f_c')^{1/4} \qquad [2.18]$$

where $t_r = 9.6R_r + 0.28$ and $t_d = 0.78d_b + 0.22$ are parameters account for the geometry of the reinforcing bar; R_r is the relative rib area of the reinforcing bar (ratio of projected rib area normal to the bar axis to the product of nominal bar perimeter and center-to-center spacing of ribs). It is noted that both the $f_c'^{1/4}$ and $f_c'^{3/4}$ effects have been accounted for in Eqs. [2.17] and [2.18] and the influence of transverse reinforcement yield strength (f_{yt}) was removed.

Harajli et al. (Harajli, Hamad, and Karam, 2002) proposed a local bond stress-slip relation for steel FRC, as shown in Figure 2.9. The ascending portion of the monotonic envelope (pullout bond failure) is given by:

$$\tau = \tau_{\max}\left(\frac{s}{s_1}\right)^{0.3} \qquad \text{if } 0 \le s \le s_1 \qquad [2.19]$$

where $\tau_{\max}(\text{MPa}) = 2.57\sqrt{f_c'(\text{MPa})}$; $s_1 = 0.15c_0$; $s_2 = 0.35c_0$; $s_3 = c_0$; c_0 is the clear distance between the ribs; $\tau_f = 0.35\tau_{\max}$. In the absence of information about the bar geometry, $s_1 = 1.5$ mm; $s_2 = 3.5$ mm; $s_3 = 10$ mm. For the splitting bond case, the peak bond strength is expressed as:

$$\tau_{splitting} = c_f\left(0.75\sqrt{f_c'}\left(c/d_b\right)^{2/3}\right) \le \tau_{\max} \qquad [2.20]$$

where $c_f = 1.0$ for $V_f L/d_f \le 0.25$; $c_f = 1 + 0.34\sqrt{V_f L/d_f - 0.25}$ for $V_f L/d_f > 0.25$.

$$s_{splitting} = s_1 e^{1.8\left[\left(\tau_{splitting}/\tau_{\max}\right)^2 - 1\right]} \qquad [2.21]$$

$$\tau_{ps} = \left[0.33 + 0.37\left(c/d_b\right)\left(V_f L/d_f\right)\right]\sqrt{f_c'} \leq \tau_{splitting} \qquad [2.22]$$

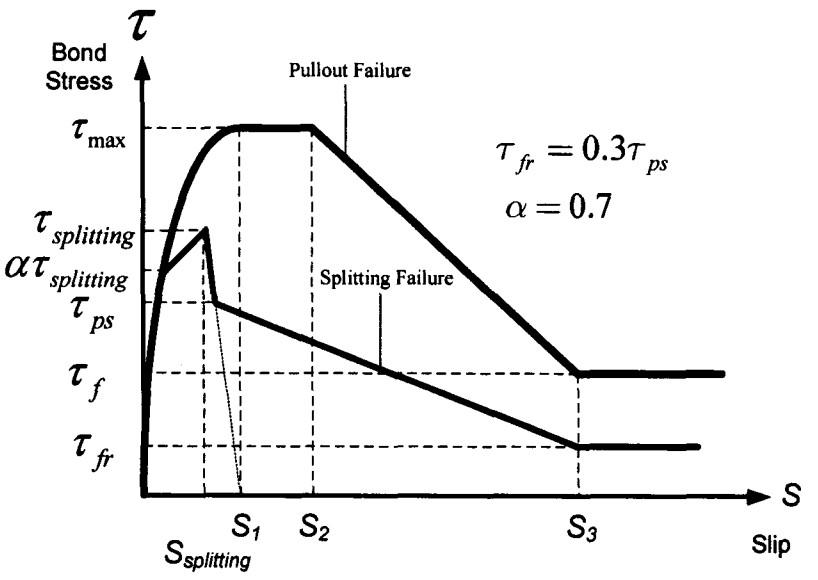

Figure 2.9 Local bond stress-slip relation of reinforcing bar embedded in SFRC (Harajli et al., 2002)

2.5 High Performance Fiber Reinforced Cementitious Composites (HPFRCCs)

In recent years, considerable attention has been paid to high performance fiber reinforced cementitious composites (HPFRCCs hereafter), which are characterized by a tensile stress-strain response that exhibits strain hardening accompanied by multiple cracking (Naaman, 2003). Figure 2.10 illustrates the typical tensile stress-strain response of a conventional FRC composite and that of an HPFRC composite, respectively. It is noted that the two responses have similar initial ascending portion (0A, which is the only portion that the conventional concrete has) and final descending portion (BC). A notable

difference is that HPFRCC shows an additional portion (AB), along which the stress keeps increasing up to relatively high strains.

Moreover, instead of a localized crack, multiple cracking develops throughout the composite. This unique portion for HPFRCCs describes their "strain-hardening" behavior. Thus large incremental strains can be involved as well as large energy-dissipation capacity (Naaman, 2000). Such performance, unlike SIFCON, can be achieved today by using less than 2% fibers by volume. Since generally, bond deterioration is the consequence of the brittle nature of concrete, and in view of the superior tensile response of HPFRCCs, they are very likely to develop superior bond behavior in RC and PC structures; particularly in preventing splitting cracks from opening should they occur.

Several types of fiber exhibit excellent high performance behavior when used in cementitious composites and two examples are given herein (Sujivorakul, 2002; Chandrangsu, 2003). The first one is Spectra fiber (one form of polyethylene), which has a very high tensile strength. Spectra fibers are referred to ultra high modulus PE (UHMPE) which are produced with a very high molecular orientation by gel spinning and subsequent drawing to give fibers that have up to 85% crystallinity and with 95% parallel orientation. Their polymer chains are bound together at various points by mechanical crosslinking. This produces strong inter-chain forces in the resulting filaments that can significantly increase the tensile strength of the fibers. The filaments emerge with an unusually high degree of orientation relative to each other, further enhancing strength (Laine, 2002)

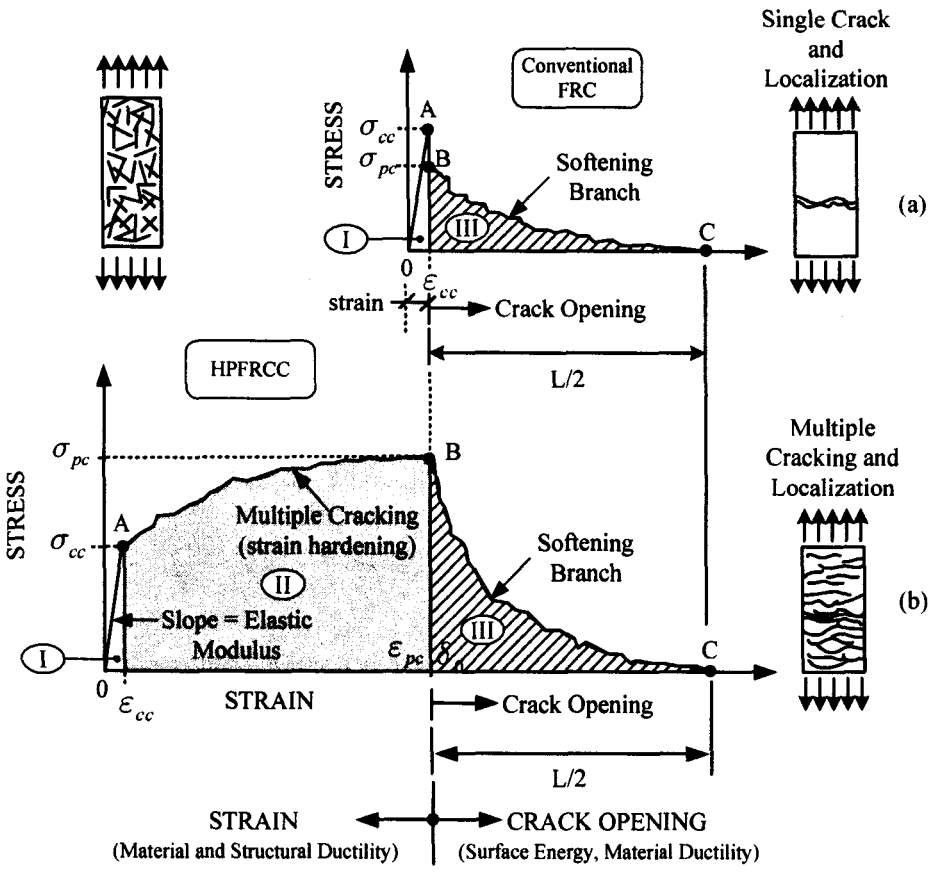

Figure 2.10 Stress-strain responses of conventional FRC and HPFRCC (Naaman, 2003)

The second high performance fiber is the Torex fiber, which is a twisted polygonal steel fiber developed at the University of Michigan. This fiber has an optimized geometry that offers a ratio of lateral surface area to cross sectional that is larger than that of round fiber, and is twisted to improve mechanical bond. An increase in the lateral surface area to cross sectional ratio of a fiber leads to a direct increase in the contributions of the adhesive and frictional components of bond. Moreover, the twisted ribs create a very effective mechanical bond. The most surprising behavior of Torex fiber is that a high level of pullout load is maintained up to very large slips, about 70 to 90% of the

embedded length (Sujivorakul, 2002). Figure 2.11 shows the microscopic view of twisted polygonal fibers having triangular and square sections. Extensive research has been conducted to investigate the bond behavior of various Torex fibers (Sujivorakul, 2002) and the results are summarized in Tables 2.1 and 2.2.

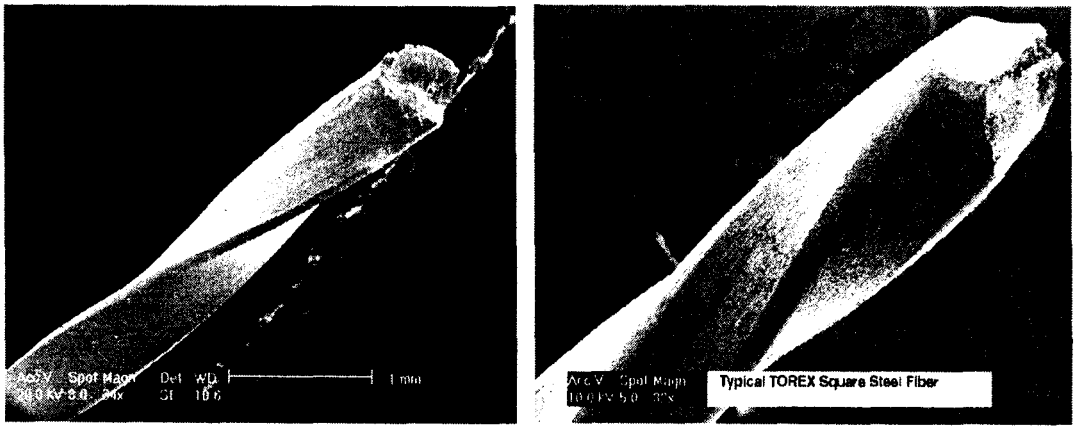

Figure 2.11 Typical examples of steel twisted triangular and square steel fibers (Torex)

Table 2.1 Properties of Torex fibers and corresponding single fiber pullout performance

A	B	C	D	E	F	G	H	I	J	K	L	
Triangular	0.327	2065	13.93	3.2/24	12.7	13	Mix-I	-	9.8	0	N	[b]
				4.2/18					12.8		Y	
				6.3/12					19.3		Y	
				12.7/6					38.8		Y	
				6.3/12		44	Mix-III		19.3		Y	[c]
	0.5	2412	10.29	3.6/21					7.3		N	[d]
				4.2/18					8.5		N	
				5.1/15					10.2		N	
				6.3/12					12.7		N	
				9.5/8					19.1		Y	
				12.7/6					25.4		Y	
				19.1/4					38.1		Y	
				38.1/2					76.2		Y	
				4.2/18		84	Mix-VI		8.5		Y	[e]
				6.3/12					12.7		Y	
				9.5/8					19.1		Y	
				12.7/6					25.4		Y	
				19.1/4					38.1		Y	
				38.1/2					76.2		Y	
				9.5/8		55	Mix-IV		19.1		Y	[f]
						20	Mix-V				N	

A	B	C	D	E	F	G	H	I	J	K	L	
Triangular	0.5	2412	10.29	9.5/8	12.7	84	Mix-VI	-	19.1	15	Y	[g]
										30	Y	
										45	Y	
										60	Y	
					6.35					0	Y	[h]
					19						Y	[i]
					25.4						N	
					6.35	68	Mix-VIII				Y	[j]
					12.7						Y	
					19						Y	
					25.4						Y	
		1998		6.35/12	6.35	84	Mix-VI		12.7		Y	[k]
					12.7						Y	
		965			6.35						Y	[l]
					12.7						N	
		1998		9.5/8	12.7	44	Mix-III		19.1		Y	
		965									Y	
	0.3	2618	17.15	4.2/18	5				8.5		Y	[m]
					8.9						Y	
					12.7						Y	
					25.4						Y	

Table 2.2 Properties of Torex fibers and corresponding single fiber pullout performance

A	B	C	D	E	F	G	H	I	J	K	L	
Triangular	0.3	2618	17.15	4.2/18	5	68	Mix-VIII	-	8.5	0	Y	[n]
					8.9						Y	
					12.7						N	
						84	Mix-VI				N	
						20	Mix-V				Y	
						55	Mix-IV				Y	[f]
					5	68	Mix-VIII			15	Y	[g]
										30	Y	
										45	Y	
										60	Y	
Square	1.0×1.0 mm; de = 1.128 mm	2065	4	12.7/8	25.4	84	Mix-VI	1.0	-	0	Y	[o]
				16.9/6							Y	
				25.4/4							Y	
				102/1							Y	
				12.7/8	12.7						Y	
	0.7×0.7 mm; de = 0.79 mm		5.71	8.5/12							Y	[p]
				12.7/8							Y	
				25.4/4							Y	
				8.5/12		44	Mix-III				N	
				12.7/8							N	
				25.4/4							N	

A	B	C	D	E	F	G	H	I	J	K	L	
Square	0.7×0.7 mm	2065	5.71	9.5/8	12.7	55	Mix-IV	1.0	-	0	Y	
						13	Mix-I				N	
Rectangular	0.5	2412	9.16	6.3/16.1		84	Mix-VI	1.39			Y	[q]
			9.54					1.94			Y	
			10.45					3.03			Y	
			9.16			44	Mix-III	1.39			N	
			9.54					1.94			Y	
			10.45					3.03			Y	
	0.3	2618	15.41					1.52			Y	[q]
			15.94					2.01			Y	
			17.54					3.13			Y	

Note:

A: Cross-Sectional Shape

B: Diameter, d_e (mm)

C: Tensile Strength (MPa)

D: FIER per unit length

E: Pitch / no. of twist (mm) / (ribs/in.)

F: Embedded length (mm)

G: Matrix Compressive strength, f_c' (MPa)

H: Interfacial Property[a]

I: Width to thickness ratio (rectangular section)

J: Pitch/d_e (triangular)

K: Initial inclination (degree)

L: Pseudo Plastic Behavior

[a] Mix-III, Mix-V, Nix-VI, Mix-VII, Mix-VIII: Ottawa Silica Sand ASTM 50-70;
Mix-IV: Sand ASTM 270;
Mix-I, Mix-II: Flint Sand ASTM 30-70

[b] Maximum Pullout Load (in terms of pitch) 3.2mm > 4.2mm > 6.3mm > 12.7mm

[c] Maximum Pullout Load (in terms of Sand) Ottawa Silica Sand ASTM 50-70 > Flint Sand ASTM 30-70

[d] Maximum Pullout Load (in terms of pitch) 3.6mm $\approx$ 4.2mm $\approx$ 5.1mm $\approx$ 6.3mm $\approx$ 9.5mm > 12.7mm > 19.1mm > 38.1mm

[e] Maximum Pullout Load (in terms of pitch) 4.2mm $\approx$ 6.3mm >9.5mm $\approx$ 12.7mm > 19.1mm > 38.1mm

[f] All else being equal, Mix-IV (f_c' = 55MPa) with Sand ASTM 270 has lower maximum pullout load than the Mix-III (f_c' = 44MPa) with Ottawa Silica Sand ASTM 50-70

[g] $\theta > 60^\circ$, maximum pullout load has significantly reduction

[h] Maximum Pullout Load (in terms of embedded length) 25.4mm $\approx$ 19mm >12.7mm > 6.35mm

[i] Fiber fails when L_e=25.4mm

[j] Maximum Pullout Load (in terms of embedded length) 25.4mm >19mm >12.7mm > 6.35mm

[k] Maximum Pullout Load (in terms of embedded length) 12.7mm > 6.35mm

[l] Maximum Pullout Load (in terms of embedded length) 12.7mm > 6.35mm; however, fiber fails in tension when L_e=12.7mm

[m] Maximum Pullout Load (in terms of embedded length) 25.4mm > 12.7mm > 8.9mm > 5mm

[n] Maximum Pullout Load (in terms of embedded length) 12.7mm > 8.9mm > 5mm

[o] Maximum Pullout Load (in terms of pitch) 12.7mm > 16.9mm > 25.4mm > 102mm

[p] The smaller pitch, the higher maximum pullout load

[q] The smaller width-to-thickness ratio, the higher maximum pullout load

CHAPTER 3

FIRST PHASE EXPERIMENTAL PROGRAM

3.1 General

The first phase experimental work (see Figures 1.8 and 1.9) was conducted with specimens using both reinforcing bars (No. 4, No. 5, and No. 8) and prestressing strands (0.5 inch diameter) with various fiber reinforced cement composites. The first phase bond tests consisted of pull-out type bond stress-slip tests with loading types including monotonic, unidirectional cyclic (both force and displacement controlled) and fully reversed cyclic (both force and displacement controlled) loadings.

3.2 Materials

3.2.1 Cement-Based Matrices and Fibers

The compositions of the matrices and average compressive strength (obtained from 4×8 in. cylinders) are listed in Table 3.1. Properties of fibers employed in this study are summarized in Table 3.2. Figure 3.1 shows the fibers used in this study.

Spectra fiber (polyethylene, PE) has a very high tensile strength but relatively weak bond strength. Spectra fiber is referred to ultra high modulus PE (UHMPE), which is

produced with a very high molecular orientation by gel spinning and subsequent drawing to give fibers that have up to 85% crystallinity and with 95% parallel orientation. The polymer chains of UHMPE are bound together at various points by mechanical crosslinking. This produces strong inter-chain forces in the resulting filaments that can significantly increase the tensile strength. The filaments emerge with an unusually high degree of orientation relative to each other, which further enhancing strength (Laine, 2002). Although the bond strength of Spectra fiber is relatively weak, it exhibits a slip-hardening behavior during fiber pullout, which is caused by an "abrasion effect" (Li, Wu, and Chan, 1996). When a Spectra fiber is pulled out from cementitious matrix, the fiber surface is damaged and stripped into small fibrils due to abrasion effect. These small fibrils jam the tunnel surrounding the fiber, which in turn prevents the fiber from being pulled out. This mechanism significantly increases the frictional bond between the Spectra fiber and cement matrix, which leads to a slip-hardening response.

PVA (polyvinyl alcohol) has a tensile strength about 1/2~1/3 that of Spectra fiber, but with a cost of 1/8 that of Spectra fiber. On the other hand, PVA has much stronger chemical bond between fiber/matrix interface because it can develop strong affinity to hydroxyl groups present in the neighboring hydrated cement (Li et al., 2001). However, the high bond strength and low tensile strength leads to a tendency of fiber rupture during opening of a matrix crack, rather than pullout. Therefore, an oiling agent is usually applied onto the fiber surface during the production process to reduce bond (Li et al., 2002), which is the case of PVA K-II listed in Table 3.2

It is well-known that fiber/matrix interface bond is a key issue to develop HPFRC

composites that exhibit multiple cracking and tensile strain-hardening behavior. In this regard, steel fibers have the advantage over other fibers in terms of ease to be deformed to improve their mechanical bond, as well as of high tensile strength and ductility. The mechanical bond of steel hooked fibers comes from the hooked ends, which contribute to bond strength through the work needed to straighten the fiber during pullout.

Torex fiber is a twisted polygonal steel fiber, which has an optimized geometry that offers a ratio of lateral surface area to cross sectional are larger than that of round fiber. An increase in this ratio of a fiber leads to a direct increase in the contributions from the adhesive and frictional components of bond. In addition, the twisted ribs create a very effective mechanical bond. Unlike conventional steel fibers, when pulled out from a cement matrix, Torex fibers can maintain a high level of resistance up to slips representing 70% to 90% of the embedded length. This unique bond behavior is due to the successive untwisting and locking of the fiber embedded portion in its tunnel of matrix during slip (Naaman, 1999). Microscopic view of two types of Torex fibers used in this study, with square and rectangular cross sections, are shown in Figure 3.1(c).

Single fiber pull-out tests were conducted for the two types of Torex fibers used in this investigation and Figure 3.2 (d) shows the single fiber pullout apparatus. As can be seen in Figures 3.2 (a) and 3.2 (b), both types of Torex fiber maintained significant bond resistances up to very large slips. In addition, some of the square Torex fibers exhibited a slip-hardening pullout response. The main reason for the superior pullout response exhibited by square fiber compared to rectangular fiber is that the untwisting torque strength increases with a decrease in aspect ratio of the fiber cross section, thereby giving

highest mechanical bond in the twisted fibers with square cross section (Sujivorakul, 2002). Figure 3.2 (c) shows the average pullout response curves for these two types of Torex fibers, where it can be seen that the square Torex fiber, in average, exhibited a higher bond resistance. The untwisted square Torex fiber after pulling out is highlighted in Figure 3.2 (e).

Results from direct tension tests on 1 by 2 in. (25 by 50 mm) cross section dog-bone shaped specimens (Figure 3.3(a)) yielded the typical tensile stress-strain curves for the FRCC materials used in this investigation shown in Figures 3.3(b) and 3.3(c). As can be seen, the specimen with 2.0% volume fraction of Torex fibers exhibited a tensile strain-hardening behavior up to approximately 0.6% strain with a peak strength close to 1.7 ksi (11.7 MPa), which in turn led to the formation of multiple cracks, as shown in Figure 3.3(d). The main reason for the larger tensile strength exhibited by the composite with square Torex fibers compared to that with rectangular fibers was the increase in the untwisting torque strength with a decrease in aspect ratio, as explained earlier. An accompanying curve in Figure 3.3(b) shows that, with same fiber volume fraction (2.0%), the composite with hooked steel fibers exhibited a tensile softening response at strains larger than 0.2%. However, the stress decay was gradual, and the FRCC composite maintained approximately 50% of the peak strength at a tensile strain of 1.0%. The Spectra FRCC composite exhibited a similar behavior compared to the FRCC with hooked steel fibers, but with a longer stress plateau, while the PVA 13 FRCC showed the lowest tensile strength and strain capacity.

Figure 3.3(c) gives tensile stress-strain curves for three FRCC composites (with

rectangular Torex, Helix, and PVA K-II fibers) with a 7.6 ksi average compressive strength. The Helix fiber (triangular twisted fiber) was made out of a relatively low strength stainless steel and less ribs per inch of length compared to the Torex fiber. Properties of both the Helix and PVA K-II fibers can be found in Table 3.2. It is seen that although the Helix fiber FRCC material showed a relatively high ductility, its peak tensile strength was lower than that of the FRCC containing rectangular Torex fibers. This is attributed to the shape and less number of twists of Helix fibers, as shown in Figure 3.1 (d), in which it can be seen that the shaping was not perfectly triangular and the rib was much less deep than the square and rectangular Torex fiber used in this study (Figure 3.1 (c)). Clearly, the use of a twisted fiber with appropriately tailored mechanical and geometrical properties is essential to ensure a strain-hardening behavior of the composite. The FRCC with PVA K-II fiber showed a lower strength and strain capacity compared to the FRCC with Helix fiber. It is worth mentioning that the cement-based matrix composition was the same for all FRCCs and not specifically tailored for PVA K-II fibers.

Tension test data from the FRCC materials with 1.0% fiber volume fraction were not available. However, it has been shown that a tensile softening response is expected in composites with 1.0% volume fraction of Spectra, PVA, or steel hooked fibers. A strain-hardening behavior, on the other hand, has been obtained in composites with 1.0% volume fraction of Torex fibers (Sujivorakul, 2002).

In addition to the matrix compressive strength, the deformation capacity of the FRCC materials under compression was determined by a compressometer that complied with ASTM C 469-94 (ASTM, 1994), and was composed of two rotation yokes and three

LVDTs (Figure 3.3 (e)). The compressometer was attached to the cylinder specimen to measure the average deformation in its middle region. This was done in order to avoid measurement errors due to deformations from the sulfur compound at the top and bottom of the cylinder. Two test specimens are presented in Figure 3.3 (f), in which it can be seen that the specimen with 1% rectangular Torex fiber sustained a substantially higher deformation capacity compared to the control specimen. Typical compressive stress-strain responses of the FRCC materials with 1% fiber volume fraction used in this study are shown in Figure 3.3 (g). It is seen that the strain at peak strength was approximately 0.003. It is also noted that over 50% of the compressive strength was maintained at 1% strain in the specimen with 1% rectangular Torex fiber. Note all tested specimens had mortar matrices and without coarse aggregates.

3.2.2 Reinforcing Bar and Prestressing Strand

Grade 60 No. 4 (diameter = 0.5 in.), No. 5 (diameter = 0.625 in.), and No. 8 (diameter = 1.0 in.) reinforcing bars with actual yield strength and tensile strength of 65 ksi and 105 ksi, respectively, were used in this study. The length for all bars was seventeen inches, with a five inch long threaded part at each end for attachment to the test setup through bolts. The rib spacing of the No. 4 bars was 9/32" and the rib height 1/32". The rib spacing of the No. 5 bars was 5/16" and the rib height was close to 1/32", while the rib spacing and height of the No. 8 bars were 5/8" and 1/16", respectively. The geometries of the reinforcing bars used in this study are shown in Figures 3.4 (a), 3.4(b), and 3.4(c).

The prestressing strands used in this study were uncoated seven-wire strands with a diameter of 0.5 in. (13 mm) and a nominal tensile strength of 270 ksi (1860 MPa). The length of the tested strand was 19.5 inches. No threading was needed since the strand could be attached to the test setup by strand chucks. It should be mentioned that a significant restraint against twisting was provided through the friction created between the loading apparatus and the strand chuck as the strand was loaded. The strands were used in "as-received" condition and had no surface rust, as shown in Figure 3.4(d).

3.3 Specimen Preparation and Mixing Procedure

The pull-out type specimens had a prismatic shape with dimensions $6\times6\times4$ in. ($150\times150\times100$ mm), as shown in Figure 3.5. The specimen molds were made out of Plexiglas and each mold was used to prepare three specimens (Figure 3.6). A total of six specimens were prepared for each set of specimens (for instance, No. 8 bar with 1% Spectra fiber, matrix compressive strength = 11 ksi).

The molds were lightly oiled before pouring of the FRCC materials and the reinforcing steel was pre-positioned. Except for water and, if needed, superplasticizer (High Range Water Reducing Admixture), all the ingredients were poured into the mixer and dry-mixed for about one minute. Then, water and part of superplasticizer were poured slowly into the mixer and the process continued for another 2-3 minutes. Finally, for the specimens reinforced with fibers, the fibers were added slowly while mixing continued. It was done in a sprinkling fashion in order to distribute the fibers thoroughly

throughout the mix and to ease any burden caused to the mixer, in particular for Spectra and PVA fibers. Steel fibers, such as Torex fiber and hooked fiber, generally require less effort in the mixing process. The whole process lasted about 10 minutes, and the remainder superplasticizer was added during the last five minutes of this process. The molds were then placed on a vibration table and a proper vibration frequency was used to enhance the compactness. The molds were slowly filled up with the mix and tamped with a rod. Both the rodding and vibration were used in order to consolidate the mix and allow for air to escape. Cast specimens can be seen in Figures 3.6 (c) and 3.6 (d)

After the specimens were poured, the molds were placed on a table. Then, a plastic sheet or burlap was used as a cover and water cups were placed next to them to maintain a high humidity level. This was done in order to prevent shrinkage cracks. One day was allowed for specimen curing in this manner. Then, the specimens were removed from their molds and water cured for 14 days in a water tank. They were finally left in a laboratory environment (at about $20^{\circ}C$, 70% RH) for at least another 14 days until tested.

3.4 Specimen Test Setup and Testing Procedure

3.4.1 Test Setup

A test apparatus (Hota and Naaman, 1997) designed to accommodate the various types of loadings conditions considered in this study, was used. The test setup is shown in

Figures 3.7 thru 3.9 for specimens with a reinforcing bar and a prestressing strand, respectively. The prismatic specimen was supported at its eight corners by $2\times1.5\times0.5$ in. ($50\times38\times13$ mm) plates. No bearing plate was used for pulling the reinforcing steel through as in previous investigations (e.g. Abrishami et al., 1992; Cousins et al., 1992; Russell et al., 1999), thus minimizing the confinement effect in the loading direction. It is worth mentioning that conventional pull-out type bond tests using bearing plates, while placing the steel in tension, result in compressive forces on the concrete. However, in most reinforced or prestressed concrete members, both the steel and surrounding concrete are subjected to tension. Further, ACI Committee 408 suggests that in order to achieve a representative stress state in a bond test, the compressive force must be located away from the reinforcing steel by a distance approximately equal to the embedded length of the steel. In the test setup employed in this study, the effect of compressive forces on bond behavior was minimized by providing a distance between the strand and the compressed concrete zones (4.2 in.) slightly larger than the embedded length of the strand (4 in.).

The slip data was recorded using a pair of Linear Variable Differential Transformers (LVDTs) connected to a data acquisition system, while the applied load was monitored through a load cell. LVDTs were placed close to two corners of the specimen because no movement would occur in these regions during the pullout process. In this investigation, slip is defined as the permanent movement of the steel in the vertical direction with respect to the fixed concrete specimen. The average of the two LVDT readings was then used to get a representation of the slip. A photo showing the location of the LVDTs is shown in Figure 3.10. Because the reinforcing bar or prestressing strand behaved

elastically and the embedment length (4 inches) was short, the slip values at the unloaded and loaded bar or strand ends did not differ significantly from each other should strand elastic deformations be ignored (the strain of reinforcing steel is approximately in the range of $10^{-5} \sim 10^{-3}$ and the total elastic elongation was generally less than 0.004 in. for a typical maximum load). Therefore, the measured slip was believed to represent the average local slip in the middle of the embedment length with sufficient accuracy.

The average equivalent bond stress, σ, was calculated in terms of the load P applied to the reinforcing bar or prestressing strand as:

$$\sigma = \frac{P}{p_{ps} L} \qquad [3.1]$$

where P is the applied load (kips), L is the embedment length (4 in.). p_{ps} is the bar or strand perimeter, equal to πd for reinforcing bar and equal to $\frac{4}{3}\pi d = \frac{4}{3}\pi(0.5) = 2.094$ in. for 0.5 in. strands where d is the nominal diameter of the reinforcing bar or prestressing strand

The testing machine was a closed-loop servo controlled hydraulic universal testing machine (INSTRON 1325). This machine consisted of a 220 kip capacity frame, and a 110 kip actuator with 6 inch stroke. The machine had a load and stroke digital voltmeter readout. The testing machine was equipped with a load cell calibrated for 110 kips, full capacity. The whole test system, including the testing machine and data acquisition system is shown in Figure 3.11.

3.4.2 Testing Procedure

As mentioned earlier, monotonic, cyclic, and reversed cyclic loading tests were conducted. The adopted standard loading rate was 0.001 in. slip per second (1.5 mm per minute). However, to save on testing time, it was sometimes increased to 0.005 in. per second (7.6 mm per minute) especially for the fully reversed cyclic loading tests. The test setup was specially designed so that only the nut or chuck position needed to be changed when changing loading protocols.

3.4.2.1 Monotonic Loading

The monotonic test consisted of a simple pullout test of a reinforcing bar or prestressing strand. A monotonically increasing displacement was applied to the bar or strand and the response of the specimen was recorded beyond the peak load, for each of the different types of materials. Only one nut or chuck was needed to perform the monotonic loading test, as shown schematically in Figure 3.12, position 1.

3.4.2.2 Unidirectional Cyclic Loading

The setup for unidirectional cyclic loading is similar to the monotonic load setup; that is, it uses only one nut (chuck) for the test. This type of loading was intended to simulate fatigue loading and was performed either load control or displacement control mode (Figure 3.12, position 1). It should be noted that, in this investigation, when a displacement control test was conducted, the reloading was ended when zero load was

reached, rather than a zero displacement.

3.4.2.3 Fully Reversed Cyclic Loading

The fully reversed cyclic loading test was intended to simulate earthquake-induced loading. In order to perform this type of loading, the test setup had to be designed with the use of one actuator to simulate a fully reversed cyclic motion. This was achieved by using two or four nuts (chucks) placed at different locations. When two nuts (chucks) are used, as shown in Figure 3.12 position 2, a pull-push cyclic loading mechanism is allowed. When only one nut (chuck) is tied at the top of the setup and one at the bottom of the setup, a pull-pull reversed cyclic loading mechanism is achieved, as shown in Figure 3.13 position 3. Furthermore, in order to simulate the bar loading conditions that may take place in a beam-column joint subjected to earthquake-type loading (i.e. bar is pulled and pushed simultaneously), four nuts can be used to allow the pull-push & push-pull cyclic loading condition; this is shown in Figure 3.13 position 4. All cyclic motions could be performed either by load control or displacement control (detail described in next section). In this study, position 1 (Figure 3.12), and position 3 (Figure 3.13) were chosen for the monotonic (and unidirectional cyclic) and fully reversed cyclic loading tests, respectively, for reinforcing bar specimens. Similar placements of chucks were used for the strand specimens, as shown in Figure 3.14.

3.4.3 Loading Protocol

Four types of loading protocols, as shown in Figure 3.15, were employed in this

study depending on the purpose of each test. Figure 3.15(a) gives the loading protocol employed for unidirectional cyclic loading with force control. The applied force was 50% (3 cycles), 65% (3 cycles), 80% (5 cycles), 90% (5 cycles), and 100% (if achieved, then until failure) of the peak bond strength obtained from the monotonic bond tests. The test was performed until the bond strength degraded to 50% of the monotonic peak bond strength. The preceding test procedure was also used for fully reversed cyclic loading with force control, as illustrated in Figure 3.15(b).

Two displacement-controlled cyclic loading histories, one unidirectional and the other fully reversed, were employed in this study to investigate the effect of loading history, especially on the bond characteristics of strands embedded in FRCC materials. Both loading histories are illustrated in Figures 3.15(c) and 3.15(d).

Table 3.1 Composition of matrix mixtures by weight ratio and average compressive strength

Matrix	Cement (Type III)	Fly Ash	Sand*	Silica Fume	Super-plasticizer**	Water	f_c', ksi (MPa)
Mix 1	0.8	0.2	1.0	0.07	0.04	0.26	11 (76)
Mix 2	1.0	0.15	1.0	-	-	0.40	7.6 (52)
Mix 3	0.8	0.2	1.0	-	-	0.45	5.9 (41)

*Flint Sand ASTM 30-70

**High Range Water Reducing Admixture (RHEOBUILD®1000)

Table 3.2 Properties of Fibers

Fiber Type	Diameter in. (mm)	Length in. (mm)	Density pcf (g/cc)	Tensile Strength ksi (MPa)	Elastic Modulus ksi (GPa)
Spectra	0.0015 (0.038)	1.5 (38)	60.6 (0.97)	375 (2585)	17000 (117)
PVA 13	0.0075 (0.19)	0.5 (13)	81.8 (1.31)	130 (900)	4200 (29)
PVA K-II	0.0016 (0.04)	0.3 (8)	81.8 (1.31)	230 (1600)	5800 (40)
Steel Hooked (Dramix)	0.02 (0.5)	1.2 (30)	490 (7.9)	185 (1275)	29000 (200)
Rectangular Torex*	0.012 (0.3)***	1.2 (30)	490 (7.9)	370 (2570)	29000 (200)
Square Torex*	0.012 (0.3)***	1.2 (30) & 0.8 (20)	490 (7.9)	400 (2750)	29000 (200)
Helix (Twisted triangular fiber) **	0.02 (0.5) ***	1.4 (35)	490 (7.9)	260 (1800)	29000 (200)

*12 ribs/in.

** 9 ribs/in.

*** equivalent diameter

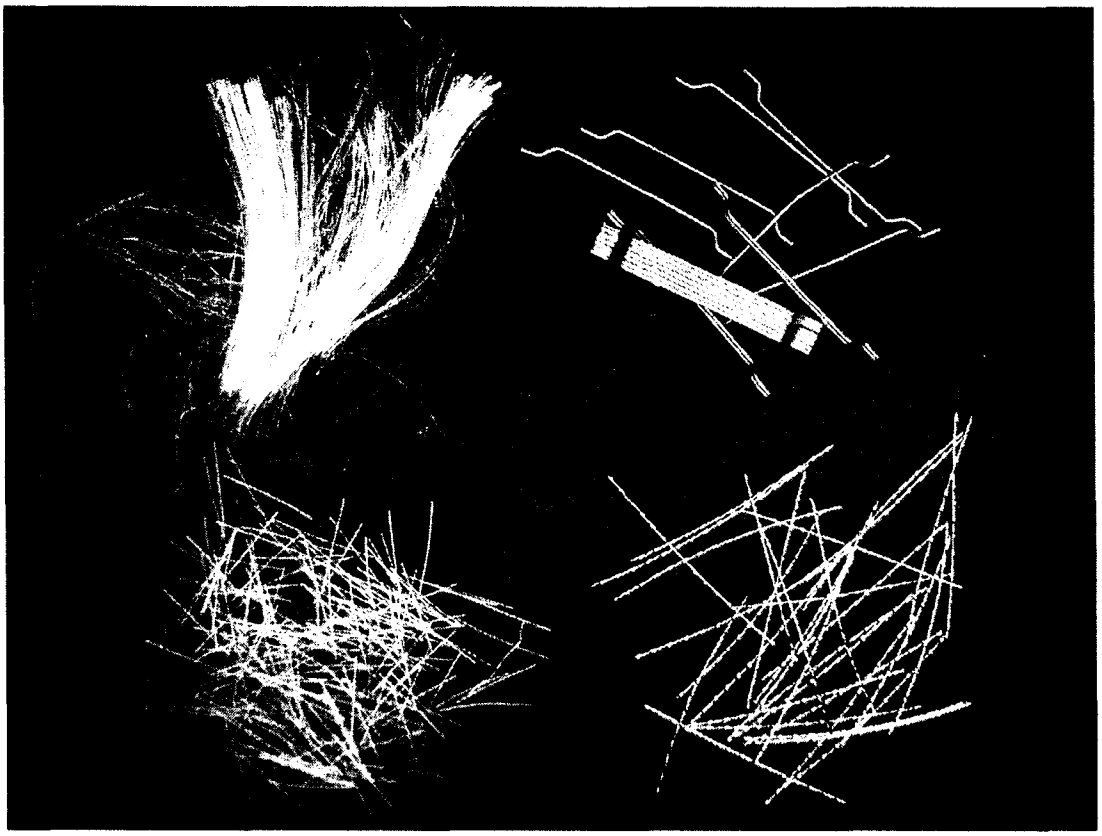

Figure 3.1 Fibers used in this study: (a) Spectra (upper left); Steel Hooked (upper right); PVA 13 (lower left); Rectangular Torex (lower right)

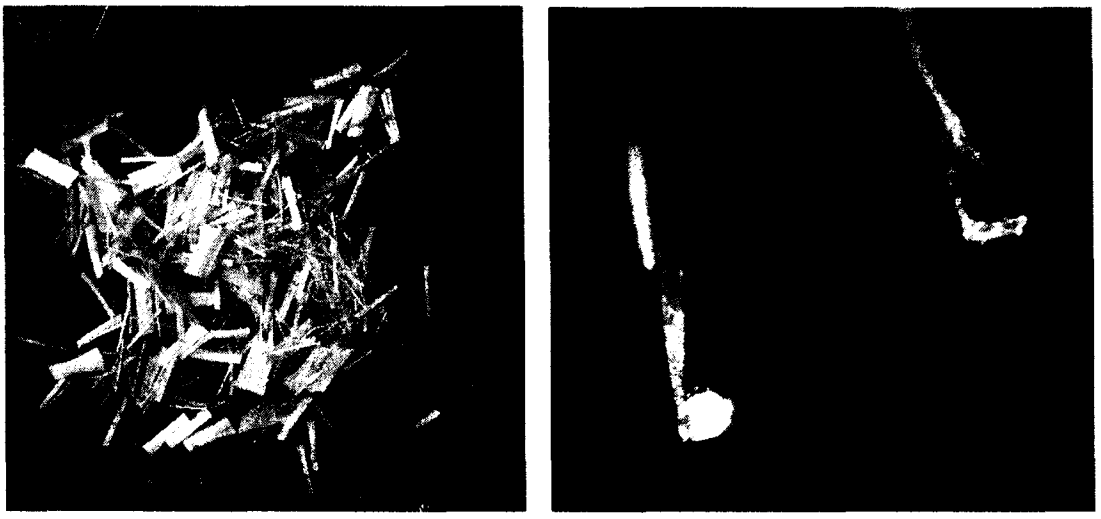

Figure 3.1 Fibers used in this study: (b) Left: PVA K-II fiber; Right: microscopic view of Torex fiber with square and rectangular cross sections

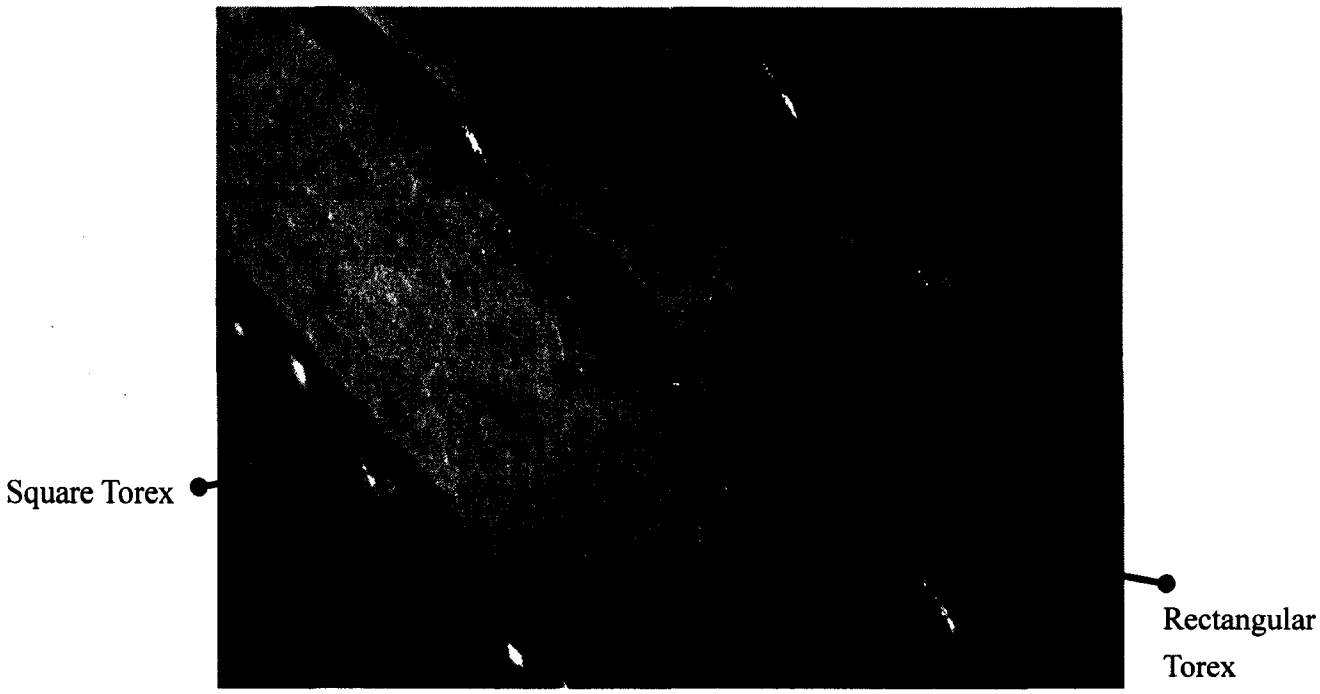

Figure 3.1 (c) Microscopic view of square and rectangular Torex fibers showing their twisted ribs

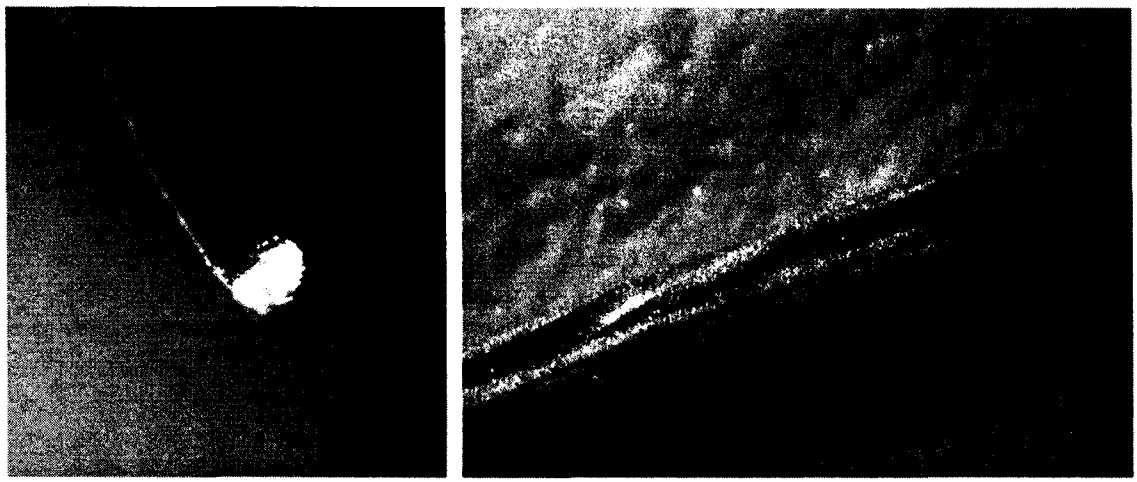

Figure 3.1 (d) Microscopic view of Helix fiber (Triangular Torex) showing its cross section and ribs

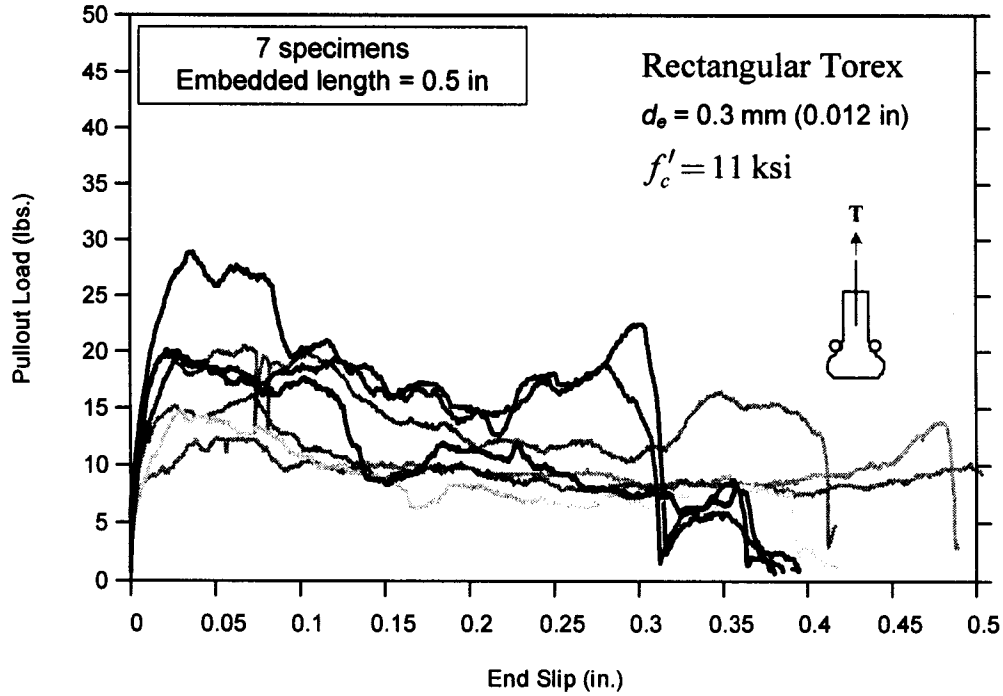

Figure 3.2 (a) Single fiber pullout response of rectangular Torex fiber

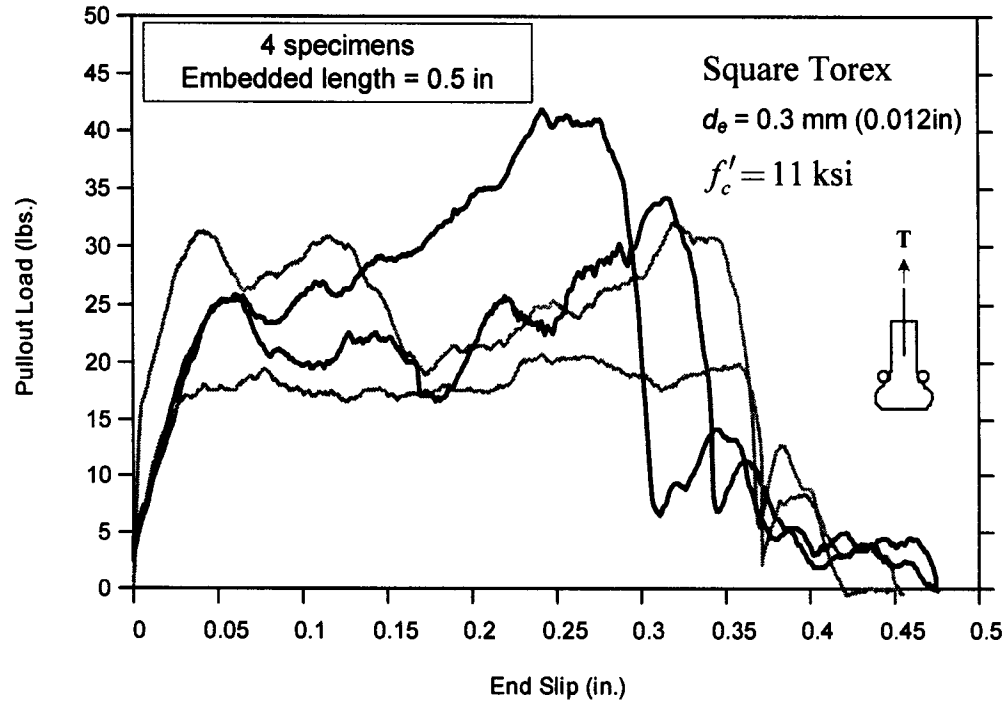

Figure 3.2 (b) Single fiber pullout response of square Torex fiber

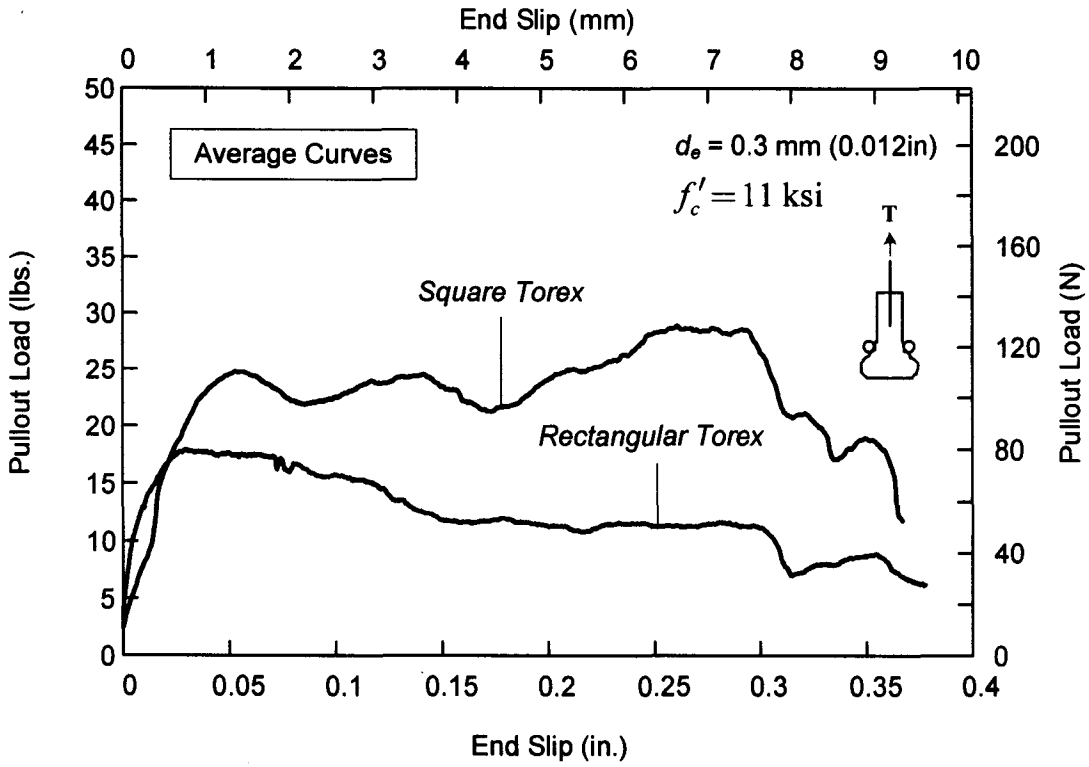

Figure 3.2 (c) Comparison of pullout load versus slip average responses for square and rectangular Torex fibers

(d) (e)

Figure 3.2 (d) Test setup for single fiber pullout test; (e) Untwisting before (upper one) and after (lower one) pullout of square Torex fiber

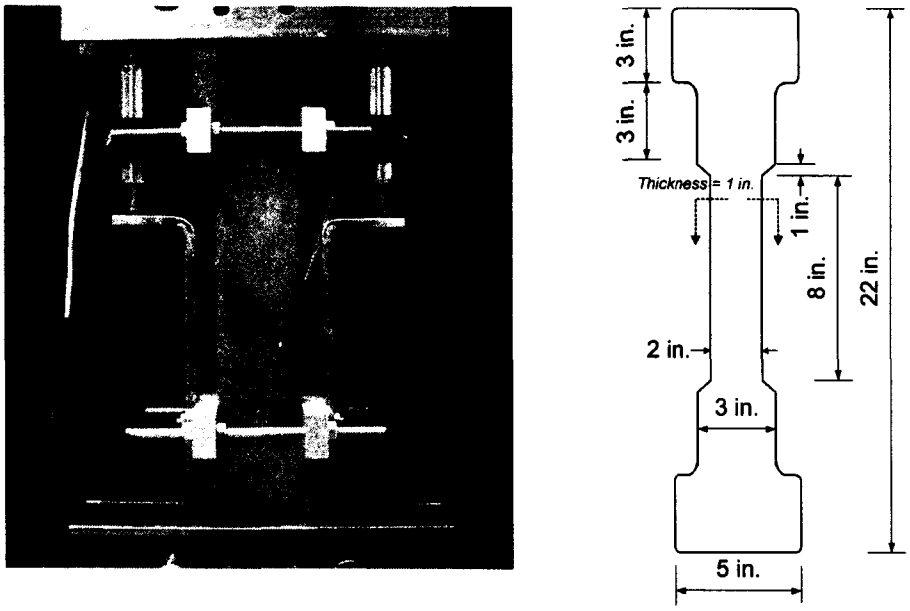

Figure 3.3 (a) Test setup for material tensile test

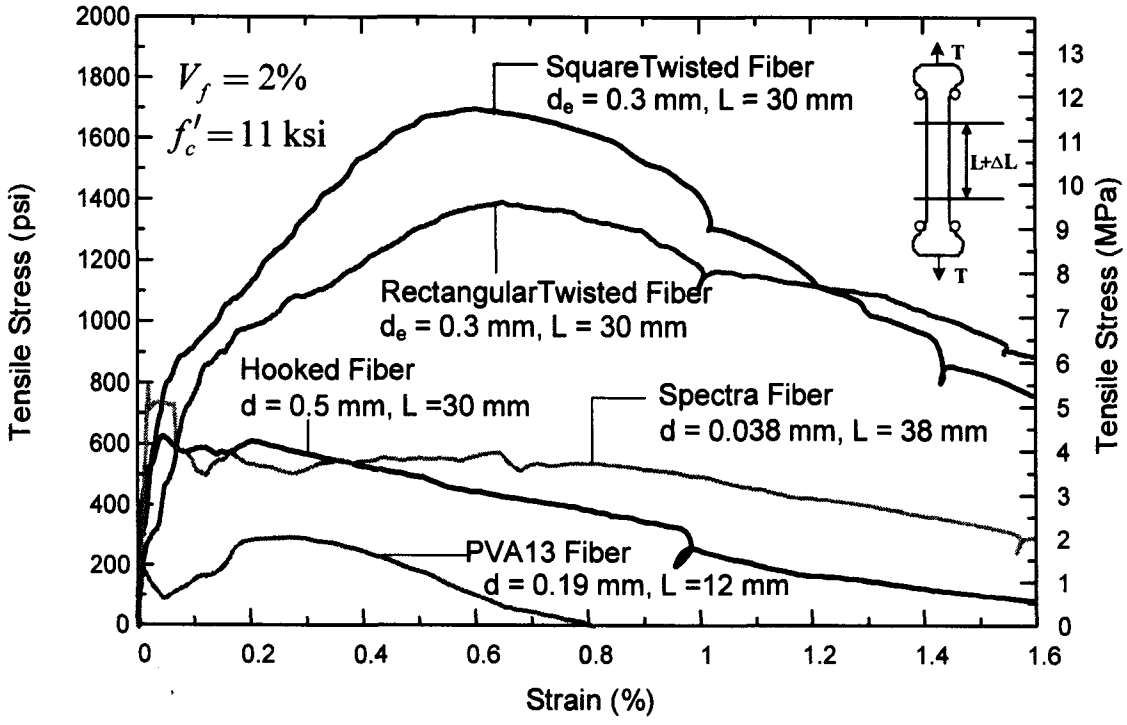

Figure 3.3 (b) Tensile stress-strain behavior of cementitious composites (f_c' = 11 ksi)

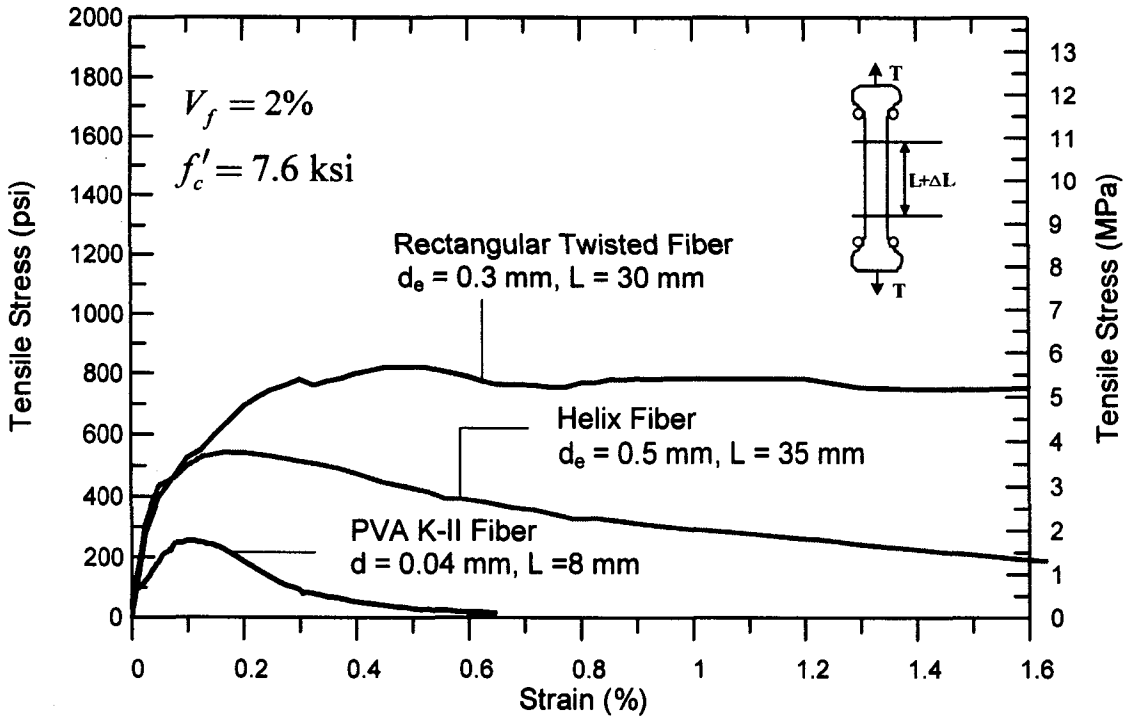

Figure 3.3 (c) Tensile stress-strain behavior of cementitious composites (f'_c = 7.6 ksi)

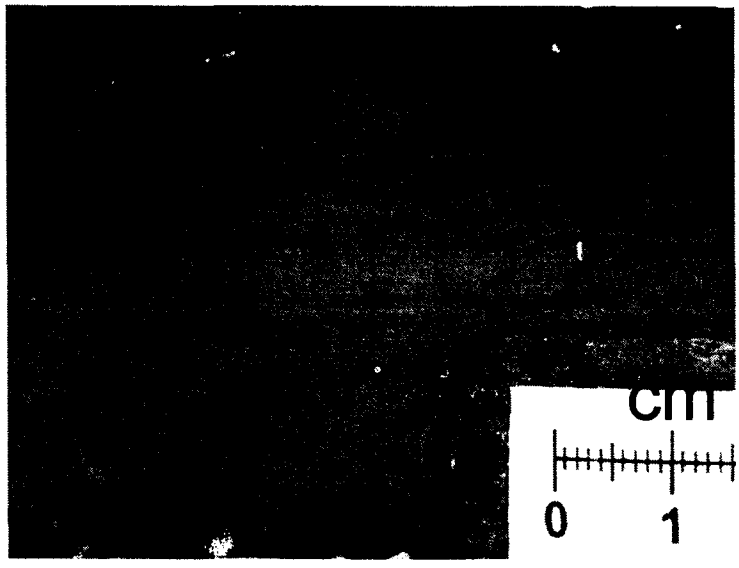

Figure 3.3 (d) Multiple cracking in specimen with rectangular Torex fiber (f'_c = 11 ksi)

Figure 3.3 (e) Compression test setup

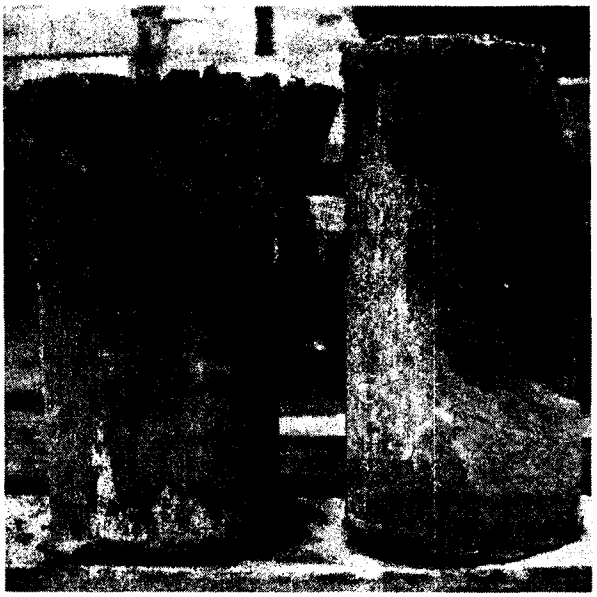

Figure 3.3 (f) Tested cylinders: 1% Rectangular Torex fiber specimen (left); plain mortar control specimen (right)

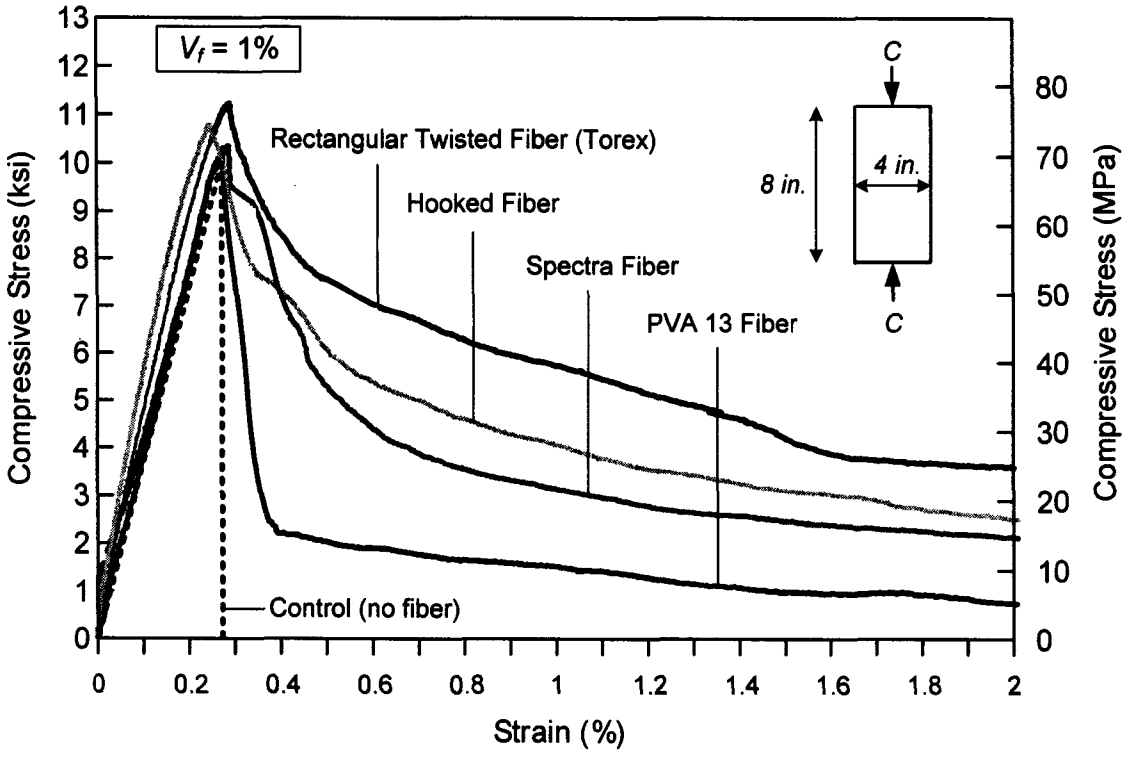

Figure 3.3 (g) Typical compressive stress-strain responses of FRCC materials

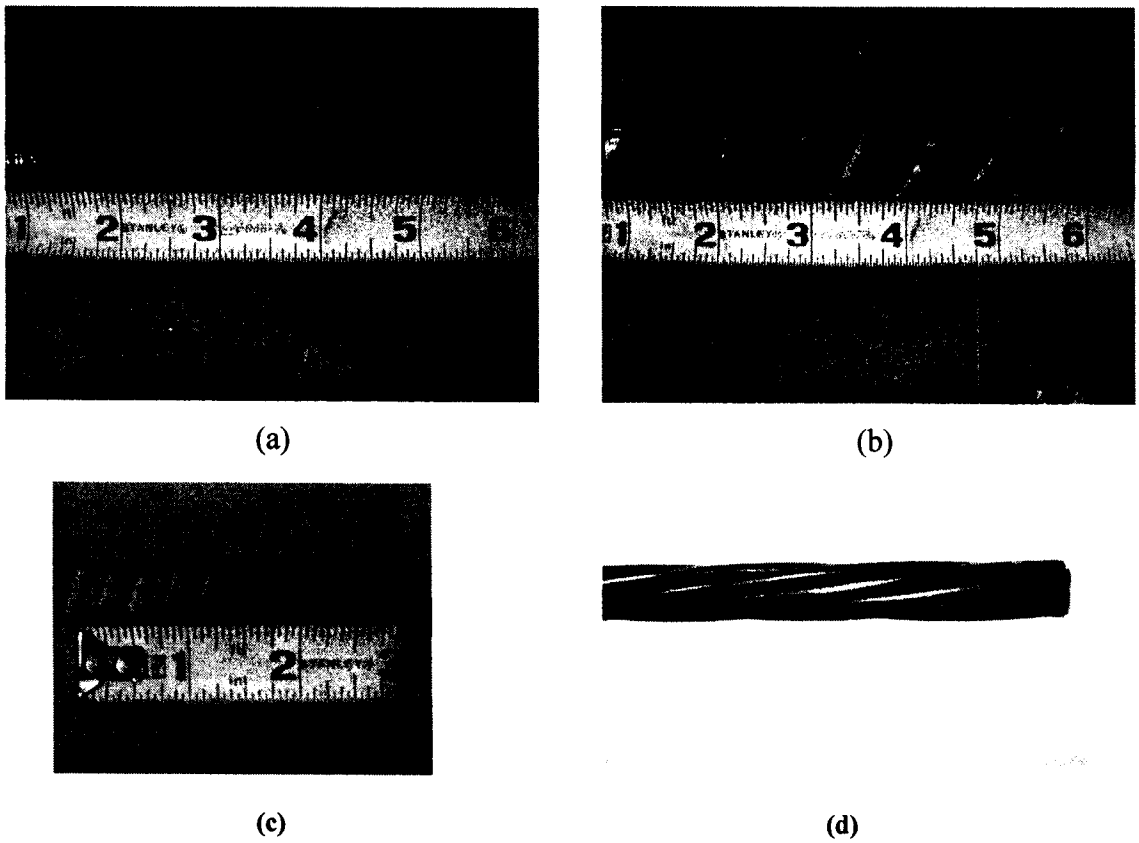

Figure 3.4 Geometry of reinforcing steel: (a) No. 5 bar; (b) No. 8 bar; (c) No. 4 bar; (d) 0.5 in. seven-wire strand (unit: inch)

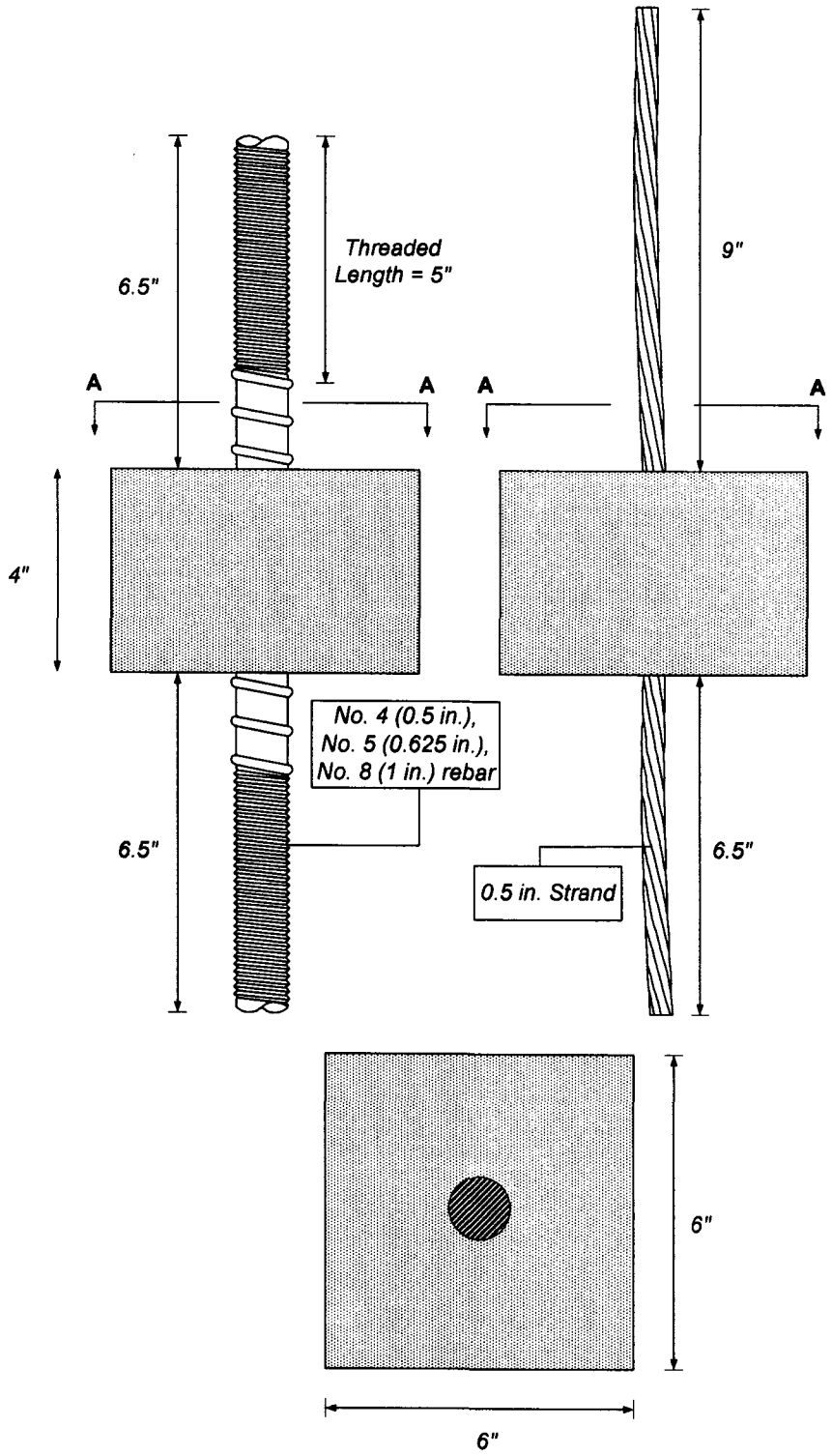

Figure 3.5 Specimen geometry

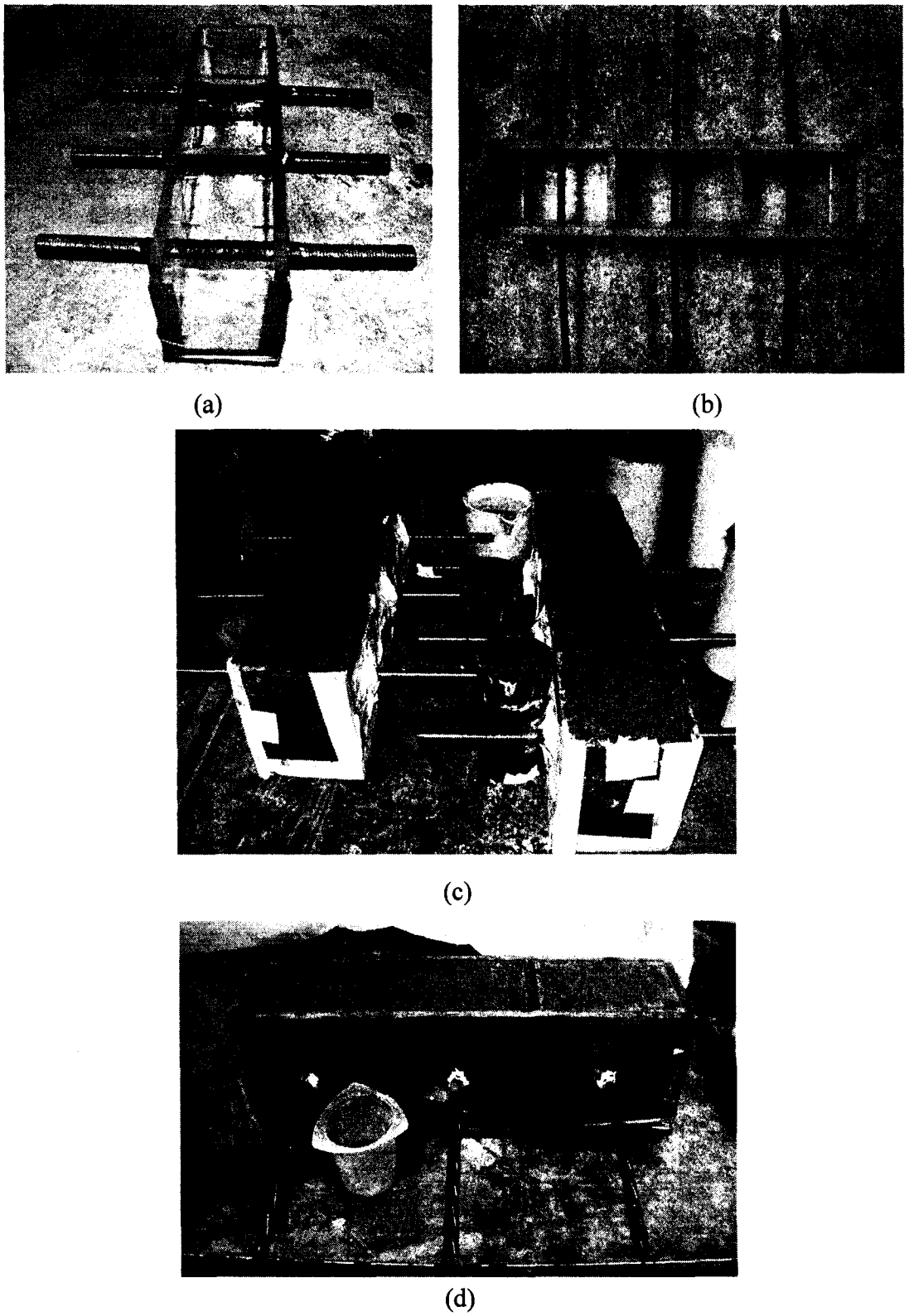

Figure 3.6 (a) Specimen mold with No. 8 bars; (b) Specimen mold with strands; (c) Cast specimens (reinforcing bar); (d) Cast specimens (strand)

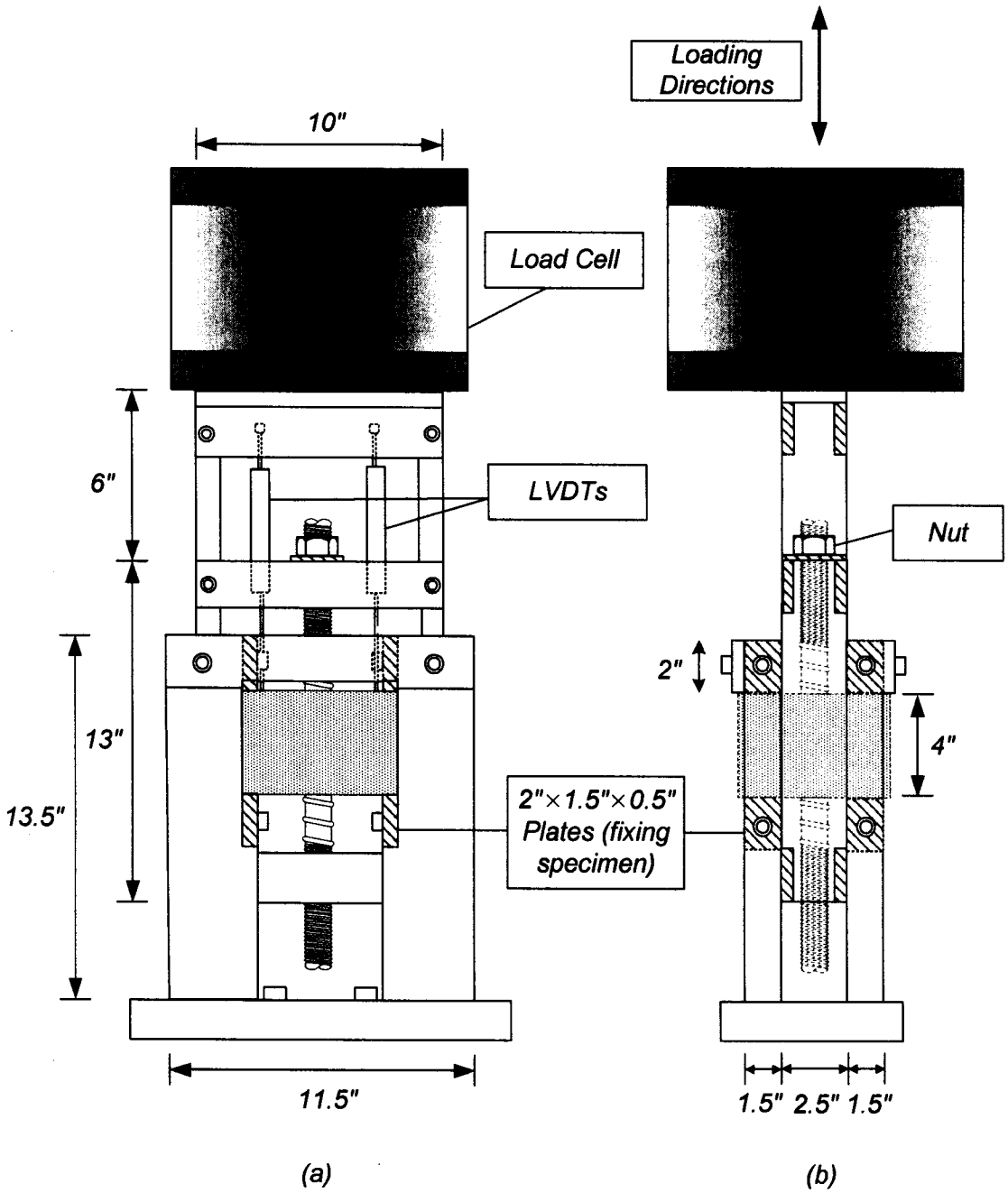

Figure 3.7 Pull-out bond test setup for reinforcing bar specimens: (a) front view; (b) side view

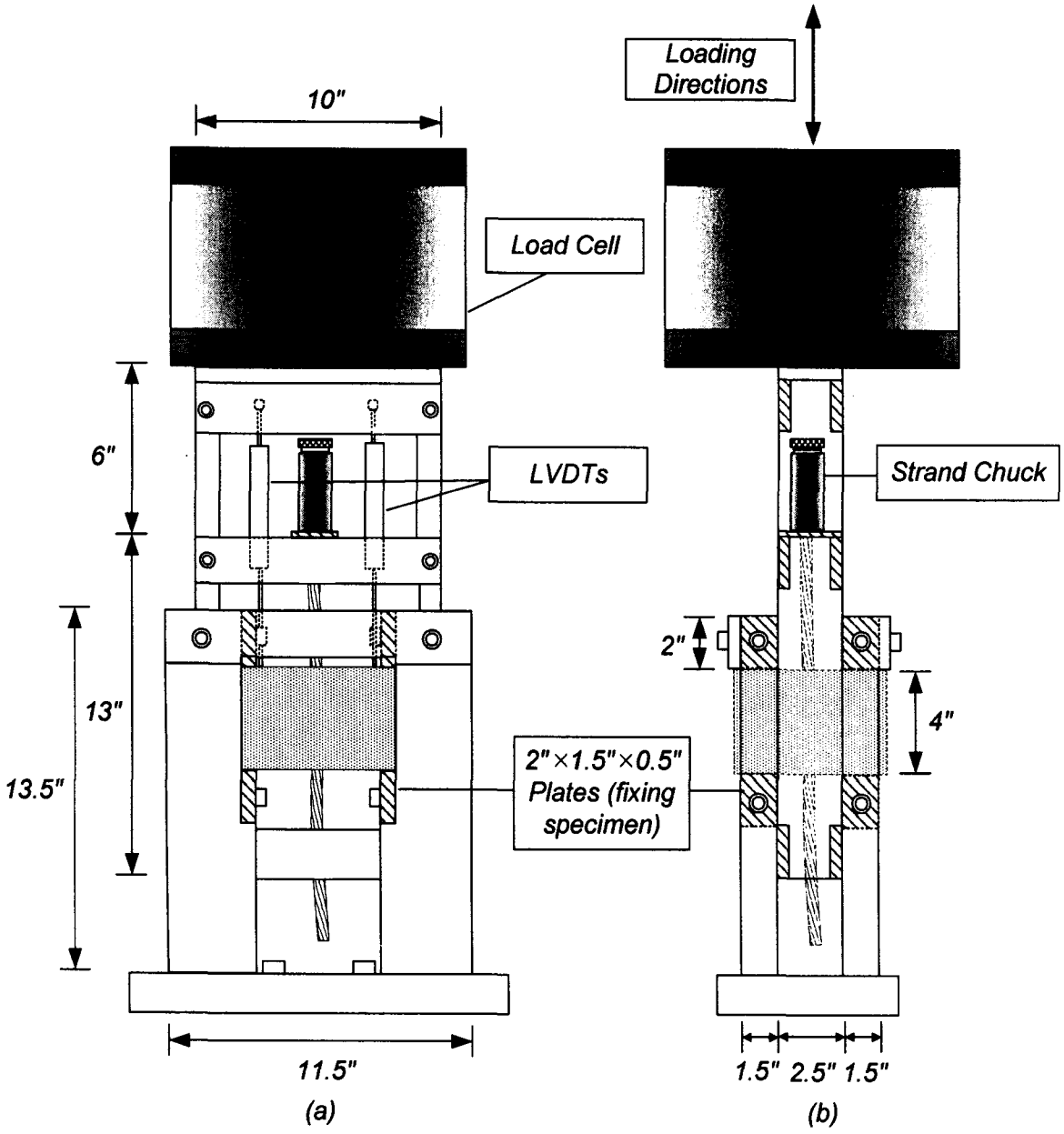

Figure 3.8 Pull-out bond test setup for strand specimens: (a) front view; (b) side view

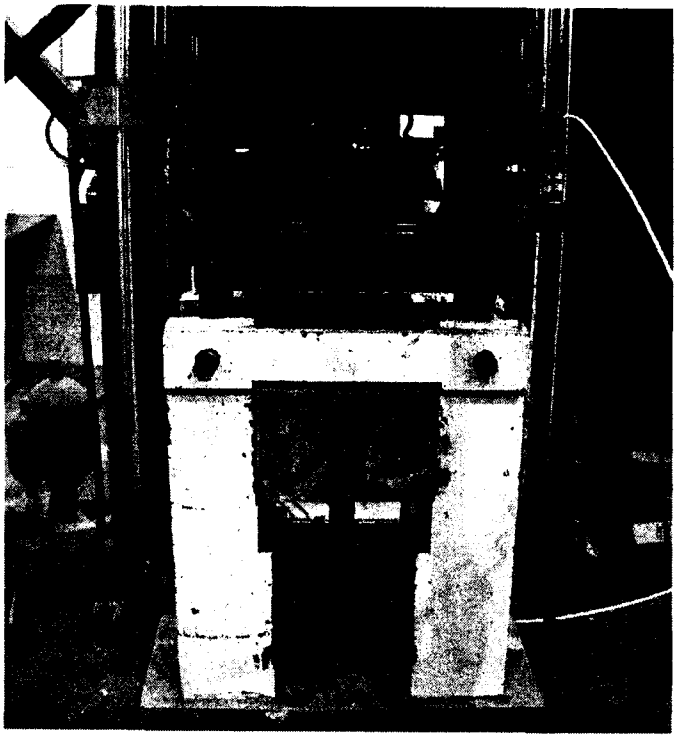

(a)

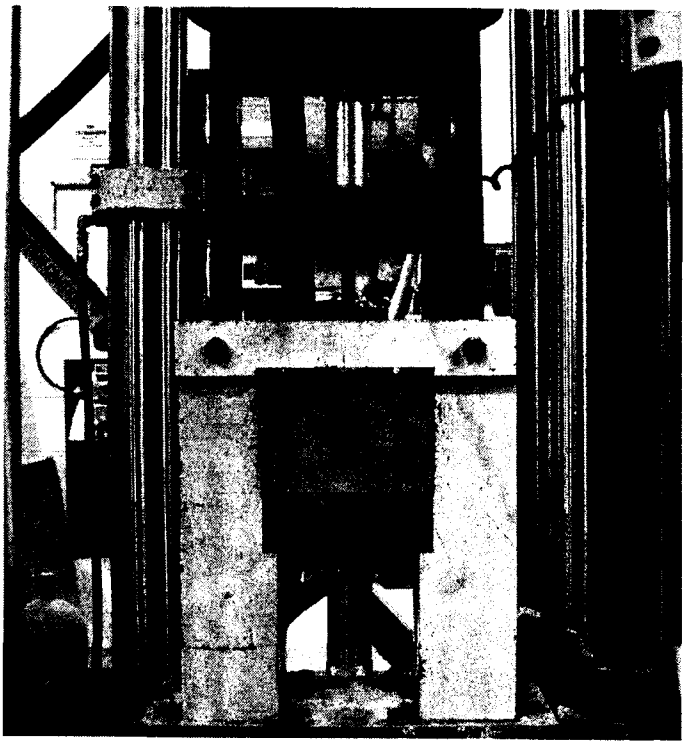

(b)

Figure 3.9 Photos of test setup: (a) reinforcing bar specimen; (b) strand specimen

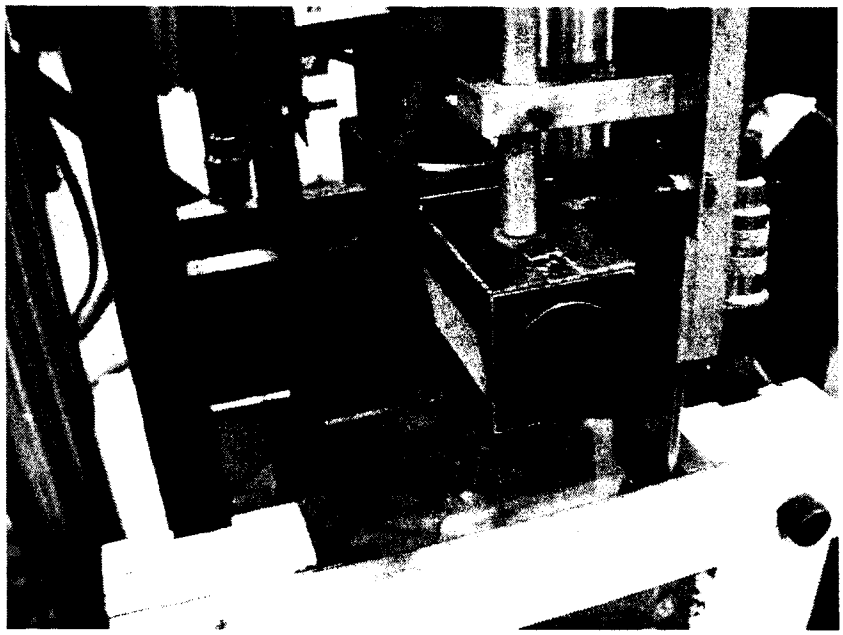

Figure 3.10 Close view of layout of LVDTs

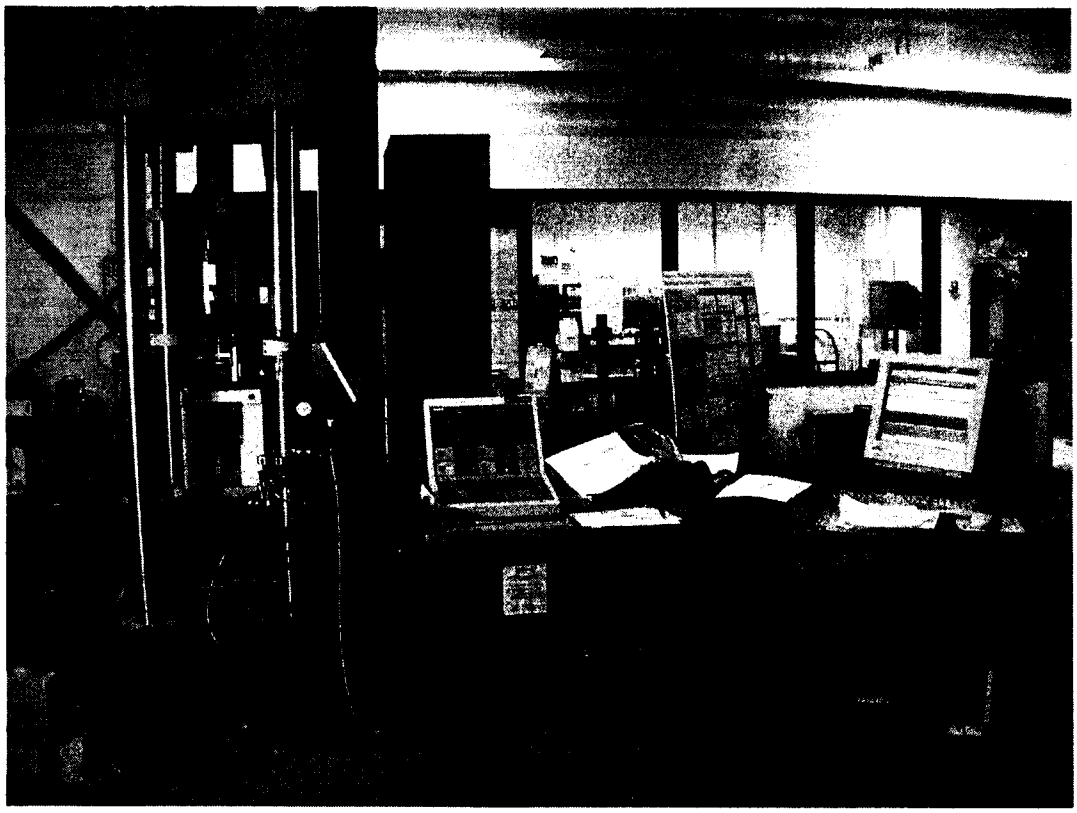

Figure 3.11 Test machine and data acquisition system

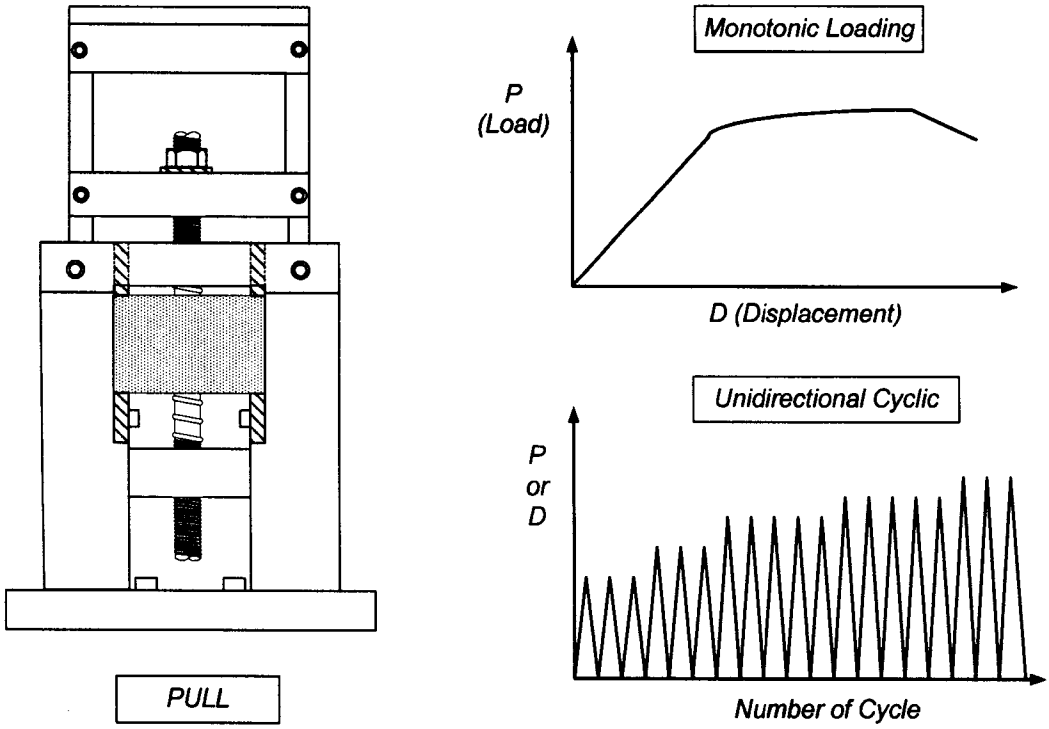

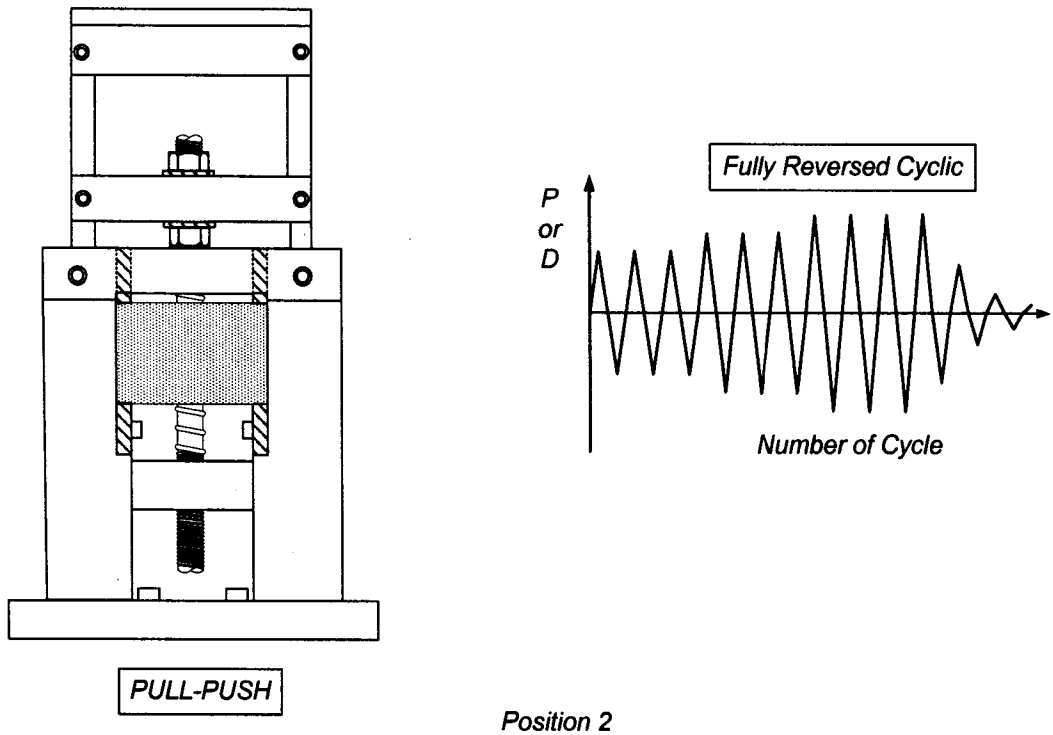

Figure 3.12 Nut position and related loading type for specimens with reinforcing bar

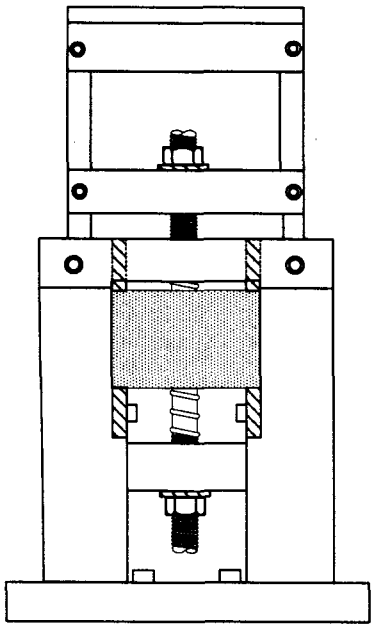

PULL-PULL

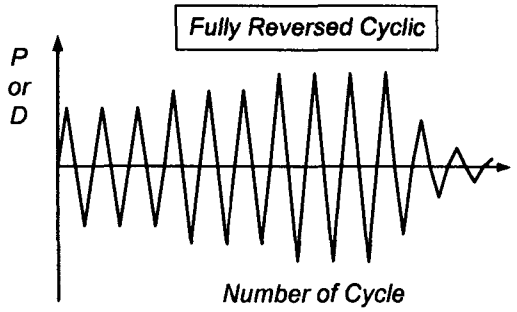

Position 3

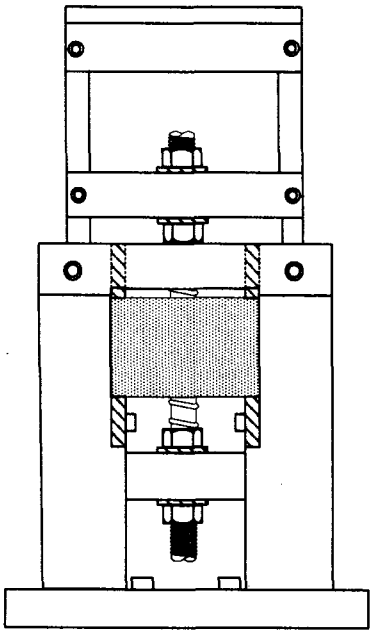

PULL-PUSH & PUSH-PULL

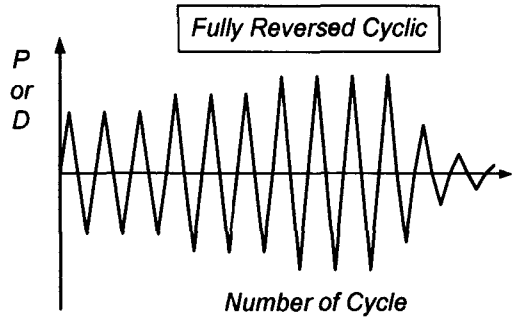

Position 4

Figure 3.13 (continued) Nut position and related loading type for specimens with reinforcing bar

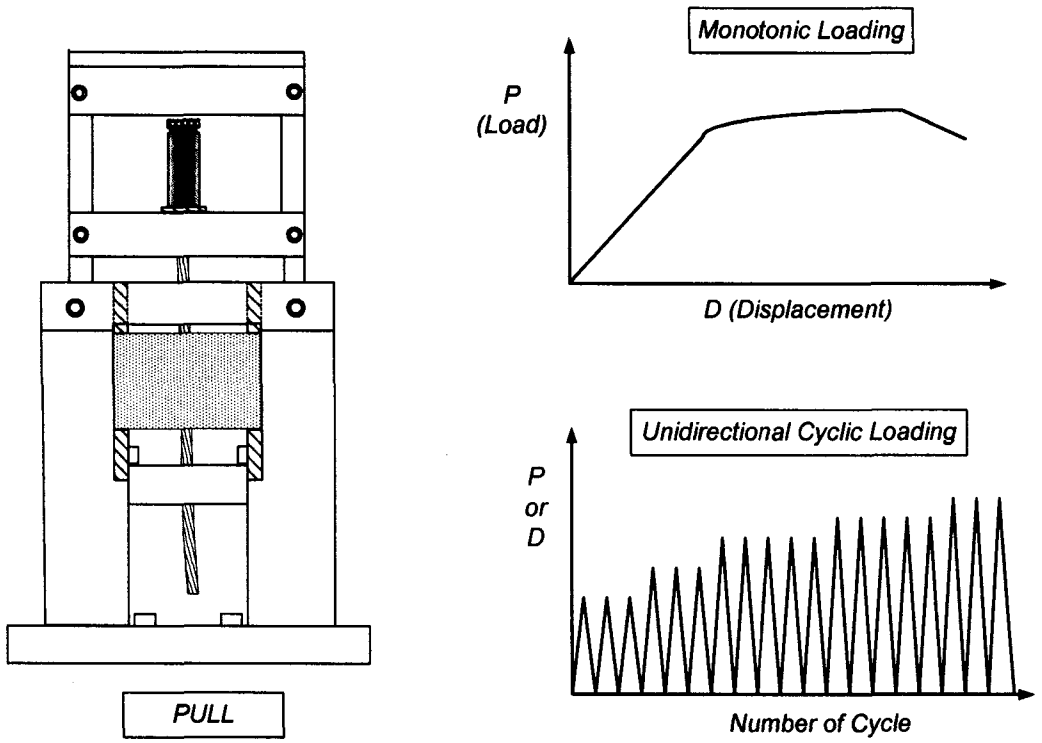

Figure 3.14 Chuck position and related loading type for specimens with strand

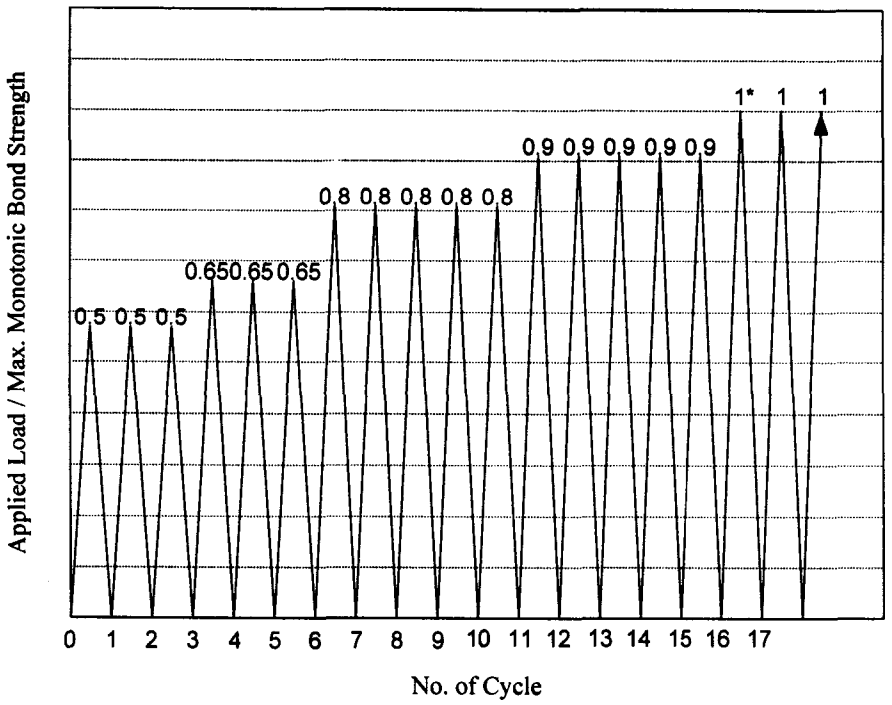

Figure 3.15(a) Loading protocol for unidirectional loading (force controlled tests)
***Note: if peak monotonic bond strength could not be attained, then specimen was monotonically loaded until failure**

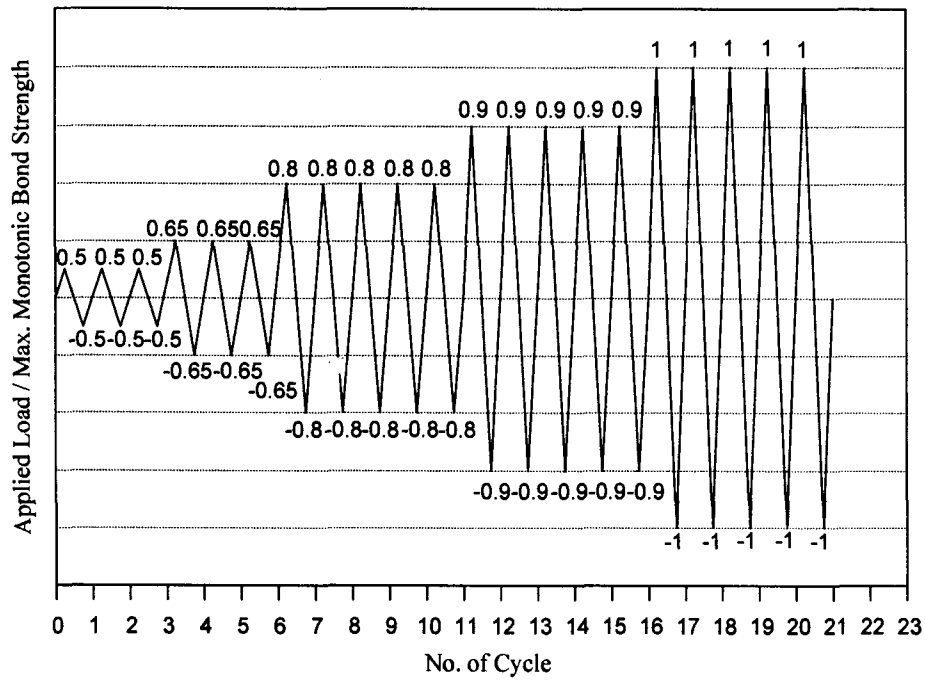

Figure 3.15(b) Loading protocol for fully reversed cyclic loading (force controlled tests)

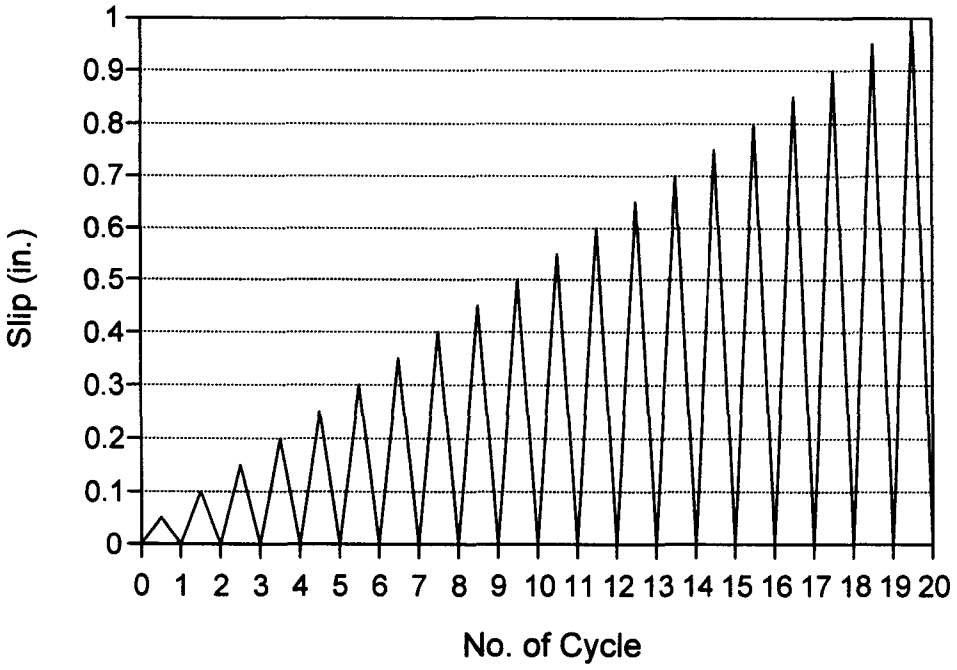

Figure 3.15(c) Loading protocol for unidirectional loading (displacement controlled tests)

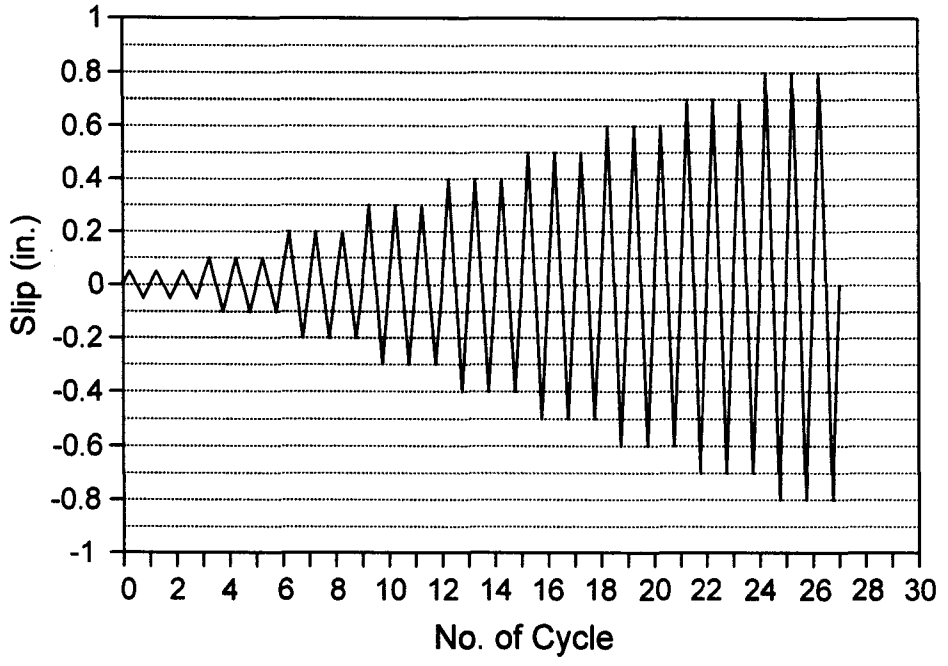

Figure 3.15(d) Loading protocol for fully reversed cyclic loading (displacement controlled tests)

CHAPTER 4

EXPERIMENTAL RESULTS OF SPECIMENS WITH REINFORCING BARS

4.1 General

Previous research (Hota and Naaman, 1995) has shown that addition of hooked steel fibers into cementitious matrix can improve the bond properties of reinforcing bars. However, splitting failures still have been observed in the FRC specimens (2% hooked steel fiber). Friction pullout failure was observed in the specimens with 9.7% fiber content (SIFCON). In this study, reinforcing bars were embedded in high performance fiber reinforced cementitious composites with fiber content up to only 2% to investigate their bond characteristics. Loading includes monotonic, unidirectional cyclic (both force and displacement controlled) and fully reversed cyclic loadings.

4.2 Monotonic Loading

4.2.1 Control Specimens

4.2.1.1 Specimens with No. 8 Bar

No fiber or confinement reinforcement was added in the control specimens and all test specimens failed by splitting of the concrete matrix. The pullout load versus slip response is largely influenced by the crack pattern of the tested specimen due to opened cracks formed after fracture. As illustrated in Figure 4.1, if a through crack develops in the 1-1 direction (Figure 4.1(b)), the cracked specimen is able to freely open in the 2-2 direction without restriction. On the other hand, if a through crack occurs in the 2-2 direction (Figure 4.1(c)), passive compression is provided by the testing setup which in turn results in confinement as shown in Figure 4.1(d). This confinement would lead to increase in bond strength at large slip.

Three control specimens with No. 8 reinforcing bar were tested under monotonic loading and all of them failed by splitting. The crack patterns varied, giving widely different load-slip curves. The crack patterns and load-slip relationship are shown in Figures 4.2 and 4.3, respectively. The monotonic load-slip curve adopted in this study is the average curve of specimen 1 and 3, which reflects more realistic failure characteristics of the control specimen (Note that the presence of cracks in the 2-2 direction in specimens 1 and 3 can cause passive confinement to certain degrees, see Figure 4.2). In any case, the ascending branching and the peak bond strength were not altered by the passive confinement (i.e. before open crack occurred).

4.2.1.2 Specimens with No. 5 Bar

The crack patterns of three test specimens with No. 5 bars are shown in Figure 4.4 and the corresponding load-slip curves of these specimens are given in Figure 4.5. As

discussed previously, the load-slip shape highly depends on the crack patterns of the control specimens, especially for the descending portion or large slip stage. Specimens 1 and 2 had through cracks in the 2-2 direction (Figure 4.4), thus leading to significant passive confinement and bond strength. The tail portion of the curve for Specimen 2 shows an increase of bond at larger slip resulting from further opening of the cracks when the bar was pulled out. Load-slip curve for Specimen 3 reflects more realistic bond characteristics without confinement because the through crack was mainly in the 1-1 direction. The curve of Specimen 3 was used as representative of the bond-slip curve for control specimen with No. 5 bar.

4.2.2 Specimens with Fibers

The general bond behavior of specimens with fibers are first illustrated using specimen with Spectra fibers, then a detailed comparison with specimen with other types of fibers are given later.

4.2.2.1 Bond Behavior of Specimens with Spectra Fiber

4.2.2.1.1 No. 8 bar

The bond behavior of the specimens with fibers is distinct from that of control specimens. The widening and propagation of cracks were inhibited due to the presence of fibers. The failure mode of most specimens was switched to friction pullout from separation failure depending on fiber type and content. For instance, Spectra fibers can

effectively bridge the cracks and redistribute the forces (from the lugs of the reinforcing bar) to the uncracked portion of the matrix. This led to the formation of multiple cracks as shown in Figure 4.6, where only the visible cracks were marked. Wide cracks were observed in the test specimens at larger slip along with cone shape fracture at the end of reinforcing bar; however, as can be observed in Figure 4.6 (b), the fiber bridging effect hindered the widening and propagation of such cracks. It is also observed in Figure 4.7, that the bond strength was largely enhanced due to the presence of Spectra fibers. Unlike the control specimens, the test setup did not apply passive compression onto the specimens with Spectra fiber because the widening of crack is hindered by the fibers. Hence, little or no confinement was offered by the test apparatus. Figure 4.7 also shows that the two test specimens exhibited similar load-slip curves which were not affected by the crack orientation.

Increasing the Spectra fiber volume fraction from 1% to 2% did not increase too much the bond strength, as shown in Figure 4.8. However, it is evident from Figure 4.9 that the crack width in the specimens with 2% Spectra fibers was less than that in the specimens with only 1% Spectra fibers. Note that only visible cracks were marked. Figure 4.9 shows that a cone surrounding the reinforcing bar tended to be pulled off from the specimen with 1% fiber content at large slip. Yet, no evident formation of this cone was observed in specimen with 2% fiber volume fraction. This shows the advantage of increasing fiber content in terms of limiting the degree of damage. The distance between first peak bond stress and the point at which the bond stress increased again as highlighted in Figures 4.7 and 4.8 is equal to the lug spacing of the used reinforcing bar (0.63 in, see Section 3.2.2), which will be elaborated later in Section 4.6.2.

Comparison of tested specimens with various Spectra fiber volume fractions under monotonic pullout loading is given in Figure 4.10. As can be observed, addition of Spectra fiber largely increases the bond strength and ductility compared with the control specimen. Peak bond strength of the fiber reinforced specimens was approximately 7 times that of the control specimens. Considerable energy (approximately 25 times of that of control specimens) can be absorbed by the fiber reinforced specimens before excessive bond loss occurs. It is noted that the difference of peak bond strength under monotonic loading between specimens with 1% fiber and 2% fiber is insignificant; however, increasing fiber volume fraction can effectively prevent the widening and propagation of the cracks, thereby maintaining the integrity of the matrix and reducing the damage degree.

4.2.2.1.2 No. 5 Bar

The load-slip characteristics of specimens with No. 5 bars are basically similar to that of specimens with No. 8 bars. However, average bond stress is much higher and the crack width is generally smaller even if only 1 % fiber was used. Furthermore, no cone shape piece fractured away around the No. 5 bar at larger slip. The load-slip and average bond stress versus slip curve are shown in Figures 4.11 thru 4.13. No significant bond strength was observed by increasing the fiber volume fraction from 1% to 2% under monotonic loading, as indicated by Figure 4.13. Energy dissipated by fiber reinforced specimens is approximately 25 times the energy dissipated by control specimens. Note that the peak loads are very close to the force corresponding to the nominal yield strength of the No. 5 bars used in this study, i.e., 20 kips. The overall crack patterns of specimens

with various fiber contents are presented in Figure 4.14, in which only visible cracks were marked. The distance between first peak bond stress and the point at which the bond stress increased again as highlighted in Figures 4.11 and 4.12 is equal to the lug spacing of the used reinforcing bar (0.32 in, see Section 3.2.2).

Comparison between Figures 4.10 and 4.13 indicates that the slip at peak bond strength increases with smaller bar diameter. However, the degradation of bond strength is more rapid in No. 5 bar specimens. The average slope for the descending portion of specimen with No. 8 bar is approximately 2000 psi/in (bond stress/slip) and the slope for specimen with No. 5 bar is about 8000 psi/in. The larger slip at peak load for smaller bar was also observed in specimen reinforced with straight steel fiber (Krstulovic-Opara, Watson and LaFave, 1994). They suggested that this can be attributed to the higher confinement level, i.e. cover thickness, of the smaller bar specimens. In this study, the cover thickness for No. 8 bar specimen is 3 bar diameters, whereas the cover thickness for No. 5 bar specimen is 4.8 bar diameters. In addition, the larger slip may also be primarily the result of higher bond stress developed in the smaller size bar specimens. It can be seen from Figures 4.10 and 4.13 that the maximum bond stress in No. 5 bar specimens is about 1.5 times that of No. 8 bar specimens, which is approximately the diameter ratio No. 8 bar to No. 5 bar. Table 4.1 summarizes the test results of specimen with Spectra fibers.

4.2.2.2 Comparison of Bond Behavior for Specimens with Various Fibers

4.2.2.2.1 No. 8 Bar and 1% Fiber Volume Fraction

Figure 4.15 shows the comparison of bond behavior between specimens with various types of fibers. All specimens with only 1% fiber volume fraction and a matrix compressive strength equal to 11 ksi. For study purposes, specimen with conventional spiral reinforcement ($d_b = 0.162$ in.; $f_y = 30$ ksi; $f_u = 46$ ksi) as shown in Figure 4.16 (a) in a 2% volumetric ratio (ρ_s) was also tested. The stress-strain curve of the steel spiral reinforcement is illustrated in Figure 4.16 (b). It is noted that, as indicated by ACI Committee 408 (2003), while the amount of transverse (spiral) reinforcement is able to enhance the bond performance, the yield strength of the transverse reinforcement does not play a role in the contribution to bond strength.

It is observed in Figure 4.15 and Table 4.2 that, while specimen with Spectra fiber has the highest monotonic bond strength (1470 psi), specimen with PVA 13 fiber has smallest bond strength (720 psi). Specimens with other types of fibers generally reached same peak bond stress. It is further observed that, when fiber volume fraction is low (1% in this case), the fiber length play an important role to the bond strength, especially for larger size reinforcing bar. When a reinforcing bar is pulled out from a matrix, the cracks need to open in order for bar moving through. Since the rib height of bar is generally proportional to the bar diameter, a larger size bar needs wider crack to allow the bar to pull through. As a consequence, the longer fiber offers better bridging effect, thus increasing the bond strength. Increasing fiber amount, by using higher volume fraction or shorter fiber but same volume fraction, the bond strength is also able to be enhanced. The enhancement is not only in the strength, but in the improvement of limiting damage. Due to the ample fiber amount thus the more effective fiber bridging, the cracks need not to be

wide and reinforcing bar is pulled out along with grinding off the concrete-to-steel interface (friction type bond failure). It has been shown that the fiber bridging effect, as well as the fiber-induced confinement effect, can be expressed by a fiber reinforcement index (Li, 1992):

$$\tau_b = f(s) \qquad [4.1a]$$

$$s = g\tau_f\left(\frac{L_f}{d_f}\right) \qquad [4.1b]$$

where,

τ_b is the fiber bridging stress

s is the reinforcement index

g is the snubbing coefficient accounting the fiber inclination (Euler friction pulley effect)

τ_f is the interface bond strength between fiber and matrix

L_f is the length of fiber

d_f is the diameter of fiber

According to Equation [4.1b], the larger the τ_f and L_f or the smaller the d_f, the higher is the reinforcing effect. In terms of bond performance, L_f may have even higher importance, in particular for large size bars. The fiber amount also has significant influence on the bond performance. The number of fiber in one unit volume composite can be calculated by the following equation (Naaman, 1972):

$$N_v = \frac{4V_f}{\pi d_f^2 L_f} \qquad [4.2]$$

where,

N_v is the number of fiber per unit volume ($\#/in^3$)
V_f is the fiber volume fraction (%)
d_f is the diameter of fiber (in.)
L_f is the length of fiber (in.)

For instance, knowing the geometry of Spectra and Torex fibers (Table 3.2), the ratio of fiber number of Spectra to Torex fiber can be obtained, assuming the same fiber volume fraction:

$$\frac{(N_v)_{Spectra}}{(N_v)_{Torex}} = \frac{\frac{4V_f}{\pi(0.0015)^2(1.5)}}{\frac{4V_f}{\pi(0.012)^2(1.2)}} = 51 \qquad [4.3]$$

That is, the number of fiber of specimens with Spectra fiber is 51 times that of specimens with Torex fiber. This large amount of Spectra fibers can effectively hinder the extension and expansion of cracks, thus leading to multiple fine cracks and better bond characteristics.

The crack patterns at larger slip of all typical specimens with various fibers are shown in Figure 4.17. Except for PVA 13 specimen, bridging was maintained at larger slip for specimens with other fibers. It is noted that conventional way to improve bond performance by using transverse reinforcement still resulted in severe damage in terms of spalling and fracturing, although bond strength was able to be raised (Figure 4.17 (h)). The matrix spalling and reinforcing bar pullout process is illustrated in Figure 4.18 for

spirally reinforced specimen. Bond failure caused by the separation of concrete cone was also observed by Viwathanatepa et al. (1979). It is seen that a relative heavy confinement using 2% spiral reinforcement cannot maintain the integrity of the specimen, which generally was not happening to specimens with fibers. In this regard, apparently, fiber reinforced concrete is easier to achieve the current performance-based design goal; that is, reduce the structural damage. Rather than splitting cracks, the failure mode in a spirally confined specimen was a cone-shaped fracture as indicated in Figure 4.18.

4.2.2.2.2 No. 8 Bar and 2% Fiber Volume Fraction

Figures 4.19 thru 4.21 give the comparison of bond behavior between 1% and 2% fiber specimens. It is noted here that at the moment that loading was applied the nut and washer may not intimately touch the setup therefore the bond stiffness of the initial portion of some curves is relatively low. This initial portion was removed for ease of comparison. PVA 13 fiber was not selected due to its relatively poor behavior. It is seen that no improvement on bond strength in specimens with steel hooked fiber by increasing fiber volume fraction from 1% to 2%. Specimens with Spectra fibers exhibited similar characteristics (see Figure 4.10). On the other hand, peak bond stresses were significantly increased by using 2% fiber volume fraction in specimens with Torex fibers. The increase is approximately 60% for square Torex (20 mm long) specimen and 40% in rectangular Torex specimen as summarized in Tables 4.2 and 4.3. It is evident that the unique fiber-to-matrix bond characteristics of Torex fiber (Section 3.2.1) can compensate for the lack of fiber amount and further enhance the ultimate bond strength. As indicated by Table 4.3, both with 2% reinforcement, specimen with square Torex fibers had 1.5 times

the bond strength of specimen with conventional transverse reinforcement. Figure 4.22 compares all specimens with 2% fiber volume fraction, as well as specimen with 2% spiral reinforcement and Figure 4.23 presents the crack patterns of corresponding specimens. Comparison between Figures 4.23 and 4.17 indicates that increasing fiber amount from 1% to 2% is able to reduce the crack width and damage at large slip.

4.2.2.2.3 Specimens with No. 5 Bar

Two types of fibers, Spectra and rectangular Torex fibers, were selected for studying the influence of smaller size bar on bond performance. It has been shown in Section 4.2.2.1.2 that, with Spectra fiber, the maximum bond stress in No. 5 bar specimens is about 1.5 times that of in No. 8 bar specimens, which is approximately the diameter ratio of No. 8 bar to No. 5 bar. The same trend was also observed in specimens with rectangular Torex fibers, as shown in Table 4.1. Figure 4.24 indicates that, increasing fiber volume fraction from 1% to 2% generally improves the bond performance in terms of peak bond stress in rectangular Torex specimens, which is consistent with No. 8 specimens. The merit using smaller bar is the damage and crack width are more limited than that of large size bar due to less height of the bar lugs. Figure 4.25 shows the crack patterns of specimens with No. 5 bar and rectangular Torex fibers. Compared with Figures 4.17 (d) and 4.23 (b), the reduced cracking width is evident.

4.2.3 Influence of Matrix Compressive Strength on Bond Behavior

As mentioned in Section 2.3, current design codes recognize that bond strength is

proportional to the square root of the concrete compressive strength, $f_c'^{1/2}$. However, ACI Committee 408 (2003) recommends using $f_c'^{1/4}$ to represent the effect of concrete compressive strength based on a large test database. For bars confined by transverse reinforcement, they found $f_c'^{3/4}$ is more suitable to represent the influence of compressive strength on bond strength. In this study, three different matrix compressive strengths were selected: 11 ksi, 7.6 ksi, and 5.9 ksi. The other factors were kept the same; that is: No. 8 bar, 2% rectangular Torex fiber. Figure 4.26 shows the three averaged monotonic pullout curves. Several observations are made. First, while the 5.9 ksi specimens had reduced bond strength, the 7.6 ksi specimens reached even higher bond strength than that of 11 ksi specimens. This may be due to the limited tested specimens or the degraded influence of matrix strength when certain matrix strength value is reached. For design purposes, however, it might be on the safe side to assume that the bond strength is proportional to the compressive strength. Second, the ascending bond moduli of 7.6 ksi and 5.9 ksi specimens (18000 psi/in) are similar but smaller than that of 11 ksi specimens (37000 psi/in). Third, the 7.6 ksi and 5.6 ksi specimens exhibited higher toughness thus dissipating more energy during the descending portion. This can be attributed to relatively weaker strength of matrix, which can form more multiple cracking and the steel-to-matrix interfaces can be more easily sheared and ground off, leading to more energy dissipation. Photos for comparison of steel-to-matrix interface taken after tests for 11 ksi and 7.6 ksi specimens are shown in Figure 4.27. It is evident that the 7.6 ksi specimen suffered more grinding. The higher energy-dissipation capacity can be also observed from the multiple cracking shown in 7.6 ksi and 5.9 ksi specimens shown in Figure 4.28, which is different from the cracking pattern of the 11 ksi specimen shown in

Figure 4.23 (b). The optimized compressive strength which maintains both high bond strength and energy-dissipation capacity needs further research.

The normalized bond strengths (bond strength of 11 ksi and 7.6 ksi specimen/ bond strength of 5.9 ksi specimen) are plotted in Figure 4.29, along with three predicted equations according to ACI codes or ACI Committee 408. It is seen that in general $f_c'^{1/4}$ can be taken as lower bound and as design basis.

Two more types of fibers described in Section 3.2, i.e. stainless triangular Torex fiber (Helix) and PVA K-II fiber, were also used in specimens with 7.6 ksi compressive strength. These two fibers have relatively lower composite tensile strength (Figure 3.3 (c)) using the adopted matrix composition. Monotonic pullout test shows that both specimens (Figure 4.30) reached approximately 75% peak bond strength of the rectangular Torex fiber specimen, when 2% fiber volume fraction was used. However, the specimens showed much severe damage as shown in Figure 4.31. Complete fracture occurred in specimen with PVA K-II fiber. It is also noted that bond moduli of all specimens are consistent.

4.2.4 Comparison of Bond Behavior between HPFRCC and SIFCON

Slurry infiltrated fiber concrete (SIFCON) is featured by infiltrating a very high steel fiber content network with fine cement slurry, which generally leads to improved mechanical properties. Bond performance of reinforcing bar embedded in SIFCON has

been reported by Hota and Naaman (1995), which used the same specimen geometry as the one tested in this study. The monotonic bond behavior of a typical SIFCON specimen with 9.7 % fiber content of steel hooked fiber was compared with specimen with steel fibers used in this study, as shown in Figure 4.32. Although the matrices have minor difference in strength, the comparison gives a general idea how the Torex fiber can enhance the overall bond behavior by using much less fiber content. It is seen from Figure 4.32, with only 2% fiber content, the Torex fiber specimens outperformed the SIFCON specimen in terms of the peak bond strength. It is also observed that, generally, the bond strength was only up to 1.3 times by using five times amount of steel hooked fibers (9.7% to 2%). The test SIFCON specimen is shown in Figure 4.33 and a comparison of the cut-open SIFCON and Torex fiber specimens is given in Figure 4.34. Figure 4.34 (a) shows that the bond interface was totally sheared and ground off, together with multiple cracking and crushing inside the specimen, signifying frictional type of pullout failure and high toughness of this composite. The square Torex fiber specimens, as shown in Figure 4.34 (b), showed minor shearing at the steel-to-matrix interface but significant multiple cracking and crushing inside the specimen. This indicates that, during the pullout process of the reinforcing bar, Torex fiber offered clamping resistance through its unique fiber-to-matrix bond characteristics, which in turn led to multiple cracking and breaking of the matrix inside the specimen.

In general, Torex fiber is able to provide superior bond performance at significantly lower fiber content than SIFCON, which is essential for practical applications.

4.2.5 Calculated Development Length

As discussed in Section 2.1.5, instead of dealing with bond stress directly, the design codes usually use the development length for the purposes of design. The required development length for tested specimens was calculated according to the ACI code (2005) and compared with the needed development length based on available bond stress obtained from experimental results. The ACI development length is calculated using Equation [2.10] and the corresponding parameters are: $\Psi_t = \Psi_e = 1.0$; $\Psi_s = 1.0$ for No. 8 bar and $\Psi_s = 0.8$ for No. 5 bar; $\lambda = 1.0$; $c_b = 3$ in.; $f_y = 65$ ksi (actual yield strength); $f_c' = 11$ ksi; $d_b = 1$ in. for No. 8 bar and $d_b = 0.625$ in. for No. 5 bar; $K_{tr} = 0$ for control specimen and $K_{tr} =$ 1.65 for spirally reinforced specimens ($A_{tr} = 0.02\ \text{in}^2$; $f_{yt} = 30$ ksi; s= 0.5 in.; n=1). Note that in both cases the $(c_b + K_{tr})/d_b$ term is larger than 2.5 (for example $(c_b + K_{tr})/d_b$ =4.65 for spirally reinforced specimens); therefore only $(c_b + K_{tr})/d_b$ =2.5 was used. This leads to a required development length equal to $18.6\,d_b$ for No. 8 bar and $14.9\,d_b$ for No. 5 bar.

It has been pointed out that (Krstulovic-Opara, Watson, and LaFave, 1994; Harajli, Hamad, and Rteil, 2005), the ductility of bond failure is significantly increased by using HPFRC composite or confined reinforcement, due to the force redistribution. This ductility allows more bar lugs to participate in resisting the bar tension force through the bond action, which in turn leads to more uniform bond stress distribution along the development length. Based on test results of beam type specimens with SIFCON, Hamza and Naaman (1992, 1996) also pointed out that bond stress distribution was more uniform for the SIFCON specimen than for plain concrete specimen. As a consequence, the

development length in specimens with fibers tested in this study was calculated assuming uniformly distributed bond stress. The expected development length is obtained by:

$$\text{Development Length} = \frac{f_y}{\left(\frac{P_{max}}{A_s L}\right)} \qquad [4.5]$$

where P_{max} is the average peak bond force (kips); A_s is bar area (in^2); L is embedded length = 4 in.; $P_{max} / A_s L$ is the uniformly developed stress per unit length in the test specimens (kips/in).

Table 4.4 summarizes the calculated development length for all specimens as well as the ACI requirement for No. 8 with 11 ksi matrix. The ACI development length, $18.6d_b$, is slightly larger than that of spirally reinforced specimen ($15d_b$). It is noted that the ACI equations (see Equations [2.10] and [2.11]) conservatively disregard the contribution of transverse reinforcement in this case: i.e. $(c_b + K_{tr})/d_b = 4.65 > 2.5$, 2.5 was used herein.

Development length in specimen with Spectra is approximately 60% of the ACI requirement, whether 1% or 2% fiber content is used. With only 1% steel fibers (Hooked, square Torex, or rectangular Torex), the development length needed is 75% to 90% of the ACI requirement. Significant reduction in development length is obtained by using 2% square Torex fiber, in which only 50% that of ACI requirement is needed. No. 5 bar specimens showed similar results as indicated in Table 4.5, where 2% rectangular Torex fiber was able to cut down the development length up to 50% of that required by ACI

code. Generally, with suitable fiber and volume fraction, the current development length specified in design codes can be reduced up to 50%.

It is interesting to note that, as has been described in Section 2.4.3, tests on SIFCON (5% steel hooked fiber) using beam type specimen indicated that only 50% the development length as required by the ACI code is needed to prevent bond failure before reinforcing yielding occurred (Hamza, 1992; Hamza and Naaman, 1996). Also, it was observed that SIFCON specimen had an increase in the average bond stress of 40% in comparing to heavily confined concrete (about 2% transverse reinforcement by volume), which is close to the observation found in this study. For instance, as shown in Table 4.3, the specimens with 2% fiber by volume (square Torex, rectangular Torex, and Spectra fibers) gave 40% to 50% higher bond stress compared to specimen with 2% spiral reinforcement.

In Hamza's tests, the maximum bond stresses recorded for beam-type SIFCON, confined concrete, and plain concrete specimens were 3.44 ksi, 2.44 ksi, and 1.35 ksi, respectively (5% steel hooked fiber, bar embedment length = 4 in., No. 8 bar, concrete cover = 1.5 in., and concrete strength = 6.2 ksi). However, pullout type SIFCON specimens (9.7% steel hooked fiber bar embedment length = 4 in., No. 8 bar, concrete cover = 3.0 in., and concrete strength = 9 ksi) gave a highest bond stress only about 1.4 ksi (Hota and Naaman, 1995), as shown in Figure 4.32. This seems to imply that the pullout type test would underestimate the bond strength for reinforcing bar embedded in HPFRC composites in a real structure.

4.2.6 Bond Modulus

Bond modulus (bond stiffness) is defined as the slope of ascending branch of the bond stress-slip responses. As indicated in Section 4.2.3, specimens with higher matrix compressive strength generally have higher bond modulus. As shown in Figure 4.26, for example, the bond modulus of rectangular Torex fiber specimen with 11 ksi matrix (No .8 bar) had a bond modulus of 37000 psi/in., while the 5.9 ksi specimen showed a bond modulus of 18000 psi/in. The ratio of bond modulus between 11 ksi and 5.9 ksi specimens (2.0) is generally equal to the ratio of matrix compressive strength (1.9).

Comparison between Figures 4.20 and 4.24 indicates that, while the fiber volume fraction has no influence on the bond modulus, the bond modulus is smaller for specimens with smaller diameter bars. For example, No. 5 bar specimen with rectangular Torex fiber (11 ksi matrix) had a bond modulus approximately equal to 24000 psi/in., while the No. 8 specimen showed much higher bond modulus (37000 psi/in.). The lower bond modulus of smaller diameter bar specimen can be attributed to the confinement effect (see Section 4.2.2.1.2). It is also observed that the ratio of bond moduli between No. 8 and No. 5 bar specimens (1.54:1) is generally equal to the ratio of bar diameter between No. 5 and No. 8 bars (1.6: 1).

It suffices to say, therefore, the bond modulus is proportional to the product of matrix compressive strength and bar diameter, i.e., bond modulus $\propto \left(f_c' \cdot d_b\right)$.

4.2.7 Pullout Work

Monotonic pullout work (up to complete failure) for all tested specimens is listed in Table 4.6. Several observations can be made:

1. Fiber reinforced specimens exhibited much higher pullout work than the control specimens. For example, the pullout work of specimen with Spectra fiber (11 ksi matrix strength, No. 8 bar), i.e., 8830 lb-in., is approximately 30 times that of the control specimen (290 lb-in.).

2. Pullout work was increased up to 60% by increasing the fiber volume fraction from 1% to 2% for Torex fiber having an aspect ratio of 100, while no pullout work increase was observed for specimens with Torex fiber having an aspect ratio of 67.

3. With same steel reinforcement content (2% steel fiber or spiral steel), the pullout work of fiber reinforced specimens are 1.2~1.6 times of the spirally reinforced specimen.

4. Specimens with smaller size bars showed higher pullout work than the larger size bar specimens if the bond failure mode is separation type (e.g. rectangular Torex fiber specimen with 11 ksi matrix); on the other hand, specimens with smaller size bars showed lower pullout work than the larger size bar specimens if the bond failure mode is friction type (e.g. Spectra fiber specimen with 11 ksi matrix).

5. Specimens exhibited friction type bond failure generally showed much higher pullout work than the specimens with separation type bond failure. For example, 2% rectangular Torex fiber specimen having 11 ksi matrix strength (No. 8 bar) showed separation type failure (see Figure 4.23 (b)), it had a monotonic pullout work equal to 5310 lb-in. The pullout work was raised to 9300 lb-in. while a lower strength matrix (7.6 ksi) was used and a friction type bond failure occurred (see Figure 4.28 (a)). This pullout work is even higher than that of Spectra specimen (8830 lb-in.). It is evident again that a suitable tailoring of matrix strength is essential for the bond performance of HPFRC composites

4.3 Unidirectional Displacement-Controlled Cyclic Loading

This type of loading was used to investigate the bond strength as well as stiffness retention capacity under half cyclic loading up to large slip. The monotonic bond load-slip curve is the upper bound curve for this type of loading (Balaguru, Gambarova, Rosati, and Schumn, 1996). The cyclic curve may be under this governing curve due to gradually crushing of matrix or crack-opening. The loading protocol shown in Figure 3.15 (c) was used for prestressing strand specimens only and a slightly different loading protocol used by Hota and Naaman (1995) was adopted for reinforcing bar specimens and described as follows.

Specimens tested under this type of loading were subjected to half cycle at each displacement level. The specimen was first loaded to 50% of its estimated maximum

bond strength (obtained from the monotonic bond load-slip curve), the displacement was recorded and then the specimen was unloaded to zero load. Next, the specimen was loaded to maximum capacity; corresponding displacement identified here as peak displacement was monitored and recorded, and the specimen was unloaded again. From this step on, the test was under displacement control. The specimen was loaded up to 1.5 times the peak displacement previously recorded. After unloading, the specimen was loaded up to 2 times the peak displacement and unloading occurred. This procedure was performed with incremental displacement equal to half the peak displacement until the residual displacement (after unloading) reached about 1.0 inch (e.g. fiber reinforced specimen), or until total failure occurred (e.g. control specimen). The loading protocol is schematically shown in Figure 4.35. Bond degradation under this type loading was observed.

4.3.1 Specimens with No. 8 Bar

Four types of reinforcement were selected for specimens under the unidirectional displacement controlled loading: Spectra, rectangular Torex, square Torex, and spiral reinforcement.

Test result for control specimen is shown in Figure 4.36, in which the monotonic curve is also plotted. The load-slip curve does not match the monotonic curve due to the crack pattern shown in the accompanying figure. Through cracks formed in both 1-1 and 2-2 directions, therefore some confinement was provided by the test fixture. This is evident by the second peak of the unidirectional load-slip curve. Nevertheless, the

degradation of bond had the same trend compared to the monotonic curve. Bond stiffness of loading and unloading paths are almost identical and minor deterioration in stiffness was observed at slip level beyond 0.2 inch.

Figures 4.37 and 4.38 give the unidirectional load-slip curves for specimens with 1% and 2% Spectra fibers, respectively. As can be seen, the monotonic envelopes generally govern the cyclic responses. The loading and unloading paths of each cycle have almost the same stiffness without noticeable degradation. Minor stiffness degradation was observed in the 1% fiber specimen at very large slip level. Some deterioration in bond strength in comparison with the monotonic curve was observed beyond the peak bond strength. Results of specimens with rectangular Torex fibers are shown in Figures 4.39 and 4.40, while Figures 4.41 and 4.42 present the load-slip curves of specimens with square Torex fibers. It is seen that both the stiffness and strength capacities are slightly superior to that of Spectra fiber specimens. Specimen with 2% volumetric steel spiral reinforcement exhibited degraded bond stiffness and strength under cyclic displacement, as indicated by Figure 4.43.

Figures 4.44 and 4.45 show the tested specimens with 1% and 2% fiber volume fractions, respectively. As can be seen, both 1% and 2% Spectra fiber specimens exhibited multiple cracks and the wider cracks formed in the 1% Spectra specimen only. Severe spalling occurred in spirally reinforced specimen, leading to the degradation in bond stiffness and strength. In general, specimens with either Spectra or Torex fiber outperformed specimen with conventional transverse reinforcement when subjected to unidirectional displacement type loading, in terms of bond stiffness retention and the

damage control capacity.

4.3.2 Specimens with No. 5 Bar

Two types of fibers were selected: Spectra and rectangular Torex. Figure 4.46 gives the test result of control specimen, in which the load-slip curve matches the monotonic curve quite well. Since the through cracks formed in the 1-1 direction only (see the accompanying figure), therefore no confinement was provided by the test fixture. The degradation of bond strength had the same trend observed in the monotonic tests. Evident stiffness degradation was observed at slip beyond 0.1 inch.

Figures 4.47 and 4.48 give the unidirectional load-slip curves for specimens with 1% and 2% Spectra fibers, respectively. Similar to the No. 8 specimens, the monotonic envelopes generally govern the cyclic responses. The loading and unloading paths of each cycle have almost the same stiffness without noticeable degradation. Some deterioration in bond strength occurred beyond the peak bond strength. The cracking patterns of these two specimens are shown in Figures 4.50 (a) and 4.50 (b), where only very narrow multiple cracks are present. Results of specimens with 1% rectangular Torex fibers are shown in Figure 4.49 while test data for 2% fiber is not available. A more significant degradation in bond stiffness was noticed in this specimen. This resulted from wider crack formed after cyclic displacement as shown in Figure 4.50 (c). The damage is more severe compared with specimen subjected to monotonic loading (Figure 4.25 (a)).

4.4 Unidirectional Force-Controlled Cyclic Loading

This type of loading was employed to investigate the bond strength as well as stiffness retention capacity under repeat cyclic forces. The cyclic response is very likely to lead to increasing residual slip as more cycles are applied. This occurs because the reinforcing bar faces a more and more crushed matrix and gradually extended cracks. Fibers or steel spiral were used to delay this process and the effectiveness of these reinforcements was the major investigation. Specimens tested under this type of loading were subjected to three to five cycles at each pre-selected force level, as shown in Figure 3.15 (a). The specimen was first loaded to 50% of its estimated peak load (obtained from the monotonic envelope curve) and unloaded to zero load, this loading continues for three cycles. Next, the specimen was loaded to 65% of its estimated peak load and unloaded to zero load for another three cycles. Five additional cycles were applied to the specimen to 80% of its estimated peak load. Then the specimen was subjected to higher load (to 90% or higher its estimated peak load) if the strength did not degrade. The cyclic test was stopped when the strength had dropped to approximately 50% to 60% of its measured peak load or more than 18 cycles had been applied. Then the reinforcing bar was monotonically pulled out. Bond strength and stiffness deterioration and corresponding residual slip under this type loading were studied. Only fiber or spirally reinforced specimens were tested under this type loading.

4.4.1 Specimens with No. 8 Bar

Five types of reinforcement were selected for specimens under the unidirectional

force controlled loading: Spectra, rectangular Torex, square Torex (20 mm), square Torex (30 mm), and spiral reinforcement.

4.4.1.1 Specimens with Spectra Fiber

A total of 11 cycles were applied for the 1% fiber content specimen before excessive drop of bond strength was observed. Then the specimen was loaded until the reinforcing bar was pulled out. The loading sequence was applied according to the pre-selected loading protocol (Figure 3.15 (a)); i.e., 50%, 65%, 80%, 90% the target load (monotonic peak bond load)). However, some fluctuation might occur during test and the actual applied load had minor difference with the pre-selected ones as revealed by Figure 4.51. As can be seen in Figure 4.52, if the average bond stress is less than about 70% of the bond strength obtained from the monotonic bond-slip curve, no bond strength and stiffness degradation were observed when repeated cycles were performed at the same stress level. Below this stress, residual slip was quite small and less than 0.03 inch. The first visible crack was observed at the 4th cycle. When the bond stress (1170 psi) approaches 80% of the monotonic bond strength, specimen was still able to sustain four cycles with no strength and stiffness degradation (Figure 4.52 (b)); however, more significant residual slip occurred. Unlike the unidirectional displacement controlled loading (one cycle only for each load level, Figure 4.37), the ultimate load (14745 lbs) is well below the estimated ultimate load (18850 lbs) obtained from the monotonic curve. That is, only 78% of the monotonic peak load can be achieved. The bond performance is summarized in Table 4.7.

For the 2% Spectra fiber specimen, a total of 18 cycles were performed before significant drop of bond strength was observed. Then the specimen was loaded until the bar was pulled out. The actual loading sequence is shown in Figure 4.53. Figure 4.54 shows that, if the average bond stress is less than about 90% of the bond strength obtained from the monotonic bond-slip curve, no bond strength and stiffness degradation occurred when repeated cycles are performed at the same stress level. This is better than the (70%) level for specimen with 1% Spectra fibers. Below this stress, residual slip was quite small. The first visible crack was observed at the 4th cycle. When the bond stress (1425 psi) approached 95% of the monotonic bond strength, specimen was still able to sustain two cycles without strength and stiffness degradation (Figure 4.54 (b)); however, significant residual slip occurred. The peak load (19324 lbs) was less than the estimated monotonic peak load (19650 lbs), but the difference is smaller than that for the specimen with 1% fiber content. That is, 98% of the monotonic peak load can be achieved if 2% fiber by volume was added. Note that the residual slip is only 0.09 in. after 18 cycles, whereas the residual slip is 0.18 in. after 11 cycles for 1% fiber content specimen. Comparison between Figure 4.52 (b) and 4.54 (b) indicates that specimen with 2% volume fraction Spectra can sustain more cycles and higher bond stress level and with less residual slip than 1% fiber content specimen.

4.4.1.2 Specimens with Torex Fiber

Figures 4.55 thru 4.59 give the results for specimens with Torex (rectangular and square) fibers and the detailed bond characteristics are summarized in Table 4.7. Several observations can be made based on those figures:

1. In general, with same fiber volume fraction, specimens with Torex fibers exhibited smaller residual slip than specimens with Spectra fiber when subjected to same bond stress level. It is noted that in some specimens, e.g. Figure 4.59, the initial slip is quite large due to the less contact of the nut or washer to the test setup, which should be ignored.

2. Specimens with Torex fibers generally were able to sustain more cycles and higher bond stress level than specimens with Spectra fibers before excessive residual slip or bond strength drop occurred; e.g. Figures 4.54 (b) and 4.56 (b).

3. Specimens with 2% Torex fiber by volume were able to reach 1.5 times the bond stress of specimens with 1% Torex fiber content under unidirectional force controlled cyclic loading.

4. The first (visible) cracks formed generally were at much later stage of cycles in Torex fiber specimens.

5. With same fiber contents, specimens with Torex fibers were able to achieve or exceed the bond stress level that Spectra fiber specimens could reach, even though the fiber number of Spectra specimen is 51 times that of the Torex specimens (see Section 4.2.2.2). This observation is important for practical purposes since Torex fibers are much easier to mix with concrete matrix than Spectra fiber.

4.4.1.3 Specimens with Spiral Reinforcement

The cyclic bond performance of specimen with conventional spiral reinforcement ($\rho_s = 2\%$) was inferior to specimens with either Spectra or Torex fibers. As can be seen in Figure 4.60, the bond stress level reached is generally smaller (approximately 60% that of 2% fiber content specimens) and the residual slip is larger. The bond stiffness of spirally reinforced specimen degraded considerably after 10 cycles while bond stiffness was able to be maintained for much more cycles for specimens with fibers (e.g. Figure 4.56 (b)). Once again, it is evident that HPFRC composites give better bond responses than conventional reinforced concrete confined by transverse reinforcement.

Cracks patterns of selected specimens with fibers are shown in Figure 4.61. Multiple cracks were observed on the surface of the Spectra fiber specimen (Figures 4.61 (a) and 4.61 (b)). It is noted that a very wide crack about 4.3 mm in width formed and extended throughout the specimen depth in 1% fiber content specimen; however, the fiber bridging capacity maintained the integrity of the specimen. A small fractured cone-shaped piece eventually formed at the pullout end of the reinforcing bar at large slip (Figure 4.61 (a)). On the contrary, addition of fibers up to 2% can effectively prevent the cracks from opening for specimen with Spectra fibers. Moreover, no cone shape formation was observed (Figure 4.61 (b)). Visible multiple cracking was not observed (even with a magnifier) on the surfaces of Torex specimens. However the integrity of the specimens was maintained by the fiber bridging effect. Figure 4.62 illustrates the damage of the spirally reinforced specimen under cycle loading. The cone-shaped fracture was first noticed at 9th cycle and became obvious at 10th cycle as shown in Figure 4.62 (a). Severe spalling and fracturing shown in Figures 4.62 (b) and 4.62 (c) contributed to the poor bond performance.

4.4.2 Specimens with No. 5 Bar

Two types of fibers were selected for No. 5 bar specimens: Spectra and rectangular Torex fibers. The test results are shown in Figures 4.63 thru 4.66 and summarized in Table 4.8. The findings observed for No. 8 bar specimens generally can be applied to No. 5 bar specimens; for instance, the 2% fiber specimens outperformed the 1% fiber specimen in terms of reached peak bond stress and smaller residual slip at same bond stress level. For instance, it is noted that for specimens with Spectra fibers the residual slip of 1% fiber content specimen subjected to 11 cycles was about 0.21 in., whereas the residual slip was only 0.06 in. for 2% fiber content specimen subjected to the same number of cycles. Also, the first crack formed in Spectra fiber specimens were generally earlier than that in Torex fiber specimens.

Compared with No. 8 bar specimens, the peak bond stress is approximately 1.3~1.5 times in No. 5 bar specimens (see Tables 4.7 and 4.8), which is close to the ratio for monotonic bond strength as indicated in Table 4.1. However, the peak bond stress level reached (percentage of peak monotonic bond load) in No. 5 bar specimens is generally slightly smaller than that of No. 8 bar specimens (see column **c** of Tables 4.7 and 4.8). This may be attributed to higher bond stress experienced by smaller bar under same number of cycles.

The crack patterns of the test specimens are presented in Figure 4.67, which resemble the one of No. 8 specimens. The only differences are that no cone-shaped fracture was observed in Spectra fiber specimens and the crack widths were smaller.

4.5 Fully Reversed Force-Controlled Cyclic Loading

Fully reversed cyclic loading was used to simulate the situation in which the reinforcing steel is subjected to two-directional cyclic reversal, such as seismic forces. Bond deterioration usually occurs in reinforcing bars of concrete members when subjected to fully reversed cyclic loading, even when substantial confinement reinforcement is present (Viawathanatepa, Popov, and Bertero, 1979). This is due to concrete crushing and the formation of splitting cracks originating from the lugs of the reinforcing bars caused by high bearing stresses. An example of reinforcing bar subjected to this type loading is reinforcing bars located in a seismic beam-column joint. As mentioned in Section 1.1, very high bond stresses can occur when a bar yields after plastic hinge forms at beam end, which could lead to damage of bond and thus excessive slip of beam bars. Slippage of reinforcing bars would increase the rotations at column faces and thus the lateral displacement of the frame which in turns increases the potential dynamic instability of the frame due to $P-\Delta$ effect. Besides, analysis has shown that the energy dissipation capacity of a beam-column joint would decrease by 30%, if a 15% reduction in bond strength along a bar occurs (Filippou, Popov, and Bertero, 1983).

Leon (1989) has suggested a length of 28 bar diameters to insure that bond can maintain its efficiency during severe seismic loading for the anchorage of a straight bar in a seismic interior beam-column joint; however, a very large joint would result by using anchorage length such as 28 bar diameters (ACI-ASCE, 2002). As a consequence, the ACI Provisions specify a minimum anchorage length which generally cannot prevent deterioration of bond resistance during a major earthquake.

The required anchorage length can be obtained by using Equation [2.12] and assuming d_b is 1.0 in. (i.e. No. 8 bar) with a nominal yield strength equal to 60 ksi and 11 ksi concrete compressive strength:

$$l_d \geq 20d_b = 20(1.0) = 20 \text{ in.} \qquad [4.6]$$

This gives a required l_d equal to 20 in. For the purposes of evaluating the bond test results, an equivalent bond stress based on the above anchorage length was calculated assuming bar stress decreasing from yielding stress to zero stress along the joint. It should be noted that the real stress distribution in a beam-column joint may be more complicated after beam yielding as shown in Figure 1.4. Also, the anchorage length provisions in the ACI code are not based on equivalent bond stress.

The maximum allowed bond stress in a beam-column joint can be calculated by:

$$\sigma_{bond} \leq \frac{P}{\pi d_b l_d} = \frac{\alpha A_s f_y}{\pi d_b l_d} = \frac{(1.25)(0.79)(60{,}000)}{(\pi)(1)(20)} = 940 \text{ psi} \qquad [4.7]$$

which means the average bond stress along the No. 8 bar should not be larger than 940 psi to limit slippage of reinforcing bar. Note the α value accounts for material overstrength and strain hardening in the rebar which gives a more realistic bar stress value. If No. 5 bar and 11 ksi concrete are used, the maximum allowed bond stress would also be 950 psi (l_d=12.5 in.) according to Equations [4.6] and [4.7].

Because the required anchorage length can be translated into equivalent bond stress, and the maximum expected bar stress (including the material and strain-hardening effect) after beam yielding is close to constant and known, it is evident that a force controlled cyclic loading test is more appropriate for reinforcing bar subjected to seismic loading. As a consequence, the fully reversed cyclic loading employed in this study was force controlled and the loading protocol is shown in Figure 3.15 (b). Specimens subjected to this type of loading were tested with three to five cycles at each pre-selected force level. The specimen was first loaded to 50% of its estimated ultimate strength (obtained from the monotonic envelope curve) in two directions for three cycles. Next, the specimen was loaded to 65% its estimated ultimate strength for another three cycles. Another five cycles were applied to the specimen with 80% of its estimated ultimate strength. The specimen was subjected to more cycles (to 90% its estimated ultimate strength and so on) if the strength did not degrade. Two or three more cycles were applied to the test specimens after bond strength started dropping in order to observe the degradation rate of bond. The cyclic test was stopped when the bond strength completely lost, then the reinforcing bar was monotonically pulled out. The pull-pull loading method (Figure 3.13 Position 3) was used in this series of tests to simulate the demands from seismic excitations. Bond strength and stiffness deterioration and corresponding residual slip were evaluated.

4.5.1 Specimens with No. 8 Bar and 11 ksi Matrix

Control specimen with no reinforcement was first tested under the fully reversed force controlled cyclic loading. Then seven types of reinforcement were selected for other specimens under the same loading protocol: Spectra fiber, rectangular Torex fiber, square

Torex (20 mm) fiber, square Torex fiber (30 mm), steel hooked fiber, PVA 13 fiber, and spiral reinforcement.

4.5.1.1 Control Specimen

A total of 9 cycles were performed before excessive drop of bond strength was observed, and then the specimen was loaded monotonically until the bar pulled out. The recorded loading history and reversed cyclic load-slip curve are shown in Figures 4.68 and 4.69, respectively. As discussed earlier, the bond behavior of control specimen is highly dependent on its crack pattern. Due to the crack pattern shown in Figure 4.69 the bond strength increased during final monotonic pull out. The first visible crack formed at the 4th cycle and corresponding bond characteristics are listed in Table 4.9. It is noted that, in Table 4.9, column **b** gives the bond tress at which only minor strength, stiffness and residual slip occur (approximately less than 0.05 in.). This bond stress is used to be compared with the standard value (940 psi) obtained from Equation [4.7].

4.5.1.2 Specimen with Spectra Fiber

A total of 11 cycles were performed for both specimens with 1% and 2% fiber contents. After significant bond deterioration the specimen was monotonically loaded until the bar pulled out. The recorded loading histories for 1% and 2% specimens are illustrated in Figures 4.70 and 4.72, respectively. As shown by Figure 4.71 and Table 4.9, for 1% fiber content specimen, if the average bond stress is less than 70% (bond stress about 1050 psi, in both directions) of the peak monotonic bond strength, no bond strength

and stiffness deterioration were observed in both loading directions. Below this stress, the residual slip was quite small (less than 0.025 in.). When the bond stress reached 1200 psi (80% its peak monotonic bond strength), significant bond strength decay and pinching in the load-slip occurred. It is worth mentioning that once the bond strength started dropping in one direction, the bond strength in the other direction did not maintain the same magnitude even within the same cycle as shown in Figure 4.71. This is due to the interaction of cracks originated from both directions, which are elaborated later on in Section 4.5.3. The bond strength dropped 20% when slip reached 0.1 in, which is the slip for maximum bond stress of the monotonic loading curve. The first observed crack formed at the 4th cycle.

A similar bond performance was observed in specimen with 2% Spectra fiber. However, due to the increase in fiber content, the average bond stress reached at which no bond strength and stiffness degradation, as well as minor residual slip was 82% (i.e., 1290 psi, in both directions) of its peak monotonic bond strength as shown in Figure 4.73 (a). The first observed crack formed at the 7th cycle. It is seen that by adding 1% more fiber volume fraction, the cracking was delayed and 20% higher bond stress was reached. In general, addition of Spectra fiber can achieve 115% ~ 140% the required bond strength (i.e. 940 psi based on Equation [4.7]) for preventing bond deterioration under fully reversed cyclic loading.

4.5.1.3 Specimen with Torex Fiber

Figures 4.74 and 4.75 give the cyclic responses of specimens with 1% and 2%

rectangular fibers, respectively. It has been shown in Figure 4.15 that, generally, specimen with Torex fiber exhibited lower bond strength than Spectra fiber if only 1% fiber by volume was added, which is directly attributable to the number of fibers as explained in Section 4.2.2.2.1. Figures 4.74 (also see Table 4.9) indicates that the bond stress (890 psi) at which no stiffness and strength degradation in conjunction with minor residual slip for 1% rectangular Torex specimen is much smaller than that of 1% Spectra fiber specimen. This bond stress was increased 25% (up to 1110 psi) by using 2% rectangular Torex fiber as shown in Figure 4.75. Note that the maximum achieved bond stress in 2% rectangular Torex fiber specimen (1470 psi) is about 15% higher than that (1290 psi) of 2% Spectra fiber specimen. It is also noted that more cycles were able to be performed in 2% rectangular Torex fiber specimen (23 cycles).

Specimen with 1% square Torex (30 mm long, the same with rectangular Torex fiber) was also tested to investigate the influence of cross-sectional shape. Comparison between Figures 4.74 and 4.76 indicates that the performance of square Torex fiber was slightly better than rectangular Torex fiber in terms of bond strength, which has also been shown for monotonic loading in Table 4.2. As mathematically validated by Sujivorakul (2002), Torex fiber with square cross-sectional shape has highest untwisted plastic torque compared with other shapes. For instance, with same equivalent diameter, the plastic torque ratio of square Torex fiber, equilateral triangular Torex fiber, and rectangular Torex fiber (assuming width-to-height ratio is 3.0, which is approximately equal to the one used in this study, see Figure 3.1 (b)) is 1.4: 1.2: 1.0, respectively. Note the slightly higher tensile strength (about 8% higher, see Table 3.2) of square Torex fiber than the rectangular Torex fiber may also contribute to the higher bond strength.

Specimens with 20 mm long square Torex fiber were tested to evaluate the influence of aspect ratio (length/diameter) on bond performance under fully reversed cyclic loading. A trade-off is made by reducing the aspect ratio of fiber to increase the number of fiber, if the fiber volume fraction is the same. It is observed from Figures 4.76 and 4.77, however, reducing the fiber aspect ratio from 100 (30 mm long) to 67 (20 mm long) led to substantially inferior bond performance if only 1% fiber by volume was used. The bond strength of specimen using 20 mm long square Torex fiber is only 65% that of specimen with 30 mm long square Torex. This arises from the shorter pullout length of the fiber; that is, 5 mm (1/4 the fiber length based from probability considerations; Naaman, 1972; Hannant, 1978). Longer fiber pullout length becomes critical especially for large size reinforcing bar, which generally results in wider cracks during pullout. However, this defect can be compensated by increase the fiber volume up to 2% as shown in Figure 4.78. The bond stress at which no bond deterioration occurred increased 115% compared to 1% fiber specimen. The maximum bond stress reached (1490 psi) in 2% square Torex (20 mm) specimen is the highest one among all specimens. A total of 20 fully reversed cycles were performed which is comparable to specimen with 2% rectangular Torex fiber (Table 4.9).

Due to the promising performance of specimen with 2% square Torex fiber (20 mm), another identical specimen was tested under constant force cyclic loading to investigate the low cycle fatigue capacity. Based on the observation from previous specimen, a very high bond stress of 1350 psi (90% the peak monotonic bond strength) was selected. It was observed that no stiffness and strength deterioration, nor significant residual slip occurred below this stress level based on the previous test result. The extra test was

conducted under fully reversed cyclic loading at this stress level until bond strength dropped. Note this loading history was much severe than the one used for previous specimen. As can be seen in Figure 4.79, this specimen was able to sustain 25 cycles without strength decay.

In general, specimens with Torex fibers exhibited superior bond strength to Spectra fiber specimens under fully reversed cyclic loading and enhanced performance is able to be achieved by tailoring the geometry of Torex fibers. It is also noticed that specimens with Torex fiber sustained more load cycles and the cracking generally occurred at later stage. Further, the cyclic residual slip usually is much small in specimens with steel (Torex, hooked) fibers than other fibers, such as Spectra fiber, as shown in Figures 4.73 (b), 4.75 (b), 4.78 (b), 4.79 (b), and 4.81 (b).

4.5.1.4 Specimens with Other Fibers and Reinforcement

The cyclic responses of specimens with hooked fiber, PVA 13 fiber, and 2% volumetric spiral reinforcement are shown in Figures 4.80 thru 4.83. The bond performance of PVA 13 fiber specimen was relatively poor due to inability of this fiber to prevent complete separation of the specimen (due to fiber fractured), therefore very low bond strength was obtained (510 psi). Specimen with 1% hooked fiber also showed inferior bond performance in terms of bond strength as indicted by Table 4.9 and Figure 4.80. However, the bond strength was increased 80% (from 645 psi to 1190 psi) by using 2% hooked fiber (Figure 4.81). Bond strength of spirally reinforced specimen (Figure 4.83) was comparable to 2% hooked fiber specimen; both of them reached 80% of the

bond strength of 2% square Torex fiber (20 mm) specimen.

Figure 4.84 and Table 4.9 give the cumulative dissipated energy through all cycles for all specimens. It is noted that a direct comparison cannot be made among all specimens because each specimen experienced different loading histories in terms of stress level and number of cycles. However, this plot gives a general idea which fiber and what fiber content are beneficial to the bond performance under fully reversed cyclic loading. For example, specimen with 2% square Torex fiber (20 mm, 2% ST20 in Figure 4.84) was able to dissipate 22 times the energy that control specimen did and 2.5 times that the spirally reinforced specimen did.

The crack patterns in specimens with various fibers or reinforcement are shown in Figures 4.85 and 4.86. As can be seen, in general, specimens with only 1% fiber by volume showed much wider cracks. In contrast, using 2% fiber content was able to prevent cracks from opening thus dissipate more energy through shearing and crushing the rebar-to-matrix interface. Also, it is evident from Figure 4.85 (b) that the bridging effect of PVA 13 fiber is poor. Multiple radial cracks were noticed in specimens with 1% Spectra, 2% Spectra, and 2% square Torex (20 mm) fibers. Figure 4.87 presents the failure sequence of specimen with 2% volumetric spiral reinforcement. Transverse reinforcement was able to increase the bond strength but cannot prevent spalling and cone-shaped fracture in both directions. In contrast to specimen with fibers, this specimen suffered very severe damage after test as shown in Figures 4.87 (10) and 4.87 (11).

4.5.2 Specimens with No. 8 Bar and Lower Strength Matrix

The effect of different matrix compressive strengths on cyclic bond strength was investigated by using two more matrices: 7.6 ksi and 5.9 ksi. Three types of fibers were selected for the test specimens: rectangular Torex fiber, Helix fiber, and PVA K-II fiber. All specimens had fibers with 2% volume fraction. The cyclic bond responses of 7.6 ksi specimens are shown in Figures 4.88 to 4.90, while Figure 4.93 gives the response of 5.9 ksi specimen. Figure 4.91 highlights the cumulative dissipated energy of all 7.6 ksi specimens. Several observations can be made according to the test results:

1. Based on test results of 2% rectangular Torex fiber specimens with different compressive strength matrices, as summarized in Tables 4.9, 4.10, and 4.11 (Column **b**), the bond strength ratio for 11 ksi, 7.6 ksi, and 5.9 ksi specimens are 1.15: 1.14: 1.00. This ratio generally agrees with the matrix strength ratio in terms of $f_c'^{1/4}$; that is, 1.17: 1.10: 1.0.

2. Specimen with rectangular Torex fiber outperformed the Helix and PVA K-II fiber specimens in terms of bond strength. Although it showed lower bond strength, the Helix fiber specimen exhibited multiple cracking and small crack width as shown in Figure 4.92 (b). The PVA K-II specimen failed due to complete fracture as shown in Figure 4.92 (c).

3. Although the 7.6 ksi specimen showed less bond strength than the 11 ksi specimen

(2% rectangular Torex specimens), the 7.6 ksi specimens exhibited more multiple cracking and the crack width was much smaller (Figure 4.92 (a)) than the 11 ksi specimens (Figure 4.86 (b)). Also, extensive shearing and grinding were observed in the rebar-to-matrix interface of the 7.6 ksi specimen than the 11 ksi specimen as can be seen in Figures 4.92 (d) and 4.92 (e). This can be attributed to the lower matrix strength and the smaller crack width formed in the 7.6 ksi specimen. Since the crack width was small, the only way for bar pullout is to shear off the matrix surrounding the bar lugs. Multiple cracking was also observed in 5.9 ksi specimen, as shown in Figure 4.94.

According to the above observations, as well as the crack patterns under monotonic loading (e.g. Figure 4.28), it is evident that matrix strength is one of the key factor for the formation of multiple cracking. This could be directly attributable to the effect of matrix toughness. It has been pointed out by Li et al. (Li, 1998; Li, Wang, and Wu, 2001) that, other factors being equal, a saturated multiple cracking can be developed if the matrix toughness (J_c) is small. In general, matrix toughness decreases if matrix compressive strength decreases. On the other hand, low matrix toughness gives low first crack strength which is undesirable for normal service loads. Also, it is observed from this study that low matrix strength leads to low bond strength. As a consequence, material tailoring is imperative for achieving high bond strength along with multiple cracking, thus a trade-off between matrix strength and bond strength needs to be made to achieve the optimum material design.

Based on the experimental results obtained from this study, the optimized material

combination for achieving both high bond strength and multiple cracking under monotonic or cyclic loading could be: (a) 1% to 2% Spectra fiber; matrix strength is flexible, or (b) 2% Torex fiber; matrix strength of about 8 ksi.

4.5.3 Specimens with No. 5 Bar and 11 ksi Matrix

In addition to the control specimen with no reinforcement, two types of fibers were selected for specimens with No. 5 bar: Spectra and rectangular Torex fibers. Figures 4.95 thru 4.100 (a) provide their cyclic bond stress-slip responses.

A total of 8 cycles were performed for the control specimen until excessive drop of bond strength was observed. Then the specimen was loaded until the bar was pulled out. The reversed cyclic load-slip curve is given in Figure 4.95. As discussed earlier, the bond stress of control specimen is highly dependent on its crack pattern as shown by the accompanying photo in Figure 4.95. In general, the load-slip curve was not altered until large slip. As Figure 4.95 and Table 4.12 indicate, the control specimen only sustained a few reversals with small stress, and then the bond strength deteriorated rapidly at the time cracking occurred. The first visible crack formed at the 4th cycle.

Bond stresses reached 1480 psi and 1580 psi for 1% and 2% Spectra fiber specimens, respectively, with no strength and stiffness degradation in both loading directions. Very minor residual slips were observed. Significant bond strength decay and pinching in the load-slip curves were observed when the bond stresses were beyond 1820 psi and 1960 psi for 1% and 2% Spectra fiber specimens, respectively. The bond stresses had dropped

80% when the slip reached approximately 0.2 in. for both specimens, which was the slip of peak bond stress on the monotonic loading curve. Referring to Figures 4.98, 4.99, and Table 4.12, the peak bond stress under fully reversed cyclic loading for rectangular Torex fiber specimens were 87% that of Spectra fiber specimens.

It is seen by comparing Tables 4.8 and 4.12 that, No. 5 bar specimens sustained higher bond stress than No. 8 bar specimens. Except for 2% rectangular Torex fiber specimen, the peak bond stress ratio of No. 5 bar to No. 8 bar specimens is 1.5~1.6, which agrees with the bar diameter ratio of No. 8 bar to No. 5 bar (1.6).

An extra 1% rectangular Torex specimen was tested under constant force cyclic loading to investigate the low cycle fatigue behavior. Based on the observation from previous specimen, a bond stress of 1430 psi (80% the peak monotonic bond strength) was selected. It was observed that no stiffness and strength deterioration, nor significant residual slip occurred below this stress level as indicated by Figure 4.98. The extra test was conducted under fully reversed cyclic loading at this stress level until bond strength dropped. As noted earlier, loading history for this extra specimen was much severe than the one used for previous specimen. Test result in Figure 4.100 (a) shows that, no bond stress deterioration occurred until the 38th cycle, during which opened crack was observed as highlighted in Figure 4.100 (b). The cumulative energy dissipated by the specimens with various fibers under fully reverse cyclic loading is shown in Figure 4.101, which indicates that specimens with fibers were able to dissipated 14~25 times the energy of the control specimen.

The failure mechanism of fiber reinforced specimens tested in this study under fully reversed cyclic loading is directly related to the crack interaction, which is illustrated using the No. 5 bar specimen with 1% Spectra fiber as shown in Figure 4.102 and explained as follows. Figure 4.102 (a) shows that, the initial cracks that developed from the top and bottom surfaces generally started at the location where the bar comes out of the specimen, when the reversed cyclic loading was applied. Due to the presence of fibers, the crack opening and propagation were hindered, thereby leading to stress redistribution and multiple cracking as shown in Figure 4.102 (b). The first visible crack formed at the 4th cycle. Prior to the 10th cycle, cracks originating from top and bottom had not connected. However, many cracks connected at the middle of the specimen depth after the 10th cycle as indicated by Figure 4.102 (e). Once a connected crack (on any side of the specimen) formed, the bond stress drops very fast, as observed in the load-slip curve in Figure 4.96.

The crack patterns for test specimens are shown in Figure 4.103. As can be seen, contrast to No. 8 specimens (Figure 4.86), specimens with No. 5 bar exhibited finer cracks. It is also noticed that multiple radial cracks formed in specimens with Spectra fiber.

In conclusion, specimens with 2% fibers (such as Spectra, Torex, and hooked fibers) or 2% volumetric spiral reinforcement met the bond stress requirement according to Equation [4.7]; some specimens were able to reach 1.6 times the required bond stress (such as specimen with 2% square Torex fiber) with no deterioration in bond stiffness and strength, as well as with very minor residual slip.

4.6 Bond Mechanism for Reinforcing Bar embedded in HPFRC Composites

4.6.1 Bond Mechanism of Conventional Concrete

As mentioned in Section 1.2.1, forces in a reinforcing bar are transferred to the concrete primarily by radial forces, which lead to circumferential internal tensile stress in the concrete as shown in Figure 1.6. If a large size bar is used, the relatively thin cover of concrete tends to fracture and results in a splitting type failure (Figure 4.104 (a)). On the other hand, if the concrete cover is thick enough or a small size bar is used, the reinforcing bar tends to be pulled out by failing the steel-to-concrete interface (Figure 4.104 (b)).

For a deformed reinforcing bar, bond is primarily coming from the bearing of bar lugs on concrete and the strength of concrete between lugs. Goto (1971) has experimentally showed that, when a reinforced concrete specimen was subjected to tension, in addition to the primary cracks arising from direct tensile stress on the concrete, the radial forces bearing on the concrete resulted in secondary internal cracks (hence called "Goto Cracks") as schematically illustrated in Figure 4.105. These internal inclined cracks will grow wider and longer upon further tension and lead to large residual slip after reloading. If heavy transverse reinforcement is present, however, the propagation and widening of these inclined cracks will be inhibited thus degradation in bond strength and stiffness are mainly caused by concrete crushing at the toe of the lugs and shearing off of the concrete between the lugs. However, failure could still eventually occur due to

these inclined cracks as observed in the test specimens reinforced by 2% volumetric spiral reinforcement as shown in Figure 4.106. A detailed description of the bond resistance mechanism for confined reinforced concrete under monotonic and cyclic loadings can be found elsewhere (Orangun, Jirsa, Breen, 1977; Viawathanatepa, Popov, and Bertero, 1979; Eligehausen, Popov, and Bertero, 1983; Abrishami and Mitchell, 1992; Malvar, 1993).

4.6.2 Bond Mechanism of HPFRCCs

Before developing the theory of bond resistance mechanism for reinforcing bar embedded in HPFRC composites, a series of observations based on the test results are described first to assist the understanding of bond characteristics. In order to investigate the steel-to-matrix interface, several specimens were cut in half in order to observe the cracked surface after different types of loadings. Essential observations are described in the following:

1. A cone shape pullout failure was usually found in elements confined by transverse reinforcement (Viawathanatepa, Popov, and Bertero, 1979; Hota and Naaman, 1995). In this study, a cone shape fracture was also observed in HPFRCCs, as shown in Figure 4.107. However, due to the fiber bridging, this cone-shaped piece remained attached to the specimen, thus keeping the integrity of the specimen. Usually, especially for smaller size bar or 2% fiber content specimen, an evident cone-shaped piece would not form until very lager slip occurred. The diameter of the cone-shaped fracture is about 1.5 to 3 times the bar diameters (Figures 4.6, 4.28, 4.94, 4.103 (c),

and 4.107), and generally occurred in specimens exhibiting multiple cracking. The cone-shaped fracture formed in HPFRCC specimens was much smaller than in the transverse reinforcement confined specimens (see Figure 4.106), which contributed to the bond failure of these confined specimens.

2. Goto cracks did happen in some specimens reinforced with fibers. As demonstrated in Figure 4.108, however, these internal inclined cracks were very small and narrow due to the fiber bridging effect. Crushed steel-to-matrix interface was also observed. Fibers which was not able to offer sufficient bridging thus led to splitting failure of specimens, such as PVA K-II, usually showed no Goto cracks but may have severe cone-shaped fracture, as shown in Figure 4.109.

3. As can be seen in Figure 4.110, no damage or crushing was observed on the cracked surfaces and the steel-to-matrix interfaces of the control specimens or PVA fiber reinforced specimens because of the splitting failure at very small slip. Usually, as noted earlier, matrix crushing resulted from high bearing stress coming from the lugs occurs in a well confined element. No intentional confinement was offered for the control specimens in this study. On the other hand, in the specimens with fibers only, such as Spectra fibers and Torex fibers, the matrix surrounding the reinforcing bar was crushed and sheared off. This indicates that the bridging fibers provide good confinement to the matrix.

4. In addition to the crushing and shearing on the steel-to-matrix interfaces, it was also observed that ample multiple cracking and crushing occurred along the cracked

surfaces as shown in Figures 4.108, 4.111, 4.112, and 4.34 for SIFCON specimen. It has been established that once a crack initiates and propagates in a plain concrete, then softening occurs. It follows that the concrete surrounding the cracked surface is unloaded elastically (Li, 1997). Therefore the energy is only dissipated by propagating the crack with no inelastic deformation around the cracked surface, which is evidenced by Figure 4.110 (a). Confined concrete shows higher bond strength by inhibiting the development of cracks through transverse steel. However, the ultimate failure is still due to a large cone-shaped surface with a few pieces broken matrix as shown in Figures 4.18 and 4.106. On the contrary, in HPFRC composites, the fracture toughness is considerably enhanced by the addition of fibers, which bridge the cracks and transfer the force into uncracked matrix, thereby inducing extensive inelastic deformation along the cracked surfaces. For instance, when Torex fibers are used in a specimen, the pseudo strain-hardening pullout behavior (see Figure 3.2) leads to increased bond stress on the steel-to-matrix interface, while the matrix surrounding a crack keeps taking force without unloading. This eventually results in the multiple cracking and crushing on the cracked surfaces as shown in Figures 4.111 and 4.112. Therefore more energy is able to be dissipated by not only crack propagation, but the multiple cracking along the cracked surfaces. Figure 4.111 also shows that, for a Torex fiber reinforced specimen, extensive cracking occurred along the cracked surface but not on the uncracked surfaces. This observation implies that multiple cracked surfaces originated from the reinforcing bar, such as the one shown in Figure 4.28, are more desirable in terms of energy dissipation. Each surface will have its own multiple cracking and crushing along the surface during bond action as shown in Figure 4.111 (a). It is also noted that in Figure

4.112 (c), the cut surface did not necessarily went through exactly the cracked surface, therefore the multiple cracking and crushing were not on the entire cut surface as shown in this picture.

Based on the preceding observations, the following bond mechanisms for reinforcing bars embedded in HPFRC composites can be illustrated using Figure 4.113 and elaborated as follows.

There are generally two types of bond mechanisms for reinforcing bar in HPFRCCs: one is *interface-crushing type*, the other is *separation type*. Both mechanisms are able to attain high bond strength, depending on how an HPFRCC is tailor designed. The interface-crushing type bond mechanism is described by Figures 4.113 (a) thru 4.113 (d):

(a) At initial loading, the fibers are bridging the uncracked matrix and help delay its cracking, thus increasing the bond strength. With increased bar pull-out load, the radial compression exerted on the concrete by the lugs is redistributed to the whole matrix due to the presence of fibers. Multiple fine cracks can form at this stage without bond strength deterioration (Figure 4.113 (a)).

(b) Following the pullout or breaking of fibers, longitudinal cracks along the bar axis develop; this corresponds approximately to the maximum load at which the maximum bond strength is attained (Figure 4.113 (b)). Multiple cracking and crushing start to form along the surfaces of longitudinal cracks. The widening and propagation of the internal inclined cracks are hindered by the fibers.

(c) If the fibers can effectively bridge the longitudinal cracks without excessive opening, the matrix around the lugs will be eventually crushed under increasing bar slip (Figure 4.113 (c)). If an optimal combination of matrix and fiber is used (preferably with 2% fiber by volume), the multiple longitudinal cracks are able to keep increasing and multiple cracking and crushing along the surfaces of longitudinal cracks also increase. This will give rise to higher bond stress in the descending tail of a bond stress-slip curve since more fibers are participating in the resistance process. Note the matrix between lugs is sheared off only when the multiple cracking occurs or a large cover is present. This is evidenced by Figures 4.22 and 4.26, where the specimens which had multiple cracking (specimens with Spectra fibers, or specimens with Torex fiber but with lower matrix strength) showed better bond resistance in the descending portions.

(d) After the reinforcing bar is pulled out to a distance equal to the clear lug spacing, that means the lugs have traveled into the neighboring ribs. Due to the clamping effect from the fibers, there is a slight increase in resistance in the pullout force, thereby leading to an increase in bond stress as shown in Figure 4.113 (d). The distance between first peak bond stress and the point bond stress increasing again is approximately equal to the spacing of the bar lugs. This is also evident in the specimens with higher confinement, such as those embedded with smaller size bar or reinforced with higher fiber volume fraction. Note that the lug spacing is about 0.32 in. and 0.63 in. for No. 5 bar and No. 8 bar, respectively, as show in Figure 3.4. These spacings are exactly equal to the distances between first peak bond stress and the point bond stress increasing again, or two points at which bond stress increased,

as demonstrated in Figures 4.7, 4.8, 4.11, and 4. 12.

The interface-crushing type bond mechanism usually occurs in specimens with Spectra fibers or Torex fibers with specific matrix strength (about 6~8 ksi).

The separation type of bond mechanism usually occurs with only one major through crack. Only a few longitudinal cracks form as well as less multiple cracking and crushing along the surfaces of longitudinal cracks. However, due to the fiber bridging effect against the internal pressure resulting from the bar lug bearing stresses, a high bond strength can also be attained (See Figure 4.113 (e)). The bar-to-matrix usually is not sheared off therefore the bond strength in the descending branch is lower than the friction type failure. This usually occurs in specimens with 2% Torex fibers.

It is noted that in the specimens with larger size bar or lower fiber volume fraction, such as 1% by volume, the longitudinal cracks could be quite wide. In this case the bond strength can be much lower due to less fiber number thus less bridging force.

4.7 Conclusions

1. Plain concrete exhibited sudden splitting bond failure and only a relatively small bond stress (300~500 psi) was attained. On the other hand, bond behavior of specimens with fibers is distinct from that of control specimens because widening and propagation of cracks were inhibited due to the presence of fibers. Besides, the conventional way to improve bond performance by using transverse reinforcement

still resulted in severe damage in terms of spalling and cone-shaped fracturing, although bond strength was increased. It is found that a relatively heavy confinement using 2% spiral reinforcement cannot maintain the integrity of the specimen. In this regard, apparently, it is easier to achieve the current performance-based design goal with fiber reinforced concrete; that is, to reduce overall structural damage.

2. Addition of Spectra fiber greatly increased bond strength and ductility compared with the control specimen. Multiple cracking usually occurred in specimens with Spectra fibers. Peak monotonic bond strength of the fiber reinforced specimens was approximately 7 times that of the control specimens. Considerable energy (approximately 25 times that of control specimens) was dissipated by the fiber reinforced specimens before excessive bond loss occurred. It is noted that the difference in peak bond strength under monotonic loading between specimens with 1% fiber and 2% fiber is insignificant. This is due to the fact that the failure mode for Spectra specimen is pull-out (friction) type rather than separation type. Nevertheless, increasing fiber volume fraction can effectively prevent the widening and propagation of cracks, thereby maintaining the integrity of the matrix and reducing the degree of damage.

3. When fiber volume fraction is low (1%), the fiber length play an important role in the bond strength, especially for steel fibers. When a reinforcing bar is pulled out from a matrix, the cracks need to open in order for the bar to move through. As a consequence, the longer fiber offers better bridging effect, thus increasing the bar bond strength. It is noted that, with the same fiber volume fraction, the number of

Spectra fibers is approximately 50 times that of Torex fibers. This large amount of Spectra fibers can effectively hinder the extension and expansion of cracks, thus leading to multiple fine cracks and better bond characteristics, even at low fiber volume fractions. At 1% fiber content, the specimen with Spectra fiber had the highest monotonic bond strength (1470 psi), while the specimen with PVA 13 fiber had the smallest bond strength (720 psi). Specimens with other types of fibers (Torex and hooked fibers) generally reached same peak bond stress (approximately 1100 psi).

4. No improvement in bond strength was observed in steel hooked fiber specimens when the fiber volume fraction was increased from 1% to 2%. On the other hand, peak monotonic bond stresses were significantly increased by using 2% fiber volume fraction of Torex fibers. This increase was approximately 60% for the square Torex fiber specimen and 40% for the rectangular Torex fiber specimen. The specimen with square Torex fiber (20 mm long) attained the highest bond stress (1640 psi). It is evident that the unique tensile characteristics of Torex fiber composites (high tensile strength, and pseudo strain-hardening response) compensated for the lack of fiber amount and further enhanced ultimate bond strength. Further, both with 2% reinforcement, the specimen with square Torex fibers had 1.5 times the bond strength of the specimen with conventional transverse (spiral) reinforcement. It is also found that increasing the fiber amount from 1% to 2% led to a reduction in crack width and damage at large slips.

5. Peak monotonic bond stress ratio of No. 5 bar specimens to No. 8 bar specimens is

inversely proportional to their diameter ratio, no matter what type of fiber is used.

6. Generally, bond strength of bars embedded in HPFRCCs is proportional to $f_c'^{1/4}$. This was observed in both monotonic and fully reversed force-controlled cyclic loading tests. Specimens with lower matrix compressive strength (6~8 ksi) exhibited higher toughness, thus dissipating more energy than the high strength specimens (11 ksi) during the descending branch of the bond stress-slip response. This can be attributed to the relatively weaker strength matrix, which led to denser multiple cracking. In addition, the steel-to-matrix interface could be more easily sheared and ground off, leading to higher energy dissipation. In general, Torex fiber specimens with high strength matrix showed separation type failure, while interface-crushing type failure was observed in specimens with lower matrix strength.

7. With only 2% fiber content, the Torex fiber specimens outperformed the SIFCON (Slurry infiltrated fiber concrete) specimen previously tested (9.7% steel hooked fiber) in terms of peak bond strength. That is, Torex fibers were able to provide superior bond performance at relatively lower fiber content than SIFCON, which is essential for practical applications. It is also observed that, using approximately five times more steel hooked fibers (9.7% to 2%) led to only a 30% increase in bond strength.

8. Development length (calculated based on average monotonic bond strength obtained from tests) for bars in Spectra fiber cement composites is approximately 60% that required by the ACI code (assuming 2% spiral reinforcement), for either 1% or 2%

fiber content. With only 1% steel fibers (hooked, square Torex, or rectangular Torex), the development length needed corresponded to 75% to 90% of the ACI requirement. A significant reduction in development length was obtained by using 2% square Torex fibers, (50% of the ACI required development length). No. 5 bar specimens showed similar results as the No. 8 bar specimens. Thus, with suitable fiber and volume fraction selection, the current development length specified in design codes could be reduced up to 50%.

9. Under unidirectional displacement-controlled cyclic loading, specimens with either Spectra or Torex fiber outperformed specimens with conventional transverse reinforcement in terms of bond stiffness (modulus) retention and the damage control. It is observed that the monotonic envelopes generally governed the cyclic responses for HPFRCC specimens and the loading and unloading paths of each cycle had almost the same stiffness without noticeable degradation. Both the stiffness and strength capacities of Torex fiber specimens were slightly superior to those of Spectra fiber specimens. The specimen with 2% volumetric steel spiral reinforcement exhibited degraded bond stiffness and strength under cyclic displacement due to severe concrete spalling.

10. Under unidirectional force-controlled cyclic loading, Spectra fiber specimens (No .8 bar, 11 ksi matrix) showed no bond strength and stiffness degradation when repeated cycles were performed at the same stress level, if the average bond stress was less than about 70% and 90% of the monotonic bond strength for 1% and 2% fiber content specimens, respectively. Below the above stress levels, residual slip was quite small.

Only 78% of the peak monotonic strength was achieved for 1% Spectra specimen, while the 2% Spectra fiber specimen attained 98% of the peak monotonic bond strength. Residual slip was only 0.09 in. after 18 cycles for the 2% fiber specimen, whereas the residual slip was 0.18 in. after 11 cycles for the 1% fiber specimen. A small fractured cone-shaped piece eventually formed at the pullout end of the reinforcing bar at large slips in the 1% fiber specimen. On the other hand, no cone shape formation was observed in the 2% fiber specimen. Specimens with No. 5 bar showed similar performance as the specimens with No. 8 bars.

11. Under unidirectional force-controlled cyclic loading, specimens with Torex fibers exhibited smaller residual slip and sustained more loading cycles than the Spectra fiber specimens. Even though the fiber amount of Spectra specimens was about 50 times that of the Torex specimens (with the same fiber volume fraction), Torex fiber specimens sustained higher bond stresses than the Spectra fiber specimens. Specimens with 2% Torex fiber by volume were able to reach 1.5 times the bond stress of specimens with 1% Torex fiber. In the Torex fiber specimens, the first cracks were generally visible at a much later stage. Visible multiple cracking was not observed on the surface of the Torex specimens. However, the integrity of the specimens was maintained by the fiber bridging effect.

12. Under unidirectional force-controlled cyclic loading, the bond performance of the specimen reinforced with conventional spiral reinforcement ($\rho_s = 2\%$) was inferior to that of specimens with either Spectra or Torex fibers. The bond stress level reached was smaller (approximately 60% that of the 2% fiber content specimens) and the

residual slip was larger. The bond stiffness of the spirally reinforced specimen degraded considerably after 10 cycles, while bond stiffness was maintained for many more cycles (about 20~30 cycles) for specimens with fibers. Severe spalling and fracturing contributed to the inferior bond performance of specimens with spirals.

13. Under fully reversed force-controlled cyclic loading, Spectra fiber specimens (No. 8 bar, 11 ksi matrix) exhibited no degradation in bond strength and stiffness, as well as minor residual slip (less than 0.025 in.) in both loading directions, when the average applied bond stress demand was less than 70% and 82% of the peak monotonic bond strength for 1% and 2% fiber content, respectively. By increasing the fiber content from 1% to 2%, cracking was delayed, and a 20% higher bond stress was achieved.

14. Under fully reversed force-controlled cyclic loading, the bond stress (890 psi) for the 1% rectangular Torex specimen (No. 8 bar, 11 ksi matrix) at which no stiffness and strength degradation in conjunction with minor residual slip occurred was smaller than that of the 1% Spectra fiber specimen (1050 psi). However, this bond stress was increased 25% for 2% rectangular Torex fiber. The maximum bond stress achieved in 2% rectangular Torex fiber specimen (1470 psi) is about 15% higher than that of 2% Spectra fiber specimen (1290 psi). It is also noted that more cycles were able to be performed in 2% rectangular Torex fiber specimen.

15. The bond strength of the square Torex fiber specimen was slightly better than that of the rectangular Torex fiber specimen under fully reversed force-controlled cyclic loading. This is because the Torex fiber with square cross-sectional shape has a higher

untwisted plastic torque compared with the rectangular fibers used in this study (1.4: 1.0). Reducing the fiber aspect ratio from 100 (30 mm long) to 67 (20 mm long) led to substantially inferior bond performance when only 1% fiber by volume was used. The bond strength of the specimen with 20 mm long square Torex fiber was only 65% that of the specimen with 30 mm long square Torex fiber. This arises from the shorter pullout length of the fiber. For the case of large size reinforcing bars which generally results in wider cracks during bar pullout, the using of longer fiber (thus longer fiber pullout length) becomes critical. However, this drawback can be compensated by increasing the fiber volume to 2%. In this case, the bond stress at which no bond deterioration occurred increased 115% compared to the 1% fiber specimen. However, the maximum bond stress attained in the 2% square Torex (20 mm) specimen was the highest among all specimens.

16. Fully reversed low cycle high amplitude fatigue test results showed that the specimen (No. 8 bar, 11 ksi matrix) with 2% square Torex fiber (20 mm) was able to sustain 25 cycles without strength decay under a constant bond stress of 1350 psi (90% of the peak monotonic bond strength). In general, specimens with Torex fibers exhibited superior bond strength in comparison to Spectra fiber specimens under fully reversed cyclic loading. Enhanced performance can be achieved by tailoring the geometry of Torex fibers. It is also noticed that specimens with Torex fibers sustained more loading cycles and visible cracking generally occurred at a later stage.

17. The bond performance of the PVA 13 fiber specimen (No. 8 bar, 11 ksi matrix) under fully reversed force-controlled cyclic loading was rather poor due to the inability of

this fiber to prevent a complete specimen separation due to fiber fracture. Therefore, a low bond strength was obtained (510 psi). The specimen with 1% hooked fiber also showed inferior bond performance in terms of bond strength (600 psi). However, the bond strength increased 80% by using 2% steel hooked fibers. Bond strength of the spirally reinforced specimen was comparable to that of the 2% hooked fiber specimen; both of them reached 80% of the bond strength of the 2% square Torex fiber (20 mm) specimen. For the spirally reinforced specimen, the transverse reinforcement led to an increase in bond strength, but could not prevent spalling and a cone-shaped fracture in both loading directions. In contrast to the specimen with fibers, the spirally reinforced specimen suffered very severe damage at the end of the test.

18. The cumulative dissipated energy through all cycles for the specimen (No. 8 bar, 11 ksi matrix) with 2% square Torex fiber (20 mm) was 22 times that of the control specimen and 2.5 times that of the spirally reinforced specimen ($\rho_s = 2\%$). In general, specimens with only 1% fiber by volume showed much wider cracks. In contrast, using 2% fiber content prevented cracks from opening, leading to more energy dissipation through shearing and crushing of the rebar-to-matrix interface. Multiple radial cracks were observed in specimens with 1% Spectra, 2% Spectra, and 2% square Torex (20 mm) fibers.

19. Although the 7.6 ksi specimens (No. 8 bar) showed less bond strength than the 11 ksi specimen (2% rectangular Torex specimens), the 7.6 ksi specimens exhibited a more dense multiple cracking with smaller crack width compared to the 11 ksi specimens. Also, extensive shearing and grinding were observed in the rebar-to-matrix interface

for the 7.6 ksi specimens compared to the 11 ksi specimens. This can be attributed to the lower matrix strength and the smaller crack width in the 7.6 ksi specimens. Since the crack width was small, the only way for bar to pullout was to shear off the matrix surrounding the bar lugs. Multiple cracking was also observed in the 5.9 ksi specimens. According to the above observations, as well as the crack patterns under monotonic loading, it is evident that matrix strength (thus matrix toughness) is one of the key factor for the formation of multiple cracking. The optimized material combination for achieving both high bond strength and multiple cracking under monotonic or cyclic loading could be: (a) 1% to 2% Spectra fiber; matrix strength is flexible, or (b) 2% Torex fiber; matrix strength of about 8 ksi.

20. Under fully reversed force-controlled cyclic loading, No. 5 bar specimens (11 ksi matrix) sustained higher bond strength than No. 8 bar specimens. The peak bond stress ratio of No. 5 bar to No. 8 bar specimens was 1.5~1.6, which agrees with the diameter ratio of No. 8 bar to No. 5 bar (1:1.6).

21. Internal inclined cracks (Goto cracks) were observed in some specimens reinforced with fibers. However, these cracks were small and narrow due to the fiber bridging effect. It was also observed that ample multiple cracking and crushing occurred along the cracked surfaces, which are more desirable in terms of energy dissipation.

22. There are generally two types of bond failure mechanisms for reinforcing bar in HPFRCCs: one is an interface-crushing type failure, the other is a separation type failure. Both mechanisms are able to attain high bond strength, depending on how an

HPFRCC is tailored.

Table 4.1 Comparison of peak bond stress between different specimens (Spectra and rectangular Torex fibers)

Fiber	Bar	Average peak Bond Stress(psi)	Bond strength ratio (No. 5/No. 8)	Bar diameter ratio (No. 8/ No. 5)
1% Spectra	No. 8	1470	1.5	1.6
	No. 5	2190		
2% Spectra	No. 8	1530	1.5	1.6
	No. 5	2350		
1% Rectangular Torex	No. 8	1110	1.6	1.6
	No. 5	1780		
2% Rectangular Torex	No. 8	1490	1.4	1.6
	No. 5	2090		

Table 4.2 Monotonic peak bond stress of specimens with various types of fibers or reinforcement (1% fiber volume fraction and matrix compressive strength = 11 ksi)

Fiber or Reinforcement	Peak Bond Stress (psi)	Relative Strength (Compared with Control Specimen)
Control (no fiber or reinforcement)	220	1.0
Spectra (38mm)	1470	6.7
Hooked (30 mm)	1170	5.3
Square Torex (30 mm)	1150	5.2
Rectangular Torex (30 mm)	1110	5.0
Spiral reinforcement ($\rho_s = 2\%$)	1090	5.0
Square Torex (20 mm)	1000	4.6
PVA 13 (12 mm)	720	3.3

Table 4.3 Monotonic peak bond stress of specimens with various types of fibers or reinforcement (2% fiber volume fraction and matrix compressive strength = 11 ksi)

Fiber or Reinforcement	Peak Bond Stress (psi)	Relative Strength	$\frac{(\text{Bond Strength})_{2\%}}{(\text{Bond Strength})_{1\%}}$
Control (no fiber or reinforcement)	220	1.0	-
Square Torex (20 mm)	1640	7.5	1.6
Spectra (38mm)	1530	7.0	1.1
Rectangular Torex (30 mm)	1490	6.8	1.4
Hooked (30 mm)	1100	5.0	1.0
Spiral reinforcement ($\rho_s = 2\%$)	1090	5.0	-

Table 4.4 Calculated required development length for No. 8 bar (11 ksi matrix)

	Fiber or Reinforcement content	Maximum Load in Bar (lbs)	Developed Stress per unit length (ksi/in.)	Development length ($\times d_b$)
Control	0%	2800	0.89	73.2
Square Torex (20 mm)	1%	12580	3.98	16.3
	2%	20650	6.53	9.9
Square Torex (30 mm)	1%	14500	4.59	14.2
	2%	-*	-	-
Rectangular Torex (30 mm)	1%	13960	4.42	14.7
	2%	18670	5.91	11.0
Spectra (38 mm)	1%	18530	5.86	11.1
	2%	19260	6.09	10.7
Hooked (30 mm)	1%	14700	4.66	14.0
	2%	13850	4.38	14.8
PVA 13 (12mm)	1%	9010	2.85	22.8
	2%	-	-	-
Spiral	$\rho_s = 2\%$	13670	4.33	15.0
				18.6 (ACI)**

* Not tested

** Same value for 0% and 2% spiral reinforcement in this case

Table 4.5 Calculated required development length for No. 5 bar (11ksi matrix)

	Fiber or Reinforcement content	Maximum Load in Bar (lbs)	Developed Stress per unit length (ksi/in.)	Development length ($\times d_b$)
Control	0%	5300	4.28	24.3
Rectangular Torex (30 mm)	1%	14000	11.29	9.2
	2%	16380	13.21	7.9
Spectra (38 mm)	1%	17170	13.85	7.5
	2%	18440	14.87	7.0
				14.9 (ACI)*

* Same value for 0% and 2% spiral reinforcement in this case

Table 4.6 Monotonic pullout work (lb-in)

	Fiber or Reinforcement content	No. 8 Bar			No. 5 Bar
		11 ksi	**7.6 ksi**	**5.9 ksi**	**11 ksi**
Control	0%	290	-	-	320
Square Torex (20 mm)	1%	3990	-	-	-
	2%	3910	-	-	-
Square Torex (30 mm)	1%	4990	-	-	-
	2%	-*	-	-	-
Rectangular Torex (30 mm)	1%	3270	-	-	4300
	2%	5310	9300	7860	7200
Spectra	1%	6360	-	-	6400
	2%	8830	-	-	6550
Hooked	1%	4190	-	-	-
	2%	4620	-	-	-
PVA 13	1%	1100	--	-	-
	2%	-	-	-	-
Spiral reinforcement	$\rho_s = 2\%$	3270	-	-	-
Helix	2%	-	7060	-	-
PVA K-II	2%	-	4990	-	-

* Not tested

Table 4.7 Summary of bond characteristics of specimens subjected to unidirectional force controlled loading (No. 8 bar and matrix compressive strength = 11 ksi)

Fiber or Reinforcement	a	b	c	d	e
1% Spectra	10	70%	78%	1170	4
2% Spectra	18	90%	98%	1540	4
1% Rectangular Torex	15	90%	90%	1000	14
2% Rectangular Torex	26	100%	110%	1630	22
1% Square Torex (30 mm)	17	90%	100%	1195	4
1% Square Torex (20 mm)	22	100%	110%	1050	9
2% Square Torex (20 mm)	17	90%	100%	1500	13
Spiral reinforcement ($\rho_s = 2\%$)	9	80%	80%	955	*

Table 4.8 Summary of bond characteristics of specimens subjected to unidirectional force controlled loading (No. 5 bar and matrix compressive strength = 11 ksi)

Fiber or Reinforcement	a	b	c	d	e
1% Spectra	8	65%	80%	1780	4
2% Spectra	12	80%	87%	2090	4
1% Rectangular Torex	16	90%	90%	1600	15
2% Rectangular Torex	11	80%	80%	1700	8

Note: (for Tables 4.7 and 4.8)

a. Number of load cycles before strength drops
b. Load reached at which only minor strength, stiffness and residual slip occur (percentage of peak monotonic bond strength)
c. Maximum strength achieved (percentage of peak monotonic bond strength)
d. Peak bond stress under unidirectional force controlled loading (psi)
e. Cycle where first visible crack was observed
* Cone-shaped fracture formed at 9th cycle

Table 4.9 Summary of bond characteristics of specimens subjected to fully reversed force controlled cyclic loading (No. 8 bar and matrix compressive strength = 11 ksi)

Fiber or Reinforcement	a	b	c	d	e
Control	9	200 (60%)	270	4 (210)	480
1% Spectra (38 mm)	11	1050 (70%)	1200	4 (970)	9250
2% Spectra (38 mm)	11	1290 (82%)	1290	7 (1280)	8810
1% Rectangular Torex (30 mm)	15	890 (80%)	1000	13 (1000)	3390
2% Rectangular Torex (30 mm)	23	1110 (80%)	1470	13 (1000)	6530
1% Square Torex (30 mm)	15	955 (80%)	1075	7 (950)	8070
1% Square Torex (20 mm)	9	620 (65%)	765	6 (620)	2070
2% Square Torex (20 mm)	20	1340 (90%)	1490	8 (1200)	10170
2% Square Torex (20 mm)*	26	1350 (90%)	1350	-	11620
1% Hooked (30 mm)	6	600 (50%)	645	4 (650)	2060
2% Hooked (30 mm)	21	1070 (90%)	1190	4 (780)	8970
1% PVA 13 (12 mm)	14	510 (80%)	570	12 (570)	2130
Spiral reinforcement ($\rho_s = 2\%$)	15	1070 (95%)	1070	5 (720)	3990

Note:

a. Number of load cycles performed
b. Bond stress reached (psi) at which only minor strength, stiffness and residual slip occur (as well as percentage of peak monotonic bond stress)
c. Peak bond stress under fully reversed force controlled cyclic loading (psi)
d. Cycle where first visible crack was observed (and the corresponding bond stress, psi)
e. Cumulative energy (lb-in)

* Constant bond stress (1350 psi) for 26 cycles until strength dropped

Table 4.10 Summary of bond characteristics of specimens subjected to fully reversed force controlled cyclic loading (No. 8 bar and matrix compressive strength = 7.6 ksi)

Fiber or Reinforcement	a	b	c	d	e
2% Rectangular Torex	11	1090 (65%)	1340	7 (1340)	8490
2% Triangular Torex (Helix)	10	875 (65%)	1080	7 (1080)	6150
2% PVA K-II	11	800 (80%)	1020	7 (1020)	6600

Table 4.11 Summary of bond characteristics of specimens subjected to fully reversed force controlled cyclic loading (No. 8 bar and matrix compressive strength = 5.9 ksi)

Fiber or Reinforcement	a	b	c	d	e
2% Rectangular Torex	14	960 (80%)	1020	8 (960)	7700

Table 4.12 Summary of bond characteristics of specimens subjected to fully reversed force controlled cyclic loading (No. 5 bar and matrix compressive strength = 11 ksi)

Fiber or Reinforcement	a	b	c	d	e
Control	8	400 (75%)	540	4 (395)	360
1% Spectra	12	1480 (70%)	1820	4 (1460)	5900
2% Spectra	12	1580 (66%)	1960	7 (1940)	8800
1% Rectangular Torex	15	1430 (80%)	1600	12 (1600)	5000
1% Rectangular Torex*	40	1430 (80%)	1430	24 (1430)	10640
2% Rectangular Torex	12	1700 (80%)	1700	8 (1700)	5900

Note: (for Tables 4.10, 4.11, and 4.12)

a. Number of load cycles performed
b. Bond stress reached (psi) at which only minor strength, stiffness and residual slip occur (as well as percentage of peak monotonic bond stress)
c. Peak bond stress under fully reversed force controlled cyclic loading (psi)
d. Cycle where first visible crack was observed (and the corresponding bond stress, psi)
e. Cumulative energy (lb-in)

* Constant bond stress (1430 psi) for 40 cycles until strength dropped

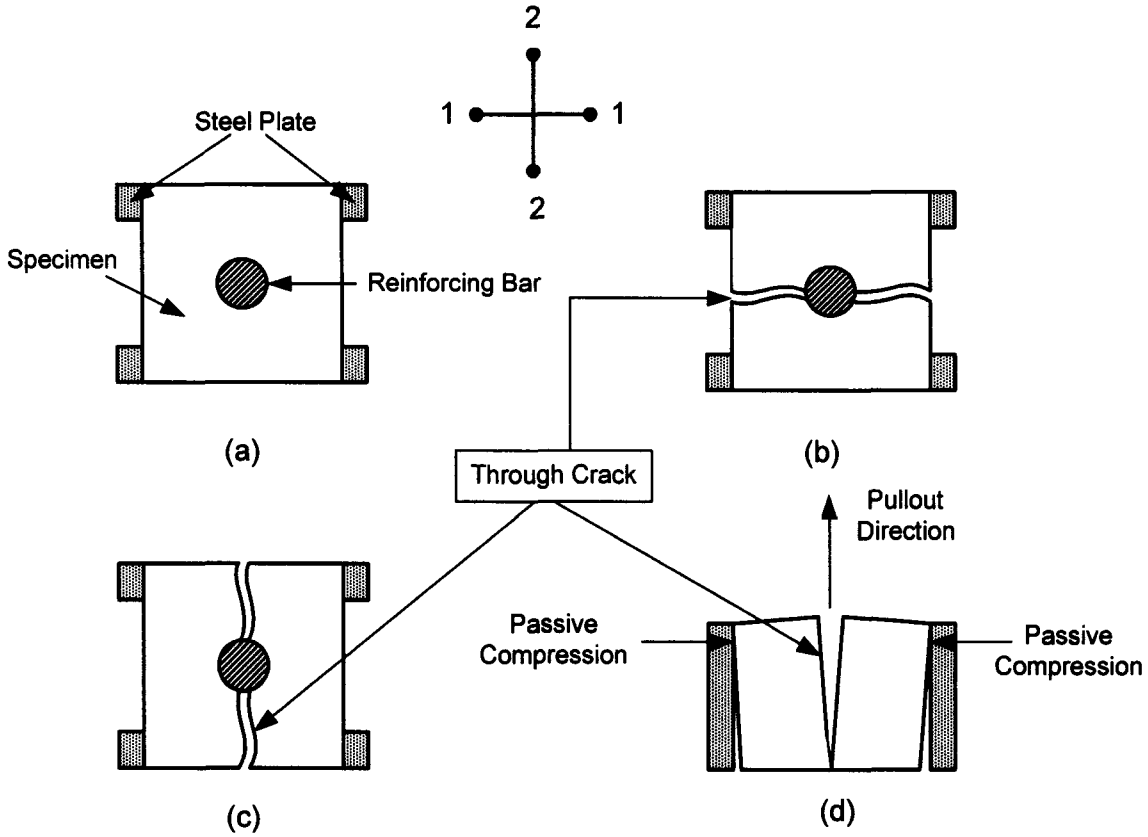

Figure 4.1 Influence of cracking pattern on the pullout behavior of control specimens (without fiber).
(a) top view of the pullout specimen: the supports are located on the sides in the 1-1 direction;
(b) Through crack in 1-1 direction: specimen fracture without passive confinement;
(c) Through crack in 2-2 direction: supports provide confinement due to the cracking;
(d) Side view of (c): the wide crack results in passive compression, thus increasing the pullout load.

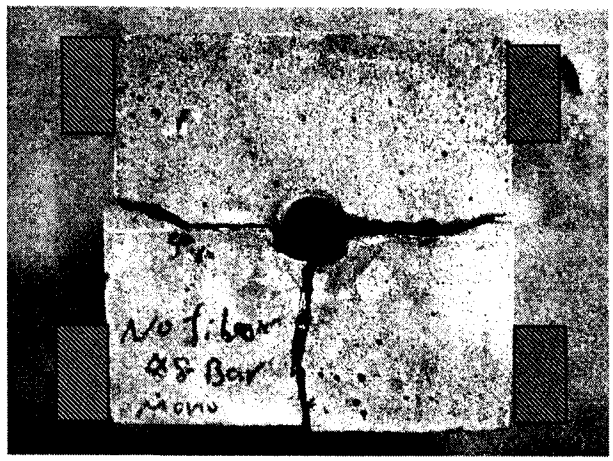

Specimen 1

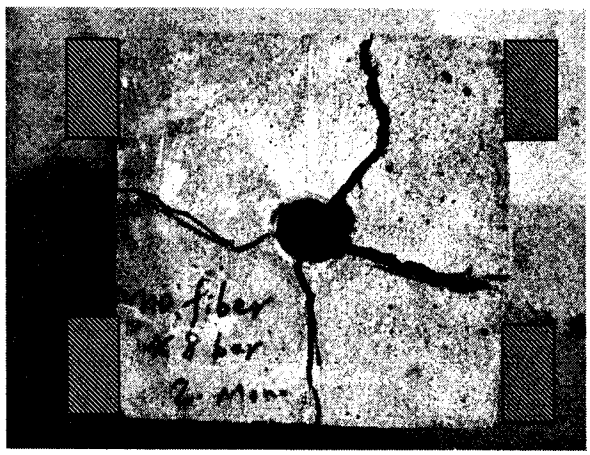

Specimen 2

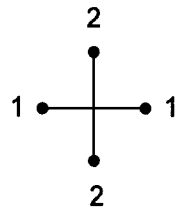

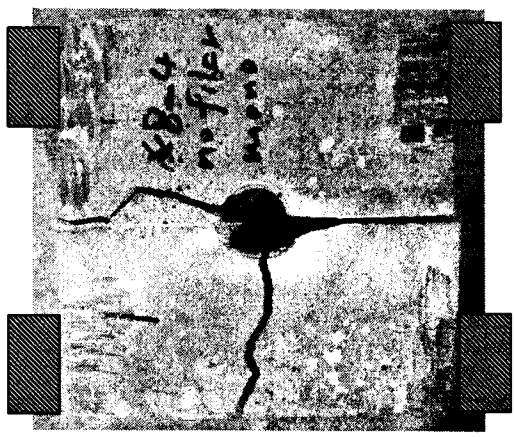

Specimen 3

Figure 4.2 Cracking patterns of three control specimens tested monotonically. Specimens 1 and 3 have through cracks in the 1-1 direction as shown in Figure 4.1, which would not result in passive compression. Specimen 2 has through cracks in both 1-1 and 2-2 directions. The through crack in the 2-2 direction causes the passive compression

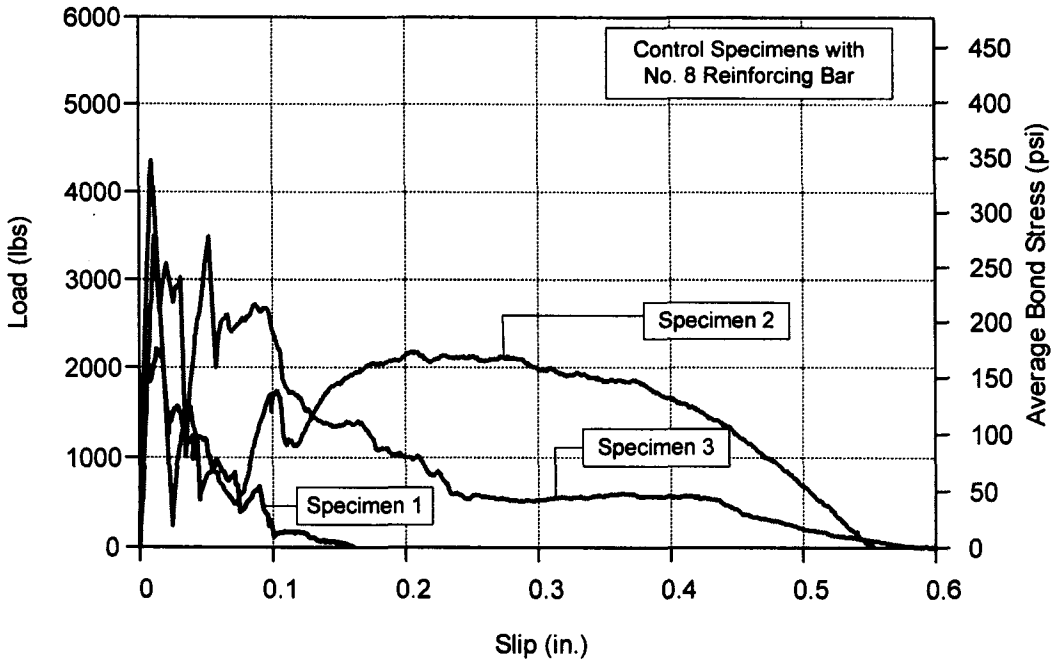

Figure 4.3 (a) Load-Slip curves of three tested control specimens (No. 8 bar) under monotonic loading. The various curve shapes on the descending branch are directly attributable to the crack patterns

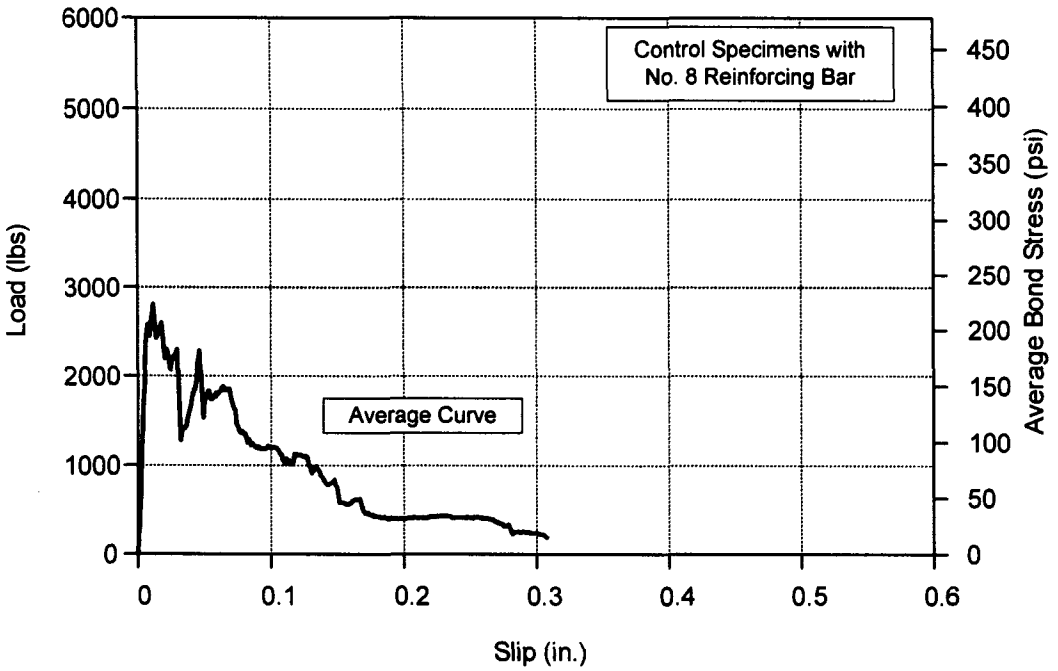

Figure 4.3 (b) Average Load-Slip curve of control specimen (No. 8 bar) under monotonic loading

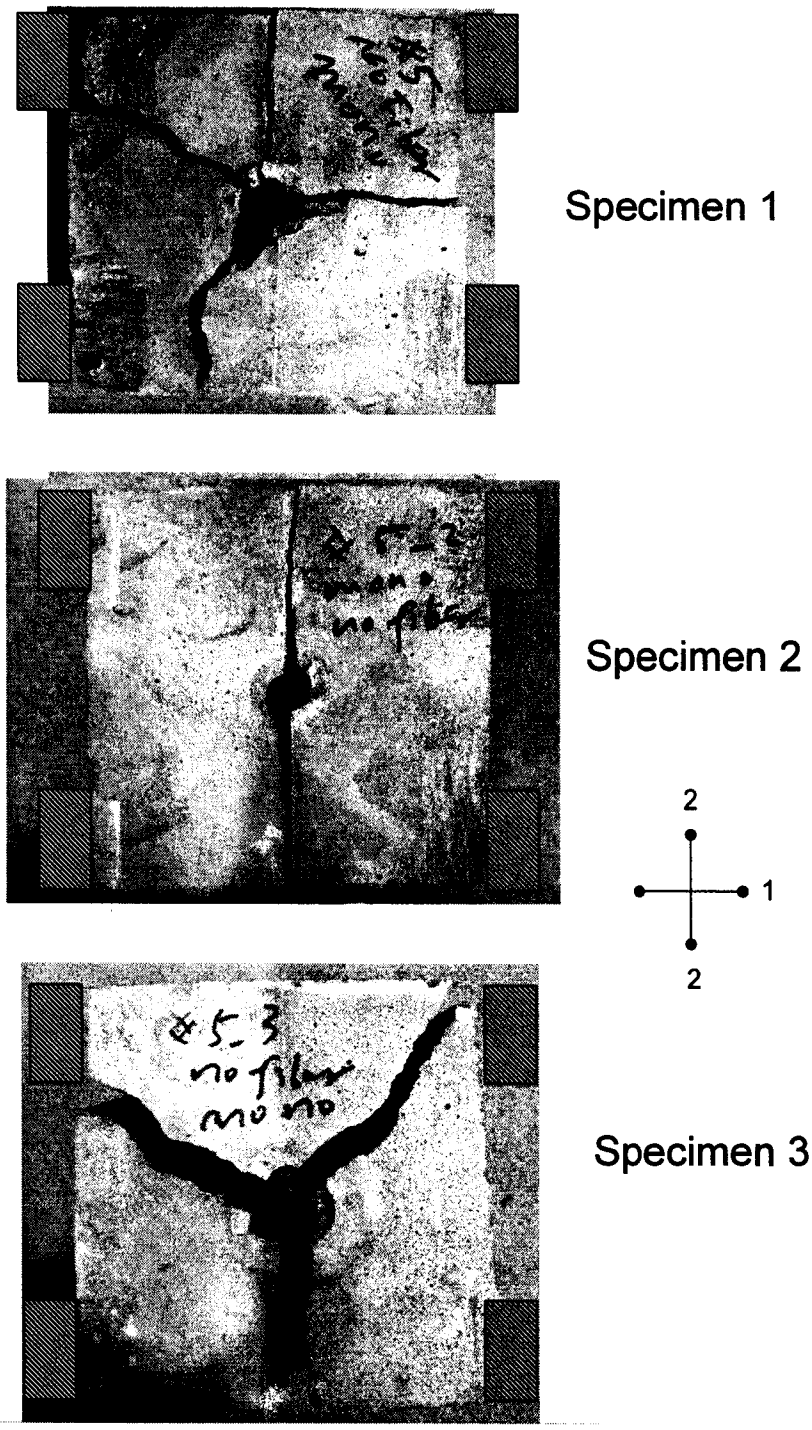

Figure 4.4 Crack patterns of three test control specimens with No. 5 bar. Specimens 1 and 2 had through cracks in the 2-2 direction, which resulted in passive compression. Specimen 3 had through cracks in transverse (1-1) directions, leading to a smaller confinement effect than that in specimen 1 and 2

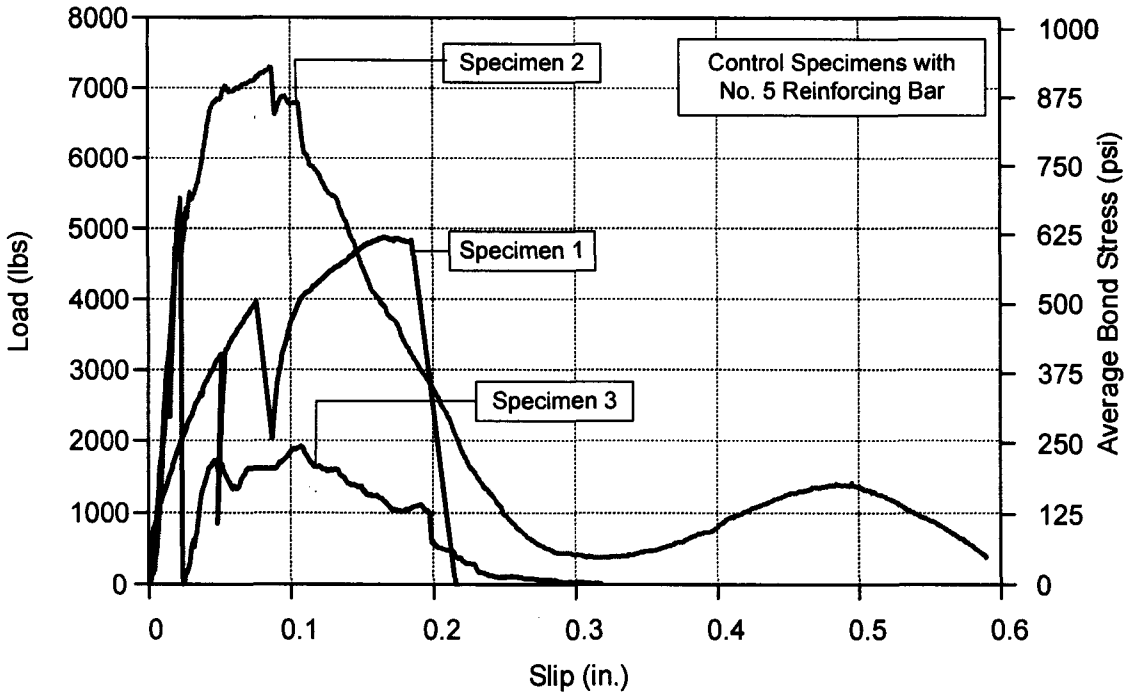

Figure 4.5 Load-Slip curves of three tested control specimens with No. 5 bar under monotonic loading. The various curve shapes are directly attributable to the crack patterns

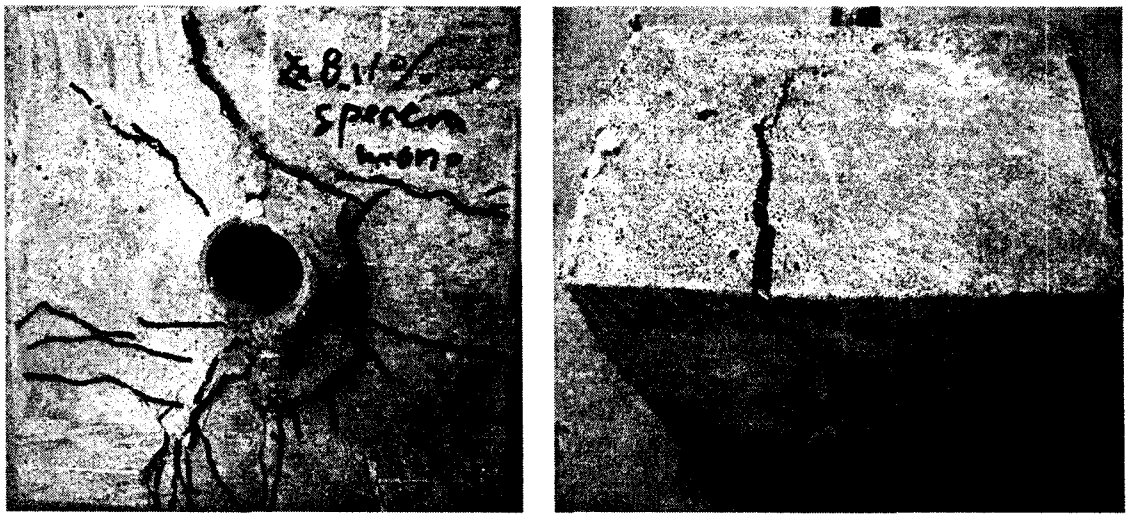

(a) (b)

Figure 4.6 (a) Multiple cracking in No. 8 bar specimen with 1% Spectra fiber; (b) Cracks are bridged by fibers

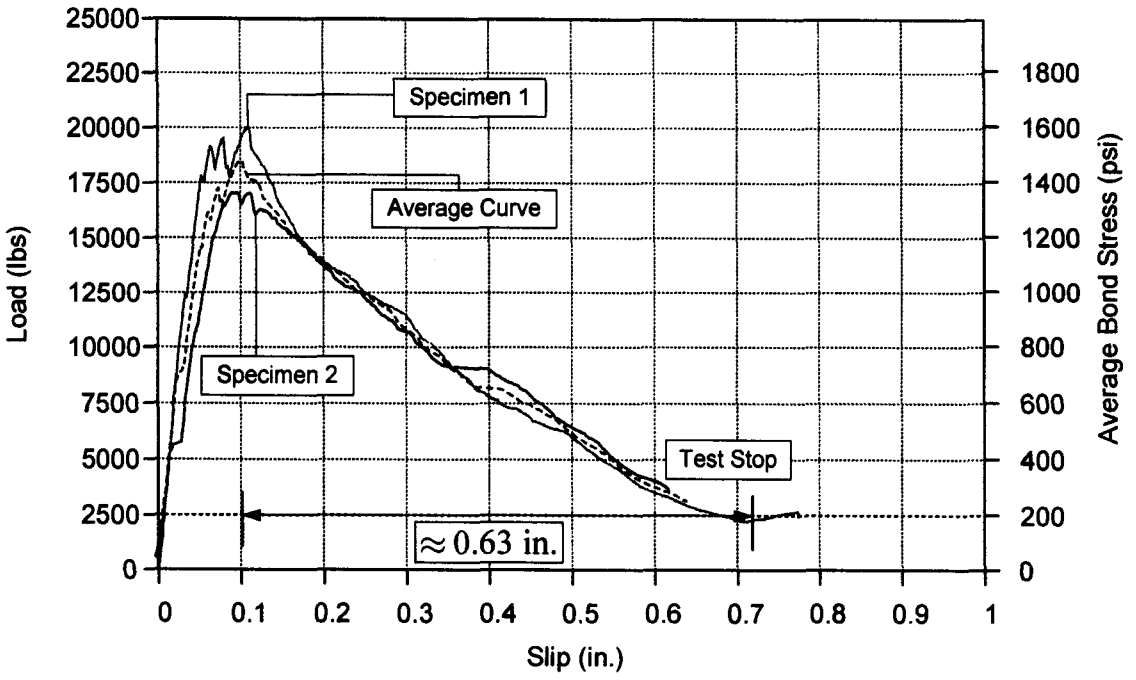

Figure 4.7 Load-Slip curves of specimens with 1% Spectra fiber (No. 8 bar) subjected to monotonic loading

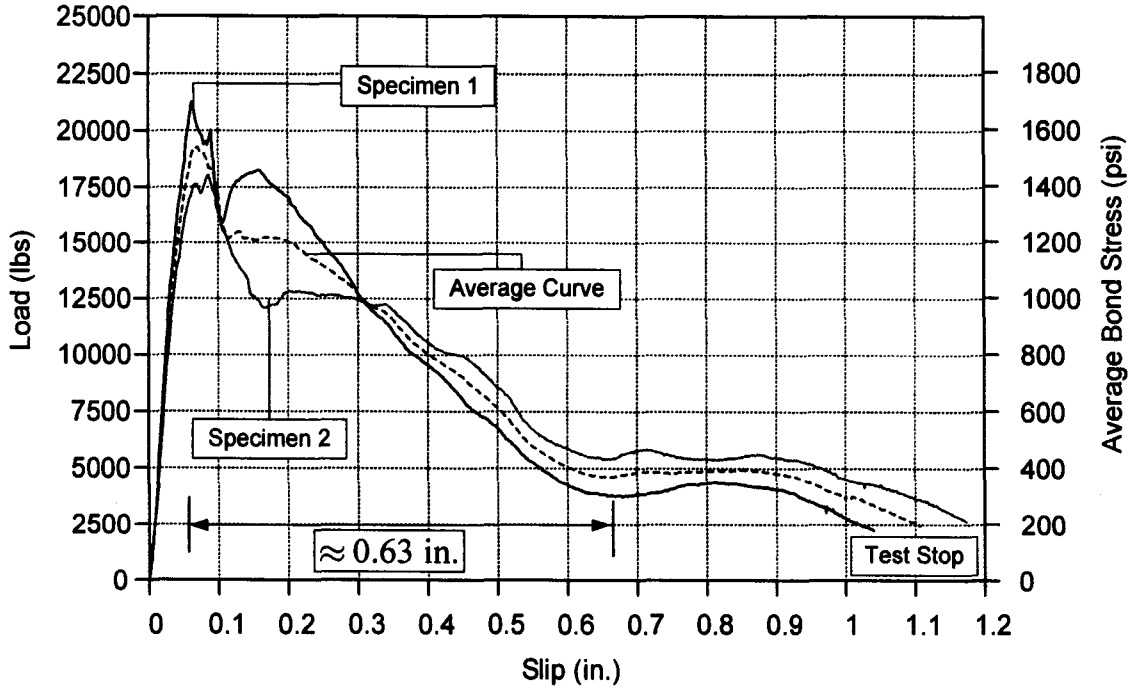

Figure 4.8 Load-Slip curves of specimens with 2% Spectra fiber (No. 8 bar) subjected to monotonic loading

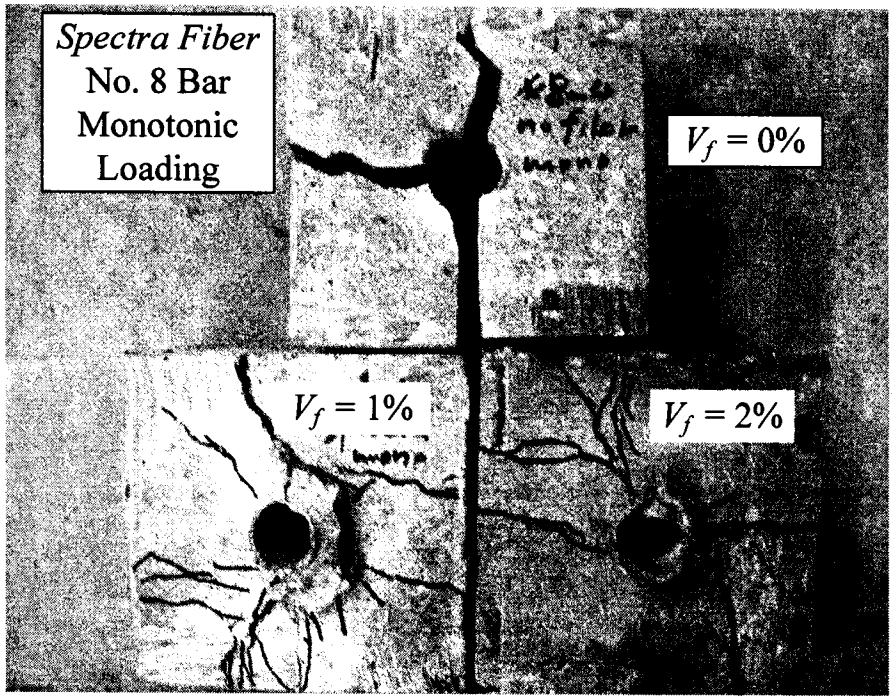

Figure 4.9 Crack patterns for specimens with different fiber contents (No. 8 bar and Spectra fiber)

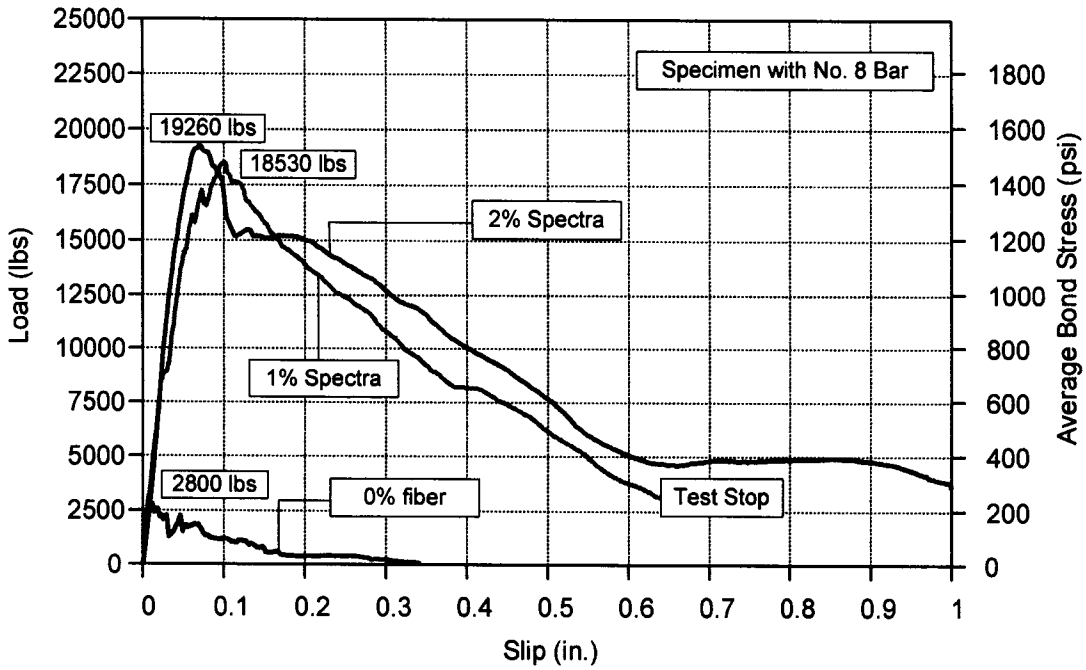

Figure 4.10 Comparison of Load-Slip curves for specimens with different fiber contents (No. 8 bar and Spectra fiber)

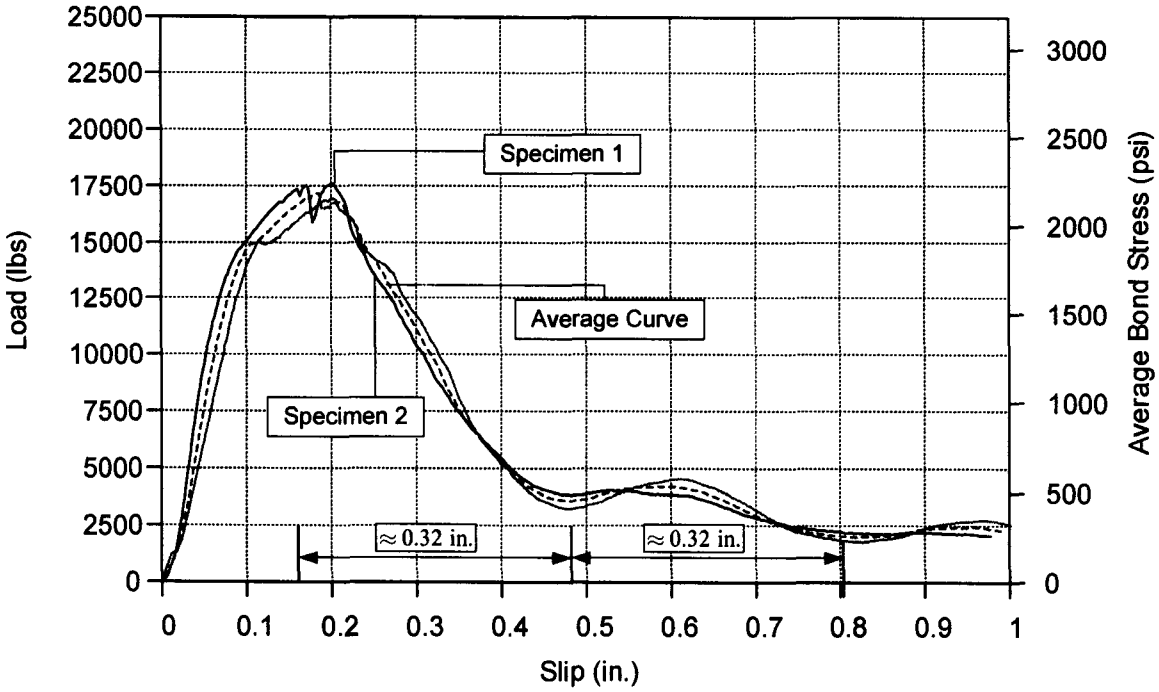

Figure 4.11 Load-Slip curves of specimens with 1% Spectra fiber (No. 5 bar) subjected to monotonic loading

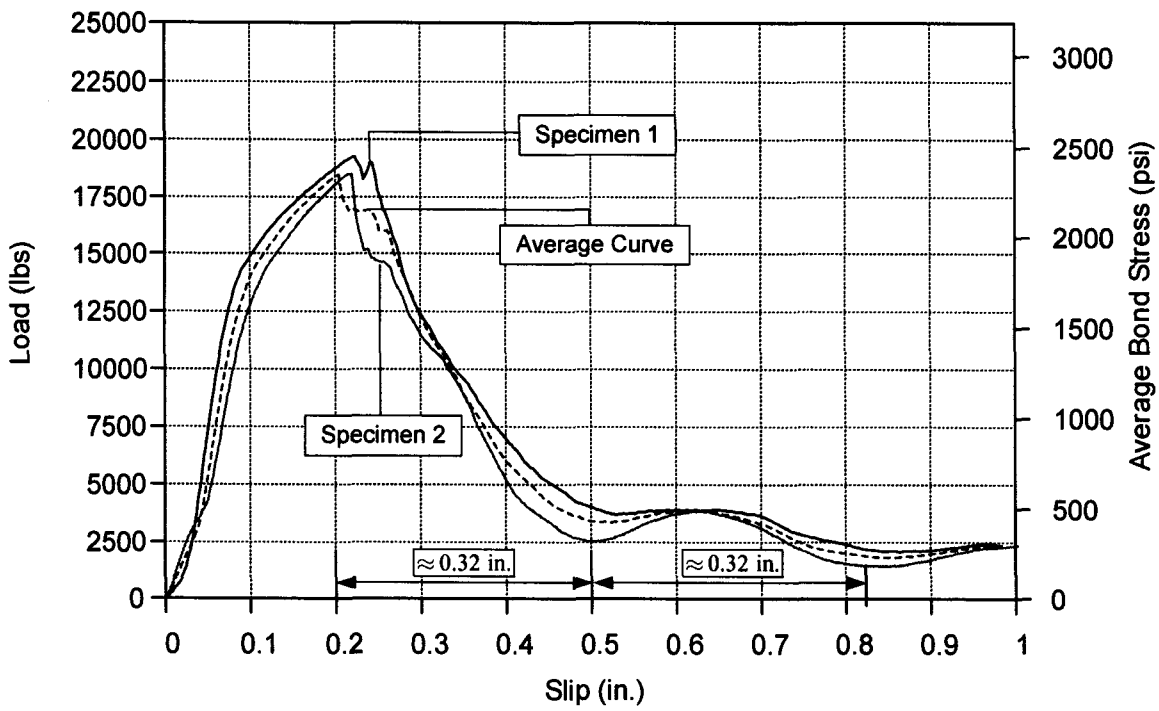

Figure 4.12 Load-Slip curves of specimens with 2% Spectra fiber (No. 5 bar) subjected to monotonic loading

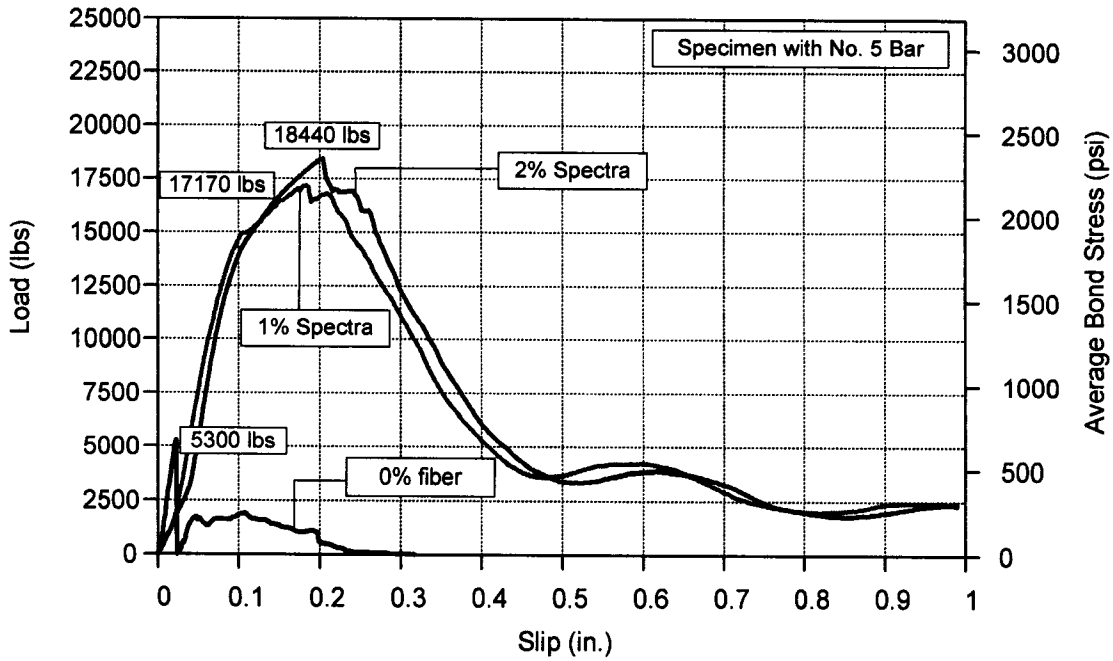

Figure 4.13 Comparison of Load-Slip curves for specimens with different fiber contents (No. 5 bar and Spectra fiber)

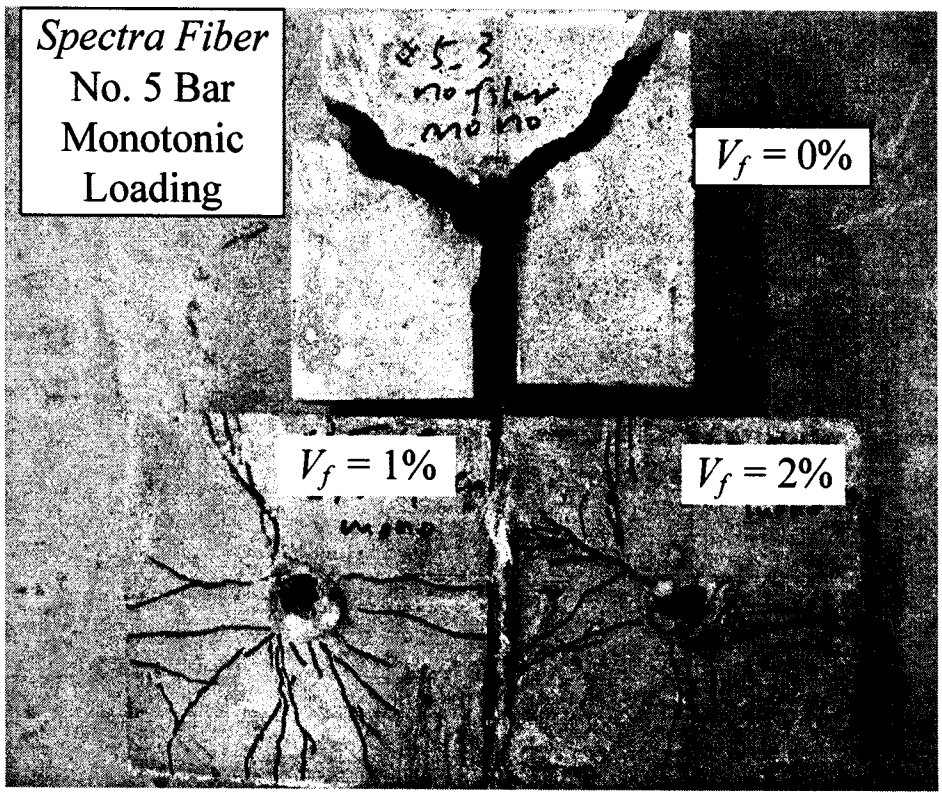

Figure 4.14 Crack patterns for specimens with different fiber contents (No. 5 bar and Spectra fiber)

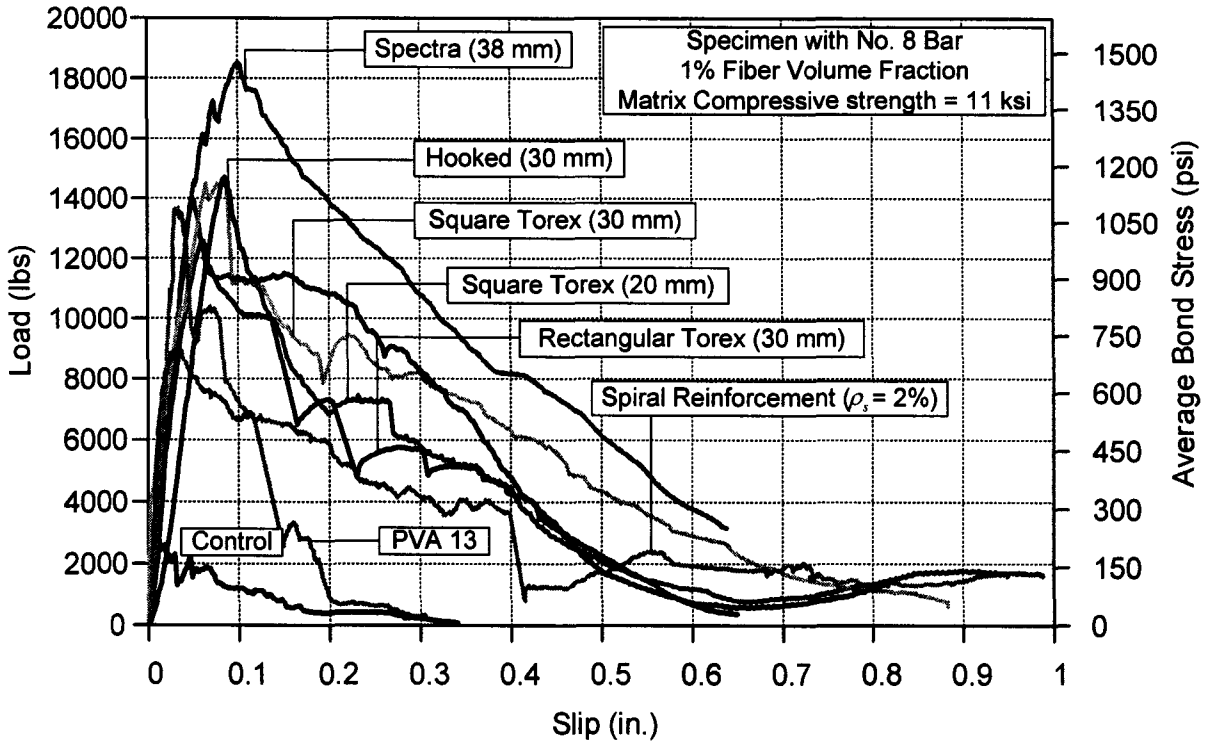

Figure 4.15 Comparison of bond stress-slip behavior of specimens with various types of fiber (No. 8; 1% fiber volume fraction; matrix compressive strength is 11 ksi)

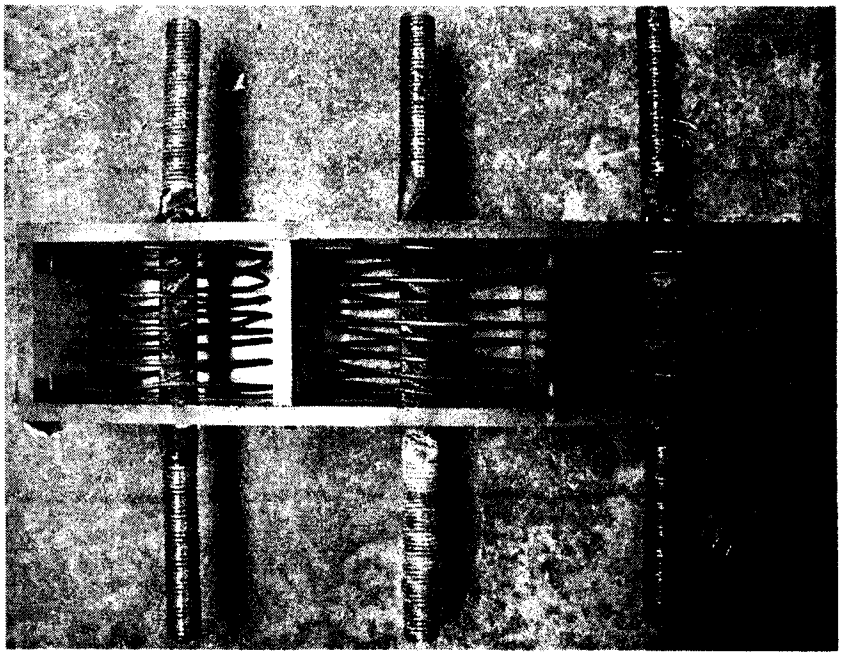

Figure 4.16 (a) Specimen with 2% steel volume fraction of spiral reinforcement

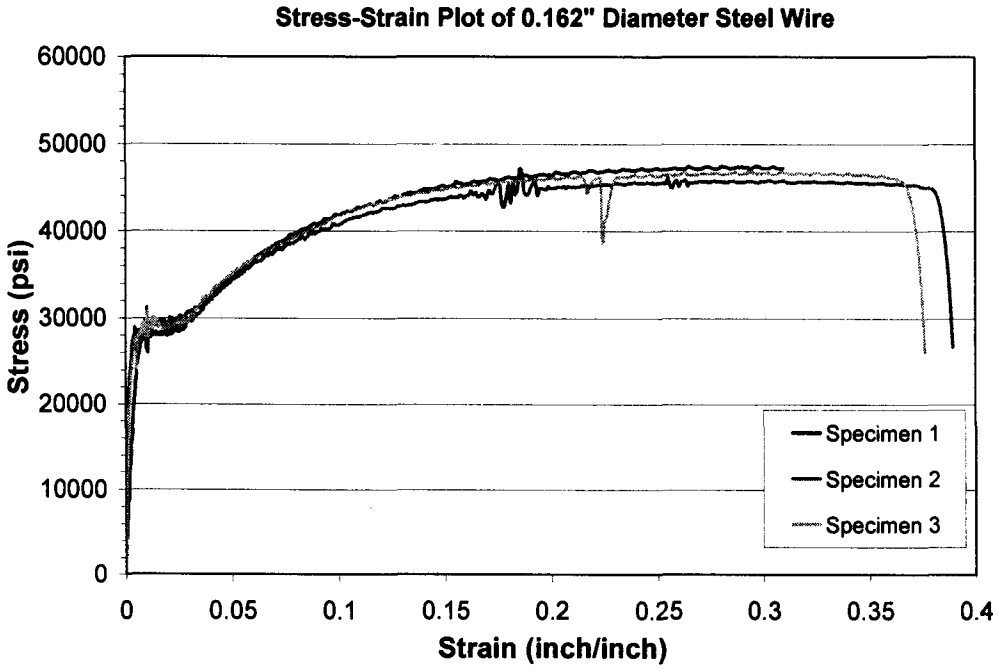

Figure 4.16 (b) Stress-Strain curve of steel wire used for spiral reinforcement

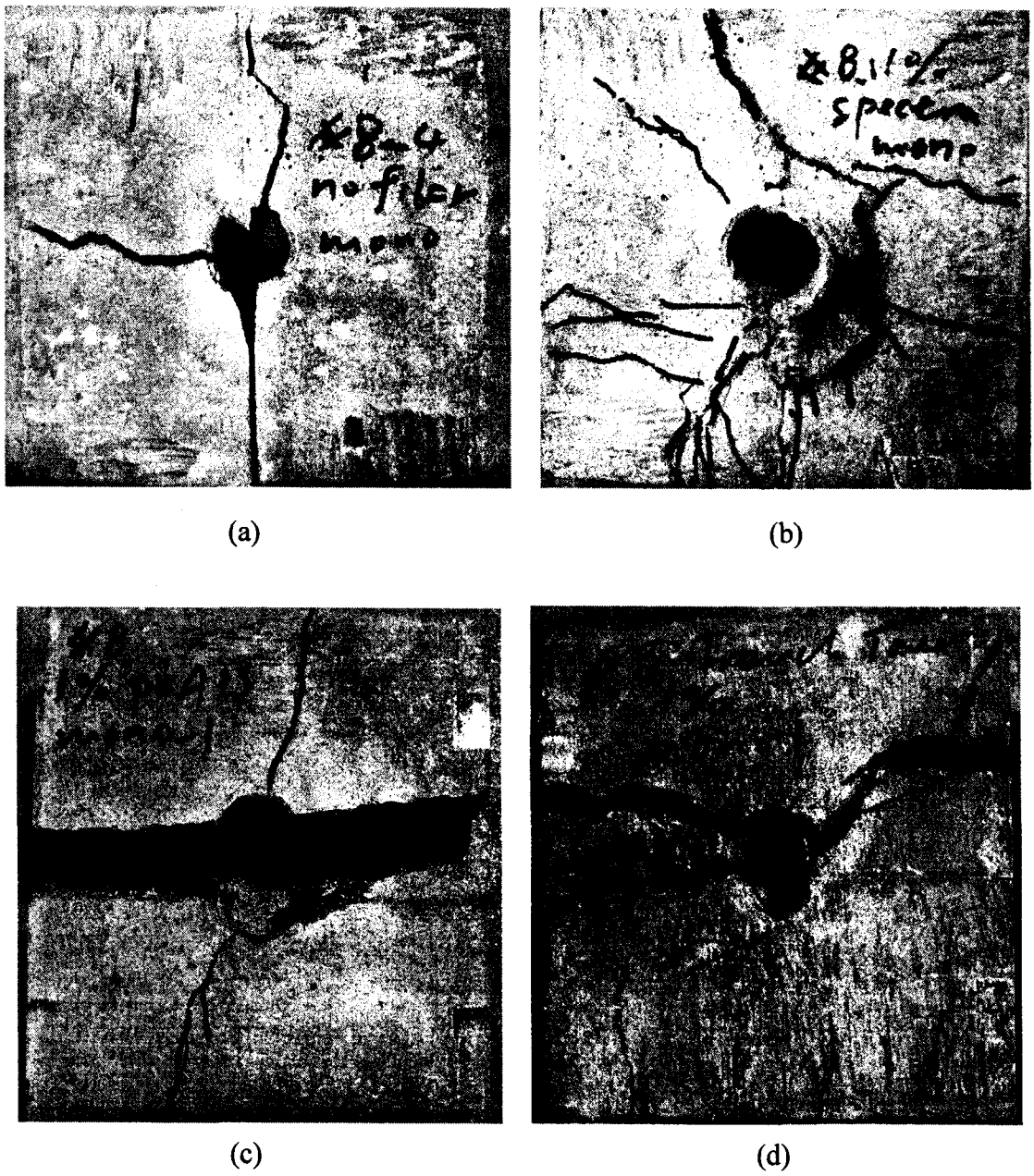

Figure 4.17 Crack patterns of No .8 bar specimens with various fibers (1% volume fraction): (a) Control specimen; (b) Spectra; (c) PVA 13; (d) Rectangular Torex

(e)

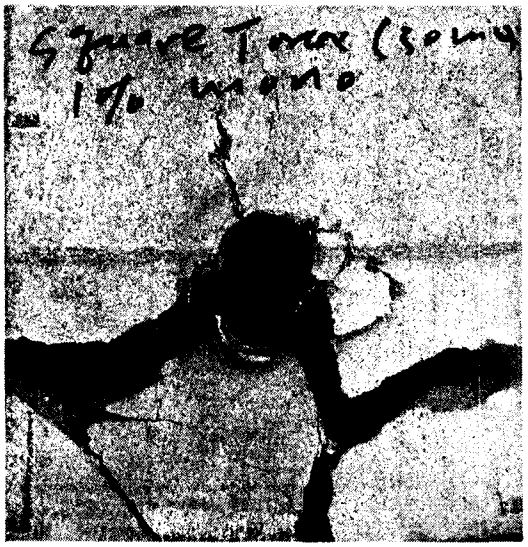

(f)

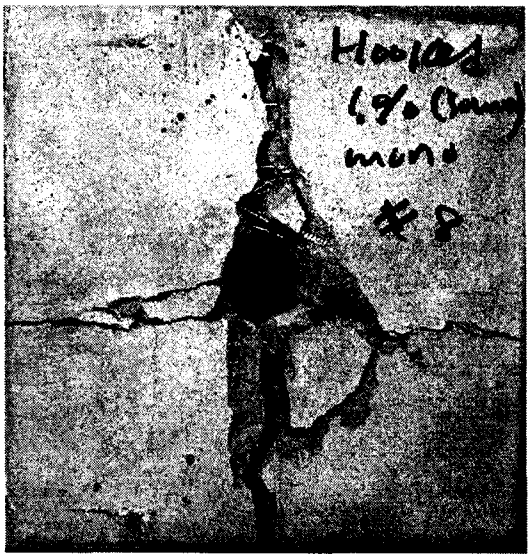

(g)

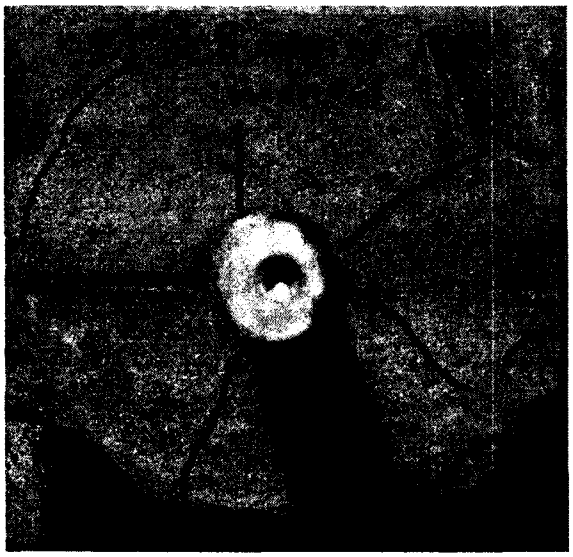

(h)

Figure 4.17 (continued) Crack patterns of No. 8 bar specimens (1% volume fraction): (e) Square Torex (20 mm); (f) Square Torex (30 mm); (g) Hooked; (h) Spiral reinforcement (2% steel volume fraction)

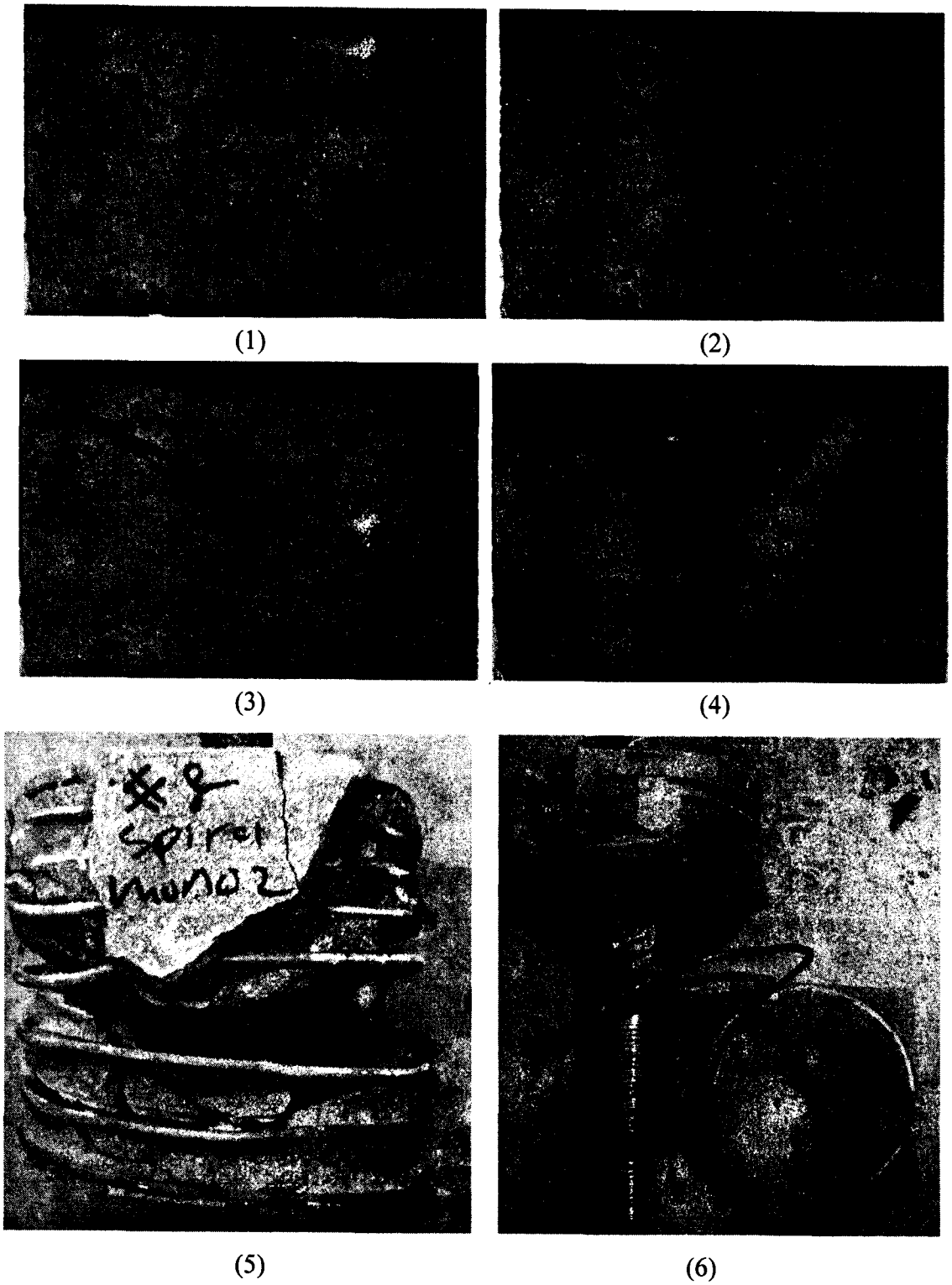

Figure 4.18 Cracking sequence of No. 8 bar specimen with 2% spiral reinforcement under monotonic pullout loading (side view)

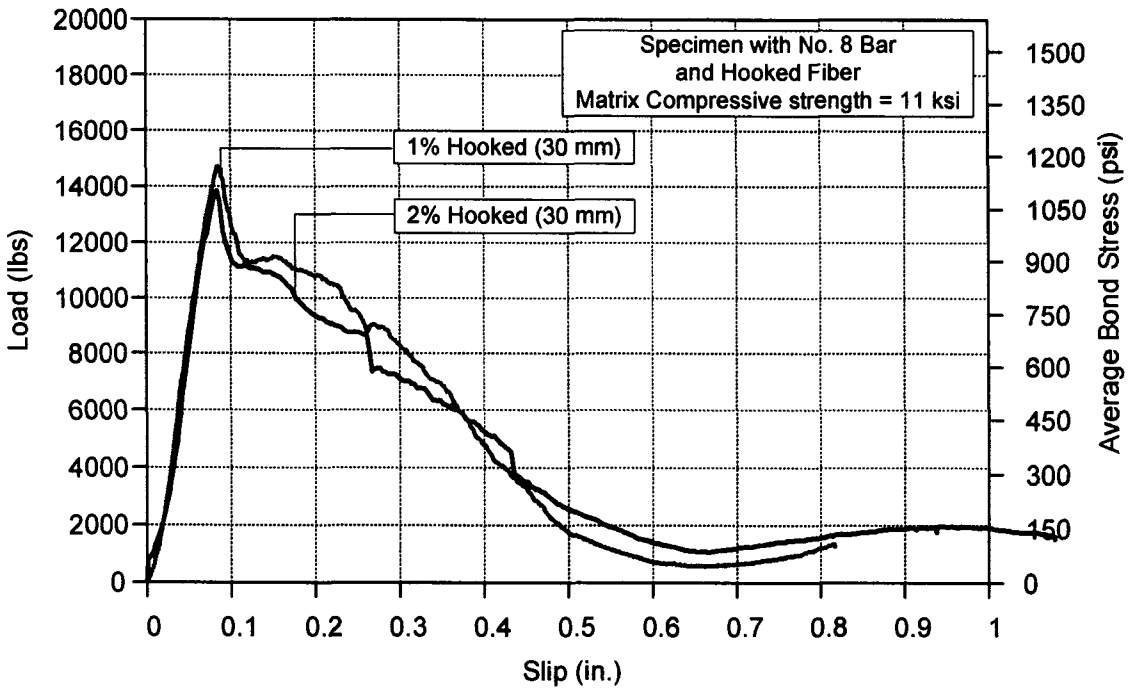

Figure 4.19 Comparison of bond behavior between 1% and 2% steel hooked fibers

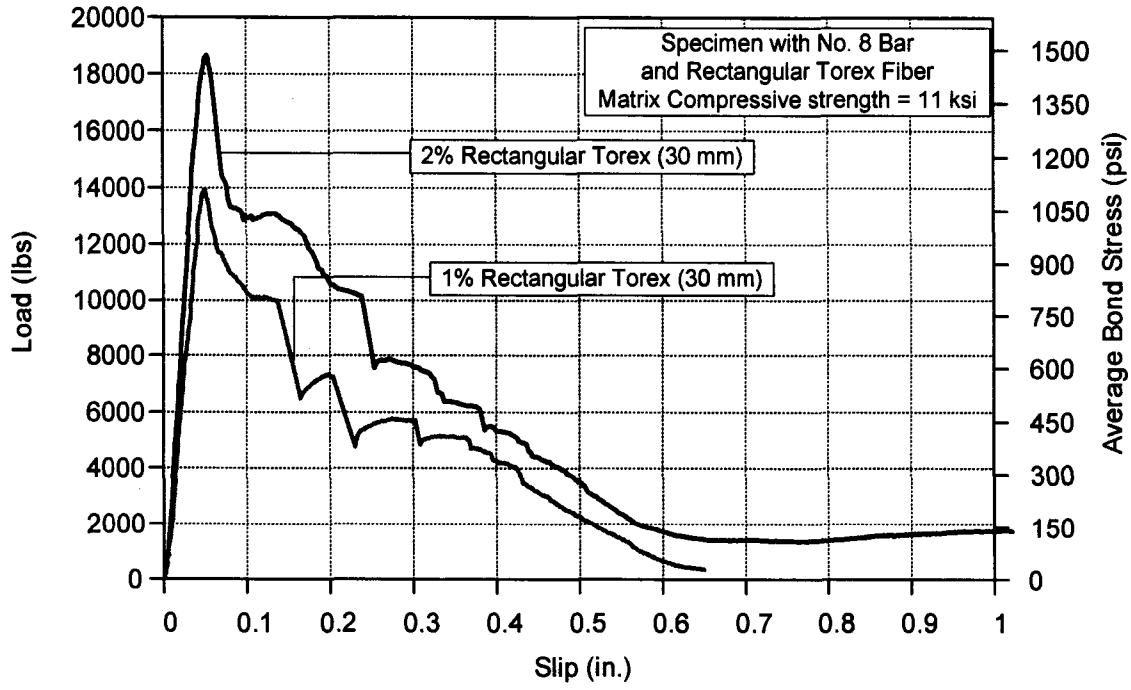

Figure 4.20 Comparison of bond behavior between 1% and 2% Rectangular Torex fibers

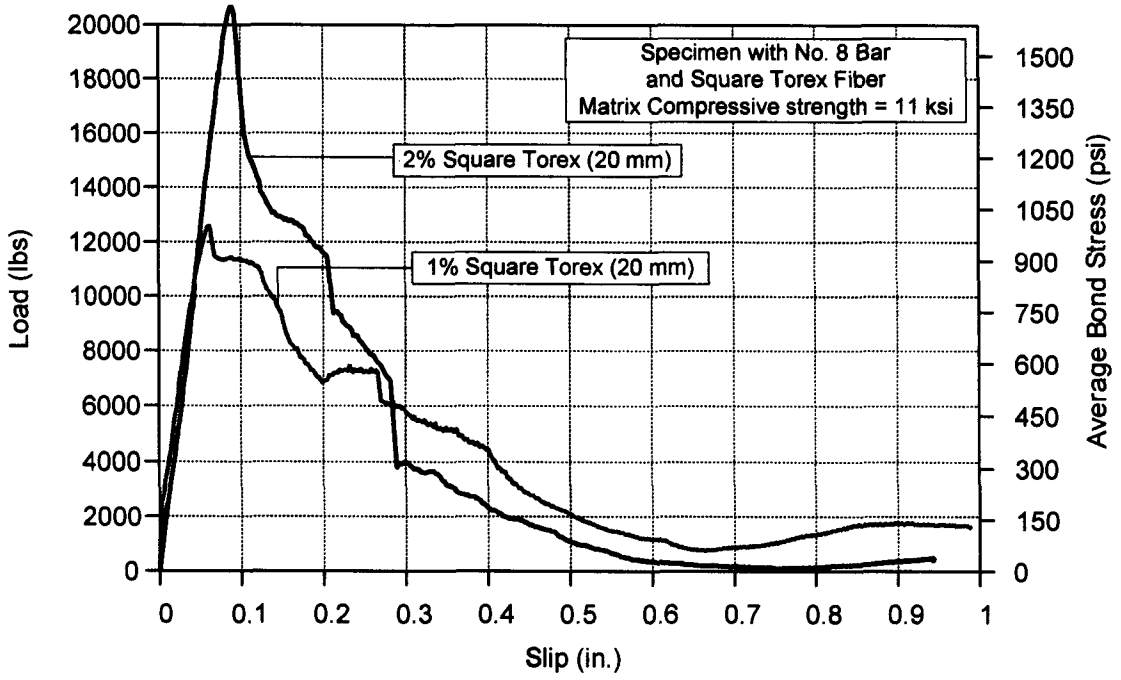

Figure 4.21 Comparison of bond behavior between 1% and 2% Square Torex fibers

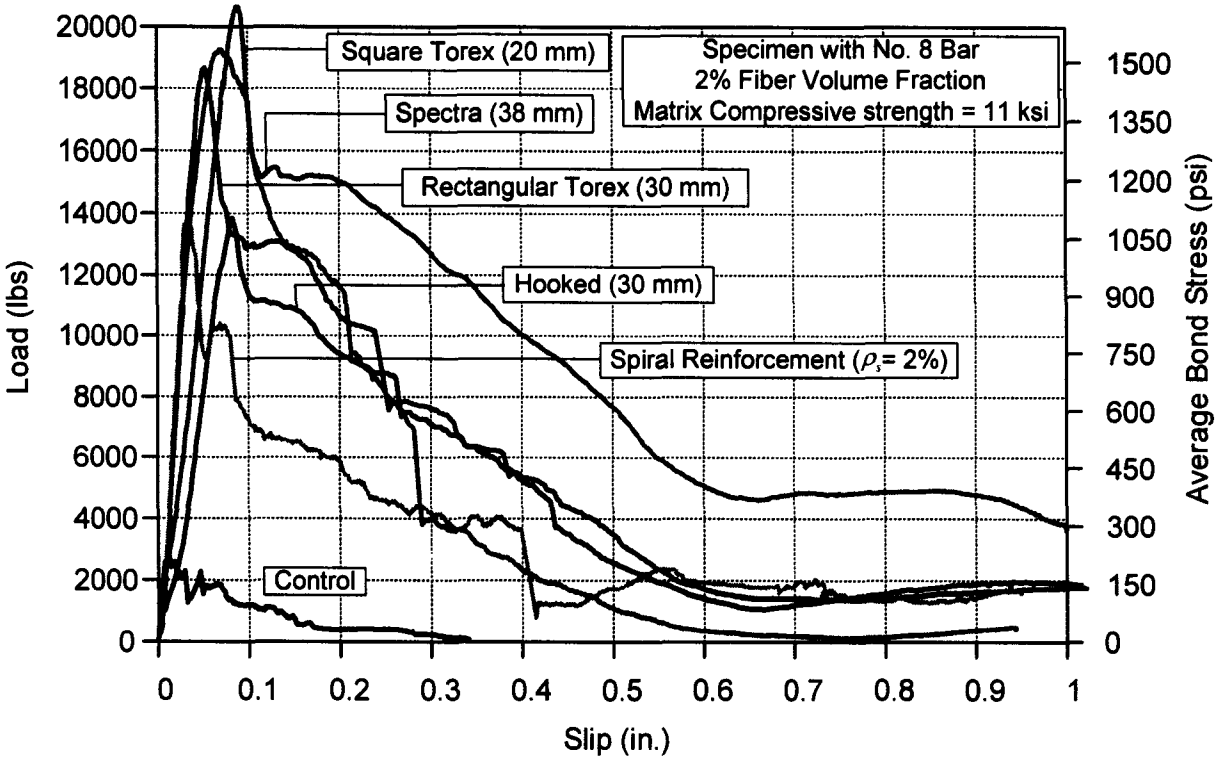

Figure 4.22 Comparison of bond strength-slip behavior of specimens with various types of fiber (No. 8; 2% fiber volume fraction; matrix compressive strength is 11 ksi)

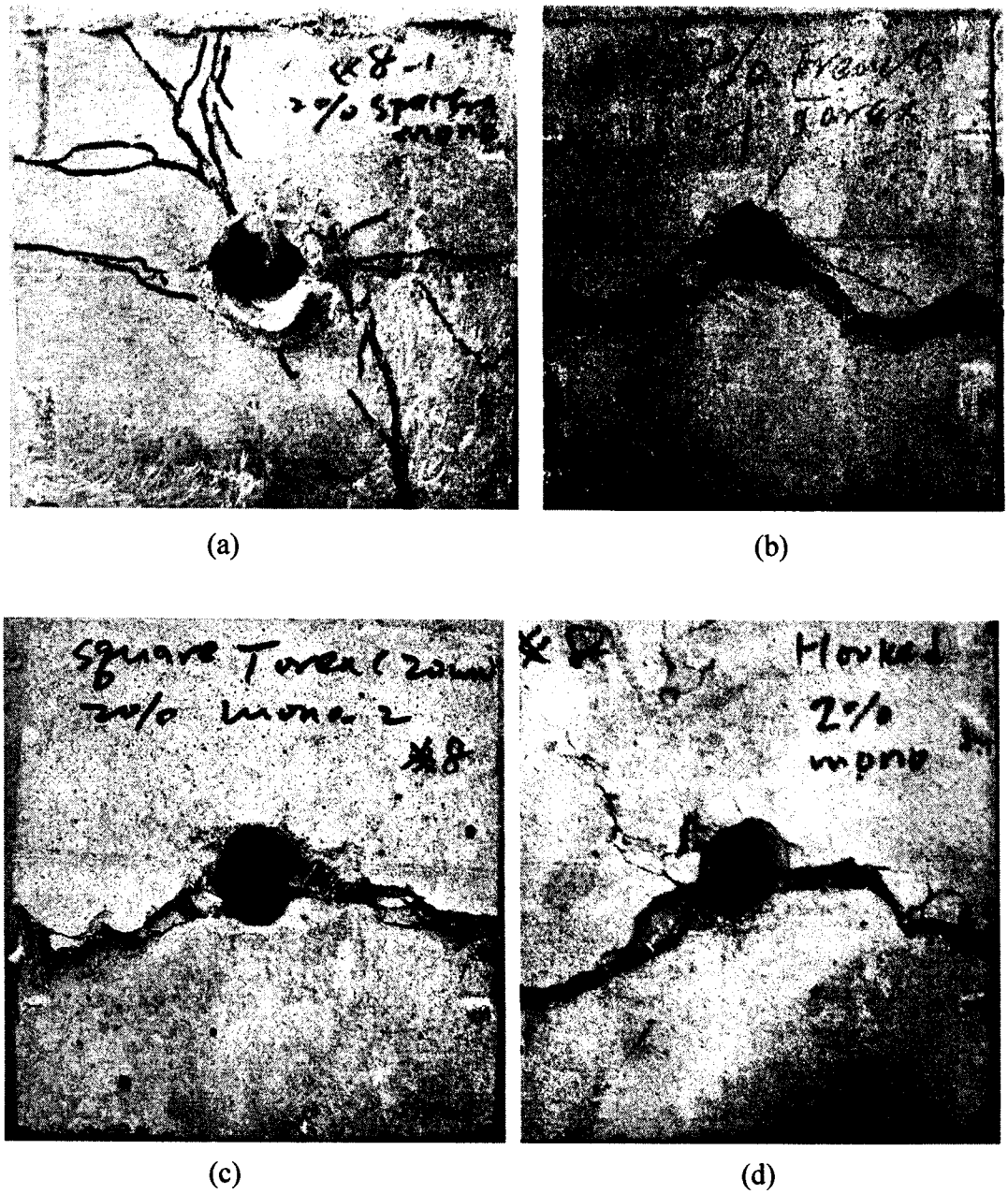

Figure 4.23 Crack patterns of No. 8 bar specimens with various fibers (2% volume fraction): (a) Spectra; (b) Rectangular Torex; (c) Square Torex (20 mm); (d) Hooked

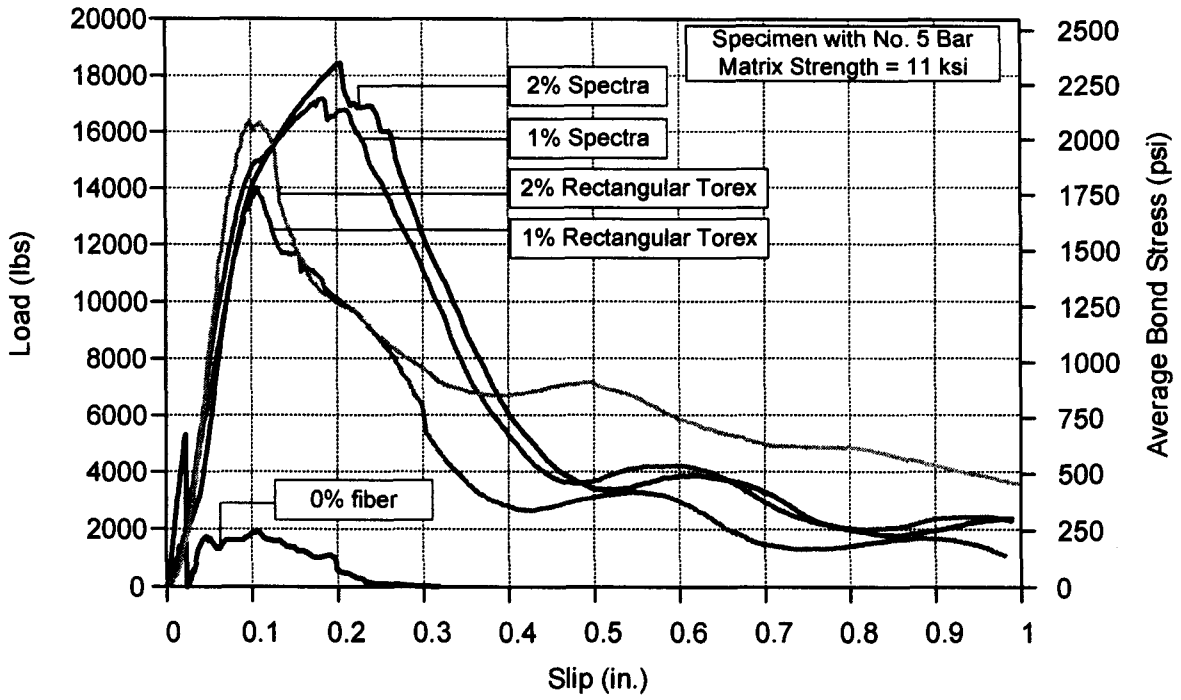

Figure 4.24 Comparison of Load-Slip curves for specimens with different fiber contents (No. 5 bar; rectangular Torex and Spectra fibers)

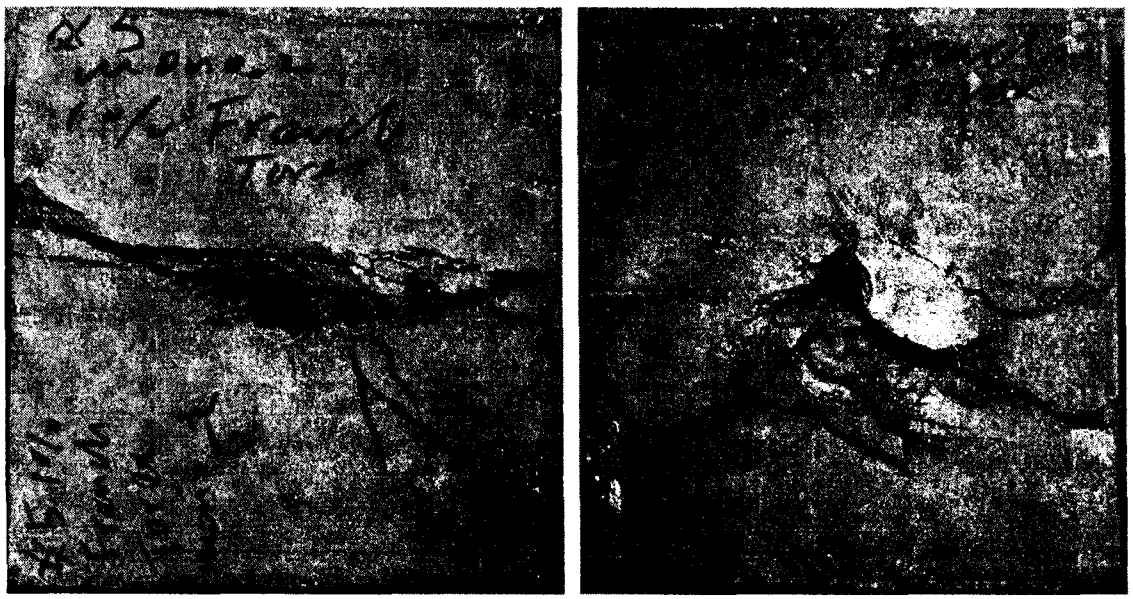

Figure 4.25 (a) Crack patterns of No. 5 bar specimens with various fibers (top view): 1% rectangular Torex (left); 2% Rectangular Torex (right)

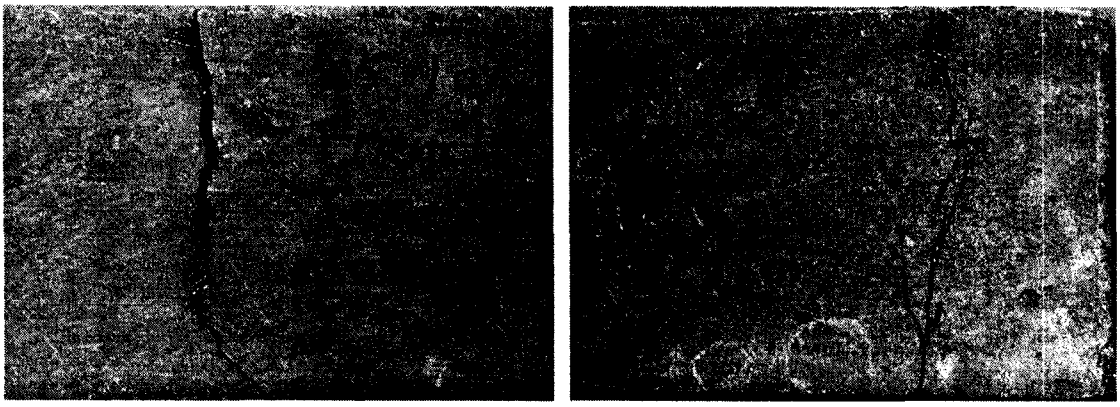

Figure 4.25 (b) Crack patterns of No. 5 bar specimens with various fibers (side view): 1% rectangular Torex (left); 2% Rectangular Torex (right)

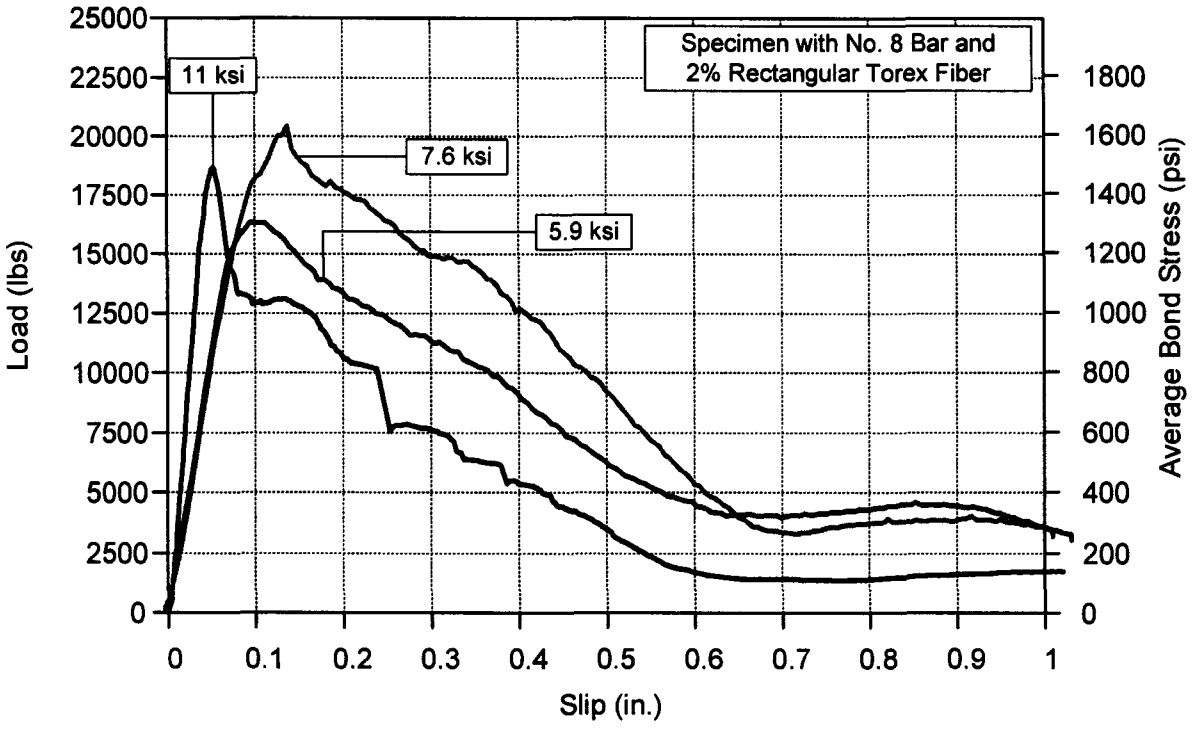

Figure 4.26 Comparison of Load-Slip curves for specimens with various matrix compressive strengths (No. 8 bar; rectangular Torex fiber)

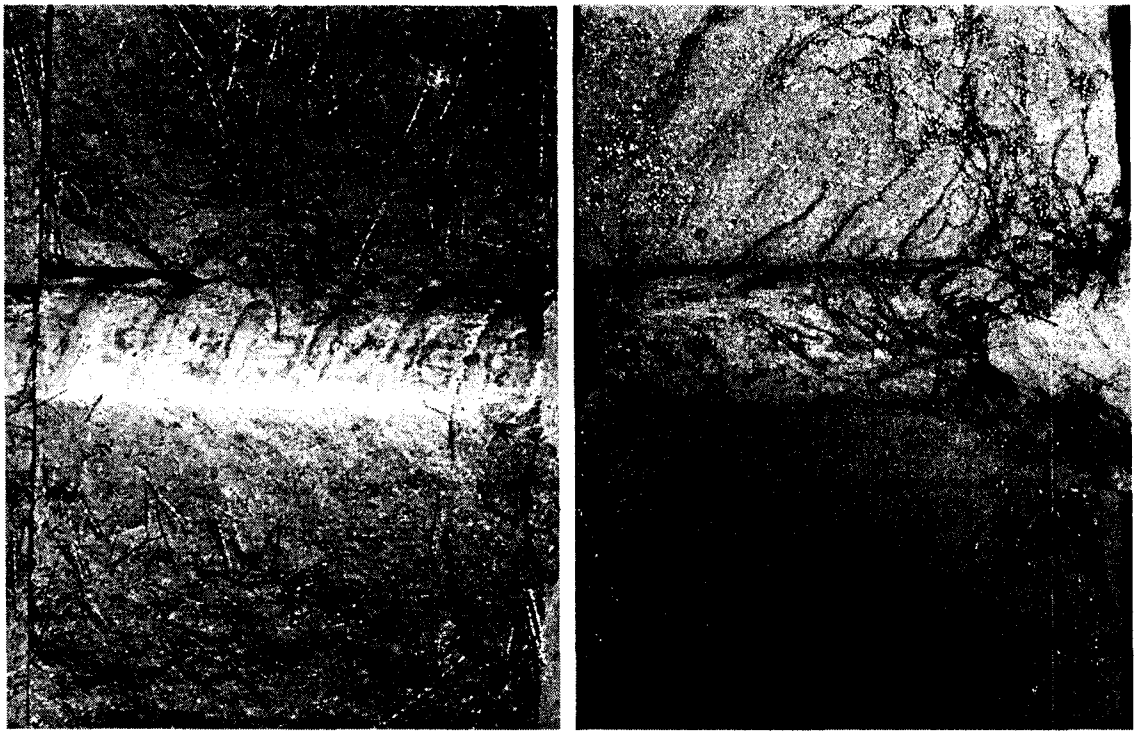

(a) (b)

Figure 4.27 Reinforcing bar-to-matrix interface after larger slip (No. 8 bar; 2% rectangular Torex fiber): (a) 11ksi matrix strength; (b) 7.6 ksi matrix strength

(a) (b)

Figure 4.28 Crack patterns after larger slip (No. 8 bar; 2% rectangular Torex fiber): (a) 7.6 ksi matrix strength; (b) 5.9 ksi matrix strength

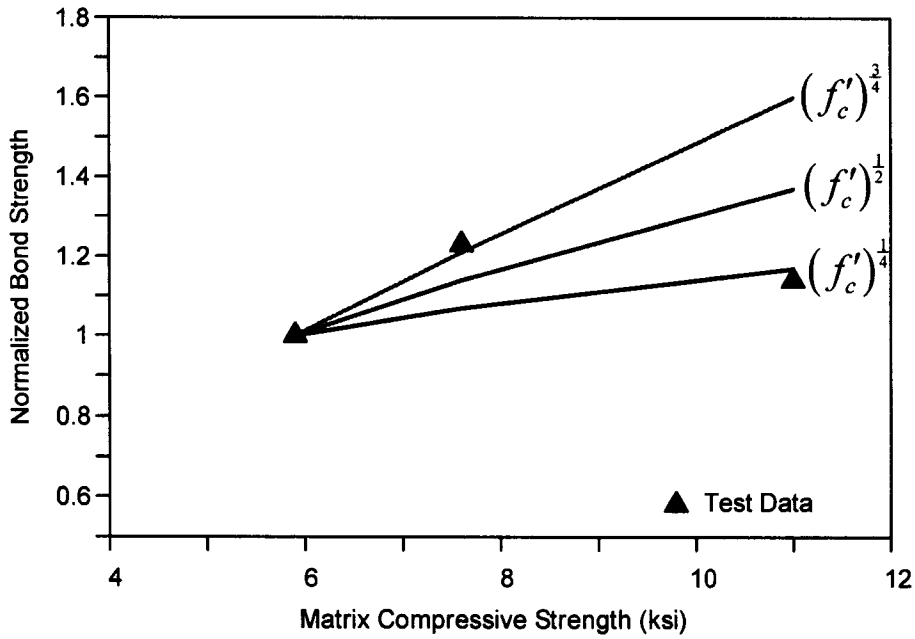

Figure 4.29 Normalized bond strength using various matrix strength index, compared with test data

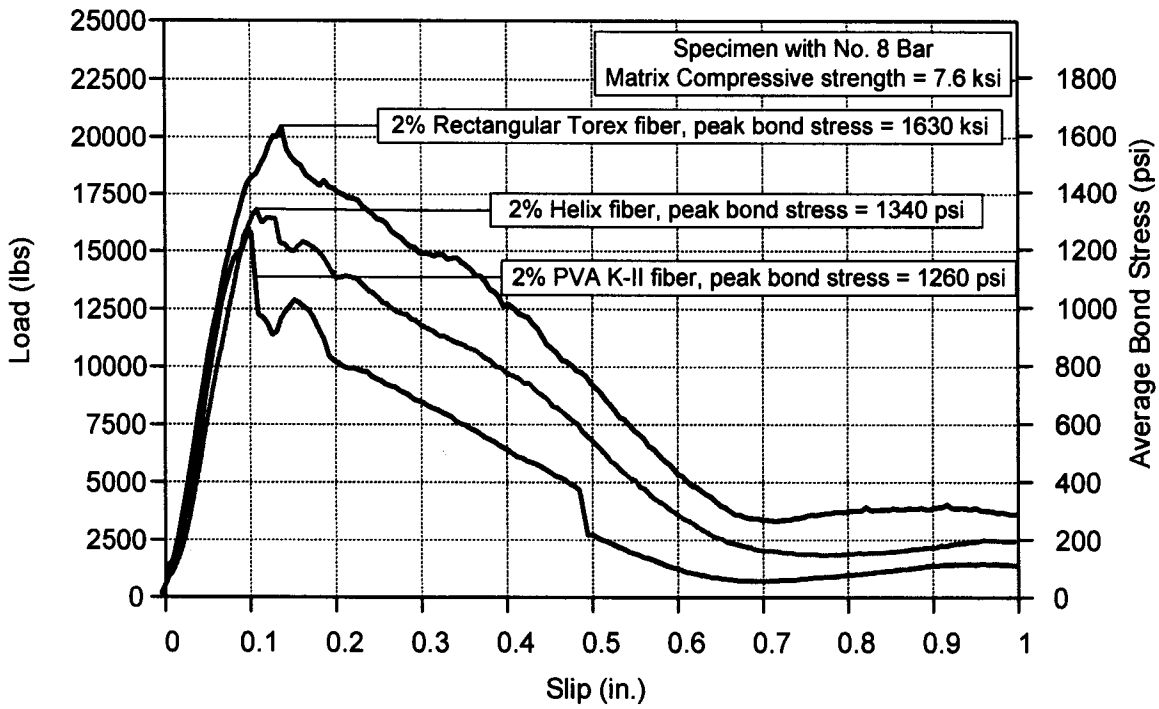

Figure 4.30 Load-slip curves of specimen with 7.6 ksi matrix strength and three different types of fibers

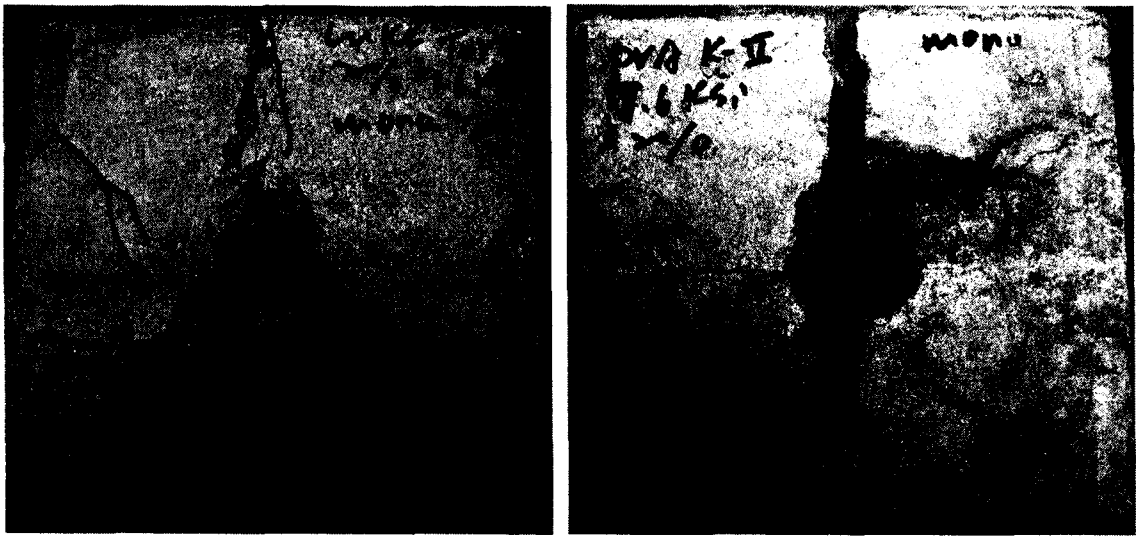

(a) (b)

Figure 4.31 Crack patterns after larger slip (No. 8 bar; 7.6 ksi matrix strength): (a) Helix fiber; (b) PVA K-II fiber

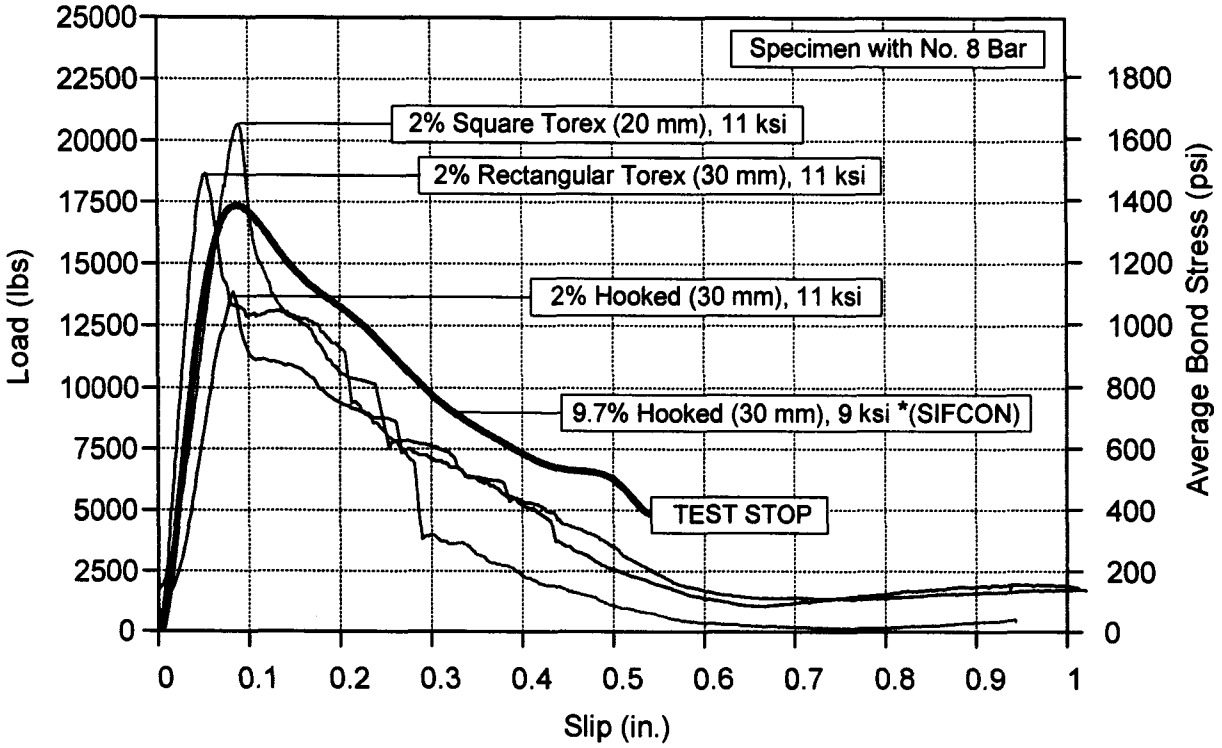

* SIFCON Specimen #81, Hota and Naaman, 1995

Figure 4.32 Comparison of bond behavior between test HPFRCCs and SIFCON

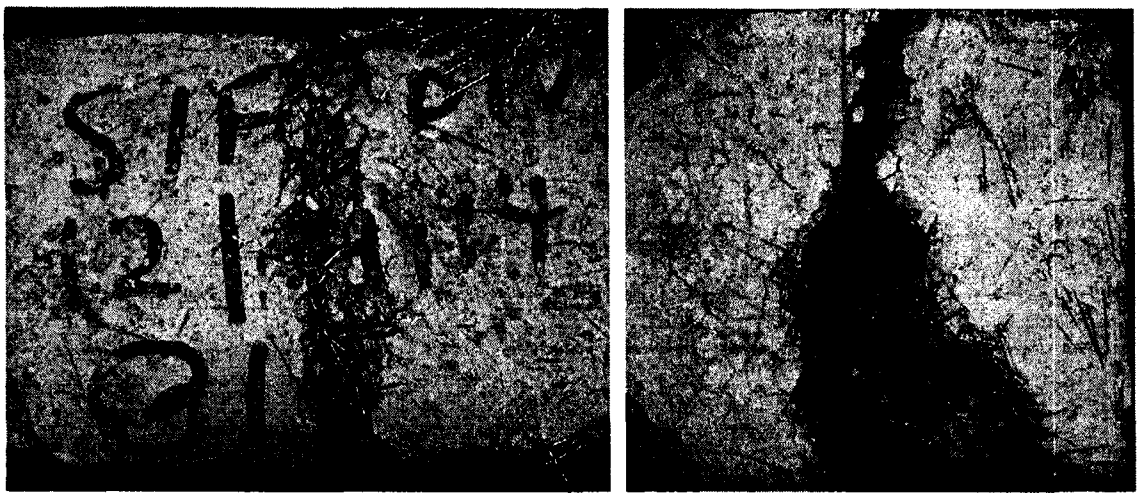

(a) (b)

Figure 4.33 SIFCON specimen (# 81, Hota and Naaman, 1995) after monotonic pullout bond test: (a) side view; (b) top view

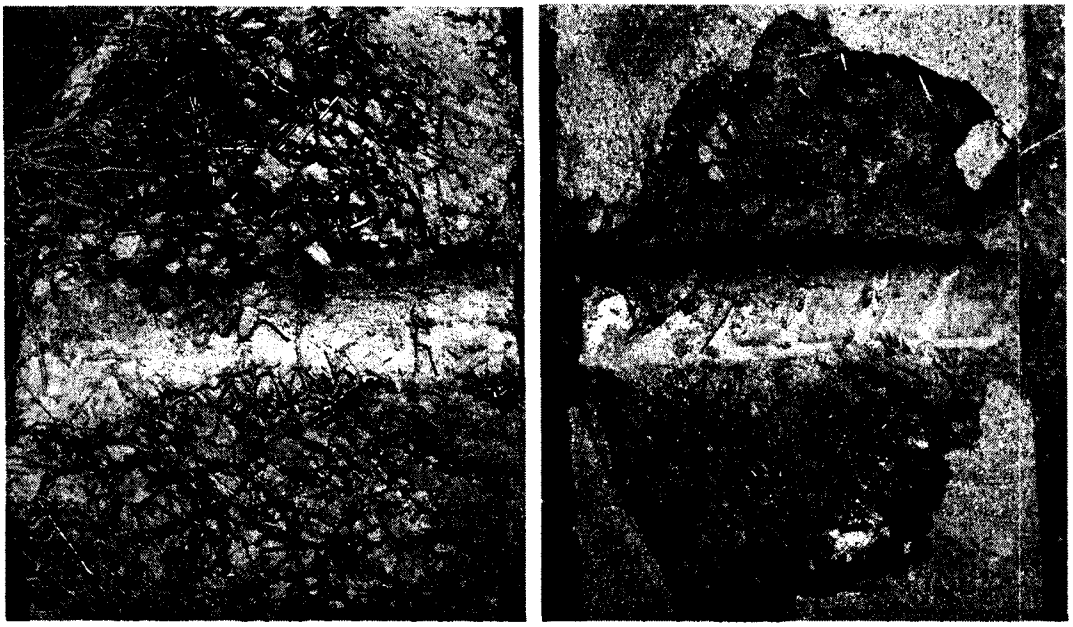

(a) (b)

Figure 4.34 Half cut-open specimen showing the crushing or shearing after large slip under monotonic pullout bond test: (a) SIFCON specimen, 9.7% hooked fiber (# 81, Hota and Naaman, 1995); (b) HPFRCC specimen, 2% square Torex fiber (20 mm)

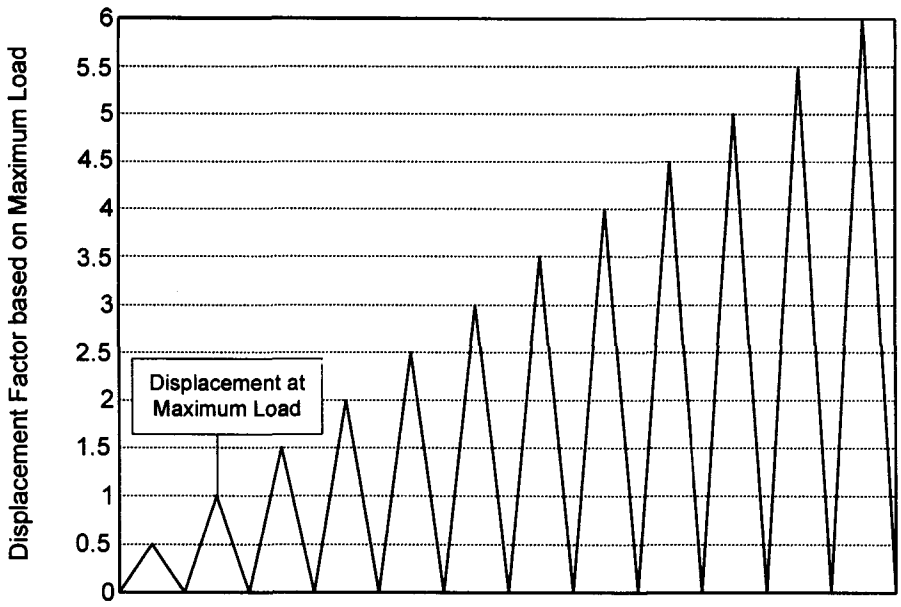

Figure 4.35 Unidirectional cyclic loading protocol for reinforcing bar (displacement controlled)

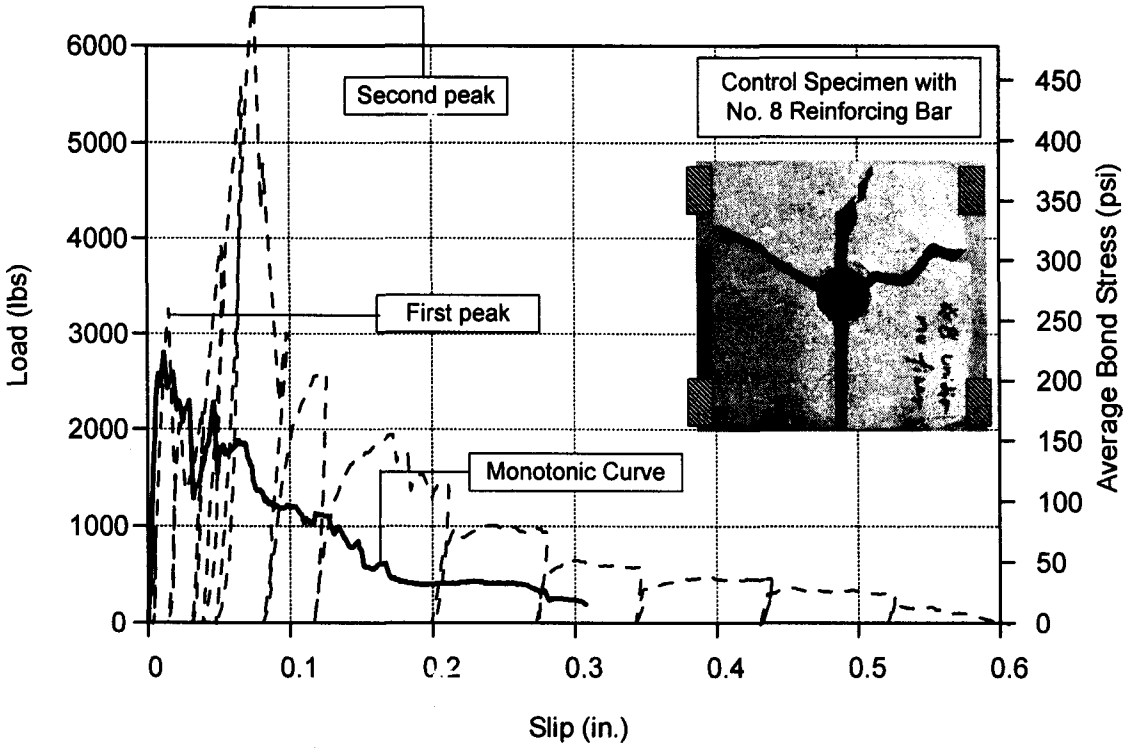

Figure 4.36 Load-slip curve for No. 8 bar control specimen subjected to unidirectional displacement controlled loading and corresponding cracking patterns

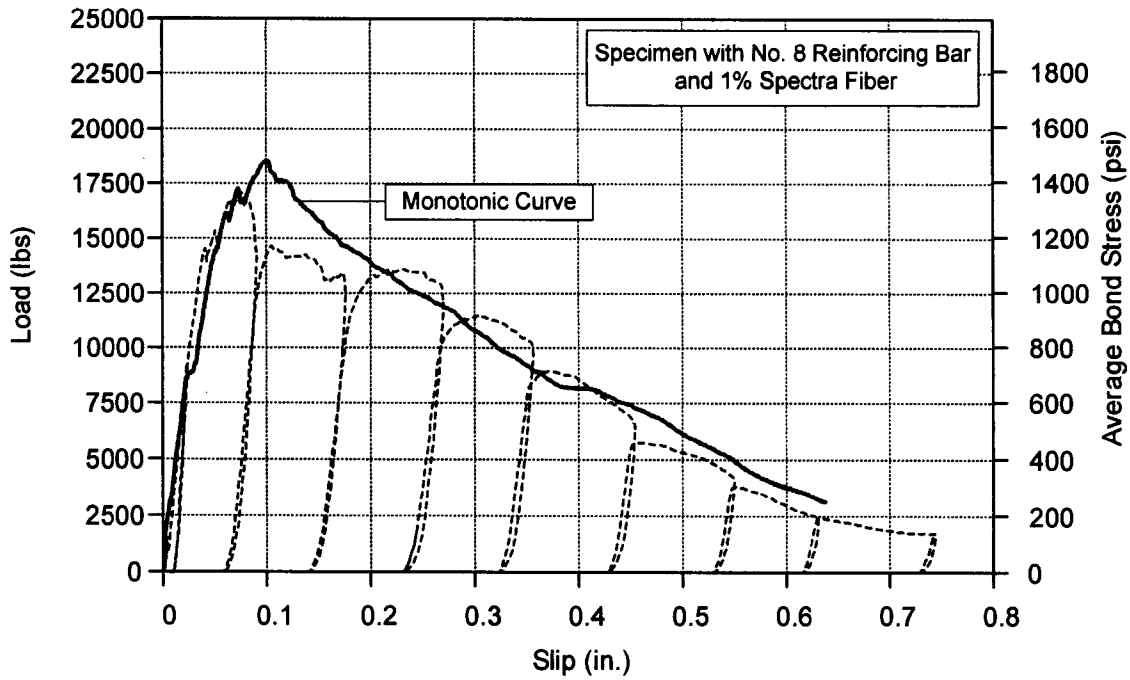

Figure 4.37 Load-slip curve for No. 8 bar specimen with 1% Spectra fiber subjected to unidirectional displacement controlled loading

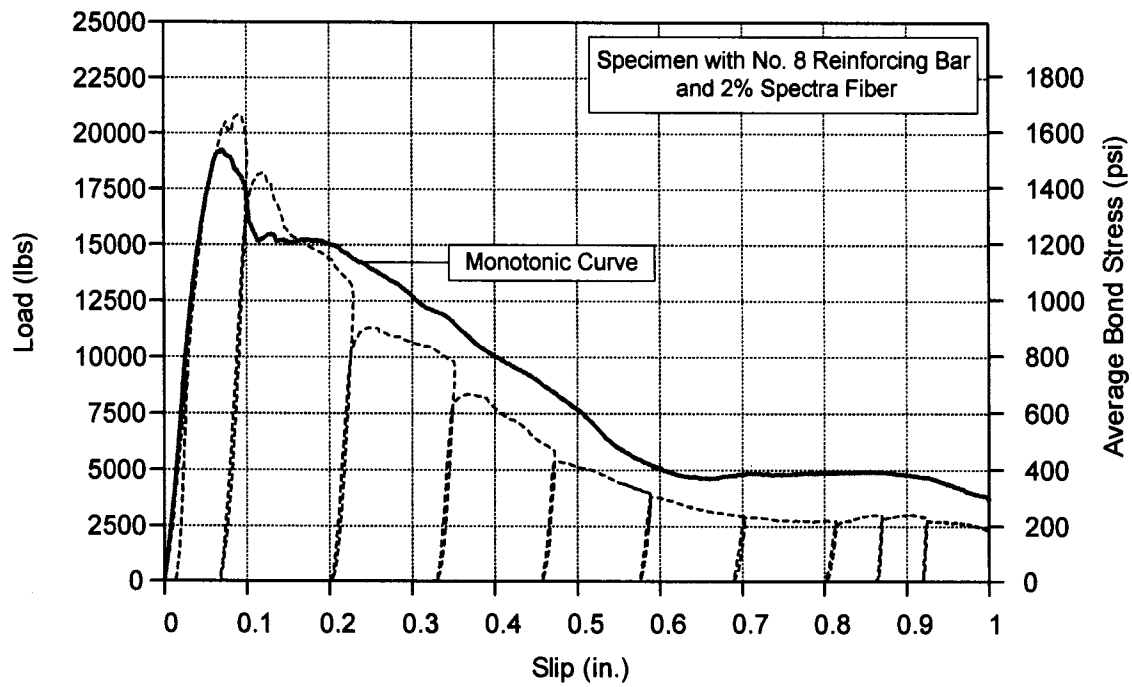

Figure 4.38 Load-slip curve for No. 8 bar specimen with 2% Spectra fiber subjected to unidirectional displacement controlled loading

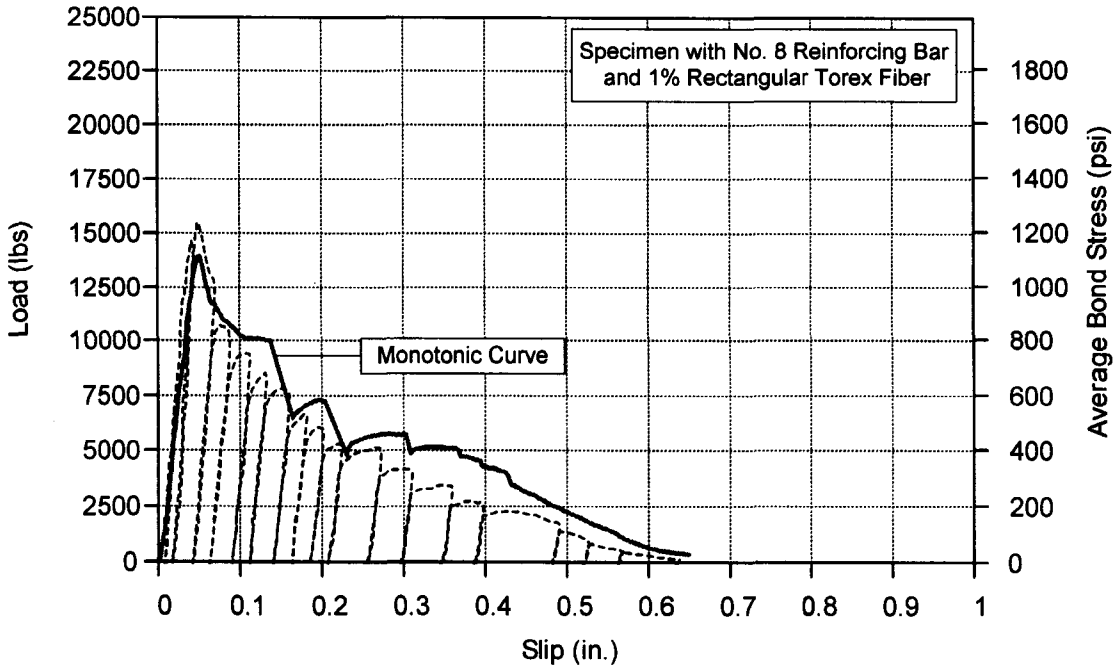

Figure 4.39 Load-slip curve for No. 8 bar specimen with 1% rectangular Torex fiber subjected to unidirectional displacement controlled loading

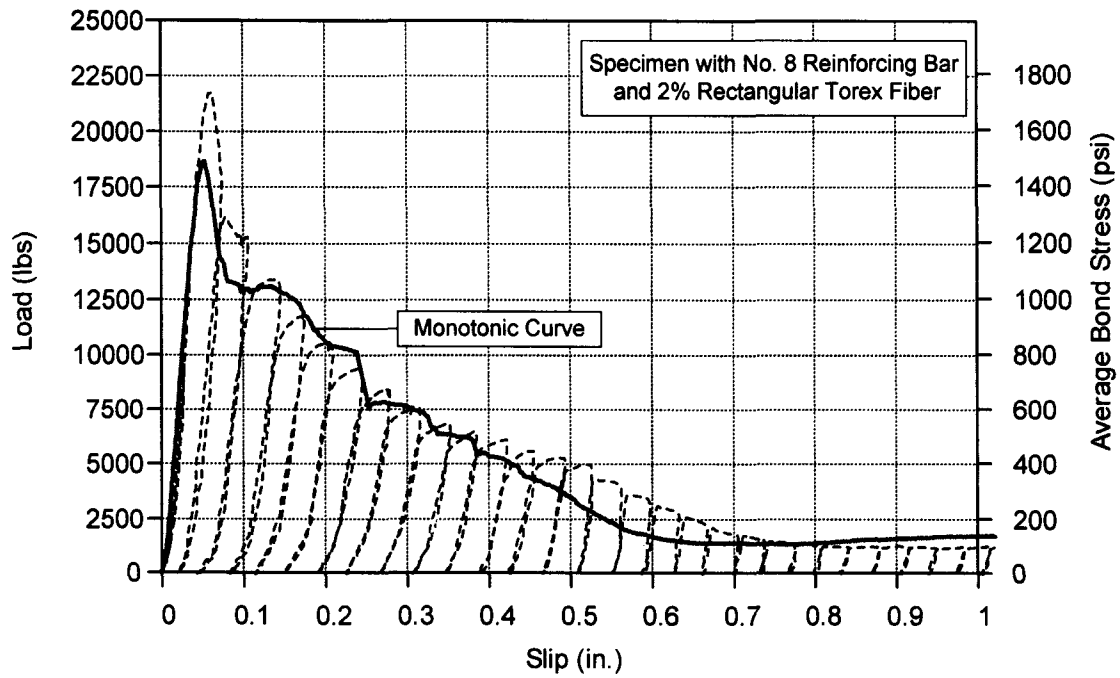

Figure 4.40 Load-slip curve for No. 8 bar specimen with 2% rectangular Torex fiber subjected to unidirectional displacement controlled loading

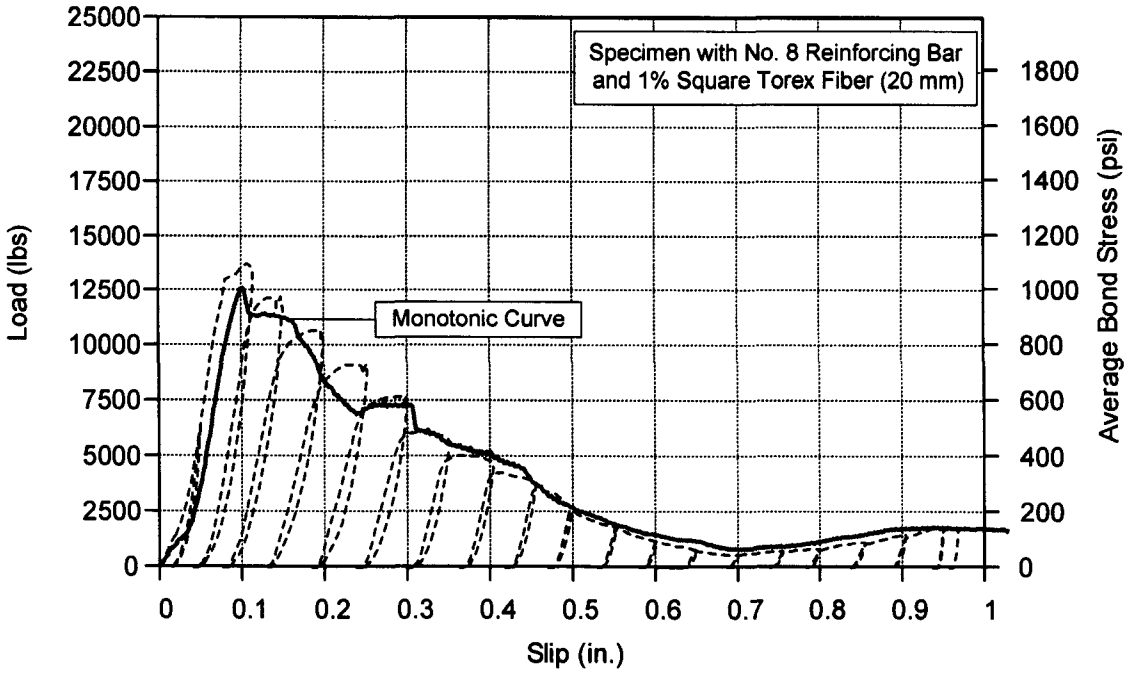

Figure 4.41 Load-slip curve for No. 8 bar specimen with 1% square Torex fiber subjected to unidirectional displacement controlled loading

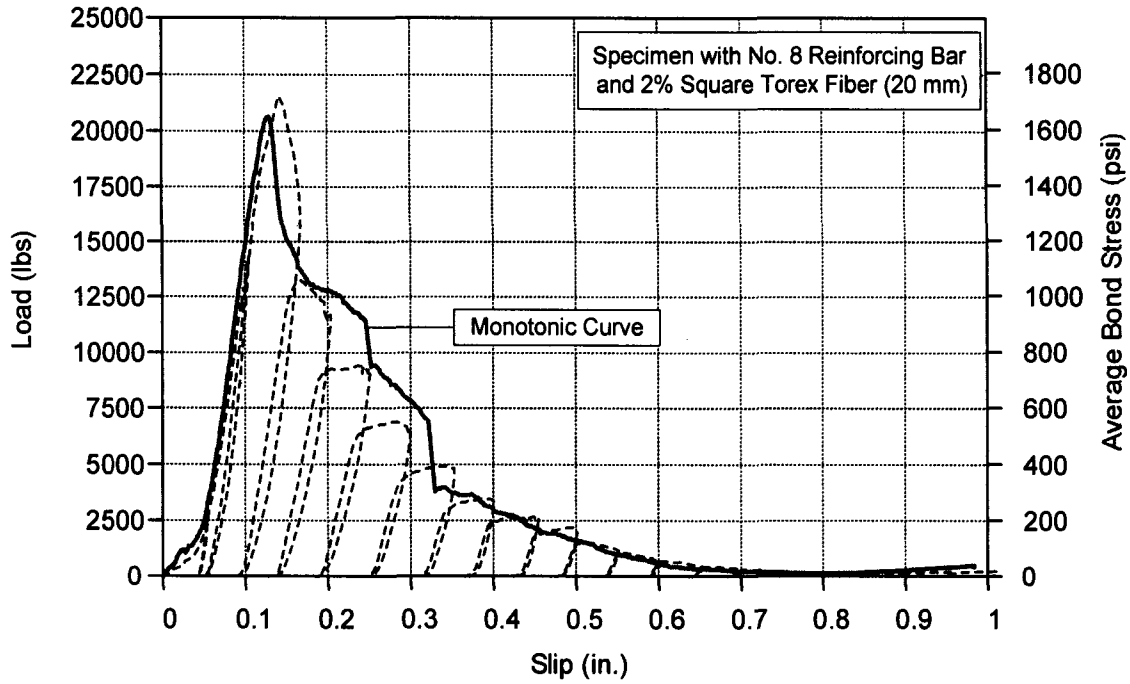

Figure 4.42 Load-slip curve for No. 8 bar specimen with 2% square Torex fiber subjected to unidirectional displacement controlled loading

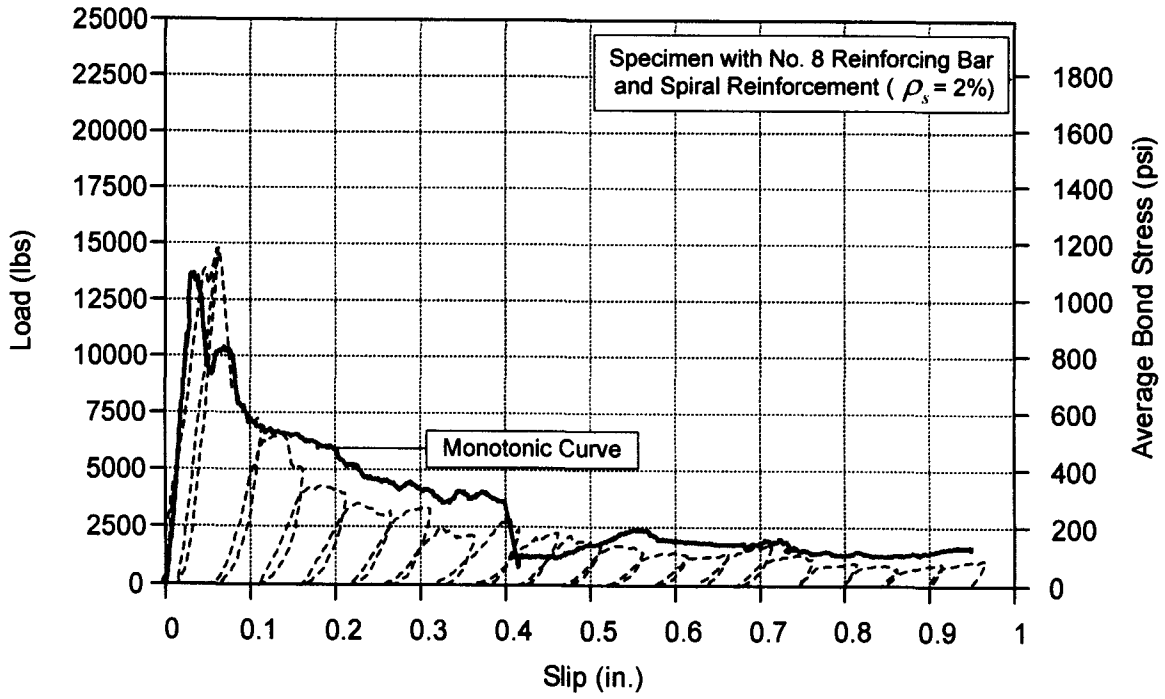

Figure 4.43 Load-slip curve for No. 8 bar specimen with spiral reinforcement subjected to unidirectional displacement controlled loading

Figure 4.44 Crack patterns of specimen with No. 8 bar and 1% fiber volume fraction subjected to unidirectional displacement controlled loading: (a) Spectra; (b) rectangular Torex; (c) Square Torex

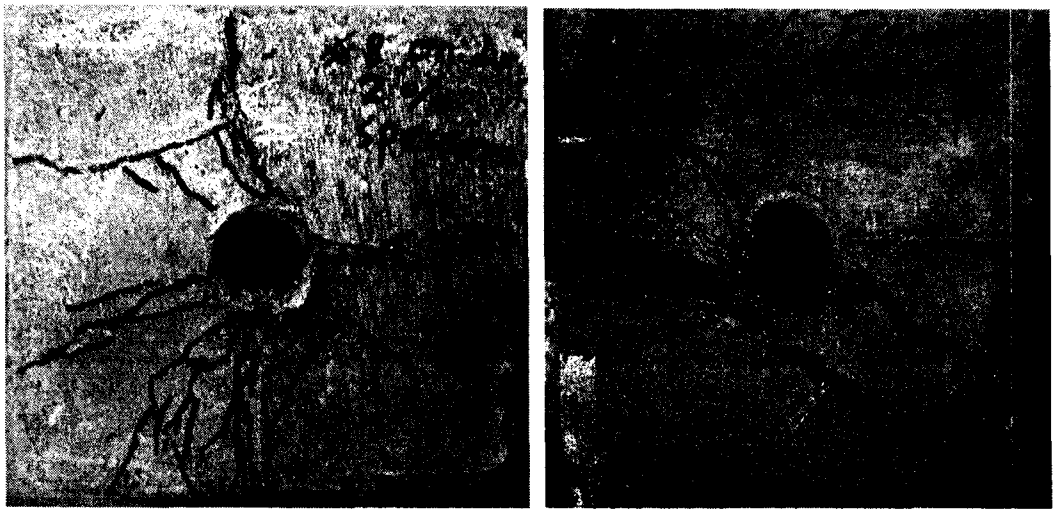

(a) (b)

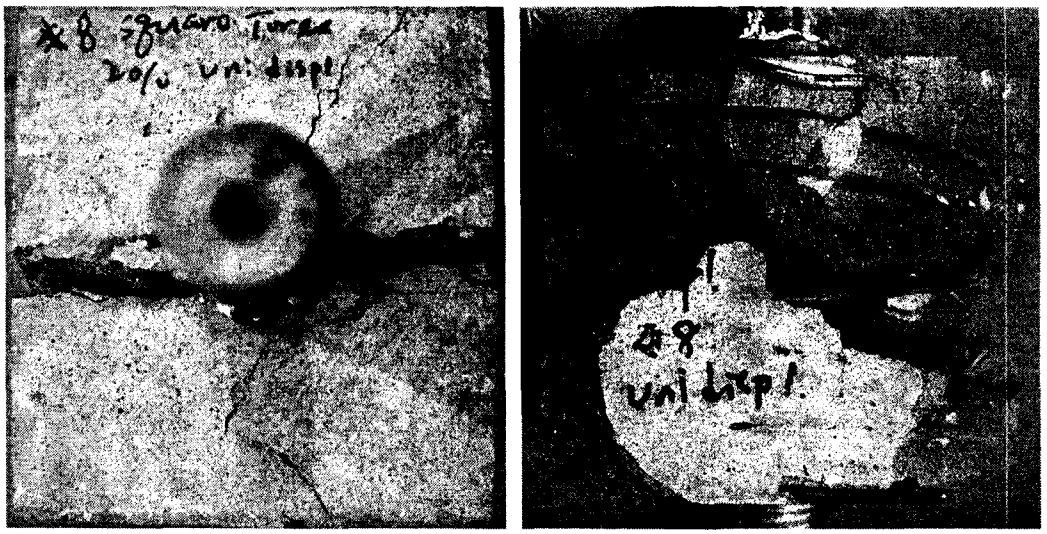

(c) (d)

Figure 4.45 Crack patterns of specimen with No. 8 bar subjected to unidirectional displacement controlled loading: (a) 2% Spectra; (b) 2% rectangular Torex; (c) 2% square Torex; (d) 2% volumetric spiral reinforcement

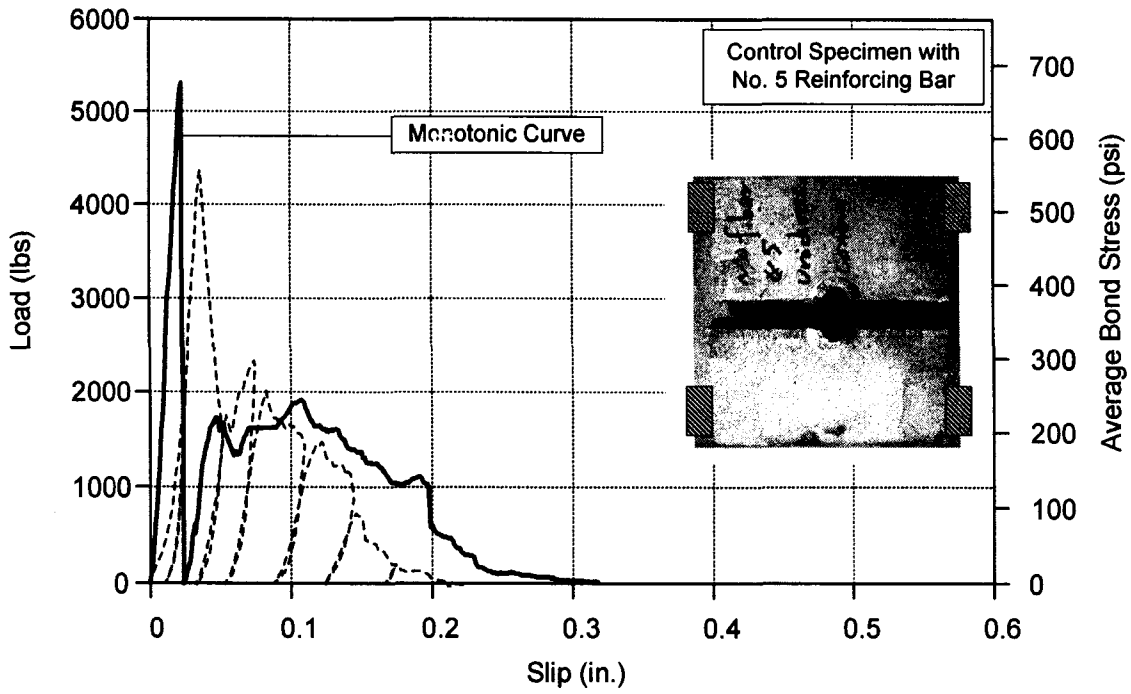

Figure 4.46 Load-slip curve for No. 5 bar control specimen subjected to unidirectional displacement controlled loading and corresponding cracking patterns

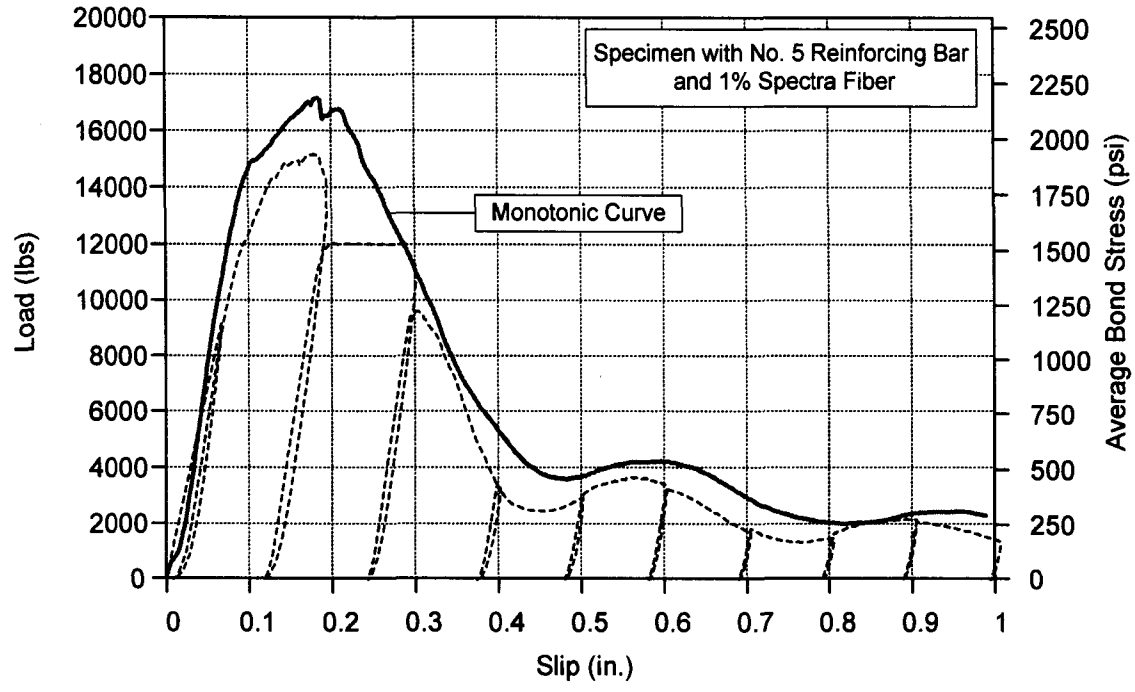

Figure 4.47 Load-slip curve for No. 5 bar specimen with 1% Spectra fiber subjected to unidirectional displacement controlled loading

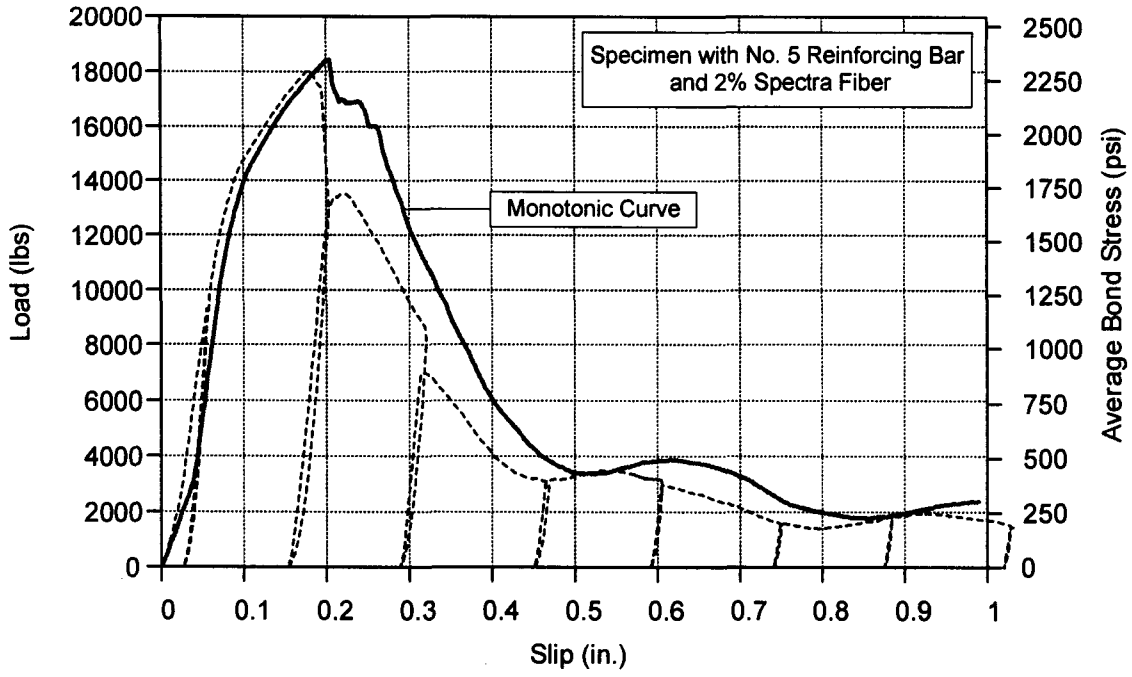

Figure 4.48 Load-slip curve for No. 5 bar specimen with 2% Spectra fiber subjected to unidirectional displacement controlled loading

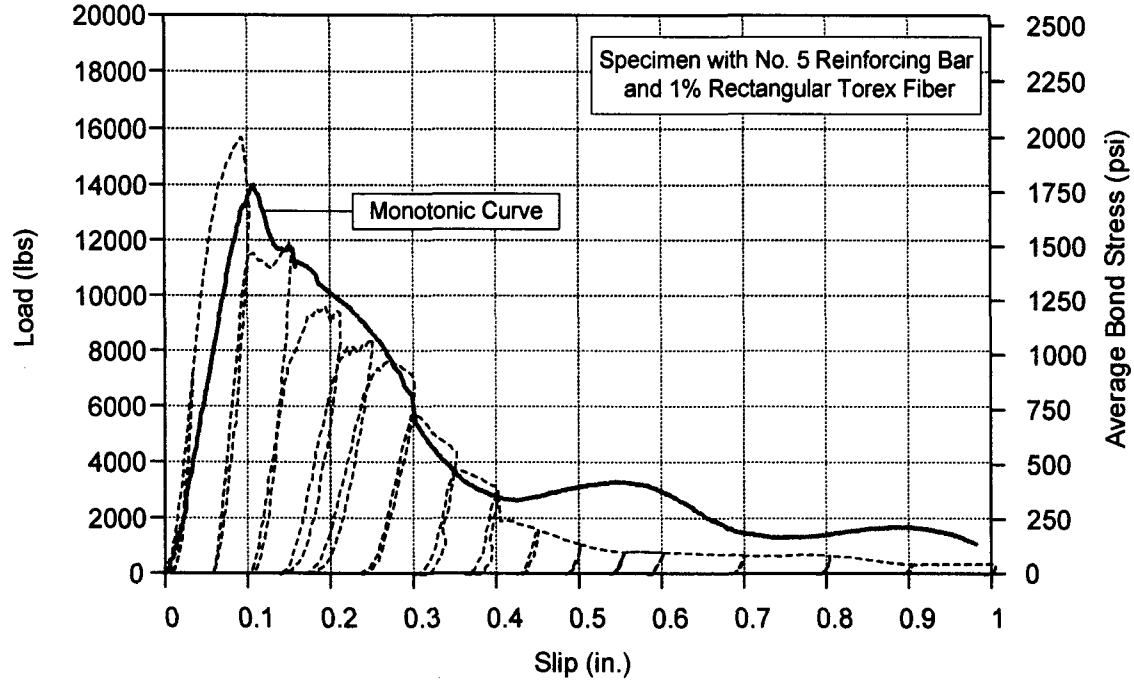

Figure 4.49 Load-slip curve for No. 5 bar specimen with 1% rectangular Torex fiber subjected to unidirectional displacement controlled loading

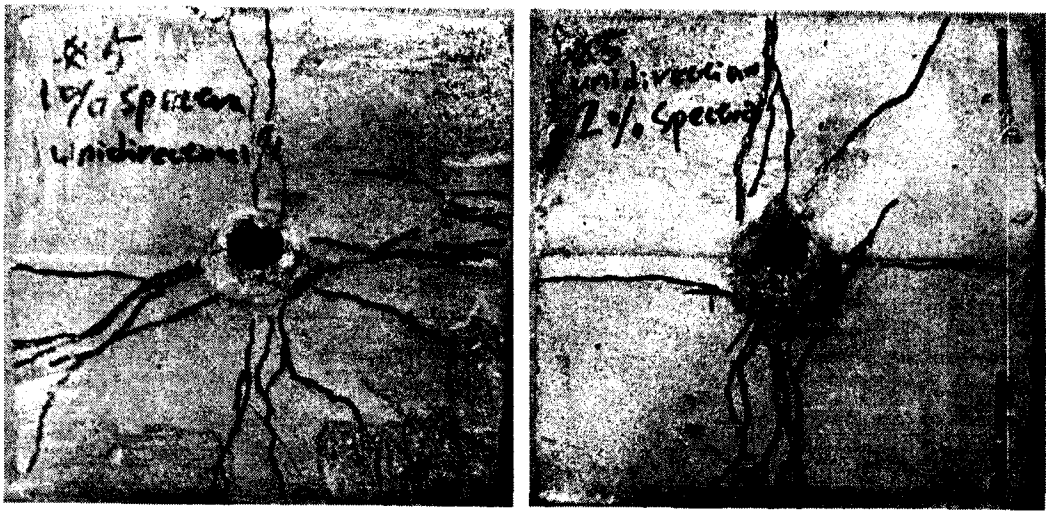

(a) (b)

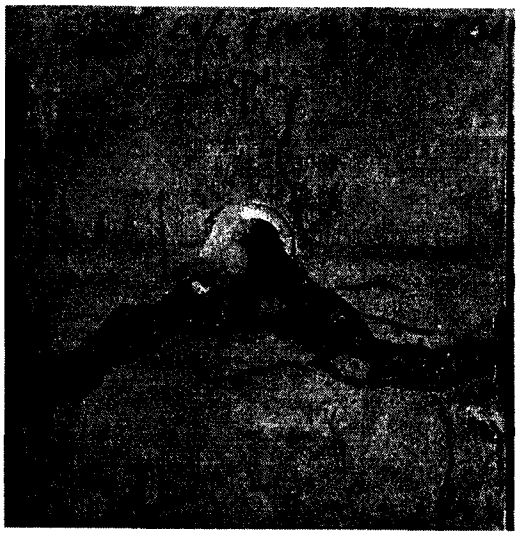

(c)

Figure 4.50 Crack patterns of specimen with No. 5 bar subjected to unidirectional displacement controlled loading: (a) 1% Spectra; (b) 2% Spectra; (c) 1% rectangular Torex

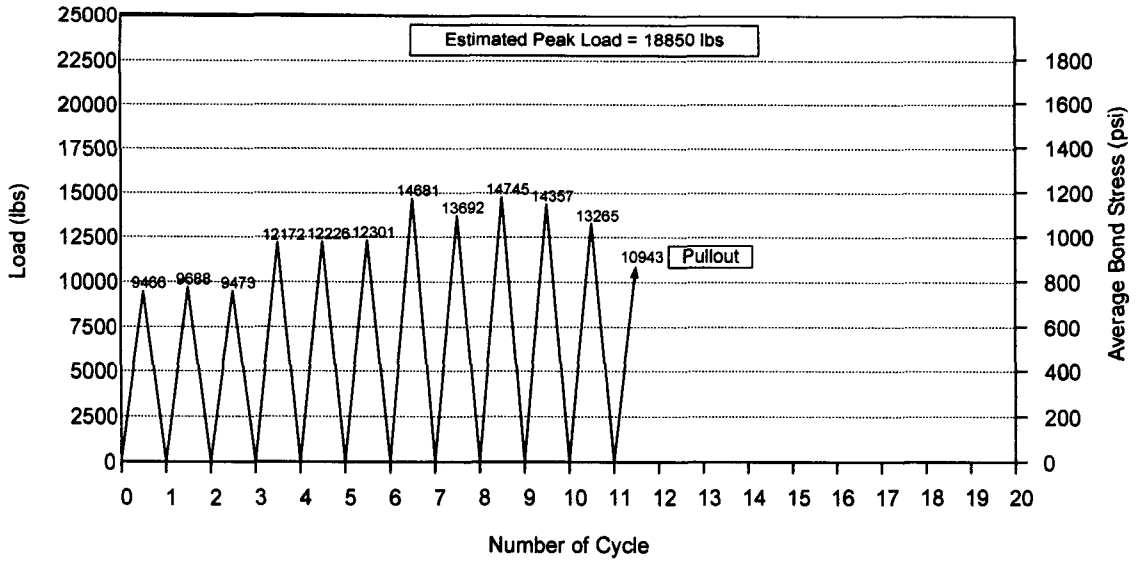

Figure 4.51 Recorded load vs. number of cycle for specimen with No. 8 bar and 1% Spectra fiber under unidirectional force controlled loading

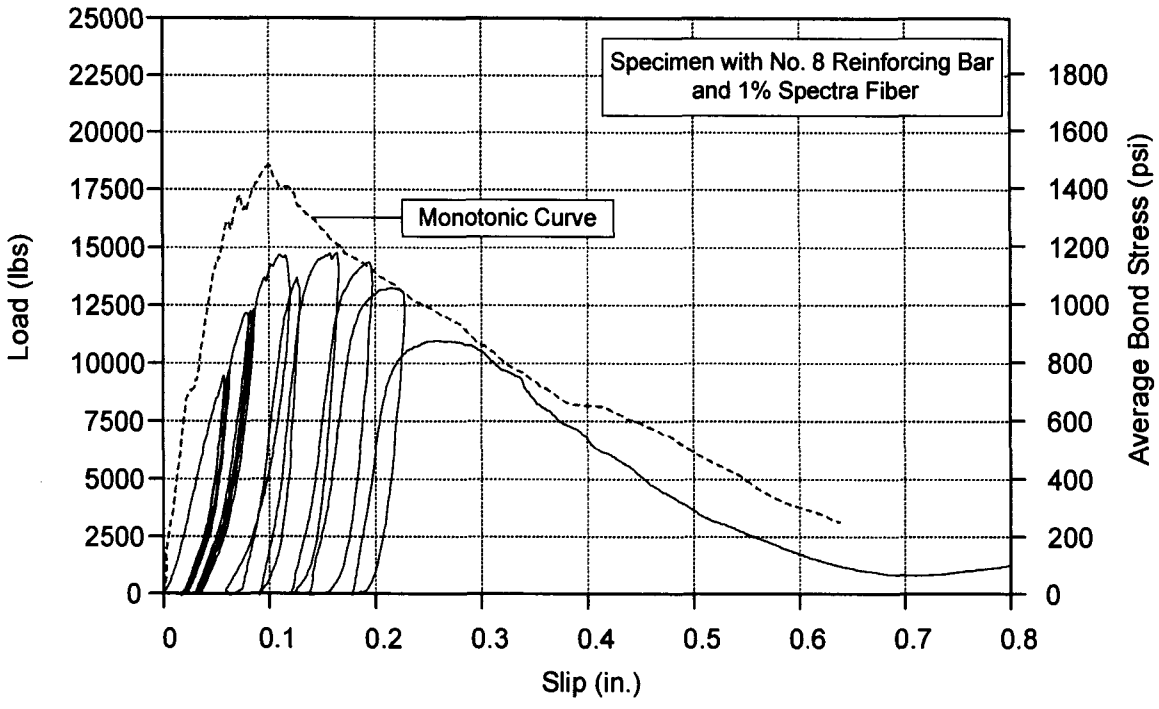

Figure 4.52 (a) Load-slip curve for unidirectional force controlled cyclic loading: No. 8 bar and 1% Spectra fiber

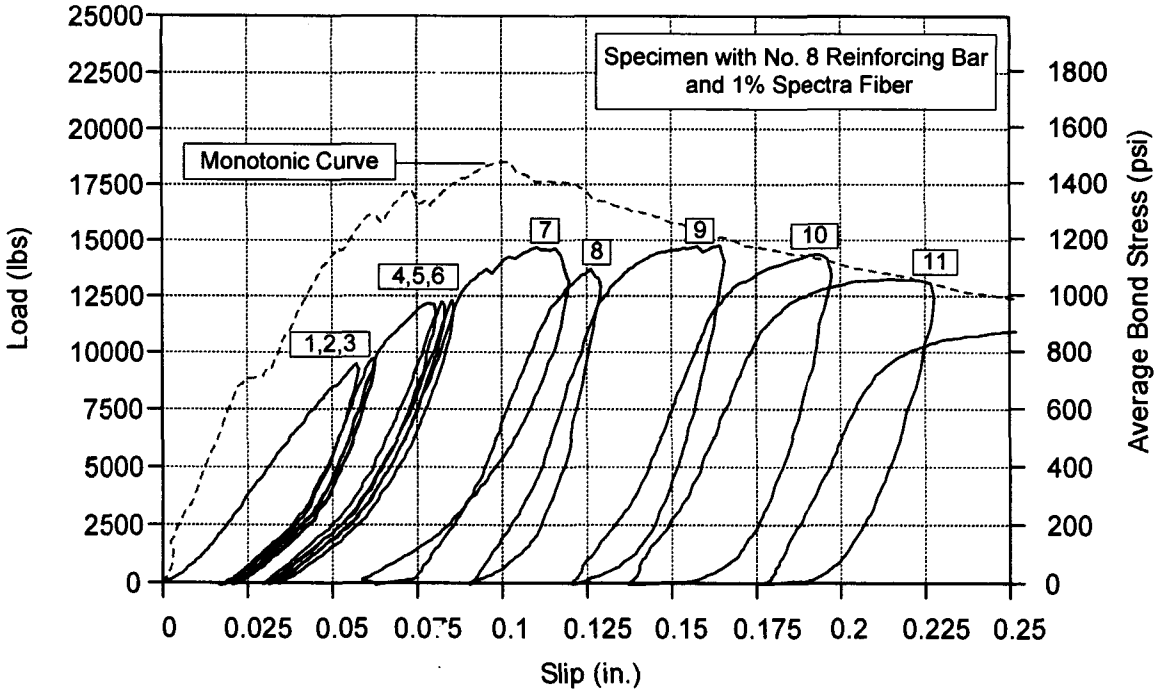

Figure 4.52 (b) Enlargement load-slip curve for the first 11 cycles: number indicates the *n*th cycle

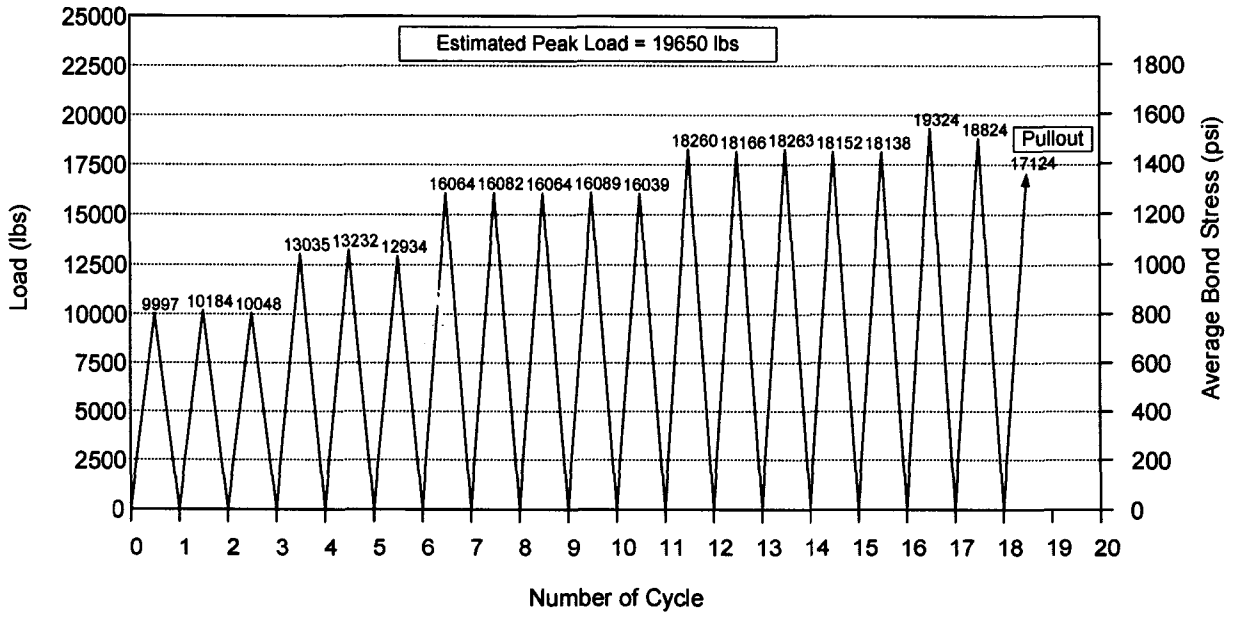

Figure 4.53 Recorded load vs. number of cycle for specimen with No. 8 bar and 2% Spectra fiber under unidirectional force controlled loading

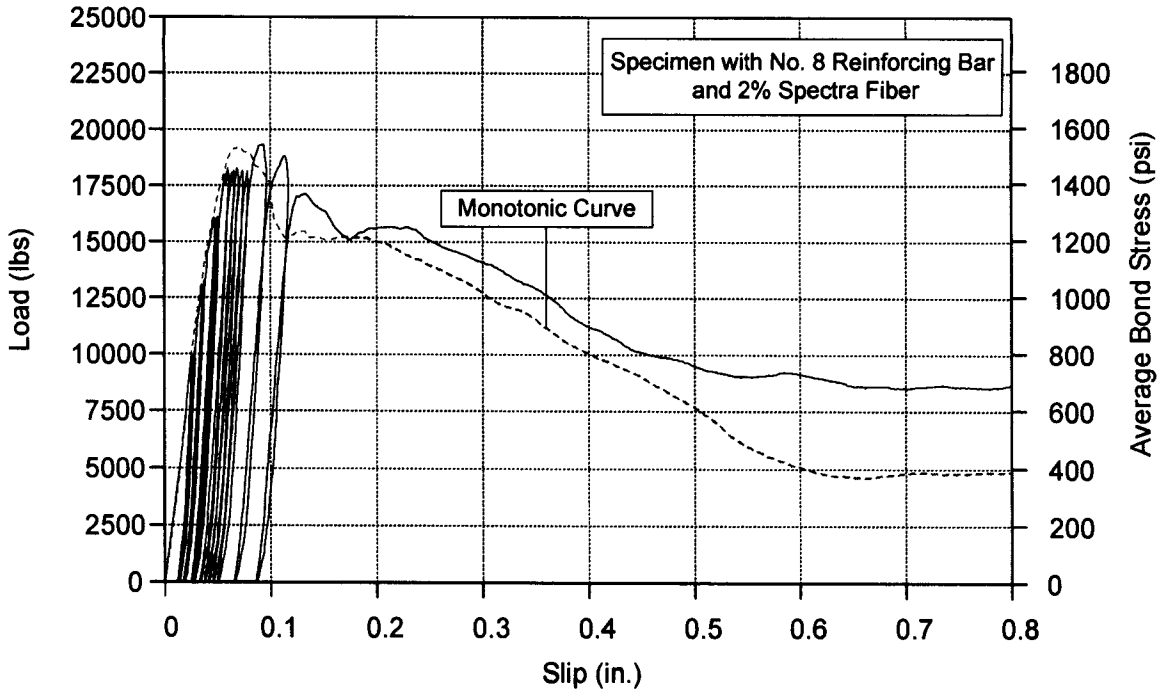

Figure 4.54 (a) Load-slip curve for unidirectional force controlled cyclic loading: No. 8 bar and 2% Spectra fiber

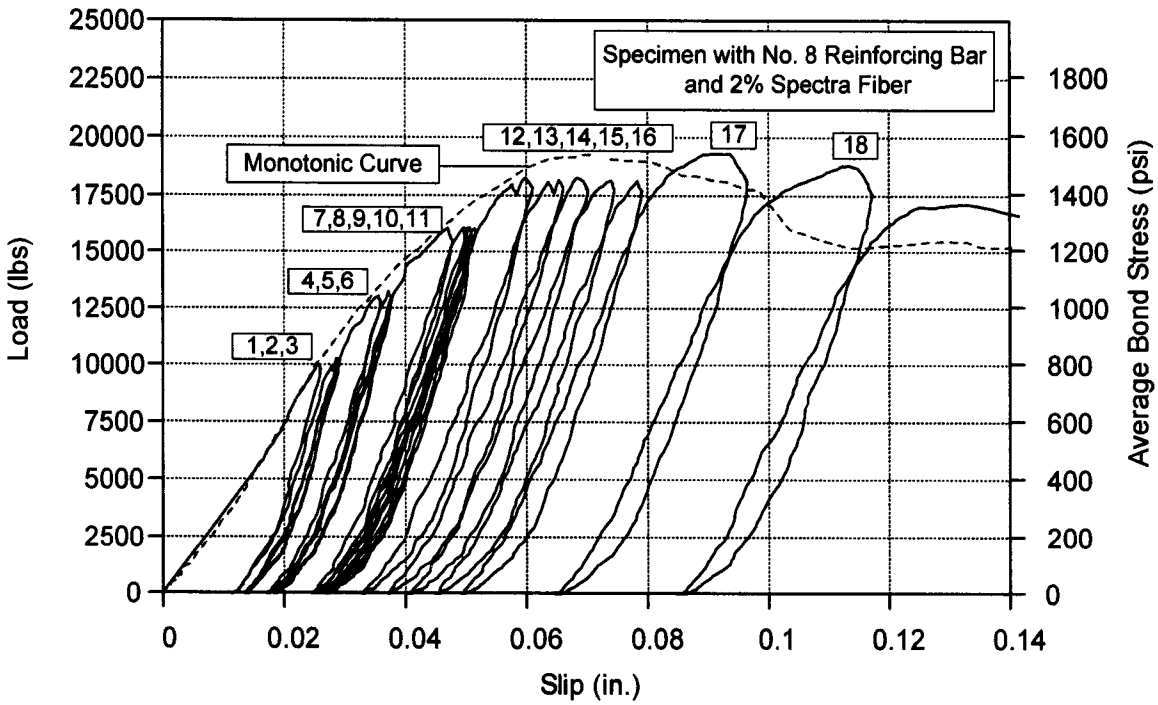

Figure 4.54 (b) Enlargement load-slip curve for the first 18 cycles: number indicates the *n*th cycle

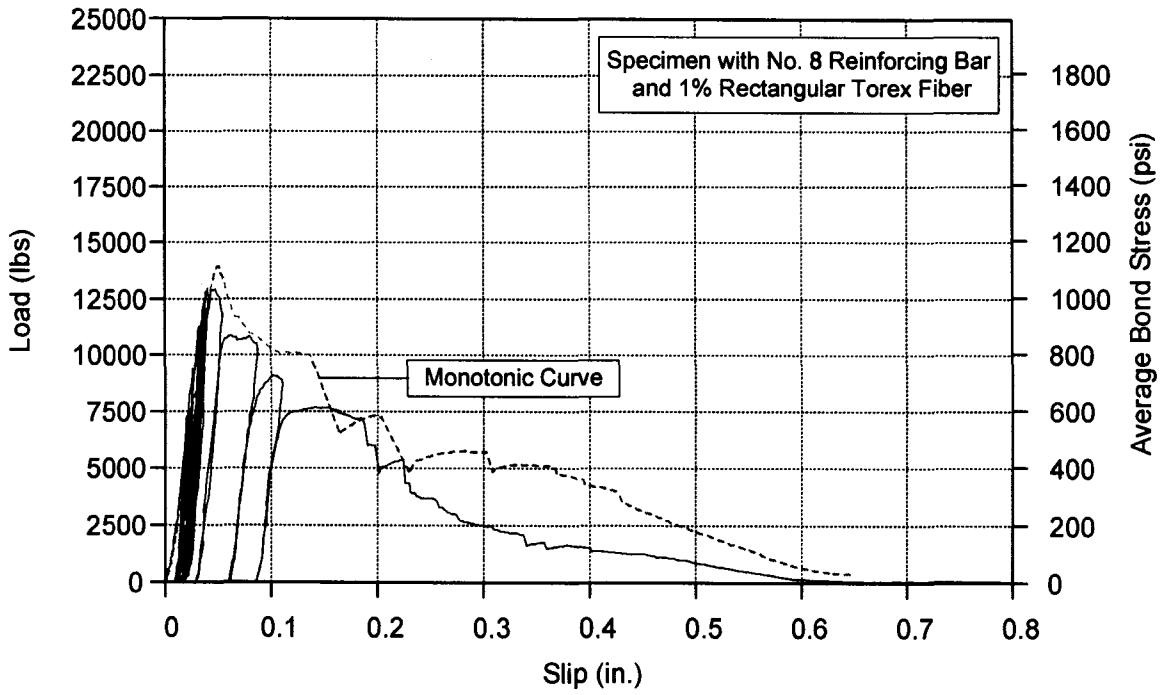

Figure 4.55 (a) Load-slip curve for unidirectional force controlled cyclic loading: No. 8 bar and 1% rectangular Torex fiber

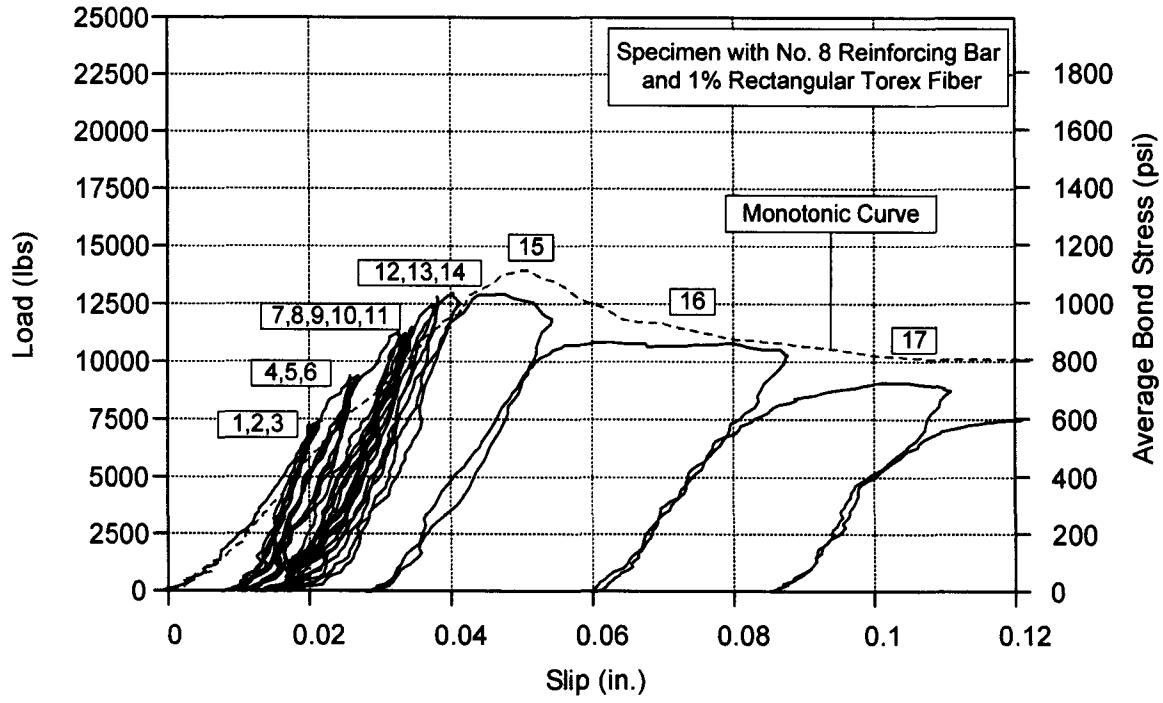

Figure 4.55 (b) Enlargement load-slip curve for the first 17 cycles: number indicates the *n*th cycle

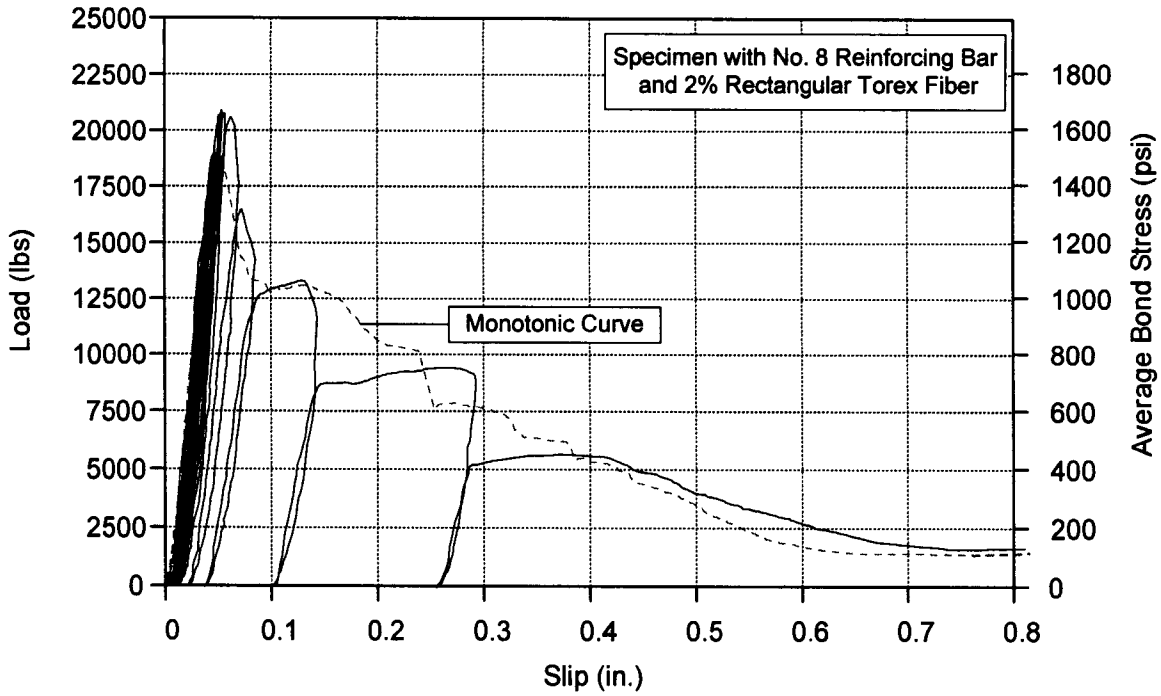

Figure 4.56 (a) Load-slip curve for unidirectional force controlled cyclic loading: No. 8 bar and 2% rectangular Torex fiber

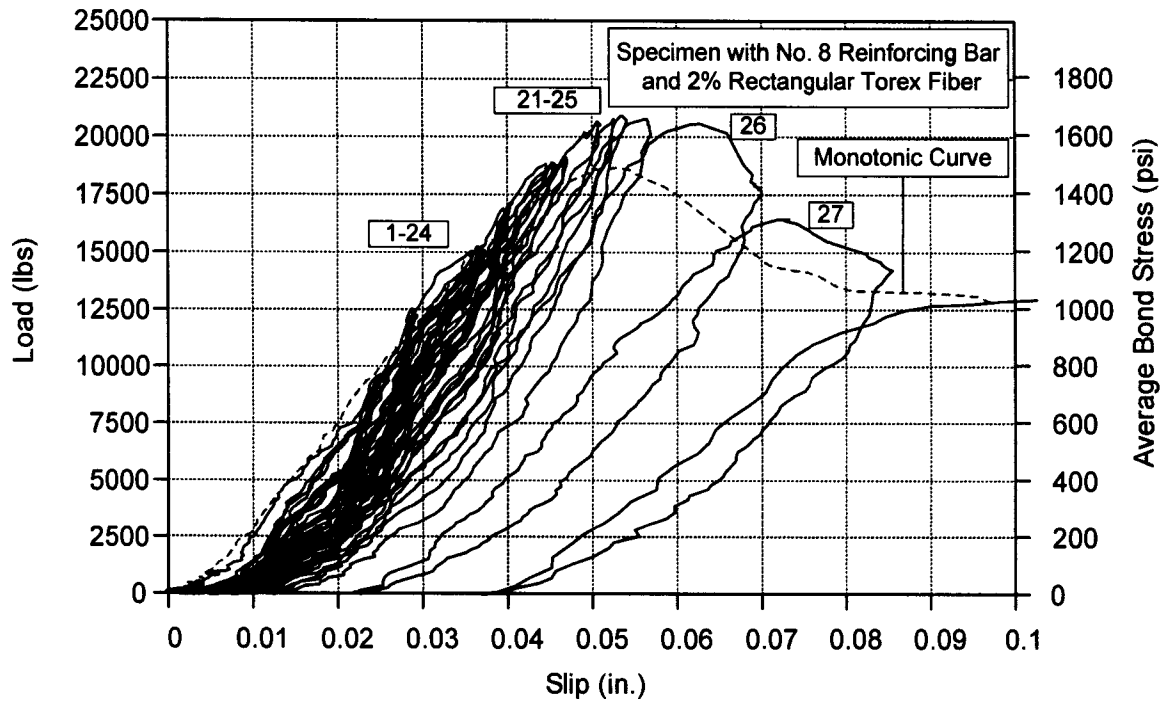

Figure 4.56 (b) Enlargement load-slip curve for the first 27 cycles: number indicates the *n*th cycle

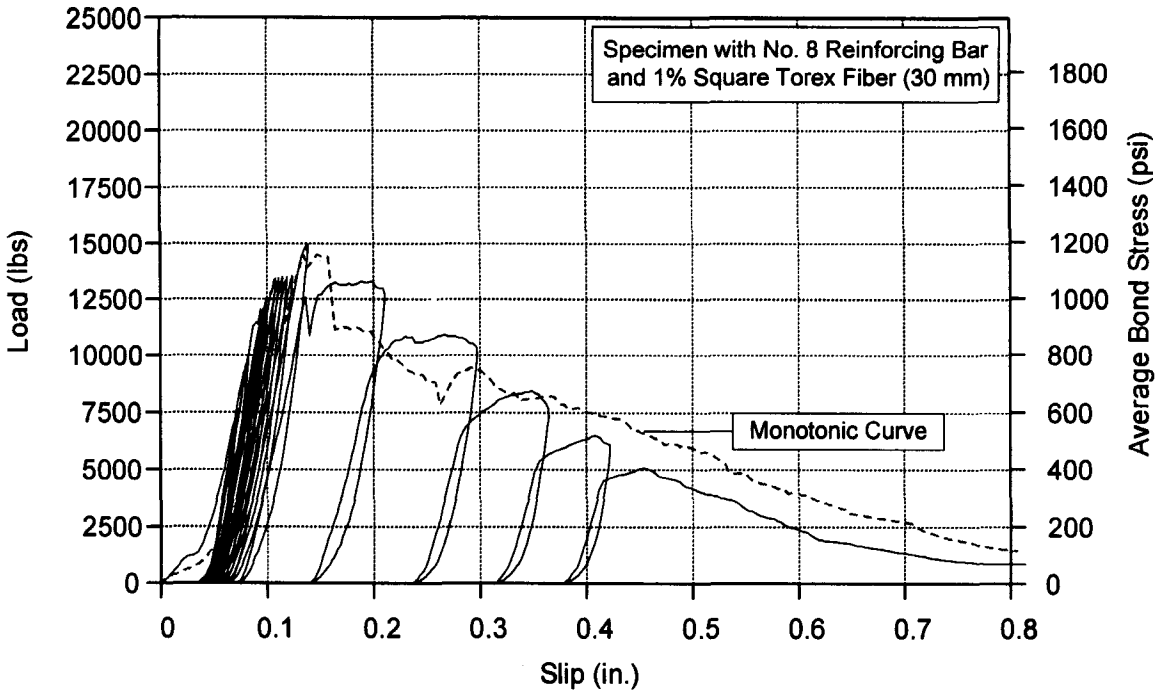

Figure 4.57 (a) Load-slip curve for unidirectional force controlled cyclic loading: No. 8 bar and 1% square Torex fiber (30 mm)

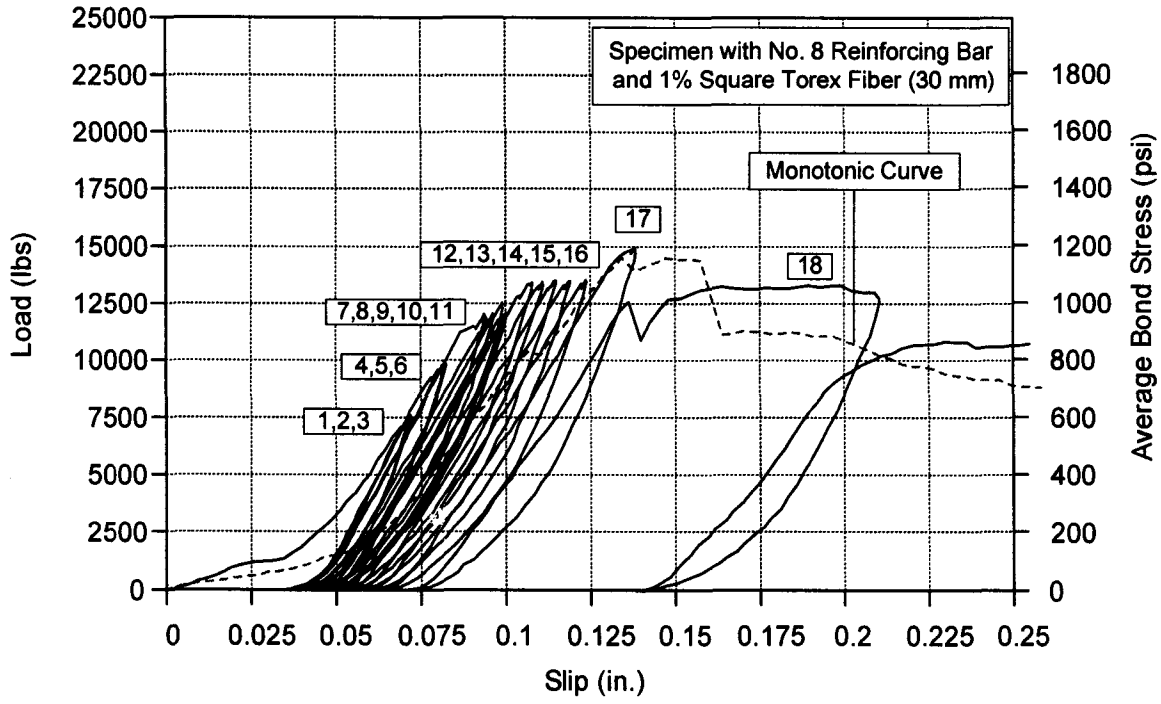

Figure 4.57 (b) Enlargement load-slip curve for the first 18 cycles: number indicates the *n*th cycle

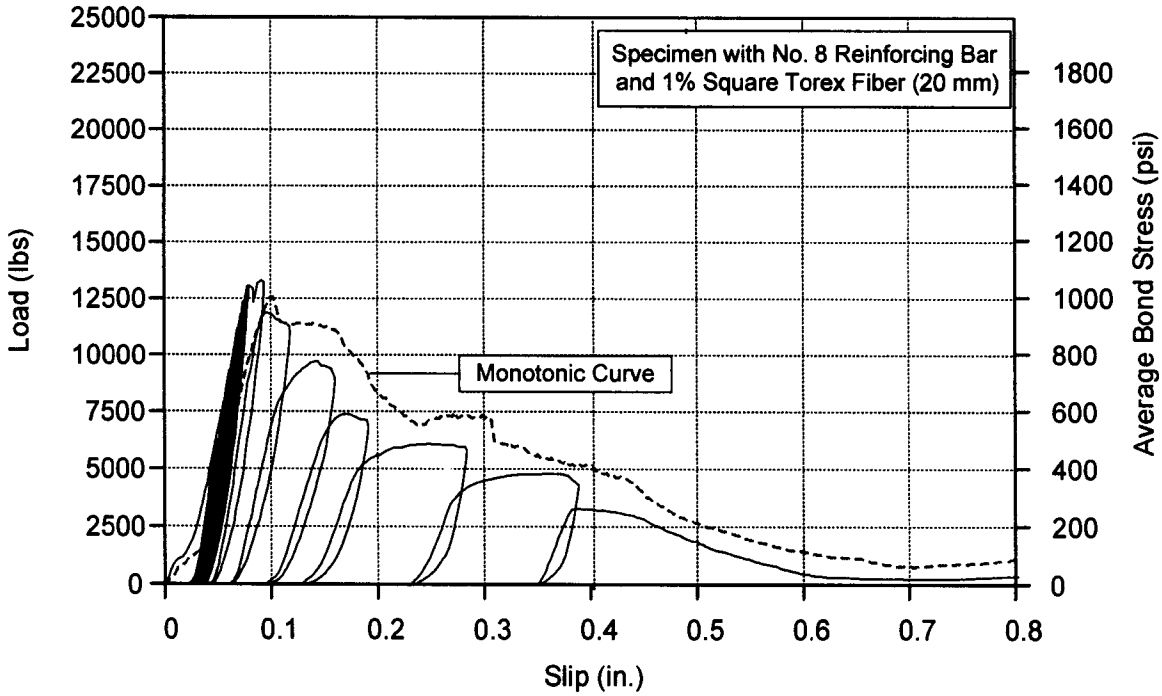

Figure 4.58 (a) Load-slip curve for unidirectional force controlled cyclic loading: No. 8 bar and 1% square Torex fiber (20 mm)

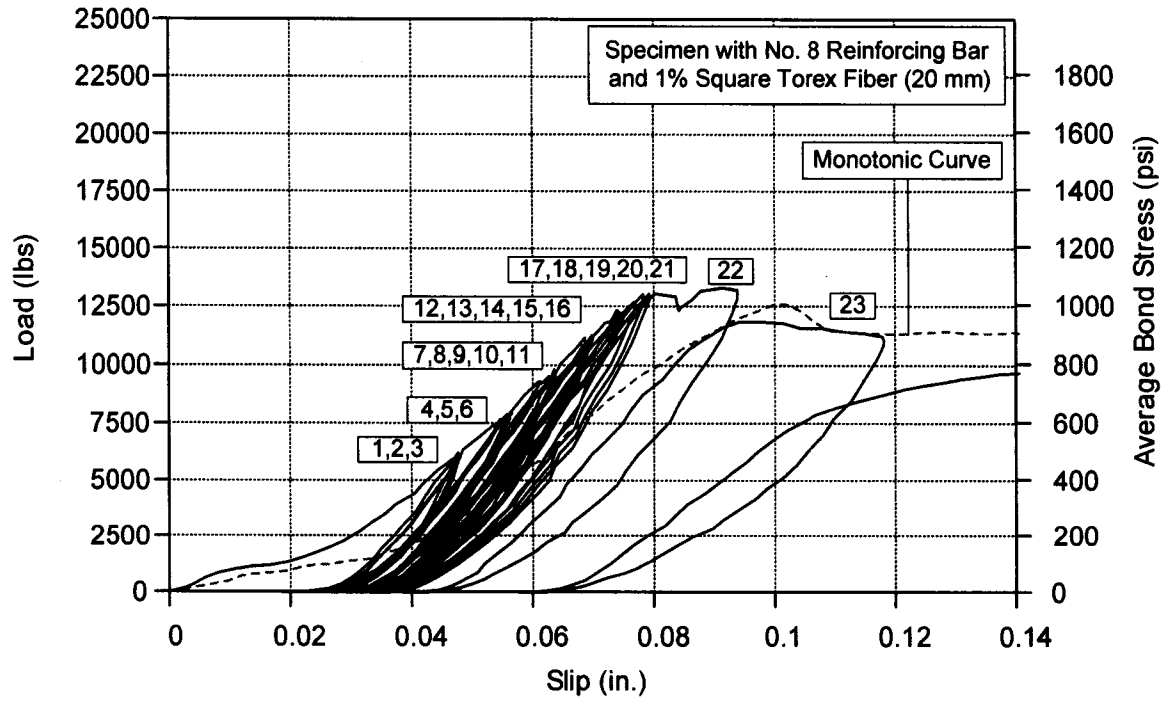

Figure 4.58 (b) Enlargement load-slip curve for the first 23 cycles: number indicates the *n*th cycle

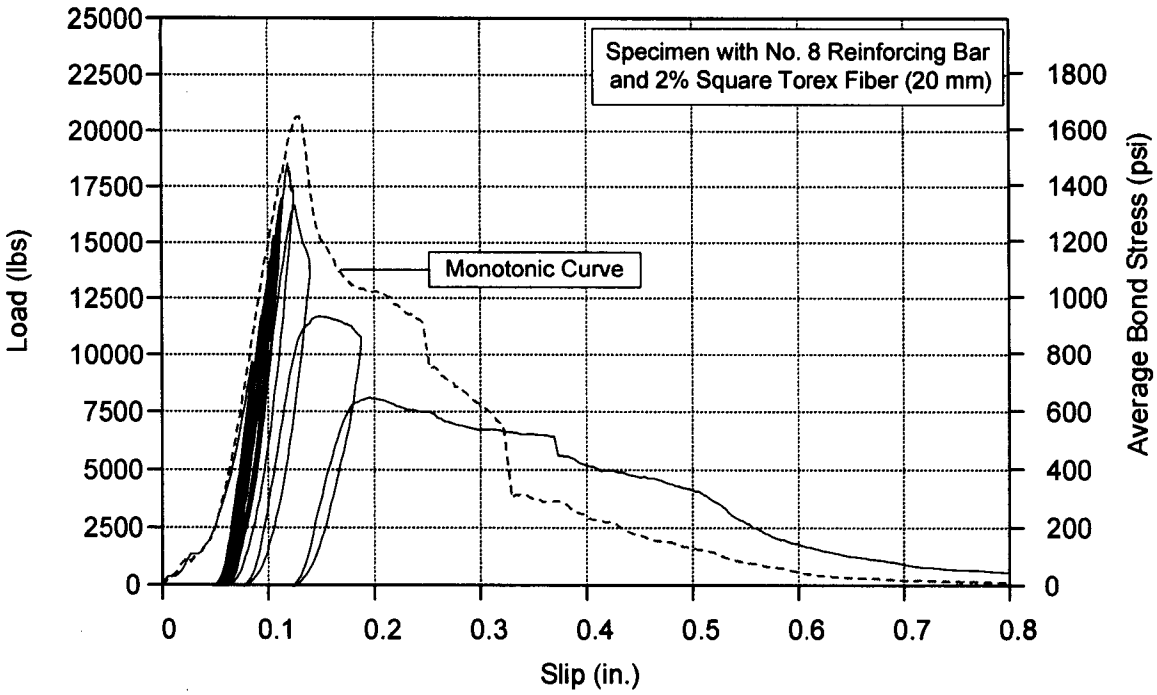

Figure 4.59 (a) Load-slip curve for unidirectional force controlled cyclic loading: No. 8 bar and 2% square Torex fiber (20 mm)

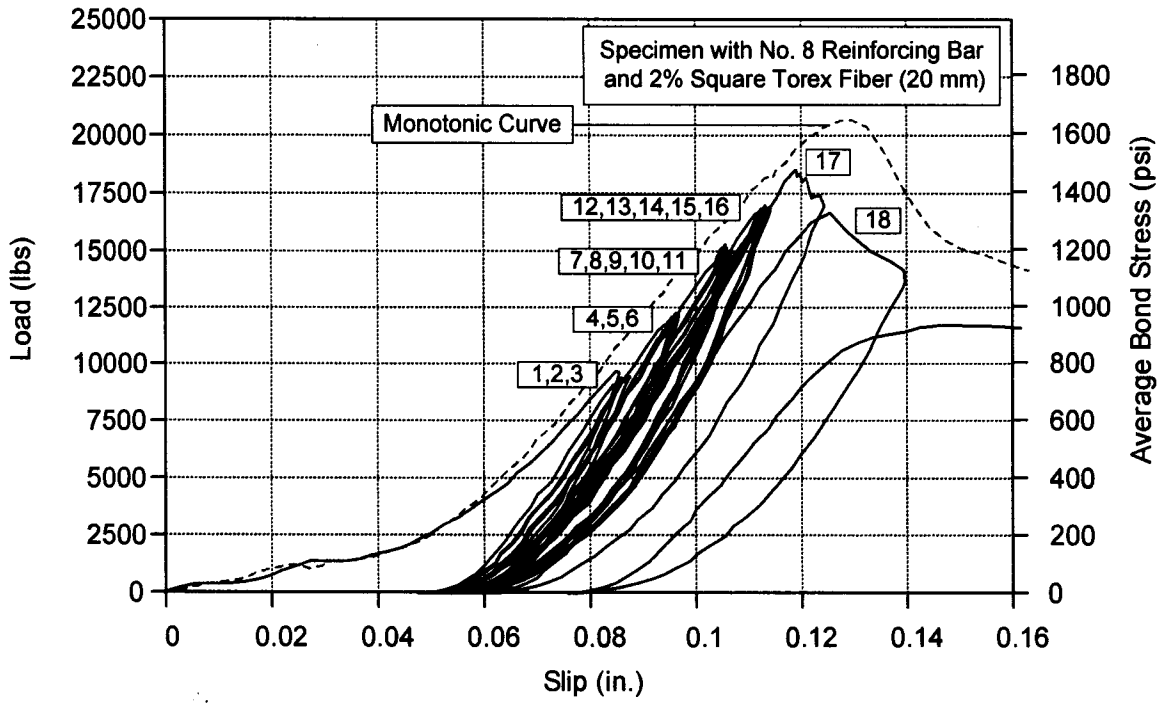

Figure 4.59 (b) Enlargement load-slip curve for the first 18 cycles: number indicates the *n*th cycle

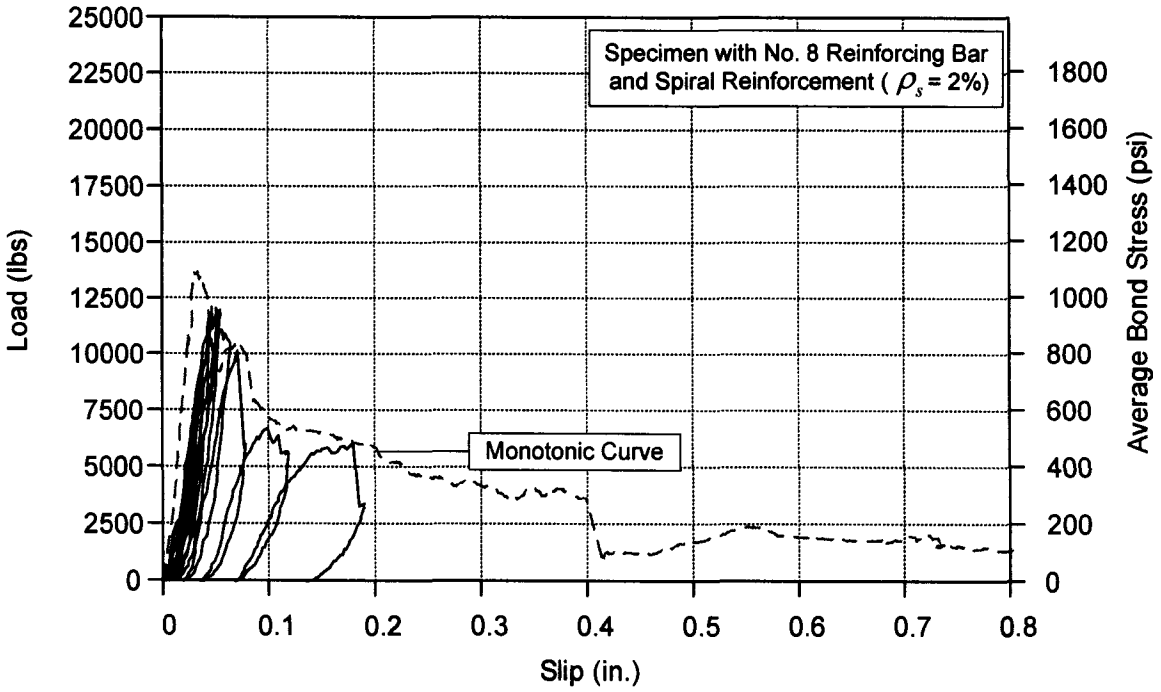

Figure 4.60 (a) Load-slip curve for unidirectional force controlled cyclic loading: No. 8 bar and 2% volumetric spiral reinforcement

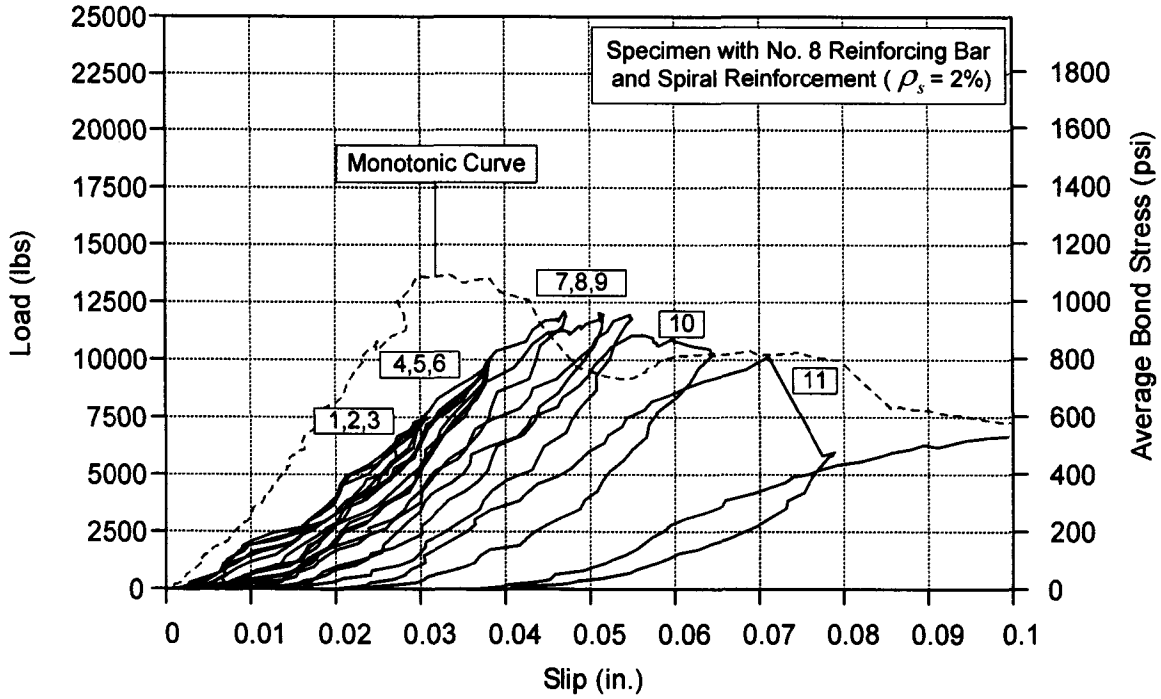

Figure 4.60 (b) Enlargement load-slip curve for the first 11 cycles: number indicates the *n*th cycle

(a) (b)

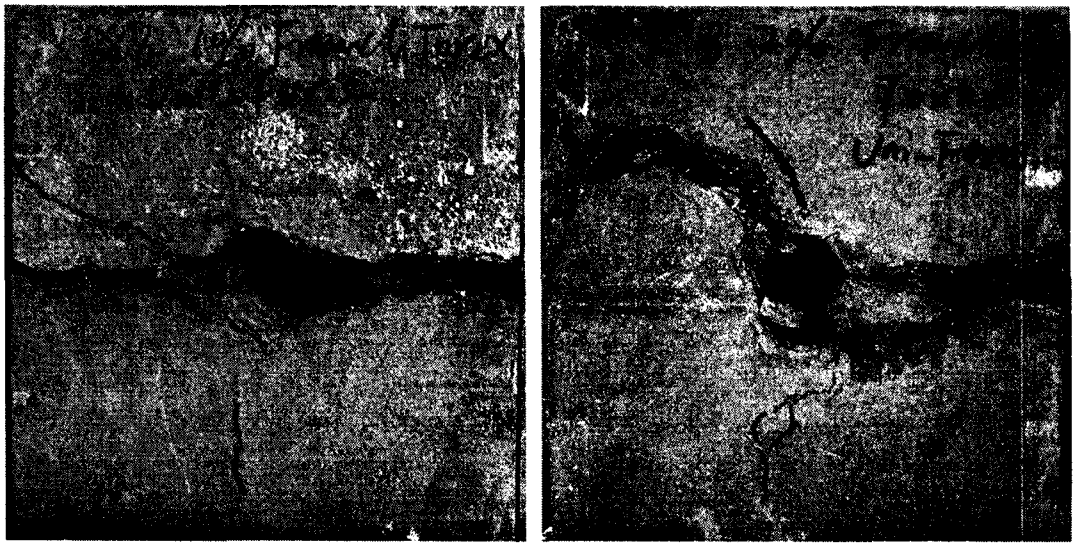

(c) (d)

Figure 4.61 Crack patterns of selected specimen with No. 8 bar subjected to unidirectional force controlled loading: (a) 1% Spectra; (b) 2% Spectra; (c) 1% rectangular Torex; (d) 2% rectangular Torex

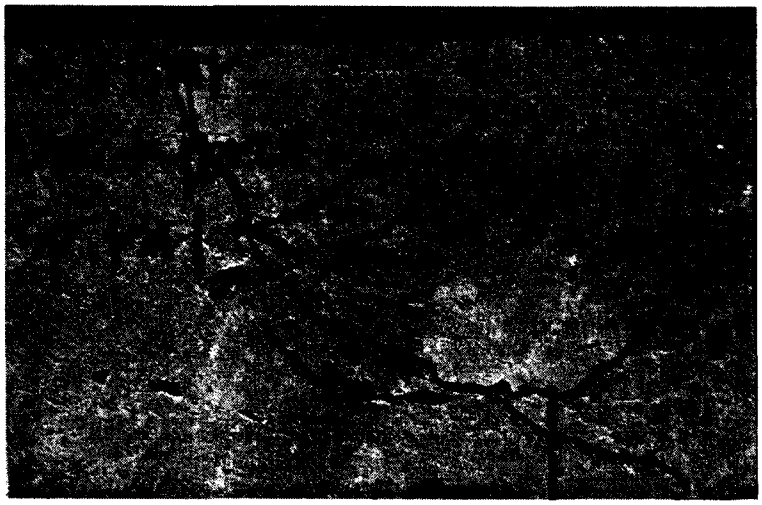

(a)

(b)

(c)

Figure 4.62 Crack patterns of spiral reinforced specimen with No. 8 bar subjected to unidirectional force controlled loading: (a) cone-shaped fracture at 10th cycle (side view); (b) picture shows the spalling and cracking after test; (c) top view of the cone-shaped fracture

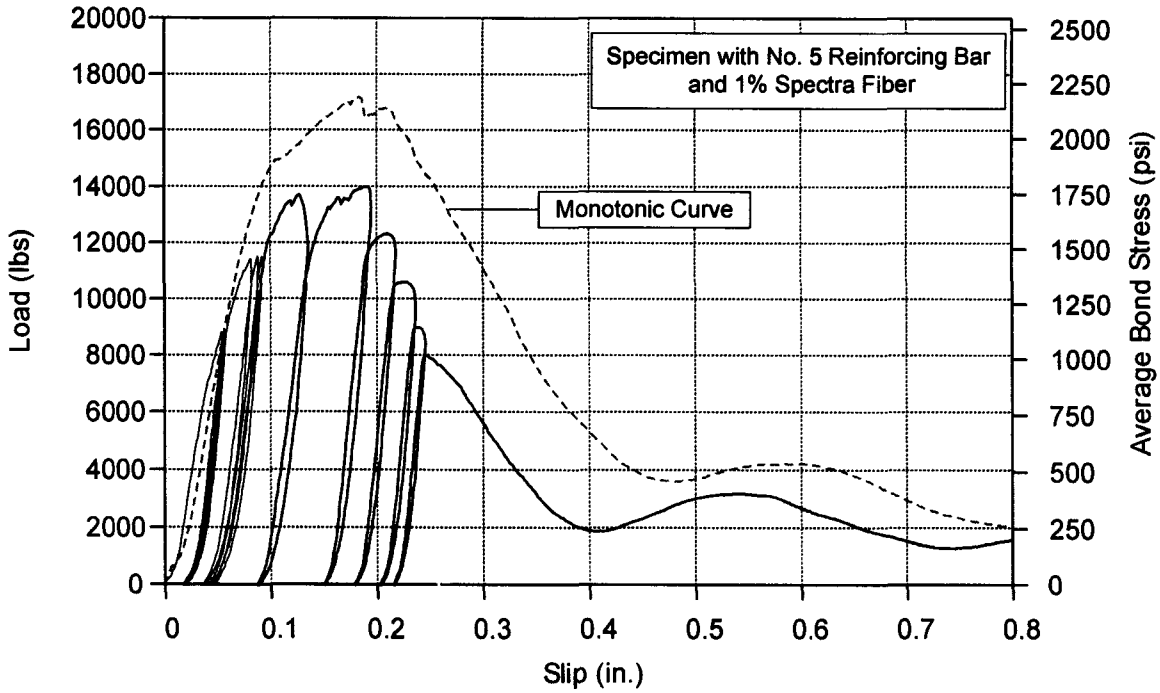

Figure 4.63 (a) Load-slip curve for unidirectional force controlled cyclic loading: No. 5 bar and 1% spectra fiber

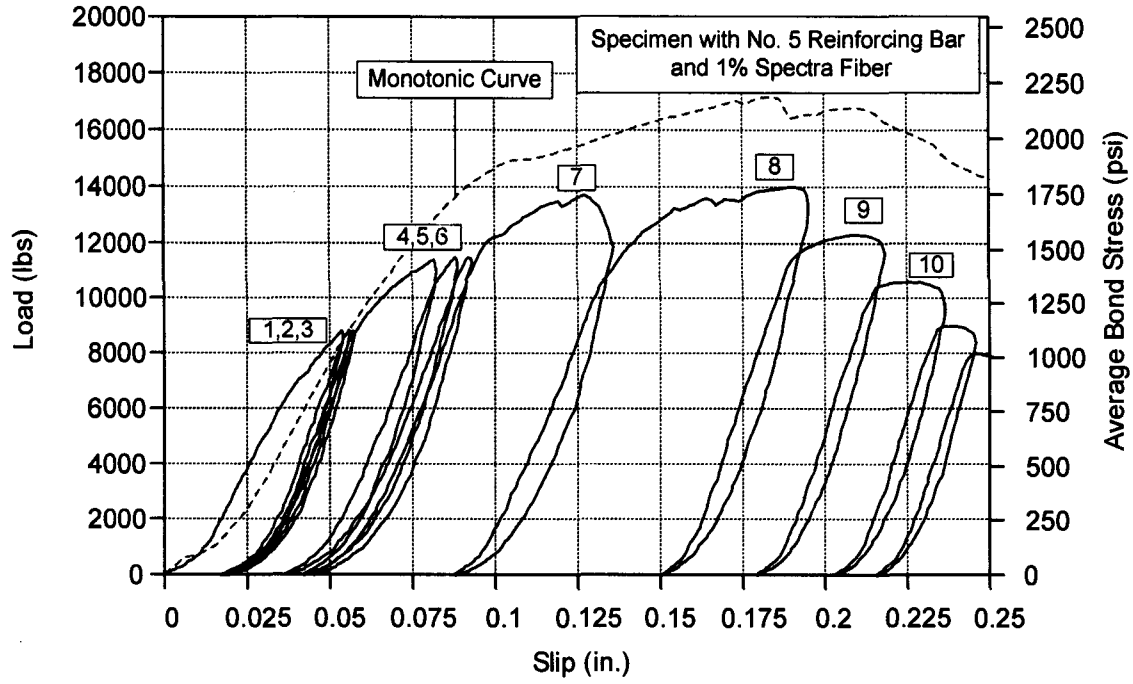

Figure 4.63 (b) Enlargement load-slip curve for the first 10 cycles: number indicates the *n*th cycle

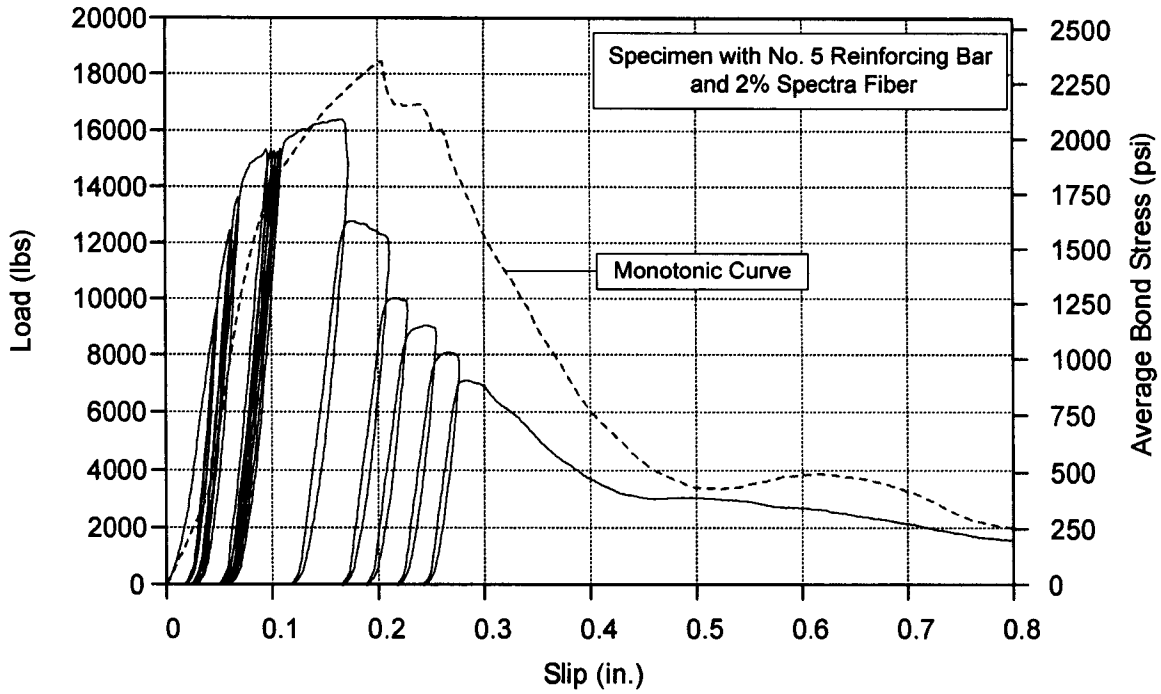

Figure 4.64 (a) Load-slip curve for unidirectional force controlled cyclic loading: No. 5 bar and 2% spectra fiber

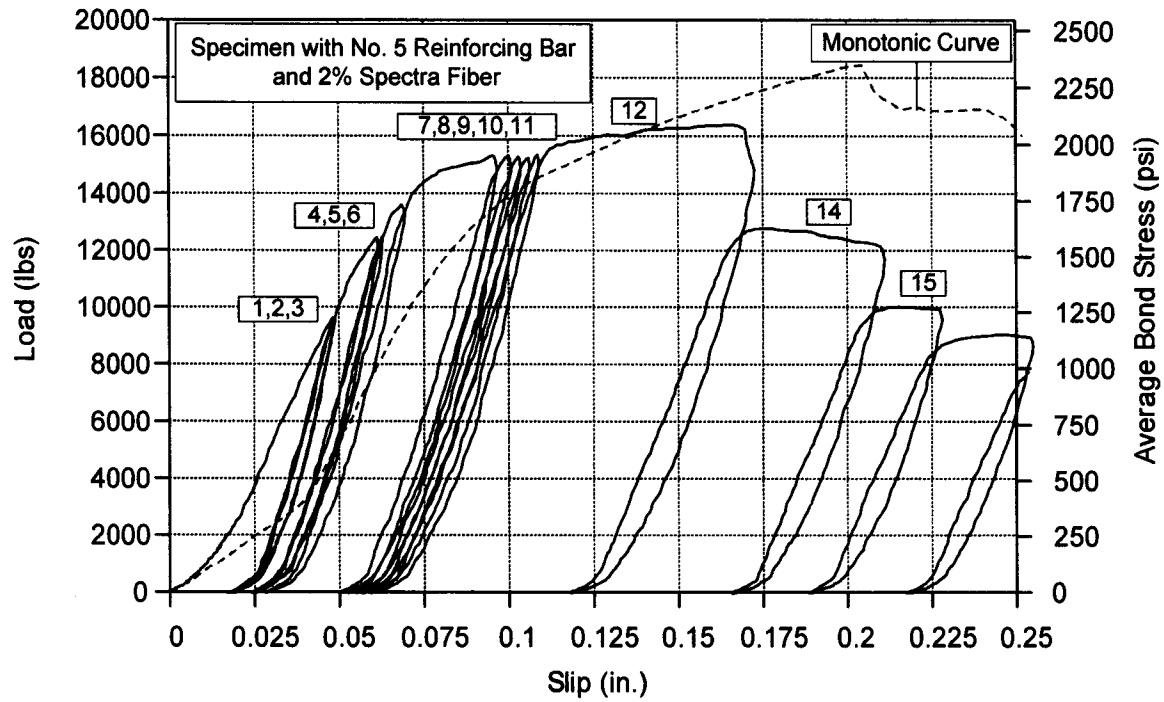

Figure 4.64 (b) Enlargement load-slip curve for the first 15 cycles: number indicates the *n*th cycle

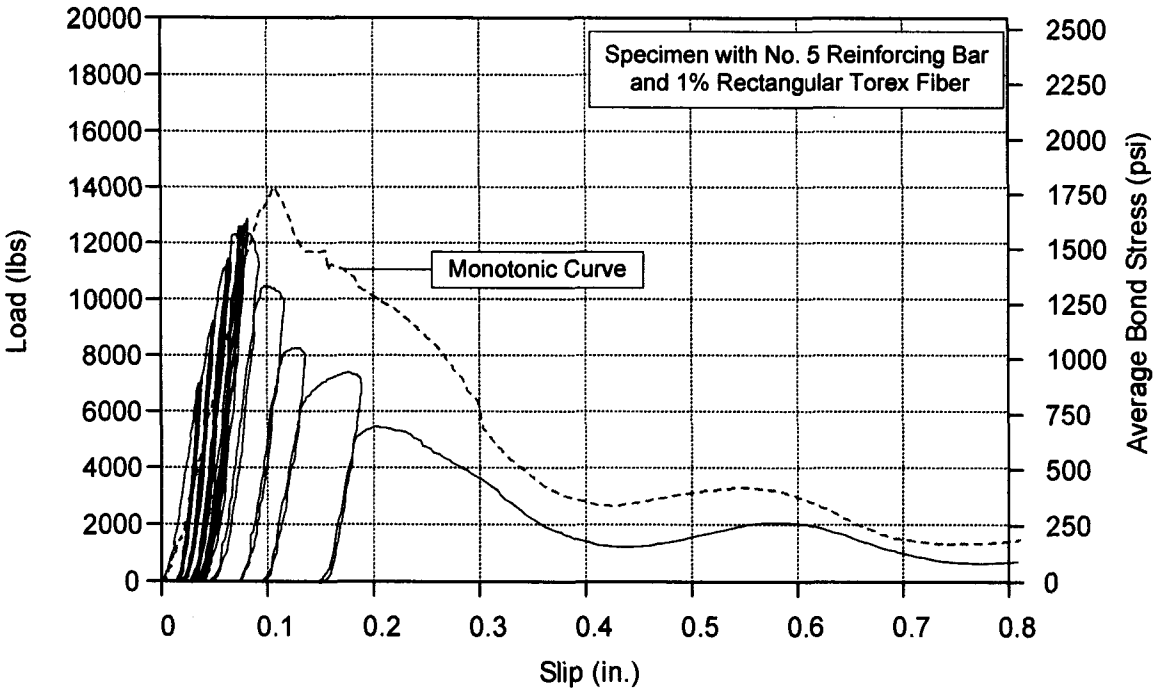

Figure 4.65 (a) Load-slip curve for unidirectional force controlled cyclic loading: No. 5 bar and 1% rectangular Torex fiber

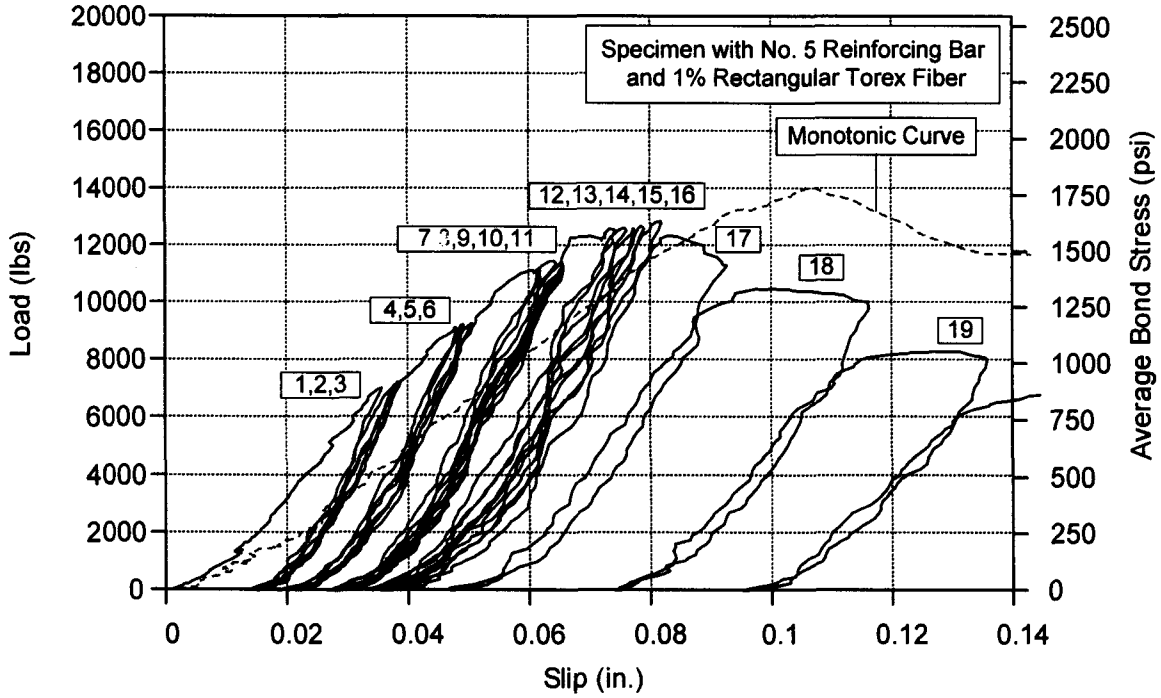

Figure 4.65 (b) Enlargement load-slip curve for the first 19 cycles: number indicates the *n*th cycle

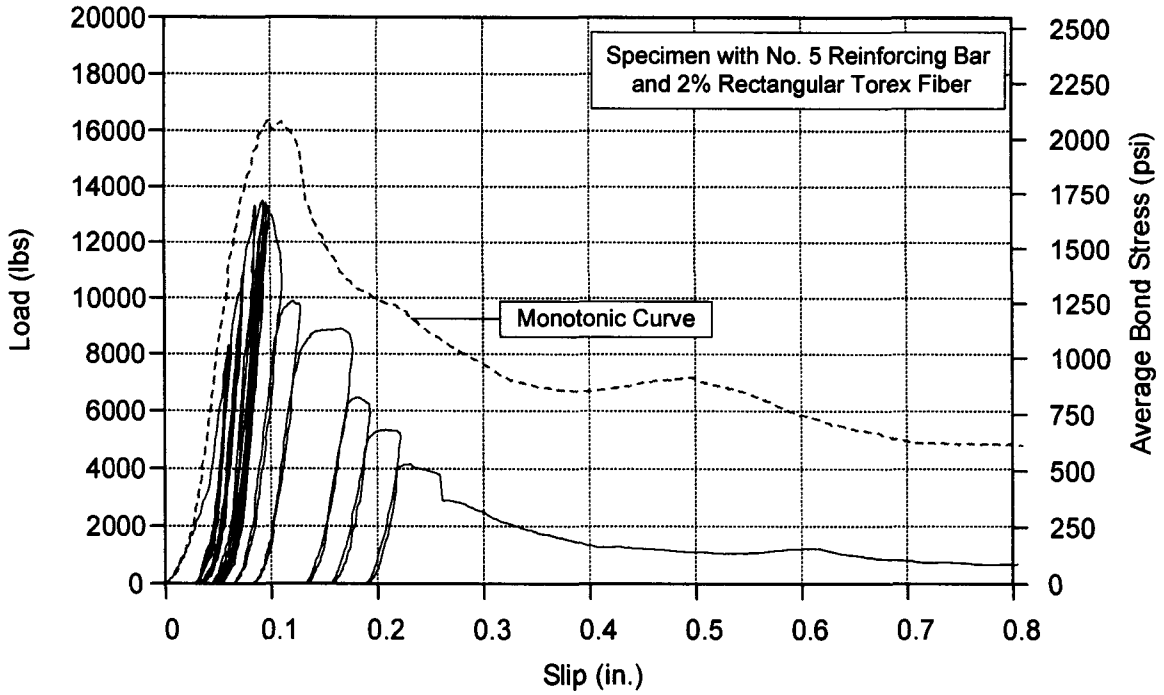

Figure 4.66 (a) Load-slip curve for unidirectional force controlled cyclic loading: No. 5 bar and 2% rectangular Torex fiber

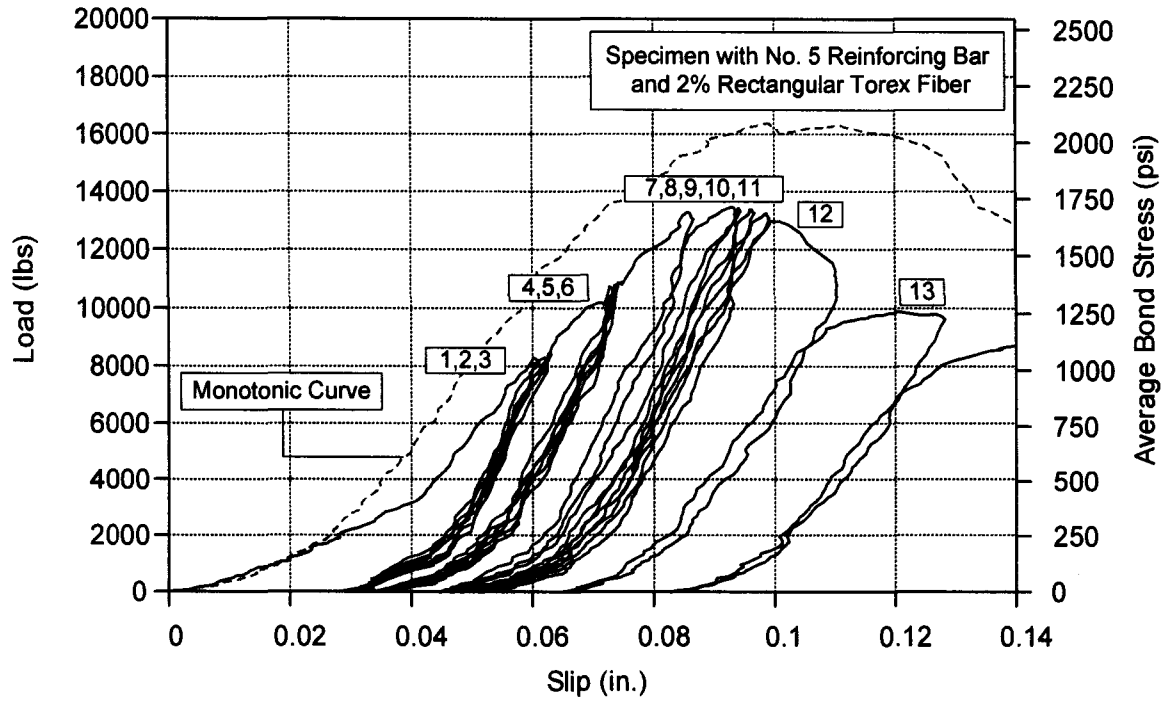

Figure 4.66 (b) Enlargement load-slip curve for the first 13 cycles: number indicates the *n*th cycle

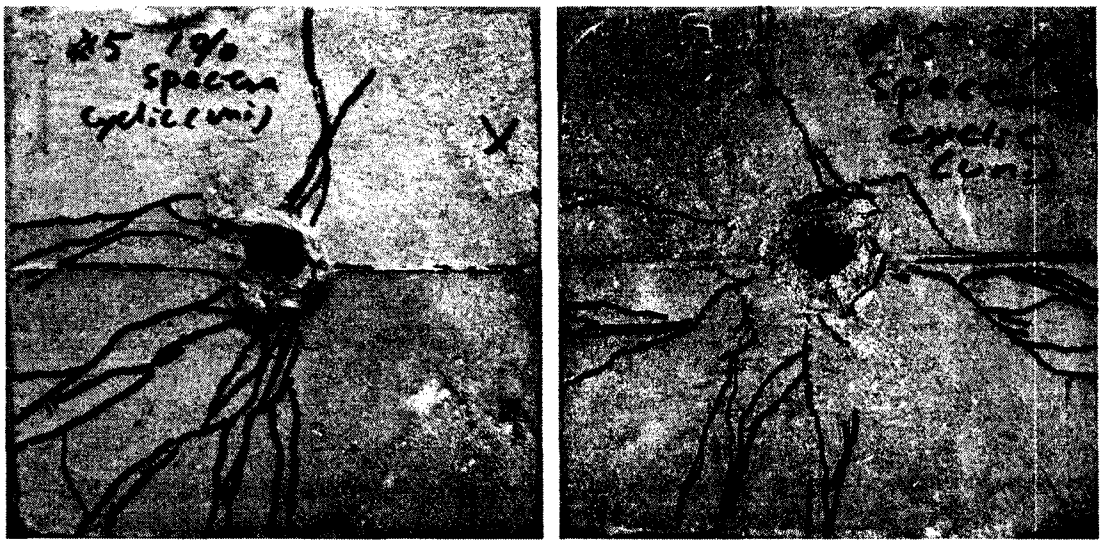

(a) (b)

(c) (d)

Figure 4.67 Crack patterns of selected specimen with No. 5 bar subjected to unidirectional force controlled loading: (a) 1% Spectra; (b) 2% Spectra; (c) 1% rectangular Torex; (d) 2% rectangular Torex

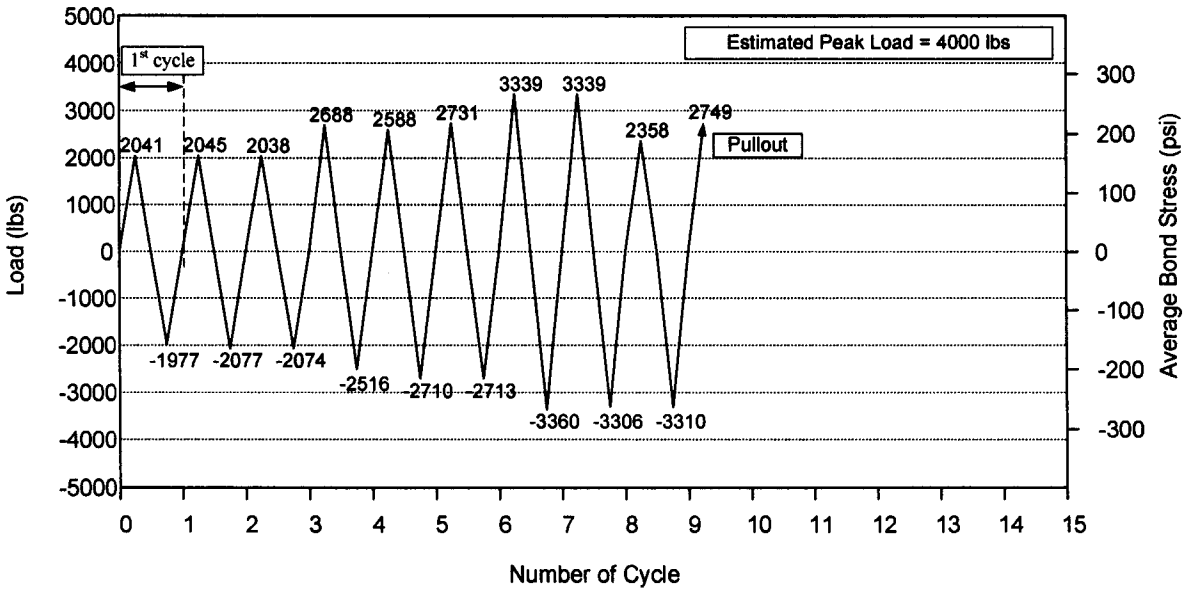

Figure 4.68 Recorded load vs. number of cycle for control specimen with No. 8 bar under fully reversed force controlled cyclic loading

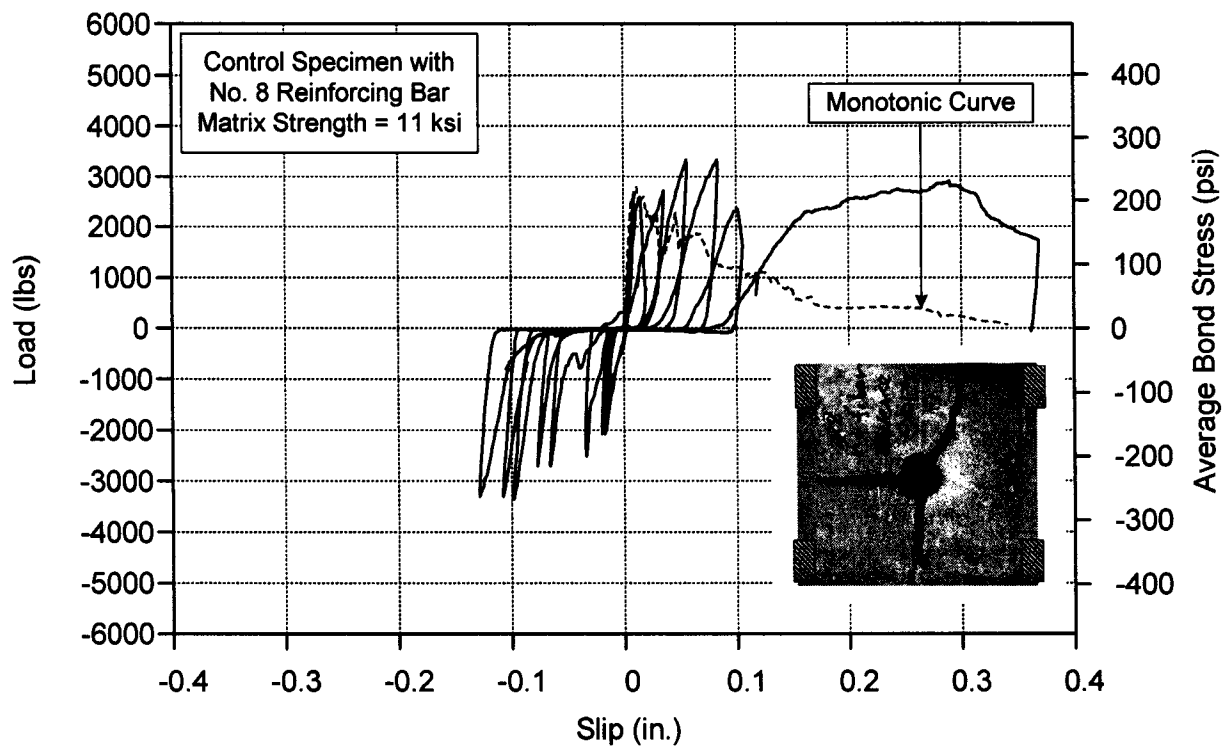

Figure 4.69 Load-slip curve for fully reversed force controlled cyclic loading: No. 8 bar, control specimen

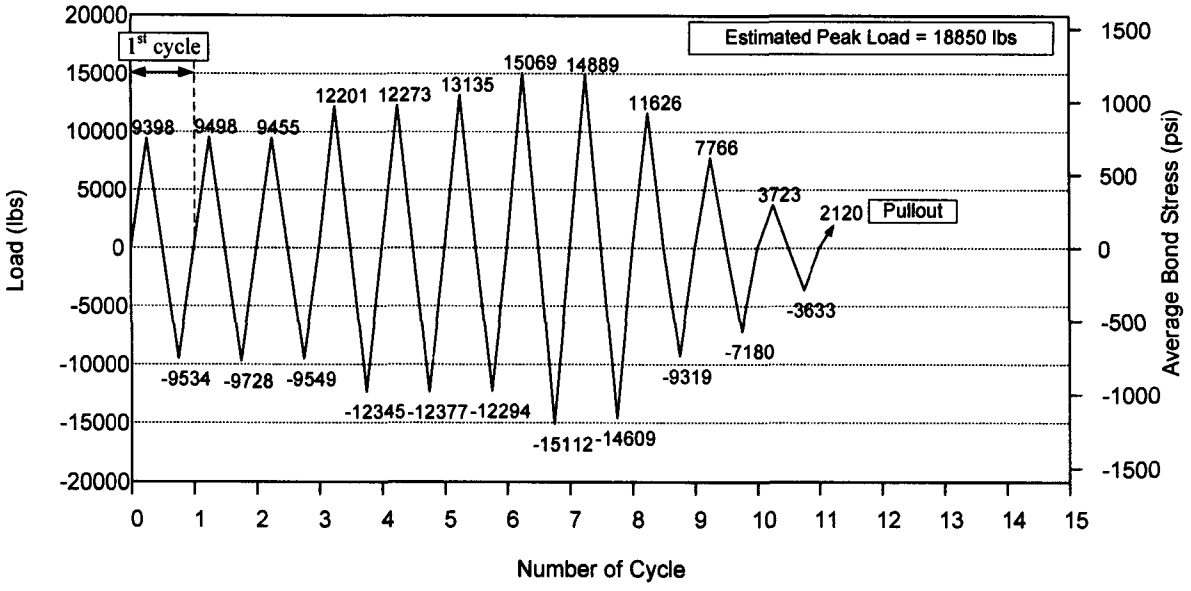

Figure 4.70 Recorded load vs. number of cycle for specimen with No. 8 bar and 1% Spectra fiber under fully reversed force controlled cyclic loading

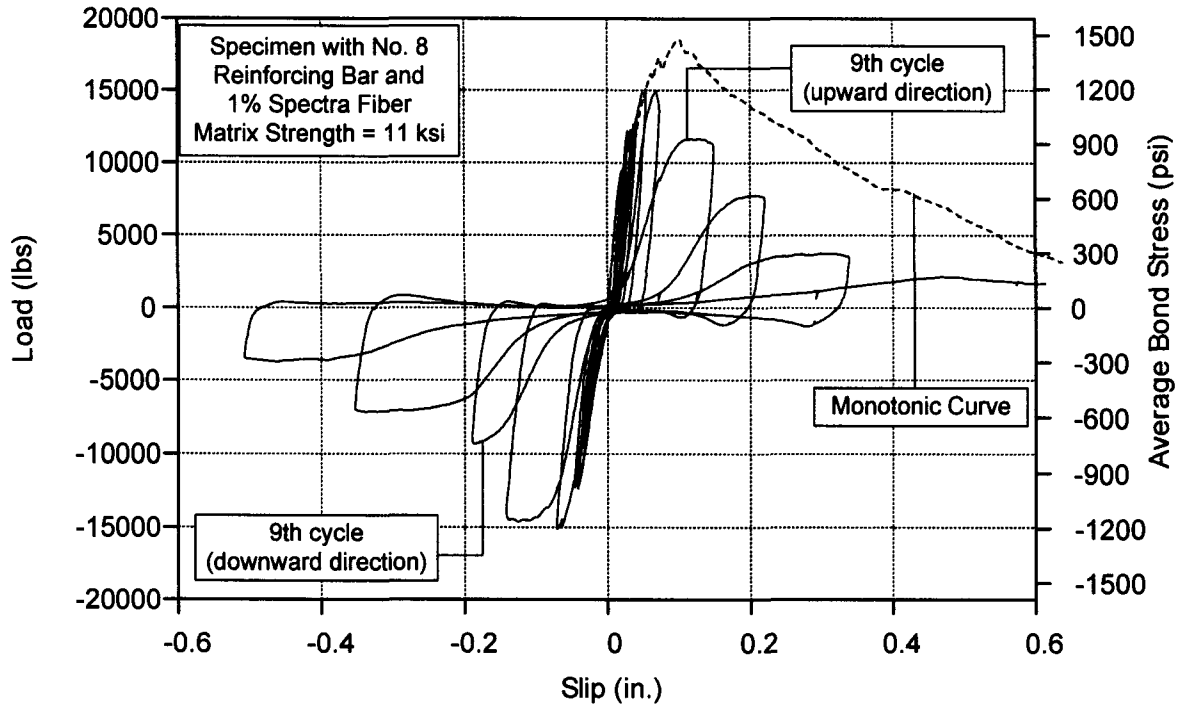

Figure 4.71 Load-slip curve for fully reversed force controlled cyclic loading: No. 8 bar and 1% Spectra fiber

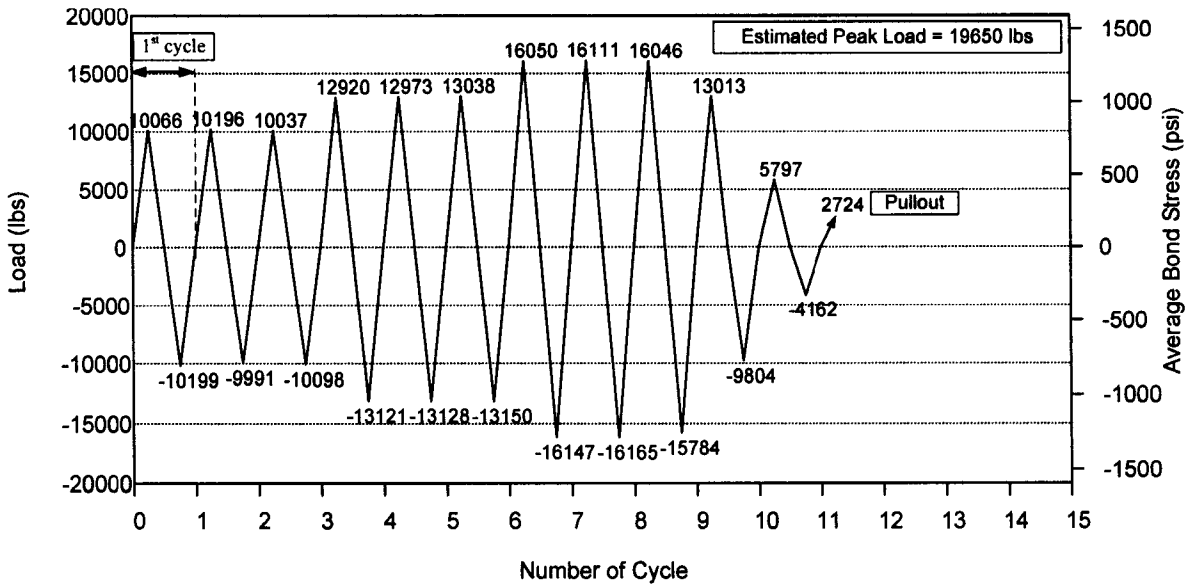

Figure 4.72 Recorded load vs. number of cycle for specimen with No. 8 bar and 2% Spectra fiber under fully reversed force controlled cyclic loading

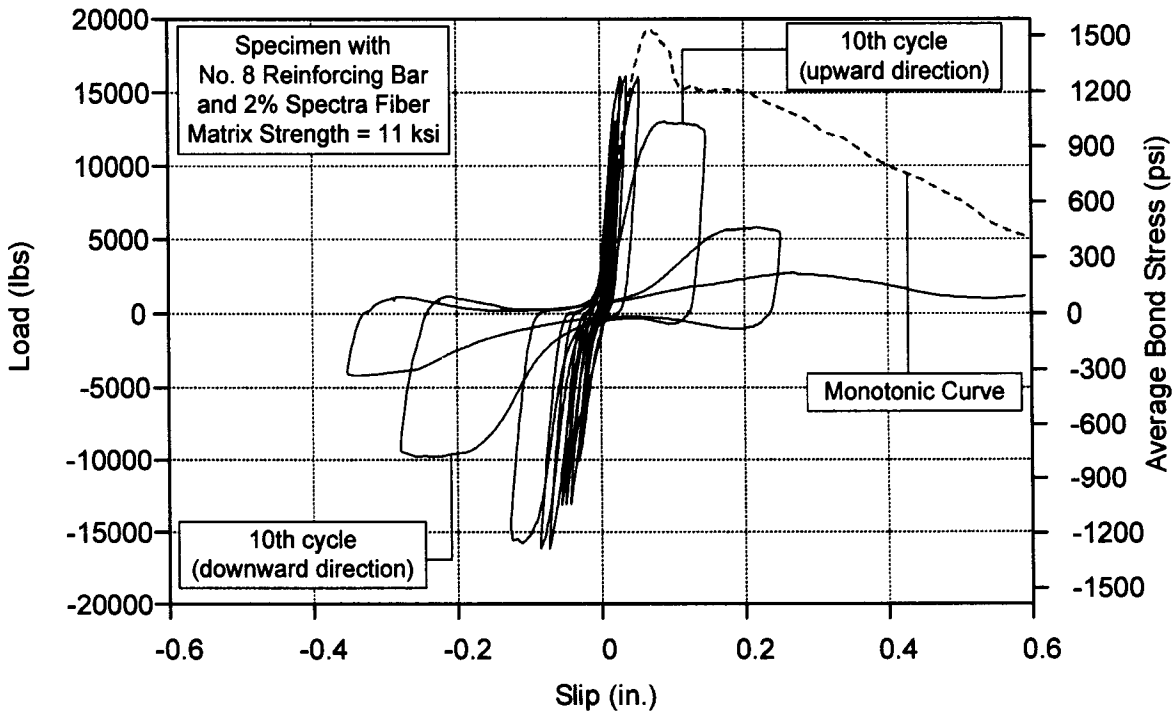

Figure 4.73 (a) Load-slip curve for fully reversed force controlled cyclic loading: No. 8 bar and 2% Spectra fiber

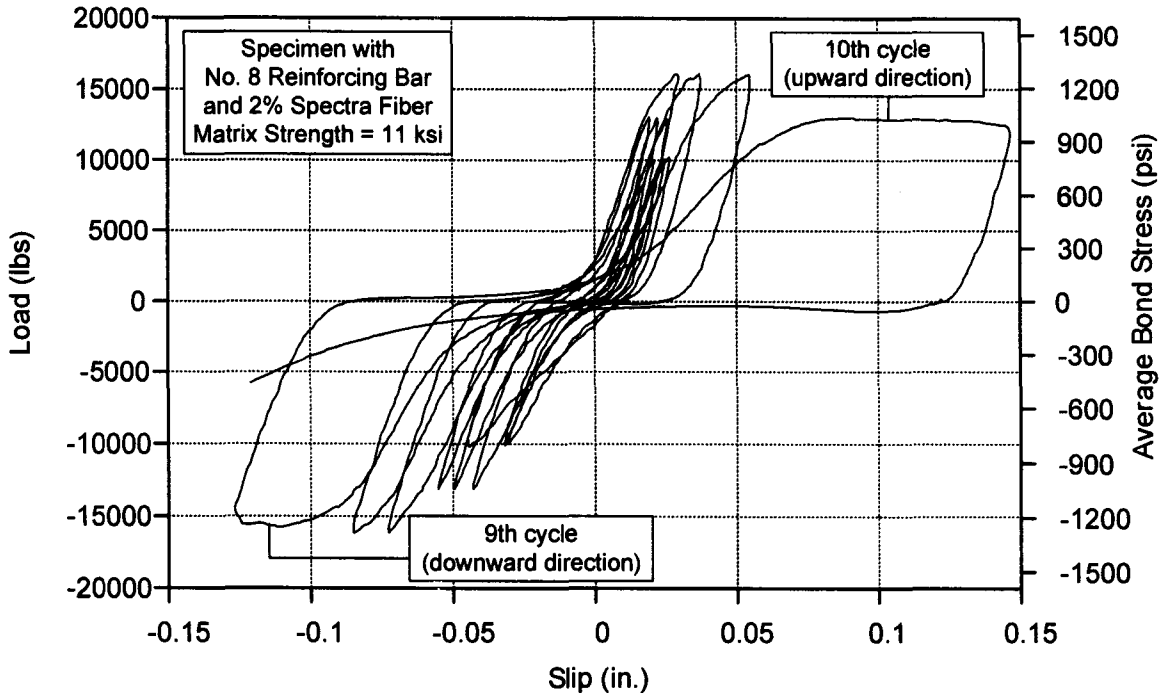

Figure 4.73 (b) Enlargement load-slip curve for fully reversed force controlled cyclic loading: No. 8 bar and 2% Spectra fiber

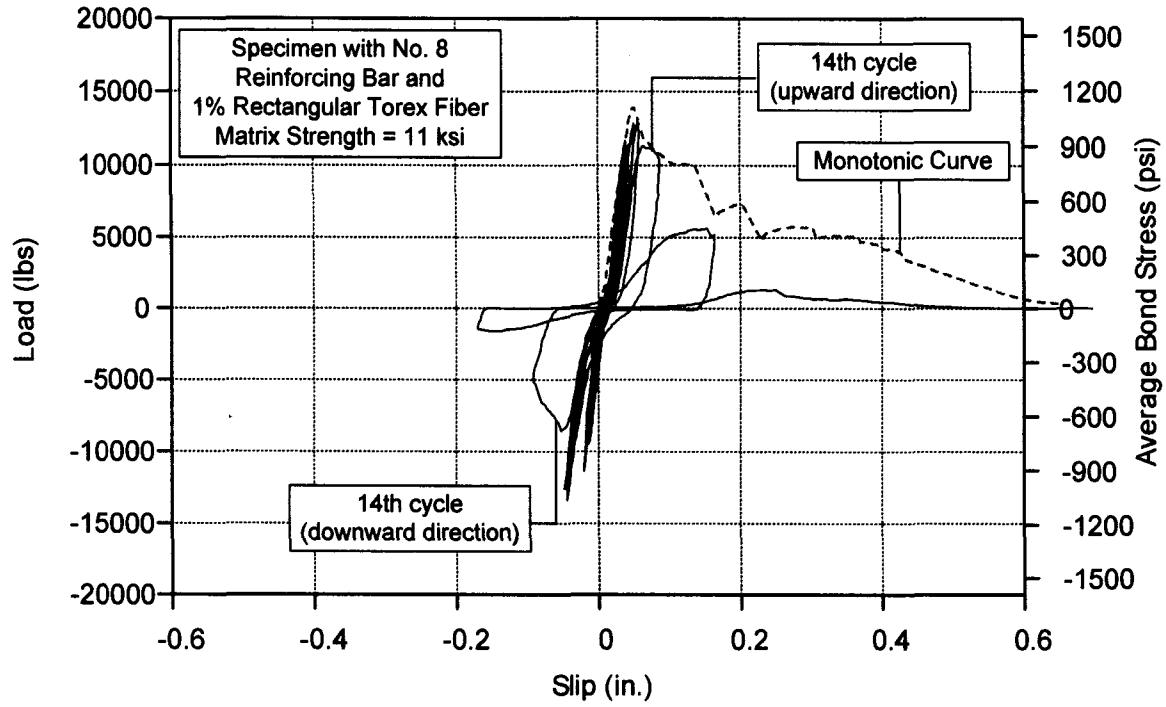

Figure 4.74 Load-slip curve for fully reversed force controlled cyclic loading: No. 8 bar and 1% rectangular Torex fiber

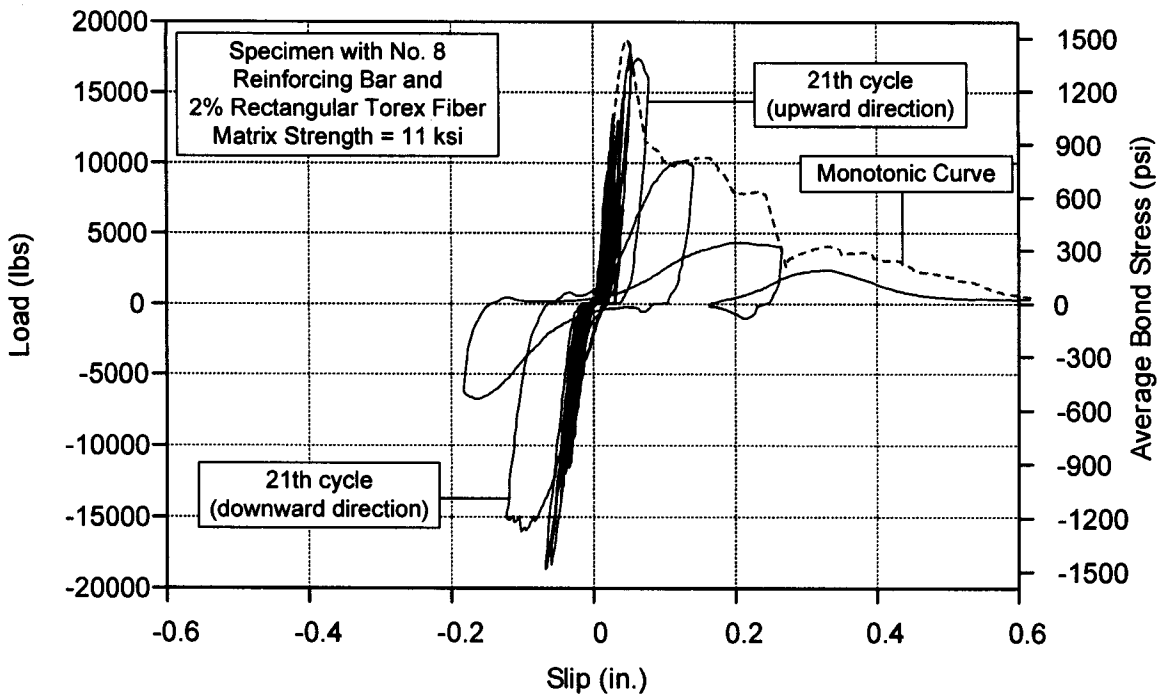

Figure 4.75 (a) Load-slip curve for fully reversed force controlled cyclic loading: No. 8 bar and 2% rectangular Torex fiber

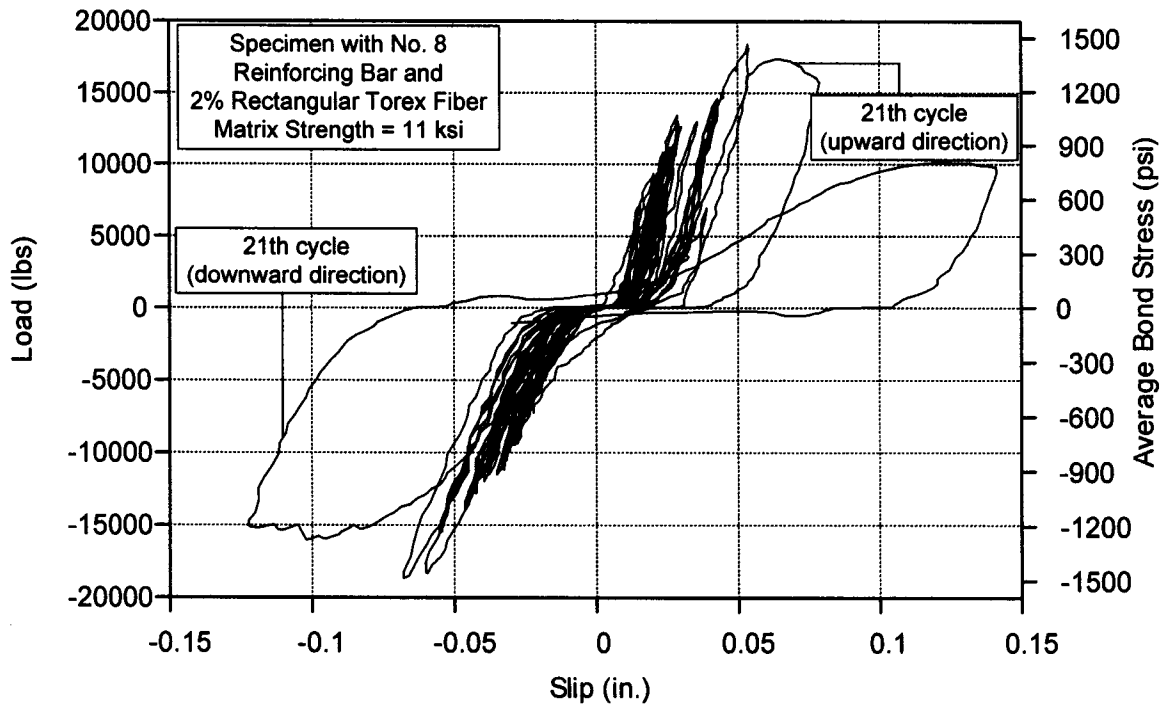

Figure 4.75 (b) Enlargement load-slip curve for fully reversed force controlled cyclic loading: No. 8 bar and 2% rectangular Torex fiber

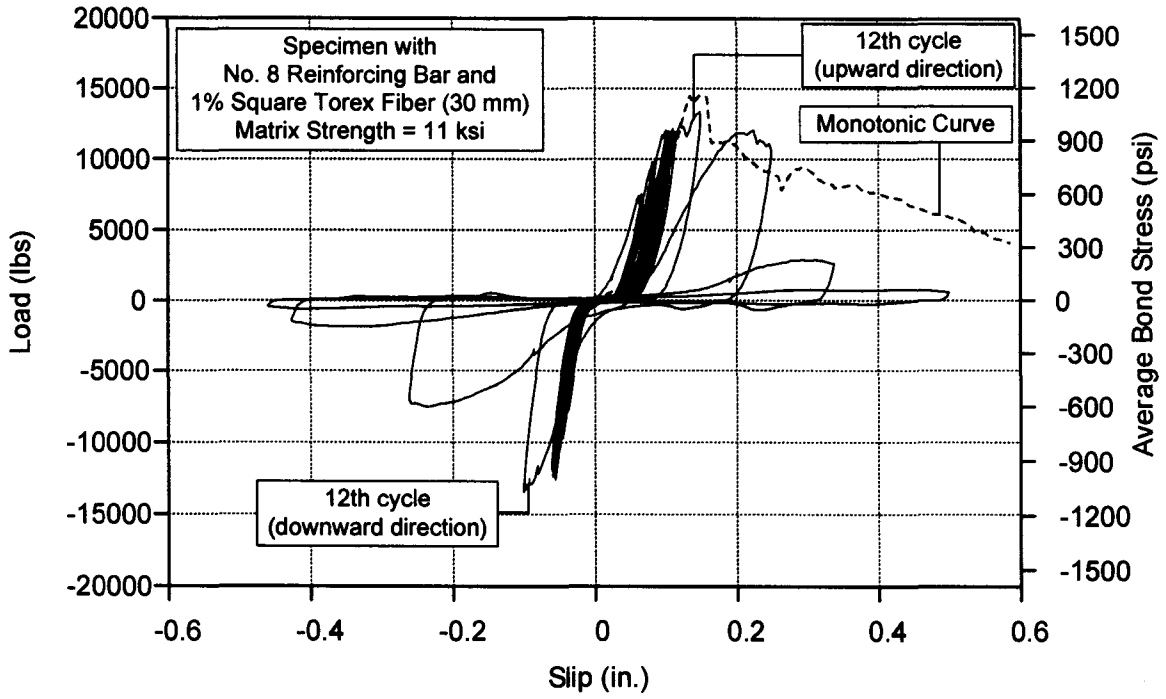

Figure 4.76 Load-slip curve for fully reversed force controlled cyclic loading: No. 8 bar and 1% square Torex fiber (30 mm)

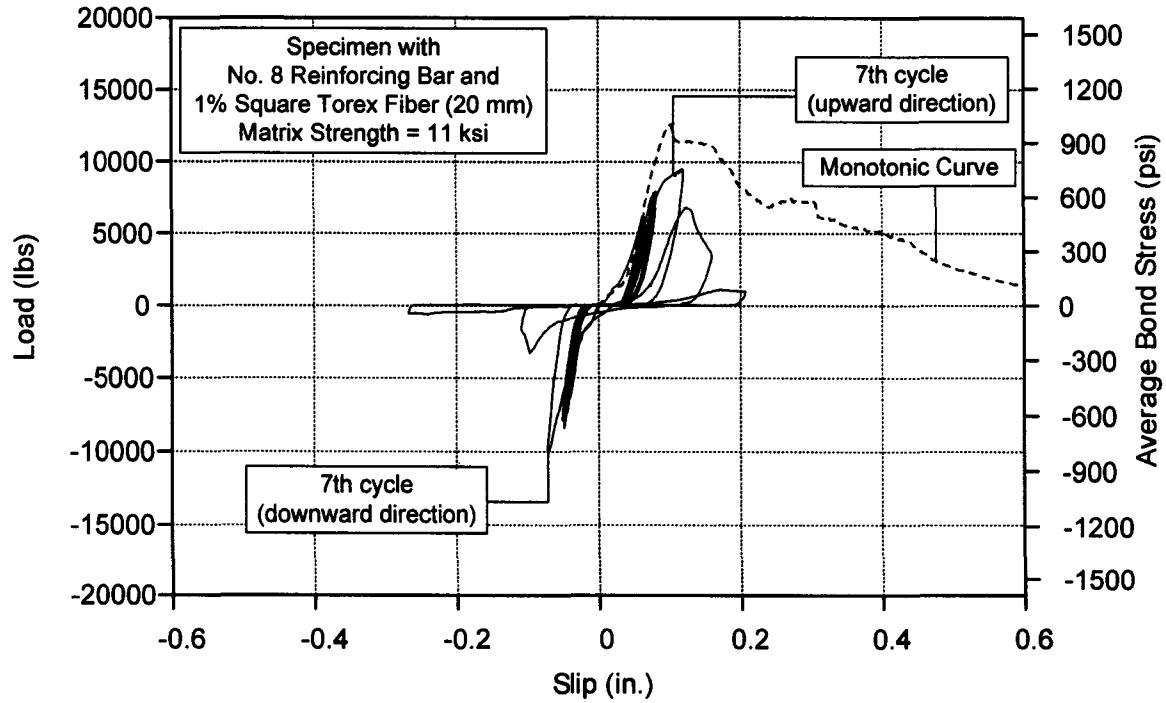

Figure 4.77 Load-slip curve for fully reversed force controlled cyclic loading: No. 8 bar and 1% square Torex fiber (20 mm)

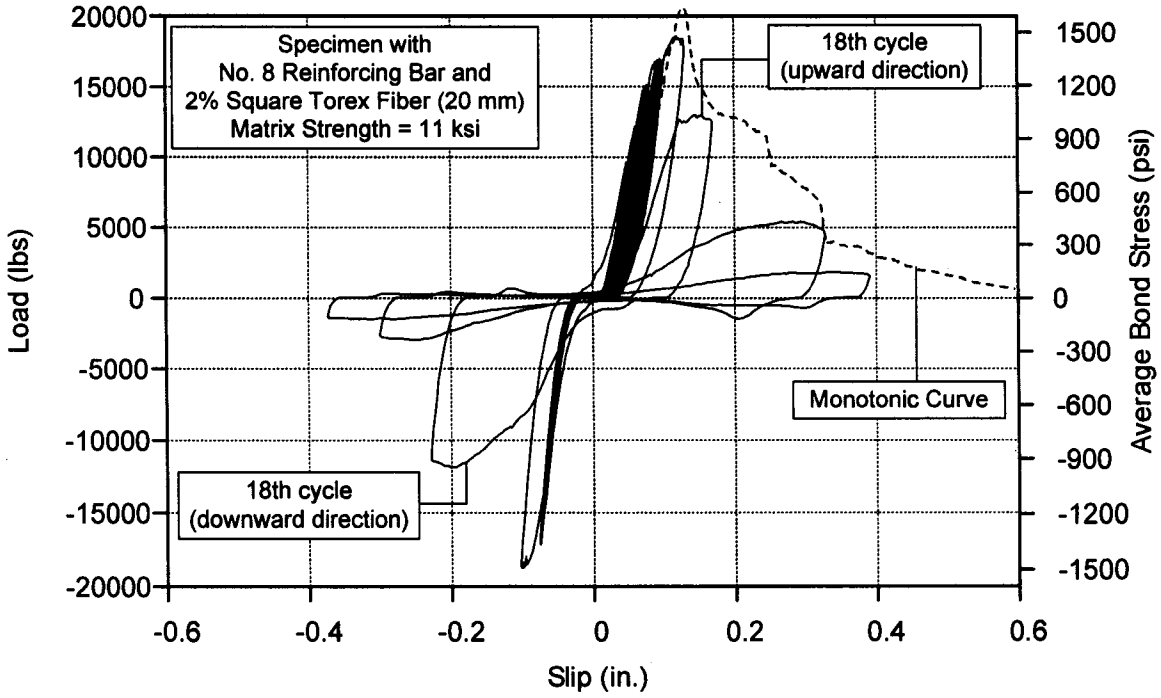

Figure 4.78 (a) Load-slip curve for fully reversed force controlled cyclic loading: No. 8 bar and 2% square Torex fiber (20 mm)

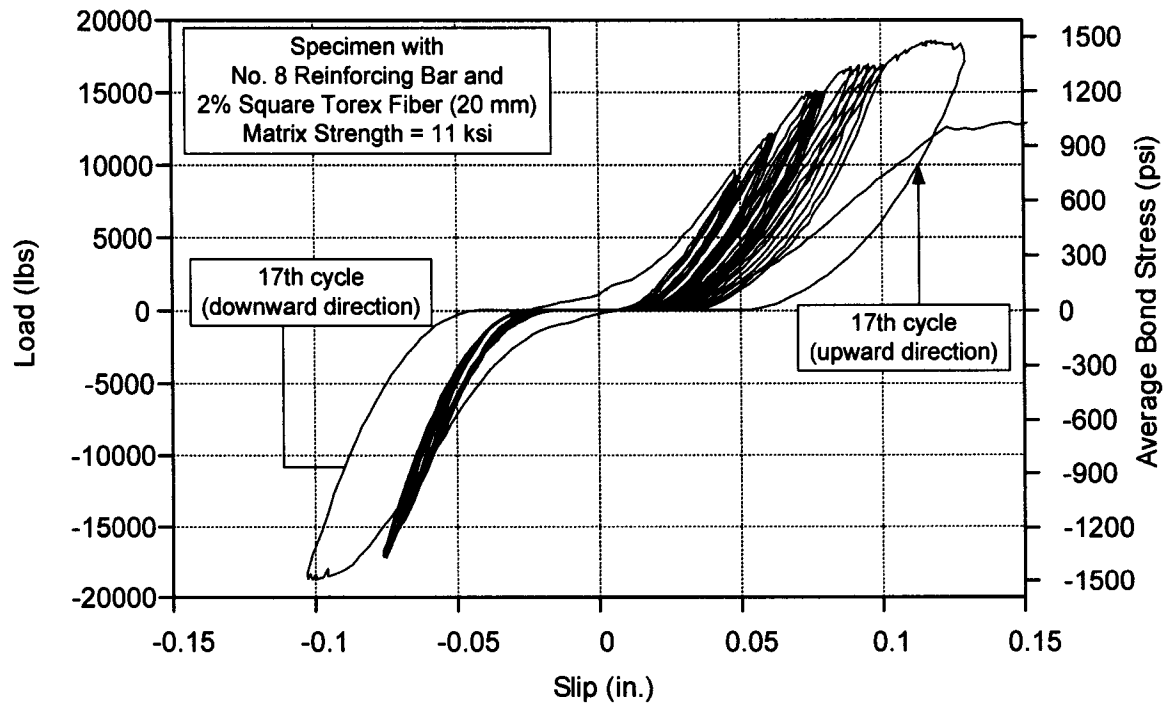

Figure 4.78 (b) Enlargement load-slip curve for fully reversed force controlled cyclic loading: No. 8 bar and 2% square Torex fiber (20 mm)

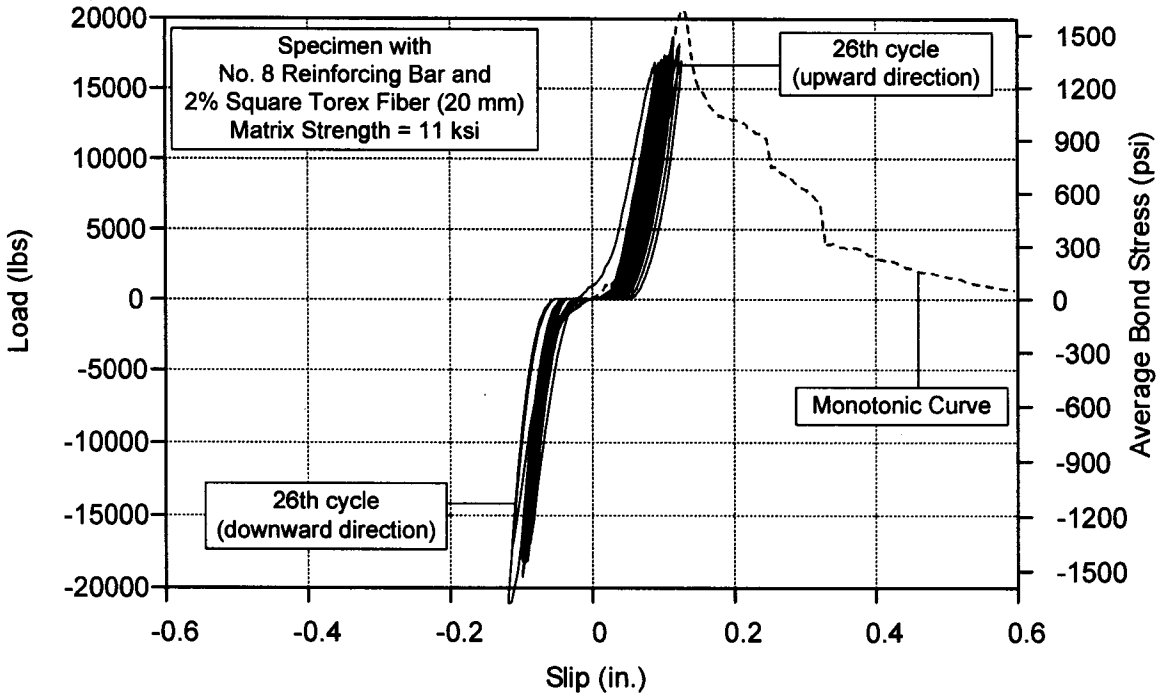

Figure 4.79 (a) Load-slip curve for fully reversed (constant) force controlled cyclic loading: No. 8 bar and 2% square Torex fiber (20 mm)

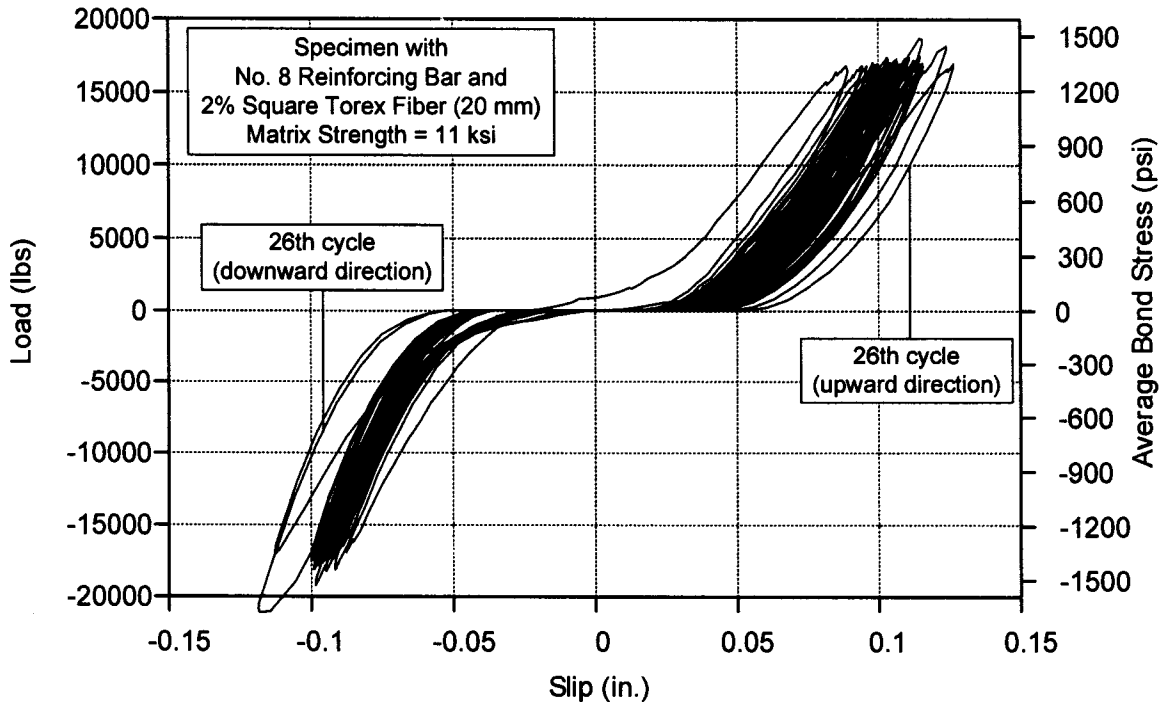

Figure 4.79 (b) Enlargement load-slip curve for fully reversed (constant) force controlled cyclic loading: No. 8 bar and 2% square Torex fiber (20 mm)

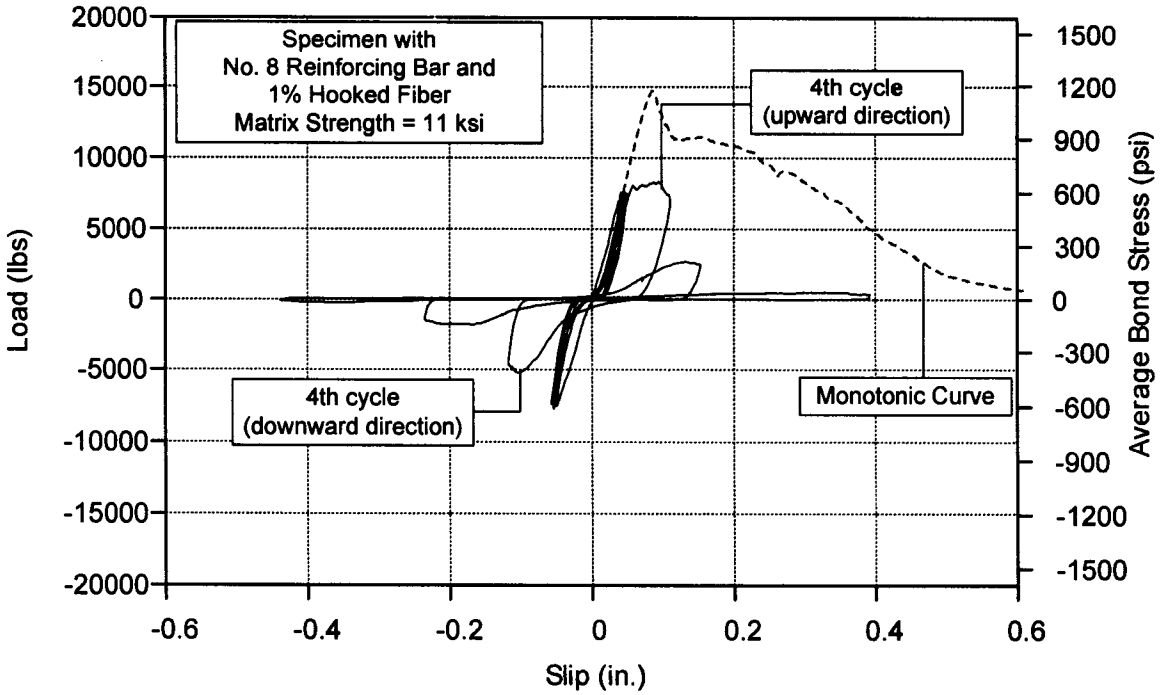

Figure 4.80 Load-slip curve for fully reversed force controlled cyclic loading: No. 8 bar and 1% hooked fiber

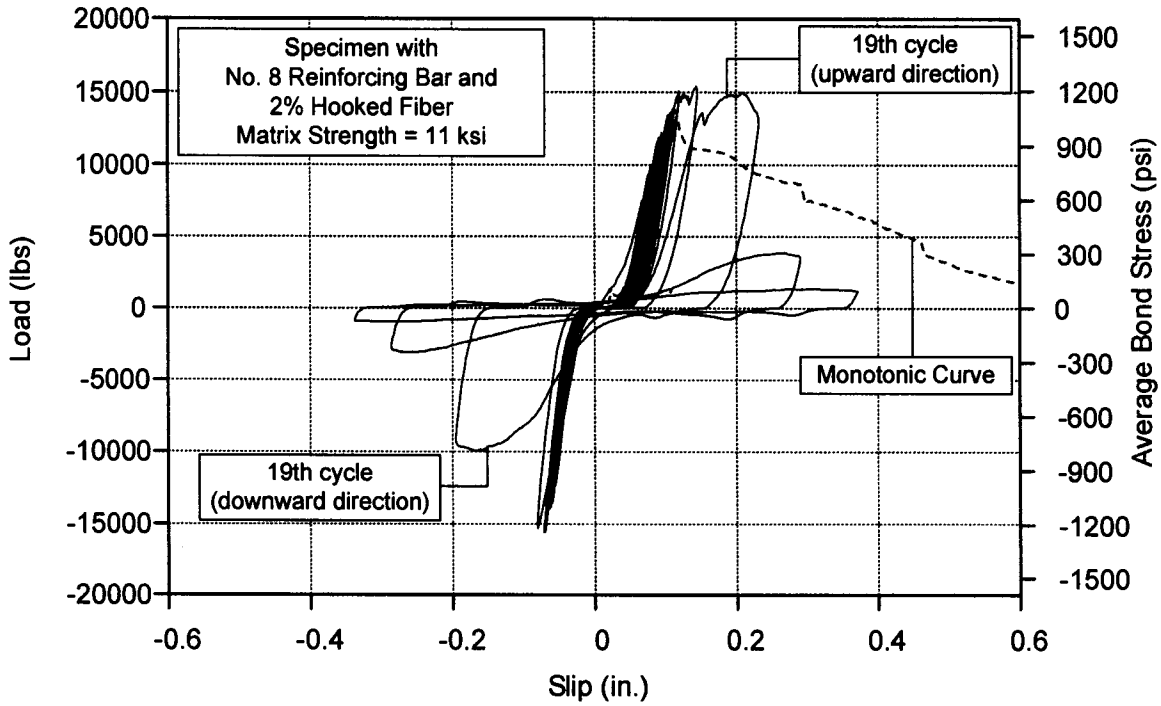

Figure 4.81 (a) Load-slip curve for fully reversed force controlled cyclic loading: No. 8 bar and 2% hooked fiber

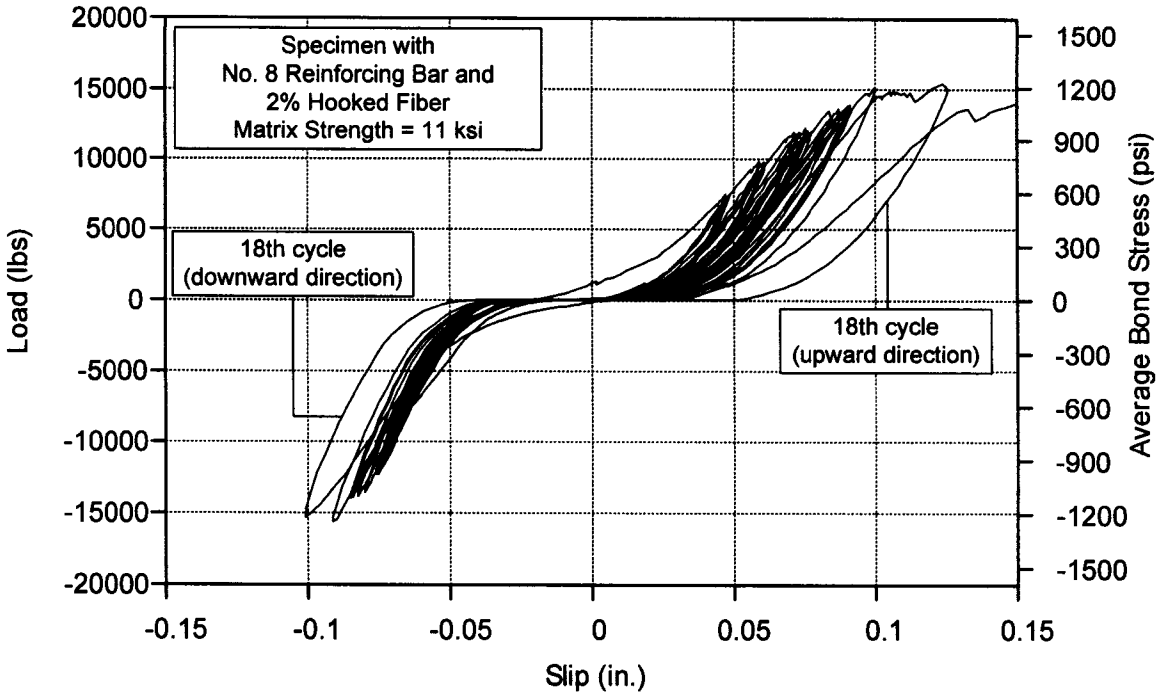

Figure 4.81 (b) Enlargement load-slip curve for fully reversed force controlled cyclic loading: No. 8 bar and 2% hooked fiber

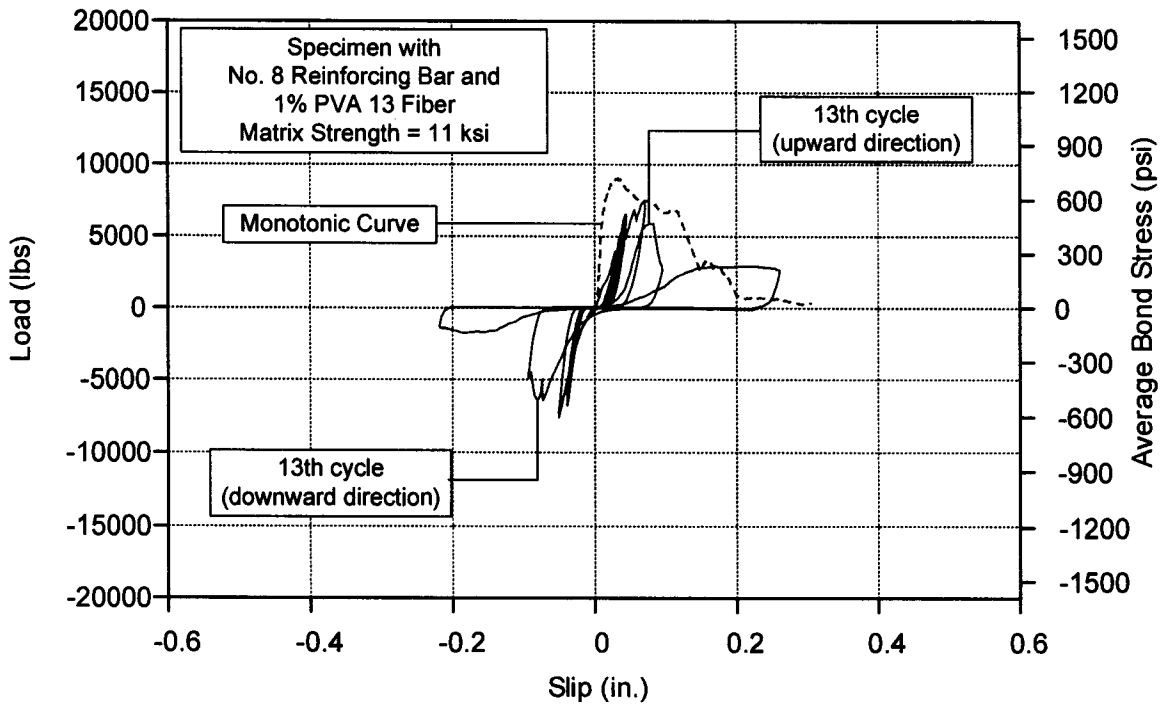

Figure 4.82 Load-slip curve for fully reversed force controlled cyclic loading: No. 8 bar and 1% PVA 13 fiber

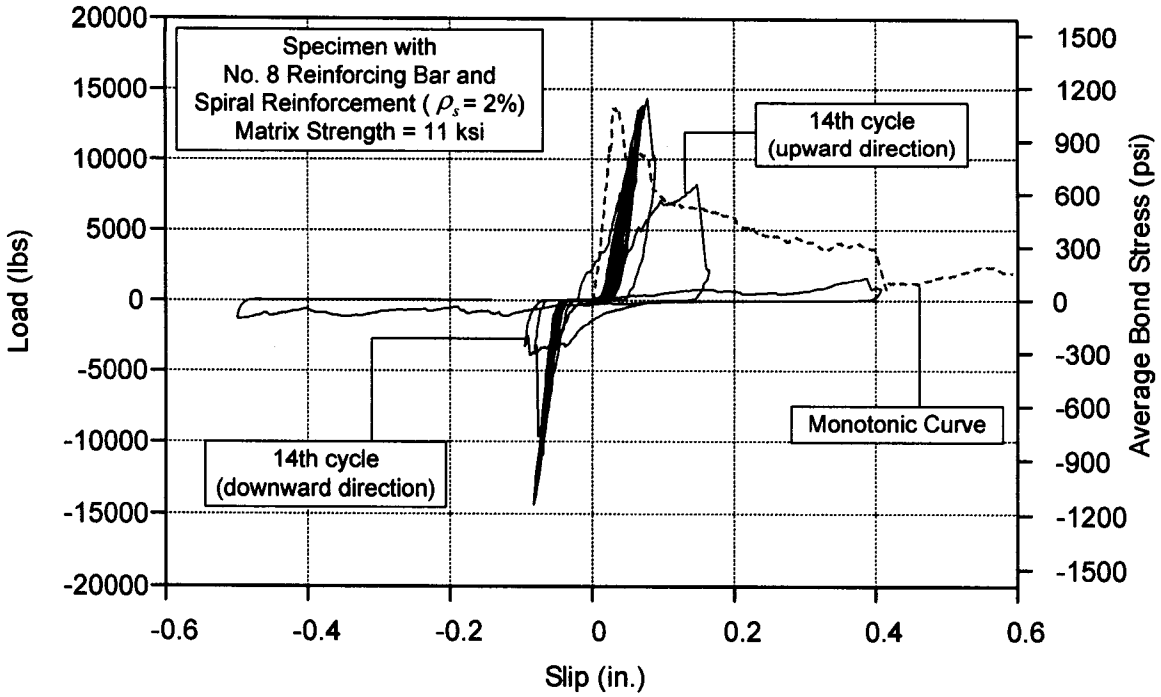

Figure 4.83 (a) Load-slip curve for fully reversed force controlled cyclic loading: No. 8 bar and 2% volumetric spiral reinforcement

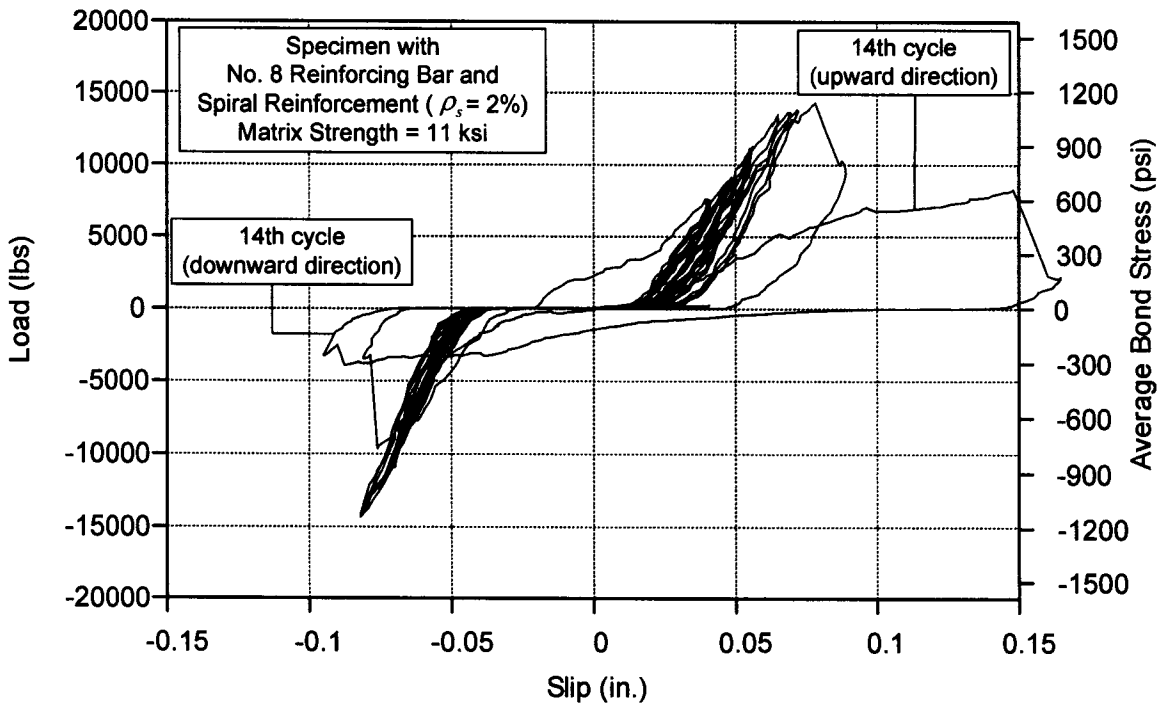

Figure 4.83 (b) Enlargement load-slip curve for fully reversed force controlled cyclic loading: No. 8 bar and 2% volumetric spiral reinforcement

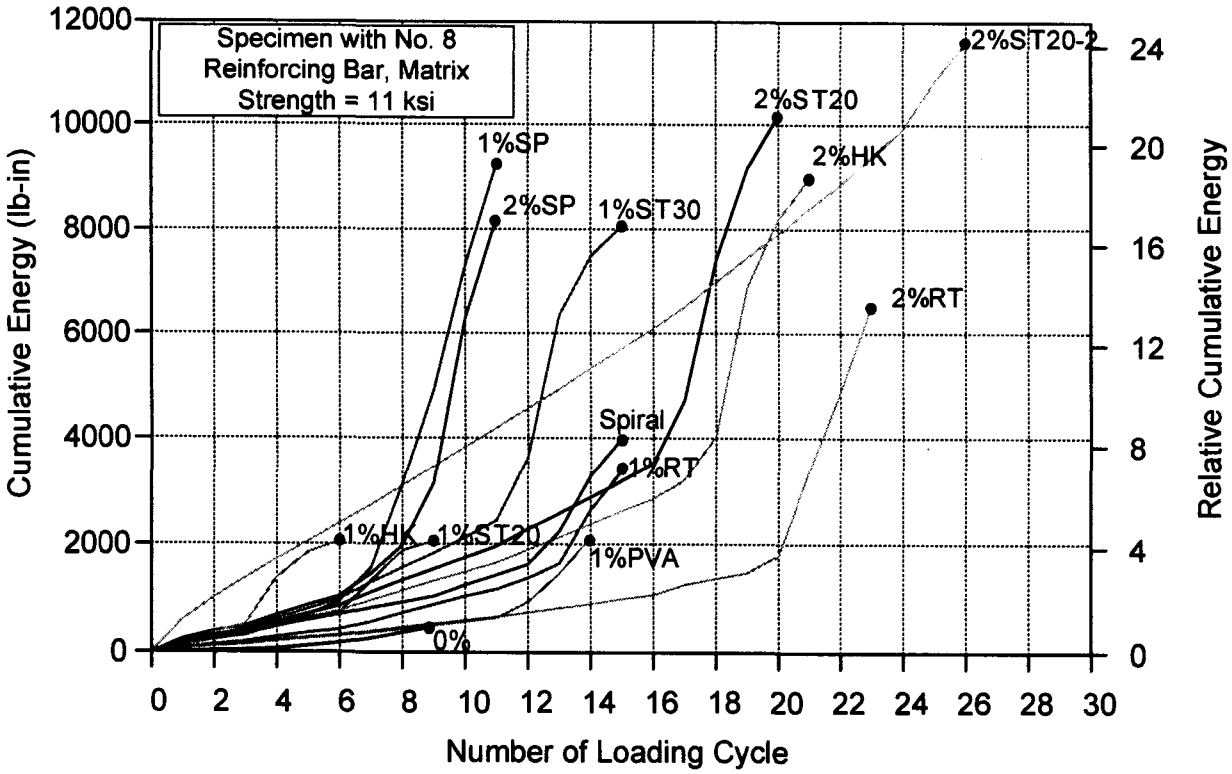

Note: 0%: Control specimen
PVA: PVA 13 fiber
HK: steel hooked fiber
ST 20: square Torex fiber, 20 mm in length
ST 20-2: square Torex fiber specimen under constant force controlled loading, see Table 4.8
ST 30: square Torex fiber, 30 mm in length
RT: rectangular Torex fiber, 30 mm in length
SP: Spectra fiber
Spiral: Spiral reinforcement (2% volumetric ratio)

Figure 4.84 Cumulative dissipated energy for specimens under fully reversed force controlled cyclic loading (No. 8 bar and 11 ksi matrix)

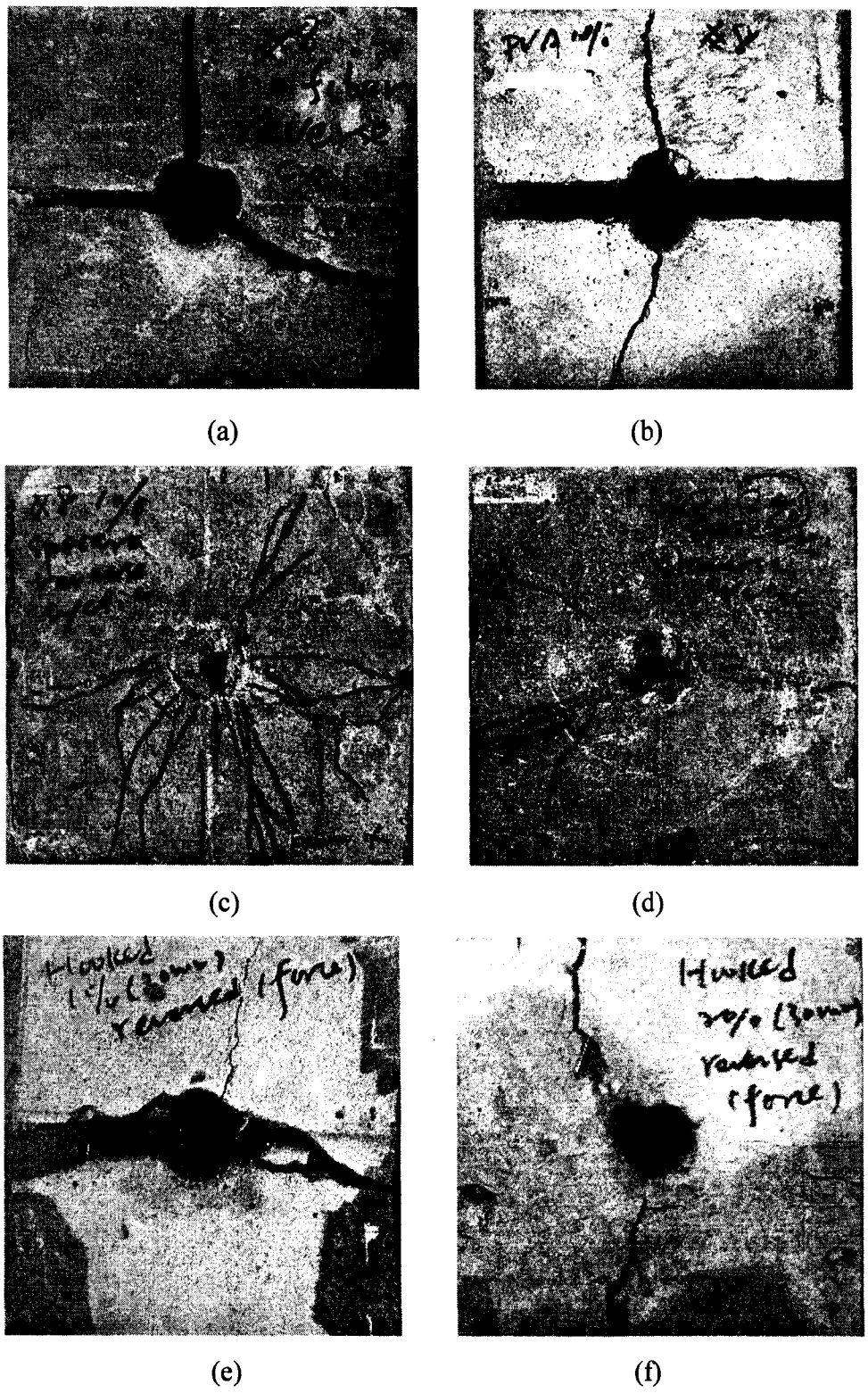

Figure 4.85 Crack patterns of specimen with No. 8 bar subjected to fully reversed force controlled cyclic loading: (a) control specimen; (b) 1% PVA 13; (c) 1% Spectra; (d) 2% Spectra; (e) 1% steel hooked; (f) 2% steel hooked

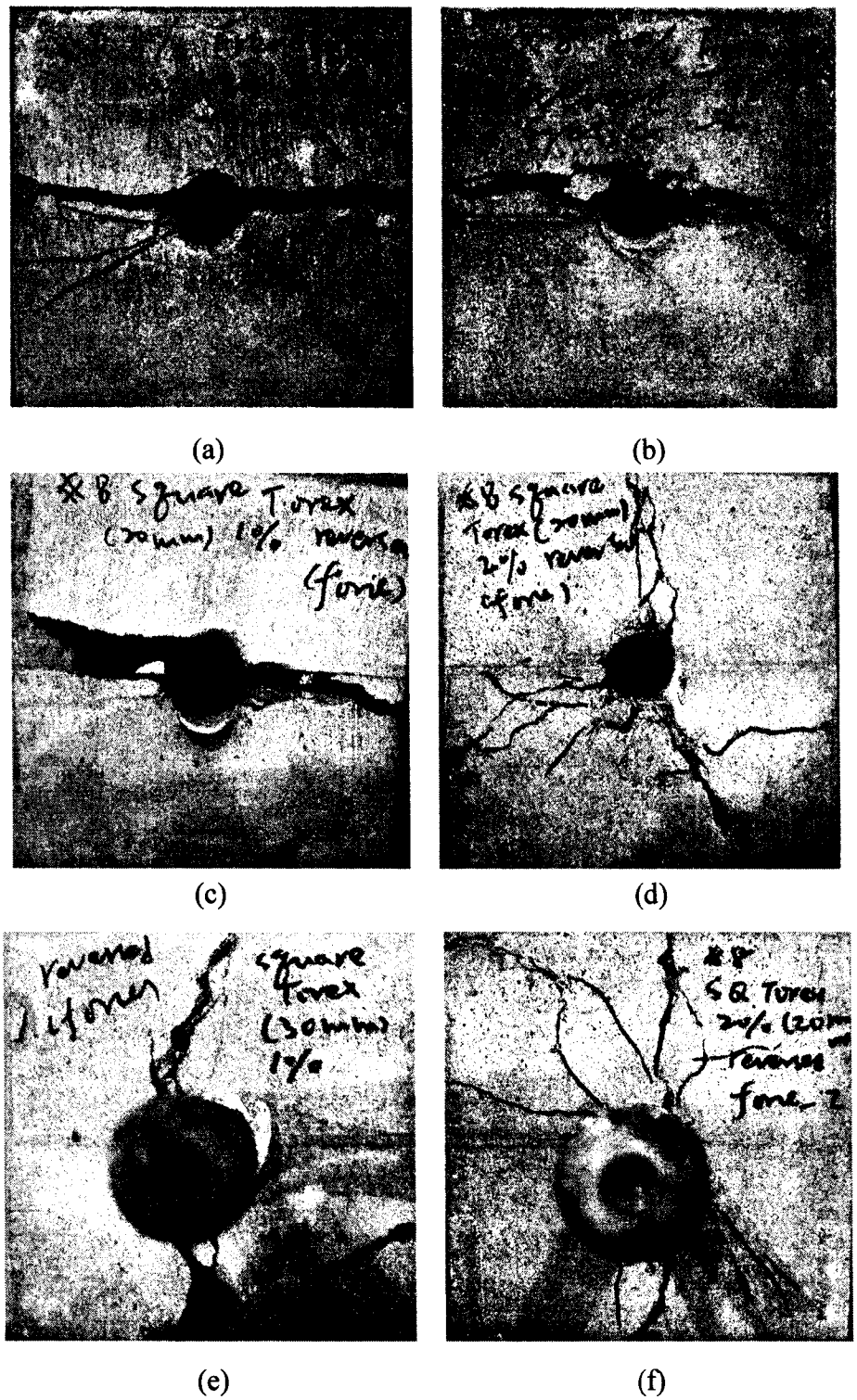

Figure 4.86 Crack patterns of specimen with No. 8 bar subjected to fully reversed force controlled cyclic loading: (a) 1% rectangular Torex; (b) 2% rectangular Torex; (c) 1% square Torex (20 mm); (d) 2% square Torex (20 mm); (e) 1% square Torex (30 mm); (f) 2% square Torex (20 mm) under constant force controlled loading, see Table 4.8

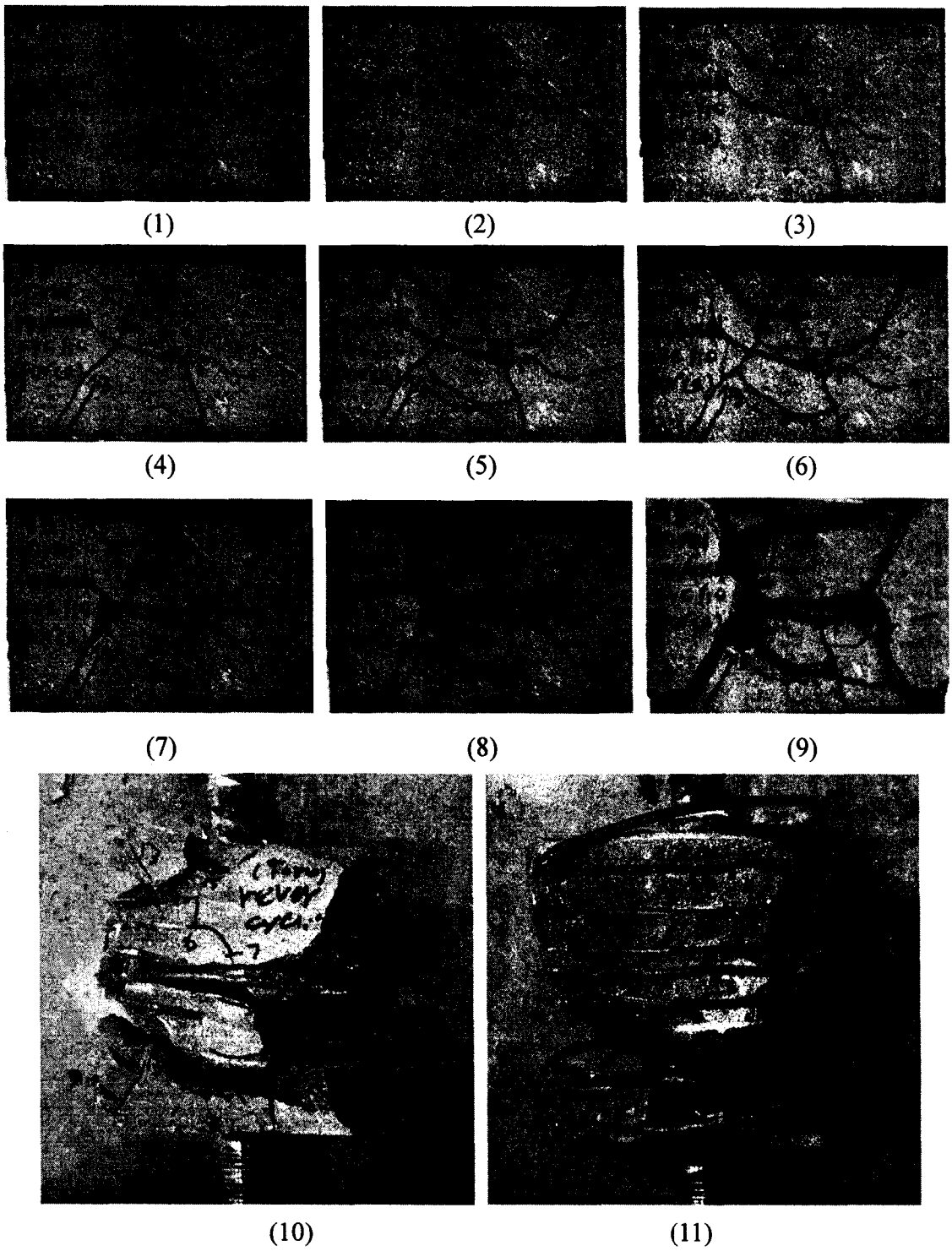

Figure 4.87 Fracture sequence of specimen with No. 8 bar and 2% volumetric spiral reinforcement subjected to fully reversed force controlled cyclic

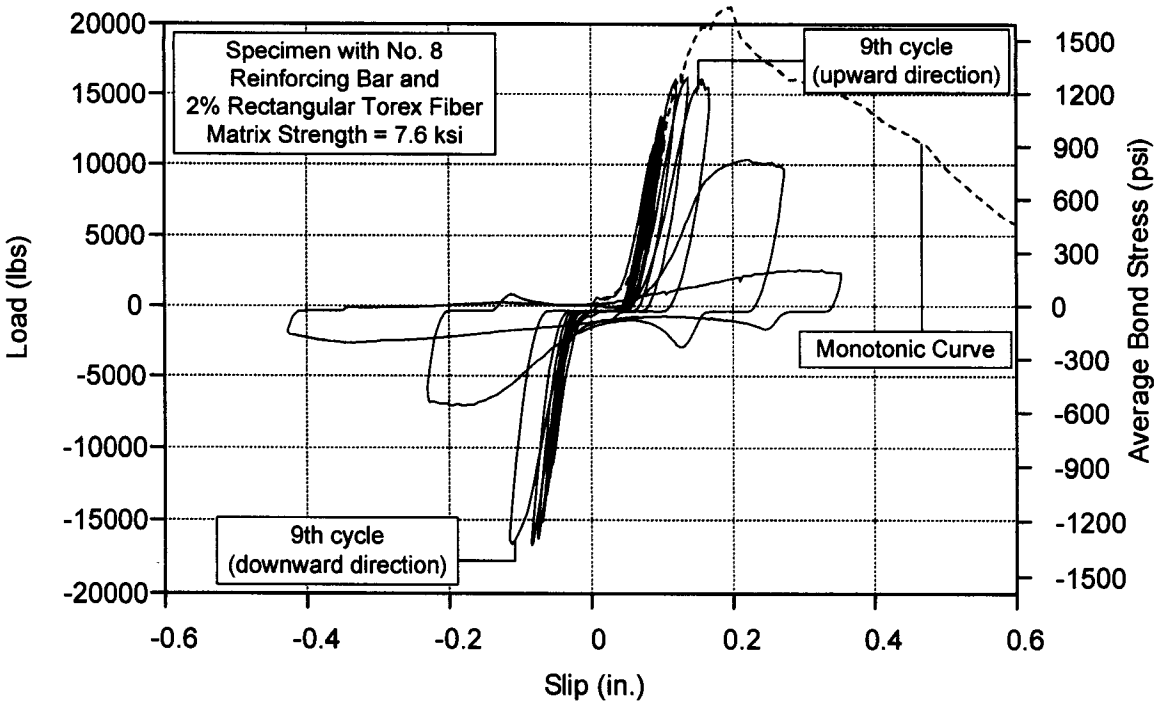

Figure 4.88 Load-slip curve for fully reversed force controlled cyclic loading: 7.6 ksi specimen with No. 8 bar and 2% rectangular Torex fiber

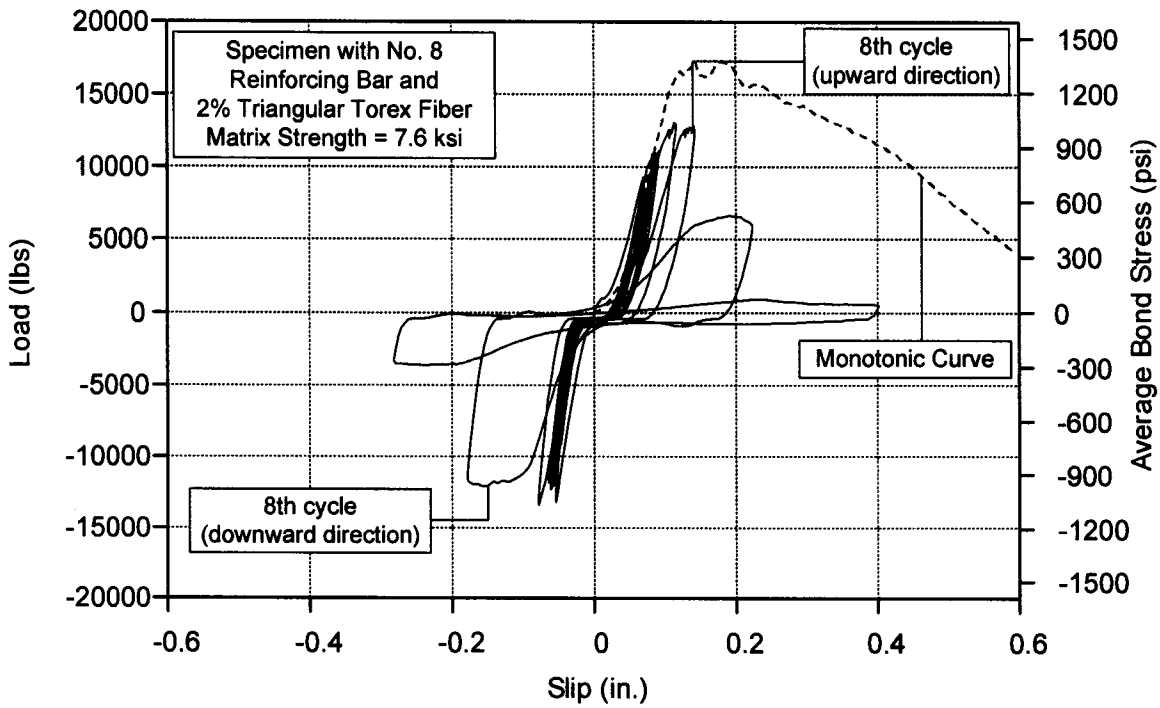

Figure 4.89 Load-slip curve for fully reversed force controlled cyclic loading: 7.6 ksi specimen with No. 8 bar and 2% triangular Torex fiber (Helix)

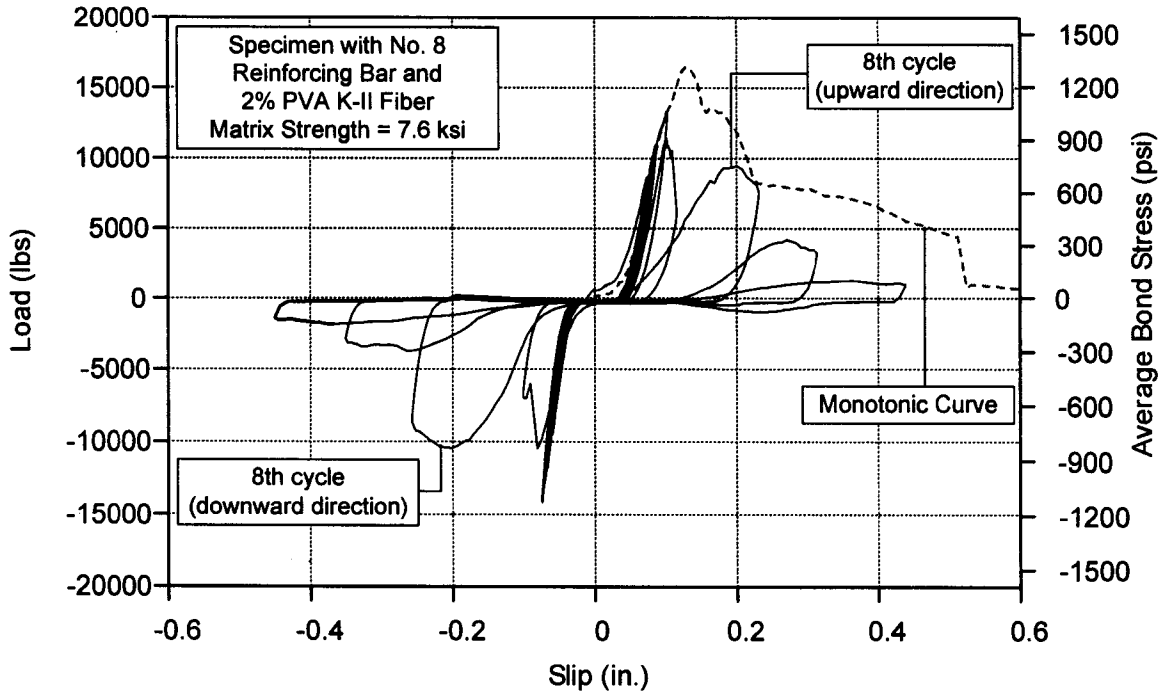

Figure 4.90 Load-slip curve for fully reversed force controlled cyclic loading: 7.6 ksi specimen with No. 8 bar and 2% PVA K-II fiber

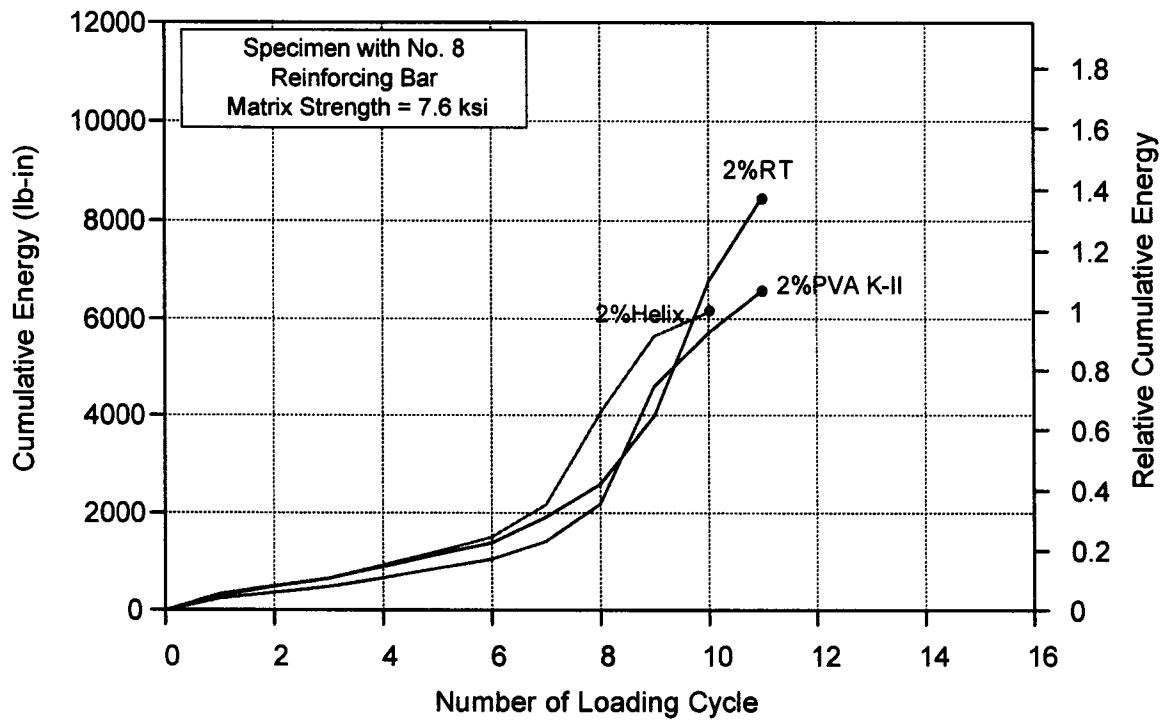

Figure 4.91 Cumulative dissipated energy for specimens under fully reversed force controlled cyclic loading (No. 8 bar and 7.6 ksi matrix)

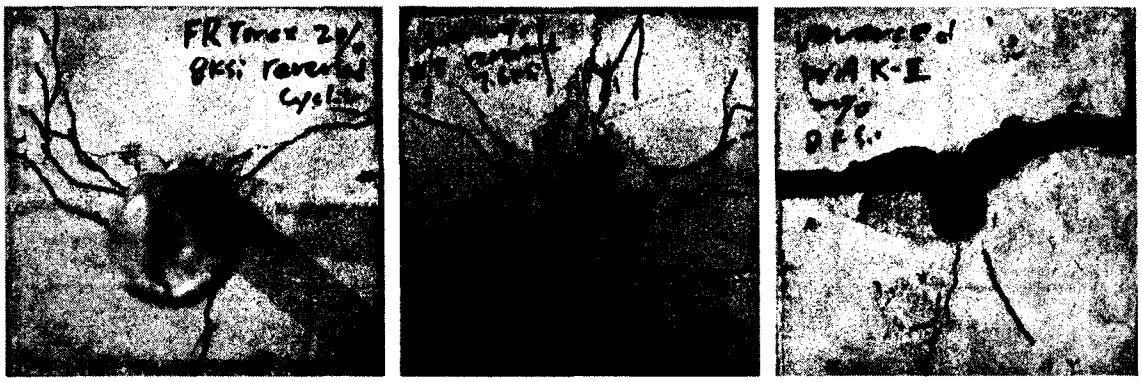

(a) (b) (c)

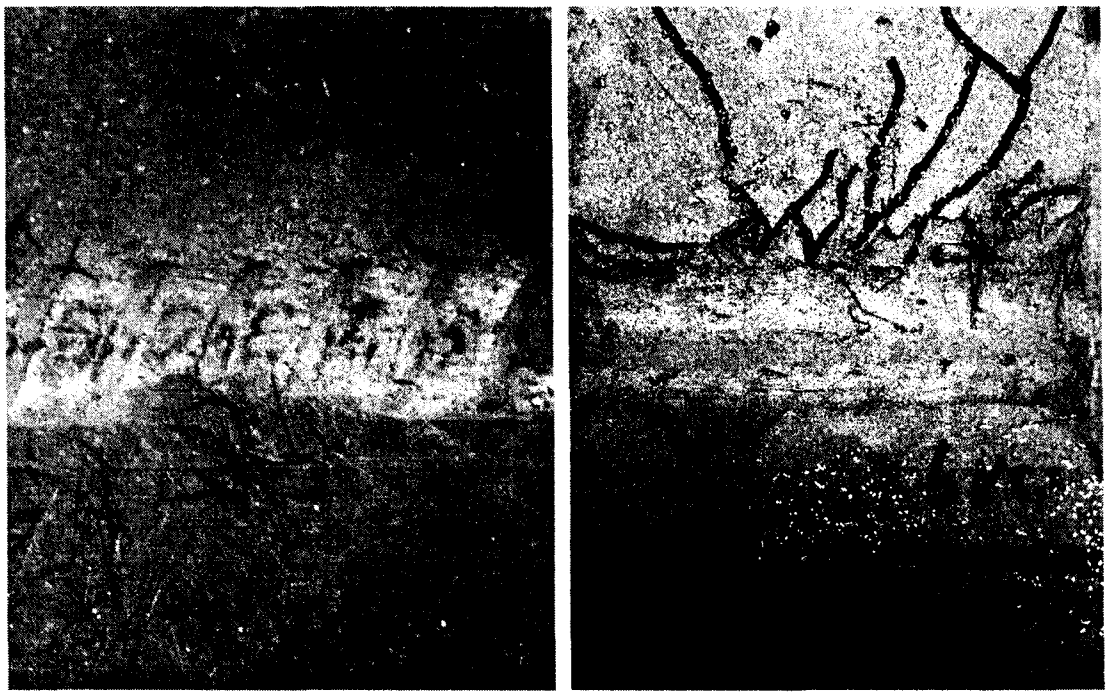

(d) (e)

Figure 4.92 Crack patterns of 7.6 ksi specimen with No. 8 bar subjected to fully reversed force controlled cyclic loading: (a) 2% rectangular Torex; (b) 2% triangular Torex (Helix); (c) 2% PVA K-II; (d) cut-half specimen with 11 ksi matrix and 2% rectangular Torex; (e) cut-half specimen with 7.6 ksi matrix and 2% rectangular Torex

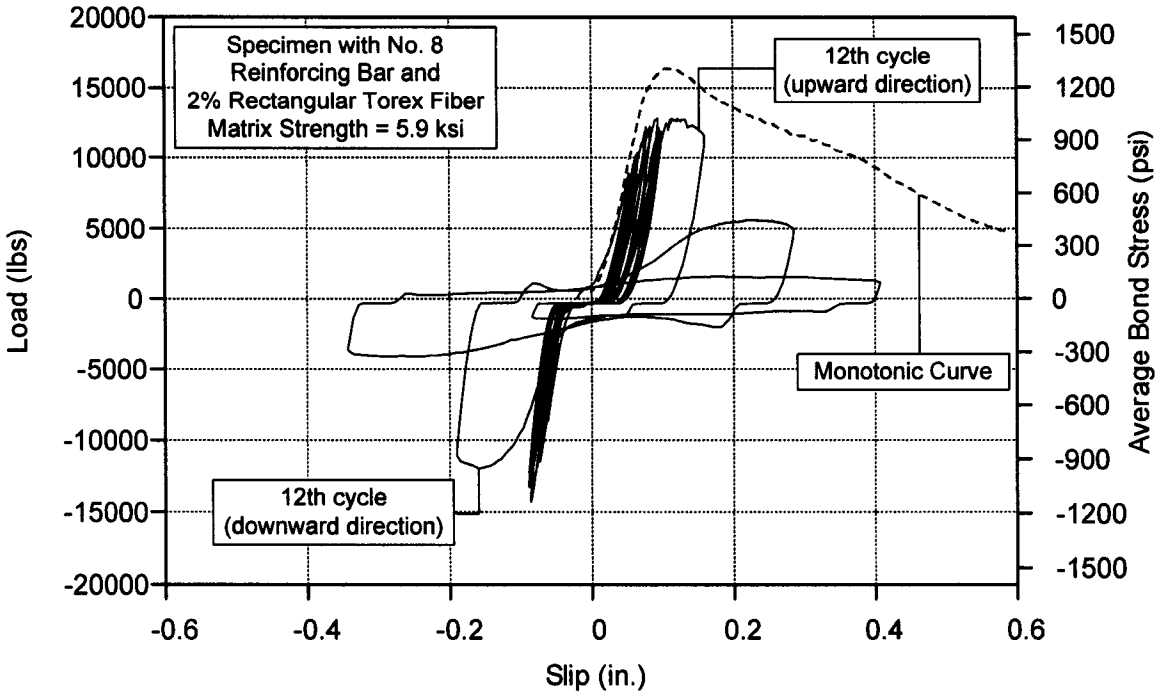

Figure 4.93 Load-slip curve for fully reversed force controlled cyclic loading: 5.9 ksi specimen with No. 8 bar and 2% rectangular Torex fiber

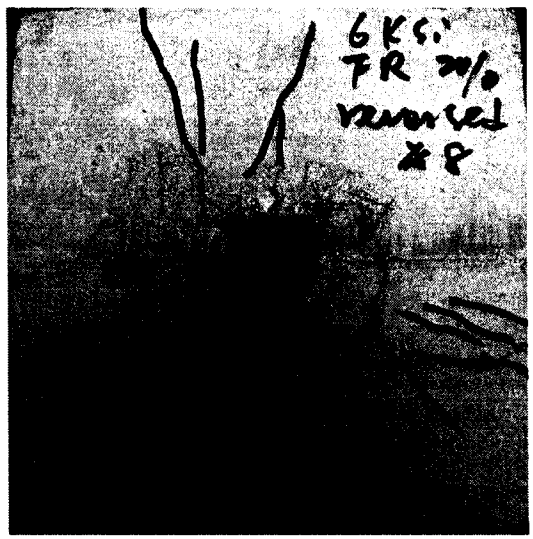

Figure 4.94 Crack patterns of 5.9 ksi specimen with No. 8 bar and 2% rectangular Torex fiber subjected to fully reversed force controlled cyclic loading

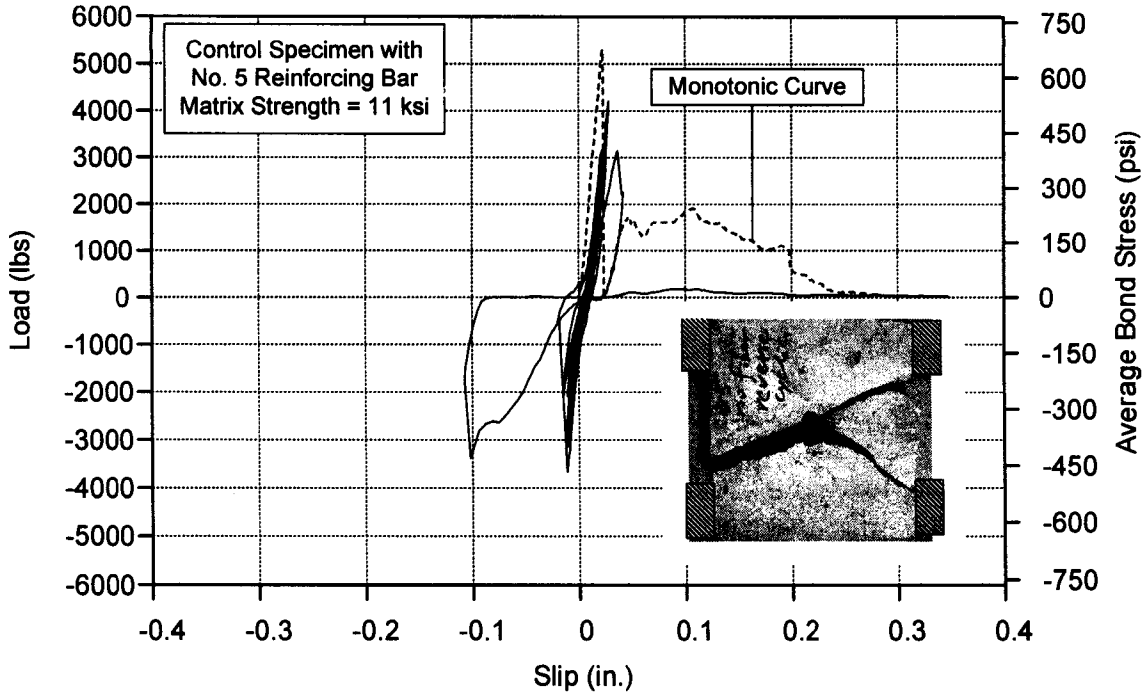

Figure 4.95 Load-slip curve for fully reversed force controlled cyclic loading: No. 5 bar, control specimen

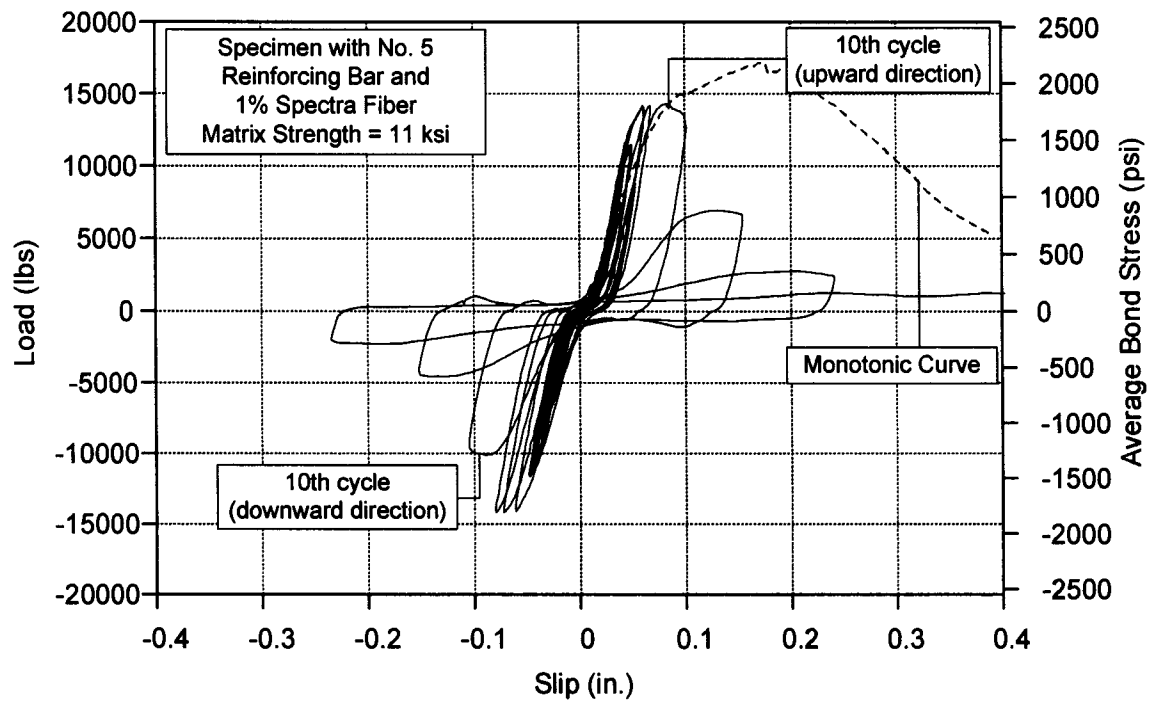

Figure 4.96 Load-slip curve for fully reversed force controlled cyclic loading: No. 5 bar and 1% Spectra fiber

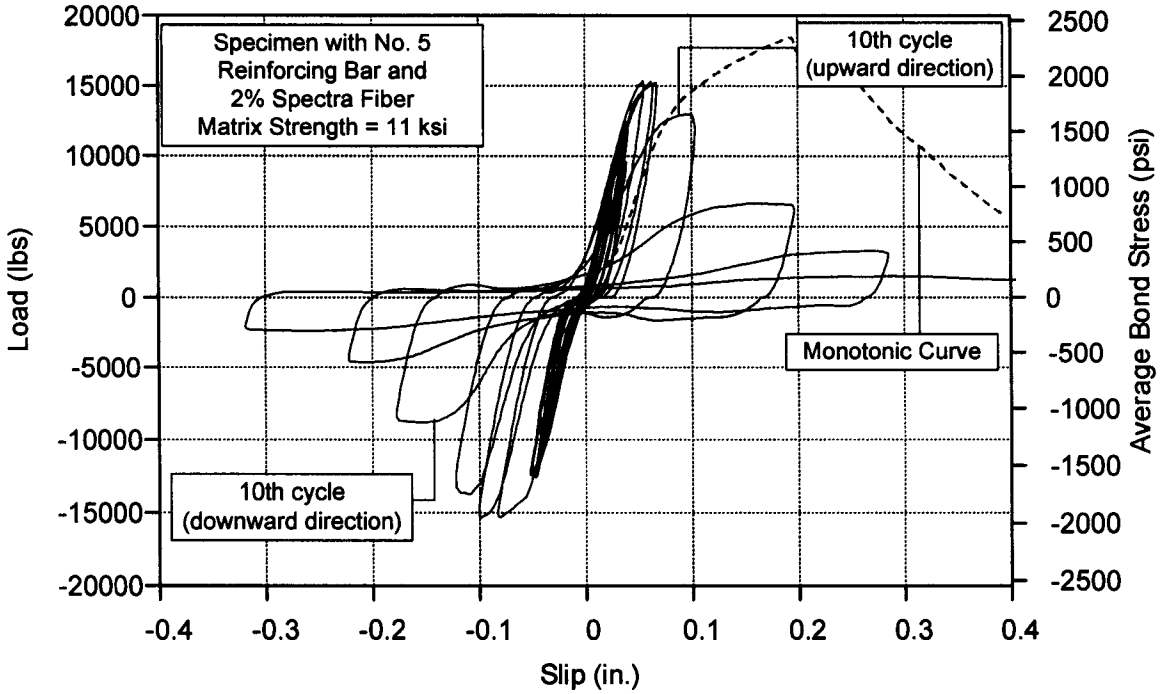

Figure 4.97 Load-slip curve for fully reversed force controlled cyclic loading: No. 5 bar and 2% Spectra fiber

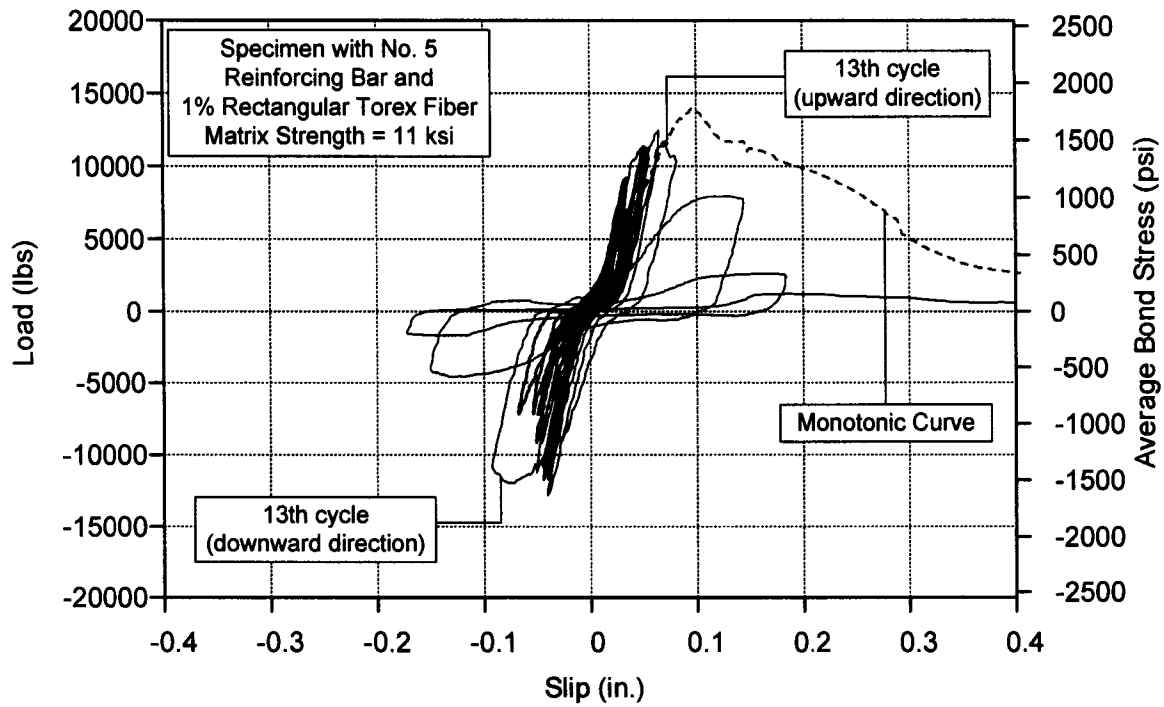

Figure 4.98 Load-slip curve for fully reversed force controlled cyclic loading: No. 5 bar and 1% rectangular Torex fiber

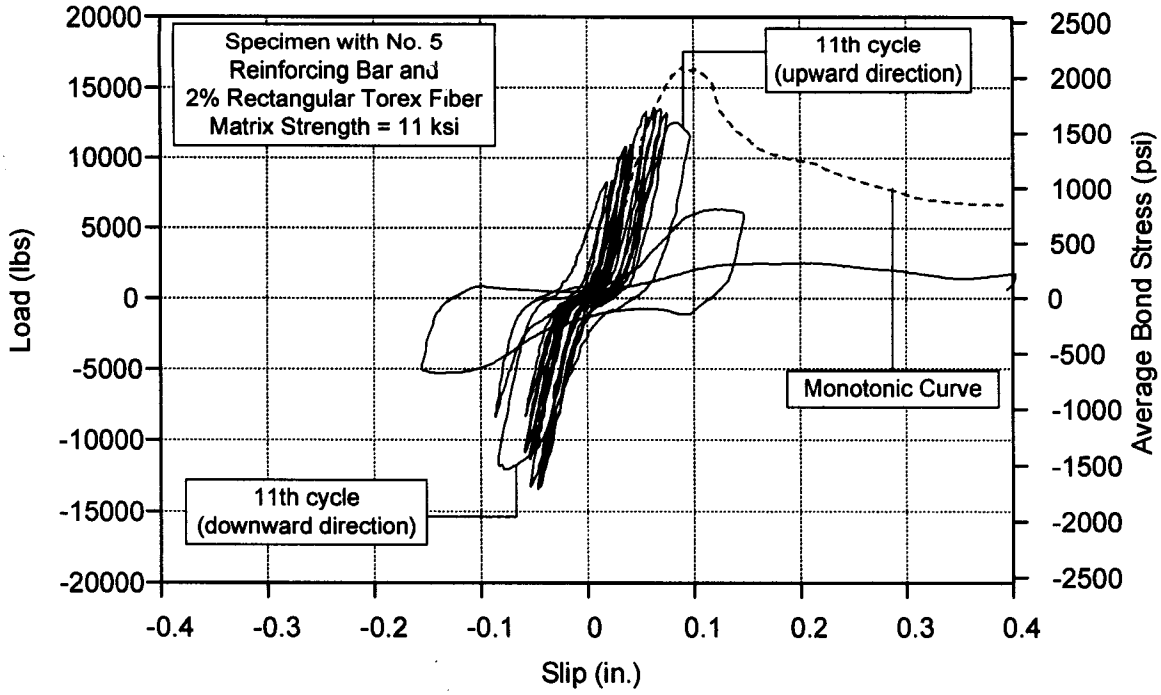

Figure 4.99 Load-slip curve for fully reversed force controlled cyclic loading: No. 5 bar and 2% rectangular Torex fiber

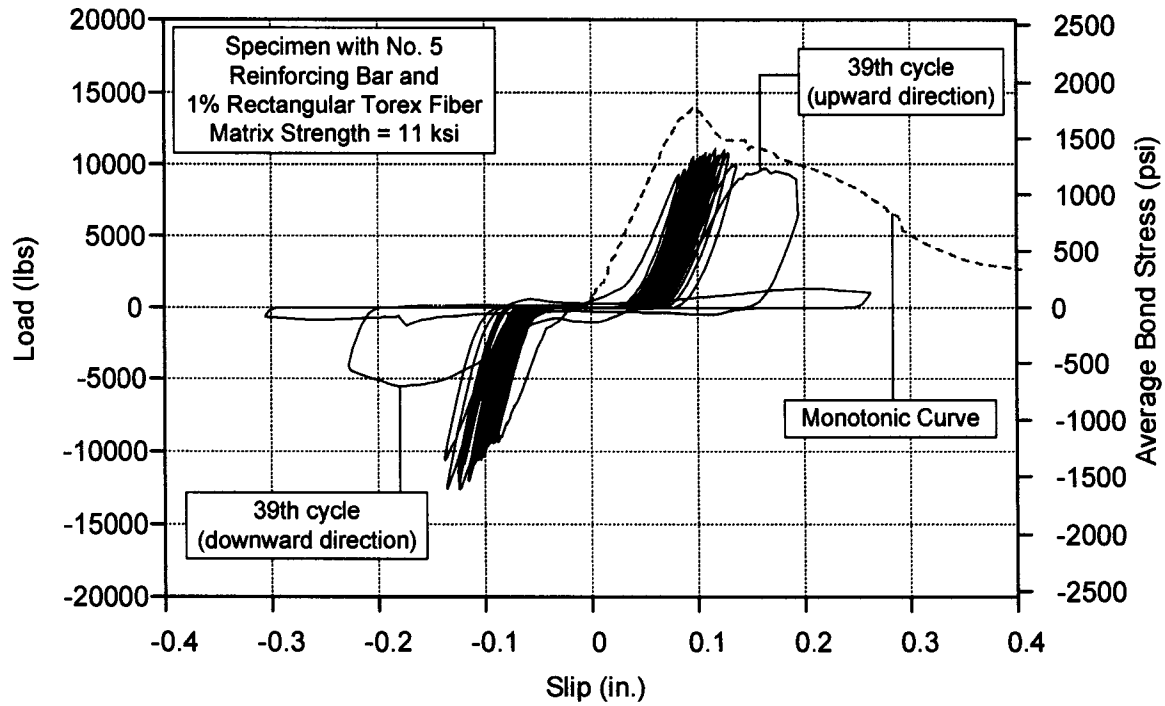

Figure 4.100 (a) Load-slip curve for fully reversed (constant) force controlled cyclic loading: No. 5 bar and 1% rectangular Torex fiber

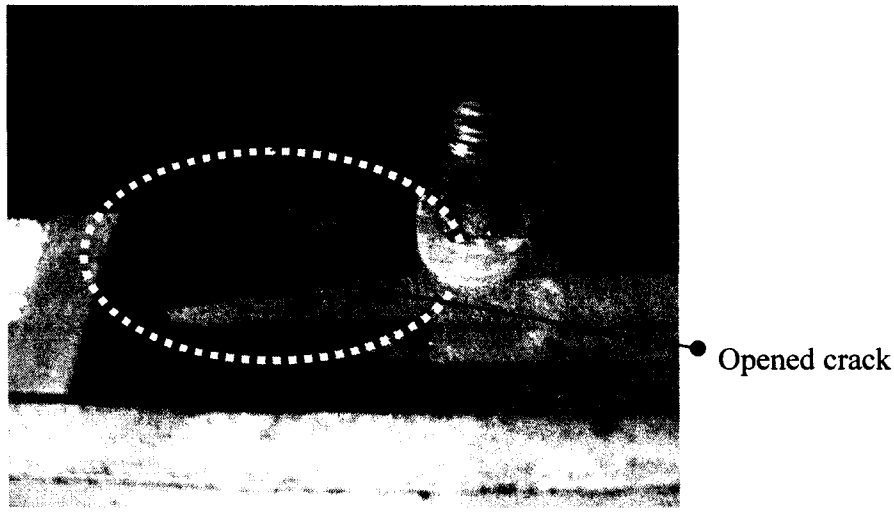

Figure 4.100 (b) Observed opened crack at 38th cycle

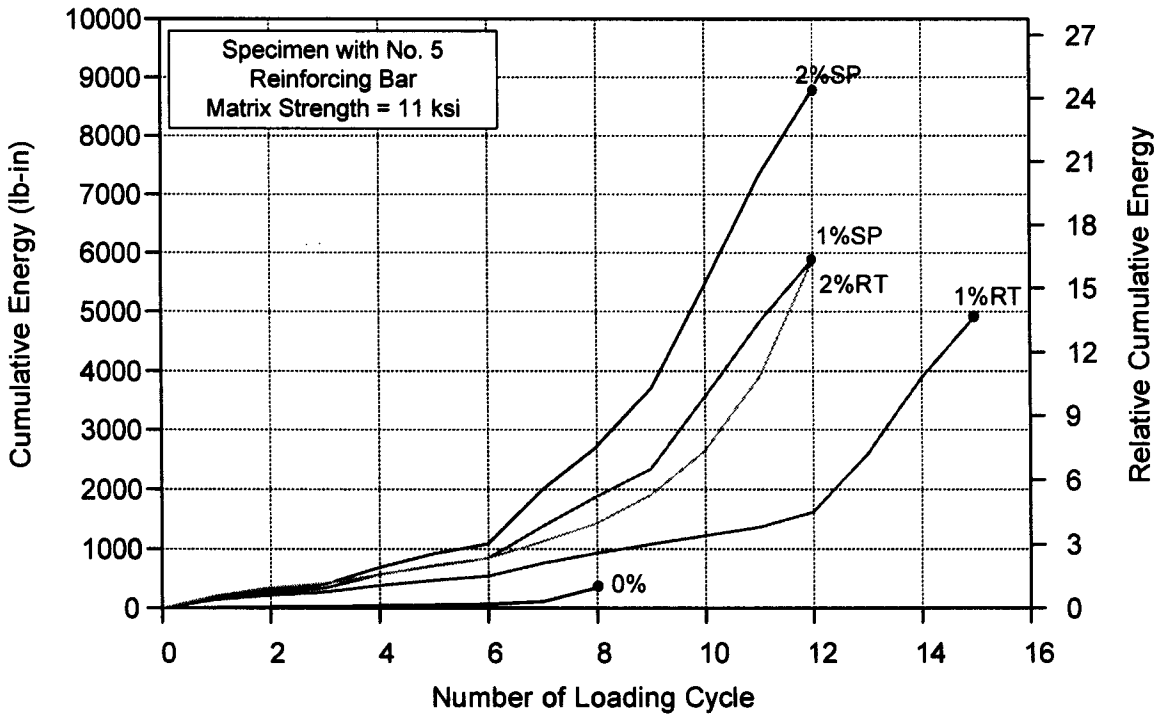

Note: 0%: Control specimen; RT: rectangular Torex fiber; SP: Spectra fiber

Figure 4.101 Cumulative dissipated energy for specimens under fully reversed force controlled cyclic loading (No. 5 bar and 11 ksi matrix)

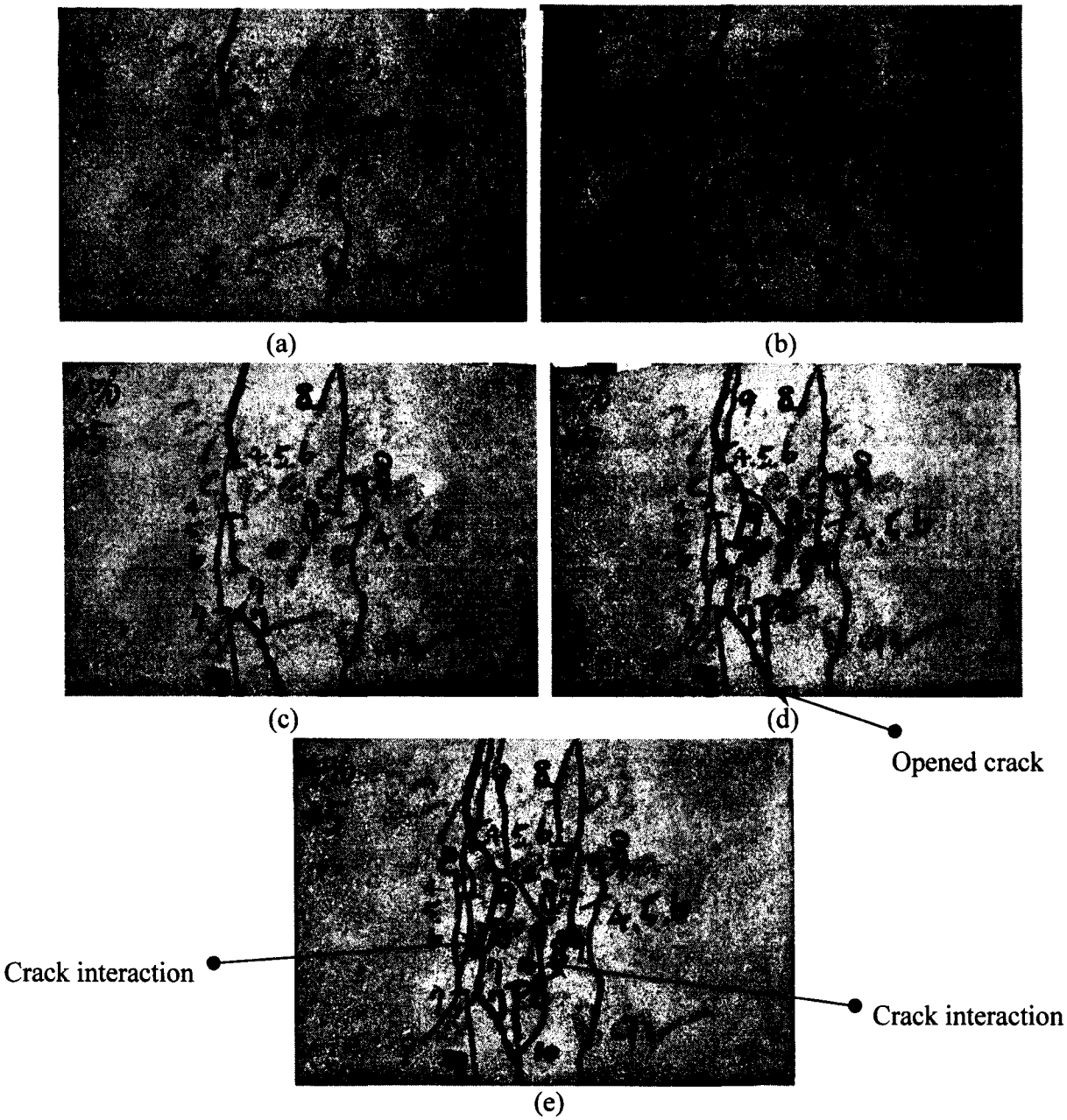

Figure 4.102 Crack development process for specimen with No. 5 bar and 1% Spectra fibers:
(a) First visible cracks formed in the 4th cycle, which extended from the top and bottom surfaces to the side faces
(b) Cracks extending after the 7th cycle. Cracks originating from the top and bottom surfaces had not met, hence no bond strength degradation
(c) Crack extending after the 8th cycle. Note that multiple cracks had developed. Cracks originating from top and bottom surfaces had not met, hence no bond strength degradation
(d) Crack extending after the 9th full cycle. Number of multiple cracks kept increasing. Cracks originating from top and bottom surfaces had not connected, hence no bond strength degradation. The bottom crack started to open.
(e) Crack extending after the 10th cycle. Number of multiple cracks continued increasing. Cracks originating from top and bottom surfaces already connected, hence bond strength degradation occurred.

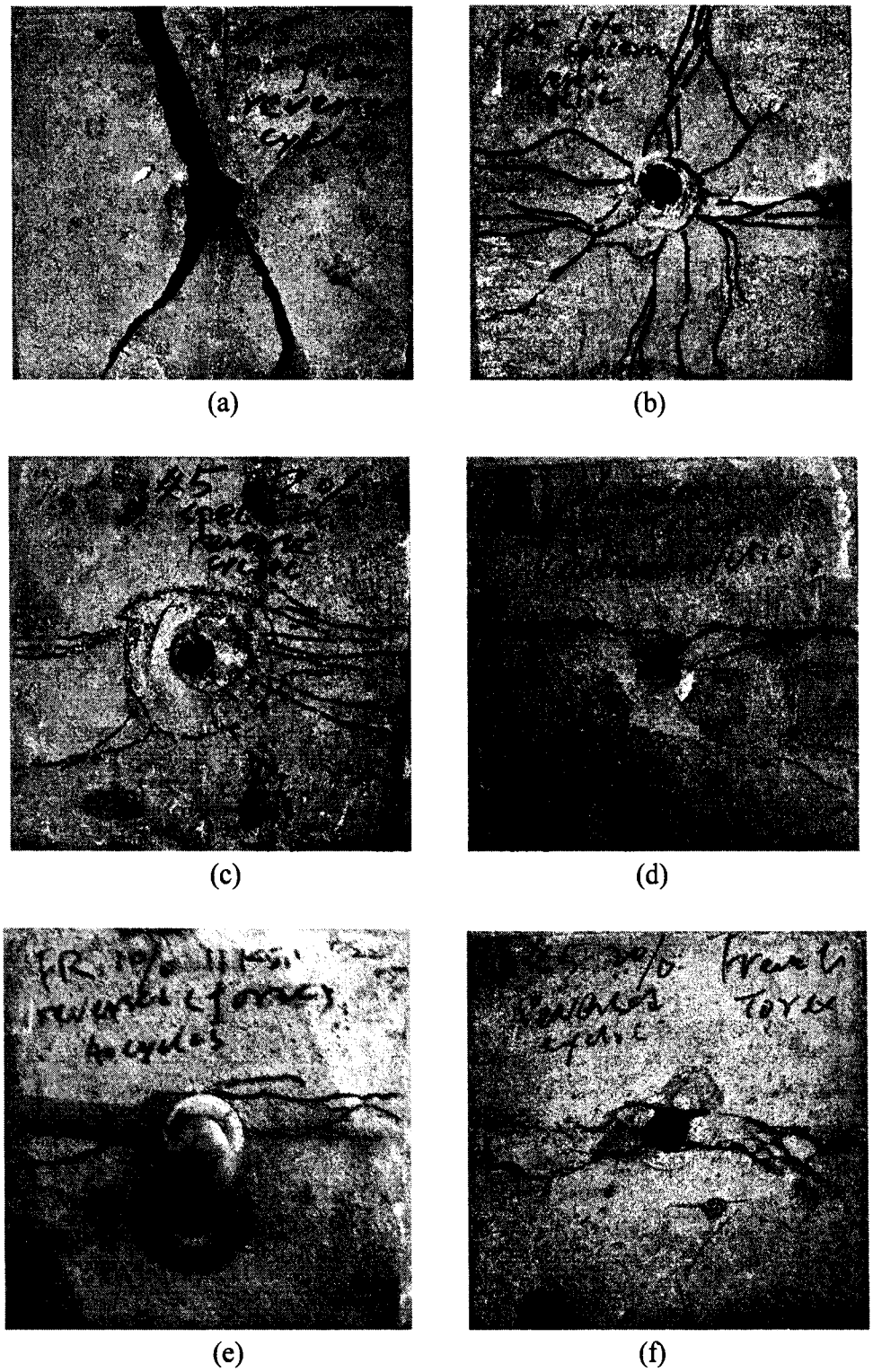

Figure 4.103 Crack patterns of specimen with No. 5 bar subjected to fully reversed force controlled cyclic loading: (a) Control specimen; (b) 1% Spectra; (c) 2% Spectra; (d) 1% rectangular Torex; (e) 1% rectangular Torex under constant force controlled loading, see Table 4.12; (f) 2% rectangular Torex

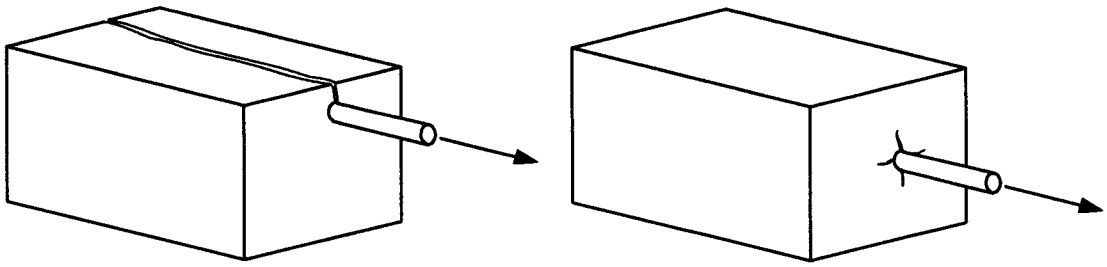

Figure 4.104 Bond failure modes of reinforcing bar: (a) Splitting failure; (b) Pullout failure

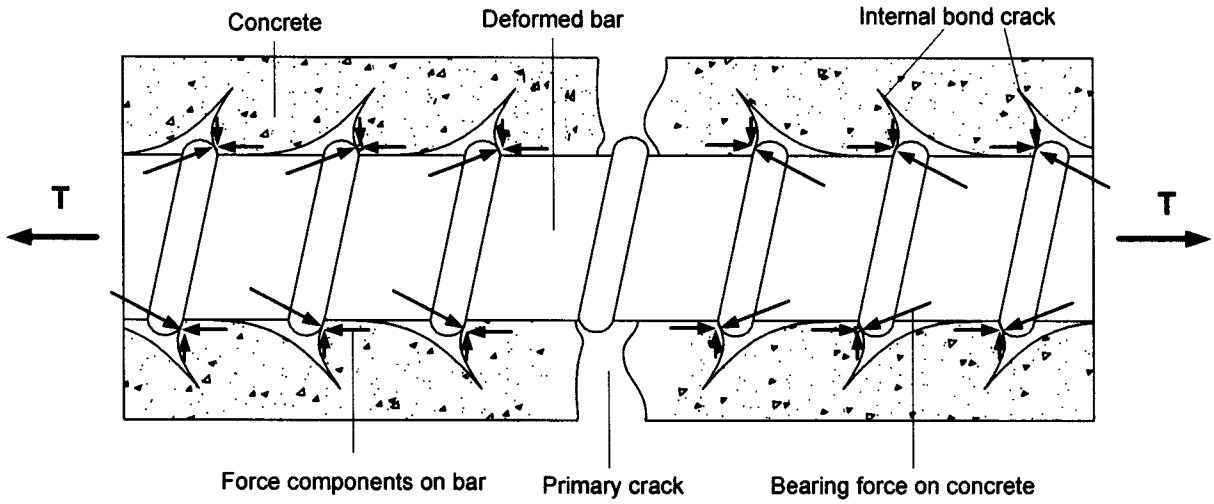

Figure 4.105 Internal cracks arise from pullout of deformed reinforcing bar (Goto, 1971)

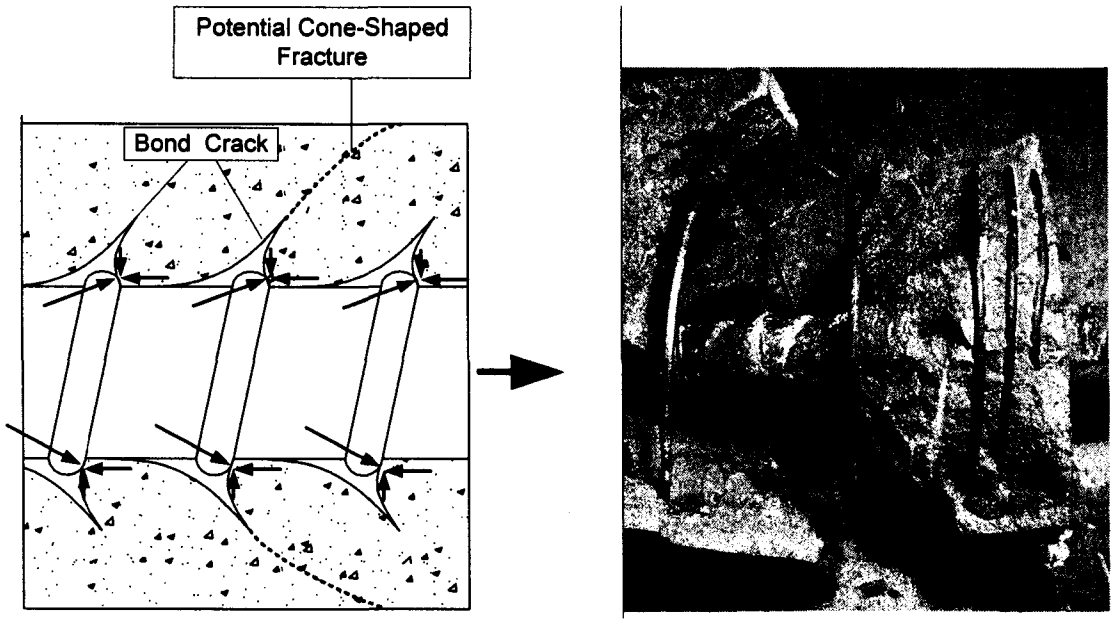

Figure 4.106 Cone-shaped fracture in transverse steel confined concrete

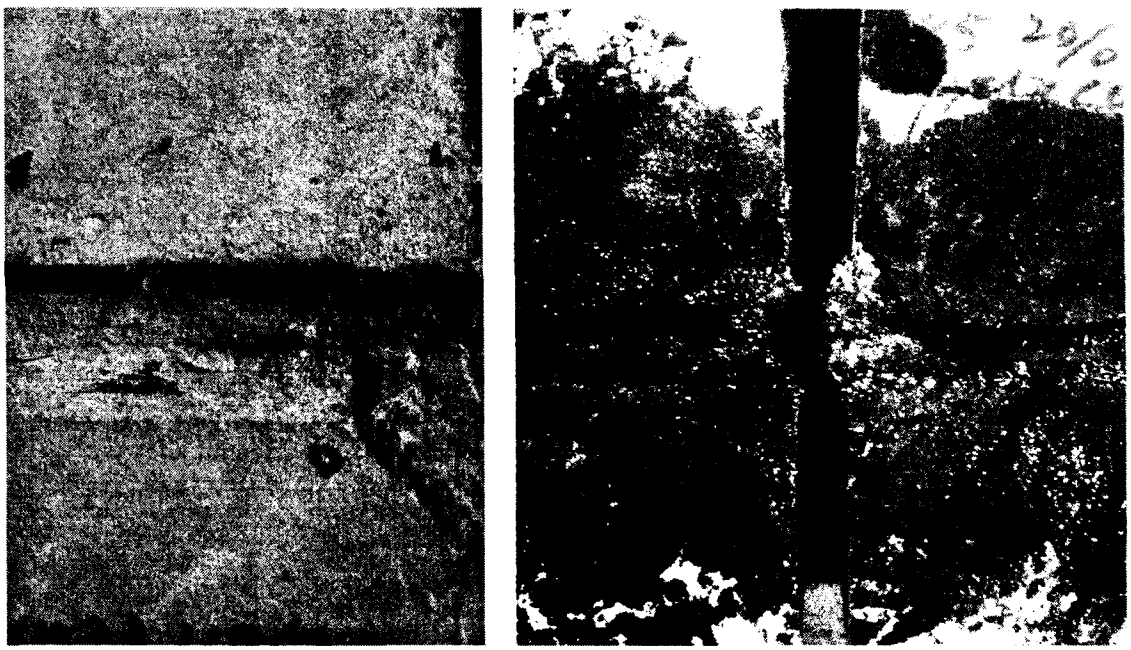

(a) (b)

Figure 4.107 Cone-shaped cracking in fiber reinforced specimens: (a) No. 8 bar, 2% Spectra, 11 ksi matrix, unidirectional force controlled cyclic loading; (b) No. 5 bar, 2% Spectra, 11 ksi matrix, unidirectional force controlled cyclic loading

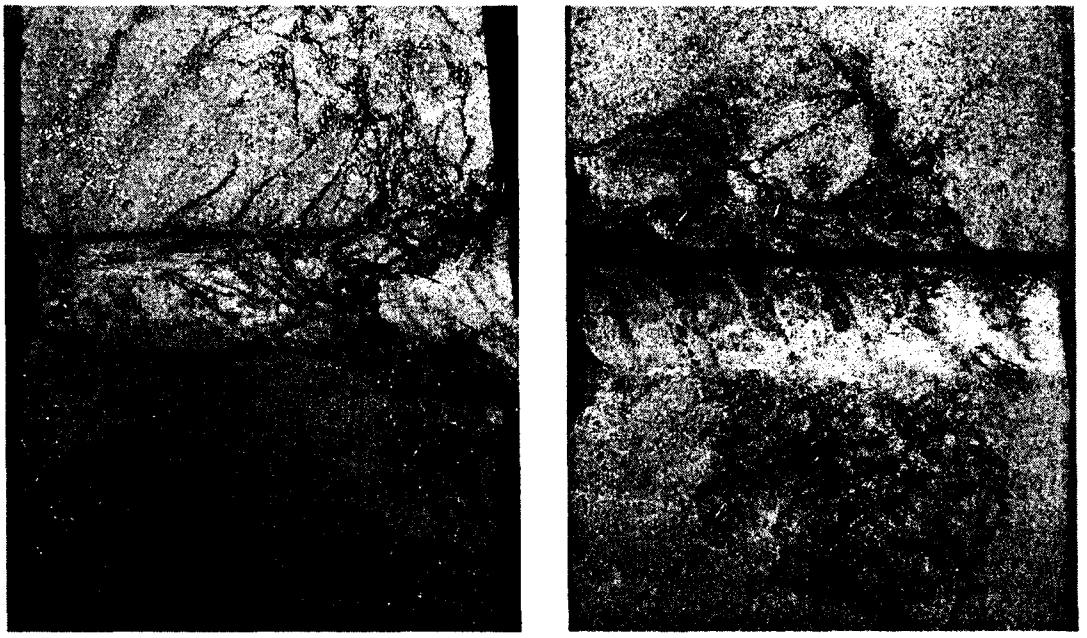

(a) (b)

(c)

Figure 4.108 Cone-shaped cracking as well as Goto cracks in fiber reinforced specimens: (a) No. 8 bar, 2% rectangular Torex, 7.6 ksi matrix, monotonic loading; (b) No. 8 bar, 2% square Torex (20 mm), 11 ksi matrix, monotonic loading; (c) No. 8 bar, 2% hooked, 11 ksi matrix, monotonic loading

Figure 4.109 Cone-shaped cracking in fiber reinforced specimens: No. 8 bar, 2% PVA K-II, 7.6 ksi matrix, monotonic loading

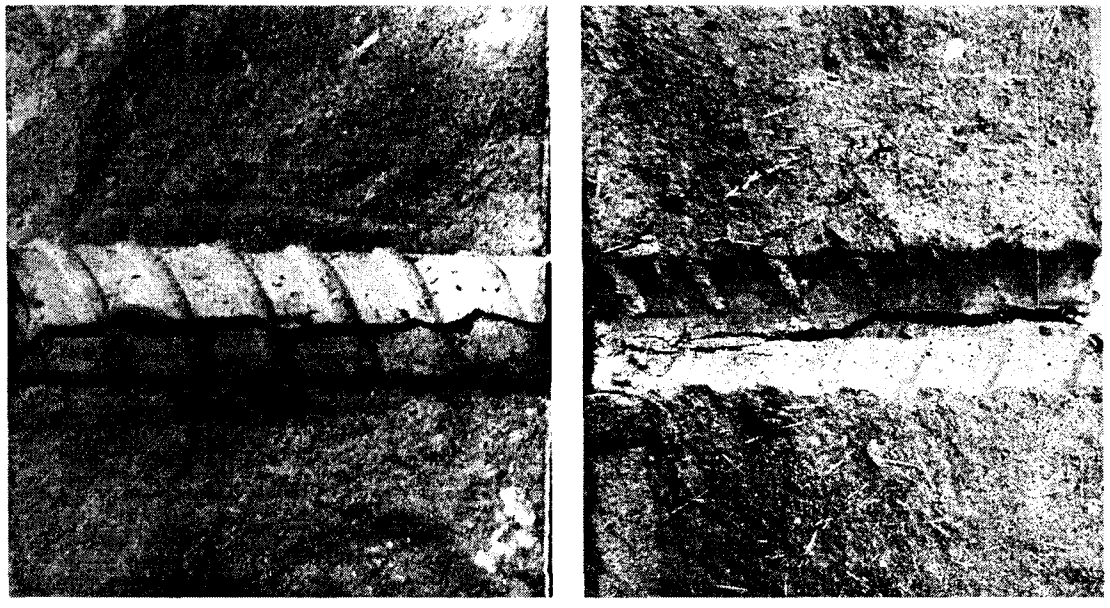

(a) (b)

Figure 4.110 Steel-to-matrix interface and the crack surface: (a) No. 8 bar, control specimen, 11 ksi matrix, monotonic loading; (b) No. 8 bar, 1% PVA 13, 11 ksi matrix, monotonic loading

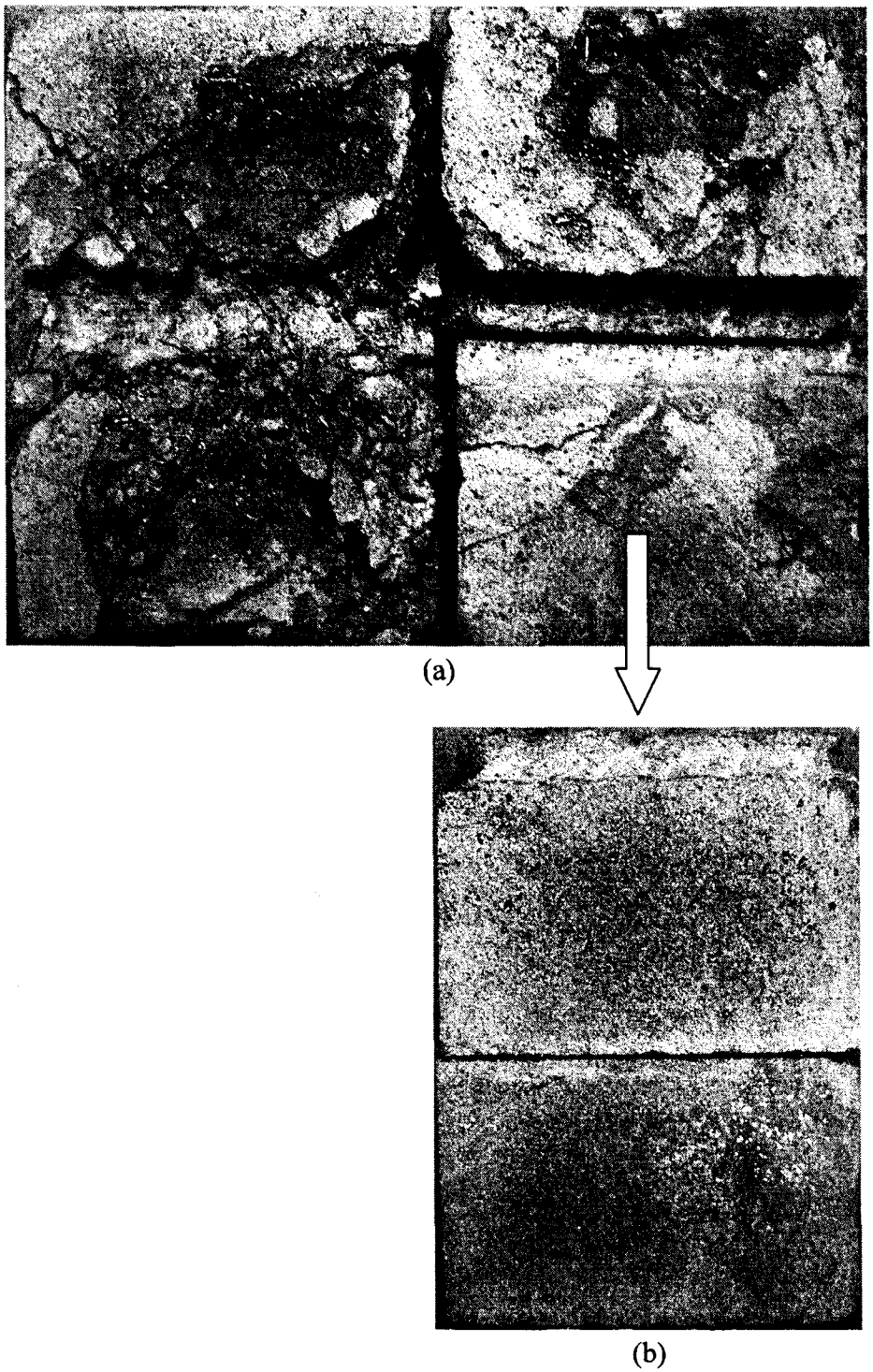

Figure 4.111 Steel-to-matrix interface and the crack surface (No. 8 bar, 2% rectangular Torex, 11 ksi matrix, fully reversed cyclic loading): (a) Multiple cracking and cracking on the crack surfaces; (b) Another cut surface which no crack went through showed no matrix cracking

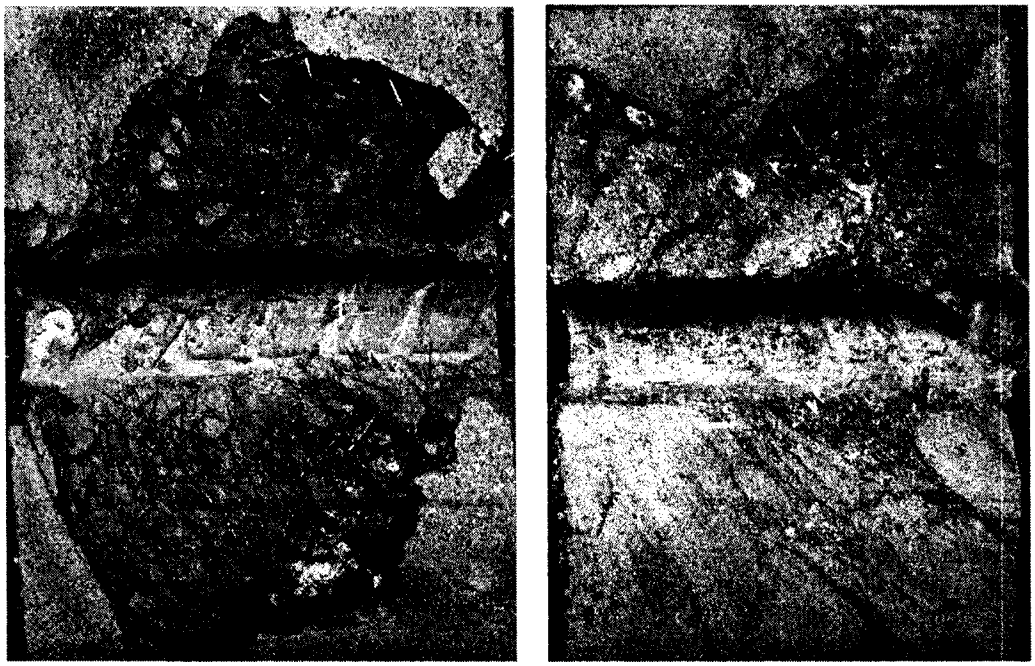

(a) (b)

(c)

Figure 4.112 Steel-to-matrix interface and the crack surface: (a) No. 8 bar, 2% square Torex (20 mm), 11 ksi matrix, monotonic loading; (b) No. 8 bar, 1% Spectra, 11 ksi matrix, unidirectional force controlled cyclic loading; (c) No. 5 bar, 1% rectangular Torex, 11 ksi matrix, fully reversed cyclic loading (constant stress for 40 cycles)

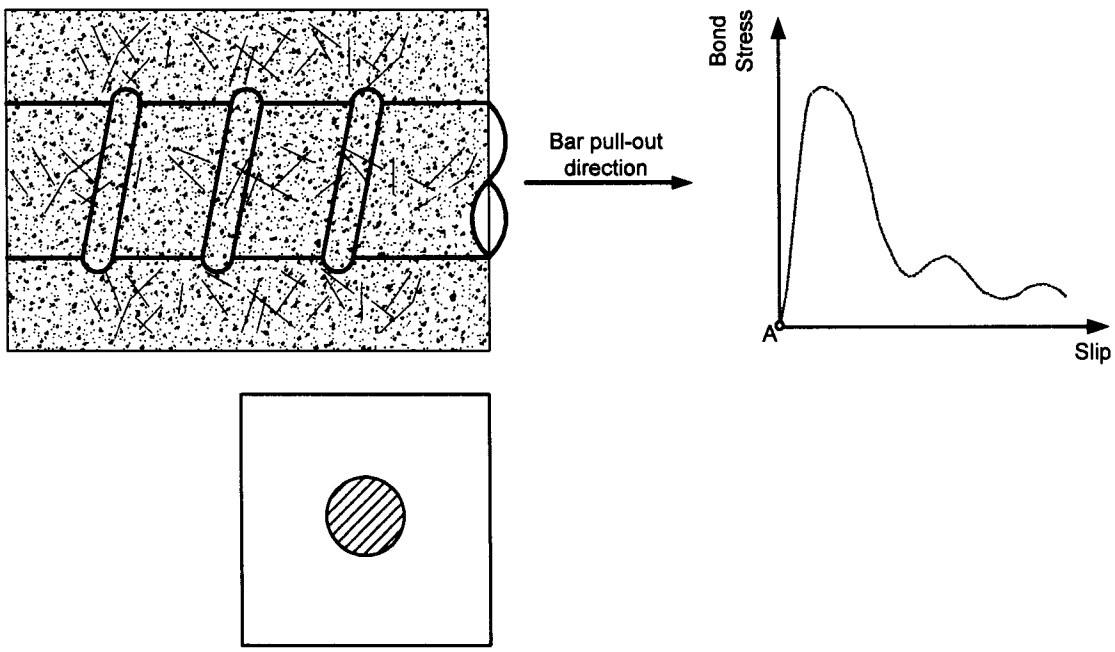

(a)

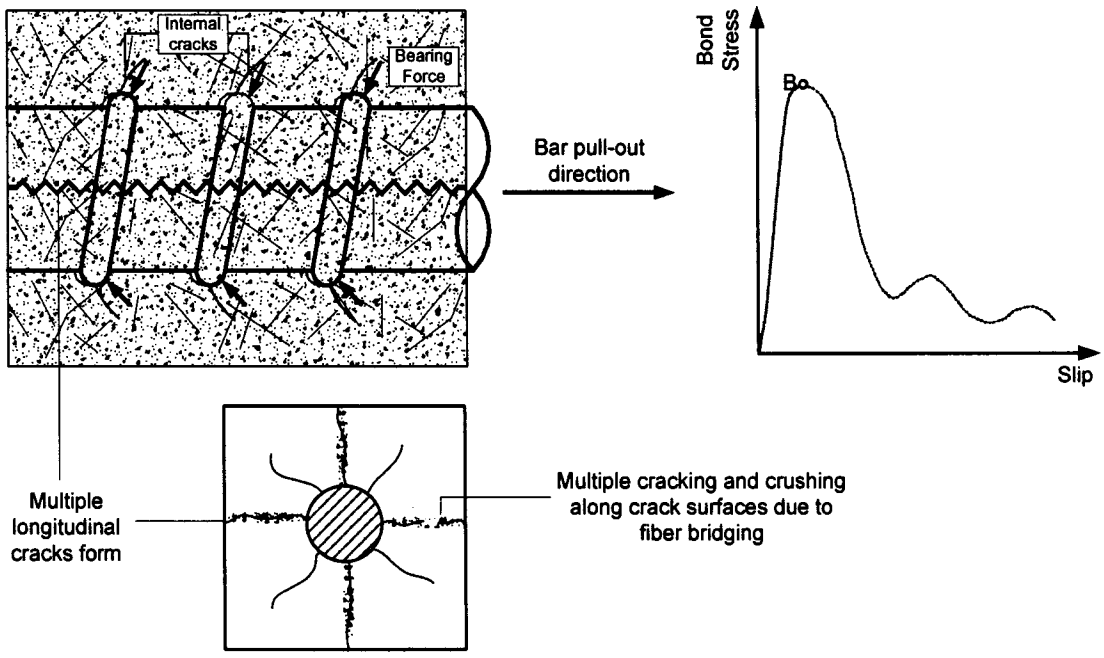

(b)

Figure 4.113 Bond mechanism of reinforcing bar embedded in HPFRC composites

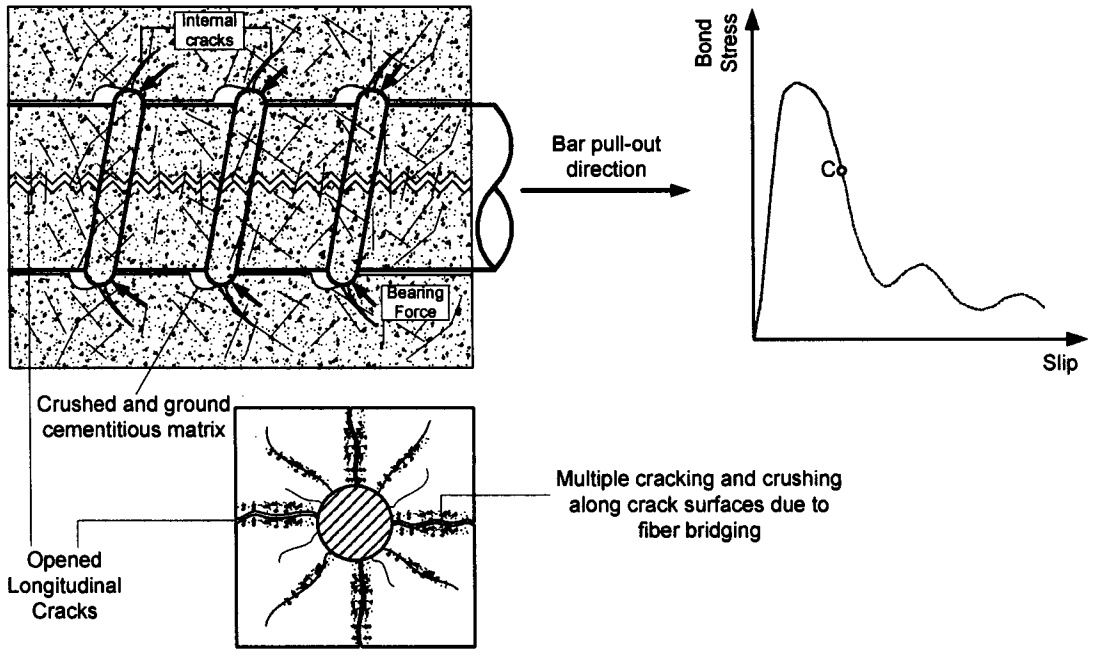

(c)

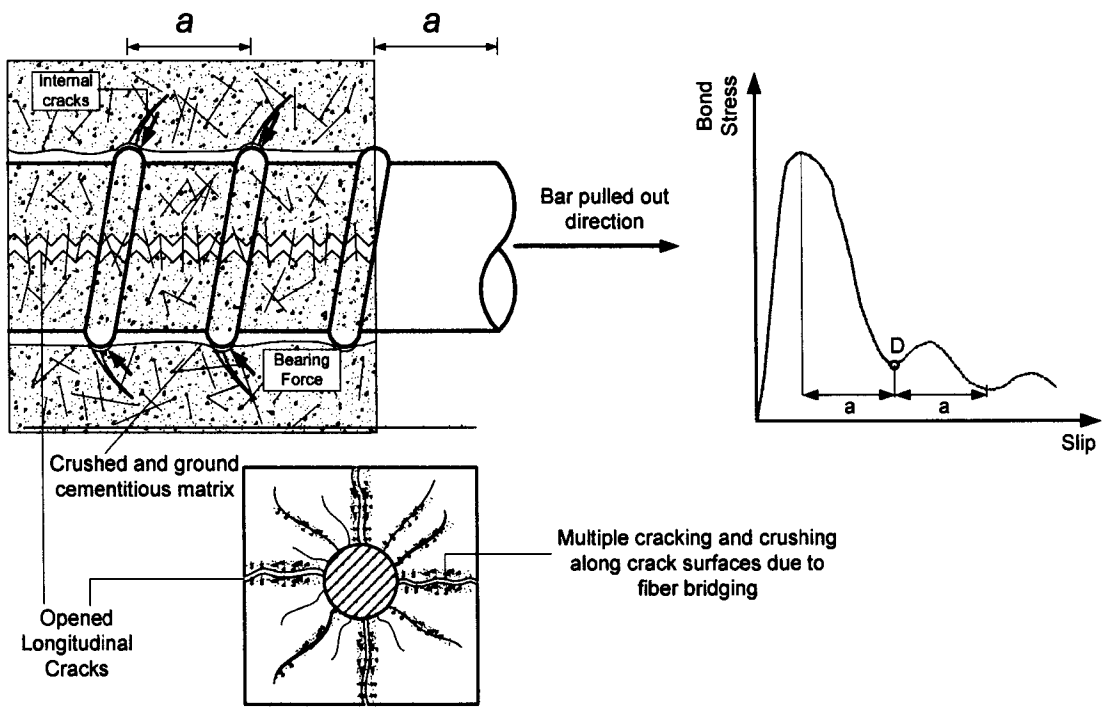

(d)

Figure 4.113 (Continued) Bond mechanism of reinforcing bar embedded in HPFRC composites

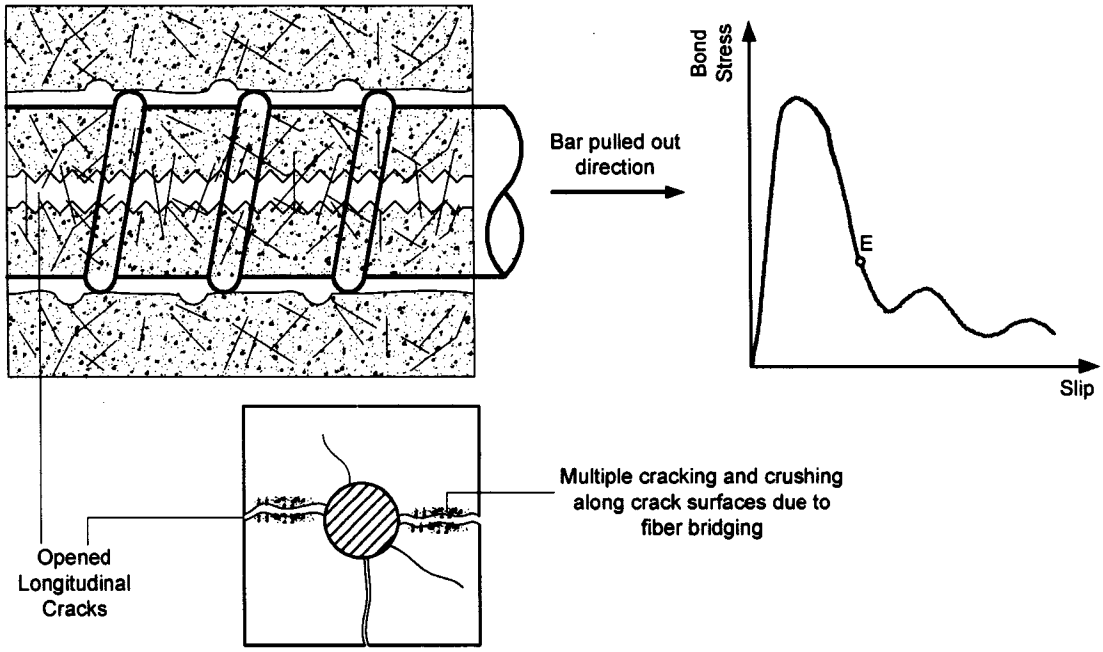

(e)

Figure 4.113 (Continued) Bond mechanism of reinforcing bar embedded in HPFRC composites

CHAPTER 5

EXPERIMENTAL RESULTS OF SPECIMENS WITH PRESTRESSING STRANDS

5.1 General

The bond properties of seven-wire strands embedded in concrete play a major role in the behavior of prestressed concrete structures. Poor bond can lead to a significant decrease in the load carrying capacity and stiffness of a structure when subjected to monotonic, cyclic or reversed cyclic loading. Bond is critical in pre-tensioned concrete structures because the entire prestressing force is transferred to the concrete through bond action. Aspects pertaining to bond behavior in pre-tensioned reinforced concrete members include transfer length and flexural bond length. In post-tension concrete structures which are partially prestressed, cracks can form under service load and the force in tendons is then transferred by bond to the concrete. Hence, the quality of bond between prestressing strands and concrete may have an appreciable effect on structural behavior (Tassios and Bonataki, 1992).

It has been mentioned in Section 2.2.1 that, along the transfer zone of a pre-tensioned element, swelling of the strand leads to the Hoyer's effect (wedge effect) which in turn gives rise to considerable radial pressure and thus larger friction forces against strand slip. In the flexural region the strand is subjected to contraction due to

tensile stress increase. This leads to reduced frictional bond resistance thus contribution to the flexural bond from mechanical interlocking augments. The mechanical interlocking of a strand comes from the helical winding shape of the seven-wires (see Figure 3.4 (d)). Unlike the protruding lugs on a reinforcing bar, this mechanical interlocking generally offers less bearing forces thus smaller bond resistance.

Russell (1992) pointed out ,however, that when splitting cracks occur and propagate along the anchorage zone, Hoyer's effect become less effective, leading to a reduction in frictional and mechanical bond resistance, and eventually, to bond failure. It is evident that cracking is the most important factor which influences the bond performance of a strand in conventional prestressed concrete elements. On the other hand, due to the superior tensile response of HPFRCCs, it is expected that the opening of splitting cracks is able to be prohibited, thereby maintaining the contact of strand and matrix. This eventually prevents the loss of frictional resistance or mechanical interlocking after cracking.

The test variables in this phase of the experimental program included fiber type, fiber volume fraction, fiber length, and loading type (see Figure 1.9). Thirteen series of specimens were tested under four types of loading, namely, 1) monotonic loading, 2) unidirectional cyclic loading (displacement control), 3) fully reversed cyclic loading (displacement control), and 4) fully reversed cyclic loading (force control). It is worth noting that, because the strands were not pre-tensioned, the Hoyer's effect had no contribution to bond resistance.

5.2 Monotonic Loading

5.2.1 Specimen with 11 ksi Matrix

Figure 5.1 (a) shows the monotonic pullout load versus slip curves of specimens with various fibers at 1% volume fraction. In addition, the pullout responses observed in strands embedded in plain concrete (control specimen) and in a concrete prism confined by steel spiral reinforcement ($d_b = 0.162$ in; $f_y = 30$ ksi; $f_u = 46$ ksi) in a 2% volumetric ratio (ρ_s) as shown in the Figure 5.2 were also tested for comparison purposes. Figure 5.1 (b) gives the comparison specifically between control specimen, spiral reinforced specimen, and Torex fiber specimens. The control specimen, without any reinforcement, exhibited a brittle behavior after splitting cracks formed at a slip of 0.3 in. It should be mentioned that some confinement may have resulted from the contact of the split specimen (see Figure 5.6 (a)) with the test setup during the late stages of loading, but was believed to have no significant influence on the bond behavior of the control specimen. It should also be noted that the lower bond modulus (bond stress/slip) shown in Figure 5.1 for the specimens with strands was due to the initial curvature of the strand outside the embedded length and the slip of the strand in the strand chuck. Thus, a better way to determine the bond modulus is to utilize the cyclic response curves, as will be described later.

At a fiber volume fraction of 1%, all fibers tested led to an improvement in pullout response compared to the control specimen, and the twisted steel fibers providing the best

performance (see Table 5.1). At a slip of 0.4 in., most of the bond strength in the fiber reinforced specimens had been developed and was maintained up to slips in the order of 1.0 in (twice the nominal strand diameter). For the fiber reinforced materials considered in this study, the peak bond strength ranged between 500 psi for the FRCC with PVA 13 fibers up to 1400 psi for the case of Torex FRCC. Composite materials with either Spectra or hooked steel fibers exhibited a peak bond strength of 1000 psi with a behavior nearly identical to that of the concrete prism confined by spirals. It is seen from the test results that, large bond stresses can be maintained in the strand up to large slips in most strand specimens, resulting in a "ductile" bond stress-slip response, which is characteristically different from the bond stress-slip response of reinforcing bars. Similar bond stress-slip response was also observed in a simple pull-out test where 0.5 in. strands were embedded in a large plain concrete block ($24\times36\times48$ in.) with 4 ksi concrete strength (Rose and Russell, 1997).

In order to compare the bond behavior exhibited by strands and deformed bars, the bond-slip behavior of No. 4 deformed bars, which had the same nominal diameter as the strands used in this study (d = 0.5 in.), was also evaluated. Figure 5.3 shows that, with a 1% volume fraction of Spectra fibers, the specimen with a reinforcing bar exhibited a higher bond stress up to a slip of 0.3 in., followed by a rapid bond strength deterioration (It is noted that the nominal yield force is 13,000 lb; therefore some measured slip value might result from inelastic deformation of the No. 4 bar). On the other hand, the specimen with a strand showed a lower bond strength, but a substantially more ductile response with no significant bond degradation up to a 1.0 in. slip. Thus, the monotonic pullout work up to 1.0 in. slip was almost equivalent for the two specimens and

approximately seven times that of the control specimen. It is noted that comparison of bond stress was made between 0.5 in. strand and No. 4 bar using two bond stress axes in the same figure because they have different perimeters even with the same diameter (i.e., for strand: $p_{ps} = \frac{4}{3}\pi d$; for deformed bar: $p_{ps} = \pi d$).

In addition to the evaluation of the pullout behavior of strands embedded in FRCC matrices with 1% fiber volume fraction, the effect of varying fiber volume fraction and fiber aspect ratio on strand pullout response was also investigated. The post-cracking strength (σ_{pc}) of fiber reinforced cement composites is directly proportional to the fiber reinforcing index, $\tau \times V_f \times \frac{l}{d_f}$ (τ : average bond strength at the fiber matrix interface; V_f : fiber volume fraction; l : fiber length; d_f : fiber diameter; Naaman and Reinhardt, 1996). Thus, to achieve the same level of performance a trade-off can be made between fiber volume fraction and fiber aspect ratio (or fiber length if the fiber is of a given diameter). For a given fiber, increasing the volume fraction should in theory lead to better performance at least up to a certain degree. Thus, increasing the fiber volume fraction should enhance the bond behavior of strands or reinforcing bars due to the increased number of fibers bridging cracks (higher confining effect). Figure 5.4 shows the effect of fiber volume fraction on bond strength using monotonic pull-out tests for FRCC specimens with Spectra and Torex fibers (square and rectangular). It is observed that, for the three fibers used, increasing the volume fraction led to an increase in bond strength. However, the difference in bond strength between the specimens with 1% and 2% volume fraction of fibers was generally small and within 10% of the maximum value. It is also

noted that specimens with square Torex fibers exhibited the highest bond resistance. The reason for the high performance of Torex fiber specimens is elaborated in Section 5.4.1.

The effect of fiber length was investigated only for the FRCC materials containing square Torex fibers, in which 20 mm and 30 mm long fibers were used. However, as shown in Figure 5.5, no significant differences in behavior were obtained when a change in fiber length was introduced.

Crack patterns of specimens with 1% various fibers and 2% spirals are shown in Figure 5.6. It is seen, except for the control specimen, all specimens maintained their integrity due to the addition of fibers or reinforcement. Some spalling occurred in the spiral specimen at the location where the strand was entering the prism. Figure 5.7 gives the crack pattern of No. 4 bar specimen with 1% Spectra fiber. In general, compared to reinforcing bar specimens shown in Figure 5.7 or Chapter 4, strand specimens with fibers showed very narrow cracks and multiple cracking was less than the reinforcing bar specimens. Figure 5.8 shows the crack patterns of specimens with 2% fiber contents for Spectra and rectangular Torex fibers.

The maximum splitting crack width in specimens with strands was generally less than 0.01 in. (0.25 mm) at peak pullout load. On the other hand, the maximum crack width in specimens with reinforcing bars depended on the bar diameter and lug height, and for the case of specimens with No. 4 bars, was usually larger than 0.04 in. (1 mm) at peak load. As noted in Section 5.1, preventing cracks from opening is essential for bond performance of strands, to be able to maintain the friction and mechanical interlocking between the helical wires of a strand and the surrounding matrix.

5.2.2 Comparison of Test Results with Flexural Bond Stress in Design Codes

5.2.2.1 Flexural Bond Stress

As pointed out by Russell (1992), the current codes for both the transfer length and flexural bond length are based on an assumed value for bond stresses based on transfer length testing and flexural bond testing. As noted in Section 2.2.2, both ACI (2005) and AASHTO (2002) recommend an empirical equation for development length l_d used in pretensioned application, as follows:

$$l_d = l_t + l_f = \left(\frac{f_{pe}}{3}\right)d + \left(f_{ps} - f_{pe}\right)d \qquad [5.1]$$

where f_{pe} is the effective stress in prestressing strand after losses; d is the nominal diameter of prestressing strand; f_{ps} is the nominal strength of prestressing strand; l_t is the prestress transfer length; l_f is the flexural bond length. For a Grade 270 strand, f_{ps}=270 ksi, and assuming the effective stress f_{pe} is 150 ksi, then:

$$l_d = l_t + l_f = \left(\frac{150}{3}\right)d + (270-150)d = 50d + 120d = 170d \qquad [5.2]$$

It is seen that the transfer length is about 50*d* and the flexural bond length is 120*d*. This indicates a lower bond strength along the flexural bond length than along the transfer length. This can be translated into a lower flexural bond stress than the transfer bond stress. A lower flexural bond stress was used because flexural cracking occurs under

loading and will disturb bonding between strands and concrete, thus reducing bond strength (Russell, 1992).

Recently, the Federal Highway Administration (FHWA, 1998) proposed a new equation for development length l_d based on FHWA full-size beam data and available new research results:

$$l_d = l_t + l_f = \left(\frac{4 f_{pt} d}{f_c'} - 5\right) + \left(\frac{6.4\left(f_{ps} - f_{pe}\right) d}{f_c'} + 15\right) \qquad [5.3]$$

where f_{pt} is the stress in prestressing strand prior to transfer of prestress. Note this new equation accounts for the influence of concrete strength. It has been recognized that a pullout test correlates more closely with flexural bond situation than transfer bond situation, whereby a "pull-in" occurs due to release of strand rather than "pull-out" (Uijl, 1998; Burnett and Marefat, 1992). Therefore, only the second terms on the right side of Equations [5.1] and [5.3], *i.e.* the flexural bond length, are used to calculate the code-specified bond stresses and compared with that obtained from the tests in this study.

It has been shown by Russell (1992) that, the average flexural bond stress based on ACI (AASHTO) development equations can be calculated by solving equilibrium on strand:

$$l_f \cdot u_f \cdot p_{ps} = \left(f_{ps} - f_{pe}\right) \cdot A_{ps}$$

$$\Rightarrow u_f = \frac{\left(f_{ps} - f_{pe}\right) \cdot A_{ps}}{l_f \cdot p_{ps}} \qquad [5.4]$$

where u_f is the average flexural bond stress needed if strand reaches ultimate strength; $p_{ps} = \frac{4}{3}\pi d$ is the perimeter of the seven-wire strand; $\left(f_{ps} - f_{pe}\right)$ is the additional stress in strands due to external loading; $A_{ps} = \frac{7}{36}\pi d^2 = 0.153 \text{ in}^2$ is the cross-sectional area of 0.5 inch strand.

The calculated bond values are shown in Table 5.1 for both the ACI (AASHTO) and FHWA bond stress, together with the average bond stress obtained from test results. As suggested by Table 5.1, FRCC materials can significantly increase the bond resistance, especially for FRC composites exhibited strain-hardening tensile behavior. For instance, specimens with Torex fibers, depending on fiber volume fraction, exhibited 8 to 10 times the bond strength expected by ACI (AASHTO) Code and 3.5 to 4 times that expected by FHWA. This can be directly attributable to the strain-hardening tensile capacity of the Torex fiber composites as well as the high stiffness of Torex fiber used, which led to multiple fine cracks and thus maintaining friction and mechanical interlocking between strand and surrounding matrix. It is also noted that, since the maximum stress in the strand is merely 80 ksi in this study, reduction in bond stress could occur if strands are loaded to ultimate due to the lateral contraction of strand and disturbance on bonding from cracks. However, this contraction would only occur in the vicinity of cracks, which usually are very small in HPFRC composites, thereby minimizing the potential disturbance.

5.2.2.2 Note on the Transfer Bond Stress

Transfer length for a prestressing strand is generally inversely proportional to the average transfer bond strength. Although the transfer bond strength may not be directly evaluated by the pullout type test, it is believed that HPFRCC material is able to effectively reduce the required transfer length specified by the current codes. As pointed out by Barnes et al. (2003), after release of the tendon, the compressive stresses coming from the radial expansion of tendon will lead to inelastic deformation of surrounding concrete along the transfer length. This inelastic deformation can result in radial cracking and softening of the surrounding concrete. Hence, the radial compressive stresses and resulting frictional stresses (Hoyer's effect), thus the bond resistance, are significantly dependent on the tensile strength and the stiffness of the surrounding concrete. Validated by experimental results, Barnes et al. proposed an expression for transfer length, which is inversely proportional to the square root of the concrete compressive strength at tendon release (based on the normal practice that concrete tensile capacity is approximately proportional to the square root of the concrete compressive strength).

Intuitively, the transverse reinforcement would shorten the transfer length by confining the concrete subjected to bursting stresses upon force transfer of the pretensioned strands. However, as demonstrated by experimental results from prestressed girders (Russell, 1992), conventional transverse reinforcement will not provide confining effect until concrete is subjected to lager lateral strains. This maybe also because that, should splitting cracks occur, the crack width is large, thereby reducing the confinement effect. As a consequence, no difference was observed in transfer length with or without

transverse reinforcement.

On the other hand, as shown in Figure 3.3 (b), the tensile strength as well as the strain capacity in an HPFRCC is considerably enhanced. This infers, upon the expansion of released strands, the surrounding HPFRCC matrix is able to sustain high tensile stress until very larger strain, along with fine multiple cracks, thereby more effectively transferring forces into the concrete. However, a larger scale beam test is still suggested to verify this inference.

5.2.3 Influence of Matrix Compressive on Bond Behavior

As indicated by Equations [5.1] and [5.3], while ACI (AASHTO) does not recognize the influence of concrete compressive strength on bond strength (or development length), FHWA suggests the bond strength of strands is approximately proportional to concrete compressive strength, f_c'. Note this is different from the case of reinforcing bar, where bond strength is generally assumed proportional to $f_c'^{1/2}$ (ACI, 2005) or $f_c'^{1/4}$ (ACI Committee 408, 2003).

In order to investigate the influence of matrix compressive strength on the bond strength of strands embedded in HPFRC composites, tests were conducted by using 2% rectangular Torex fiber specimens with three different matrix compressive strengths: 5.9 ksi, 7.6 ksi, and 11 ksi. Figure 5.9 and Table 5.2 provide clear evidence that compressive strength of the matrix has an appreciable effect on bond strength. The relative bond

strengths (bond strength of 11 ksi specimen/ bond strength of 5.9 ksi specimen, etc.) are plotted in Figure 5.10 (a), along with the normalized values according to ACI(AASHTO) and FHWA. For example, the flexural bond strength according to FHWA is obtained by using Equation [5.4]:

$$u_f = \frac{(f_{ps} - f_{pe}) \cdot A_{ps}}{p_{ps} \cdot \left(\frac{6.4(f_{ps} - f_{pe})d}{f_c'} + 15 \right)} = \frac{17500}{\frac{384}{f_c'} + 15} \text{ (psi)} \qquad [5.5]$$

It should be noted that the actual bond stress values from tests are much higher than the FHWA and ACI/AASHTO predictions (see Table 5.2 and Figure 5.10 (b)), Figure 5.10 was plotted to show that the rate of the bond stress change with the increase of matrix compressive strength from the test data compared with the rate of FHWA expression . As can be seen in Figure 5.10 (a), FHWA equation has good agreement with the test data in terms of the ascending slope, while ACI (AASHTO) equation apparently underestimates the bond strength when higher strength matrix is used (It should be added here that, FHWA suggests to use f_c' = 10 ksi when value of f_c' greater than 10 ksi due to limited test data. However, f_c' = 11 ksi was still used for the plot in Figure 5.10). This result can be expected since the frictional resistance contributes significantly to the bond strength due to confinement effect of fibers and, generally, abrasion resistance capacity of concrete improved as the concrete compressive strength increases (Mindess, Young, and Darwin, 2003).

5.3 Unidirectional Displacement-Controlled Cyclic Loading

This type of loading was used to investigate the bond strength as well as stiffness retention capacities under half cyclic loading up to large slip. The monotonic bond load-slip curve was taken as the upper bound to evaluate the bond strength degradation. The loading protocol used for tests is shown in Figure 3.15 (c). The testing was performed with incremental displacement equal to 0.05 inch until the residual displacement (after unloading) reached 1.0 inch (e.g. fiber reinforced specimen), or until total failure occurred (e.g. control specimen).

Experimental results from unidirectional tests are presented in Figures 5.11 thru 5.23, along with the responses obtained from monotonic tests. Bond strength of the control specimen dropped immediately after peak bond stress was reached, with a residual strength of 20% the peak bond stress up to 0.8 inch slip (see Figure 5.11). No significant bond stiffness degradation was observed in the control specimen.

For the strand specimen with a 2% volumetric ratio of spiral reinforcement and no fibers (Figure 5.12), the peak bond strength reached only 75% of the monotonic peak bond strength. However, the bond strength was maintained at this level throughout all 20 cycles, and no significant bond stiffness degradation was observed.

Figures 5.13 and 5.14 show that, the strands embedded in FRCC materials with Spectra fibers developed bond strengths close to those obtained from monotonic tests (95% and 100% of the monotonic peak bond strengths for 1% and 2% fiber specimens,

respectively), maintaining most of the strength throughout the 20 loading cycles and up to slips of 1.0 in.

Specimens with 30 mm long, i.e. aspect ratio of 100, Torex fibers (either 1% or 2% fiber volume) were able to attain the peak monotonic bond strengths for both rectangular and square fiber sections, as shown in Figures 5.15 to 5.18. Bond strength dropped 20% after 11 cycles in specimen with 1% 30 mm long square Torex fiber (Figure 5.17). Torex fiber with smaller aspect ratio (67) showed somewhat inferior performance in terms of bond strength retention ability. As shown in Figures 5.19 and 5.20, specimens were able to reach 90% to 95% the monotonic peak bond strengths but only maintained 10 cycles. The bond strengths gradually degraded to approximately 70% of the monotonic peak bond strengths when reached slips of 1.0 in. Nevertheless, Torex fiber specimens exhibited highest bond stresses among all tested specimens. No significant bond stiffness degradation was observed in all the specimens.

As can be seen in Figures 5.21 and 5.22, the strands embedded in FRCC materials with 1.0% volume fraction of either hooked or PVA 13 fibers developed bond strengths close to those obtained from monotonic tests (90% and 100% of the monotonic peak bond strengths for hooked and PVA 13 fiber specimens, respectively), maintaining most of the strength throughout the 20 loading cycles and up to slips of 1.0 in.

In general, FRCC specimens with seven-wire strand developed bond strengths close to the peak monotonic values and were able to maintain high percentage of these strengths up to 1.0 in. slip when subjected to unidirectional displacement controlled

cyclic loading. Bond stiffness was also retained throughout all cycles.

For comparison purposes, the behavior obtained from the cyclic load test of a No. 4 deformed bar embedded in an FRCC material with 1% volume fraction of Spectra fibers is shown in Figure 5.23. As can be seen, the bond strength in the No. 4 bar specimen reached a peak value corresponding to 80% of the monotonic peak bond strength at a slip of nearly half the slip at peak stress obtained during the monotonic load test. Once the peak strength was attained, most of the bond strength was lost within five cycles, as opposed to the excellent bond strength retention capacity up to large slips observed in the strand specimens.

As mentioned earlier, the initial curvature in the strands and the slip that occurred in the strand chuck did not allow the determination of the bond modulus during the monotonic load tests. However, the determination of the bond modulus during both loading and unloading was possible in the cyclic load tests after the application of the first loading cycle. From Figures 5.13 thru 5.22, average values of bond modulus of 15,000 and 27,000 psi/in. (bond stress/slip) were determined for the loading and unloading branches, respectively.

Crack patterns of selected strand specimens after testing were presented in Figure 5.24. It is seen that only a few cracks, generally smaller than 0.01 in. (0.25 mm), were visible and marked. Specimen with No. 4 bar is shown in Figure 5.25, where multiple cracking was observed and the maximum crack width was about 0.08 in. (2 mm).

5.4 Fully Reversed Displacement-Controlled Cyclic Loading

5.4.1 Specimen with 11 ksi Matrix

Bond resistance usually deteriorates rapidly after peak bond stress is attained in reinforcing bars of concrete members when subjected to fully reversed cyclic loading, even when substantial confinement reinforcement is present (Viawathanatepa, Popov, and Bertero, 1979), as evidenced in Figure 4.83. This is due to concrete crushing and formation of splitting cracks originating from the ribs of the reinforcing bars caused by high bearing stresses. In this investigation, the behavior of strands embedded in various FRCCs under reversed cyclic loading was evaluated and compared with that of strands in plain and confined concrete, as well as deformed bars embedded in FRCCs. As shown in Figure 3.15 (d), testing was performed with incremental displacement equal to 0.05 inch for three full cycles until the residual displacement (after unloading) reached 0.8 inch (e.g. fiber reinforced specimen), or until total failure occurred (e.g. control specimen). The loading method is shown in Figure 3.14, position 2.

Strands embedded in an FRCC material or in regular concrete confined by spiral reinforcement exhibited distinct hysteresis bond stress-slip responses, as illustrated in Figures. 5.26 to 5.38. As can be seen, for specimens with fibers or spiral reinforcement, relatively full hysteresis loops were obtained up to slips of 0.8 in., indicating good ductility and energy dissipation capacity after large slips occurred. On the other hand, the bond strength developed in the strand embedded in plain concrete degraded quickly at slips less than 0.2 in, (Figure 5.26).

Unlike the unidirectional cyclic loading, specimens subjected to fully reversed cyclic loading can hardly attain the peak monotonic bond strength. For instance, while maximum bond stress attained was 95% of the monotonic bond strength for 1% Spectra specimen under unidirectional cyclic loading, only 78% was reached when subjected to fully reversed cyclic loading, as shown in Figure 5.27 and Table 5.3. In general, the specimens with Torex fibers (Figures 5.30 thru 5.35) exhibited superior performance compared to all other fibers in terms of bond strength retention and energy-dissipation capacities. In particular, specimens with square Torex fiber having an aspect ratio of 100 (i.e. 30 mm long) gave the best results. From Figures 5.30 thru 5.35, it is noted that increasing the fiber volume fraction of Torex fibers from 1% to 2% considerably enhanced bond performance under fully reversed cyclic loading, whereas no significant improvement was observed in specimens with Spectra fibers (Figures 5.28 and 5.29). The best bond strength retention capacity was observed in 2% Torex fiber specimens, which were able to attain 85% ~95% the peak monotonic bond strengths (see Table 5.3).

Specimen with 2% volumetric spiral reinforcement showed relatively low bond stress under reversed cyclic loading, which was only better than the control specimen. This can be attributed to the severe spalling and cracking occurred under displacement reversals, as indicated in Figure 5.39 (b). PVA 13 fiber specimen, although exhibited a peak bond stress higher than that of the spiral specimen, showed a very narrow hysteresis loops which presented a low energy-dissipation capacity. Specimen with steel hooked fiber showed similar performance with Spectra fiber specimens in terms of peak bond stresses.

The No. 4 deformed bar embedded in an FRCC with 1% volume fraction of Spectra fibers also showed severe bond deterioration and "pinching" after a slip of 0.2 in. was reached as shown in Figure 5.38. Compared with strand specimens, reinforcing bar specimen exhibited severe bond strength deterioration when subjected to incremental displacement reversals. As can be seen, the bond strength was completely lost at 0.4 in. slip in the No. 4 bar specimen (1% Spectra fiber) while 50% bond strength was maintained in the strand specimen (1% Spectra fiber, see Figure 5.28). In the strand specimen with 2% square Torex fiber (30 mm), no bond strength deterioration occurred at 0.4 in. slip and only 35% the bond strength was lost at 0.8 in. slip, as demonstrated by Figure 5.33. Figures 5.39 and 5.40 present the cracking patterns of selected specimens. Note that only the cracks visible to the naked eye were marked.

Since all specimens were tested under the same loading history, a direct comparison of dissipated energy can be made. The cumulative energy dissipated through all cycles under fully reversed displacement controlled cyclic loading is plotted in Figure 5.41. This cumulative energy, besides being expressed in absolute terms, is also presented with respect to the energy dissipated by the control specimen (no fibers). The cumulative energy was calculated by summing up the areas enclosed by all the hysteresis loops in a given test. It is seen that although the specimen with a reinforcing bar showed larger peak bond strength (Figure 5.38), the dissipated energy represented only 13% of the energy dissipated by the specimens with a strand (both with 1% volume fraction of Spectra fibers). Overall, the specimens with 2% volume fraction of square Torex fibers (30 mm) showed the best performance; they dissipated approximately 140 times the energy of the control specimen (no fiber reinforcement), 2.7 times that of 2% spiral reinforced

specimen, and 20 times that of the reinforcing bar specimen with 1% volume fraction of Spectra fibers. The specimen with 2% volumetric ratio of steel spiral reinforcement dissipated only an amount of energy comparable to the specimens with 1% volume fraction of Spectra fibers due to spalling of the cover of the cementitious matrix under reversed cyclic loading. In contrast, as shown in Figure 5.39, the specimens with fibers maintained their integrity throughout all applied cycles due to the fiber bridging effect, which prevented cracks from opening widely.

The superior behavior observed in strands embedded in FRCCs with Torex fibers, compared to those with Spectra fibers or with spiral reinforcement, can be explained as follows. In concrete members confined by transverse reinforcement such as a spiral or rectangular hoops, a minimum lateral expansion is required (leading to cracking) in the cementitious matrix before this reinforcement is effective in providing confinement. A similar situation occurs in FRCC materials with fibers of relatively low elastic modulus (compared to steel) such as Spectra; their high tensile strength will not be utilized until some appreciable strain level or crack width is achieved in the cementitious matrix. These initial cracks may reduce the bond contribution from friction and mechanical interlocking, especially under reversed cyclic loading. On the other hand, the crack bridging resistance of steel fibers, such as hooked or Torex fibers, can be activated much earlier than that of Spectra fibers because of their higher elastic modulus and bond modulus, which makes FRCCs with steel fibers more effective for controlling crack growth and for energy-dissipation at early loading stages. Further, due to the superior tensile characteristics of FRCCs with Torex fibers, especially for square Torex fiber used in this study, in terms of high tensile strength and ductility (see Figure 3.3 (b)), Torex fiber

specimens exhibited better performance than steel hooked fiber specimens.

5.4.2 Comparison of Specimens with Various Matrix Compressive Strengths

The influence of matrix compressive strengths was investigated by using 2% rectangular Torex fiber specimens with 11 ksi, 7.6 ksi, and 5.9 ksi matrices. The test results can be seen in Figures 5.31, 5.42, and 5.43, as well as in Table 5.4. It is noticed that the peak bond stress was improved by increasing the matrix compressive strength. The cumulative energy of 11 ksi and 7.6 ksi specimens are comparable. Also noticeable in Figures 5.42 and 5.43, an apparent increase in bond strength was present at large slips. This may be due to the "lack of fit" mechanism (Stocker and Sozen, 1971) occurred at large slip, which has been used to describe one possible contribution of the radial compressive stresses, in addition to the Hoyer's effect. This theory states that, upon movement of the strand relative to the surrounding matrix, a wedging action would result due to the small changes in the strand cross section, thereby inducing high bond stress. Photos of tested specimens are shown in Figure 5.44. More evident damage at the location strand entering the prism was observed in the lower strength specimens than in the high strength specimens (see Figure 5.39 (h)).

5.5 Low-Cycle Fatigue Tests

Low-cycle high amplitude fatigue tests were conducted to investigate the bond performance under repeated large slip demands or large bond stresses. Only specimens

with square and rectangular Torex fibers were tested in this phase of the investigation due to their superior bond performance in prior tests. In a first type of test, cycles to a target slip demand of 0.4 in. were applied to specimens with 1.0% square Torex fibers (length = 20 mm long). As can be observed from Figure 5.45, after 130 cycles, the bond strength dropped only 30% in comparison to the initial strength, with an incremental residual slip of about 0.075 in.

The second type of test was a force-controlled fully reversed low-cycle fatigue test carried out on specimens with square (20 mm long) and rectangular (30 mm long) Torex fibers. In the first tests, reversed loading cycles to a target bond stress level equal to approximately twice the peak bond strength exhibited by the control specimen (without fibers) under reversed cyclic loading (400 psi – see Figure 5.26) were applied. As can be seen in Figure 5.46, specimen with 1% square Torex fiber was able to sustain 40 full cycles without bond strength and stiffness degradation. A second specimen with 2% square Torex fiber was also tested with the 800 psi target bond stress. As shown in Figures 5.47 (a) and 5.47 (b), the test specimen was able to retain a bond strength of about 800 psi for 37 full cycles. Bond strength started to degrade at the 38th cycle, accompanied by large residual slips (Figure 5.47 (c)). Given the large number of cycles performed to a target bond stress of 800 psi without significant strength degradation, another series of "identical" specimens was tested using a target bond stress of 960 psi. As shown in Figure 5.48, the bond strength was maintained for six full cycles, followed by a gradual strength decay accompanied by large residual slips during subsequent loading cycles. However, the bond stress-slip loops were quite full, indicating good energy dissipation capacity. The bond stress maintained 83% of the peak bond stress (960

psi) at a slip of 0.8 in. A summary of the tested square Torex fiber specimens is given in Table 5.5.

Specimen with 1% rectangular fiber was tested using a slightly higher target bond stress, 900 psi, than the 1% square Torex fiber specimen. As can be observed in Figure 5.49, no bond degradation and significant residual slip occurred before the 24th full cycle. Residual slip increased starting from the 25th cycle as well as gradual strength degradation. Test was stopped at the 38 cycle as the residual slip reached beyond 0.8 in., with a bond strength drop about 33%. Another specimen with 2% rectangular Torex fiber was then tested using the same target bond stress. It is seen from Figure 5.50, this specimen was able to sustain 61 full cycles without evident strength drop and residual slip. The residual slip was increasing gradually but much slower than the 1% rectangular Torex fiber specimen. It reached 0.8 in. residual slip at the 100th cycle, along with a 10% drop in the bond strength (decreased to 800 psi). This specimen dissipated considerable energy through its full hysteresis loops as indicated by Table 5.5. A specimen with 2% rectangular Torex but lower matrix compressive strength (7.6 ksi) was tested under 800 psi target bond stress. As can be seen in Figure 5.51, no bond strength deterioration was observed after 100 full cycles.

In general, specimens with either 1% or 2% Torex fibers exhibited high toughness under larger repeated stress and slip reversals. Contrary to reinforcing bar specimens, such the one shown in Figure 4.100, the bond strength was able to maintain very high percentage of the target bond stresses even at very large slips.

Specimens after testing are shown in Figure 5.52. Except for the locations where strand entering the prism subjected to damage, the composite maintained their integrity for all test specimens with few and very fine cracks.

5.6 Bond Mechanism for Strands Embedded in HPFRCCs

Several observations from the test specimens are examined and elaborated as following before developing the theory of bond mechanism for strand embedded in HPFRC composites.

It was noticed that, as presented in Figure 5.53, a strand has distinct behavior from a reinforcing bar when it was pulled out from the prism. Figure 5.53 (a) shows that, the stand rotated during the pull-out process as indicated by the rotated center lines. This rotating can be explained by the orientation of individual helical wires, in which the applied force is resolved into a longitudinal component and a tangential component. In a real structural element, as schematically shown in Figure 5.54, assuming strand on one side of the crack has reached its peak bond strength and slip occurs while strand on the other side of the crack still has enough anchorage length therefore no slip occurs, then the longitudinal component will pull the strand out and the tangential component tends to rotate the strand. In an unrestrained strand (or whenever the restraint has broken upon loading), instead of pulling out directly from the matrix, the strand tends to move helically along the path formed by the surrounding tunnel of concrete, like a screw coming out from its screw hole. Note that in Figure 5.53, the upper chuck provided twist

constraint so that the rotation angles of the upper and lower portions of the strand were different.

In the control specimen, the failure usually occurs without much damage along the strand-to-matrix interface, as shown in Figure 5.55 (a). On the contrary, as indicated in Figures 5.55 (b) and 5.55 (c), the strand-to-matrix interface was subjected to substantial crushing and shearing in an HPFRCC specimen, signifying effective clamping coming from fiber bridging. Furthermore, as shown in Figure 5.56, the presence of fiber led to multiple cracking and crushing along cracking surface, thereby enhancing the toughness of the entire composites.

Based on above observations and testing results, the following bond mechanism for strands embedded in HPFRC composites is proposed and illustrated in Figure 5.57:

(a) The addition of fibers, especially Torex fiber, is able to significantly increase the bond strength before noticeable slip occurs. The fiber bridging prevents the matrix from large lateral deformation; that is, it limits the widening of cracks. This leads to effective bond resistance from friction and mechanical interlocking between strand and matrix. On the other hand, conventional transverse reinforcement will not provide confining effect until the matrix is subjected to certain lateral strains (cracking) thus reduces the friction and mechanical interlocking, which in turn decreases the bond resistance.

(b) When the applied load keeps increasing until the maximum bond capacity is reached,

the radial compression exerted on the surrounding matrix eventually leads to crack development, and slip occurs. Because only very narrow cracks form, particularly in the case of strain-hardening composites (HPFRCCs), the matrix and strand remain intimate during pullout, providing ample friction and mechanical interlocking. Thus, large bond stresses can be maintained in the strand up to large slips, resulting in a "ductile" bond stress-slip response, which is characteristically different from that of reinforcing bars, for which a much wider splitting crack is needed for bar to be pulled out, which eventually leads to degradation of bond strength after crack development. It is also noticed that, the number of cracks is much less and the crack width is much finer in a strand composite than in a reinforcing bar composite.

In conclusion, strands embedded in HPFRCCs are able to develop very high bond strength. After significant slip occurs, no catastrophic failure would happen due to the retention of bond capacity.

5.7 Potential Applications of the Research Results

Possible applications which could take advantage of the superior bond behavior of strands embedded in HPFRC composites as revealed by this research could be:

1. Replacement of the Conventional Confinement Reinforcement

HPFRCCs are able to be utilized to reduce the conventional confining reinforcement

or anchorage zone of prestressed concrete beam congestion; i.e., reduce risk of splitting cracks.

2. Shortening the development length in prestressed elements

Russell has indicated that (1992), for a conventional prestressed concrete structure, a lower flexural bond stress may result because flexural cracking occurs under loading and will disturb bonding between strands and concrete, thus reducing bond strength. Also, in the case where splitting cracks propagate along the anchorage zone, the Hoyer's effect becomes less effective, leading to a reduction in frictional and mechanical bond resistance, and eventually, to bond failure along the transfer length. However, it has been shown from this research that, HPFRCC materials exhibit excellent behavior when subjected to tension, with a tensile strain-hardening stress-strain response and multiple cracks. This led to very high bond resistance upon loading. While flexural cracking results in disturbance of bond in conventional prestressed concrete element, an HPFRC composite generally shows multiple fine cracks (see Figure 5.58) and bond would not be altered since no softening occurs after cracking. As a consequence, a much shorter flexural bond length is expected in HPFRCCs. By the same reasoning, as well as the note in Section 5.2.2.2, it is anticipated that a shorter transfer bond length can also be used in HPFRCCs.

3. Facilitating the prestressed girder construction using debonding strands

Since conventional draping method to relieve over stresses in the end region is more

difficult and dangerous, debonding strands near the supports emerges to be a safer and viable alternative, which is able to simplify girder construction and be more economical compared to draped or harped strands (Shahawy, Issa, and Batchelor, 1992). However, some issues may occur in a girder with debonded strands (Russell, 1992):

a) In a beam with fully bonded strands, only one region of flexural cracking would be expected. However, in beams with debonded strands, concrete in the debond/transfer zone (there is a second transfer zone in beams with debonded strands) could also suffer flexural cracking because the beam's resistance to flexural cracking is reduced. Cracking in the transfer zone of the debonded strand will cause the debonded strands to slip and bond failure is probable.

b) Debonding prestressing strands reduces a beam's resistance to web shear cracking in the debond/transfer zone because the effective prestress force has been reduced. Therefore, beams with debonded strands are more susceptible to web shear cracking and consequently more susceptible to bond failure.

By using HPFRCC materials, however, the flexural cracking problem is able to be significantly reduced. Also, as indicated by Parra-Montesinos (2003, 2005), HPFRCC materials can considerably contribute to the shear strength due to the excellent tensile behavior, as well as delay the degradation in strength and stiffness of a reinforced concrete member under shear forces. These merits would eventually facilitate the girder construction using both debonded strands and HPFRCC materials. In fact, with HPFRCC materials, the tensile resistance is considerably increased thus there may be no need for

debonding (but camber issue needs to be considered) and only straight tendon is placed.

4. Applications where strands can be used as non-prestressed reinforcement in conventional reinforced concrete

The monotonic, unidirectional cyclic, and fully reversed cyclic loading test results conducted in this study suggest that, potentially, prestressing strands could be very beneficially used, non-prestressed, in reinforced concrete structures with HPFRCC matrices. This is particularly valuable for seismic resistance structures. For example, as depicted in Figure 5.59, untensioned strands could be used to replace reinforcing bars in a seismic beam-column joint, along with the HPFRCC matrix placed in joint region only. Assuming the limiting bond stress is 900 psi and the yield strength of Grade 270 strand (d = 0.5 in.) is 243 ksi, then the required column depth needed to anchor the strand is 19.5 in. The current ACI Committee 352 Recommendations (ACI-ASCE, 2002) specify an anchorage length of at least 20 reinforcing bar diameters for 60 ksi reinforcement passing through the joint. Note this specified anchorage length does not prevent reinforcing bars from slippage, which in turn leads to reduction in stiffness and energy dissipation capacity of the connection region due to the bond deterioration. A strand would carry a similar load for a similar embedded length, but would have a significantly better response under load reversals. By using untensioned strands as well as HPFRCC material in the critical regions (beam-column joint and locations of plastic hinge), a non-degraded bond strength could be expected. Alternately, the ductile bond characteristics of strands embedded in HPFRC composites may be used as an additional energy-dissipation mechanism, in conjunction with RC plastic hinges.

The advantage of using prestressing strand is that, with the same yield strength, a Grade 270 strand ($A_s \times f_{py} = 0.153 \text{ in.}^2 \times 230 \text{ ksi}$) is equivalent to a Grade 60 No. 7 reinforcing bar ($A_s \times f_{py} = 0.6 \text{ in.}^2 \times 60 \text{ ksi}$). However, a strand has a diameter (0.5 in.) equal to 57% of the diameter of a No. 7 bar (0.875 in.), which requires much smaller space when placed in an structural element thus eventually facilitates the construction. Also, assuming both reinforcements have the same unit weight and length, the weight of a strand is only approximately 25% of a No. 7 bar, which is able to save material and easier to deliver. Further, a strand is more flexible than a reinforcing bar because it is made with relatively small diameter wires (Naaman, 2004), therefore strands can be stored and handled easily. Strands usually show superior properties than reinforcing bars due to better quality control (Naaman, 2004).

The above potential applications, although feasible based on the test results obtained from this research, still need to be validated by large scale experiments.

5.8 Conclusions

1. Preventing cracks from opening is essential for bond performance of strands, which is able to maintain the friction and mechanical interlocking between the helical wires of a strand and the surrounding matrix.

2. The confinement effect provided by FRC composites after cracking increased friction

and mechanical interlocking between prestressing strands and the concrete matrix, leading to enhanced bond resistance compared to the case of plain concrete matrices. Unstressed (without Hoyer's effect) strands embedded in FRCCs maintained high bond stresses up to slips as large as twice the strand diameter, resulting in a nearly elastic-perfectly plastic (ductile) bond stress-slip response, which is characteristically different from the bond stress-slip response of reinforcing bars.

3. Results from monotonic pullout tests suggest that the bond strength of unstressed strands embedded in FRC composites can be up to three times the bond strength of strands in plain concrete matrices. The largest bond improvement was achieved using Torex fibers. Increasing fiber volume fraction from 1% to 2% enhanced the monotonic bond strength for strands but only by about 10%. Increasing the length of Torex fibers was not seen to affect significantly the bond strength in strands, because the maximum crack width was relatively small.

4. For the fiber reinforced materials considered in this study, the peak bond strength ranged between 500 psi for the FRCC with PVA 13 fibers and 1400 psi for the case of Torex FRCC. Composite materials with either Spectra or hooked steel fibers exhibited a peak bond strength of approximately 1000 psi with a behavior nearly identical to that of the concrete prism confined by spirals.

5. Except for the control specimen, all specimens maintained their integrity due to the addition of fibers or transverse reinforcement. Some spalling occurred in the spirally reinforced specimen at the location where the strand was entering the prism. In

general, compared to reinforcing bar specimens, strand specimens with fibers showed very narrow cracks, and multiple cracking was less than in the reinforcing bar specimens. The maximum splitting crack width in specimens with strands was generally less than 0.01 in. (0.25 mm) at peak pullout load. On the other hand, the maximum crack width in specimens with reinforcing bars depended on the bar diameter and lug height, and for the case of specimens with No. 4 bars (same nominal diameter of strand used in this study), was usually larger than 0.04 in. (1 mm) at peak load.

6. The average flexural bond strength, based on ACI (AASHTO) and FHWA for conventional concrete was calculated and compared with the test data. It was found that FRCC materials can significantly increase the bond resistance, especially those that exhibited strain-hardening tensile behavior. For instance, specimens with Torex fibers, depending on fiber volume fraction, exhibited 8 to 10 times the bond strength assumed in the ACI (AASHTO) Code and 3.5 to 4 times that assumed by FHWA.

7. Unlike the bond strength expected in ACI (AASHTO), the test results showed that the compressive strength of the matrix has an appreciable effect on bond strength. This is in agreement with the FHWA expression in which the bond strength of strands is proportional to concrete compressive strength, f_c'. This result can be expected since the frictional resistance contributes significantly to the bond strength due to confinement effect of fibers and, generally, abrasion resistance capacity of concrete improved as the concrete compressive strength increased. It is also found that the peak bond stress under fully reversed cyclic loading was improved by increasing the

matrix compressive strength.

8. Under unidirectional displacement-controlled cyclic loading, strands embedded in FRCCs maintained, at a given slip, about 90% to 100% of the bond strength achieved under monotonic loading, and the bond strength was maintained at this level throughout all 20 cycles. This was true for slips up to twice the diameter of the strands. Specimens with 30 mm long (aspect ratio of 100) Torex fibers (either 1% or 2% fiber volume) with rectangular or square cross sections were able to attain the peak monotonic bond strengths. Torex fiber with smaller aspect ratio (67) showed somewhat inferior performance in terms of bond strength retention ability. These specimens were able to reach 90% to 95% of the monotonic peak bond strength, but it was only maintained for 10 cycles. In general, Torex fiber specimens exhibited highest bond stresses among all tested specimens. For the strand specimen with a 2% volumetric ratio of spiral reinforcement and no fibers, the peak bond strength was only 75% of the monotonic peak bond strength. In comparison, the bond strength of a reinforcing bar embedded in an FRCC material deteriorated rapidly under unidirectional cyclic loading, decreasing to 50% of the peak strength after only five displacement cycles, corresponding to at 0.25 in. (6 mm) slip.

9. For strands embedded in FRCCs, average values of bond modulus of 15,000 and 27,000 psi/in. (bond stress/slip) were determined for the loading and unloading branches, respectively.

10. Under fully reversed cyclic loading, strands embedded in FRCCs showed a ductile

bond stress versus slip behavior with relatively full hysteresis loops, indicating large energy dissipation capacity. Everything else being the same, such behavior was quite distinct from that of reinforcing bars, where a rapid bond deterioration occurred with cycling. Further, the behavior of strands embedded in FRCC matrices was generally superior to that observed in specimens with spiral confinement reinforcement. In general, the specimens with square Torex fibers gave the best results in terms of strength retention and energy-dissipation capacity. Specimens with 2.0% volume fraction of Torex fibers dissipated approximately 140 times the energy dissipated by the control specimen without fibers and 2.5 times the energy dissipated by specimens with 2.0% volumetric ratio of spiral reinforcement.

11. Unlike the unidirectional cyclic loading, specimens subjected to fully reversed cyclic loading seldom attained the peak monotonic bond strength. In general, specimens with Torex fibers exhibited superior performance in comparison to all other fiber reinforced specimens in terms of bond strength retention and energy-dissipation capacity. In particular, specimens with square Torex fiber having an aspect ratio of 100 (i.e. 30 mm long) gave the best results. The best bond strength retention capacity was observed in the 2% Torex fiber specimens, which were able to attain 85% ~95% of the peak monotonic bond strength. Specimen with 2% volumetric spiral reinforcement showed relatively low bond strength, being only slightly greater than that of the control specimen. This can be attributed to the severe spalling and cracking of both the control and spirally reinforced specimens, which occurred under displacement reversals. Although the PVA 13 fiber specimen exhibited a peak bond stress higher than that of the spirally reinforced specimen, it had very narrow

hysteresis loops, which led to a low energy-dissipation capacity. The specimens with steel hooked fiber showed a performance similar to that of the Spectra fiber specimens in terms of peak bond stresses. Compared to specimens with strands, reinforcing bar specimens exhibited severe bond strength deterioration when subjected to incremental displacement reversals.

12. An increase in fiber volume fraction from 1% to 2% led to a significant improvement in the bond behavior of strands subjected to reversed cyclic loading (especially for Torex fiber), while little influence was observed in the specimens subjected to monotonic loading.

13. Results from low-cycle high amplitude fatigue tests indicate that strands embedded in FRCC materials (especially for Torex fibers) can sustain a large number of cycles (in excess of 100) without strength/stiffness degradation or evident residual slip at bond stress levels as large as twice the bond strength of strands embedded in a plain concrete matrix. During subsequent loading cycles, when the strength dropped, it decreased gradually accompanied by large residual slips. As a consequence, the bond stress-slip loops were still quite full, indicating good energy dissipation capacity.

14. HPFRCCs can effectively limit crack width, thus preventing the bond from degrading. Torex fiber specimens led to the best bond performance due to high stiffness of the fibers and their high bond with the matrix, which led to higher composite cracking strength and post-cracking stiffness before damage localization. Spirally reinforced specimens, although exhibited ductile bond stress-slip response, showed less bond

strength than that of HPFRCC specimens. This is due to the fact that the confinement effect of spiral reinforcement cannot be activated until certain inelastic deformation in the matrix (cracking) occurs, which leads to loss of friction and mechanical interlocking between strand and matrix.

Table 5.1 Comparison of the average bond stresses (0.5 in. strand, matrix strength = 11 ksi)

	Average Bond Stress, (psi) *	a	b
Control (0% fiber)	440	3.0	1.3
1% PVA 13 (12 mm)	590	4.0	1.7
1% Steel Hooked (30 mm)	970	6.6	2.8
2% Spiral Reinforcement	1000	6.9	2.9
1% Spectra(38 mm)	1000	6.9	2.9
2% Spectra (38 mm)	1150	7.9	3.3
1% Rectangular Torex (30 mm)	1210	8.3	3.5
2% Rectangular Torex (30 mm)	1300	8.9	3.7
1% Square Torex (30 mm)	1280	8.8	3.7
2% Square Torex (30 mm)	1500	10.3	4.3
1% Square Torex (20 mm)	1400	9.6	4.0
2% Square Torex (20 mm)	1420	9.7	4.1
ACI & AASHTO	146	-	-
FHWA	351	-	-

* 1 psi = 0.006895 MPa

a. Average bond stress/ACI(AASHTO) bond stress (Equation [5.4])

b. Average bond stress/FHWA bond stress (Equation [5.4])

Table 5.2 Comparison of the average bond stresses with various matrix compressive strengths (0.5 in. strand; 2% rectangular Torex fiber, 30 mm)

Matrix Compressive Strength	Average Bond Stress, (psi)	ACI & AASHTO value (psi)	FHWA value (psi)
11 ksi	1300	146	351
7.6 ksi	1000	146	267
5.9 ksi	760	146	219

Table 5.3 Summary of bond performance for specimens under fully reversed displacement controlled cyclic loading (0.5 in. strand, matrix strength = 11 ksi)

Fiber or Reinforcement	a	b	c
Control (0% fiber)	415 (94%)	5	1100
1% PVA 13 (12 mm)	650 (110%)	7	43700
1% Steel Hooked (30 mm)	745 (77%)	7	85400
2% Spiral Reinforcement	600 (60%)	7	57300
1% Spectra(38 mm)	780 (78%)	10	58700
2% Spectra (38 mm)	785 (68%)	7	65700
1% Rectangular Torex (30 mm)	1070 (88%)	10	85200
2% Rectangular Torex (30 mm)	1220 (94%)	7	124400
1% Square Torex (30 mm)	1040 (81%)	7	127300
2% Square Torex (30 mm)	1275 (85%)	14	159400
1% Square Torex (20 mm)	950 (68%)	7	110900
2% Square Torex (20 mm)	1295 (92%)	10	151000
No. 4 bar with 1% Spectra (38 mm)	2035 (80%)	7	7600

a. Average (in two directions) maximum attained bond stress (and percentage of peak monotonic bond strength), psi

b. Cycle at which bond strength started to drop

c. Cumulative energy (lb-in)

Table 5.4 Summary of bond performance for specimens with various matrix strengths under fully reversed displacement controlled cyclic loading (0.5 in. strand; 2% rectangular Torex fiber, 30 mm)

Matrix Compressive Strength	a	b	c
11 ksi	1220 (94%)	7	124400
7.6 ksi	1140 (114%)	10	131500
5.9 ksi	780 (102%)	7	83200

a. Average (in two directions) maximum attained bond stress (and percentage of peak monotonic bond strength), psi

b. Cycle at which bond strength started to drop

c. Cumulative energy (lb-in)

Table 5.5 Summary of bond performance for strand specimens under low-cycle fatigue loading (fully reversed force controlled cyclic loading)

Fiber	a	b	c	d	e
1% Square Torex (20 mm)	800	40	-	39700	11
2% Square Torex (20 mm)	800	43	38	66000	11
2% Square Torex (20 mm)	960	9	7	32700	11
1% Rectangular Torex (30 mm)	900	38	25	99400	11
2% Rectangular Torex (30 mm)	900	100	62	269300	11
2% Rectangular Torex (30 mm)	800	100	-	41400	7.6

a. Target bond stress (psi)

b. Total cycles performed

c. Cycle at which bond strength started to drop

d. Cumulative energy (lb-in)

e. Matrix compressive strength (ksi)

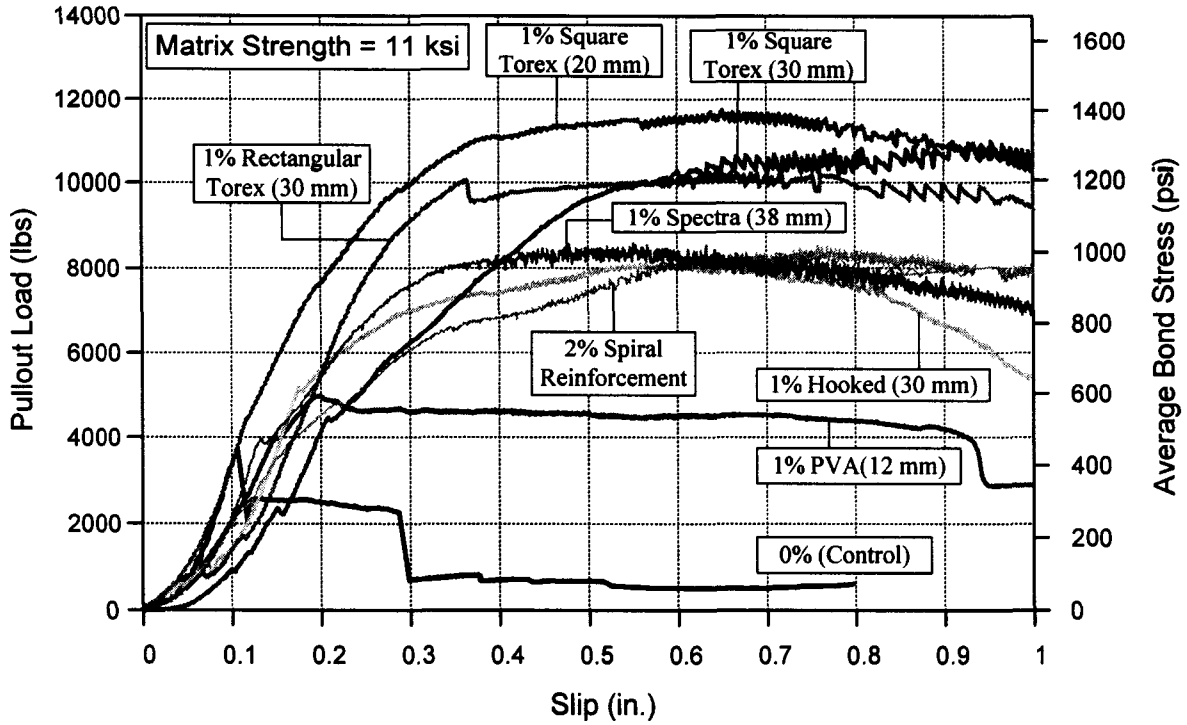

Figure 5.1 (a) Comparison of monotonic pull-out responses of strand specimens (1% fiber content, 11 ksi matrix)

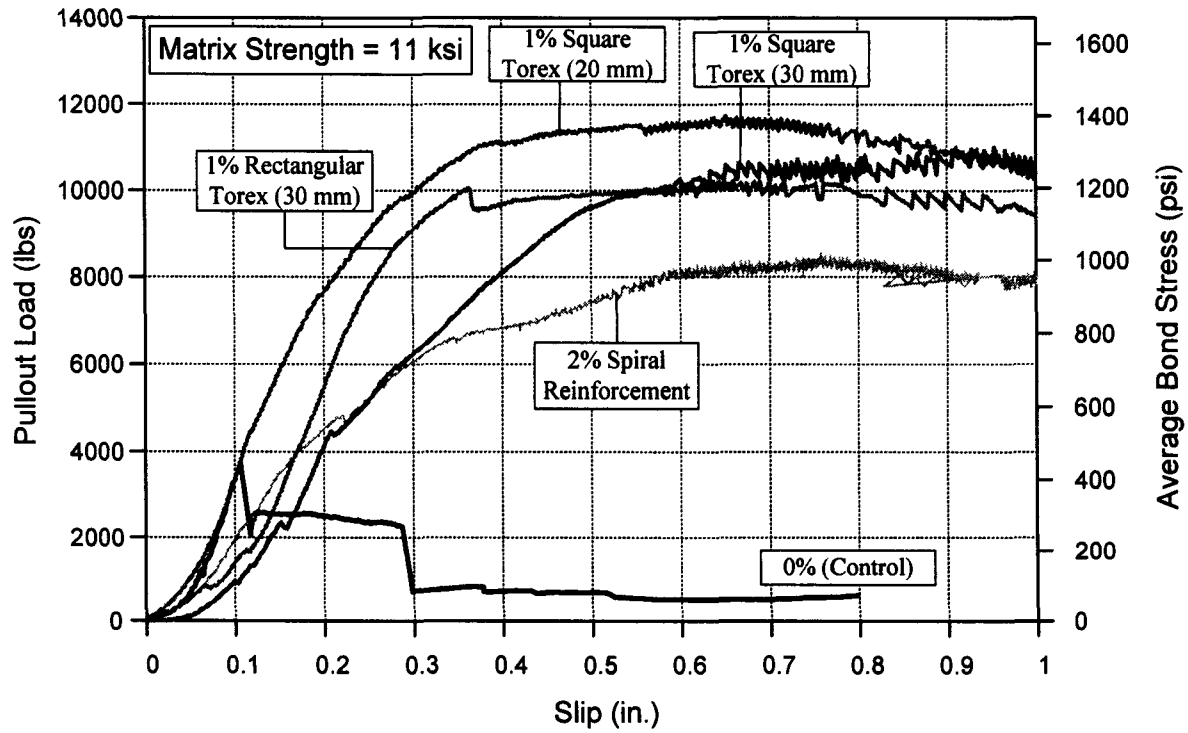

Figure 5.1 (b) Comparison of monotonic pull-out responses of strand specimens with 1% Torex fibers, 2% spiral reinforcement, and 0% reinforcement

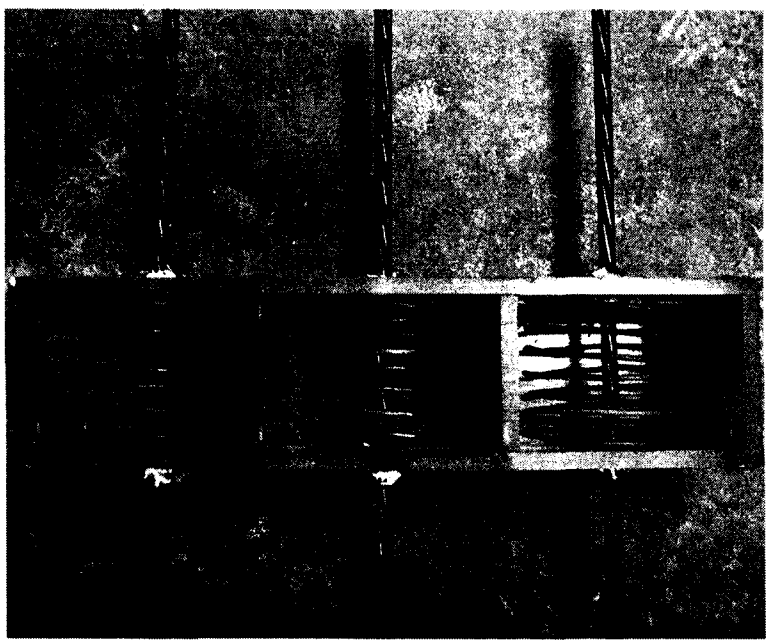

Figure 5.2 Strand specimens with 2% steel volume fraction of spiral reinforcement

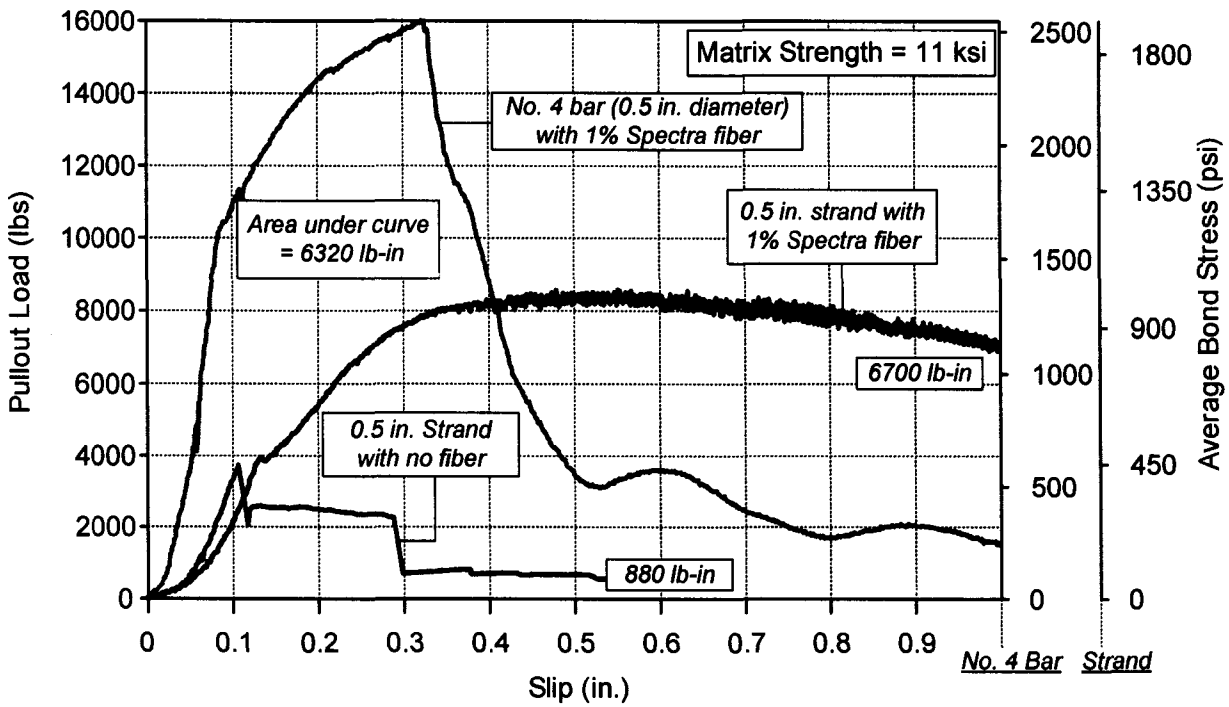

Figure 5.3 Comparison of bond behavior between reinforcing bar and strand with same diameter

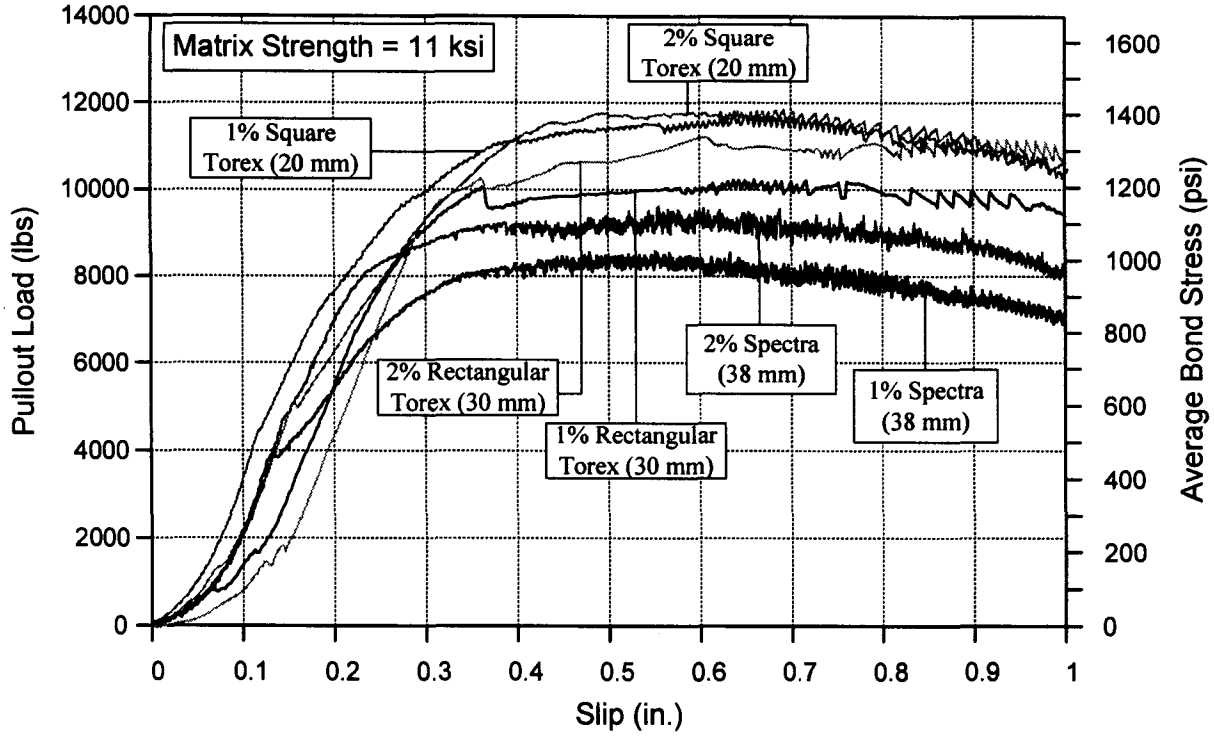

Figure 5.4 Comparison of bond behavior during monotonic pull-out loading with 1% and 2% fiber volume fractions

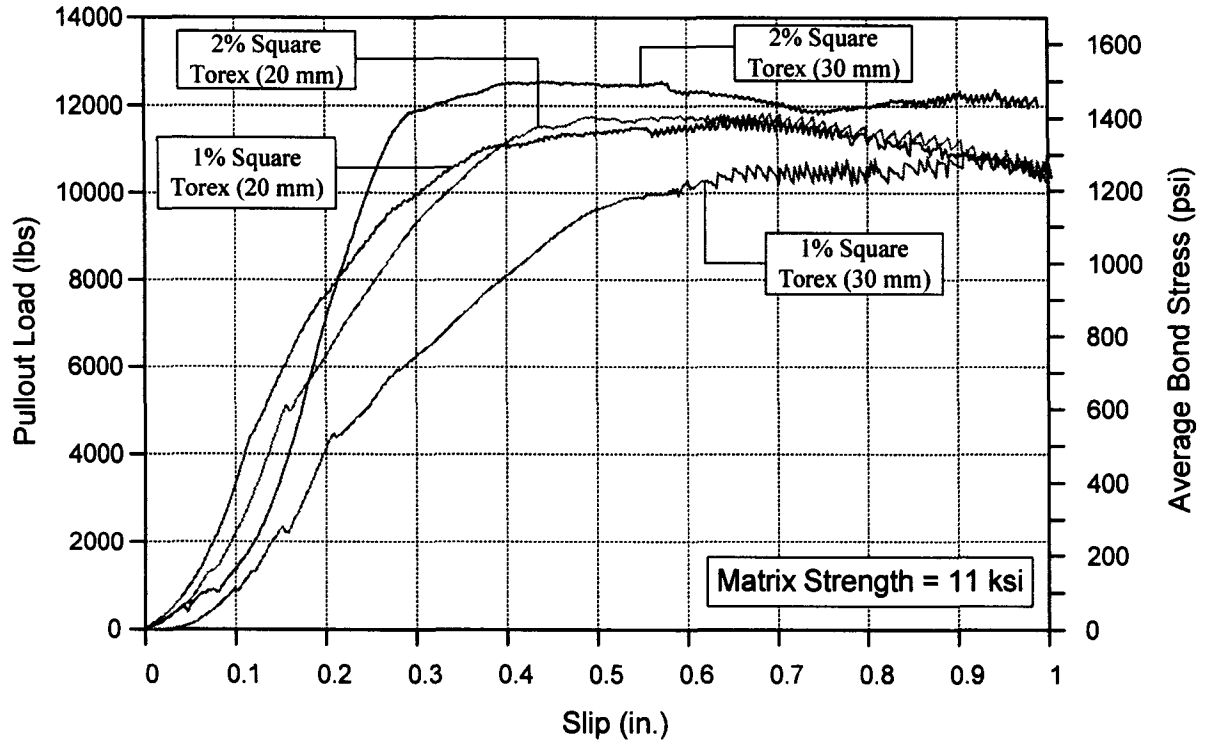

Figure 5.5 Effect of Torex fiber length and fiber volume fraction on bond behavior

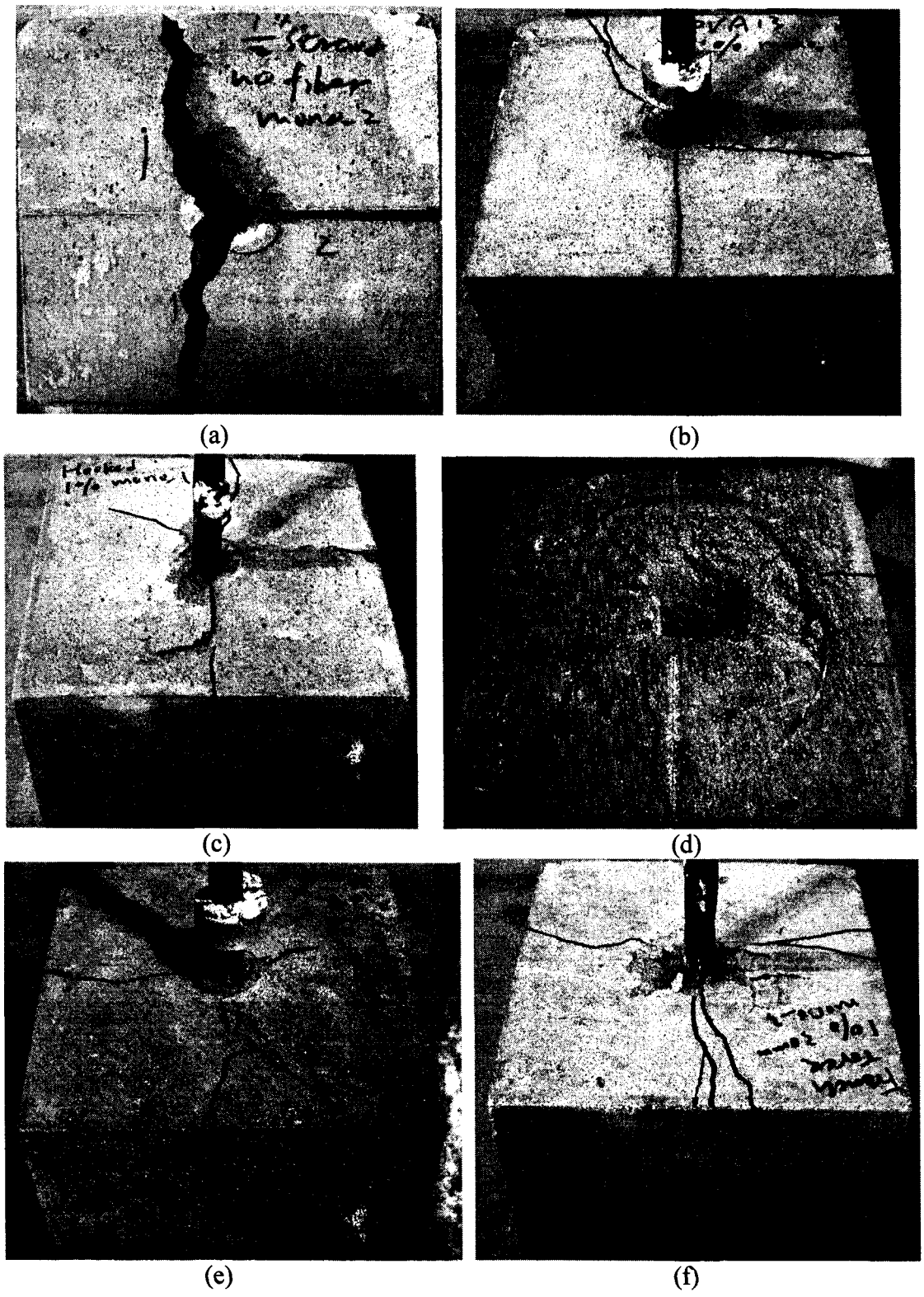

Figure 5.6 Crack patterns of 11 ksi strand specimens subjected to monotonic loading: (a) control specimen; (b) 1% PVA 13 fiber; (c) 1% steel hooked fiber; (d) 2% spiral reinforcement; (e) 1% Spectra fiber; (f) 1% rectangular Torex fiber

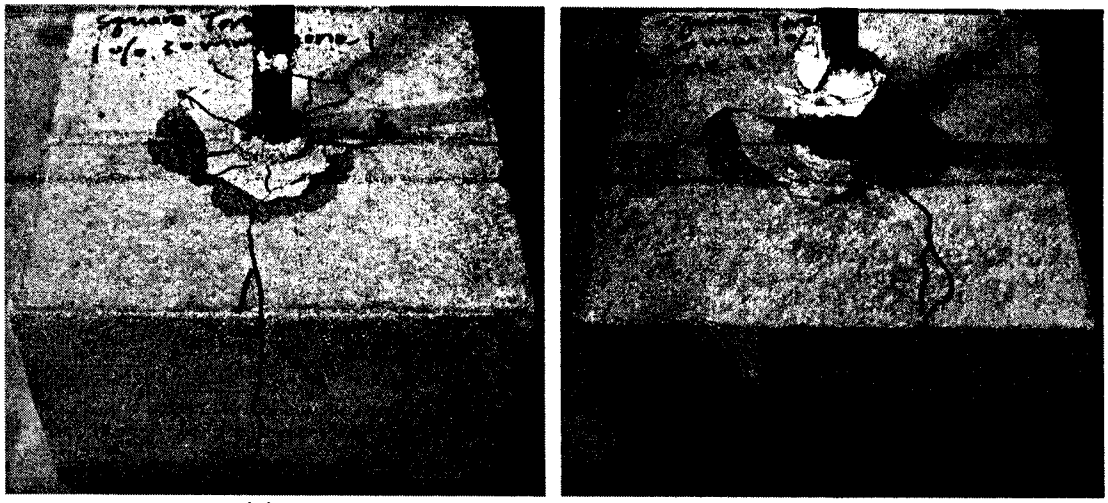

(g) (h)

Figure 5.6 (Continued) Crack patterns of 11 ksi strand specimens subjected to monotonic loading: (g) 1% square Torex fiber (30 mm); (h) 1% square Torex fiber (20 mm)

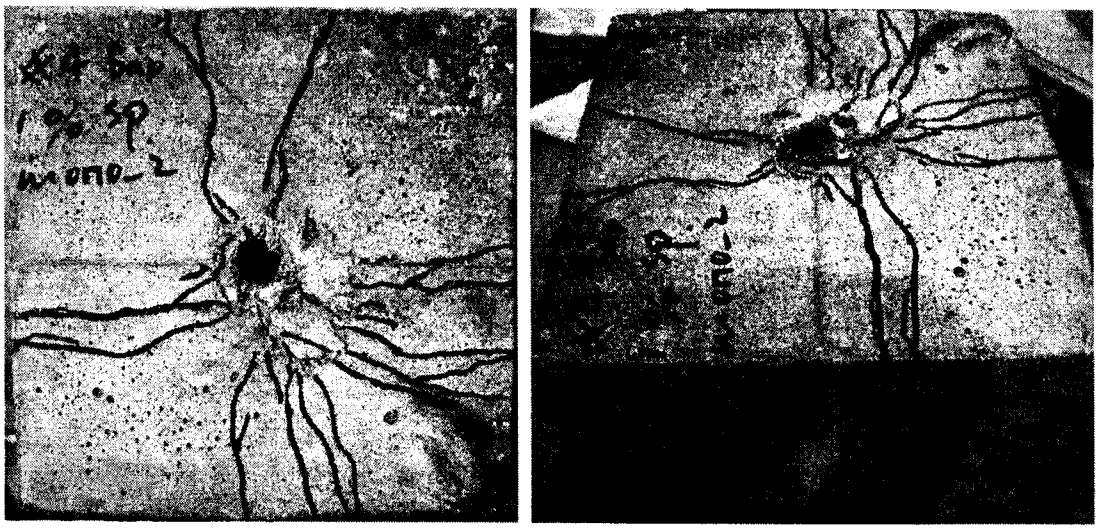

Figure 5.7 Crack patterns of 11 ksi No. 4 bar specimen with 1% Spectra fiber subjected to monotonic loading

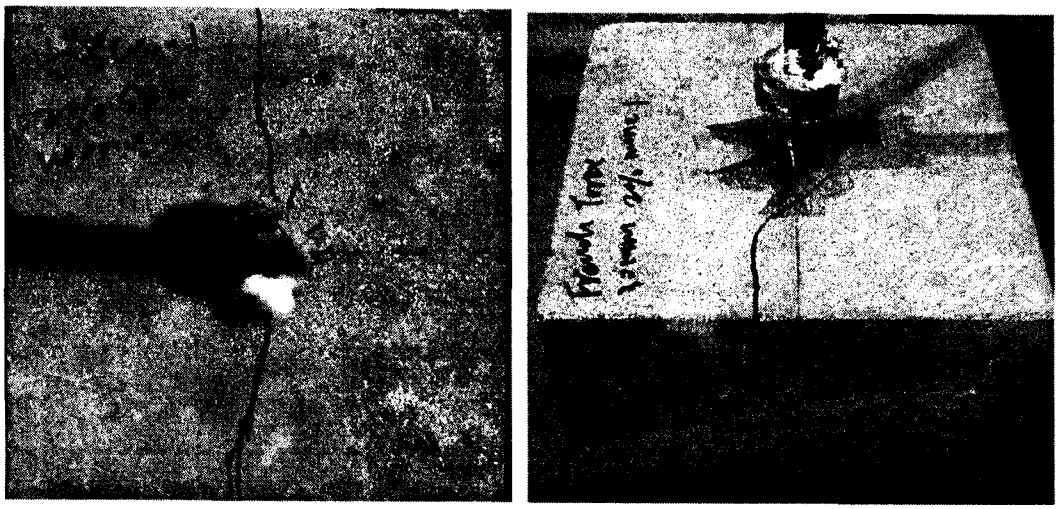

(a) (b)

Figure 5.8 Crack patterns of 11 ksi strand specimens subjected to monotonic loading: (a) 2% Spectra fiber; (b) 2% rectangular Torex fiber

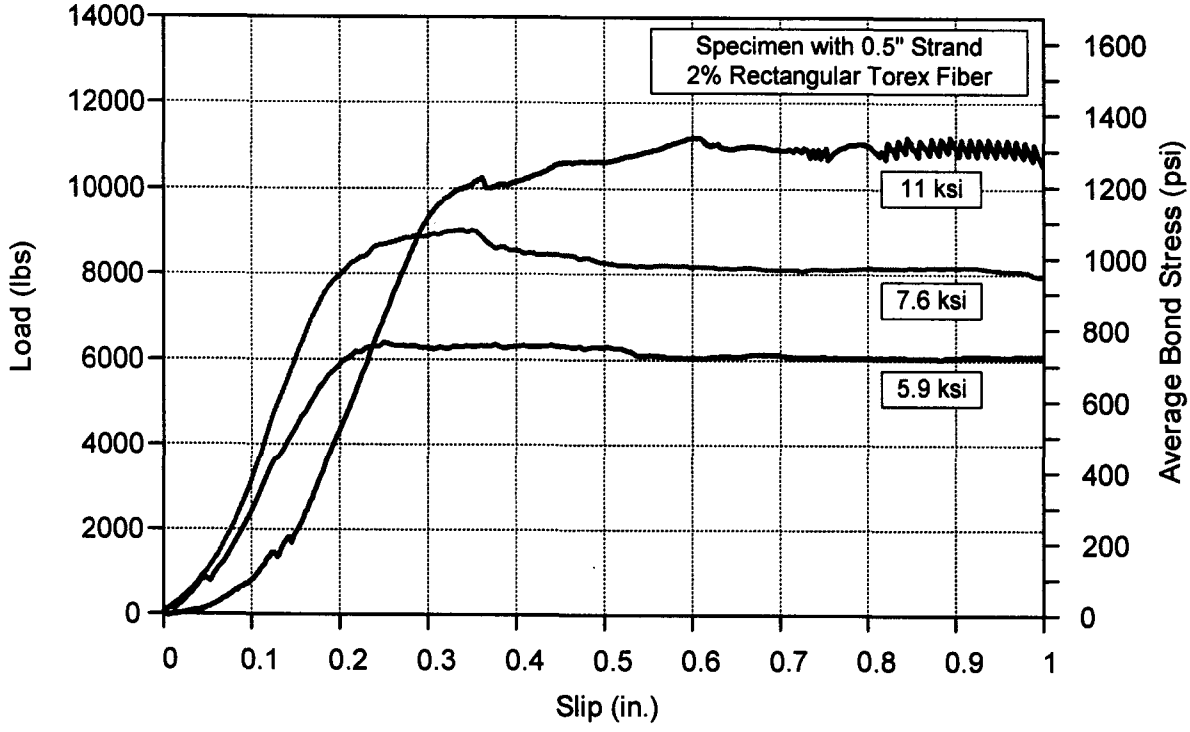

Figure 5.9 Comparison of bond stress-slip curves for specimens with various matrix compressive strengths (0.5 in. strand; rectangular Torex fiber)

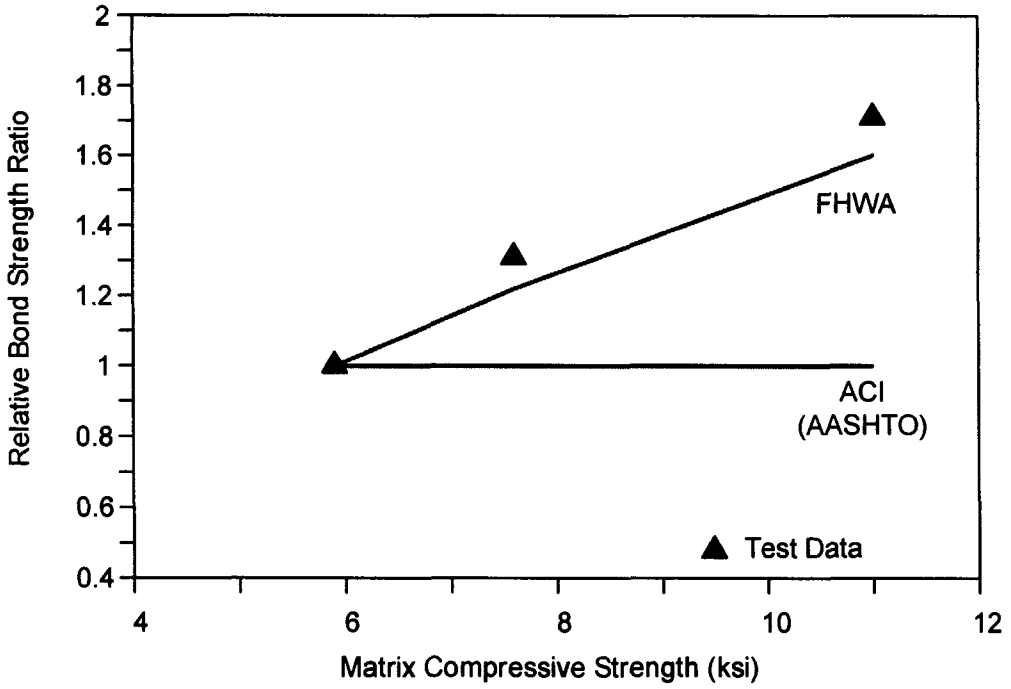

Figure 5.10 (a) Normalized bond strength for various matrix strengths (0.5 in. strand)

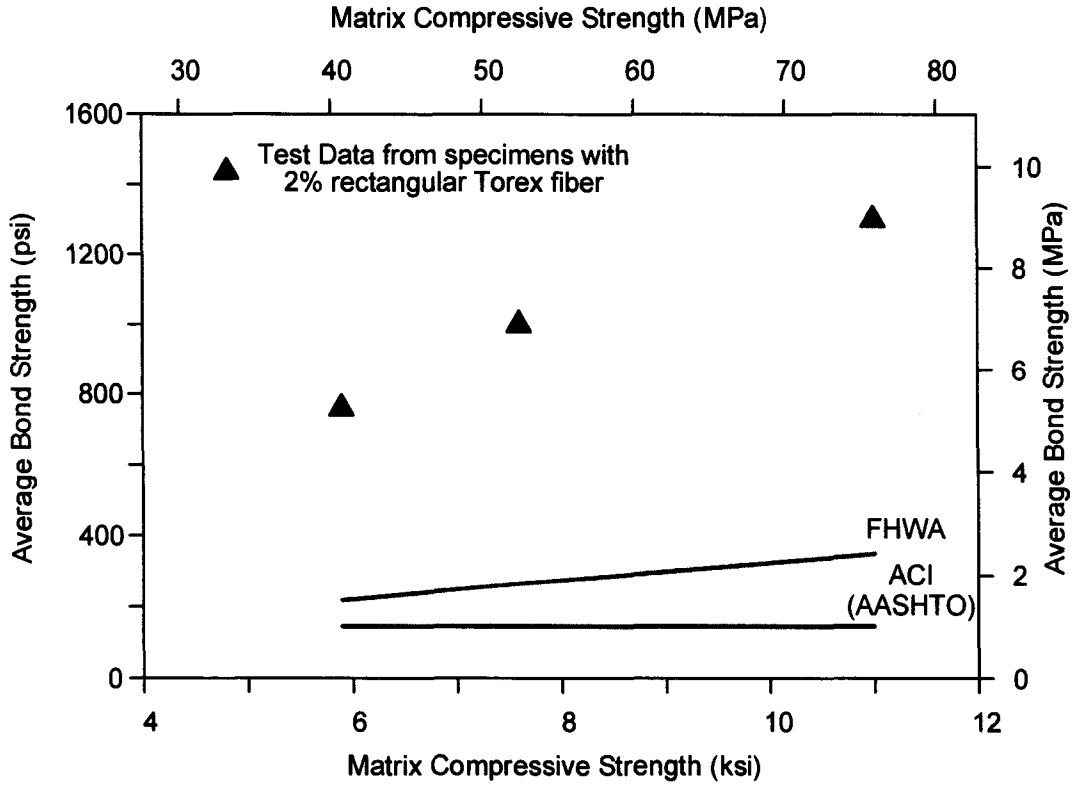

Figure 5.10 (b) Actual bond strength for various matrix strengths (0.5 in. strand)

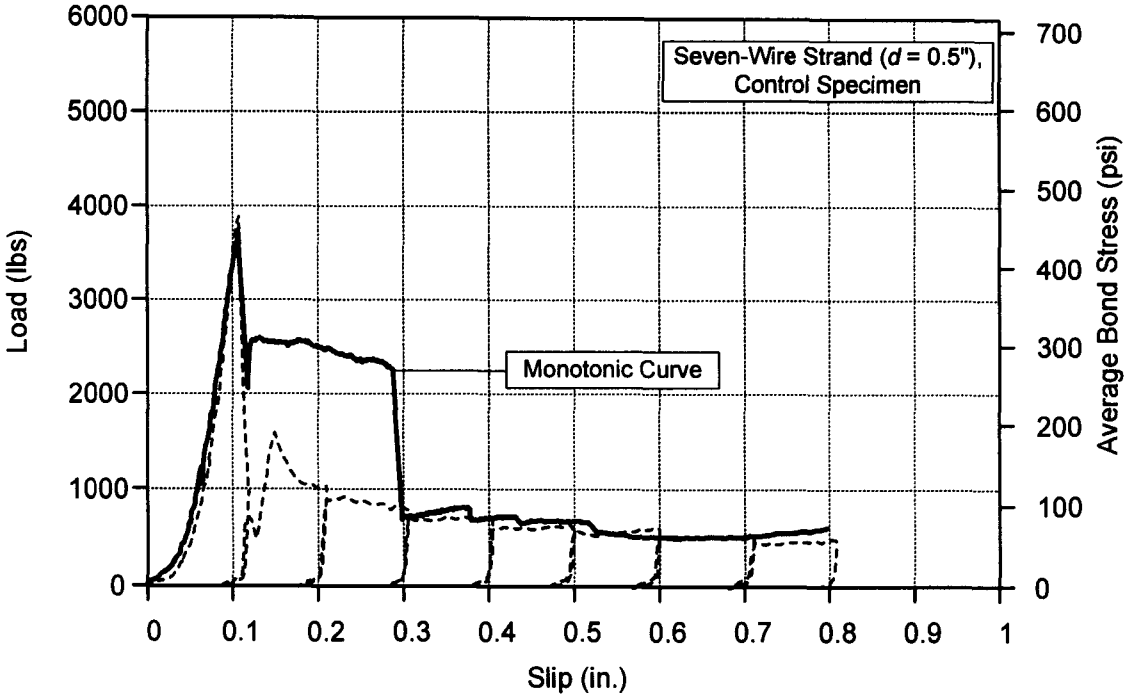

Figure 5.11 Load-slip curve for 0.5 inch strand control specimen (11 ksi) subjected to unidirectional displacement controlled loading

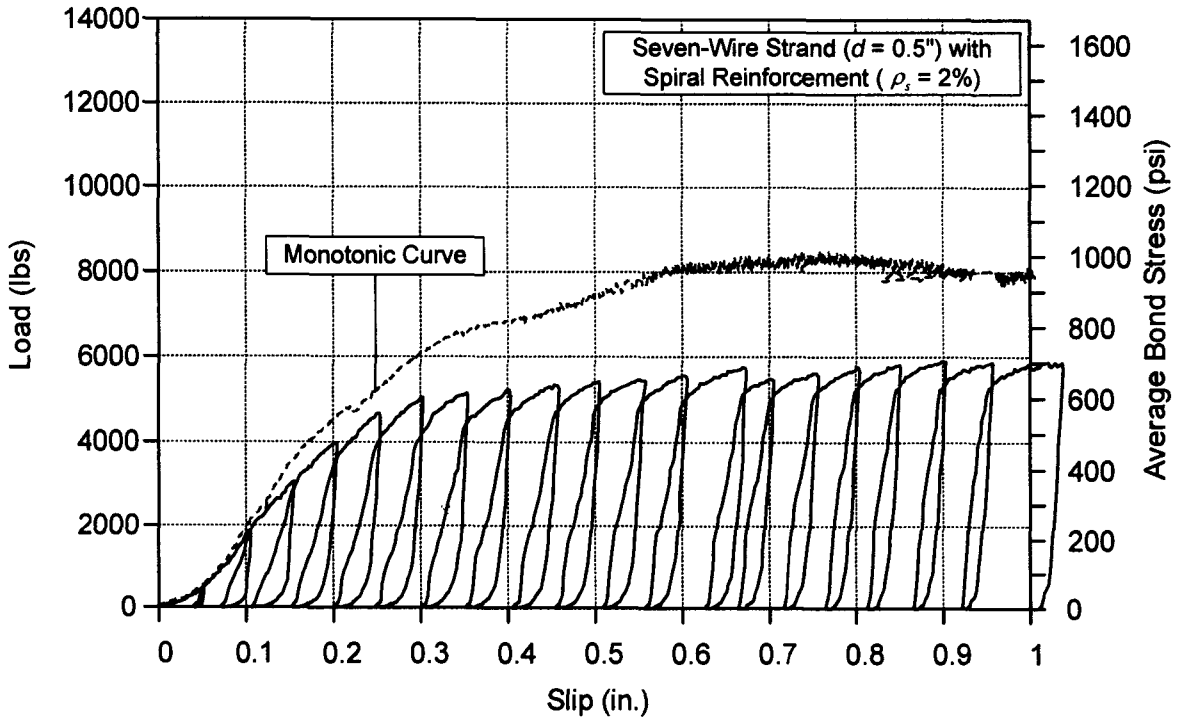

Figure 5.12 Load-slip curve for 0.5 inch strand specimen (11 ksi) with 2% volumetric spiral reinforcement subjected to unidirectional displacement controlled loading

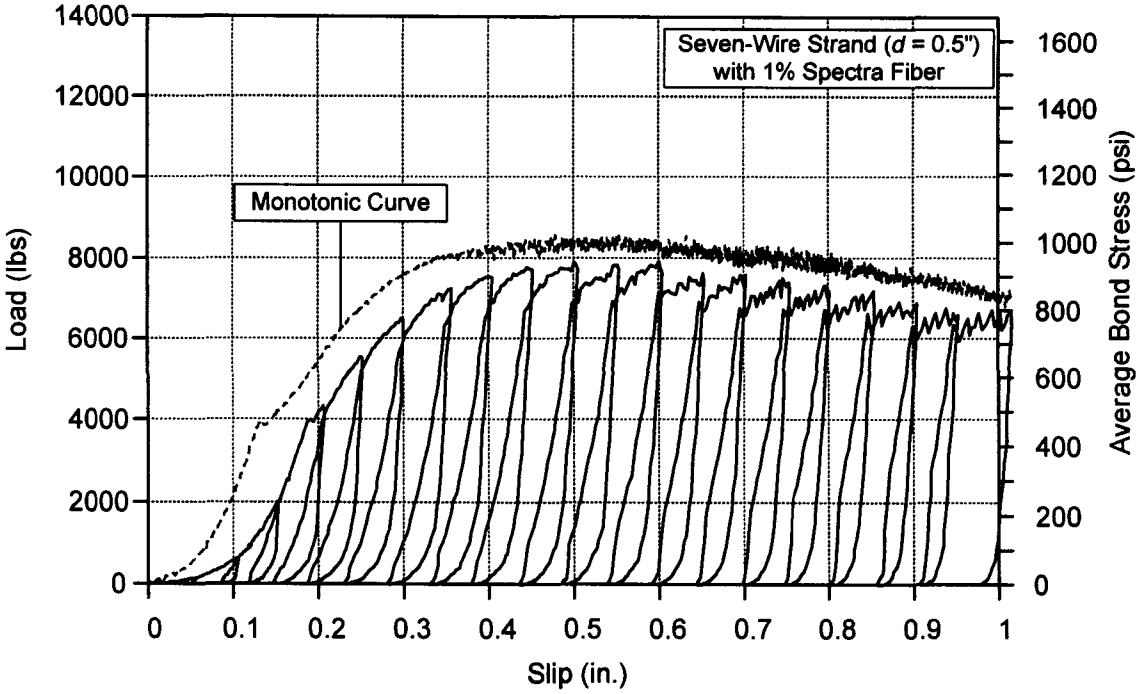

Figure 5.13 Load-slip curve for 0.5 inch strand specimen (11 ksi) with 1% Spectra fiber subjected to unidirectional displacement controlled loading

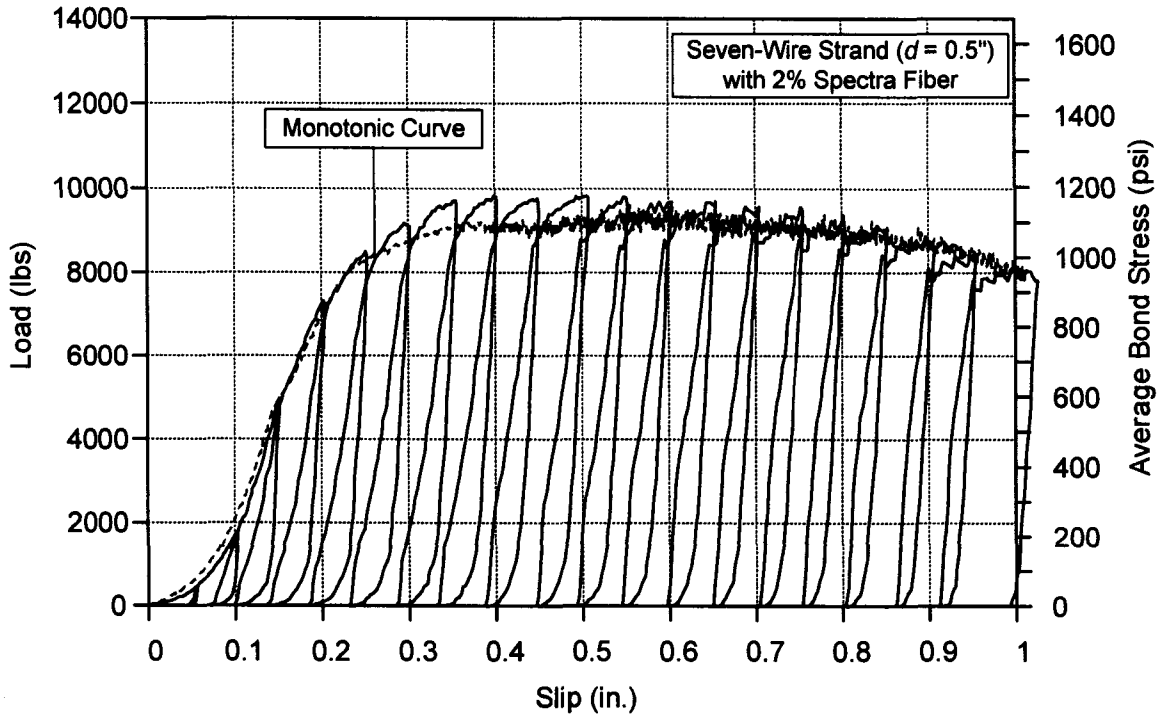

Figure 5.14 Load-slip curve for 0.5 inch strand specimen (11 ksi) with 2% Spectra fiber subjected to unidirectional displacement controlled loading

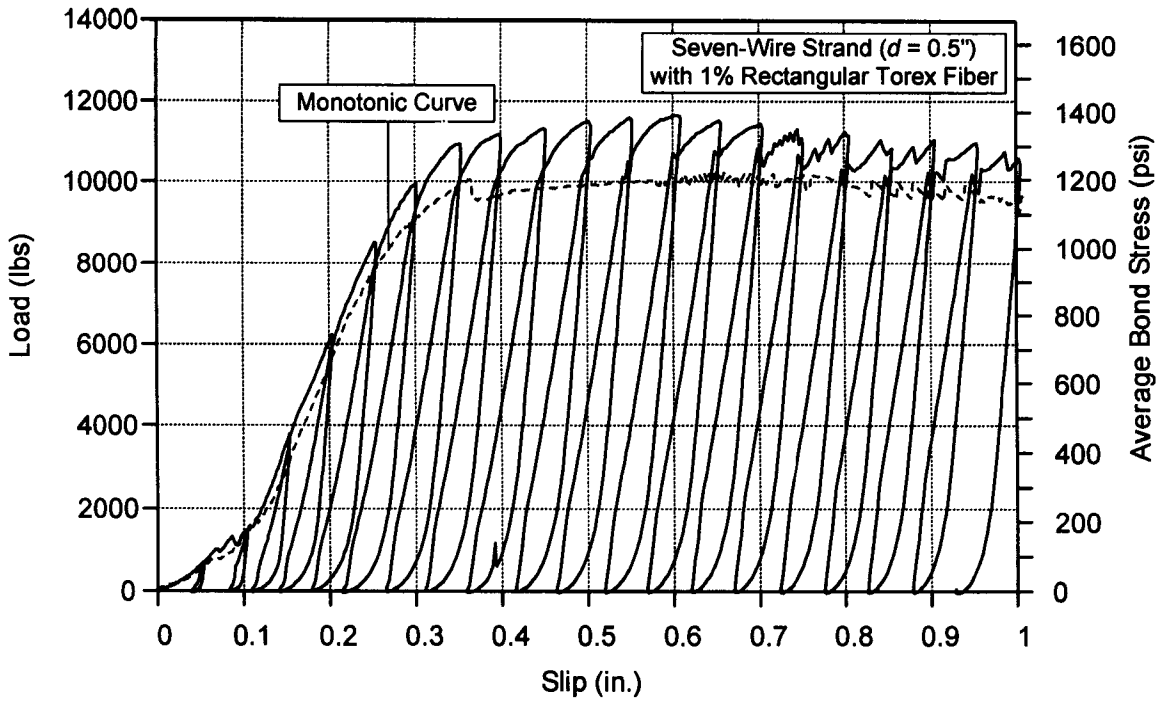

Figure 5.15 Load-slip curve for 0.5 inch strand specimen (11 ksi) with 1% rectangular Torex fiber subjected to unidirectional displacement controlled loading

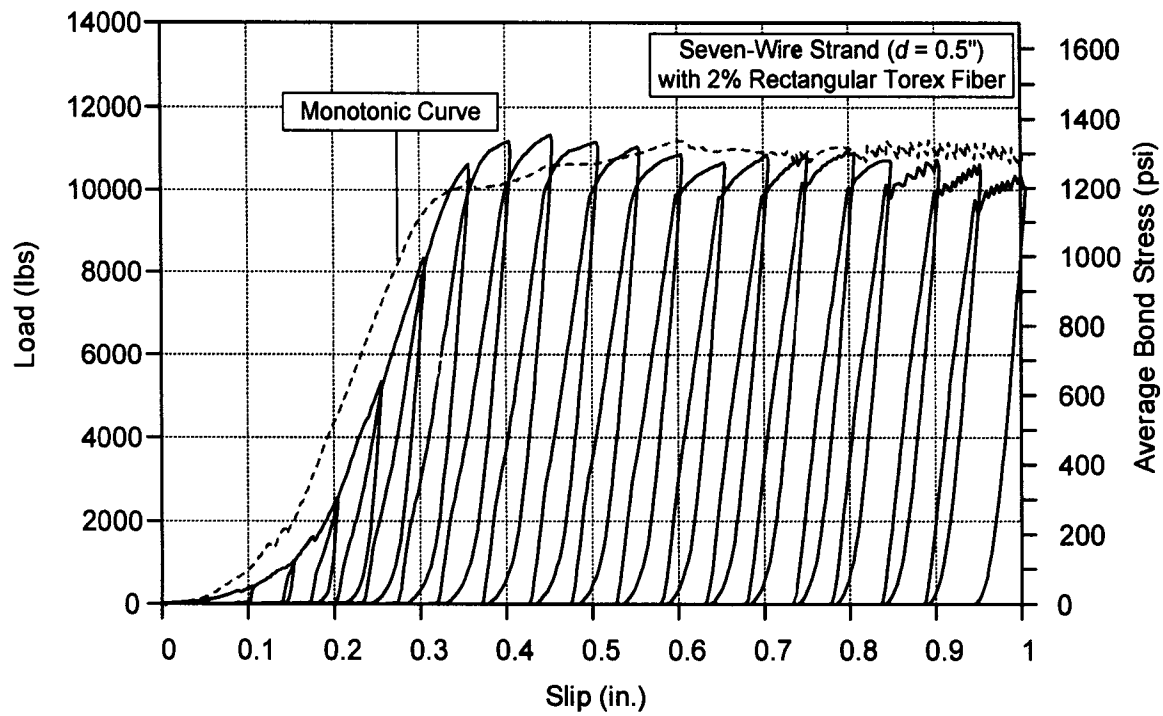

Figure 5.16 Load-slip curve for 0.5 inch strand specimen (11 ksi) with 2% rectangular Torex fiber subjected to unidirectional displacement controlled loading

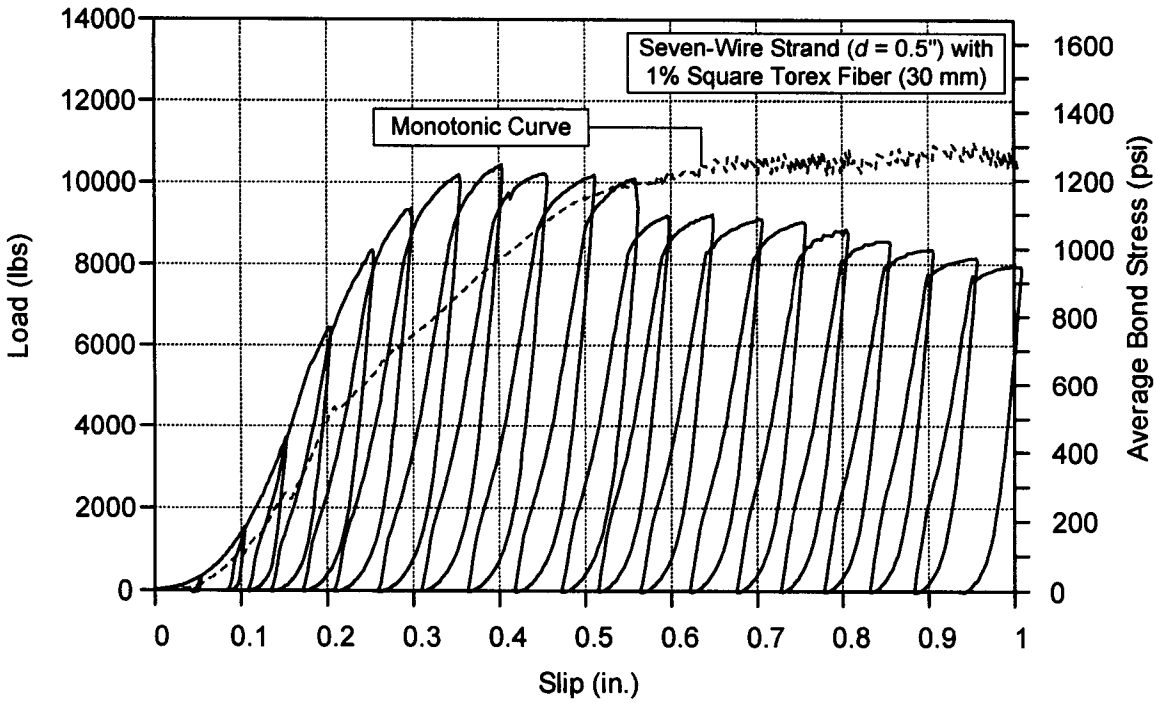

Figure 5.17 Load-slip curve for 0.5 inch strand specimen (11 ksi) with 1% square Torex fiber (30 mm) subjected to unidirectional displacement controlled loading

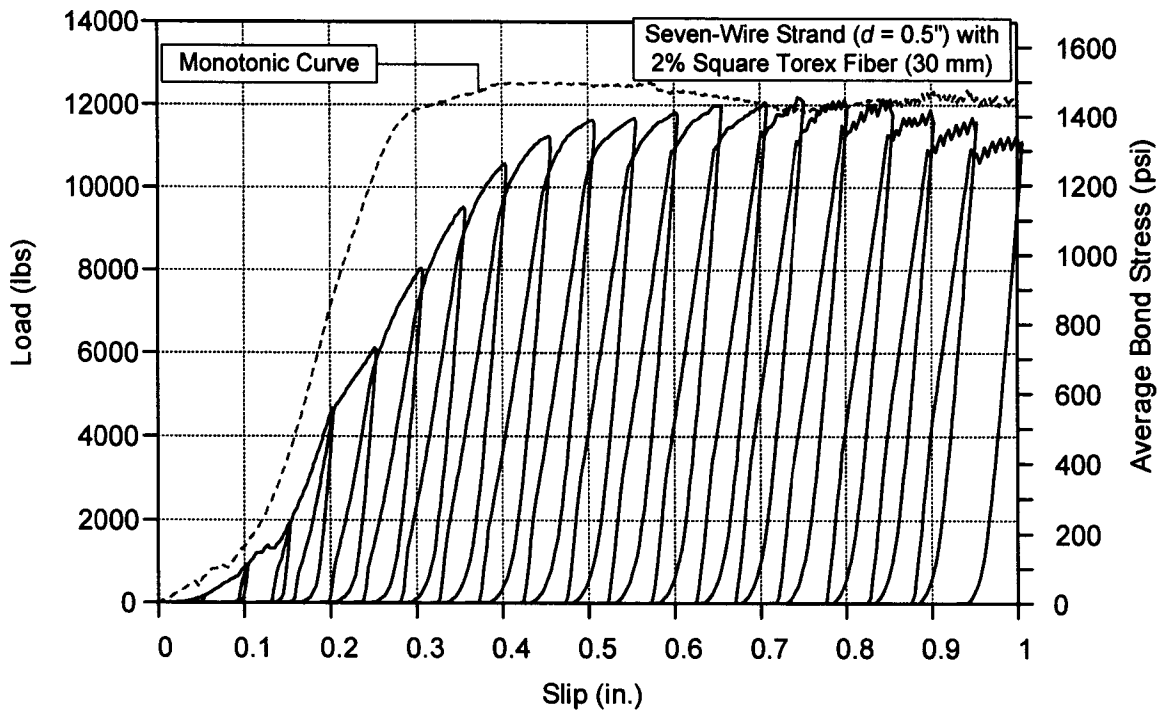

Figure 5.18 Load-slip curve for 0.5 inch strand specimen (11 ksi) with 2% square Torex fiber (30 mm) subjected to unidirectional displacement controlled loading

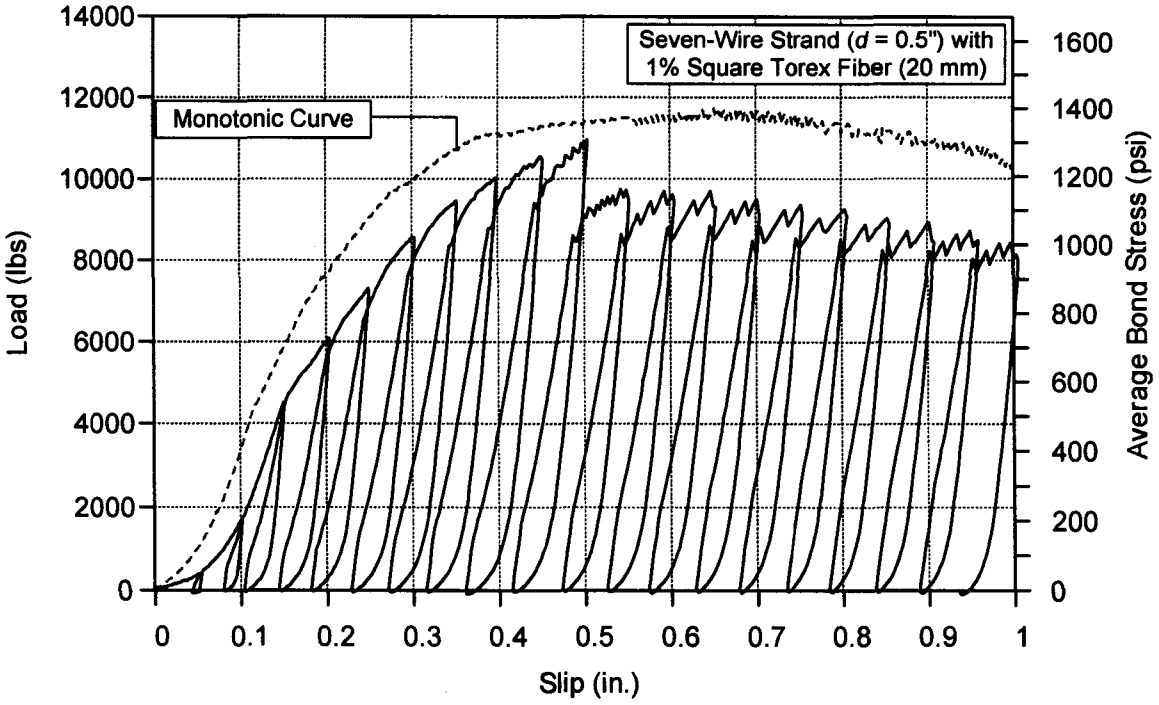

Figure 5.19 Load-slip curve for 0.5 inch strand specimen (11 ksi) with 1% square Torex fiber (20 mm) subjected to unidirectional displacement controlled loading

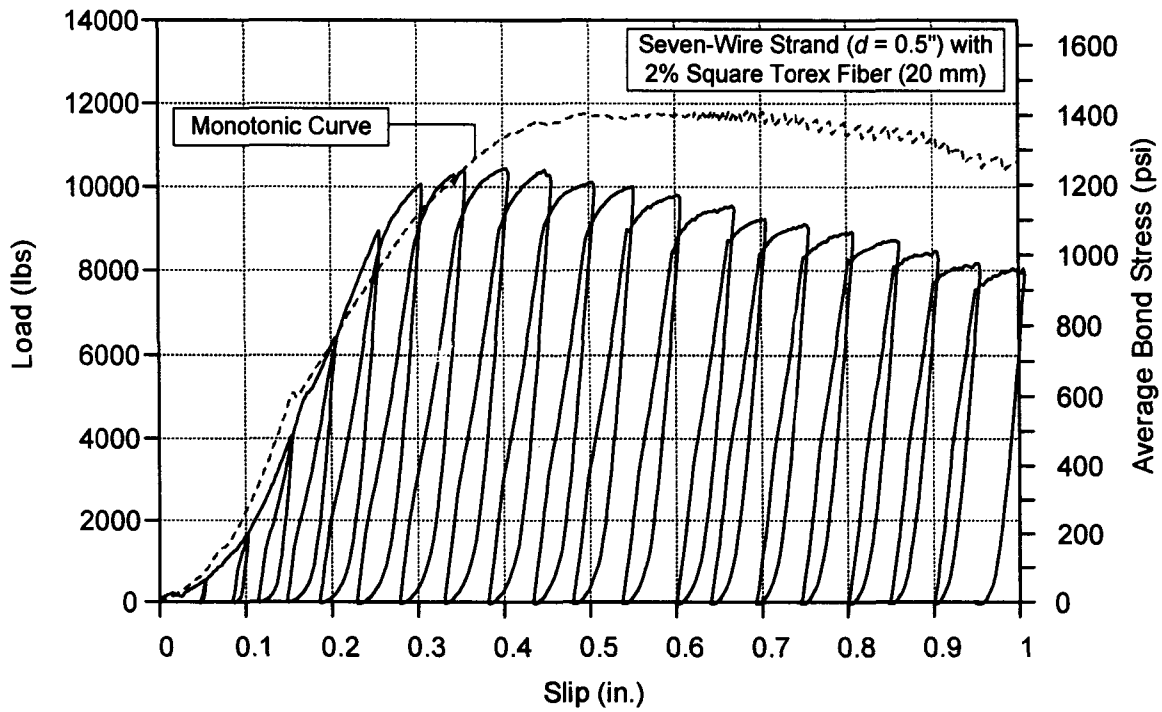

Figure 5.20 Load-slip curve for 0.5 inch strand specimen (11 ksi) with 2% square Torex fiber (20 mm) subjected to unidirectional displacement controlled loading

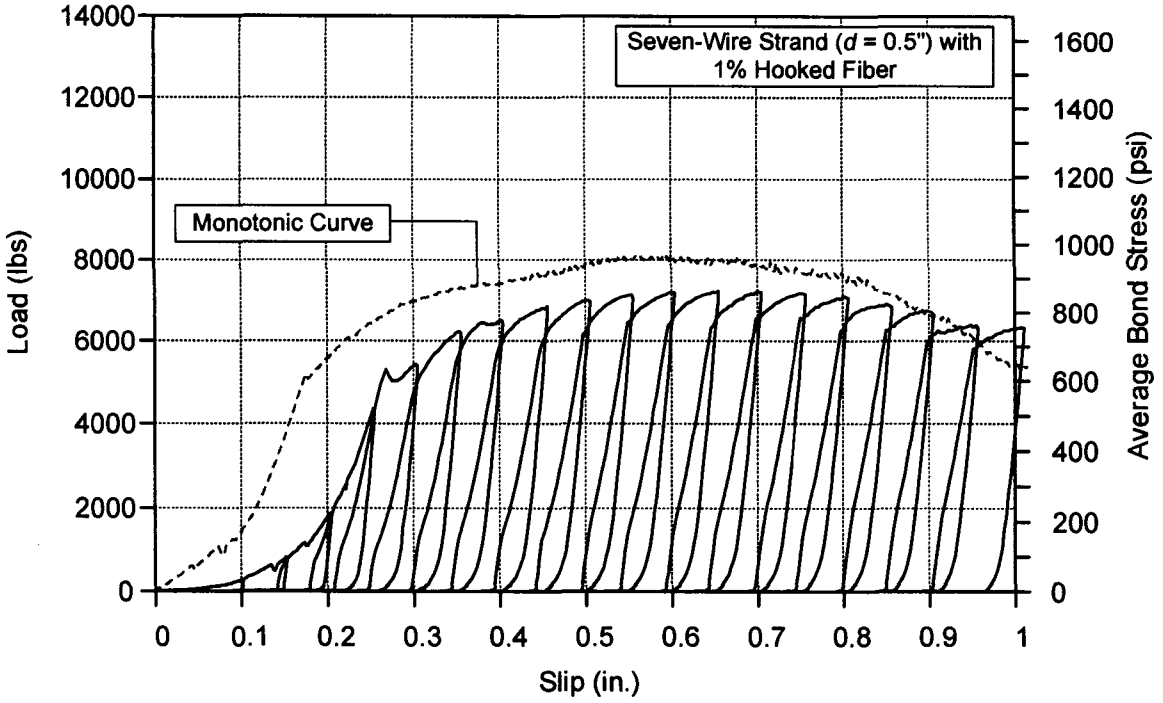

Figure 5.21 Load-slip curve for 0.5 inch strand specimen (11 ksi) with 1% steel hooked fiber subjected to unidirectional displacement controlled loading

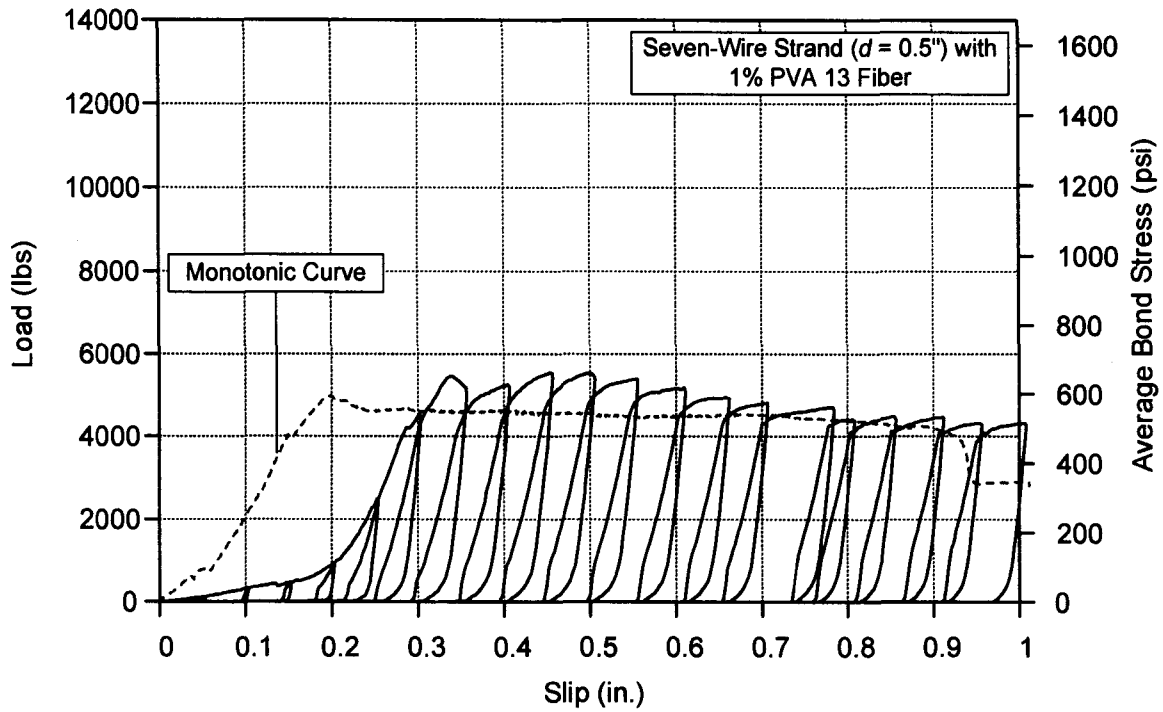

Figure 5.22 Load-slip curve for 0.5 inch strand specimen (11 ksi) with 1% PVA 13 fiber subjected to unidirectional displacement controlled loading

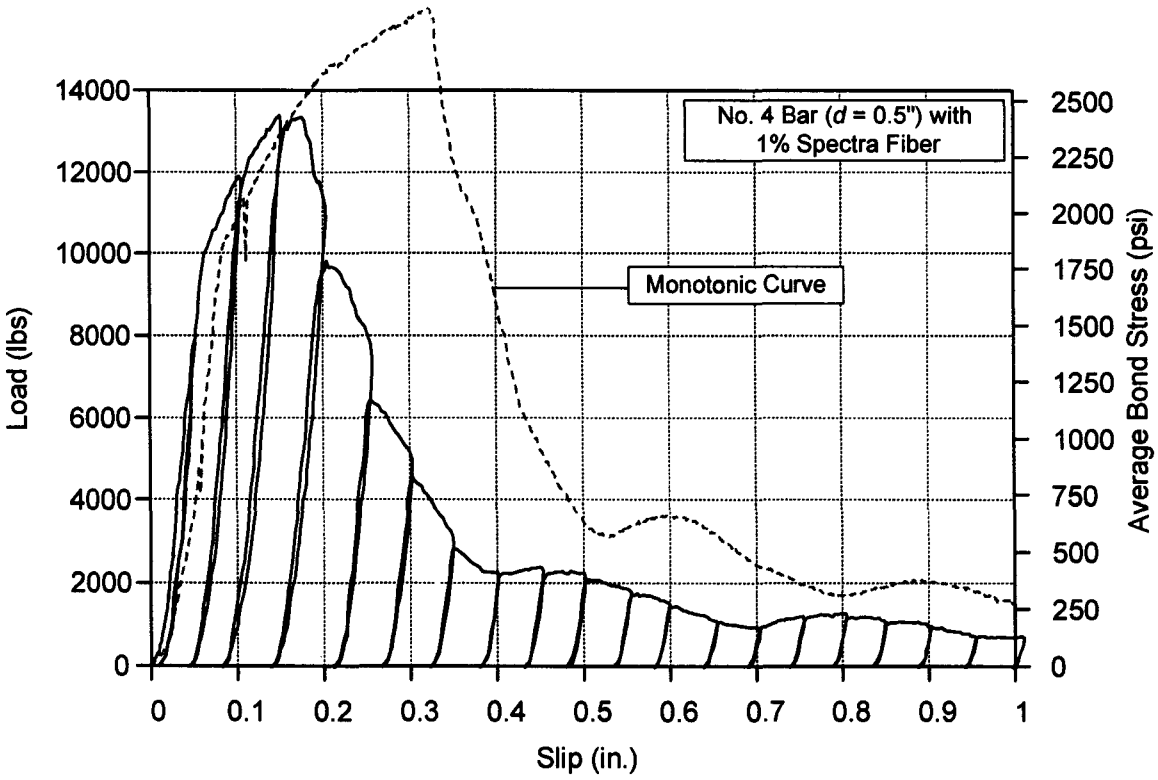

Figure 5.23 Load-slip curve for No.4 bar (0.5 inch diameter) specimen (11 ksi) with 1% Spectra fiber subjected to unidirectional displacement controlled loading

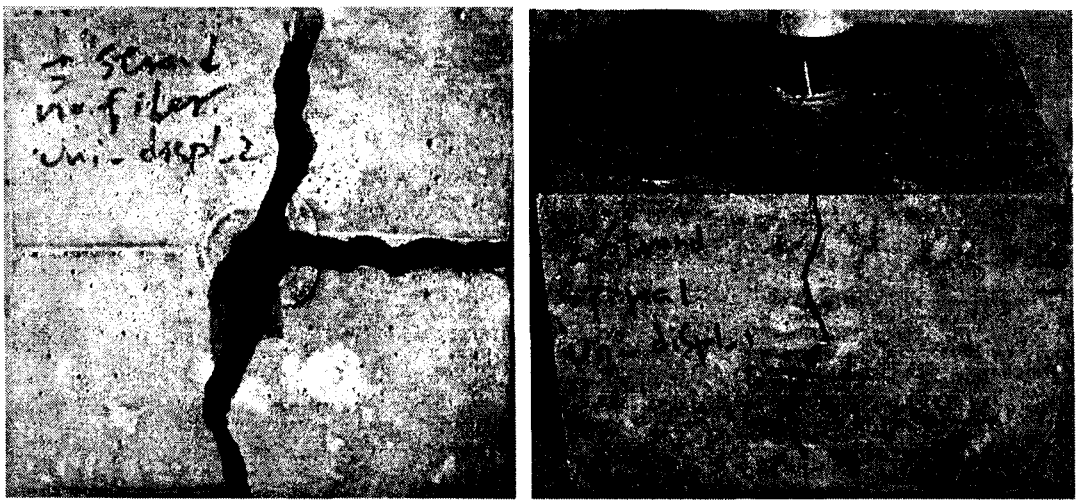

(a) (b)

Figure 5.24 Crack patterns of 11 ksi strand specimens subjected to unidirectional displacement controlled loading: (a) Control specimen; (b) 2% volumetric spiral reinforcement

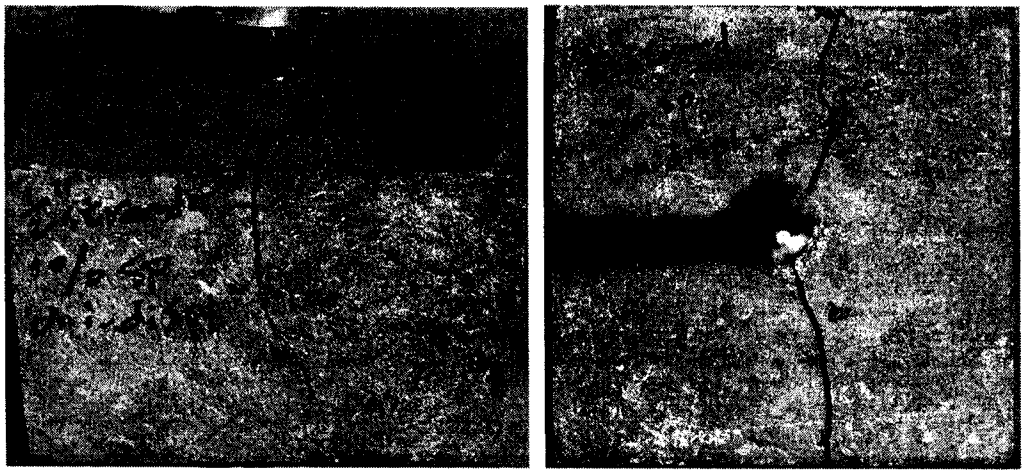

(c) (d)

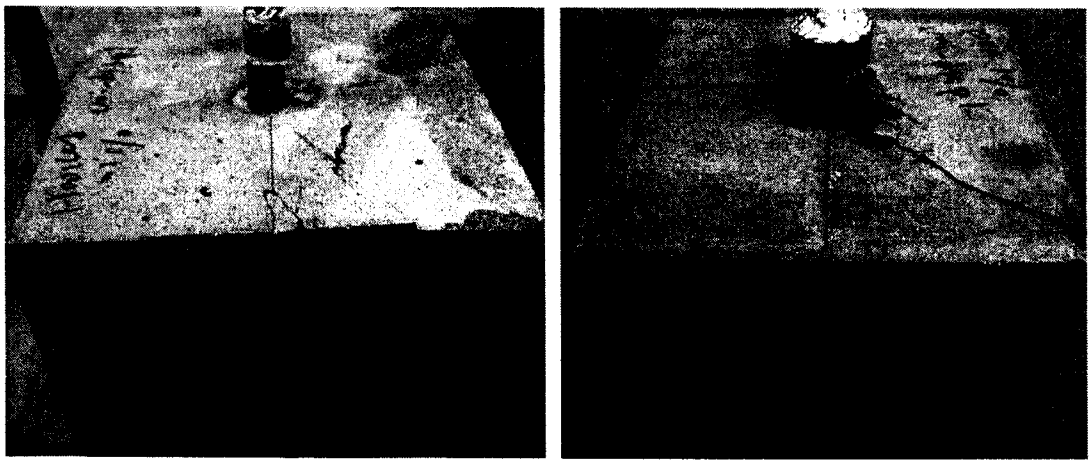

(e) (f)

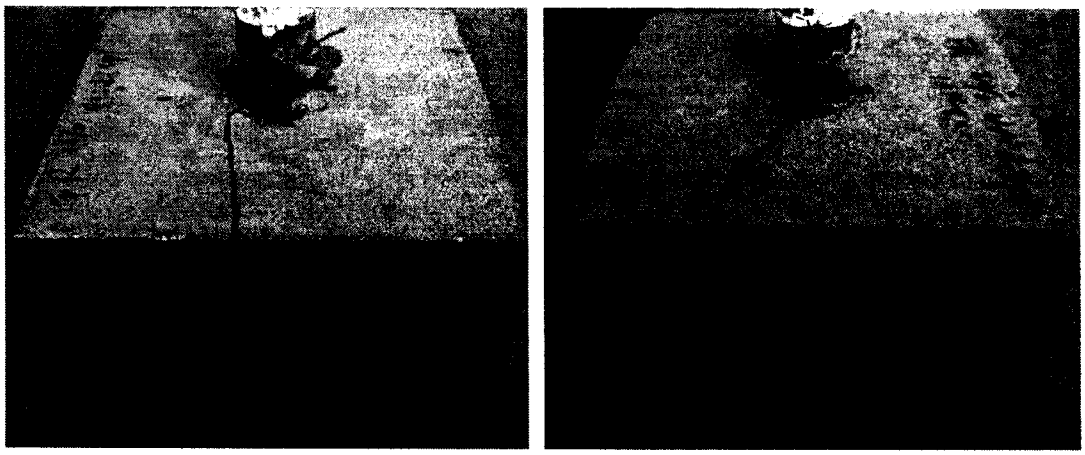

(g) (h)

Figure 5.24 (continued) Crack patterns of 11 ksi strand specimens subjected to unidirectional displacement controlled loading: (c) 1% Spectra fiber; (d) 2% Spectra fiber; (e) 1% steel hooked fiber; (f) 1% PVA 13 fiber; (g) 1% rectangular Torex fiber; (h) 2% rectangular Torex fiber

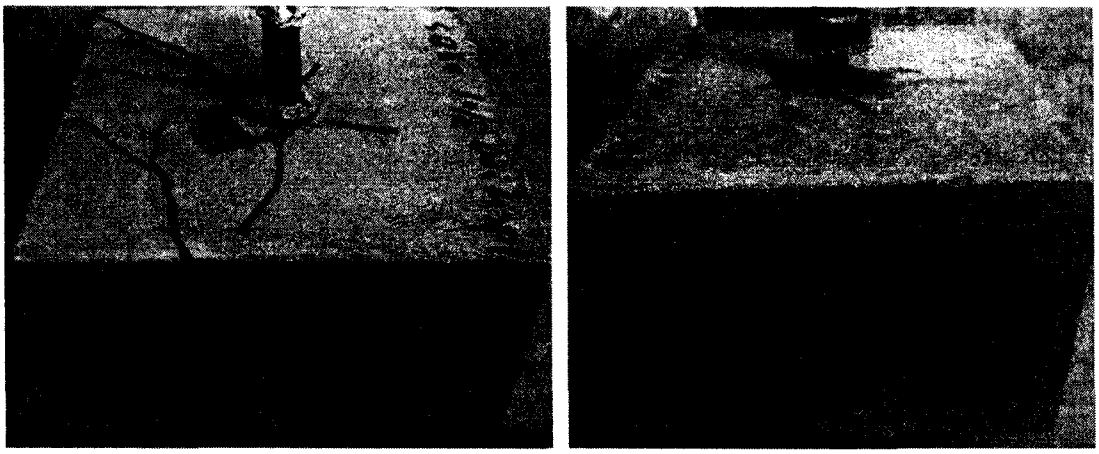

(i) (j)

Figure 5.24 (continued) Crack patterns of 11 ksi strand specimens subjected to unidirectional displacement controlled loading: (i) 1% square Torex fiber (30 mm); (j) 2% square Torex fiber (30 mm)

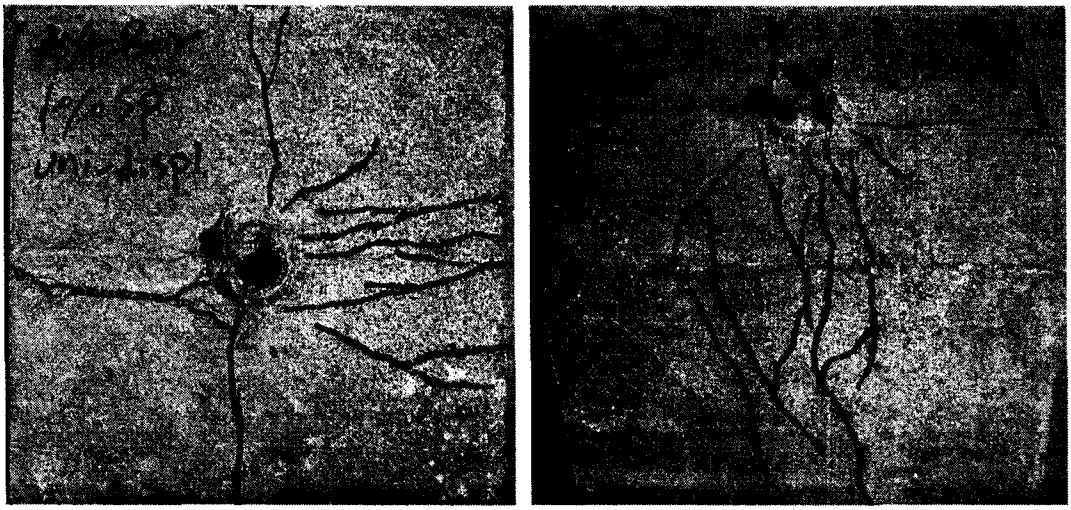

Figure 5.25 Crack patterns of No. 4 bar (0.5 inch diameter) specimens with 11 ksi matrix subjected to unidirectional displacement controlled loading

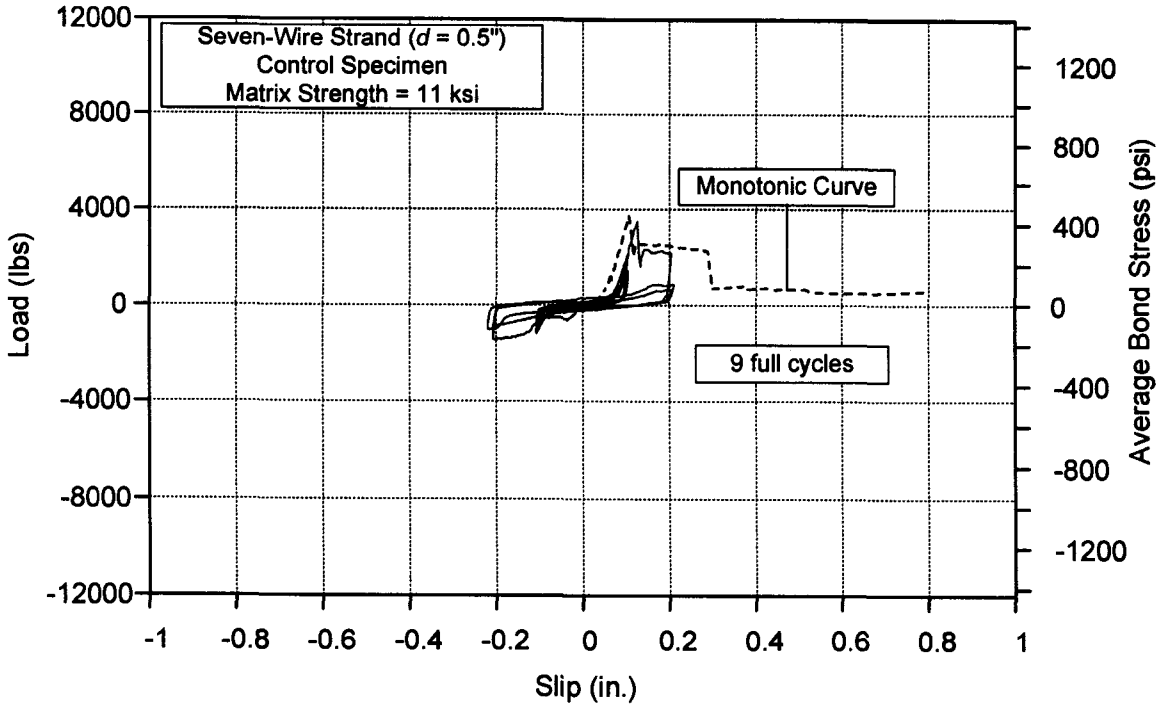

Figure 5.26 Load-slip curve for fully reversed displacement controlled cyclic loading: 0.5 inch strand, control specimen, 11 ksi matrix

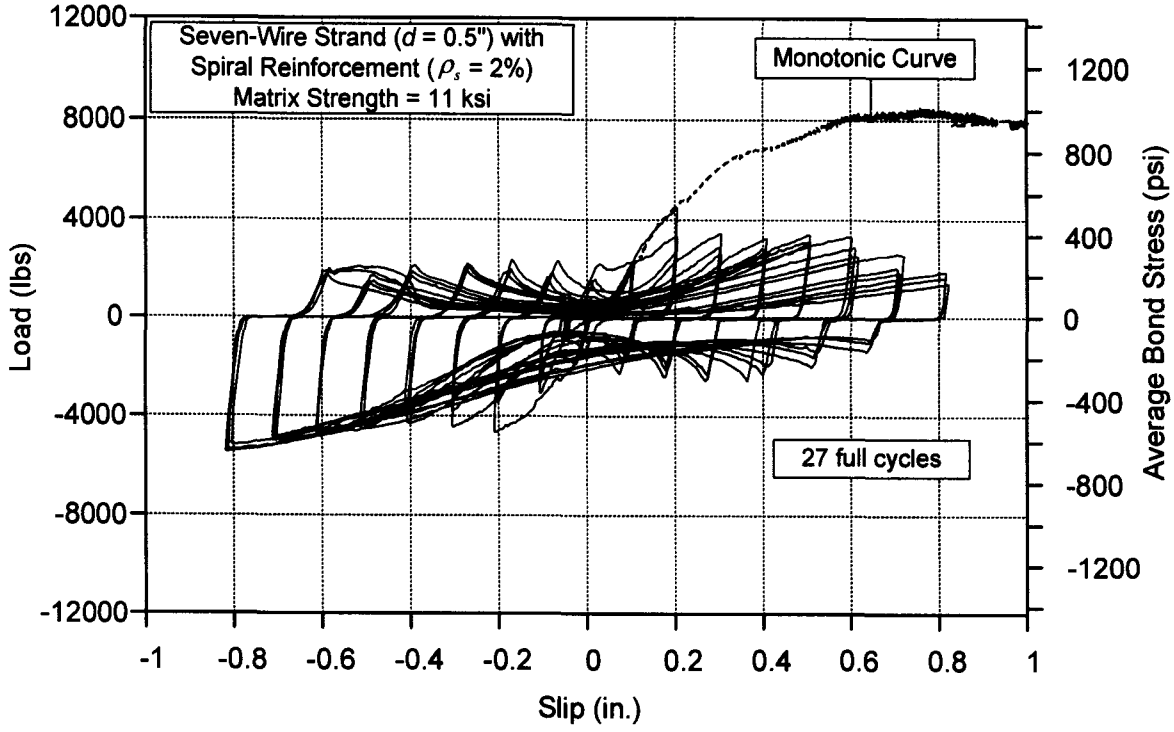

Figure 5.27 Load-slip curve for fully reversed displacement controlled cyclic loading: 0.5 inch strand, 2% volumetric spiral reinforcement, 11 ksi matrix

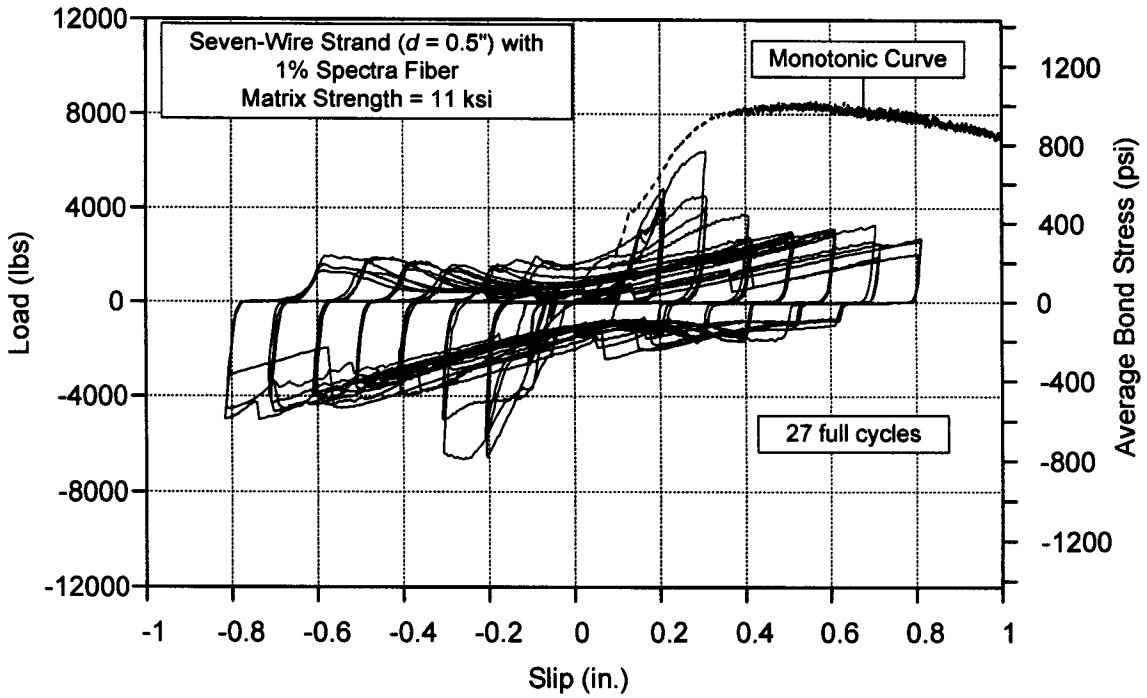

Figure 5.28 Load-slip curve for fully reversed displacement controlled cyclic loading: 0.5 inch strand, 1% Spectra fiber, 11 ksi matrix

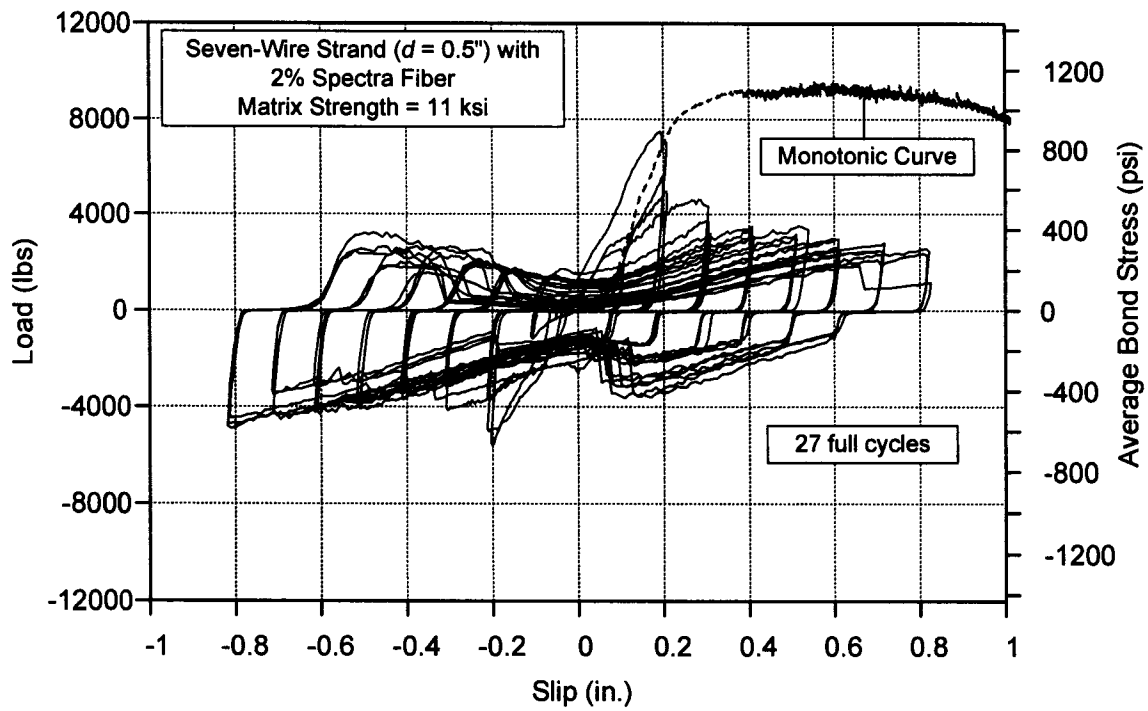

Figure 5.29 Load-slip curve for fully reversed displacement controlled cyclic loading: 0.5 inch strand, 2% Spectra fiber, 11 ksi matrix

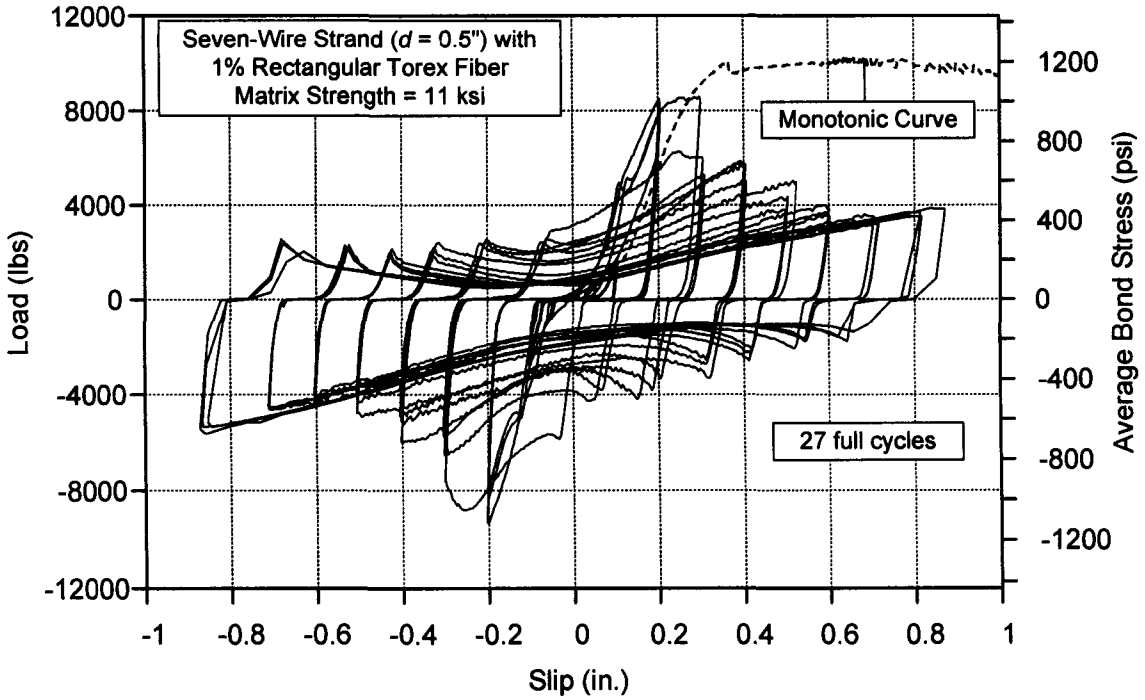

Figure 5.30 Load-slip curve for fully reversed displacement controlled cyclic loading: 0.5 inch strand, 1% rectangular Torex fiber, 11 ksi matrix

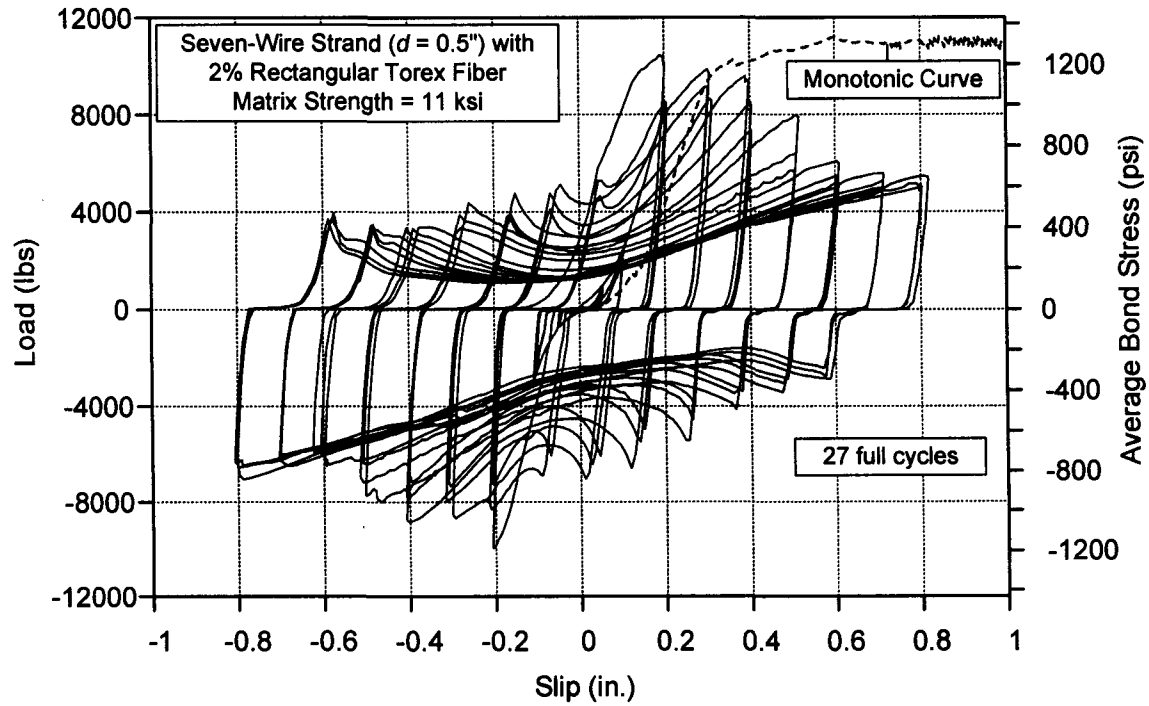

Figure 5.31 Load-slip curve for fully reversed displacement controlled cyclic loading: 0.5 inch strand, 2% rectangular Torex fiber, 11 ksi matrix

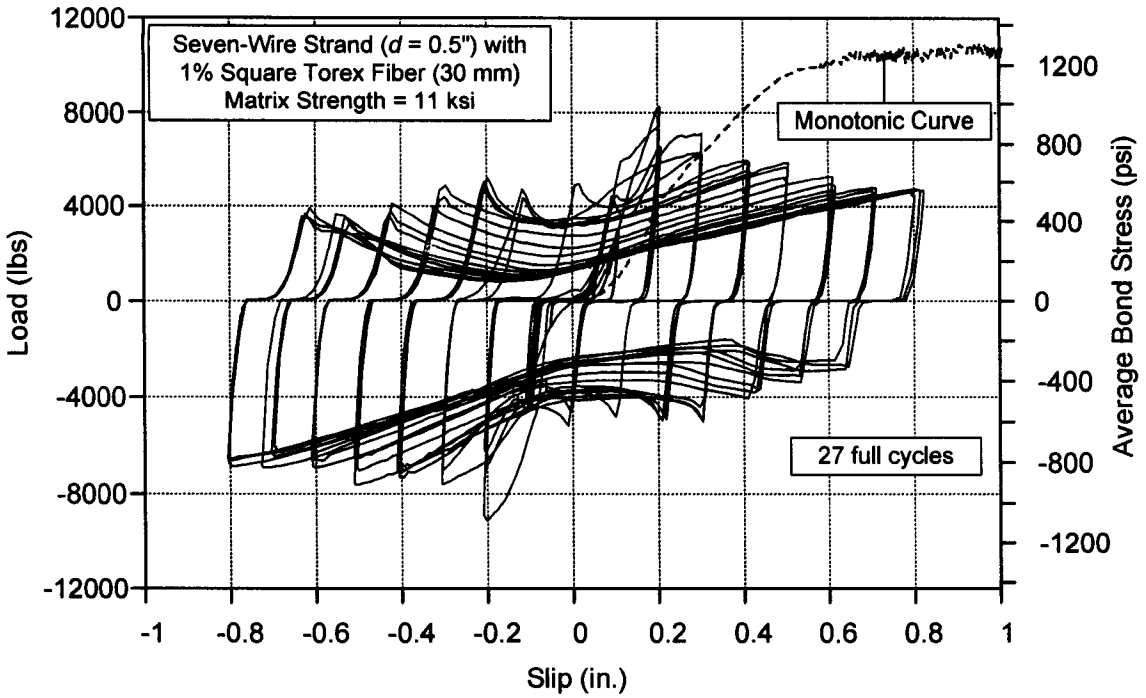

Figure 5.32 Load-slip curve for fully reversed displacement controlled cyclic loading: 0.5 inch strand, 1% square Torex fiber (30 mm), 11 ksi matrix

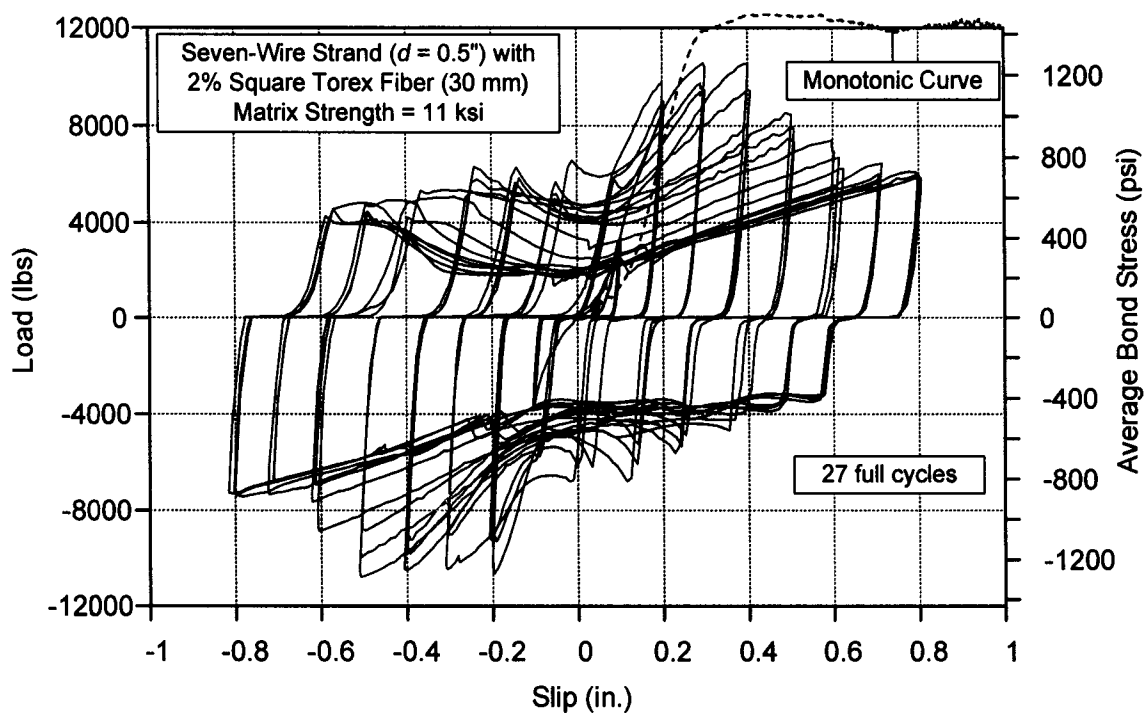

Figure 5.33 Load-slip curve for fully reversed displacement controlled cyclic loading: 0.5 inch strand, 2% square Torex fiber (30 mm), 11 ksi matrix

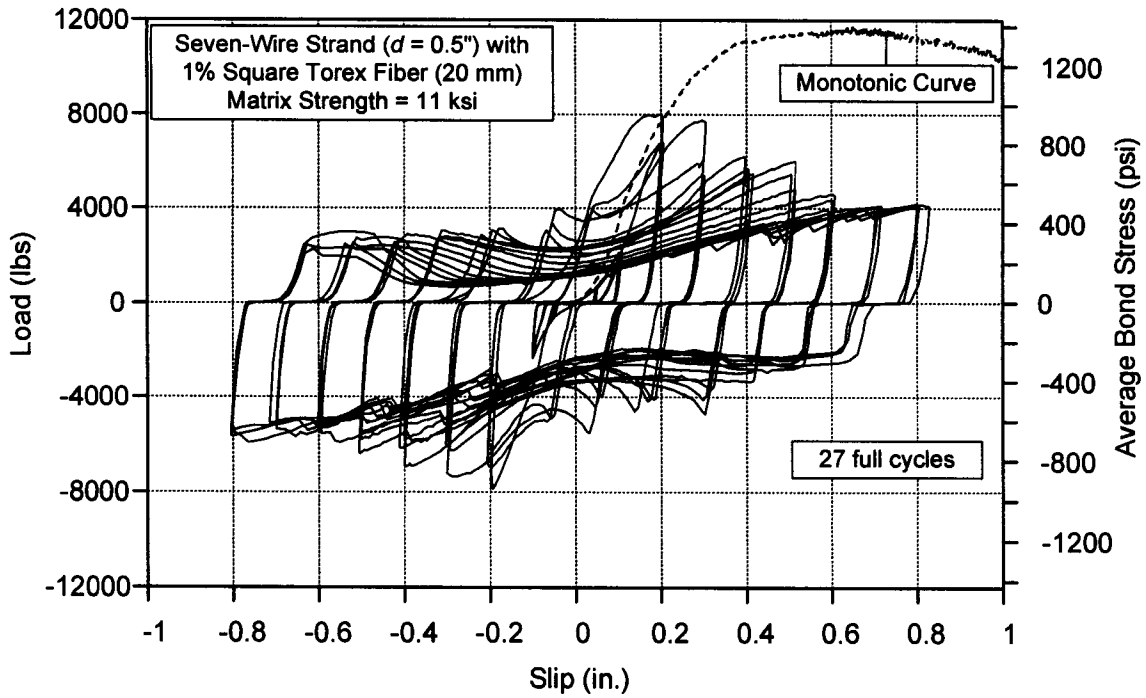

Figure 5.34 Load-slip curve for fully reversed displacement controlled cyclic loading: 0.5 inch strand, 1% square Torex fiber (20 mm), 11 ksi matrix

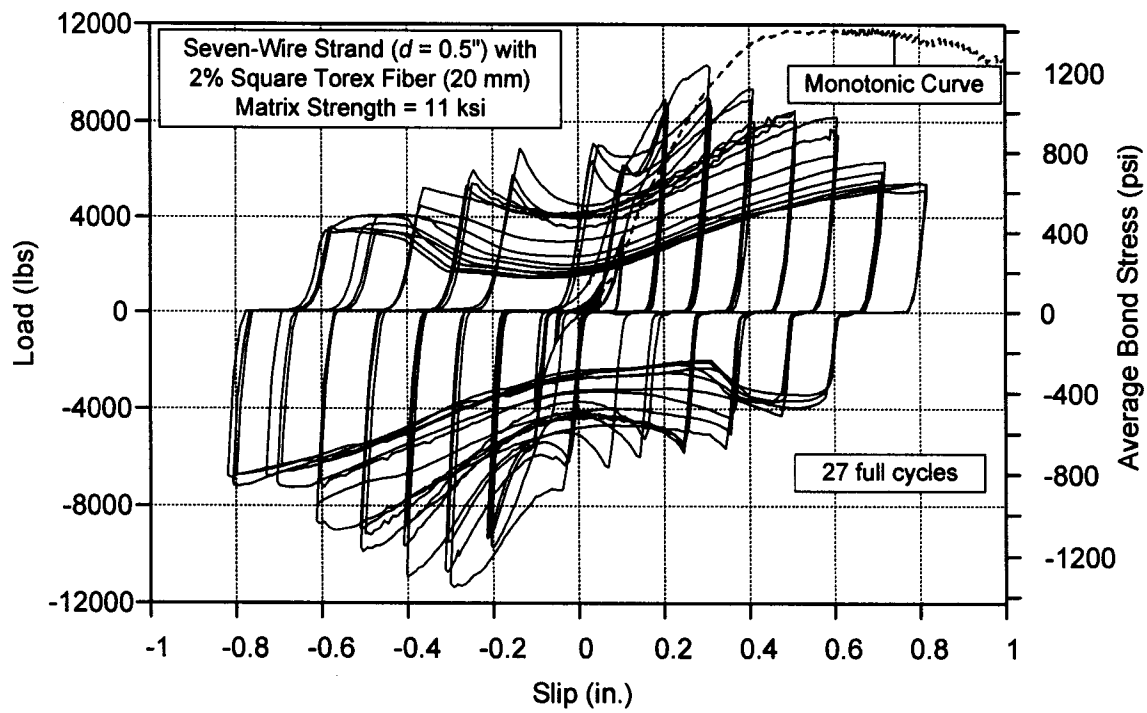

Figure 5.35 Load-slip curve for fully reversed displacement controlled cyclic loading: 0.5 inch strand, 2% square Torex fiber (20 mm), 11 ksi matrix

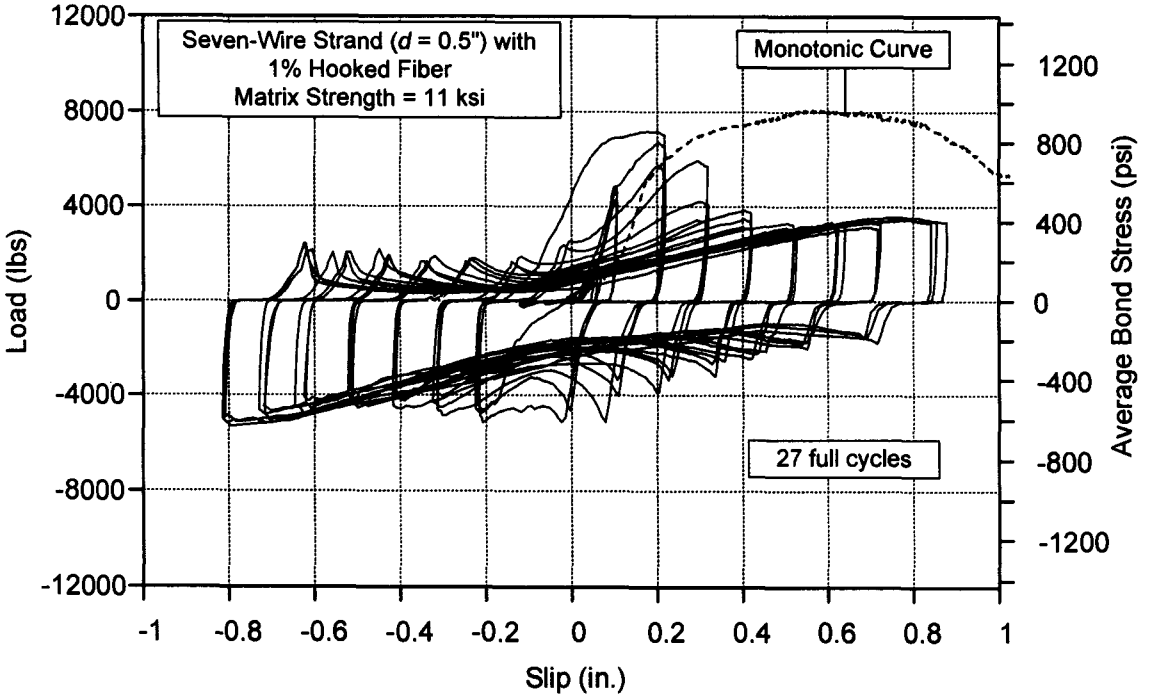

Figure 5.36 Load-slip curve for fully reversed displacement controlled cyclic loading: 0.5 inch strand, 1% steel hooked fiber, 11 ksi matrix

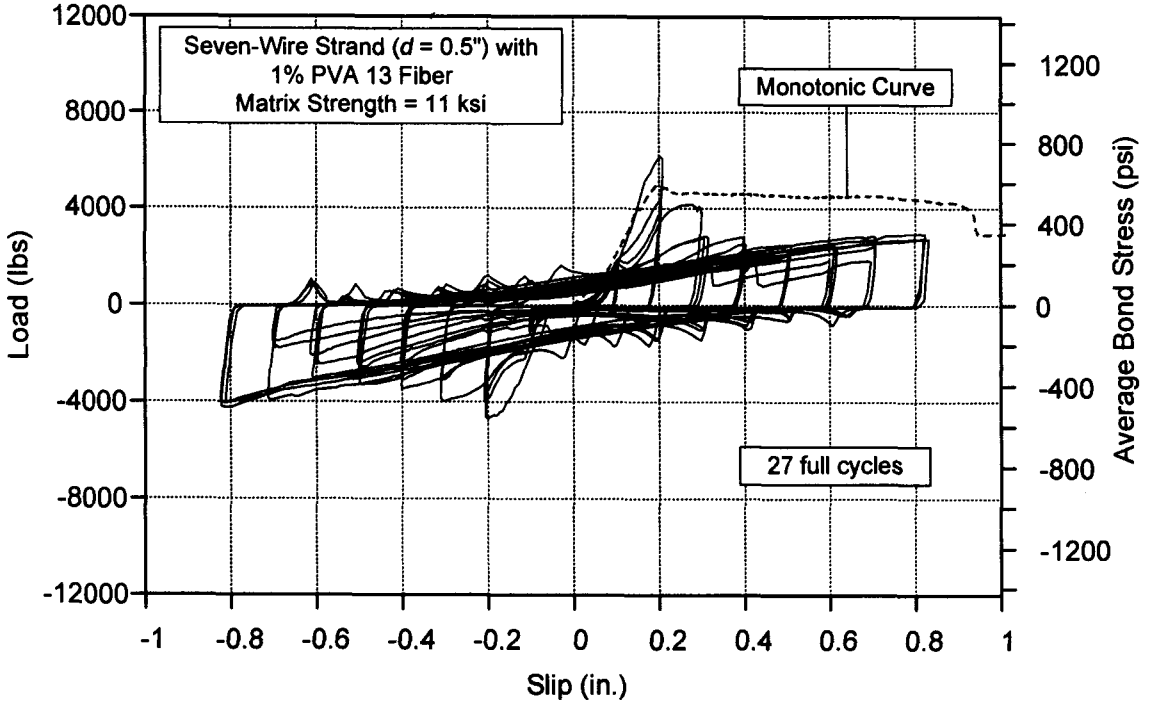

Figure 5.37 Load-slip curve for fully reversed displacement controlled cyclic loading: 0.5 inch strand, 1% PVA 13 fiber, 11 ksi matrix

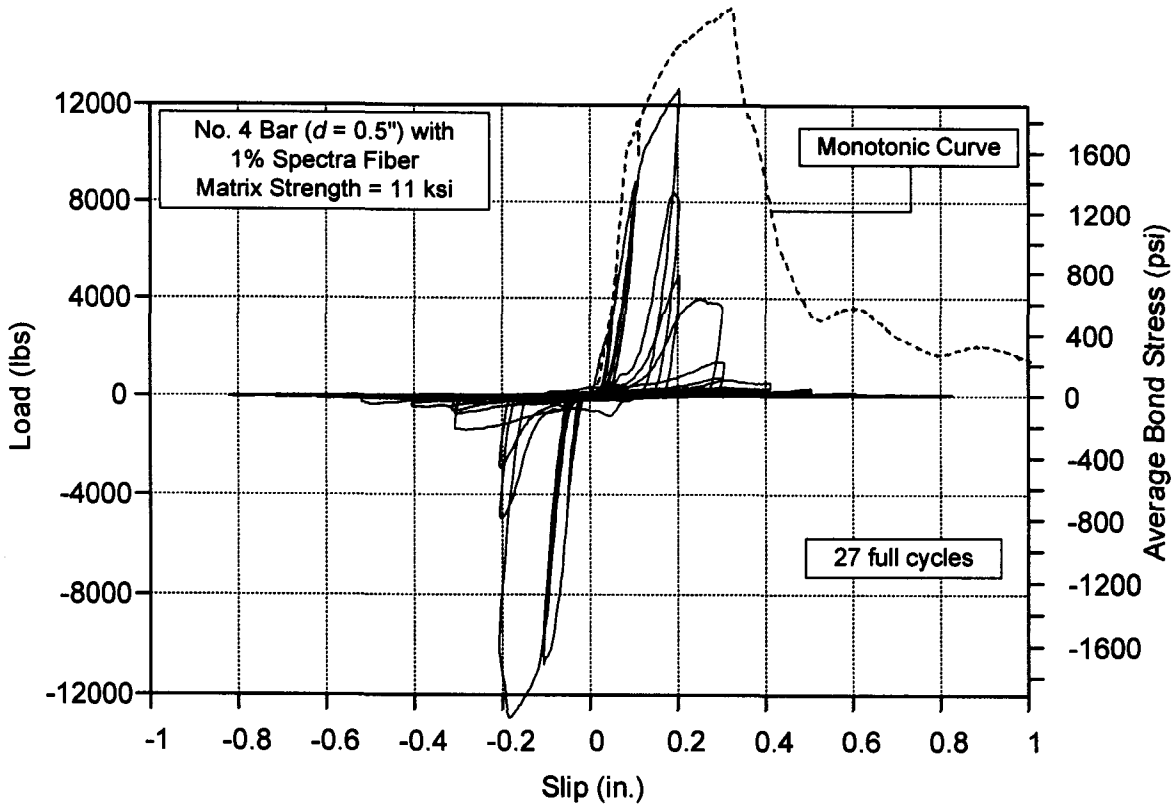

Figure 5.38 Load-slip curve for fully reversed displacement controlled cyclic loading: No. 4 bar, 1% Spectra fiber, 11 ksi matrix

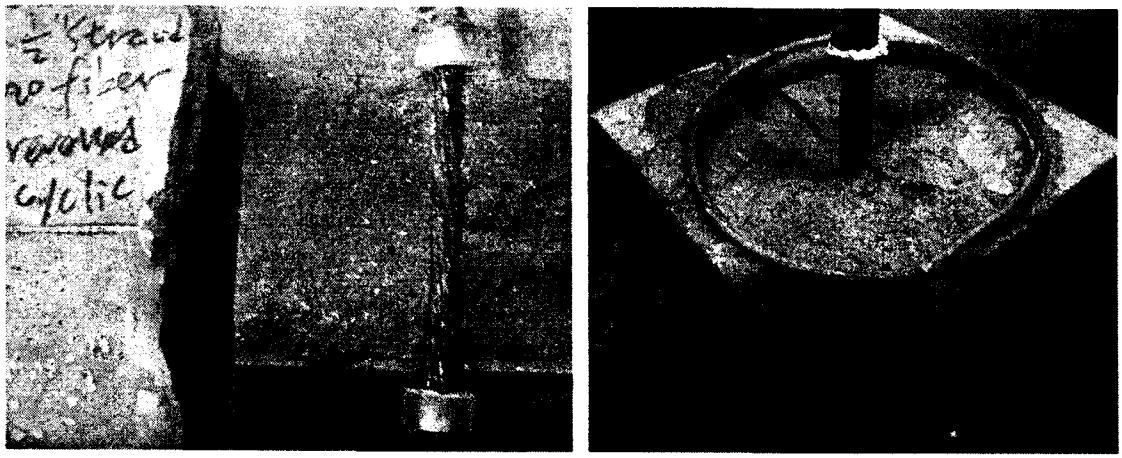

(a) (b)

Figure 5.39 Crack patterns of 11 ksi strand specimens subjected to fully reversed displacement controlled cyclic loading: (a) Control specimen; (b) 2% volumetric spiral reinforcement

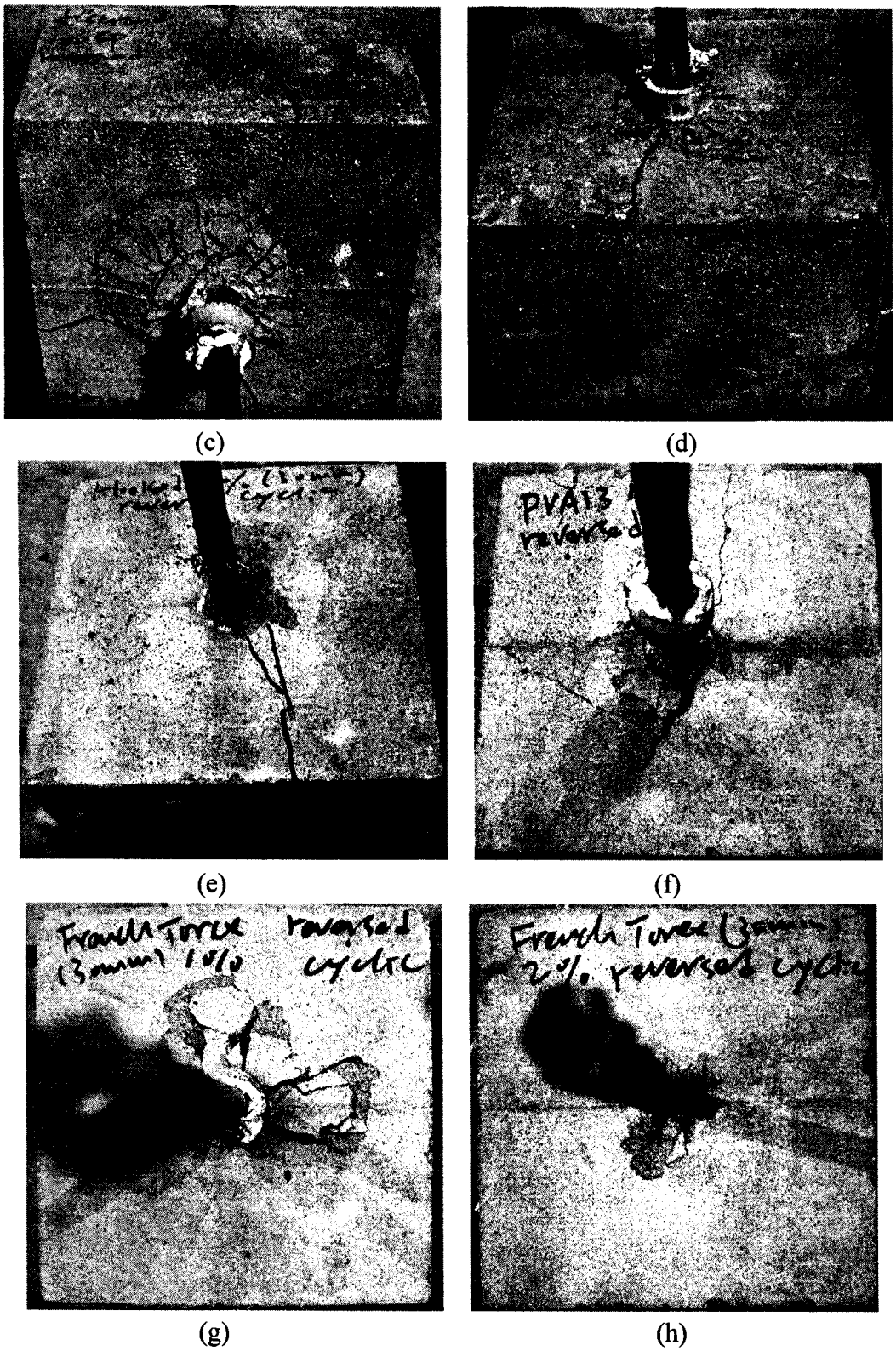

Figure 5.39 (continued) Crack patterns of 11 ksi strand specimens subjected to fully reversed displacement controlled cyclic loading: (c) 1% Spectra fiber; (d) 2% Spectra fiber; (e) 1% steel hooked fiber; (f) 1% PVA 13 fiber; (g) 1% rectangular Torex fiber; (h) 2% rectangular Torex fiber

(i) (j)

Figure 5.39 (continued) Crack patterns of 11 ksi strand specimens subjected to fully reversed displacement controlled cyclic loading: (i) 1% square Torex fiber (30 mm); (j) 1% square Torex fiber (20 mm)

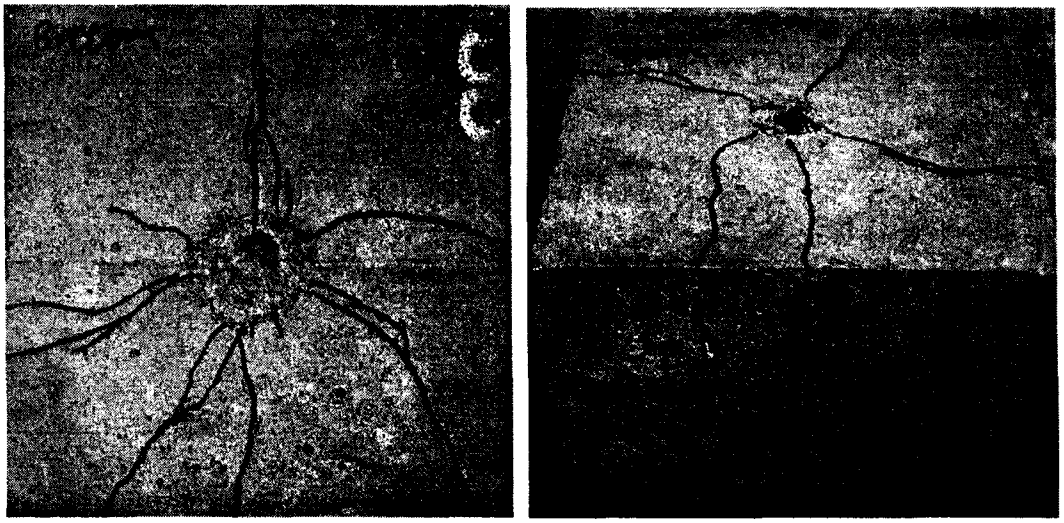

Figure 5.40 Crack patterns of No. 4 bar (0.5 inch diameter) specimens with 11 ksi matrix subjected to fully reversed displacement controlled cyclic loading

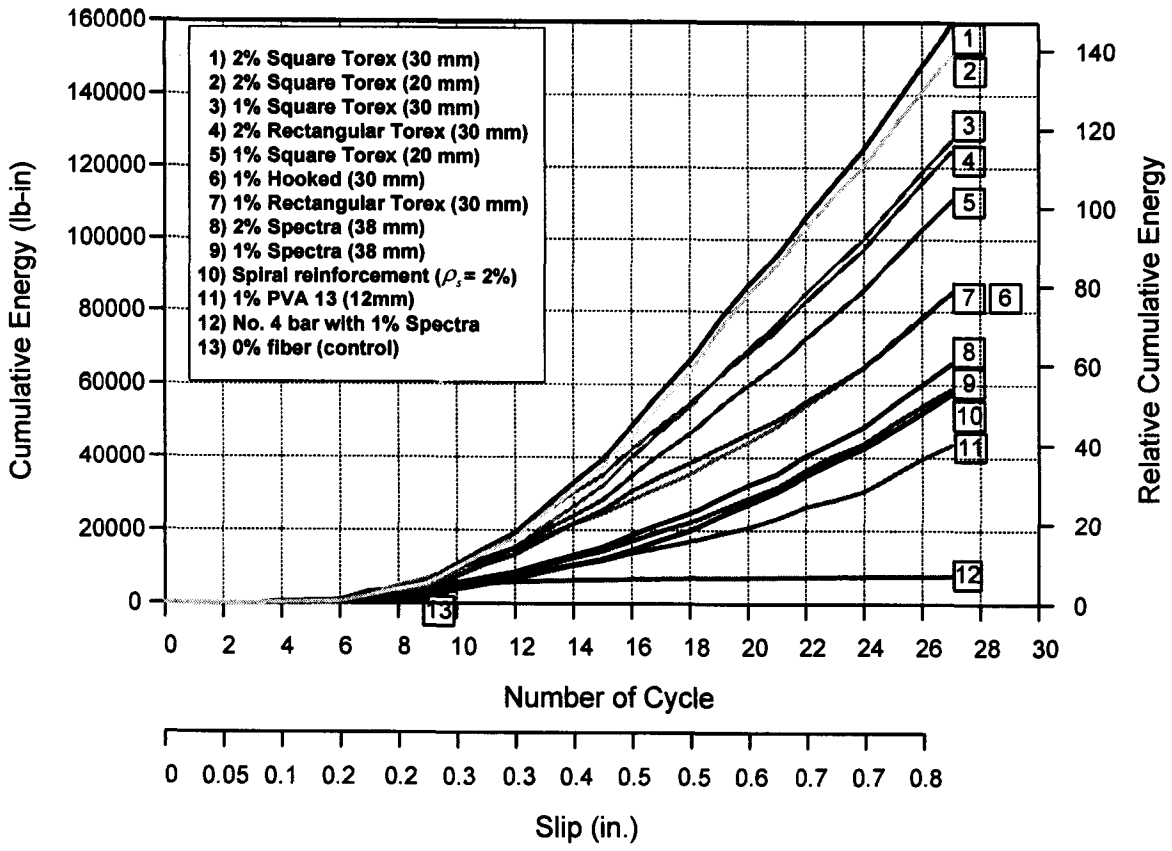

Figure 5.41 Comparison of energy-dissipation capacity

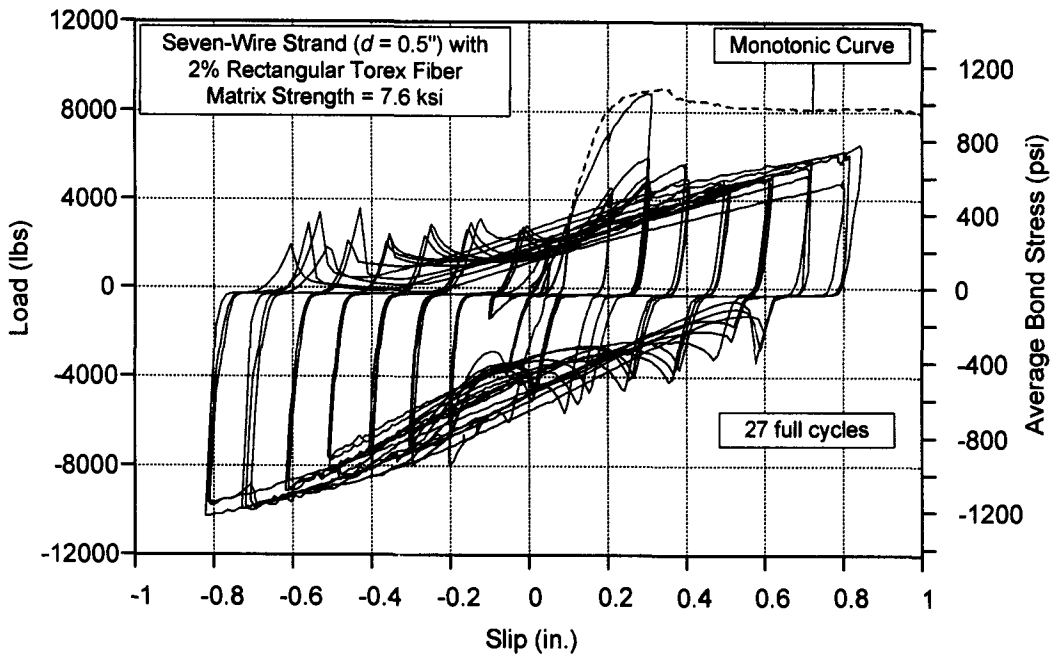

Figure 5.42 Load-slip curve for fully reversed displacement controlled cyclic loading: 0.5 inch strand, 2% rectangular Torex fiber, 7.6 ksi matrix

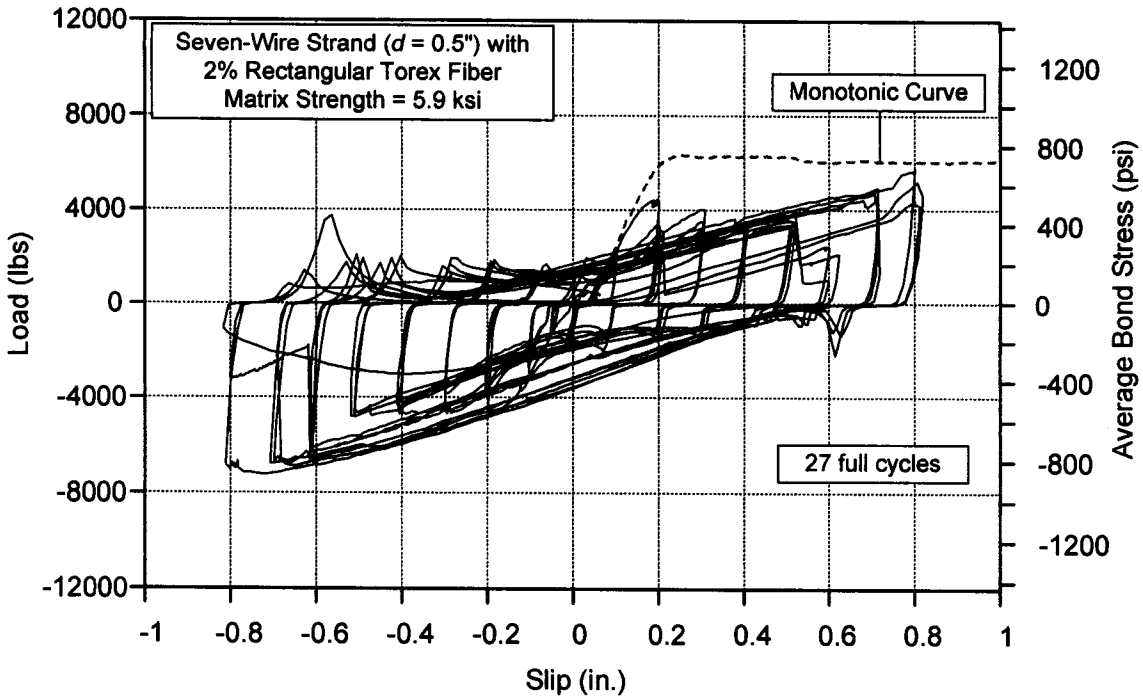

Figure 5.43 Load-slip curve for fully reversed displacement controlled cyclic loading: 0.5 inch strand, 2% rectangular Torex fiber, 5.9 ksi matrix

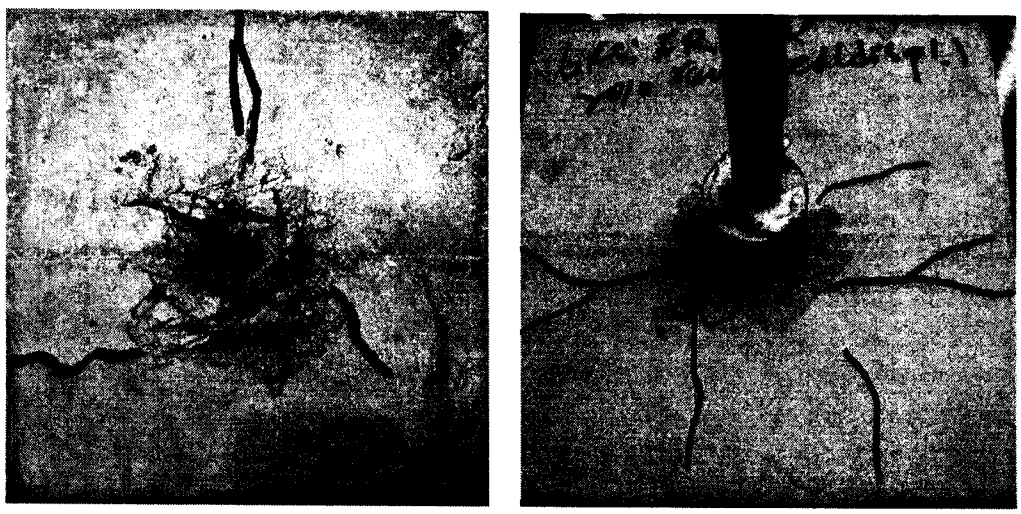

Figure 5.44 Crack patterns of strand specimens with 2% rectangular Torex fiber subjected to fully reversed displacement controlled cyclic loading: (a)7.6 ksi specimen; (b) 5.9 ksi specimen

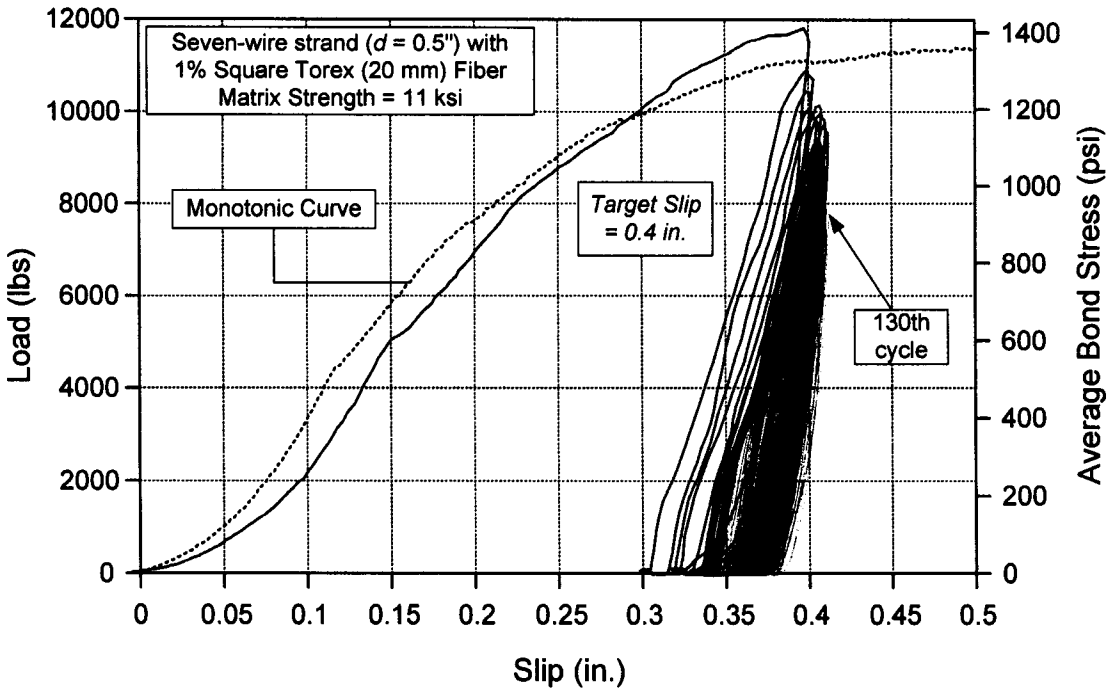

Figure 5.45 Unidirectional low-cycle fatigue test (displacement controlled test): 11 ksi specimen with 1% square Torex fiber (20 mm)

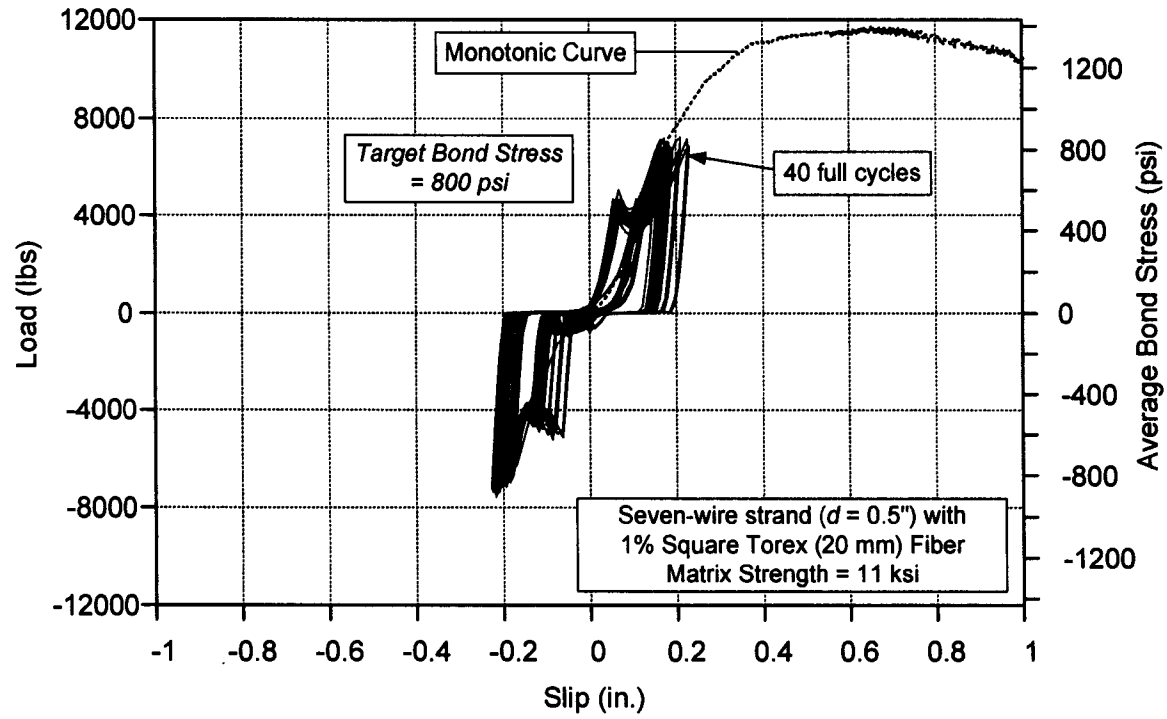

Figure 5.46 Fully reversed low-cycle fatigue test (force controlled tests, constant bond stress = 800 psi): 11 ksi specimen with 1% square Torex fiber (20 mm)

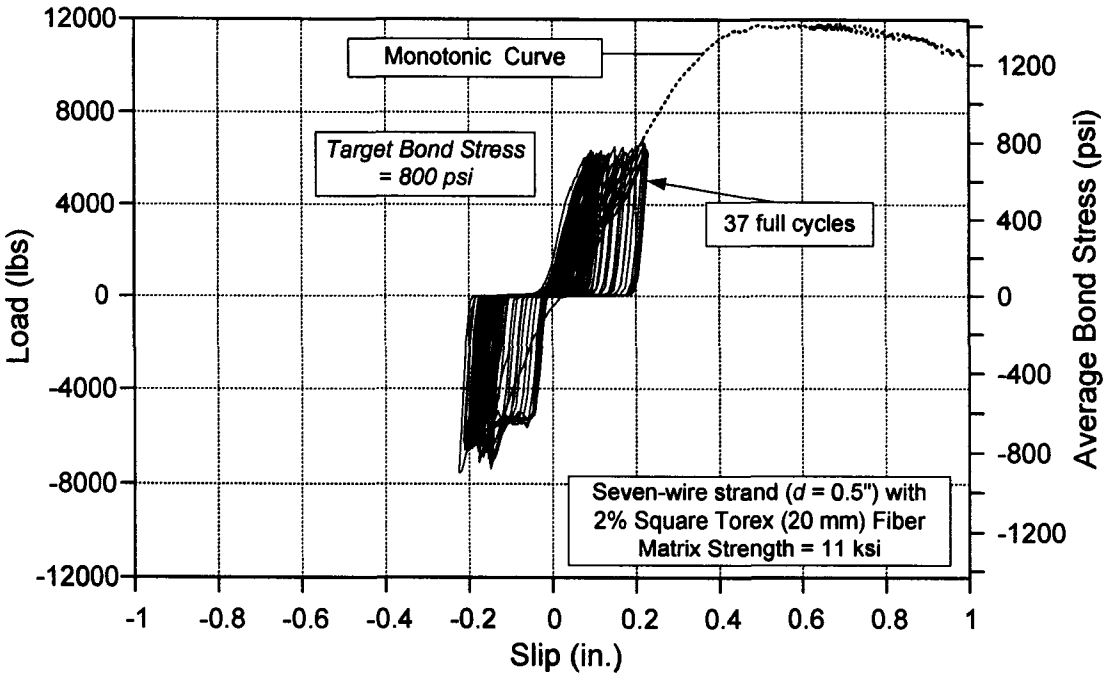

(a)

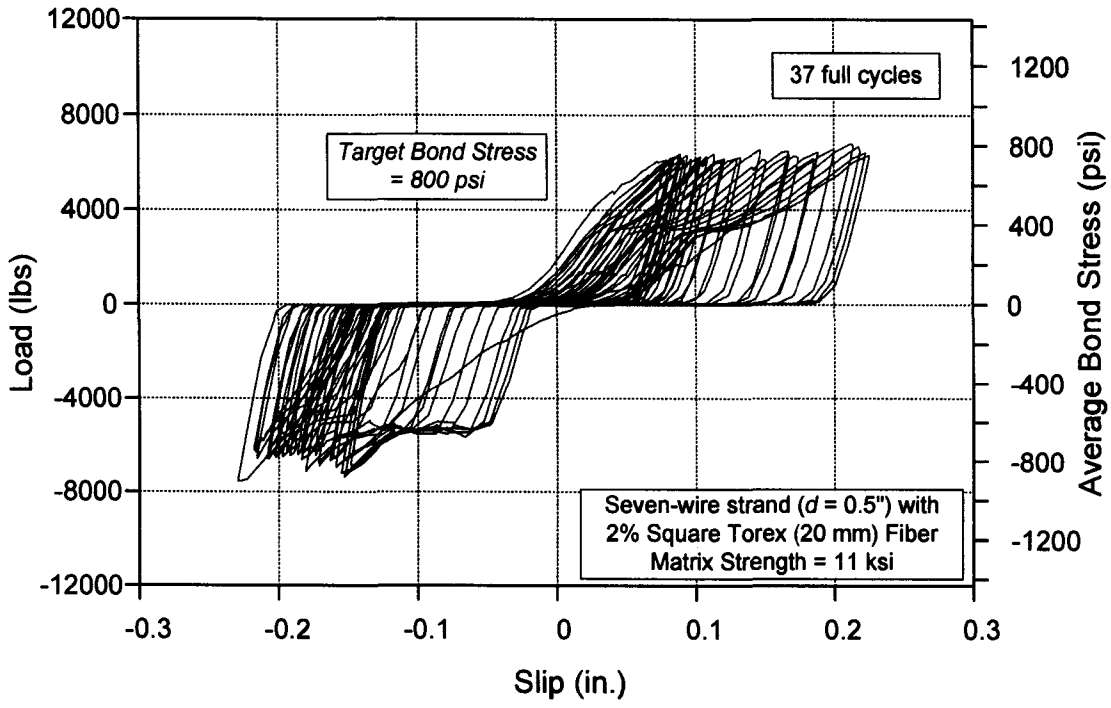

(b)

Figure 5.47 Fully reversed low-cycle fatigue test (force controlled tests, constant bond stress = 800 psi), 11 ksi specimen with 2% square Torex fiber (20 mm): (a) Hysteresis loops before strength degradation; (b) Enlarged load-slip response

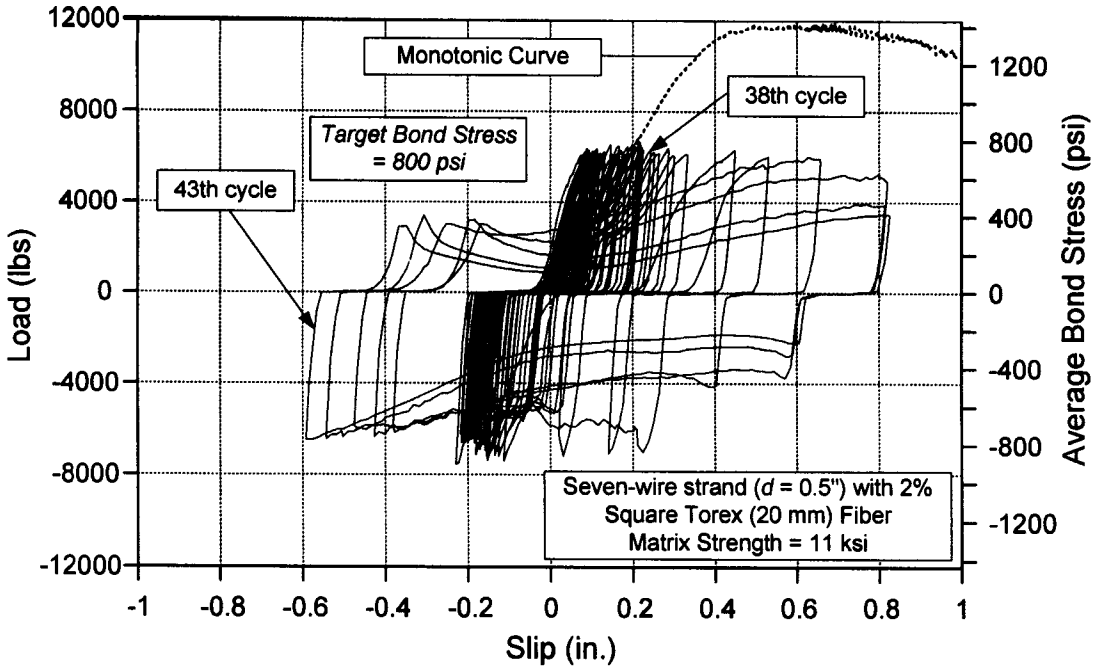

(c)

Figure 5.47 (Continued) Fully reversed low-cycle fatigue test (force controlled tests, constant bond stress = 800 psi), 11 ksi specimen with 2% square Torex fiber (20 mm): (c) Overall response

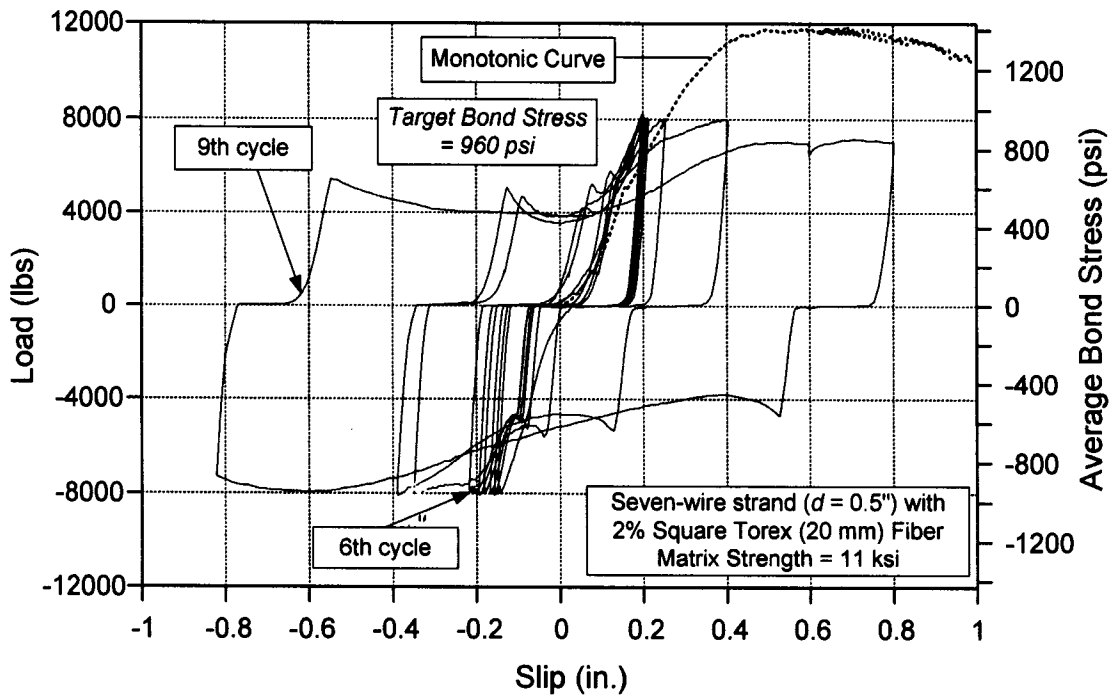

Figure 5.48 Fully reversed low-cycle fatigue test (force controlled tests, constant bond stress = 960 psi): 11 ksi specimen with 2% square Torex fiber (20 mm)

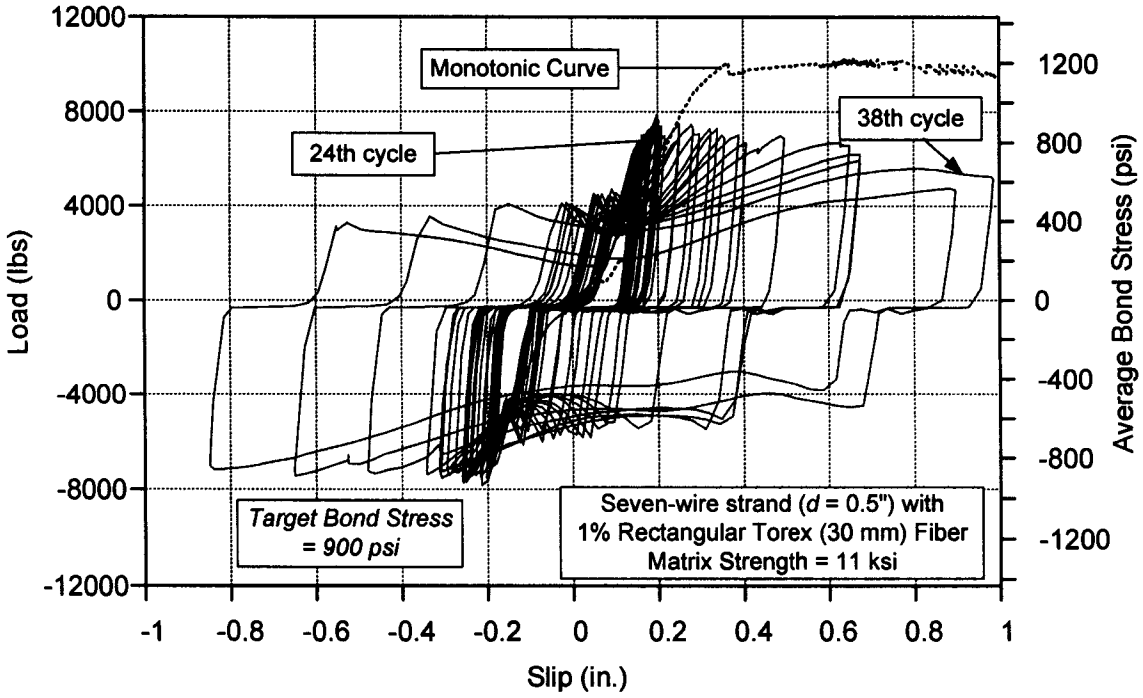

Figure 5.49 Fully reversed low-cycle fatigue test (force controlled tests, constant bond stress = 900 psi): 11 ksi specimen with 1% rectangular Torex fiber (30 mm)

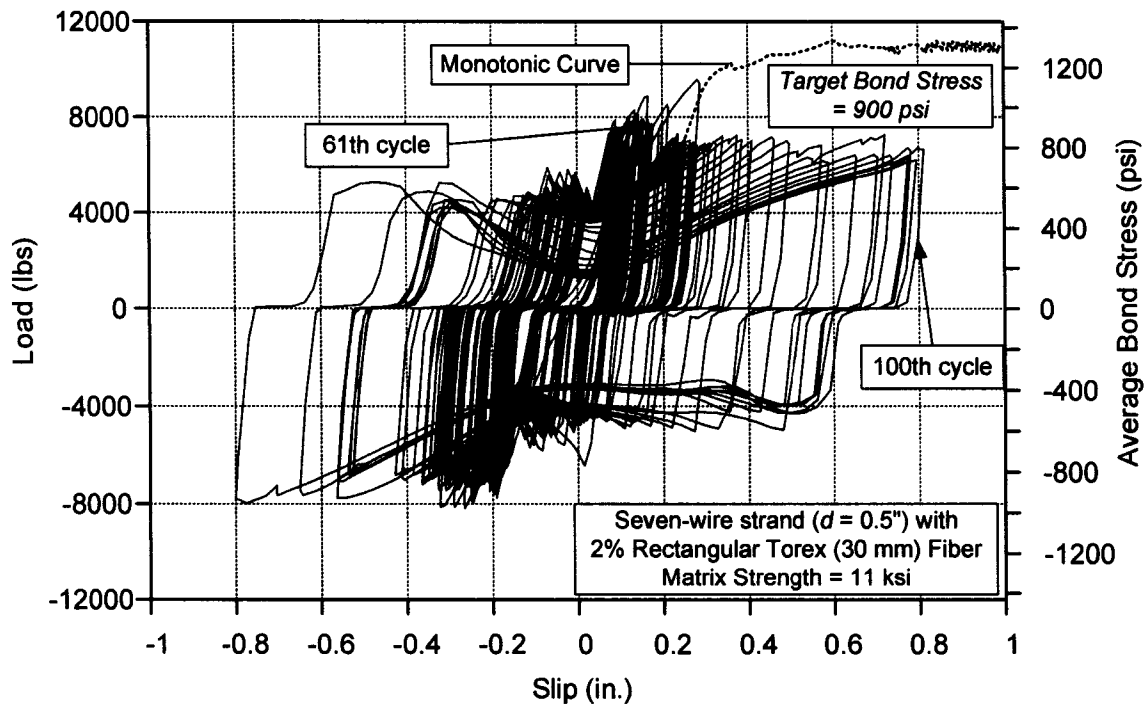

Figure 5.50 Fully reversed low-cycle fatigue test (force controlled tests, constant bond stress = 900 psi): 11 ksi specimen with 2% rectangular Torex fiber (30 mm)

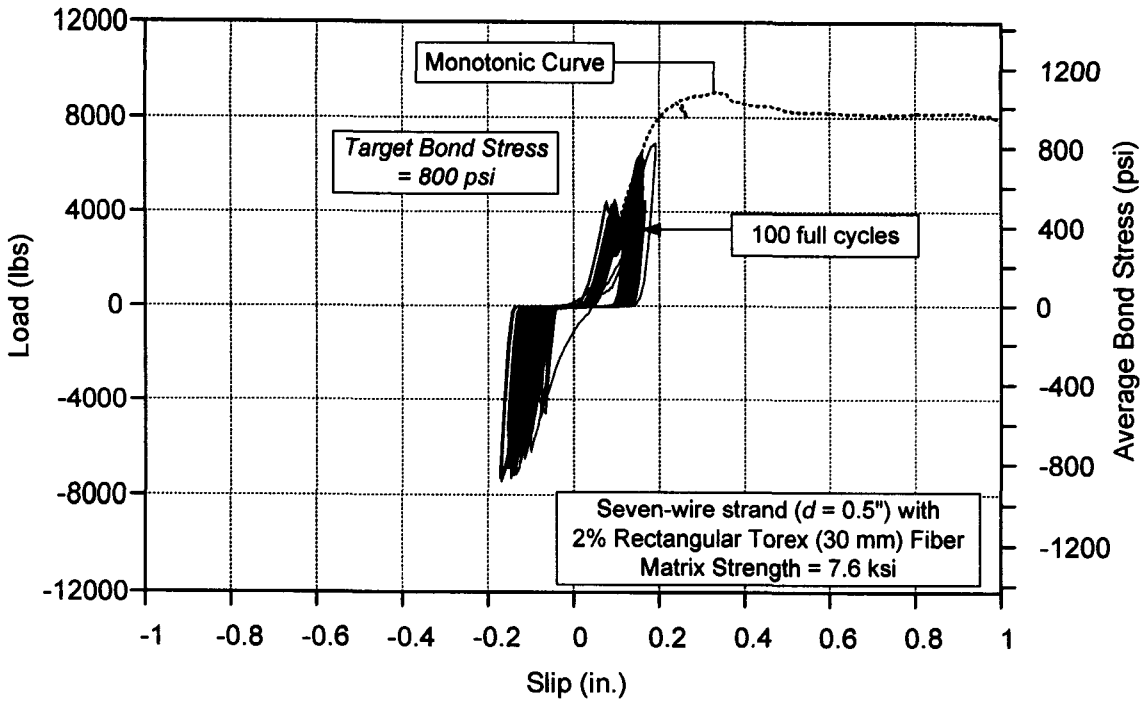

Figure 5.51 Fully reversed low-cycle fatigue test (force controlled tests, constant bond stress = 800 psi): 7.6 ksi specimen with 2% rectangular Torex fiber (30 mm)

Figure 5.52 Crack patterns of 11 ksi strand specimens subjected to low-cycle fatigue loading: (a) 1% square Torex fiber (20 mm), unidirectional test; (b) 1% square Torex fiber (20 mm), fully reversed test, target bond stress = 800 psi

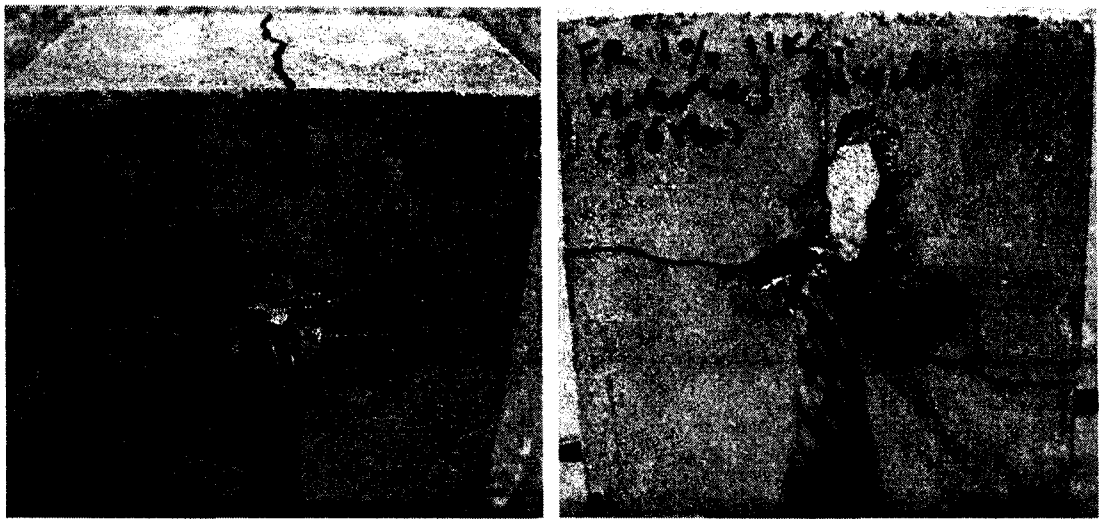

(c) (d)

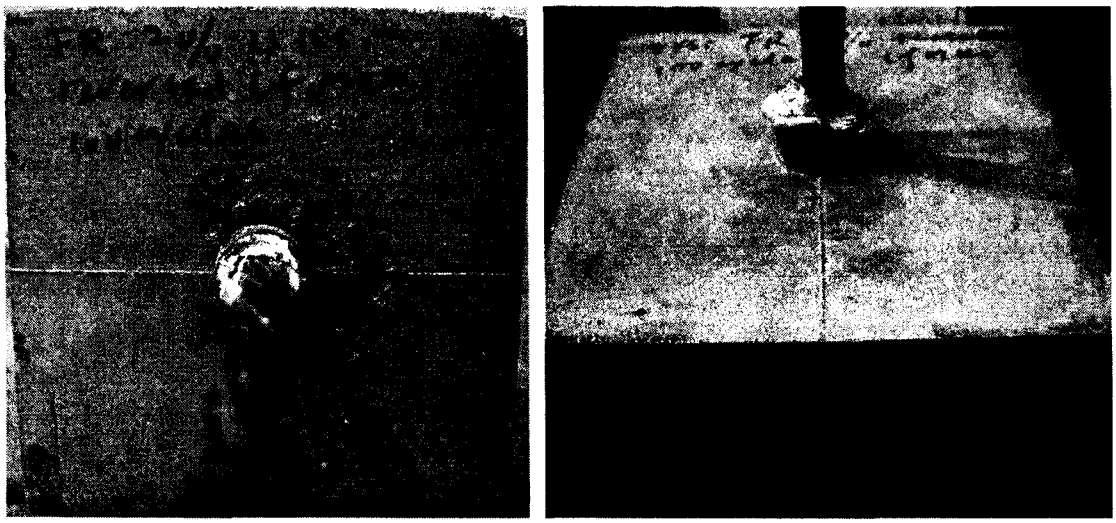

(e) (f)

Figure 5.52 (Continued) Crack patterns of strand specimens subjected to low-cycle fatigue loading: (c) 2% square Torex fiber (20 mm), fully reversed test, target bond stress = 800 psi; (d) 1% rectangular Torex fiber (30 mm), fully reversed test, target bond stress = 900 psi; (e) 2% rectangular Torex fiber (30 mm), fully reversed test, target bond stress = 900 psi, 11 ksi matrix; (f) 2% rectangular Torex fiber (30 mm), fully reversed test, target bond stress = 800 psi, 7.6 ksi matrix

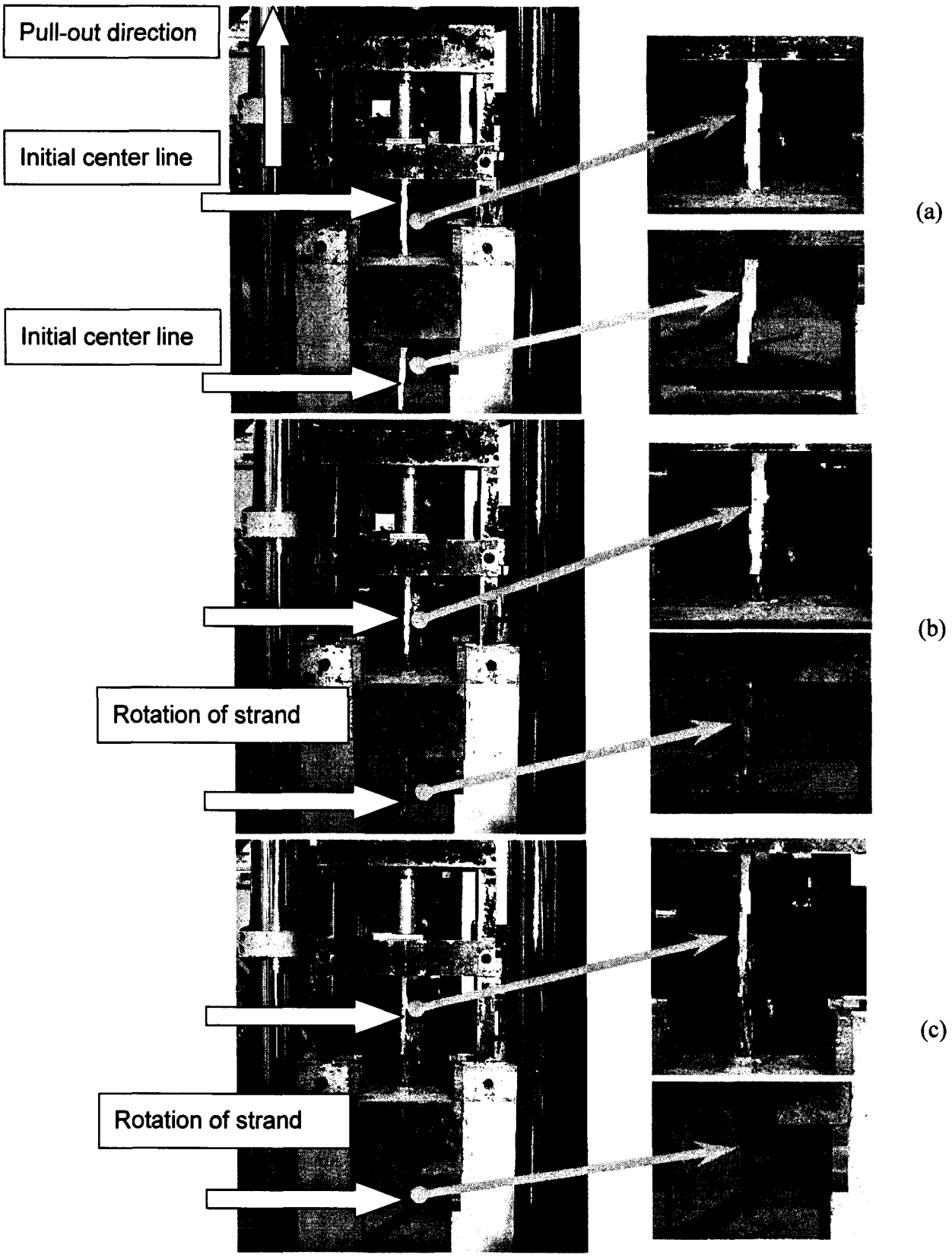

Figure 5.53 Rotation of strand during the pull-out process

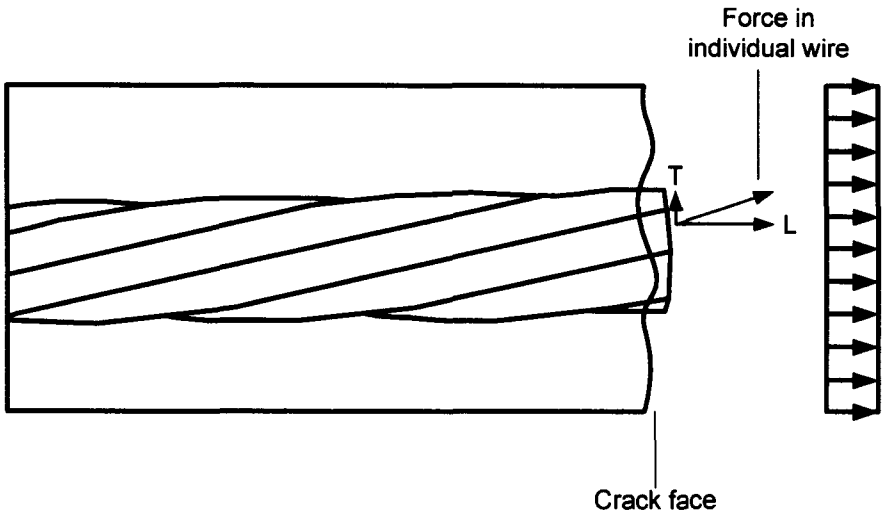

Figure 5.54 Illustration showing the internal force in an individual causing rotating action

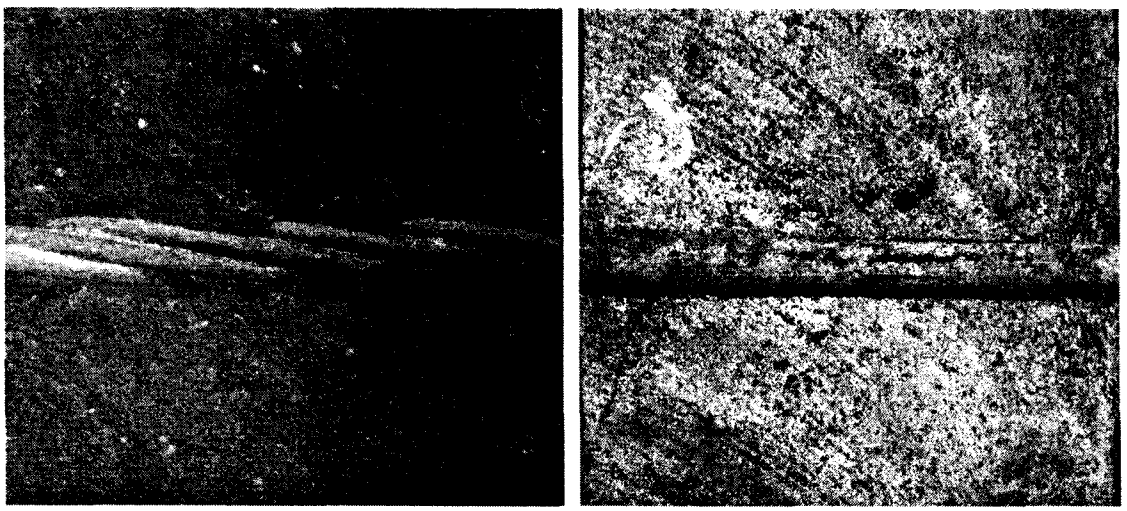

Figure 5.55 strand-to-matrix interfaces: (a) control specimen, 11 ksi matrix, monotonic loading; (b) 1% Spectra fiber specimen, 11 ksi matrix, fully reversed displacement controlled cyclic loading

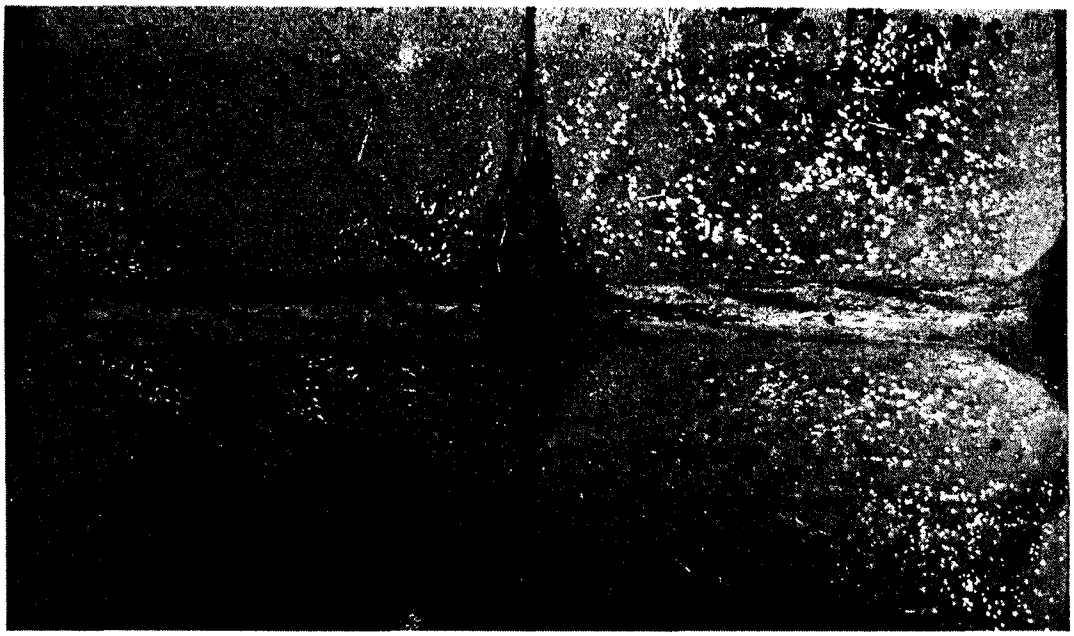

(c)

Figure 5.55 (continued) strand-to-matrix interfaces: (c) 2% rectangular Torex fiber specimen, 7.6 ksi matrix, fully reversed displacement controlled cyclic loading

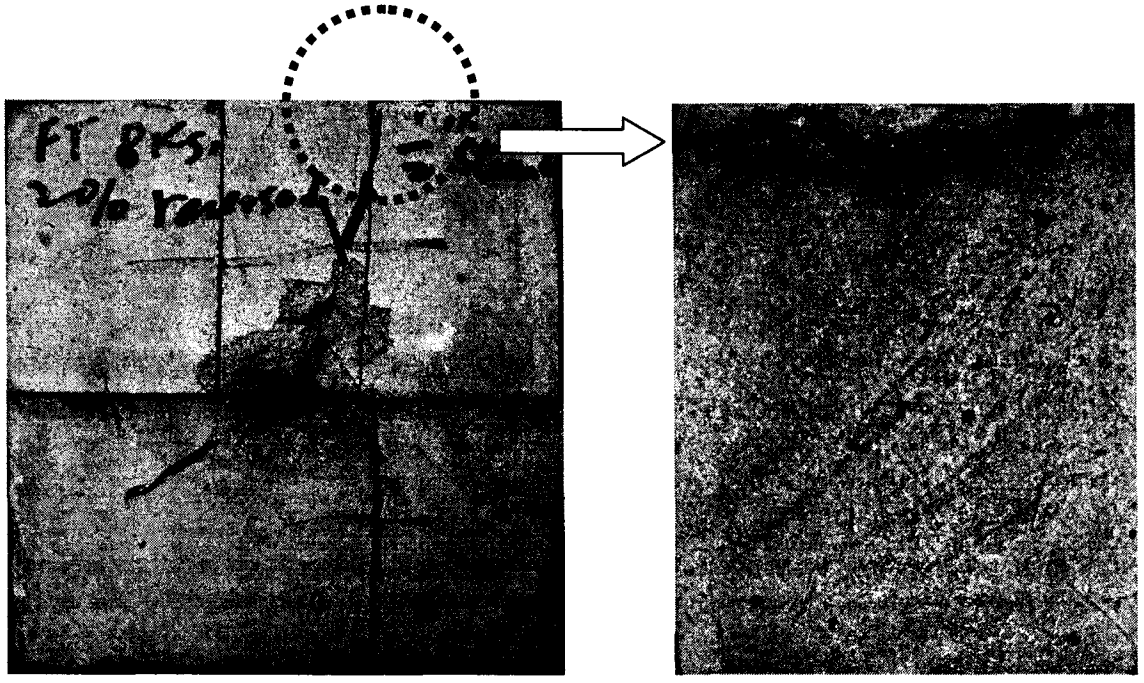

Figure 5.56 Cut section along a crack showing multiple cracking and crushing due to fiber pullout along the cracked surface: 2% rectangular Torex fiber specimen, 7.6 ksi matrix, fully reversed displacement controlled cyclic loading

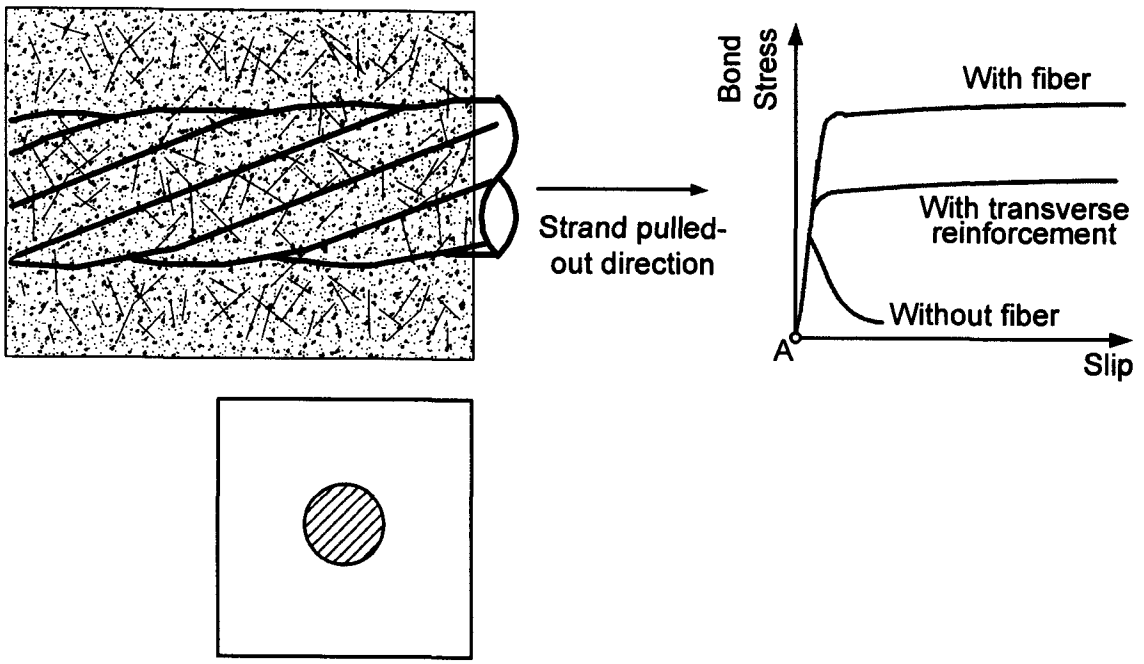

(a)

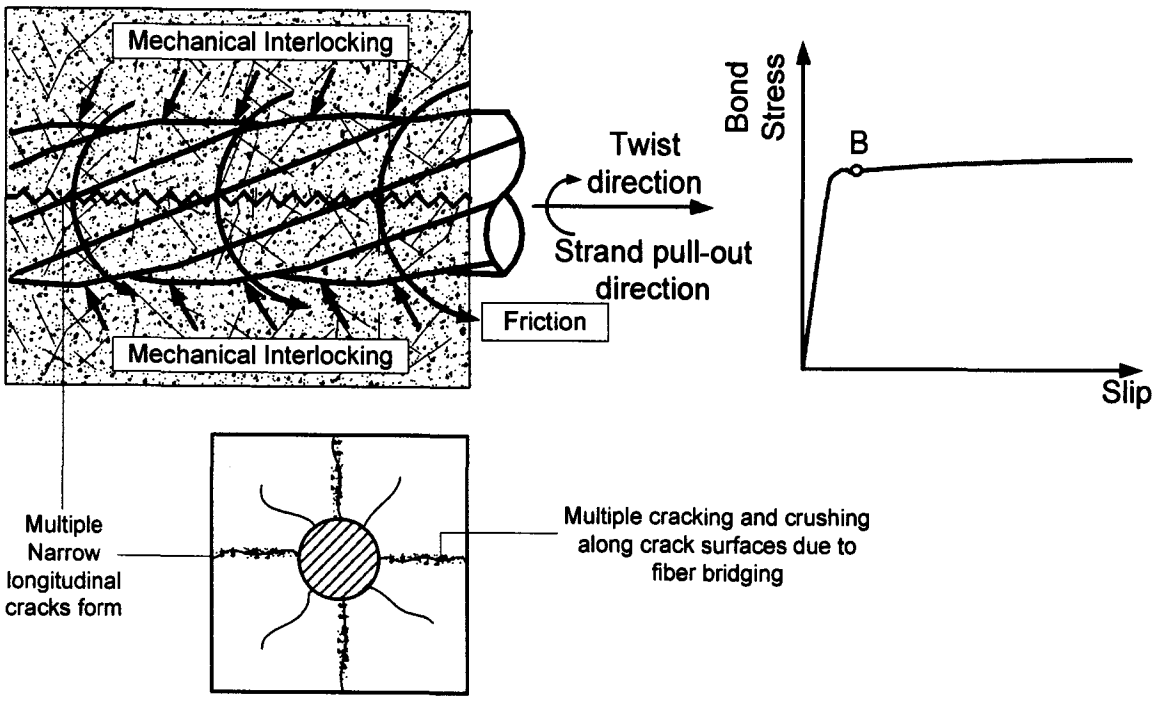

(b)

Figure 5.57 Bond mechanism of strand embedded in HPFRC composites

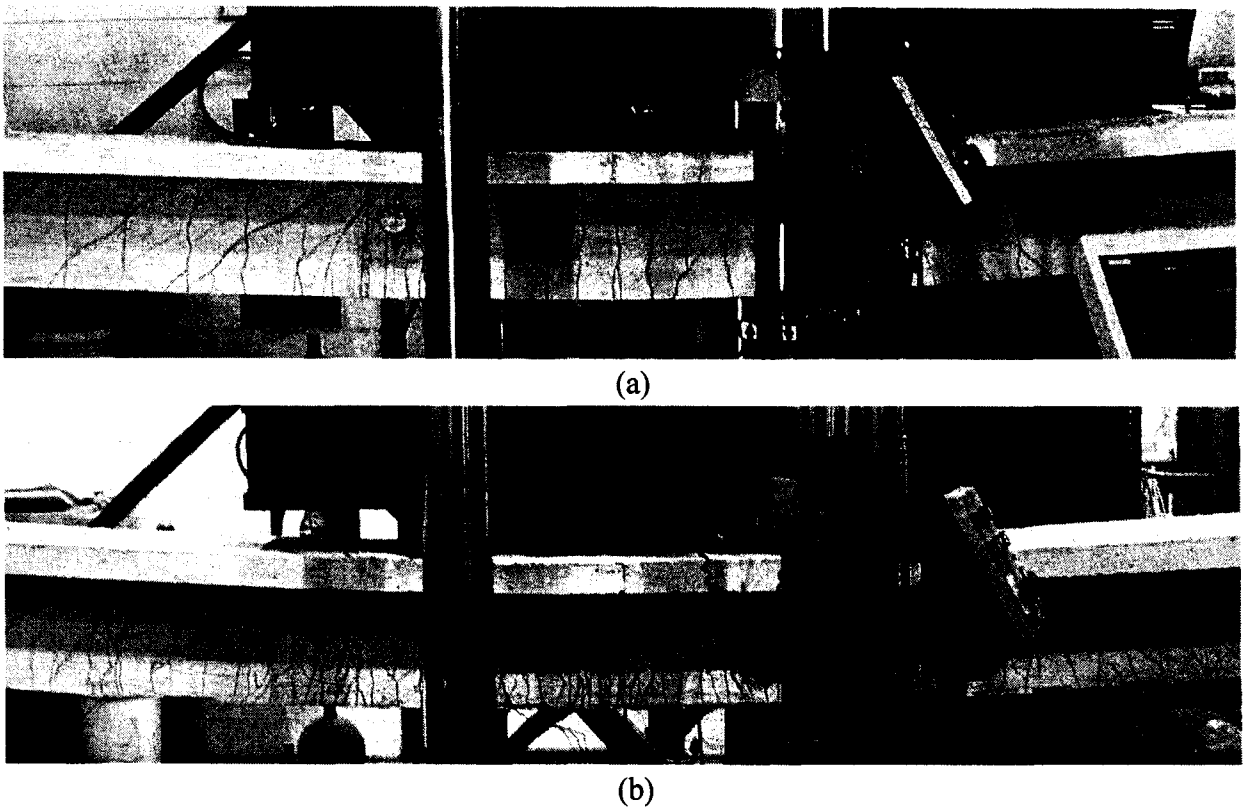

Figure 5.58 Comparison of crack development in: (a) conventional reinforced concrete beam; (b) HPFRCC beam with 2% rectangular Torex fiber (Chandrangsu and Naaman, 2005)

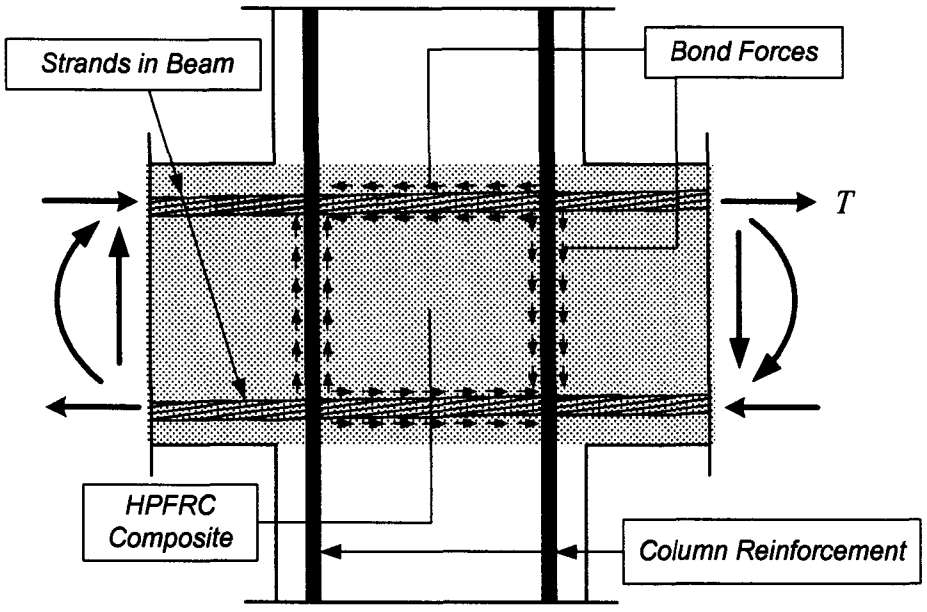

Figure 5.59 Possible application of non-prestressed strands in combination with HPFRCC material in seismic beam-column joint

CHAPTER 6

SECOND PHASE—EXPERIMENTAL PROGRAM AND RESULTS OF LARGE-SCALE HPFRCC BEAM-COLUMN JOINTS SUBJECTED TO DISPLACEMENT REVERSALS

6.1 Introduction

Reinforced concrete frames in high seismic zones are usually designed based on the concept of "strong column-weak beam", whereby plastic hinges form in the beams close to the column faces while the columns remain elastic, except at their bases, during a major earthquake. The moment gradient through the connection resulting from seismic induced loading leads to a high bond demand in beam and column bars passing through the joint. The deterioration in bond resistance in a beam-column joint subjected to displacement reversals is generally more severe than in other structural elements because reinforcing bars are under large inelastic cyclic strains and stresses (reinforcing bars will yield and enter strain-hardening due to formation of plastic hinges) and in some cases, under simultaneous pull-push action (reinforcing bars are pulled on one side of the joint and pushed on the other side in an interior beam-column joint, see Figure 1.4).

Anchorage of beam bars can be assisted by standard hooks in an exterior beam-column joint; however, this is impractical in an interior beam-column joint. To eliminate bar slippage in an interior beam-column joint, large joint dimensions would be required, which is usually not economical. From a large number of experimental tests

conducted on isolated interior beam-column joints, several unfavorable conditions for bond resistance were recognized (e.g. Paulay, Park, and Priestley, 1978; Viawathanatepa, Popov, and Bertero, 1979; Durrani and Wight, 1982; Ehsani and Wight, 1982; Popov, 1984; Leon, 1989; Paulay and Priestley, 1992). Those unfavorable conditions are summarized in Figure 6.1 and explained as follows:

1. Anchorage length can be reduced due to the formation of a cone-shaped fracture zone, as the one observed in Figure 4.106.

2. Bond resistance will further deteriorate after yielding of the longitudinal bars penetrates into the joint. This is because the bar diameter, and thus the lug height, decreases after the bar is stretched into yielding or strain-hardening, which in turn decreases the bearing area of the concrete and increases bearing stress demand. Complete loss of contact (bond resistance) could also result if a significant reduction in the bar cross section occurs. It has been shown by Viawathanatepa et al. (1979) that the reduction in bearing area can be as high as 25% when a bar goes into inelastic range in tension. Yield penetration has been considered one of the most serious causes of bond deterioration in a beam-column joint (Paulay, Park, and Priestley, 1978). The accompanying photo in Figure 6.1 shows a No. 4 bar after direct tensile testing. A decrease in the bar diameter along the inelastic portion can be observed. The dashed lines indicate the original boundary of the bar lugs.

3. Column bending induces tensile stresses and flexural cracking in the vicinity of the beam-to-column interface, which fosters the formation of longitudinal splitting cracks

along the beam bars.

4. Bond resistance can be further weakened by progressive crushing and growing of splitting cracks (Goto cracks) in front of bar lugs, as well as extensive diagonal tensile cracking in the joint for the two loading directions.

The combination of the above unfavorable conditions leads to an effective anchorage length that could be much shorter than the column width, which in turn raises the bond demand and further bond deterioration and bar slippage. Under poor bond conditions, bar tensile stresses might extend to the other side of the joint, putting the beam compression steel in tension. This leads to a reduction in flexural strength and ductility of the connection (Paulay and Priestley, 1992; Hakuto, Park, and Tanaka, 1999). Slippage of reinforcing bars through the joint also causes concentrated rotations at the column faces, which may lead to significant stiffness decay and "pinching" in the hysteretic response of the structure. It has been experimentally shown that, when bond loss occurred, up to 35% of the total displacement of a beam-column subassemblage resulted from bar slippage (Soleimani, Popov, and Bertero, 1979). Besides, analysis has shown that the energy dissipation capacity of a beam-column joint would decrease by 30% if a 15% reduction in bond strength along a bar occurs (Filippou, Popov, and Bertero, 1983). All these research results demonstrate the significance of bond in beam-column connections on overall structural performance, especially under large displacement reversals.

Because current design recommendations for anchorage length of straight beam bars

embedded in an interior beam-column joint, such as 20 bar diameters recommended by ACI-ASCE Committee 352 (2002), is not likely to prevent bars from slippage (Leon, 1989), bond deterioration and bar slip in connections of reinforced concrete frames are anticipated during a major earthquake. Unfortunately, as reported by Engindeniz et al. (2005), current repair techniques are still not able to reliably restore the destroyed bond in a beam-column joint. For example, epoxy injection has been one of the most popular methods for repairing damaged reinforced concrete members. However, damaged beam-column joints are usually not readily accessible due to the presence of transverse beams and floor slab, which increases the difficulty in injecting epoxy into the joint cracks. Limited success in restoring bond using this method has been demonstrated through experimental tests (Engindeniz, Kahn, and Zureick, 2005).

In this investigation, the use of HPFRCC materials was evaluated as a means to enhance bond resistance and to reduce bar slippage in RC beam-column joints subjected to large displacement reversals. In addition, the use of HPFRCC materials in connection regions would enhance joint damage tolerance and could allow significant relaxations in transverse reinforcement requirements. As has been seen in Figure 6.1, most of the unfavorable conditions for bond resistance are related to the cracking and fracture of concrete, such as cone-shaped fracture at the column faces, splitting and internal inclined cracks along beam bars, and diagonal tensile cracking in the joint. It has been shown in Chapter 3 and Chapter 4 that, due to the fiber bridging effect, HPFRC composites usually maintain their integrity and exhibit multiple fine cracks when subjected to large tensile strains. Extension and propagation of cone-shaped fracture, internal inclined cracks along bars, and splitting cracks are constrained due to the presence of fibers. Experimental

results discussed in Chapter 4 also showed the high toughness of HPFRCCs, even when subjected to fully reversed cyclic loading. For example, as shown in Figure 4.79, a 2% square Torex fiber specimen was able to sustain 25 fully reversed cycles of high bond stress (1350 psi) without degradation of bond strength and stiffness. Thus, it is highly likely that the use of HPFRCCs in beam-column connections would lead to an increase in bond resistance with the corresponding decrease in penetration of bar yielding in to the connection, even at large bar inelastic strains.

In view of the potential advantages of HPFRCC materials in preventing or delaying bond deterioration, as well as in enhancing joint damage tolerance, two large scale beam-column subassemblies with HPFRCC materials placed in the joint and beam plastic hinge regions were designed, constructed, and then tested under large displacement reversals. Besides enhancing bond resistance, two additional benefits were sought: 1) total elimination of joint confinement (transverse) reinforcement while maintaining comparable shear strength; 2) increased stirrup spacing in beam plastic hinge zones. These two goals, if achieved, would largely reduce the congestion of reinforcement due to current practices and facilitate the construction of reinforced concrete frames. The results from these tests have been reported elsewhere (i.e. Parra-Montesinos, Peterfreund, and Chao, 2005) and thus, only the main aspects related to bond performance are discussed in this chapter.

6.2 Experimental Program

Two approximately 3/4-scale beam-column subassemblies were tested under large

displacement reversals. HPFRCC material, due to its superior damage tolerance, was used to replace conventional concrete in the beam-to-column connection region. As shown in Figure 6.2, the proposed scheme placed the HPFRCC material in the beam-to-column joint and the adjacent beam regions (over a length of two times the beam depth). Regular concrete was used in the remaining portions of beams and columns.

6.2.1 Material Properties

As shown in Chapter 4, the HPFRCC material with Torex fibers (especially 2% by volume) exhibited better cyclic performance than the HPFRCC material with Spectra fibers in terms of bond stress-slip response and dissipated energy. Nevertheless, because of the limited availability of Torex fibers, the HPFRCC material used in the connection specimens contained Spectra fibers (see Table 3.2 for fiber properties). The mixture composition and the average compressive strength of this HPFRCC material are listed in Table 6.1. Direct tensile tests on dogbone shaped specimens (see Figure 3.3 (a)) were performed to determine the tensile properties of the HPFRCC material. A typical tensile stress versus strain response is shown in Figure 6.3 (a). As can be seen, a strain-hardening tensile behavior was maintained up to 1% strain with a peak tensile strength of about 370 psi. Beyond 1% strain, due to damage localization, tensile softening started to occur. The tensile strength was approximately 220 psi when a strain of 2% was attained. Figure 6.3 (b) shows the multiple cracking pattern in the test dog-bone specimen.

The regular concrete used outside the HPFRCC region was obtained from a local ready-mix concrete supplier, with a specified compressive strength of 5 ksi and a 6 in.

slump. The ingredients included Type I cement, fine aggregates (ASTM C-33), 3/8 in. maximum size limestone, and water. The actual average compressive strength obtained from 4×8 in. cylinders was 6.3 ksi and 6.0 ksi for Specimens 1 and 2, respectively.

No. 6 reinforcing bars with a nominal yield strength of 60 ksi were used for both column and beam longitudinal reinforcement. Actual tensile yield and ultimate strengths were obtained by testing bar samples in a Baldwin static test frame, as shown in Figure 6.4 (a). An extensometer was attached at mid length of the test bar to measure the strains. Average stress-strain curves for No. 6 bars used in Specimens 1 and 2 are given in Figure 6.4 (b). Since both specimens exhibited a sharp-kneed stress-strain diagram, the yield point can be taken at the top of the knee (ASTM A 370, 2003). The corresponding yield strengths were 79.3 ksi and 64 ksi for the No. 6 bars used in Specimens 1 and 2, respectively.

6.2.2 Specimen Design, Construction, Casting, and Instrumentation

6.2.2.1 Specimen Design

The overall specimen dimensions are shown in Figures 6.2 and 6.5. The design of these two beam-column subassemblies followed a "strong column-weak beam" principle and the ratios of nominal column moment strength to ultimate beam moment strength were 2.2 and 1.6 for Specimens 1 and 2, respectively (see Table 6.2 for details). The beam cross section was 6 in. wide and 14 in. deep, and the column cross section was 14×14 in. This gave an anchorage length equal to $18.7\,d_b$ (d_b = 0.75 in. for No. 6 bar) for

beam and column bars passing through the connection. Note that the required minimum anchorage length, based on ACI Code requirements (2005), should be $20d_b$. In other words, the anchorage length provided was approximately 93% of the ACI requirement. In addition, no confinement steel was provided in the test specimens in the joint region, where closely spaced hoops are usually required to provide joint confinement. Besides, the transverse reinforcement in the beam plastic hinge regions was designed only in accordance to Chapter 11 of the ACI Code and thus, none of the special provisions in Chapter 21 of the ACI Code (Special Provisions for Seismic Design) were applied. Multiple fine cracks were anticipated in the beam plastic hinge and joint regions by using an HPFRCC material, even though much less or even no transverse reinforcement was used in the beam plastic hinge and connection regions, respectively.

All the above factors gave a very stringent environment for bond resistance in the beam-column joint region, that is: extensive beam yielding (plus material overstrength in steel), short anchorage length, and no confinement steel. The final design and detailing of the test specimens is given in Figure 6.5. From this figure, it can be seen that four No. 3 bars were placed between the top and bottom longitudinal beam bars in the joint region. These intermediate layers of longitudinal reinforcement were provided to shift the beam plastic hinging zone somewhat away from the column face and thus, limit bar yielding penetration in the connection (Abdel-Fattah and Wight, 1987). In addition, these bars would provide a reinforcement "grid" in the connection, which would enhance cracking distribution. As indicated in Figure 6.5, the intermediate bars extended into the beam over a length of 8 in. in Specimen 1, while the projection length was only 3 in. in Specimen 2, which would lead to a more unfavorable environment for bond resistance compared to

Specimen 1.

6.2.2.2 Strain Gage Installation

Calculation of stress developed in the longitudinal reinforcement is essential for the evaluation of bond stress distribution in the joint region. Bar stress can be obtained from the strain data measured by linear electrical resistance strain gages attached to the surface of steel reinforcement through the use of material constitutive models. It should be mentioned that, in order to measure strains with a minimum of interference with bond resistance, a special technique has been used by previous researchers (e.g. Viwathanatepa et al., 1979; Hamza, 1992). As illustrated in Figure 6.6, longitudinal grooves are machined into the bar. The strain gages are then attached at the bottom of the grooves through an adhesive. Waterproof material is applied to protect the strain gages from fluid concrete, and then the grooves are covered by a strip of steel. However, in this study, strain gages were simply attached to the bar surfaces without using the aforementioned particular technique. As shown in Figure 6.7, in order to attach the strain gages, the bar surface was first ground and sanded until a smooth surface was obtained. The strain gage was then attached to the ground surface using a special adhesive that can accommodate the large deformations that result from bar yielding. Two layers of coating and a rubber tape were applied on top of the strain gages for protection. It was anticipated that the bond resistance could be somewhat affected at the locations of the strain gage due to grinding and use of rubber tapes. Therefore, bond strength was likely underestimated. The locations of strain gages on the longitudinal beam bars are shown in Figures 6.8 and 6.9 for Specimens 1 and 2, respectively. Note in Figure 6.8 (a) that the BTS series had a

relative short spacing between mounted strain gages, which could accelerate the loss of bond in the joint.

6.2.2.3 Specimen Construction and Casting

After the installation of strain gages was completed, the steel reinforcing cage was built and placed inside plywood forms, as shown in Figure 6.10. The HPFRCC region was separated from the regular concrete portion by four Styrofoam pieces (See Figure 6.11). Figure 6.12 gives a close-up view of the reinforcement in the joint region, where no transverse (confinement) steel was provided. The specimens were then cast in a horizontal position. The HPFRCC materials were poured first and the ready-mix concrete was cast after the HPFRCC portion had hardened and the Styrofoam pieces removed. Figures 6.13 thru 6.17 show the casting process of the specimens. An electrical vibrator was used to increase the compactness for both the HPFRCC material and the regular concrete, as shown in Figure 6.13. As shown in Figure 6.17, four cold joints were present at the interfaces between the HPFRCC and regular concrete regions (beam and column). However, no particular treatment, such as surface roughening, was applied at these locations. It should be noted that because floor systems are typically constructed separately from the columns, the pouring of HPFRCC materials in the joint and adjacent beam regions does not interfere with the concrete placement in the columns.

6.2.2.4 Other Instrumentation

One side of the beam-column joint was instrumented with potentiometers that were

positioned horizontally, vertically, and diagonally to record joint distortion, as shown in Figure 6.18. In addition, as can bee seen in Figure 6.19, potentiometers were placed at the top and bottom of both beams (east and west) to monitor beam plastic hinge rotations, as well as beam concentrated rotations at column faces due to slippage of beam bars. The procedure to measure bar slippage through the joint is described in Figure 6.20. Two parallel potentiometers were attached to the beam face with threaded rods. One of them measured the total deformation over an 11.75 in. gage length (up to column face), while the other monitored the total deformation over a 10.5 in. gage length. As shown in Figure 6.20 (b), the difference between the two measured data can be taken as the slip value, although some contribution may result from the deformation of the HPFRCC material in the 1.25 in. range due to beam flexure.

6.2.3 Testing Procedure

Reversals of displacement were applied at the top of the column through a hydraulic actuator (Figure 6.2). The loading history, shown in Figure 6.21, comprised displacement cycles ranging from 0.5% to 6.0% drift (lateral displacement/column height), with two cycles performed at each new drift level. The applied load and displacement were monitored through a load cell and LVDT built in the hydraulic actuator, respectively. It is worth mentioning that, as illustrated in Figure 6.2, a small axial load, approximately 4% of column axial load capacity, was applied to the column through two hydraulic jacks and prestressing cables. It has been experimentally shown (Meinheit and Jirsa, 1981) that, when the applied axial load is increased, shear cracking strength in beam-column connections is increased. To simulate a more adverse condition in which column axial

forces are significantly reduced due to overturning moment induced by seismic action, only a small axial force was applied to the columns of the test specimens.

6.3 Bond Stress Calculation

If the stress distribution in a reinforcing bar under cyclic loading is obtained, the average bond stress distribution can be calculated as:

$$\text{Average Bond Stress} = \frac{\Delta\sigma_s \cdot A_s}{\Sigma_o \cdot \Delta x} \qquad [6.1]$$

where $\Delta\sigma_s$ is the change in steel stress over a distance Δx, and A_s and Σ_o are the cross-sectional area and perimeter of the reinforcing bar, respectively.

In order to determine average bond stress from Equation [6.1], it is necessary to determine steel stresses from strain measurements obtained during testing via strain gages. This is done by means of appropriate mathematic hysteretic stress-strain model, suitable for reinforcing bars in particular. To accurately capture the cyclic stress-strain behavior of a steel reinforcing bar, several essential characteristics need to be accounted for (CEB, 1996): Bauschinger effect, isotropic strain hardening under plastic strain reversals, and cyclic strain softening (see Figure 6.22). Numerous models have been proposed to date, the most successful one likely being the Menegotto-Pinto model (Menegotto and Pinto, 1973), in which the loading and unloading response branches are easily manipulated by a few parameters. Based on the Menegotto-Pinto equation, several revised models have

been proposed and calibrated using test data by different researchers, such as Stanton and McNiven (1979), Filippou et al. (1983), and Chang and Mander (1994). Recently, Sakai and Kawashima (2003) pointed out that the Menegotto-Pinto model often develops a sudden change of stiffness after a partial unloading/reloading. Therefore, they proposed a modified Menegotto-Pinto model to represent a more realistic hysteresis behavior after partial unloading/reloading. This modified Menegotto-Pinto model was adopted in this study. It should be mentioned that, while some errors are inevitable during the strain-to-stress conversion process, it is believed that the calculated steel stresses are accurately enough for the purpose of investigating bond behavior.

The procedure for determining the bond stress distribution in the test specimens is illustrated in Figure 6.23. *First*, the strain data is obtained through strain gages and recorded by a data acquisition system. *Second*, by inputting the obtained strain data and the nonlinear monotonic envelope (see Figure 6.4) into a program that implements the Menegotto-Pinto algorithm, the hysteretic stress-strain response of the steel at a particular location is derived. *Third*, with the stress-strain responses along sections of the reinforcing bar known, the average bond stress between two particular strain gage locations is calculated according to Equation [6.1]. Then the bond stress distribution along the reinforcing bar is plotted, as shown in Figure 6.23 (b).

6.4 Experimental Results

6.4.1 Specimen 1

The steel stress-strain response, steel stress distribution, and bond stress distribution obtained based on the procedure described in Section 6.3 are shown in Figures 6.24 thru 6.31. Three reinforcing bars were monitored with strain gages during the test: BTS (Beam bar, located at Top and South side), BTN (Beam bar, located at Top and North side), and BBS (Beam bar, located at Bottom and South side) series. The BTS series comprised 8 strain gages, while both BTN and BBS series had 5 strain gages each. Locations of all strain gages are given in Figure 6.24 thru Figure 6.31. It should be noted that while a more precise bond stress distribution can be obtained by using additional strain gages, as in the BTS series, this could be potentially detrimental to the bond resistance due to the instrumentation process. It is worth mentioning that not all strain gages lasted throughout the entire testing. Therefore, the steel and bond stress distributions were only plotted at drift levels during which none of the strain gages along the reinforcing bar failed.

As can be seen in the hysteretic stress-strain responses for the beam bars shown in Figures 6.24 thru 6.31, the cyclic strain histories tended to center about an ever-increasing tensile inelastic strain. This is because, in general, the compressive force is mainly carried by the matrix (for low to moderately reinforced sections).

In the test specimens, it was expected that the beam plastic hinging zone would be pushed slightly away from the column faces due to the presence of intermediate layers of longitudinal reinforcement (see Figure 6.5). This was evident in Specimen 1, since the intermediate bars extended 8 in. into the beams. As can be seen in Figure 6.24, significant inelastic strains occurred at about 5 in. and 11 in. away from the column faces (measured by strain gages BTS1, BTS2, and BTS9), while the strain gages close to the column faces

showed much less yielding (gages BTS3 and BTS7), which indicates that the plastic hinging zones were moved away from the column faces. From Figures 6.24 and 6.25, it can also be observed that bar yielding penetrated only slightly into the joint.

Unfortunately, the bond stress distribution for BTS gage series shown in Figure 6.25 is not very consistent.

On the other hand, BTN and BBS gage series (Figures 6.27 thru 6.31) showed much more consistent bond stress distributions and thus, their data were used to evaluate the bond performance of Specimen 1. The largest yielding occurred at a short distance away from the column faces, as indicated by the beam cracking pattern shown in Figure 6.37 (b). As can be seen, the locations of cracks with maximum width were approximately 7 in. from the column faces, that is, approximately at the ends of the intermediate reinforcement. Nevertheless, the reinforcing bars were still subjected to significant yielding at the column faces (see Figures 6.26 and 6.29). It is observed that bond stress distribution was not uniform through the beam-column joint, as shown in Figures 6.27, 6.28, 6.30, and 6.31. In general, the steel subjected to high tensile stress or strain exhibited lower bond stress. For example, as illustrated in Figure 6.27, when the specimen was pushed towards the East, steel in the vicinity of strain gage BTN7 sustained the highest tensile stress and strain in the joint. This led to a reduction in bar diameter, which could in turn result in less contact between bar and matrix, thus high concentration of bearing stresses and increased damaged of the matrix. A complete loss of contact, and thus bond resistance, could also occur at highly stretched bar sections. It is noted that, however, the lack of confinement due to both column and beam in tension on

the bar tensile side is the main cause that contributed to the low bond stress. As a consequence, a low bond stress (approximately 500 psi) was observed when a bar was subjected to high tensile strains ($\varepsilon_s > \varepsilon_y$).

High bond stress, however, was calculated on the opposite side of the joint, where the reinforcing bar was in compression and located in the beam and column compression zones. The bond stresses in the compressive zone were generally in the range of 2000-2500 psi when the specimen was pushed to 4% drift. A comparison between Figures 6.27 and 6.28 (or between Figures 6.30 and 6.31) shows that the bond regained its value when the specimen was cycled to the other direction. This can be attributed to confinement effect resulted from the beam and column compressive forces. Stress in the bars decreased progressively inside a joint due to the presence of bond and this decrease was much faster at the side where the bars were in compression and surrounded by the beam and column compression zones. It is also noted that steel in the middle of the joint remained elastic during the testing, even at large drift levels.

It has been observed that significant pinching (i.e. stiffness reduction of the beam-column subassembly near zero displacement) would take place in the load versus drift hysteresis response if bond severely deteriorates, as may be the case in conventional RC beam-column joints. In Specimen a, significant pinching did not occur until 5% drift (Figure 6.32). Note that 6% drift is unrealistically high for reinforced concrete frames. Therefore, the corresponding response is represented by dotted lines. The pinching observed during the cycle at 5% drift resulted from the considerable degradation of

stiffness in the beam hinging region. Note that the column-to-beam strength ratio was 2.2 in Specimen 1 (see Table 6.2). Figures 6.33 and 6.34 indicate that the joint remained almost elastic while significant pinching occurred in both beams when the rotations exceeded 0.03 rad. It is also observed in Figure 6.32 that only minor decay (approximately 10%) of the lateral load carrying capacity occurred up to the first cycle at 5% drift.

Slippage of reinforcing bars was monitored through a pair of potentiometers, as illustrated in Figure 6.20. It should be reiterated here that the measured slippage would include the flexural deformation of the beam within a distance of 1.25 in. From the load versus slip response shown in Figure 6.35, it can be concluded that bar slippage through the joint was negligible.

Except for yielding penetration of reinforcing bars, the unfavorable conditions described in Figure 6.1 did not occur in the HPFRCC beam-column connection. Figure 6.36 shows the multiple diagonal crack patterns in the connection region at various drift levels. These cracks increased in number and extended with an increase of drift level, but the maximum width observed was only 0.6 mm (0.024 in.), as shown in Table 6.3. It is noted in Table 6.3 that the maximum joint crack width decreased during the 6% drift cycles due the fact that the HPFRCC material crushed in the beam plastic hinging region (as shown in Figure 6.52), which in turn led to a reduction in specimen strength and thus, in the shear stress demand in the joint. The maximum crack width in the beams was about 20 mm (0.8 in.), that is, about 33 times the maximum crack width in the joint. Note that no spalling or crushing of the HPFRCC was observed in the joint region.

Cracking in the beam hinging zones, as well as beam-column interfaces, is highlighted in Figures 6.37 and 6.38. It is observed that, except for the development of a multiple cracking pattern, none of the unfavorable conditions leading to a decrease in bond resistance occurred, such as cone-shaped fracture at the location of beam bars entering the joint, or splitting cracks along the beam longitudinal bars. Therefore, it can be concluded that HPFRCC materials are effective in maintaining bond resistance in beam-column joints up to very large drift levels, much beyond the allowable drift specified in design codes.

6.4.2 Specimen 2

Specimen 2 differed from Specimen 1 mainly in the beam longitudinal reinforcement ratio and thus, the column-to-beam strength ratio (1.6 in Specimen 2 and 2.2 in Specimen 1), and the length of beam intermediate longitudinal reinforcement (see Table 6.2 and Figure 6.5). It was therefore anticipated that larger joint shear distortions and damage would result due to the increased beam capacity (and joint shear demand) , as well as a higher bond demand by moving the beam plastic hinging zone closer to the column faces.

The behavior of three beam reinforcing bars was monitored with strain gages: BTS (Beam bar, located at Top and South side), BTN (Beam bar, located at Top and North side), and BBN (Beam bar, located at Bottom and North side) series. The BTN series had 6 strain gages, while both BTS and BBN series had 5 strain gages. However, only three strain gages were attached on the bars in the joint region for all series. Locations of all

strain gages, steel stress-strain responses, steel stress distributions, and average bond stress distributions are given in Figures 6.39 thru 6.47. Several observations can be made based on these figures:

1. As shown in the hysteretic stress-strain responses, strain gages at the column faces recorded the largest tensile strain, indicating that the beam plastic hinging zone was in the vicinity of the column faces.

2. As indicated by the steel stress distribution curves, yielding of bars penetrated into the middle of the joint when the specimen was pushed beyond 2% drift level. However, no penetration of yielding occurred in the middle of the joint in Specimen 1.

3. The average bond stress in the tension side was approximately 500 psi, while it was in the range of 2000-2500 psi in the compression side, which is consistent with the bond stress distribution in Specimen 1.

4. The bond stress in the compression side kept increasing until 5% drift level in most beam bars. In particular, average bond stresses in the BBN gage series reached a maximum of 2750 psi in the compression side without bond degradation up to 6% drift.

The overall lateral load versus drift response of Specimen 2 exhibited much less pinching at 5% drift with no strength degradation (first cycle), as shown in Figure 6.48. This is a consequence of increasing the beam flexural strength capacity in Specimen 2,

which led to an increase in joint shear rotation and decrease in beam plastic hinge rotation demand. Recall that in Specimen 1 the damage was primarily in the beams, which after crushing of the HPFRCC material led to pinching in the overall load versus drift response. The joint region of Specimen 2 sustained more damage than in Specimen 1, but this could still be considered minor. As can be seen in Figure 6.49, limited joint inelastic deformations occurred, with a peak shear distortion of approximately 0.008 rad. Lateral load versus beam rotation responses for both beams are given in Figure 6.50, in which no significant pinching occurred up to cycles at 5% drift, the displacement after which crushing of the HPFRCC materials occurred. Maximum crack widths in beams and joint were recorded during the test and are listed in Table 6.4. As can be seen, the maximum crack width in the joint was 3.0 mm (0.12 in.) at 6% drift. Nevertheless, the residual crack width was negligible after unloading. Crack width in beams had a maximum value equal to 4 mm (0.16 in.), which is 20% of that observed in Specimen 1.

Measured slippage of beam bars was generally small, as shown in Figure 6.51. It is noted that since the plastic hinging zone was closer to the column face, the large beam flexural deformation contributed significantly to the measured slip values. For instance, as shown in Figure 6.51 (a), a large deformation was observed when the top beam bars were in compression, due to considerable matrix crushing as highlighted in Figure 6.52.

Cracking patterns in the HPFRCC joint region, beam plastic hinging zone, and beam-column interface are shown in Figures 6.53 and 6.54. Except for multiple cracking, no through crack at the beam-column interface, cone-shaped fracture at the location of beam bars entering the joint, or splitting cracks along the beam longitudinal bars were

observed. The entire HPFRCC region (joint as well as beam portions in the vicinity of column) maintained its integrity without evident damage up to 6% drift. In general, no repair technique, such as epoxy injection, would be needed for the restoration of bond after a major earthquake since no degradation would occur when the beam plastic hinge rotation is kept below 0.04 rad. (corresponding to 4% drift in the test specimens).

6.4.3 Overall Evaluation of Bond Performance

Although the bond stress distribution in a beam-column joint is highly non-uniform, an average bond stress along the joint was calculated according to Equation [6.1], using the stress data obtained from strain gages at opposite beam-column interfaces (e.g., BTN3 and BTN 7 in Figure 6.26). The results for all bars are shown in Figure 6.55. As can be seen, the peak average bond stress over the entire column depth is in the range of 1250 to 1450 psi. It is noted that, based on Equation [4.7] and using an average bond stress of 1350 psi, the required anchorage length would be approximately 80% of the ACI requirement, i.e., $16d_b$.

The bond strength development of longitudinal beam bars in a beam-column joint was also evaluated by using a bond efficiency parameter (Leon, 1989; Parra-Montesinos, 2000), which is defined as:

$$\text{Bond Efficiency} = \frac{\Delta f_s}{f_y} \qquad [6.2]$$

where Δf_s is the variation in steel stress over the column depth, which is calculated using the stress data obtained from strain gages at opposite beam-column interfaces (e.g., BTN3 and BTN 7 in Figure 6.26), and f_y is the bar yield stress obtained from the monotonic tensile test.

A bond efficiency equal to 1.0 indicates that the bond strength in a beam-column joint is able to bring the bar from yielding (without strain-hardening) in tension on one side of the joint to zero stress at the other side. A bond efficiency value (after bar yielding) much less than 1.0 indicates bond deterioration in a joint, where the bar would be under tension through the entire joint dimension (see Figure 1.4 (c)). If the bar can be effectively anchored in the joint, steel on the tension side may undergo strain-hardening while maintaining compression or nearly zero stress on the other side; in that case the bond efficiency can be much larger than 1.0. Figure 6.56 shows plots of bond efficiency versus drift for bars in Specimens 1 and 2. As can be seen, peak bond efficiency values larger than 1.0 and as high as 2.25 were obtained for drifts ranging from 2% to 6%, indicating excellent bond strength, even when bars were subjected to substantial inelastic strains. It is worth mentioning that bond efficiency values of approximately 0.7 were reported by Leon (1989) for conventional reinforced concrete joints with a column depth equal to 20 beam bar diameters.

Based on Figures 6.55 and 6.56, it can be concluded that in an HPFRCC beam-column joint, bond strength can be maintained with no degradation up to at least 4% plastic hinge rotation (about 4% story drift in the tested specimens) when an

anchorage length of $18.7d_b$ is provided.

6.5 Conclusions

The following conclusions can be drawn based on the results from the tests of two beam-column subassemblages under displacement reversals:

1. The bond performance in an HPFRCC beam-column joint is primarily affected by the confinement effect resulting from beam and column, as well as penetration of reinforcing bar yielding. Due to the highly crack-damage tolerance of HPFRCC materials, the multiple cracking in an HPFRCC joint generally has minor influence on bond performance.

2. Most of the unfavorable conditions that influence bond resistance, such as formation of cone-shaped fracture, longitudinal splitting cracks along the beam bars, and extensive diagonal tensile cracking in the joint, were not observed in the HPFRCC connection tests. The maximum crack width recorded in the joint was 0.5 mm and 1.5 mm at 4% drift for Specimens 1 and 2, respectively.

3. The calculated average bond stress along the longitudinal beam bar had a minimum value (approximately 500 psi) close to the tension side, while it gradually increased 4 to 5 times (approximately 2000-2500 psi) close to the compression side. The peak average bond stress in the HPFRCC beam-column joint over the entire column depth was in the range of 1250 to 1450 psi, which is approximately 1.5 times the assumed

average bond stress in a conventional RC beam-column connection. Further, peak bond efficiency values larger than 1.0, and as high as 2.25, were obtained for drifts ranging from 2% to 6%, indicating excellent bond strength, even when bars had been subjected to substantial inelastic tensile strains.

4. In the HPFRCC beam-column joints, no bond strength degradation was observed up to 0.04 rad. beam plastic hinge rotation (4% story drift in the test specimens), even though an anchorage length of $18.7d_b$ was provided.

Table 6.1 Composition of matrix mixtures by weight ratio and average compressive strength of HPFRCC materials (1.5% Spectra fiber)

Matrix	Cement (Type III)	Fly Ash	Sand*	Water	f_c', ksi (MPa)
Specimen 1	1.0	0.15	1.0	0.50	5.7 (39.3)
Specimen 2	1.0	0.15	1.0	0.50	6.2 (42.7)

*Flint Sand ASTM 30-70

Note: Super- plasticizer was added to ensure good workability when necessary

Table 6.2 Summary of experimental results

Specimen	HPFRCCs		$\frac{\sum M_{nc}}{\sum M_{ub}}$	Drift Capacity (rad)*	Maximum Beam Rotation (rad)*
	σ_{pc} (psi)	ε_{pc}			
1	390	0.010	2.2	0.05	0.045
2	320	0.013	1.6	0.06	0.045

σ_{pc}: post-cracking (peak) strength

ε_{pc}: tensile strain capacity (strain at peak stress)

M_{nc} and M_{ub}: column nominal moment capacity and beam ultimate moment strength, respectively

* Drift capacity and peak beam rotation correspond to maximum values before strength decay to 80% of peak strength occurred

Table 6.3 Maximum crack width measured at various loading cycles in Specimen 1 (measured on south face of the specimen only)

No. of Cycle	Story Drift	Joint	West Beam	East Beam
10 (East)	2.5%	-	-	0.76 mm (0.03 in.)
13 (West)	3.0%	0.25 mm (0.01 in.)	1 mm (0.04 in.)	3 mm (0.12 in.)
15 (West)	4.0%	0.33 mm (0.013 in.)	4mm (0.16 in.)	6 mm (0.24 in.)
15 (East)	4.0%	0.50 mm (0.020 in.)	6 mm (0.24 in.)	6 mm (0.24 in.)
18 (West)	5.0%	0.40 mm (0.016 in.)	5 mm (0.20 in.)	12 mm (0.47 in.)
18 (East)	5.0%	0.60 mm (0.024 in.)	13 mm (0.51 in.)	6 mm (0.24 in.)
19	0%	0.10 mm (0.004 in.)	5 mm (0.20 in.)	4 mm (0.16 in.)
20 (West)	6.0%	0.40 mm (0.016 in.)	13 mm (0.51 in.)	18 mm (0.71 in.)
20 (East)	6.0%	0.40 mm (0.016 in.)	20 mm (0.80 in.)	8 mm (0.32 in.)

Table 6.4 Maximum crack width measured at various loading cycles in Specimen 2 (measured on south face of the specimen only)

No. of Cycle	Story Drift	Joint	West Beam	East Beam
1 (East)	0.5%	-	0.08 mm (0.003 in.)	0.08 mm (0.003 in.)
3 (West)	1.0%	0.08 mm (0.003 in.)	0.08 mm (0.003 in.)	0.08 mm (0.003 in.)
3 (East)	1.0%	0.08 mm (0.003 in.)	0.1 mm (0.004 in.)	0.08 mm (0.003 in.)
5 (West)	1.5%	0.2 mm (0.008 in.)	0.08 mm (0.003 in.)	0.08 mm (0.003 in.)
5 (East)	1.5%	0.08 mm (0.003 in.)	0.1 mm (0.004 in.)	0.1 mm (0.004 in.)
7 (West)	2.0%	0.4 mm (0.016 in.)	0.1 mm (0.004 in.)	0.33 mm (0.013 in.)
7 (East)	2.0%	0.2 mm (0.008 in.)	0.2 mm (0.008 in.)	0.2 mm (0.008 in.)
10 (West)	2.5%	0.5 mm (0.020 in.)	0.2 mm (0.008 in.)	0.2 mm (0.008 in.)
10 (East)	2.5%	0.25 mm (0.01 in.)	0.8 mm (0.031 in.)	0.4 mm (0.016 in.)
12 (West)	3.0%	1 mm (0.04 in.)	0.5 mm (0.020 in.)	1.25 mm (0.05 in.)
12 (East)	3.0%	0.8 mm (0.031 in.)	1.25 mm (0.05 in.)	0.4 mm (0.016 in.)
15 (West)	4.0%	1.5 mm (0.06 in.)	0.8 mm (0.031 in.)	2 mm (0.08 in.)
15 (East)	4.0%	1.0 mm (0.04 in.)	3 mm (0.12 in.)	2 mm (0.08 in.)
18 (West)	5.0%	2.5 mm (0.1 in.)	1.0 mm (0.04 in.)	3 mm (0.12 in.)
18 (East)	5.0%	2 mm (0.08 in.)	3 mm (0.12 in.)	2 mm (0.08 in.)
20 (West)	6.0%	3 mm (0.12 in.)	1.0 mm (0.04 in.)	2 mm (0.08 in.)
21 (East)	6.0%	2 mm (0.08 in.)	2 mm (0.08 in.)	4 mm (0.16 in.)

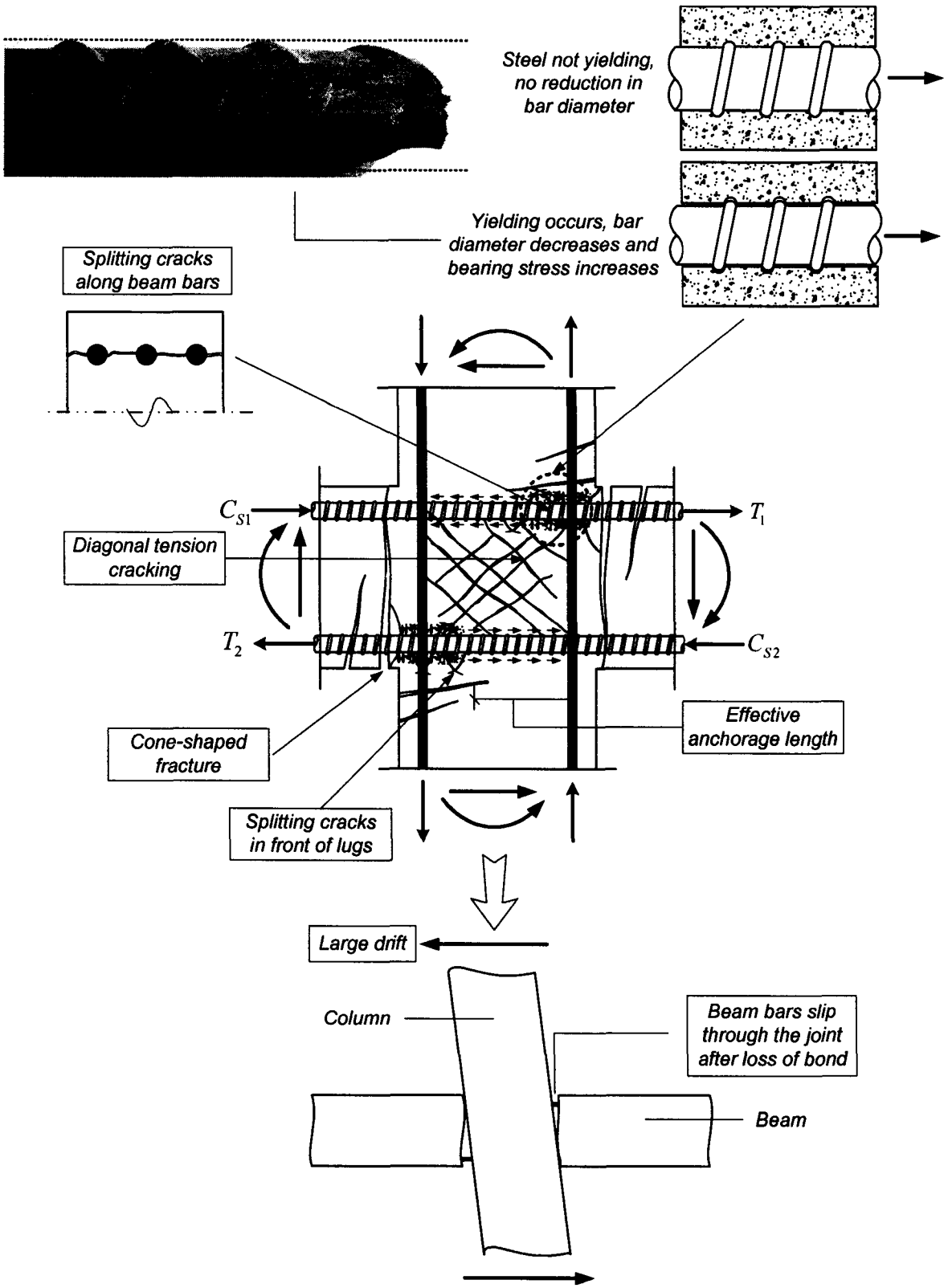

Figure 6.1 Unfavorable conditions for bond resistance in an interior seismic beam-column joint with conventional reinforced concrete (transverse hoops are omitted for clarity)

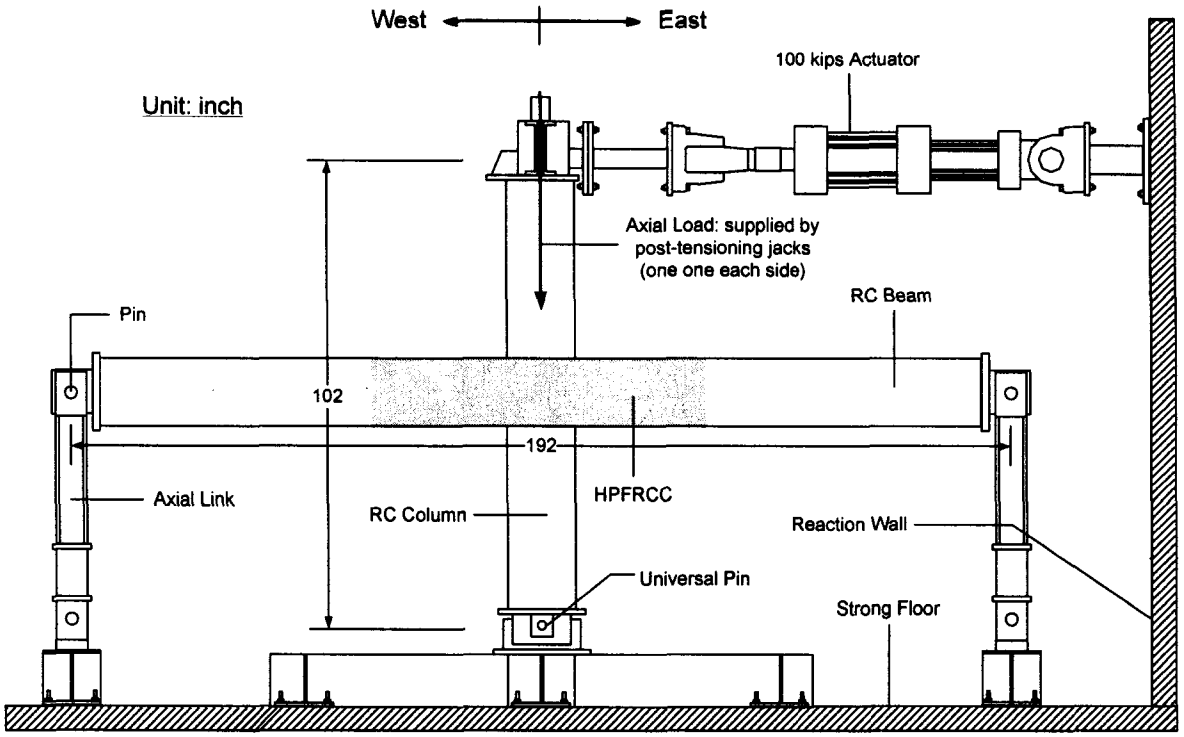

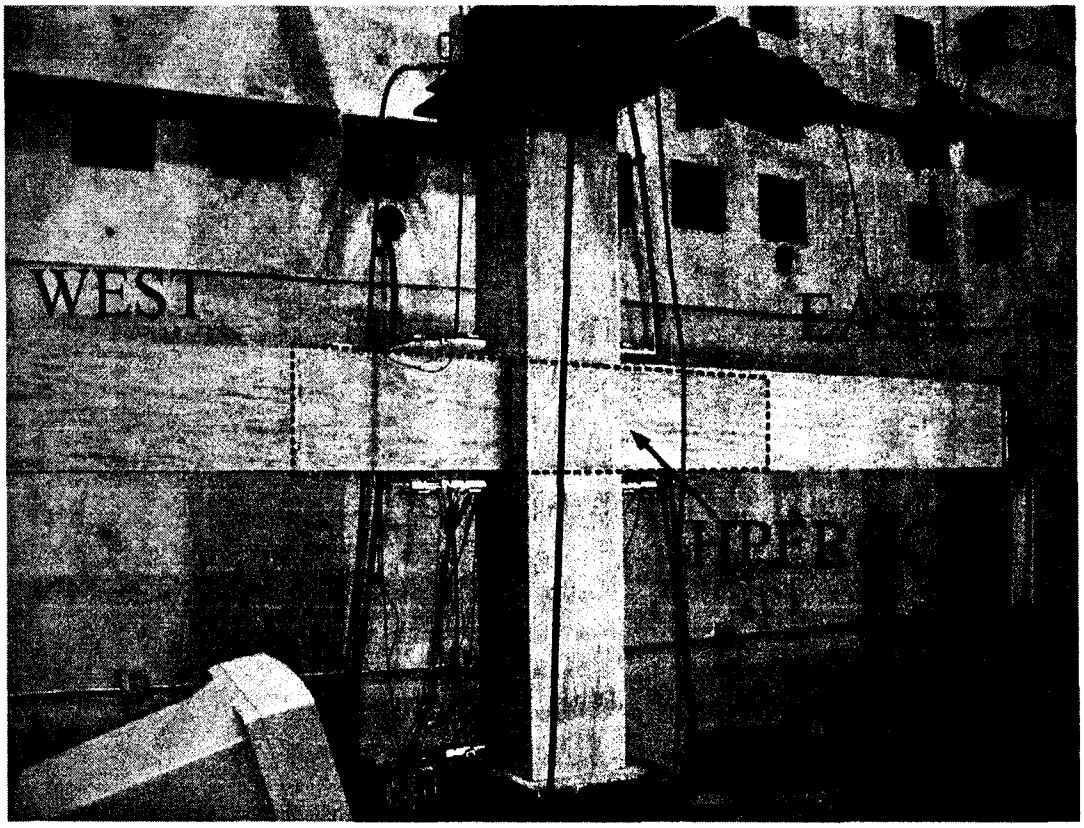

Figure 6.2 Overall view of test specimen and test setup

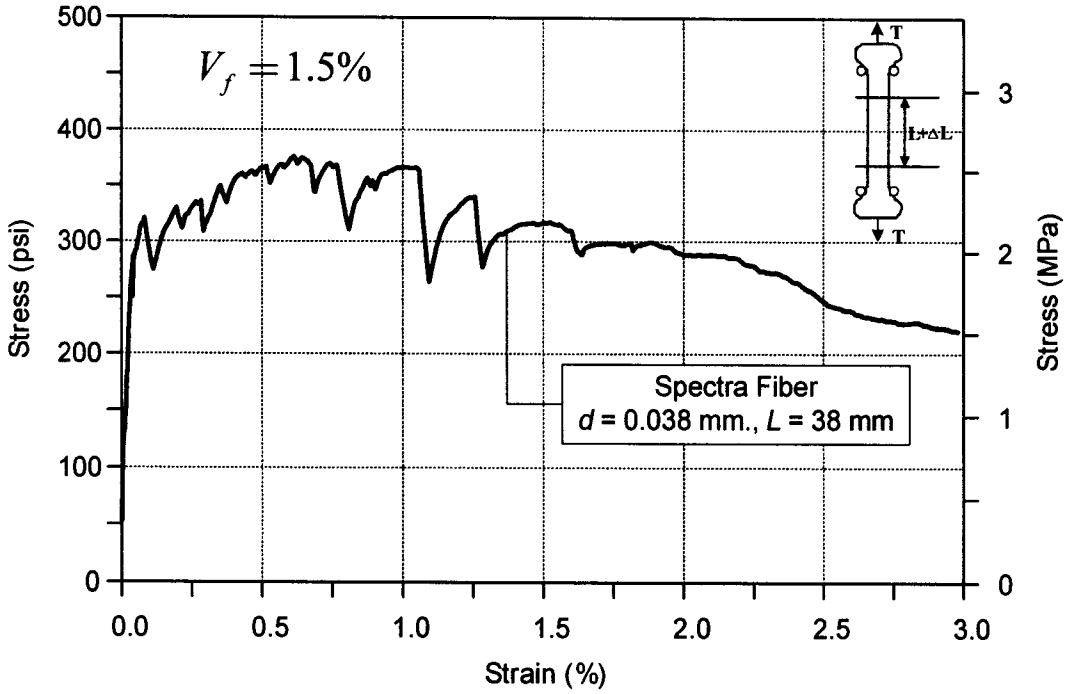

(a)

(b)

Figure 6.3 Typical tensile test results of HPFRCC material (1.5% Spectra fiber, matrix strength = 5.7 ksi): (a) tensile stress-strain response; (b) multiple cracks after test

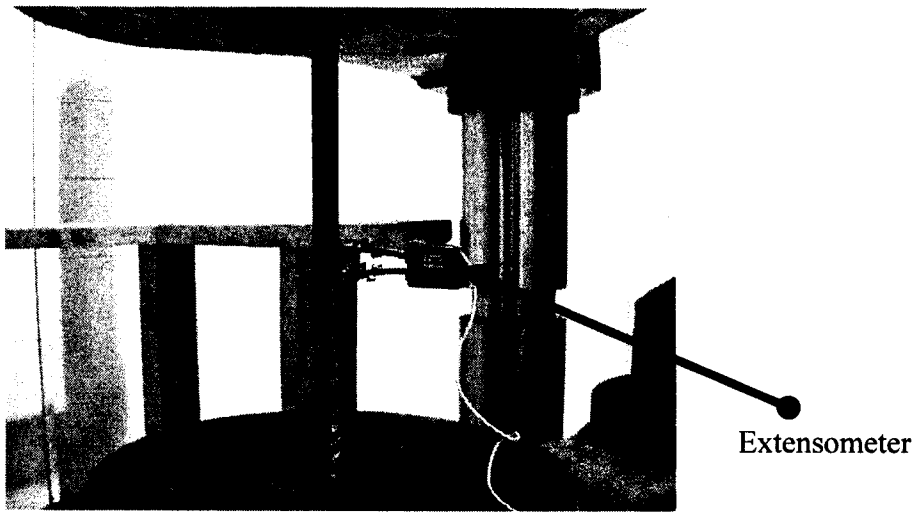

(a)

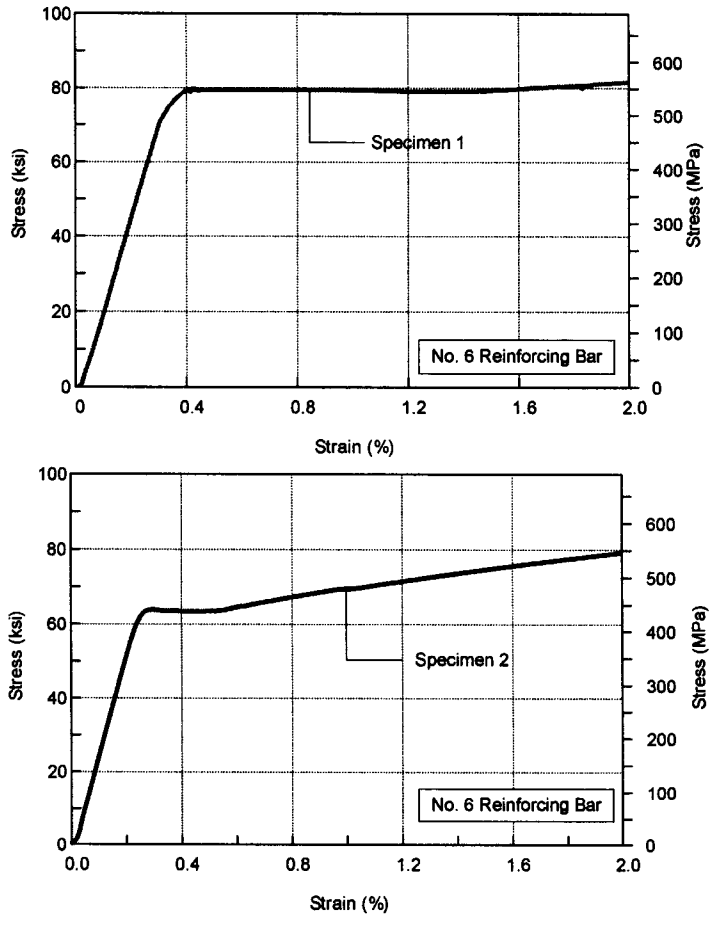

(b)

Figure 6.4 Tensile test of reinforcing bar: (a) test specimen and extensimeter; (b) average monotonic stress-strain curves for No. 6 bars used in Specimens 1 and 2

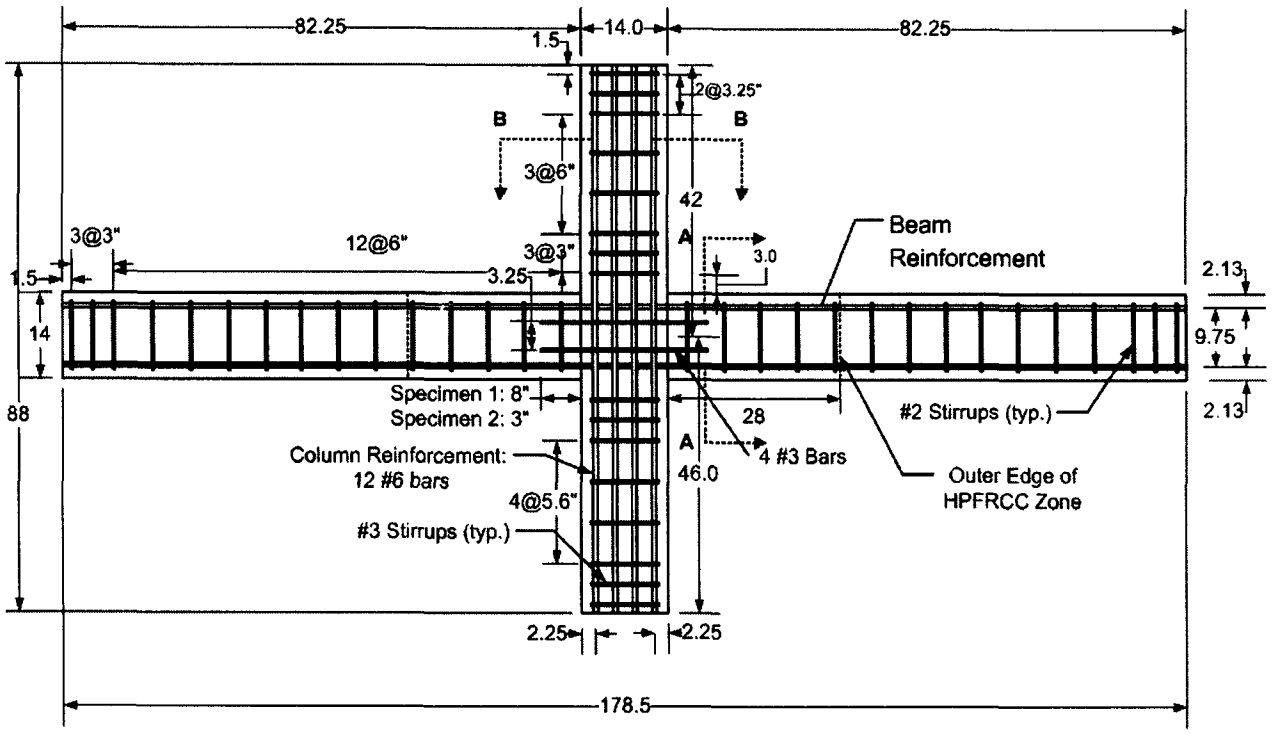

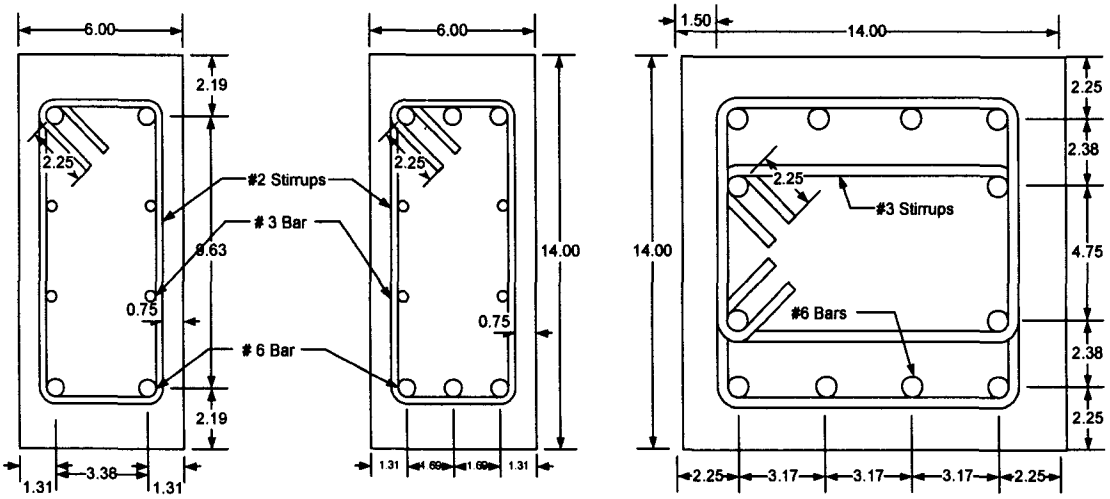

Specimen 1 **Specimen 2** **Specimen 1 & Specimen 2**

Section A-A (Beam Sections) **Section B-B (Column Section)**

Figure 6.5 Details of test specimens (unit: inch)

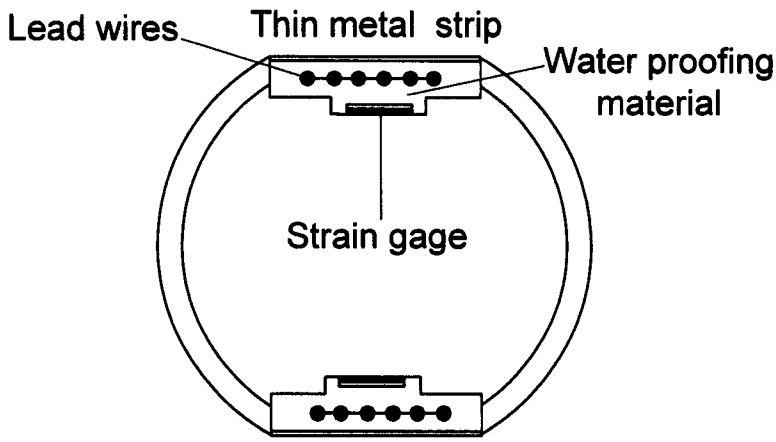

Figure 6.6 Cross section of instrumented groove in a reinforcing bar (Hamza, 1992)

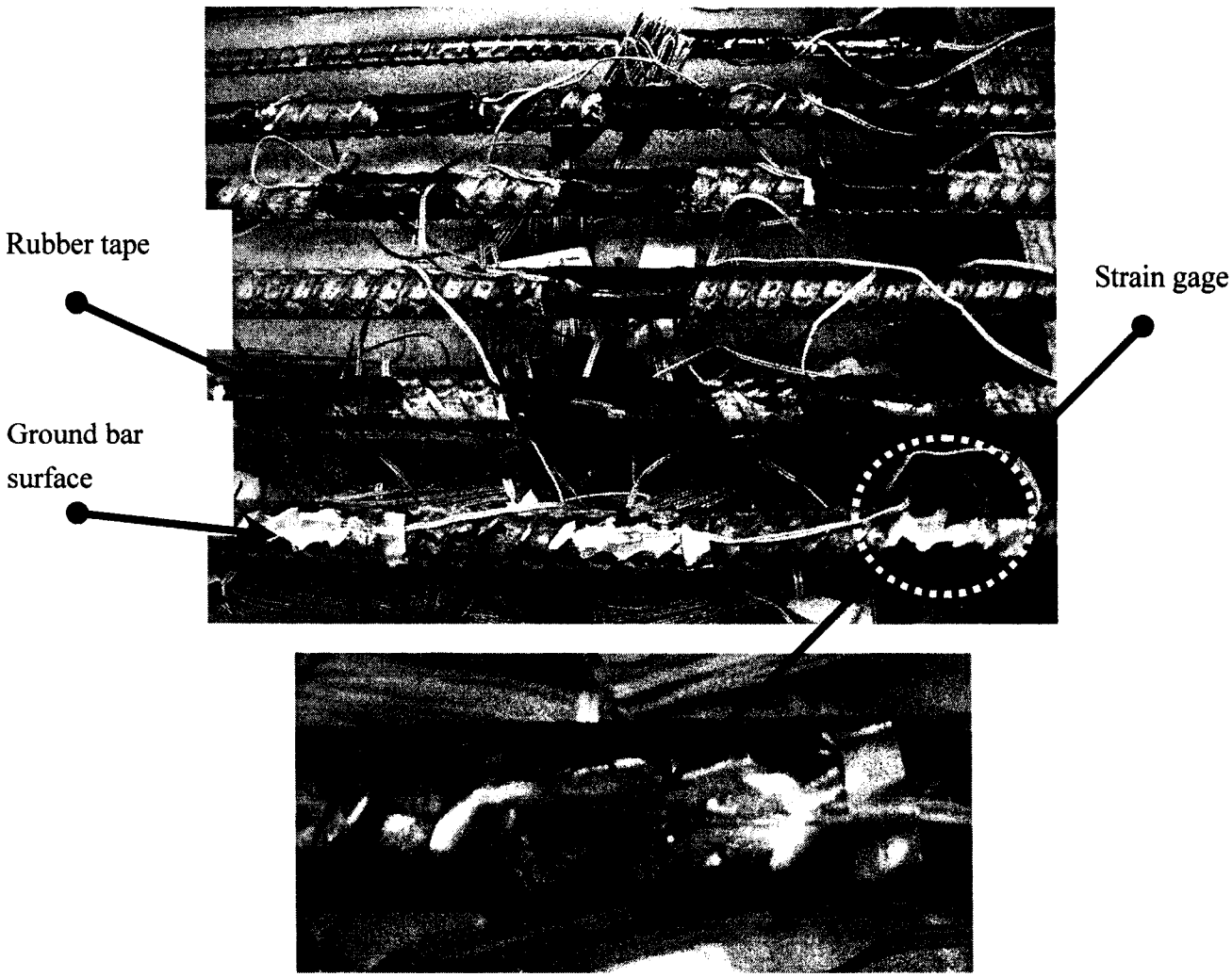

Figure 6.7 Strain gage mounting and bar surface grinding (this study)

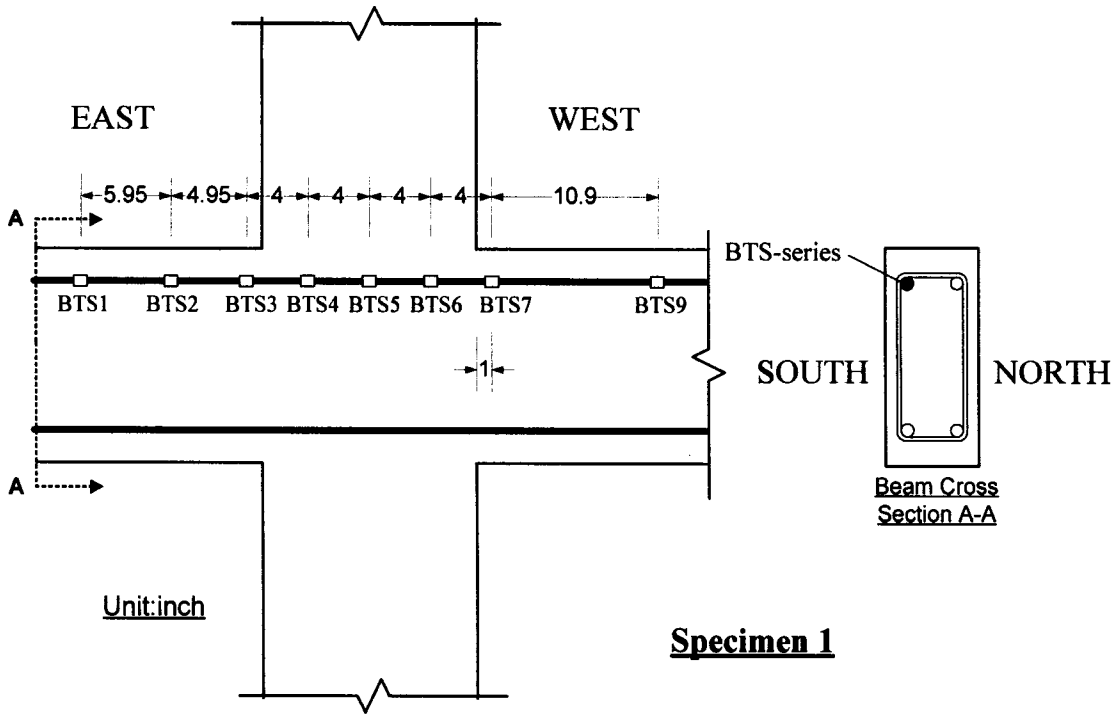

Figure 6.8 (a) Strain gage locations of BTS series in Specimen 1

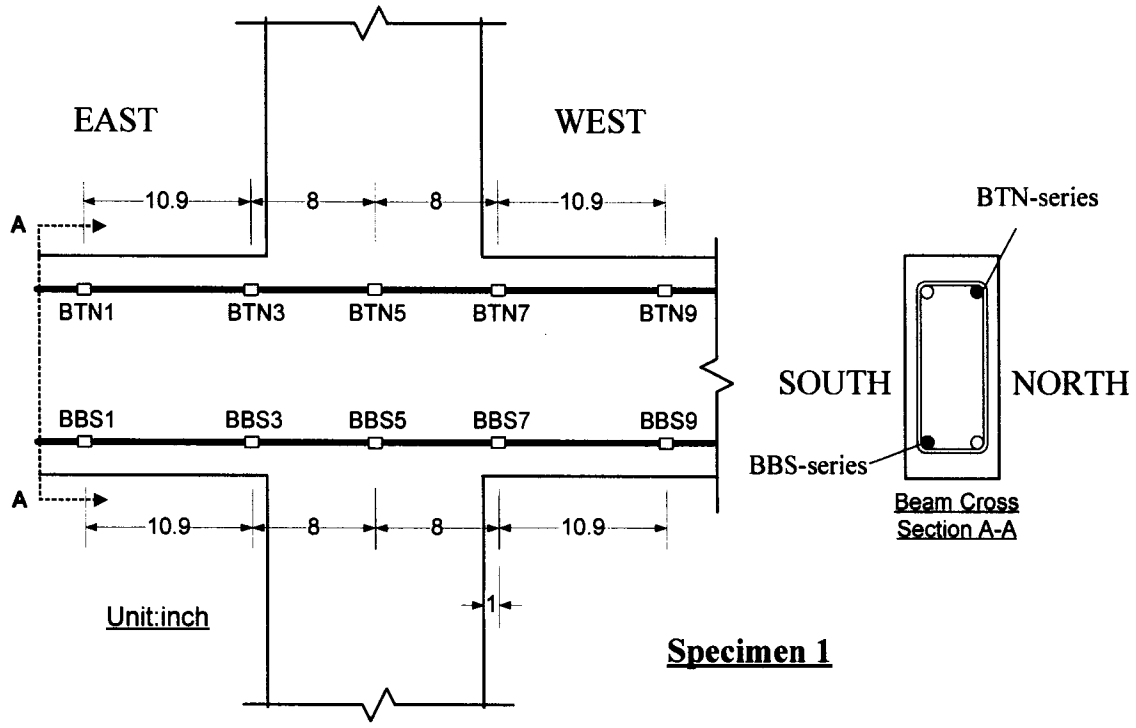

Figure 6.8 (b) Strain gage locations of BTN and BBS series in Specimen 1

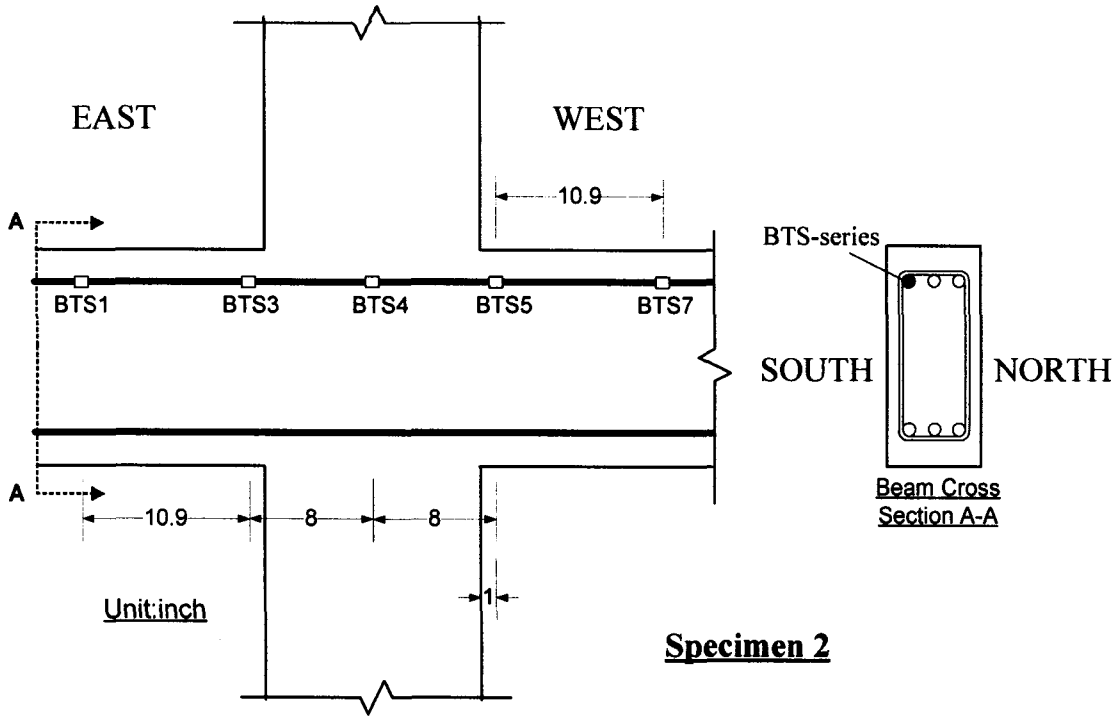

Figure 6.9 (a) Strain gage locations of BTS series in Specimen 2

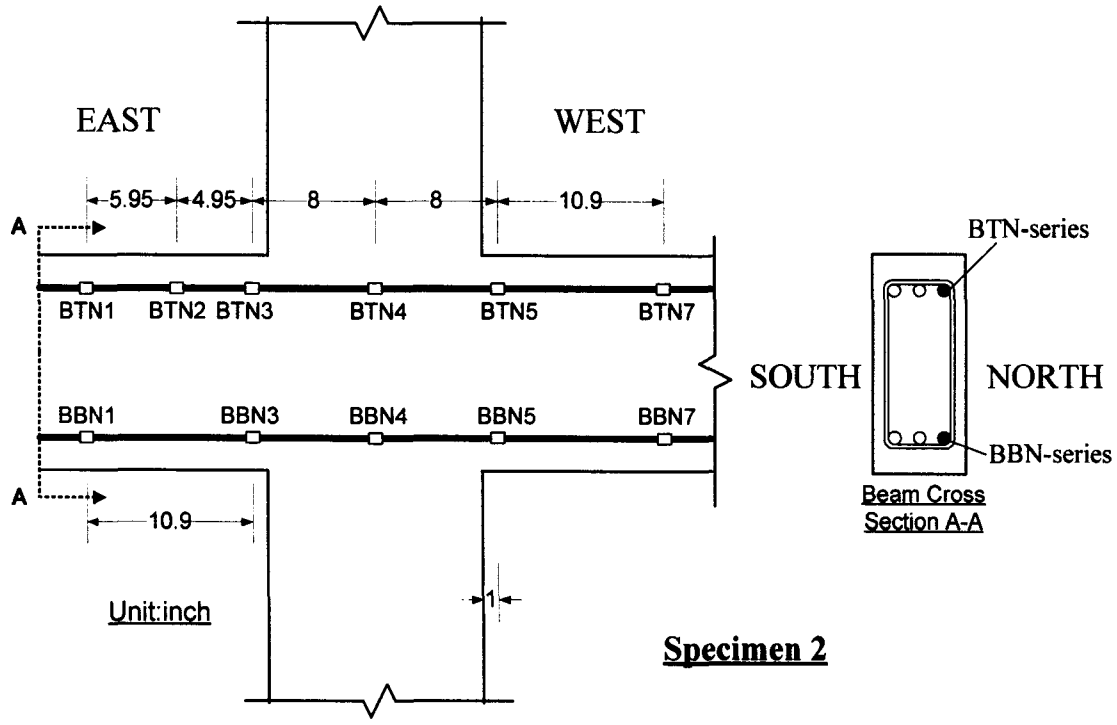

Figure 6.9 (b) Strain gage locations of BTN and BBN series in Specimen 2

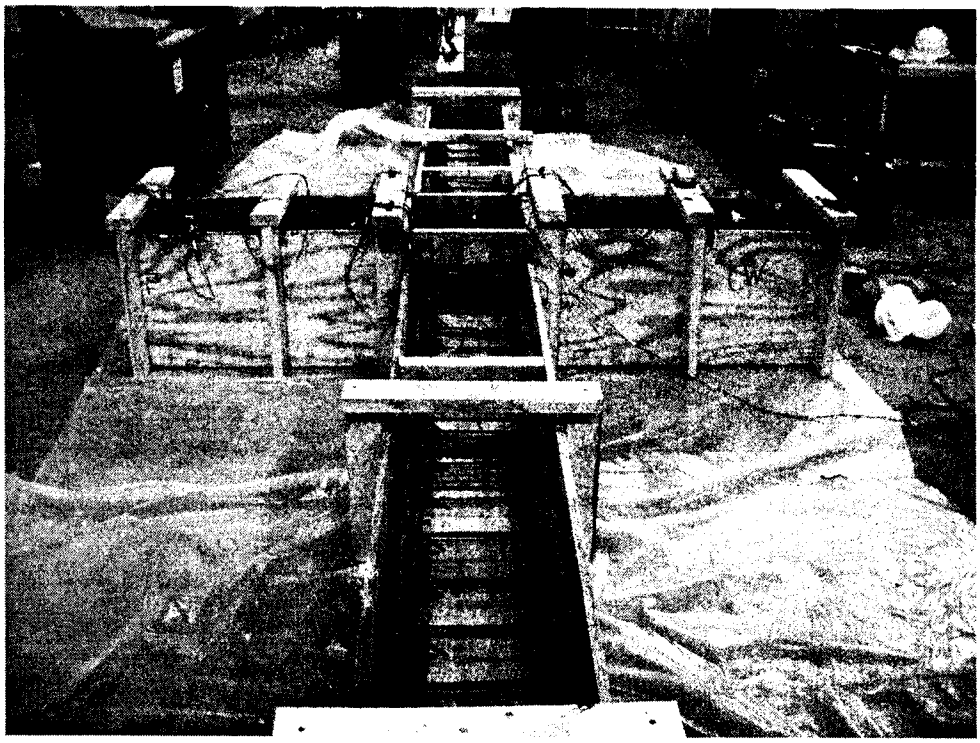

Figure 6.10 Overall view of the specimen before concrete pouring

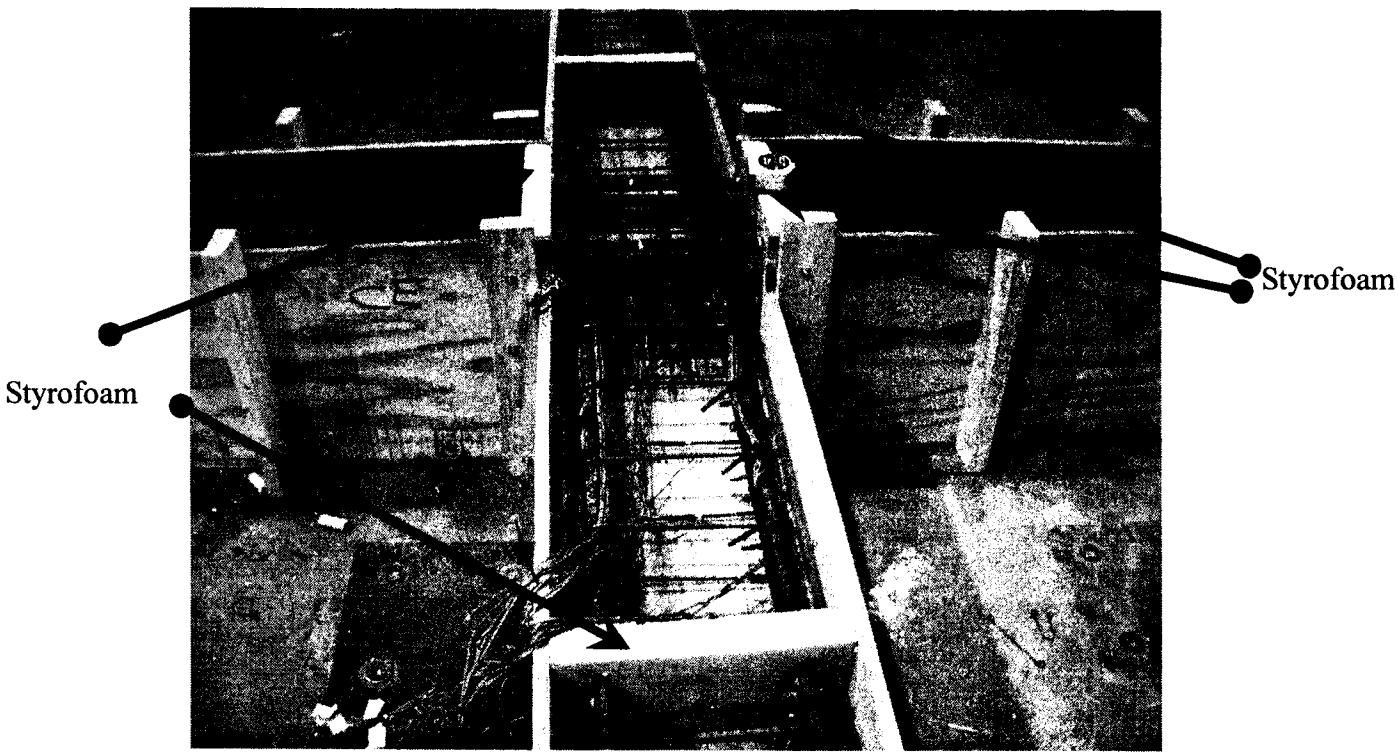

Figure 6.11 HPFRCC region of the specimen separated by Styrofoam pieces to allow the use of fiber reinforced concrete in joint

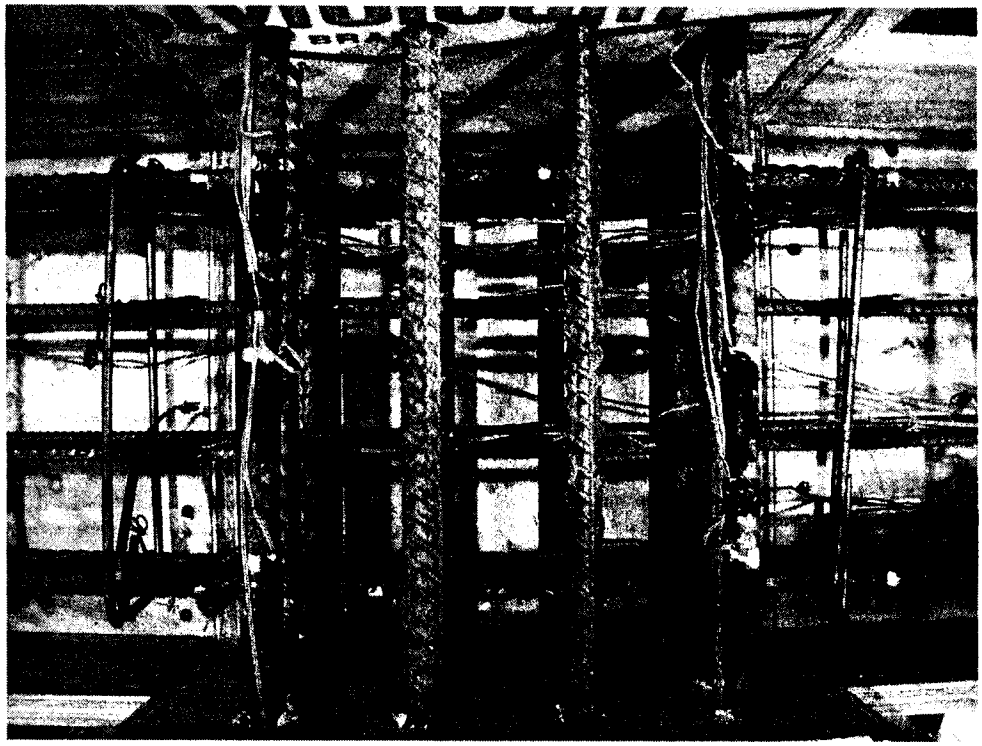

Figure 6.12 Reinforcement inside the beam-column joint; note no hoops were used (Specimen 1)

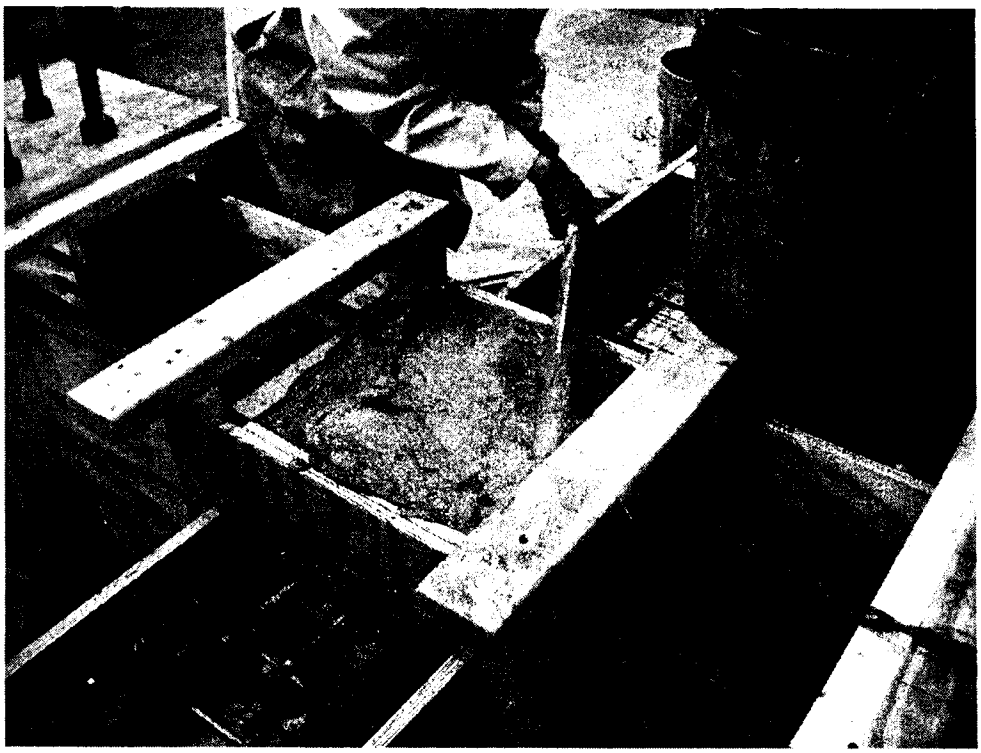

Figure 6.13 Casting and vibration of HPFRCC portion of the beam-column specimen

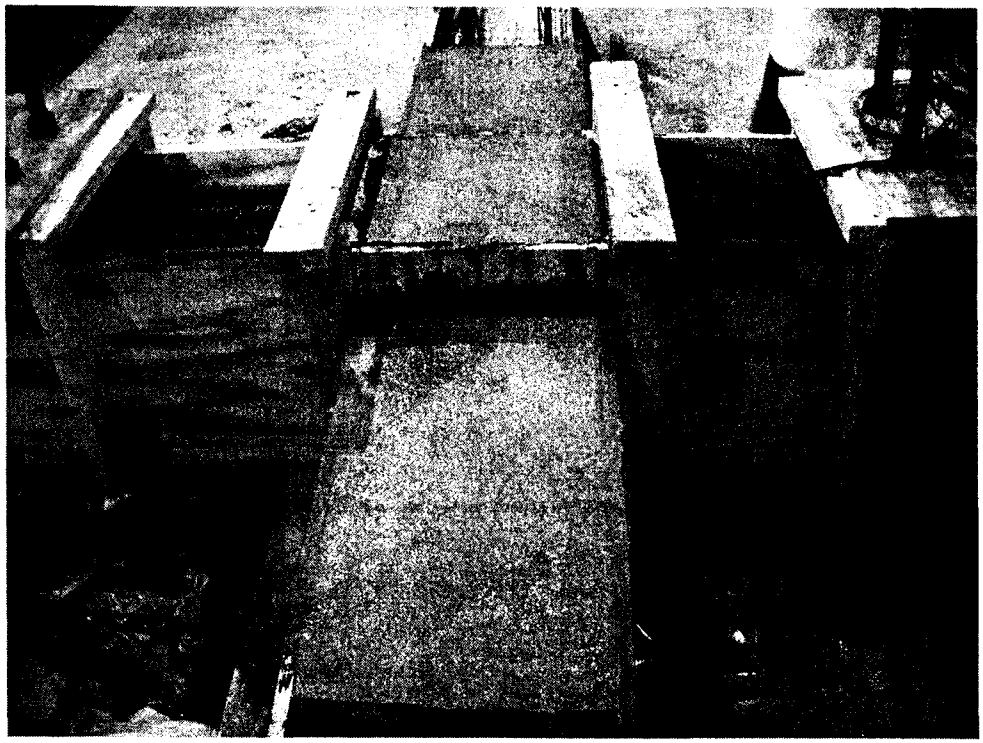

Figure 6.14 Finishing of HPFRCC portion of the beam-column specimen

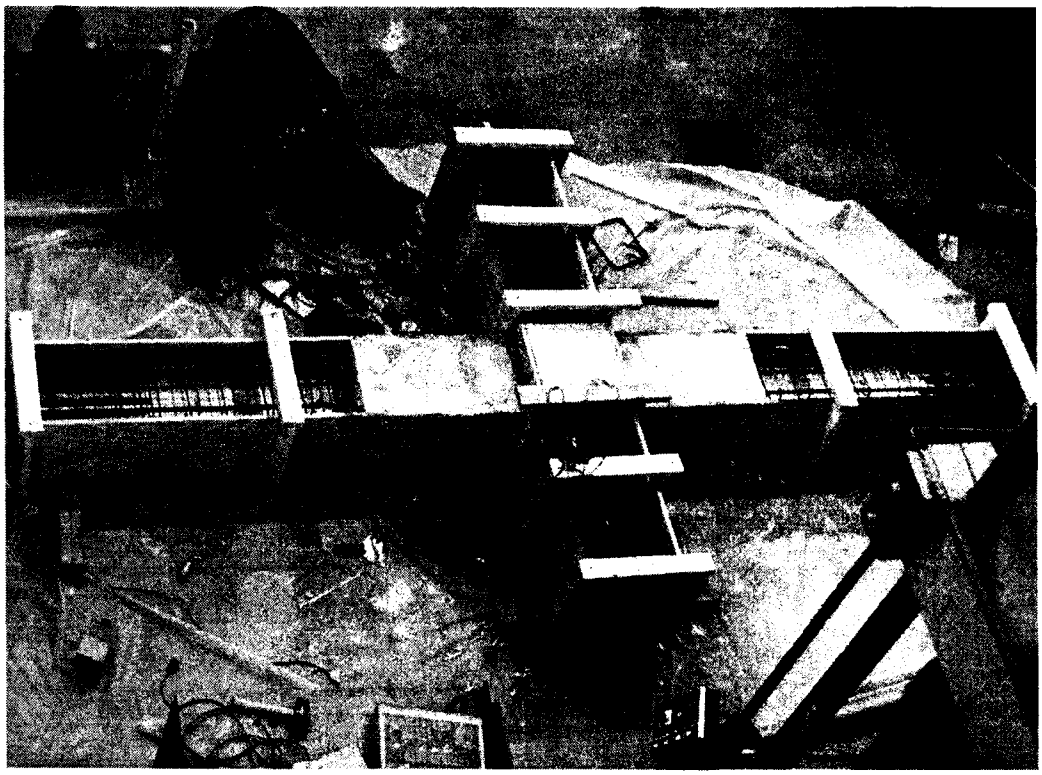

Figure 6.15 Top view of HPFRCC portion of the beam-column specimen

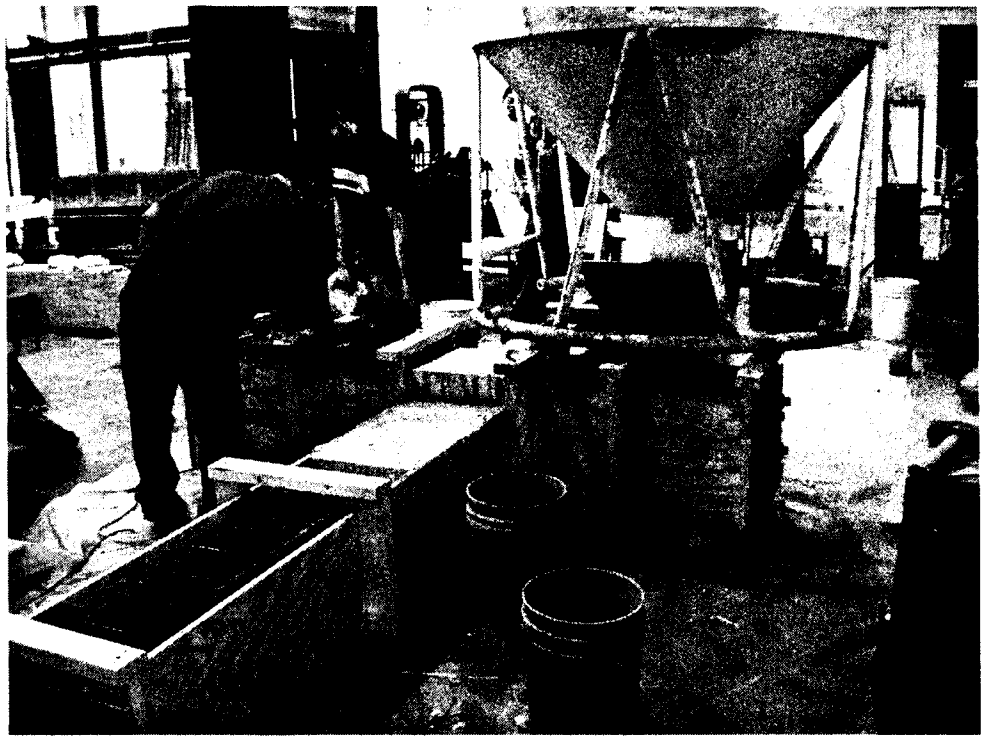

Figure 6.16 Casting of the ready-mix concrete portion of the beam-column specimen

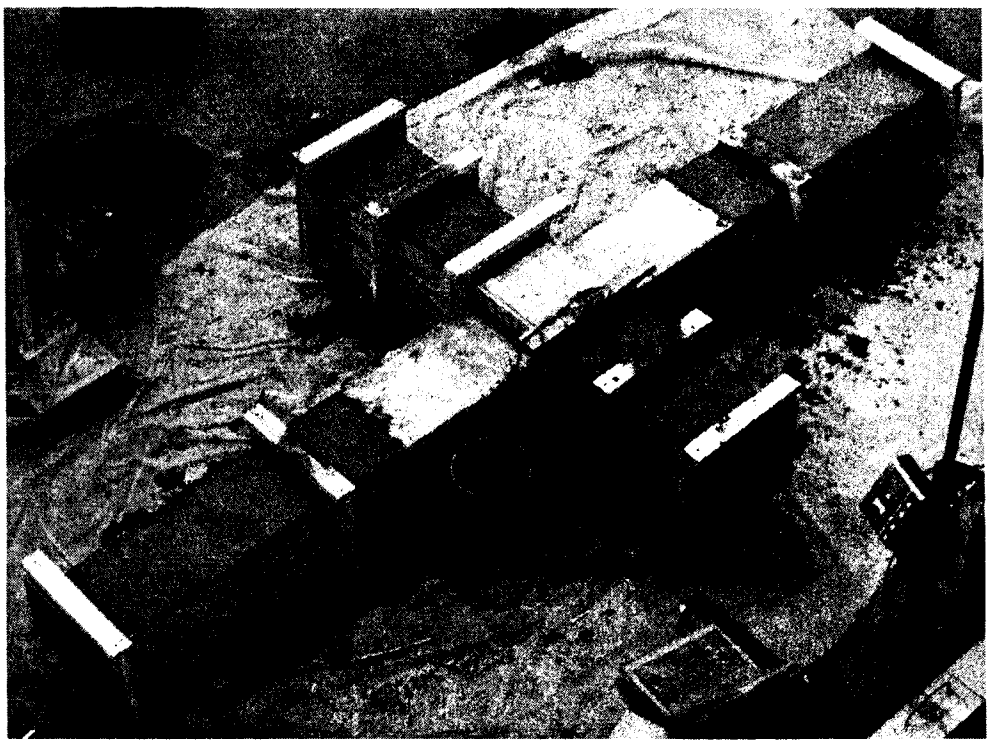

Figure 6.17 Overall view of the beam-column specimen after casting

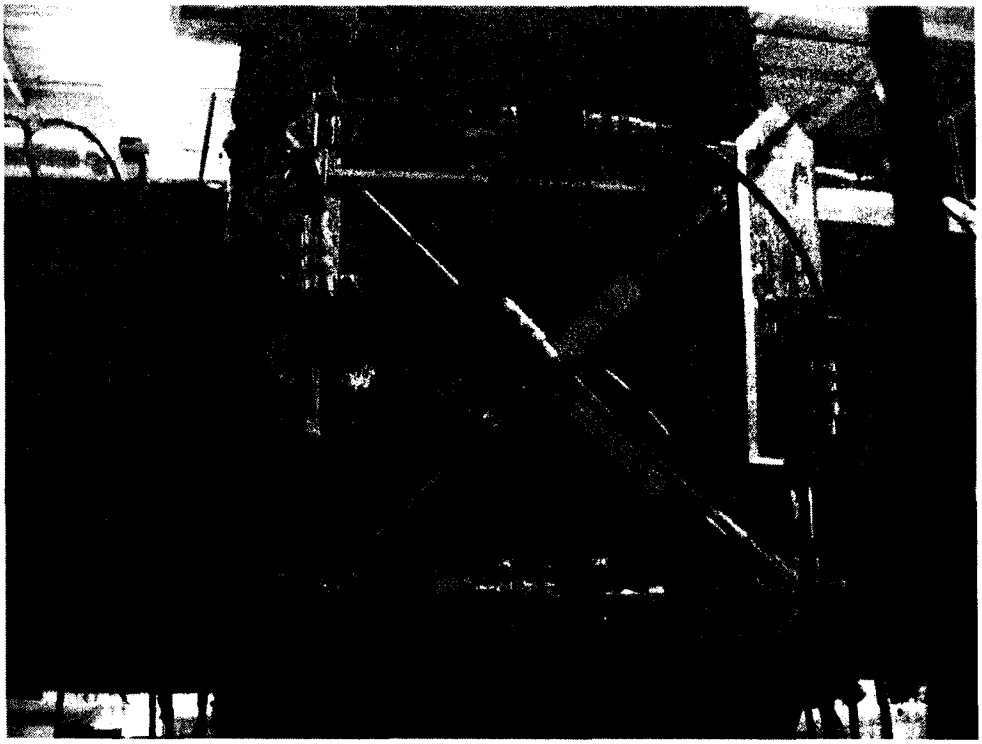

Figure 6.18 Potentiometer layout for measuring the joint distortion

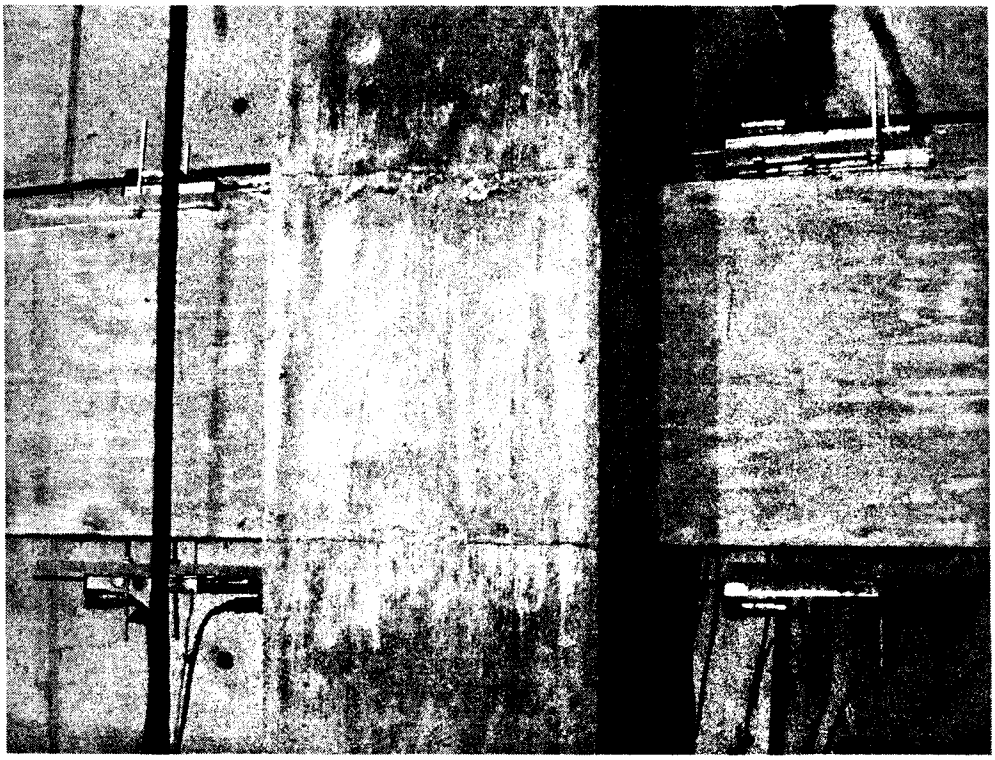

Figure 6.19 Potentiometer layout for measuring the beam end rotations and rebar slips

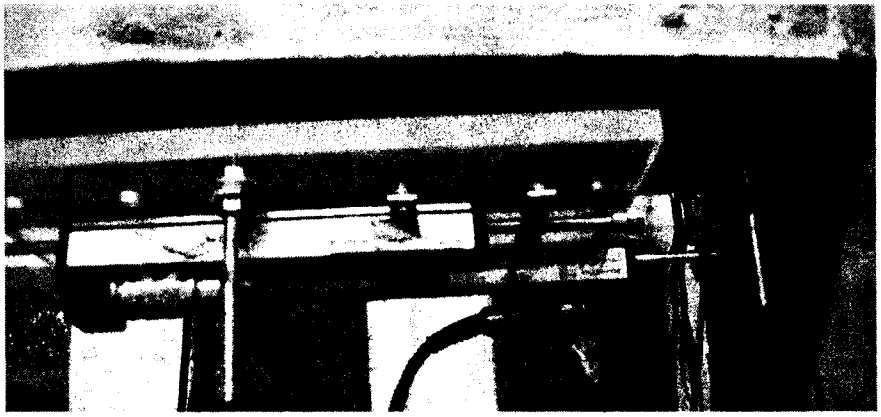

(a)

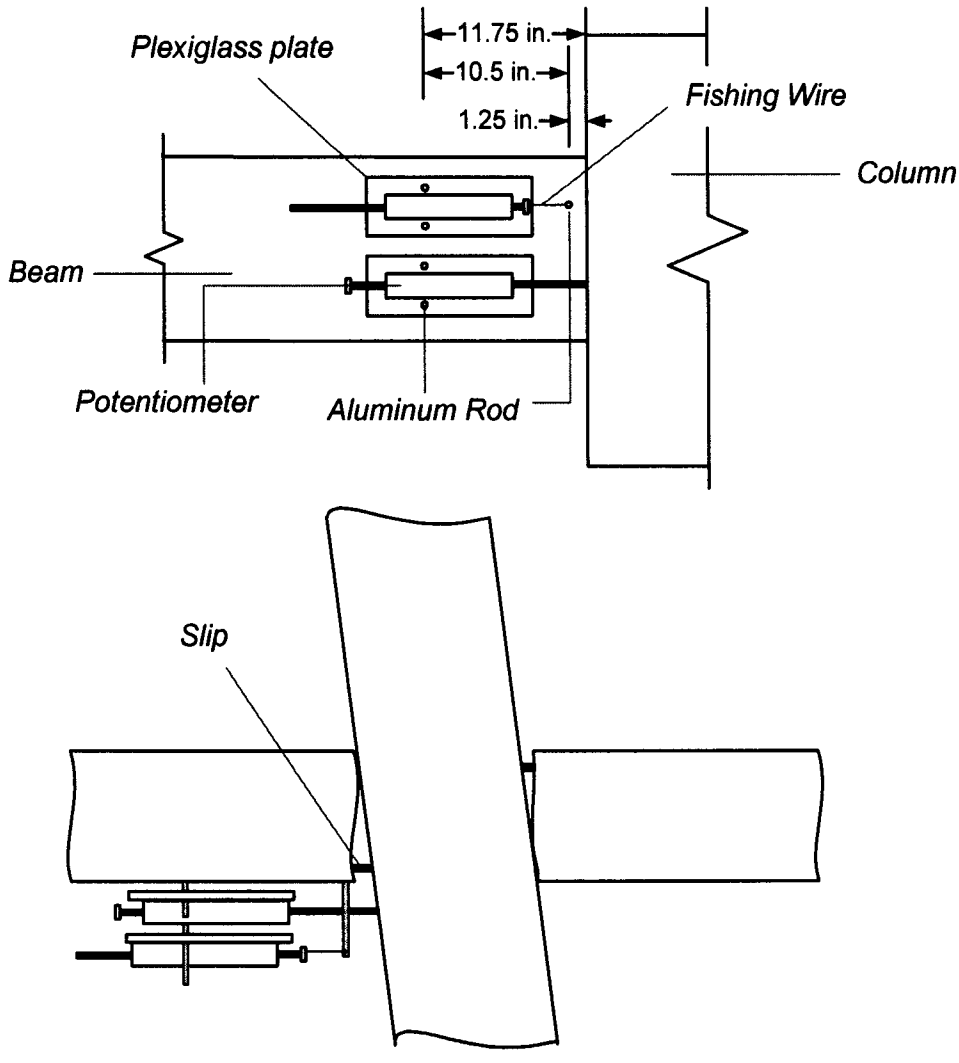

(b)

Figure 6.20 (a) A close-up view of potentiometers at bottom of the beam; (b) Details of the layout

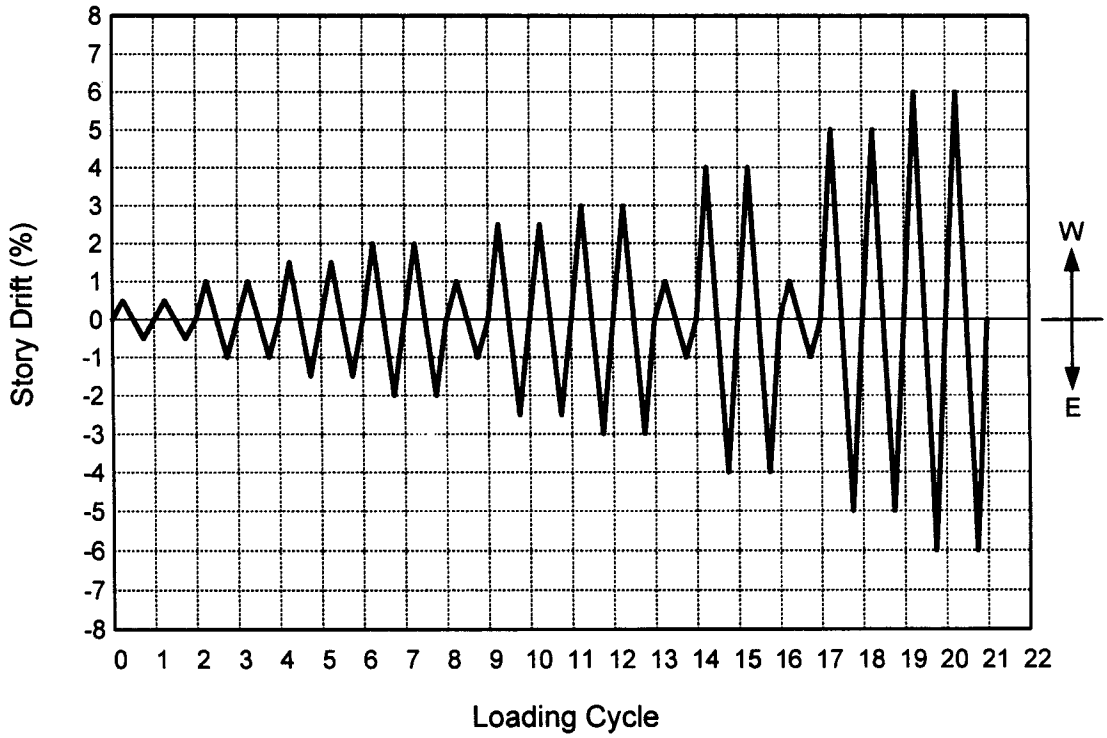

Figure 6.21 Lateral displacement history

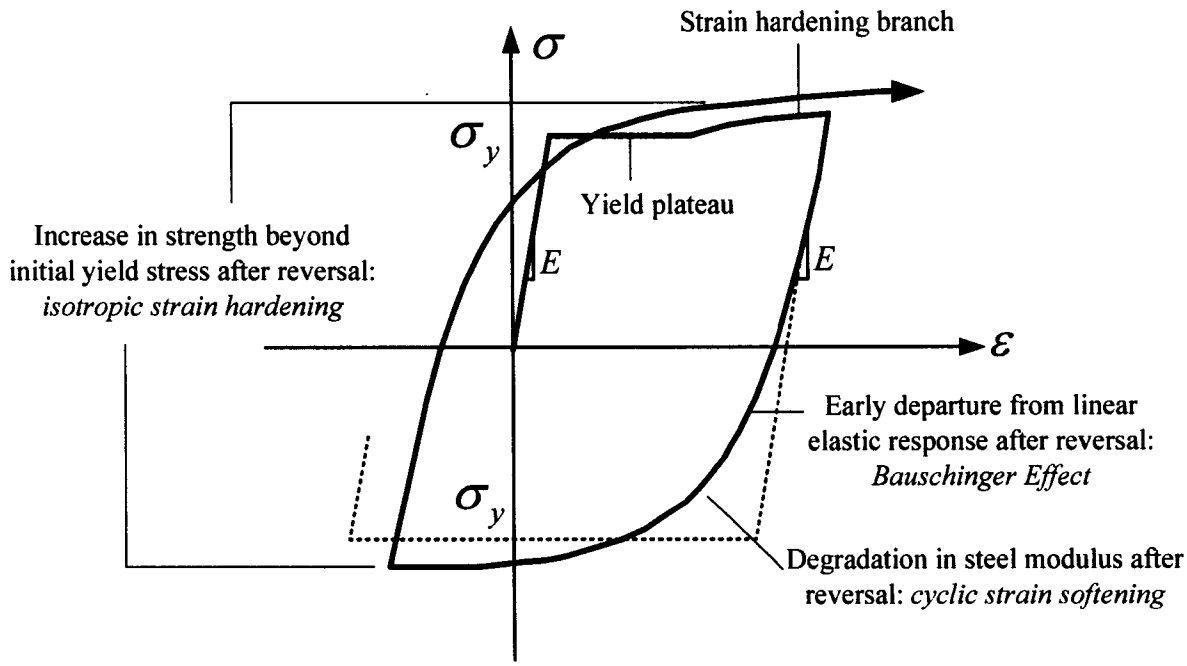

Figure 6.22 Characteristics of hysteretic stress-strain response of reinforcing steel (CEB, 1996)

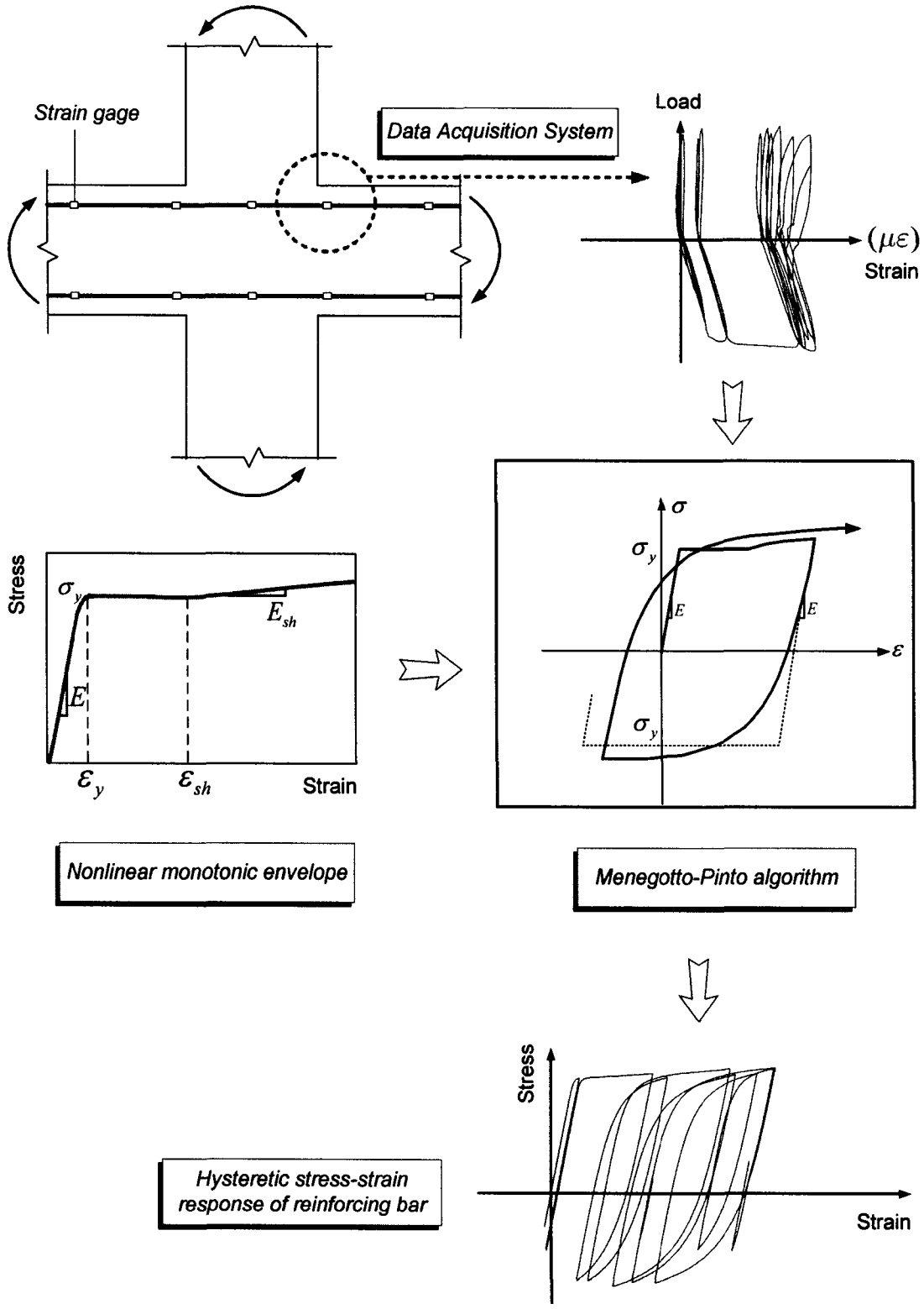

(a)

Figure 6.23 Bond stress calculation: (a) Calculating hysteretic stress-strain relation of reinforcing bar

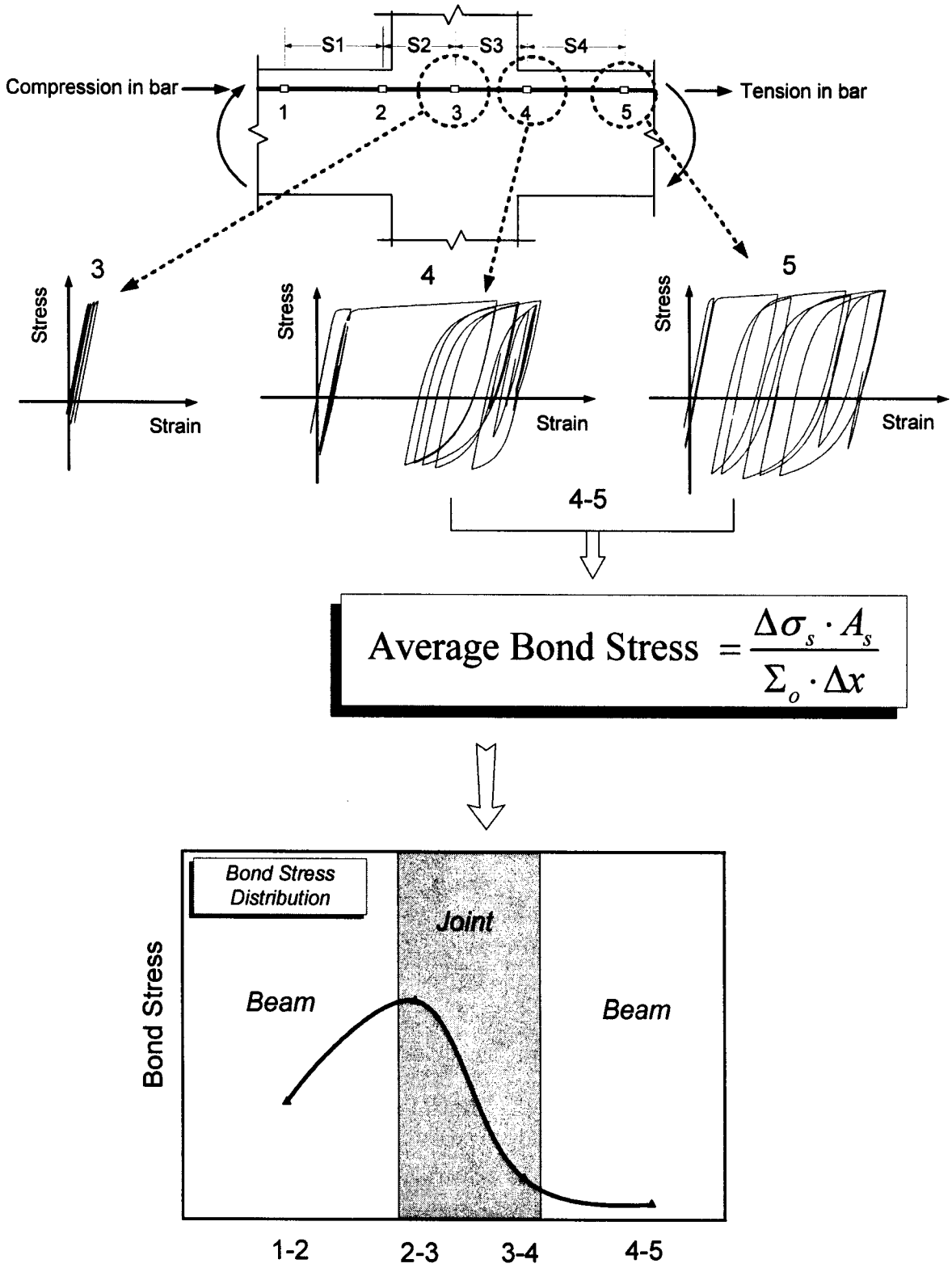

(b)

Figure 6.23 Bond stress calculation: (b) Calculating average bond stresses along reinforcing bar

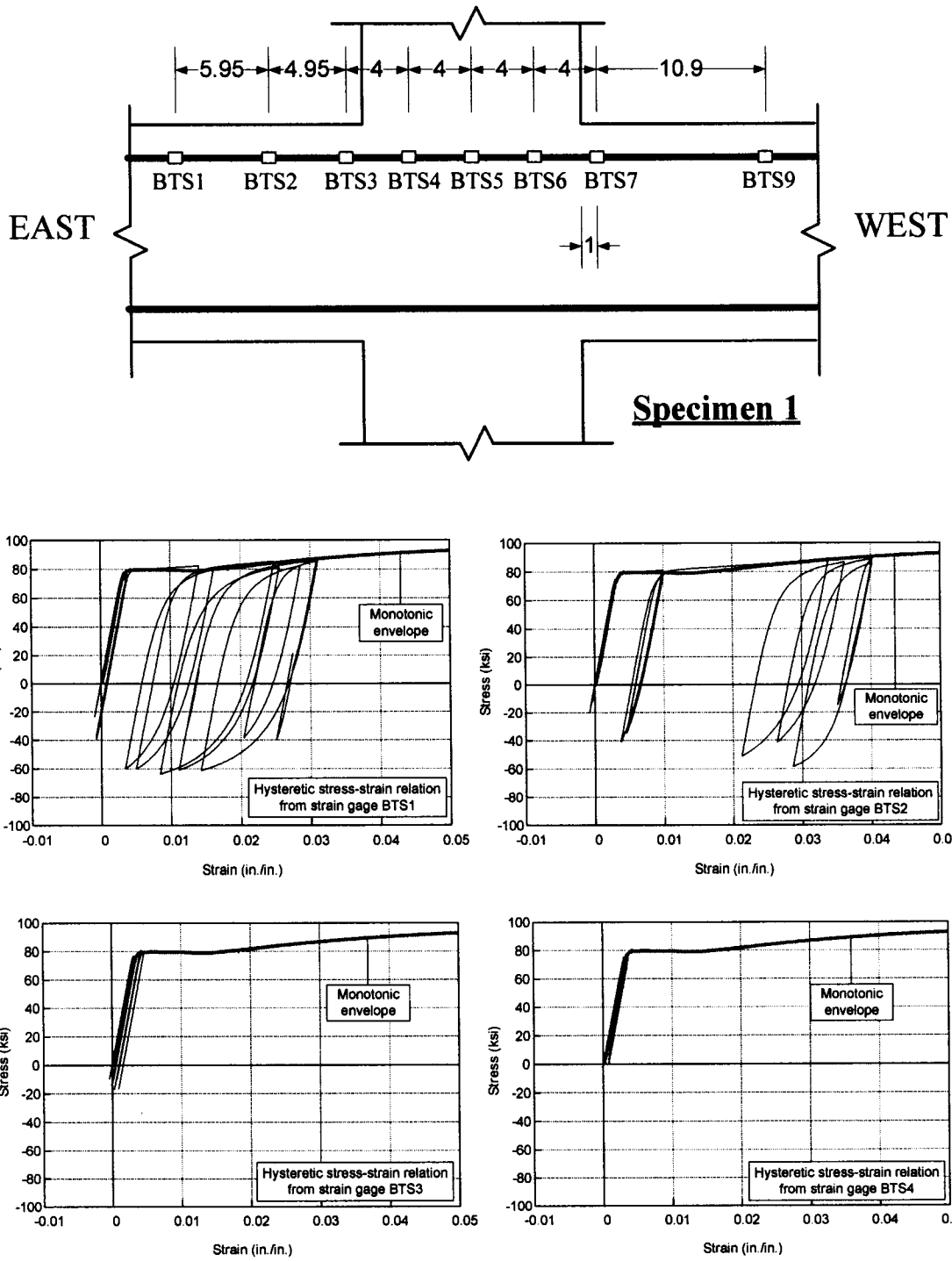

Figure 6.24 Hysteretic stress-strain responses of rebar at various locations (BTS series, Specimen 1)

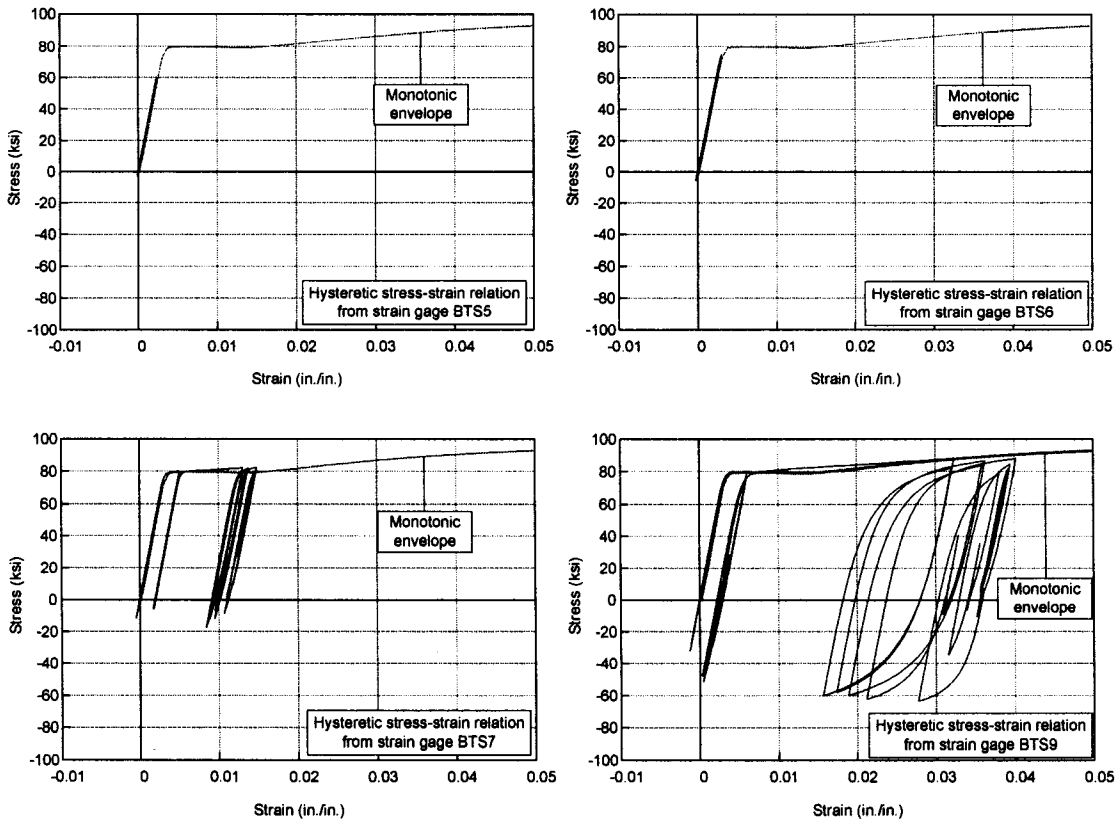

Figure 6.24 (Continued) Hysteretic stress-strain responses of rebar at various locations (BTS series, Specimen 1)

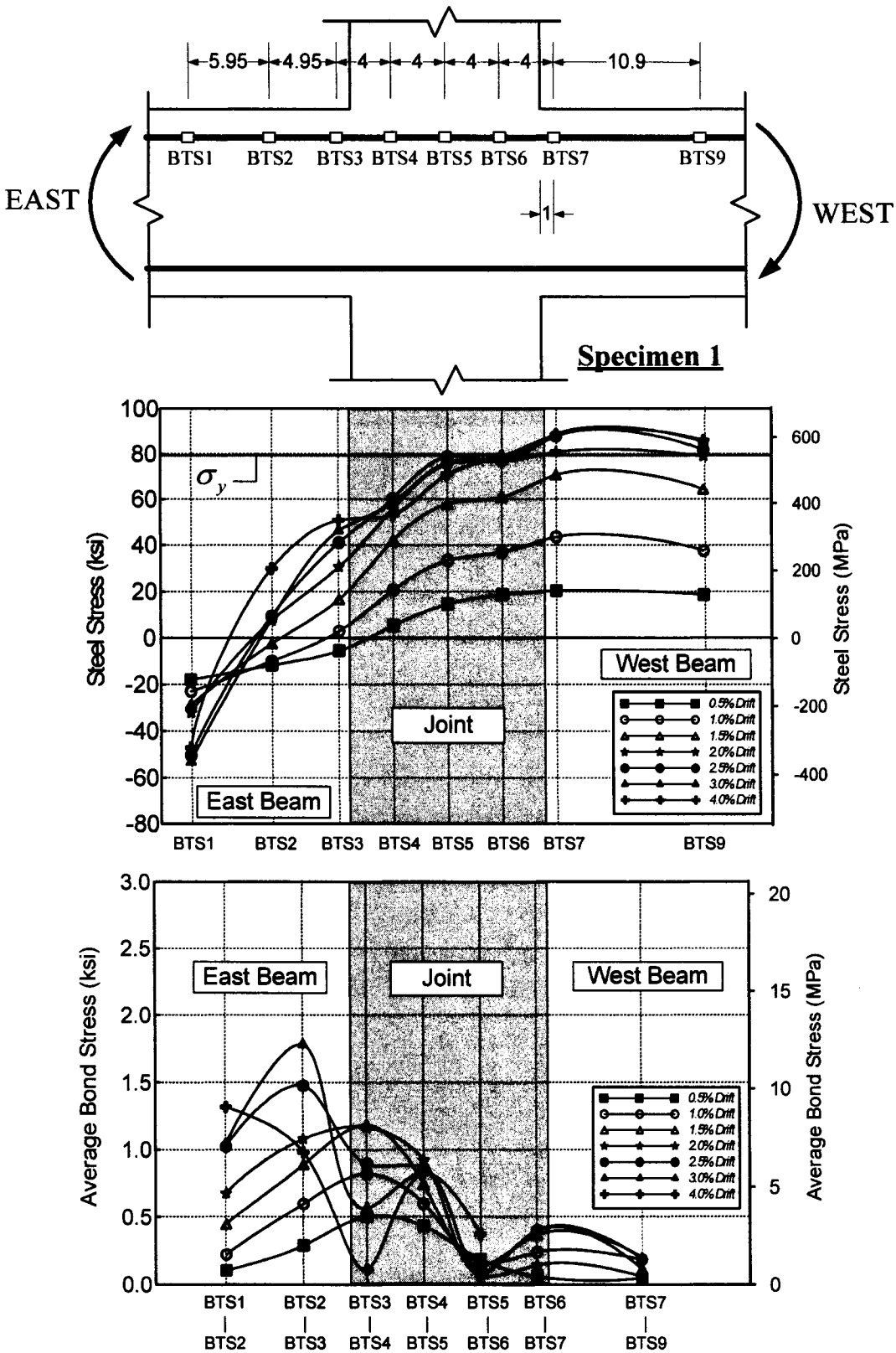

Figure 6.25 Steel stress and bond stress distributions in beam bar when specimen was pushed towards East (BTS series, Specimen 1)

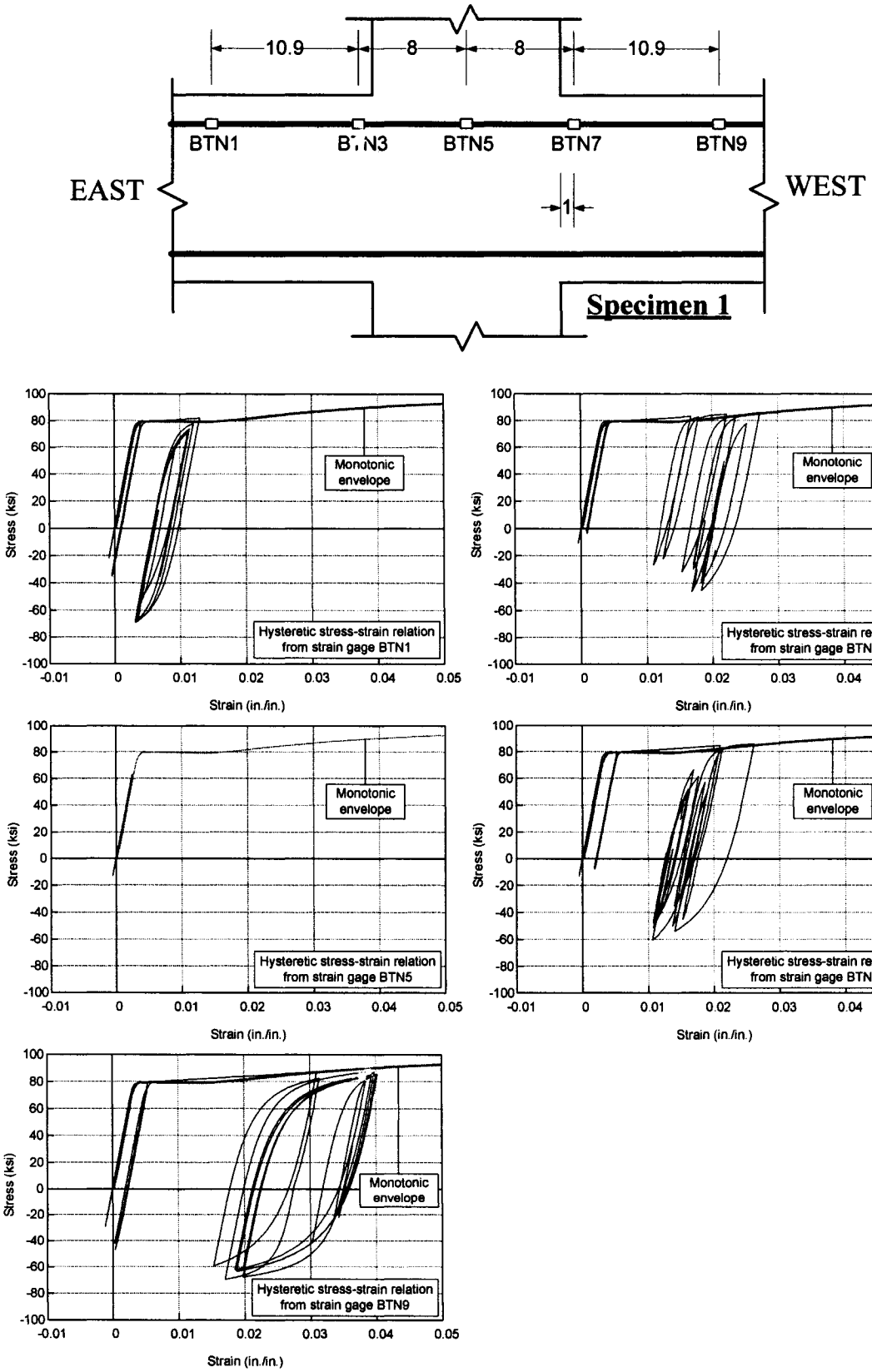

Figure 6.26 Hysteretic stress-strain responses of rebar at various locations (BTN series, Specimen 1)

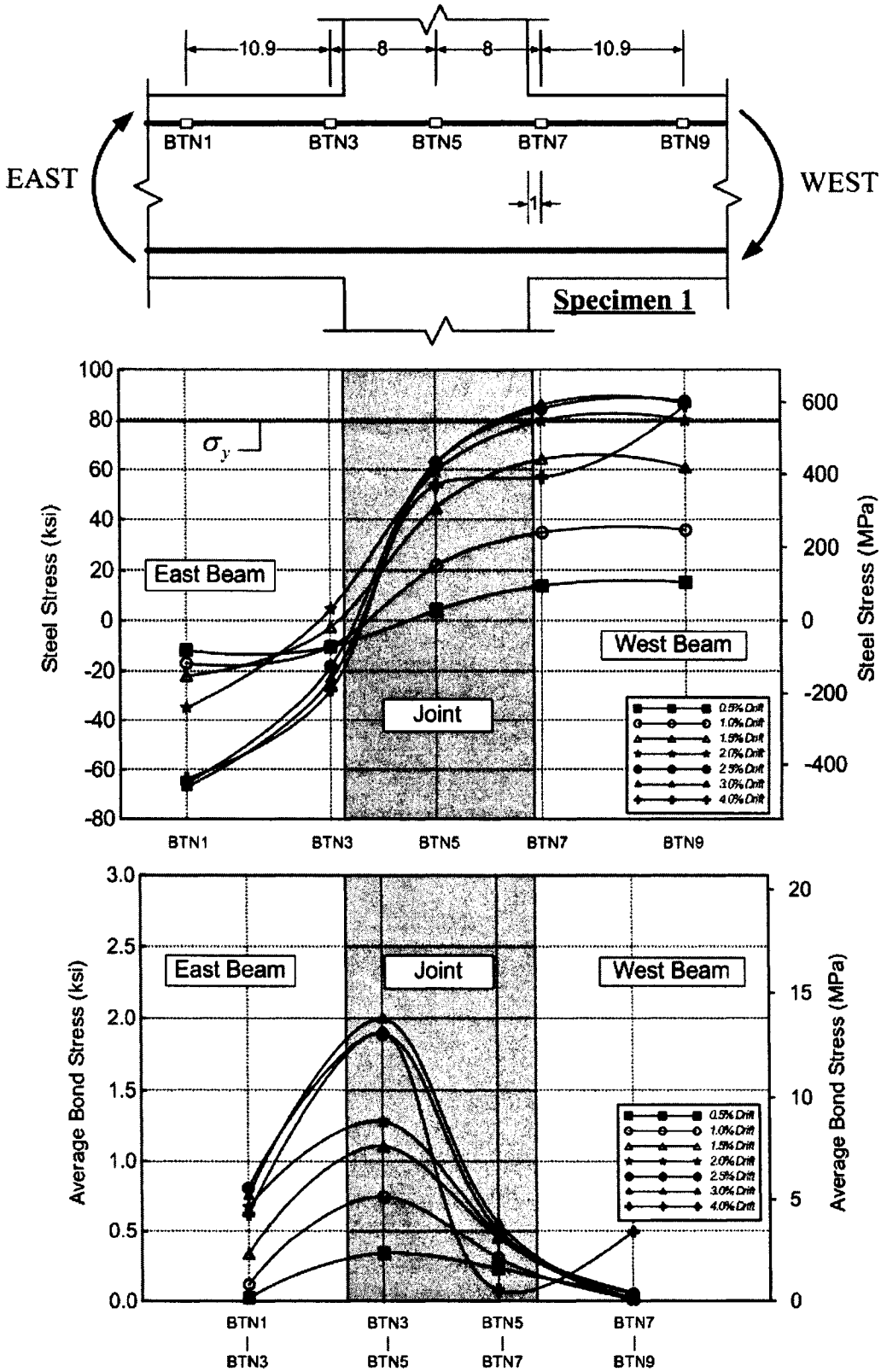

Figure 6.27 Steel stress and bond stress distributions in beam bar when specimen was pushed towards East (BTN series, Specimen 1)

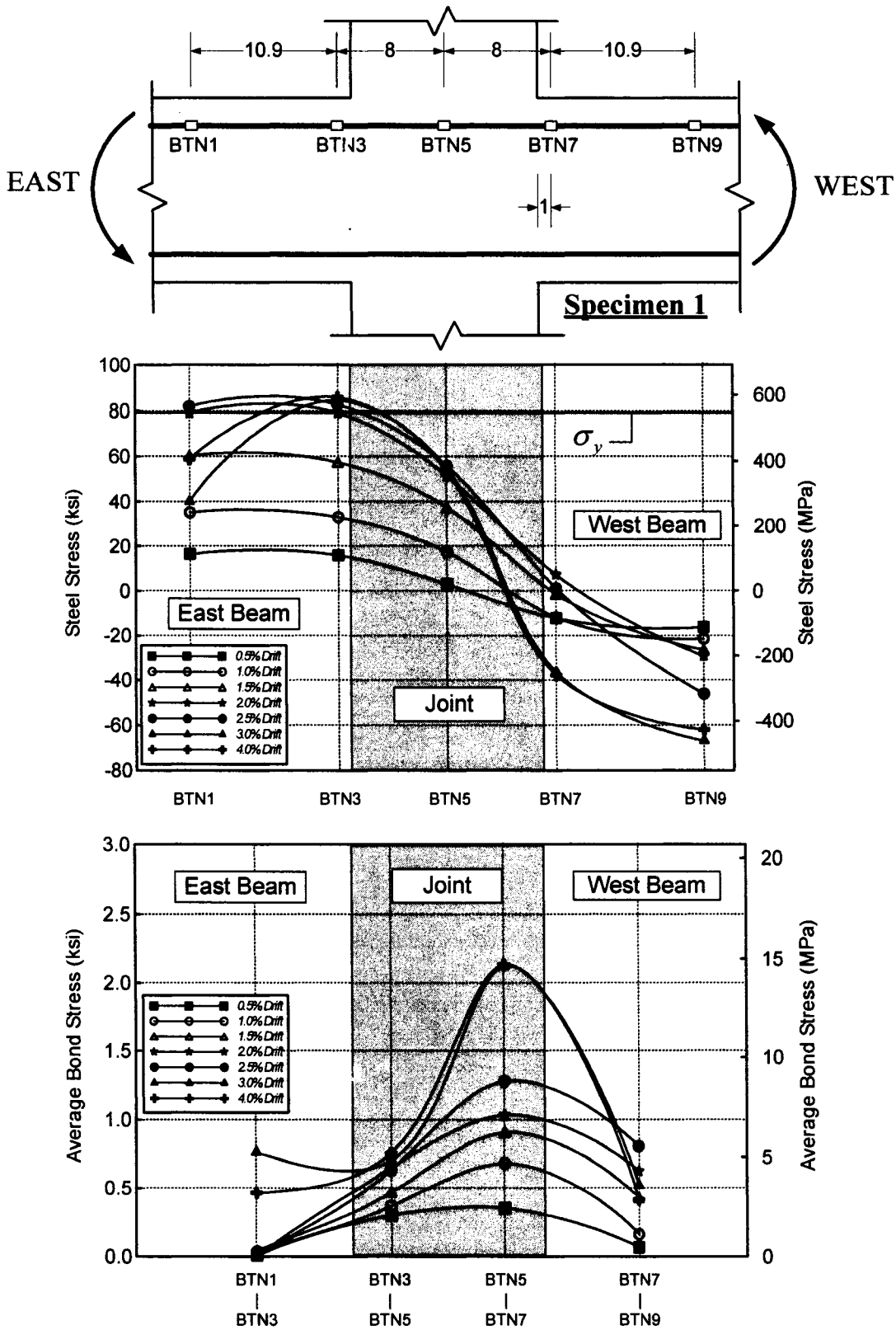

Figure 6.28 Steel stress and bond stress distributions in beam bar when specimen was pushed towards West (BTN series, Specimen 1)

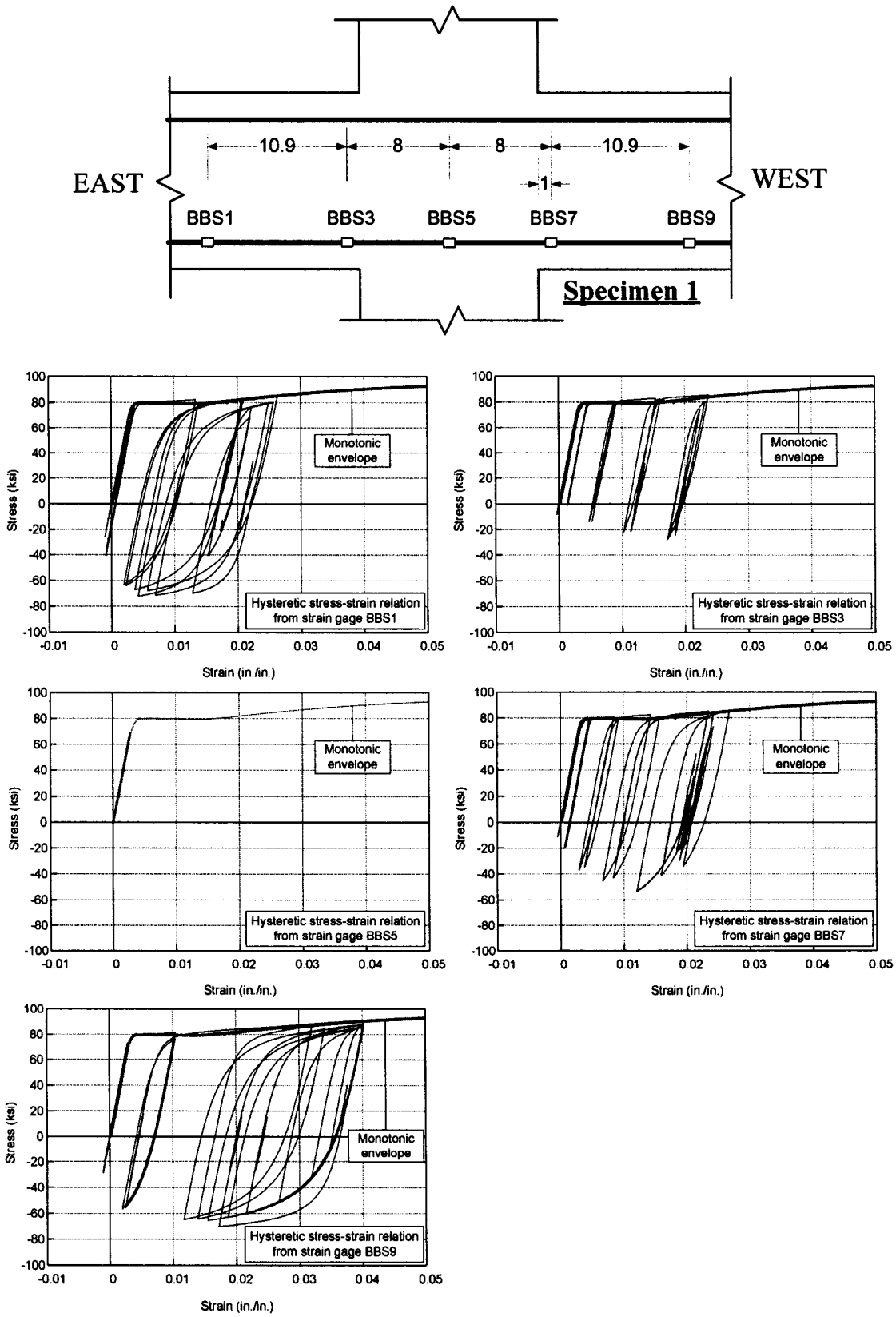

Figure 6.29 Hysteretic stress-strain responses of rebar at various locations (BBS series, Specimen 1)

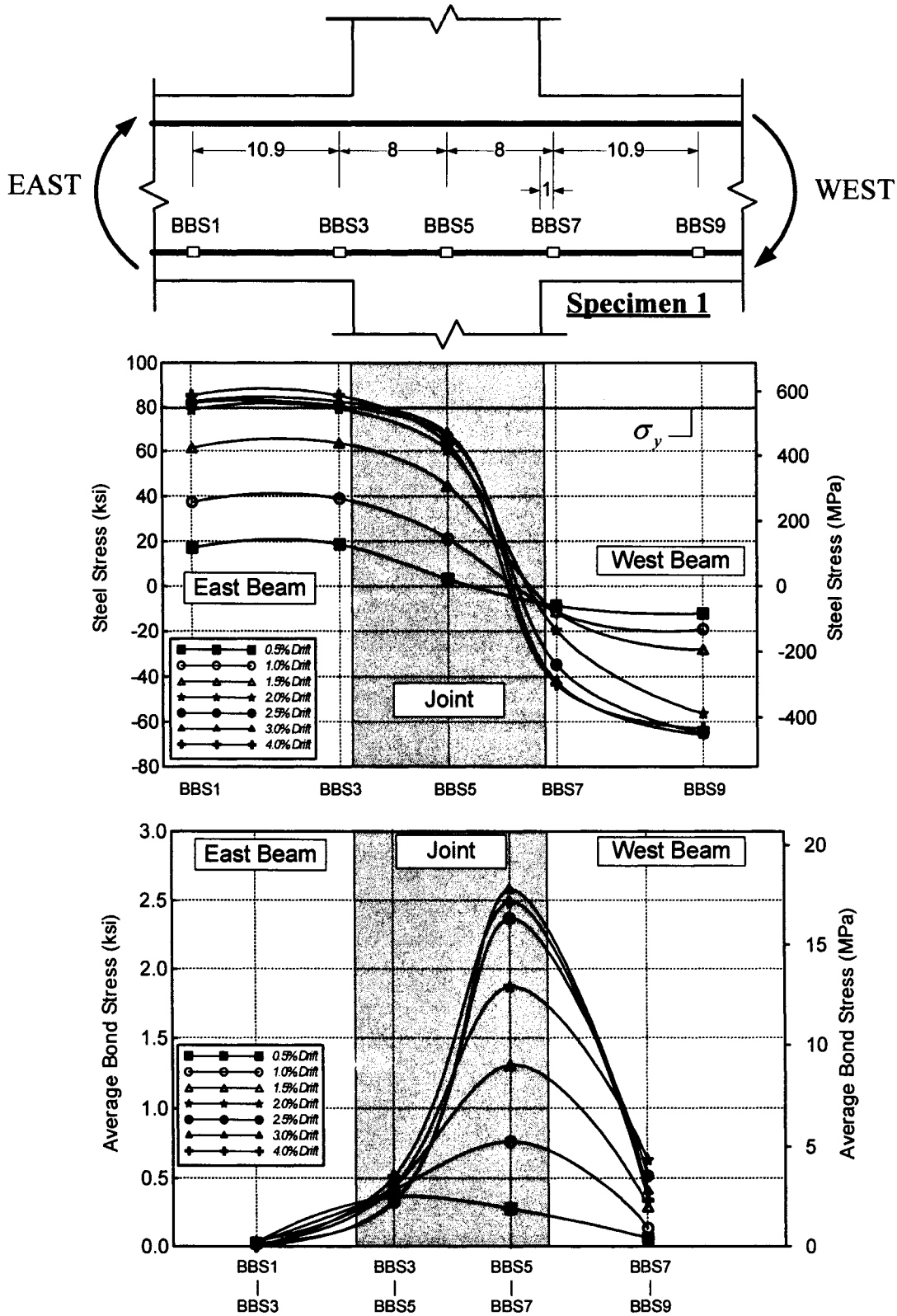

Figure 6.30 Steel stress and bond stress distributions in beam bar when specimen was pushed towards East (BBS series, Specimen 1)

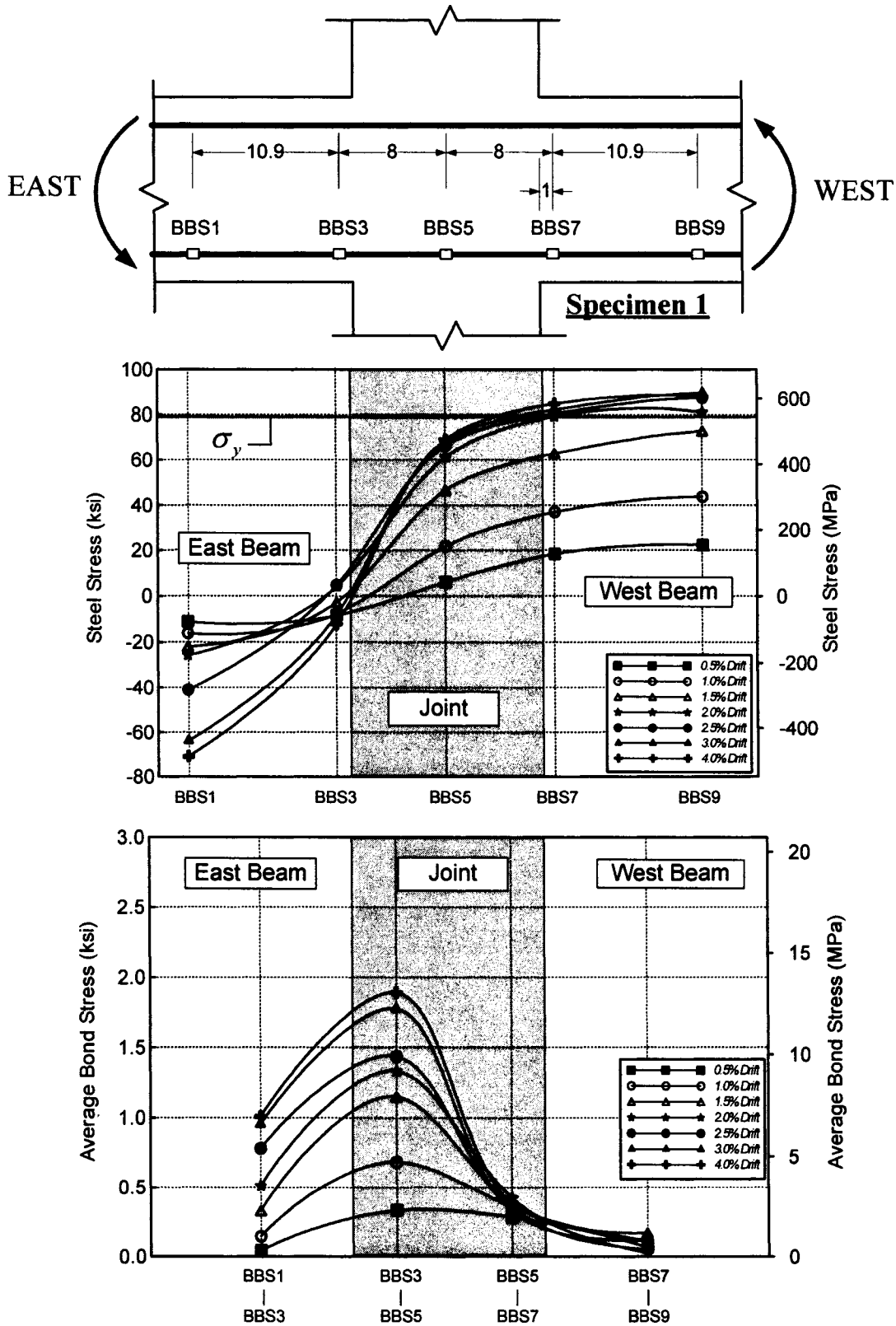

Figure 6.31 Steel stress and bond stress distributions in beam bar when specimen was pushed towards West (BBS series, Specimen 1)

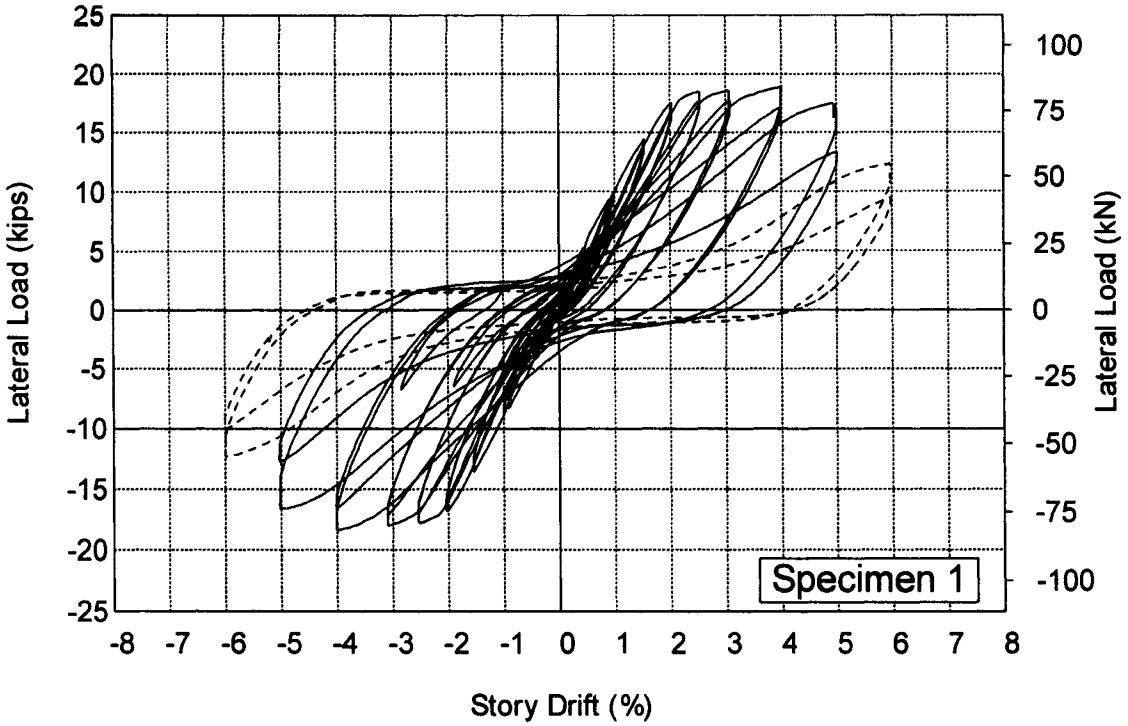

Figure 6.32 Lateral load versus drift response for Specimen 1

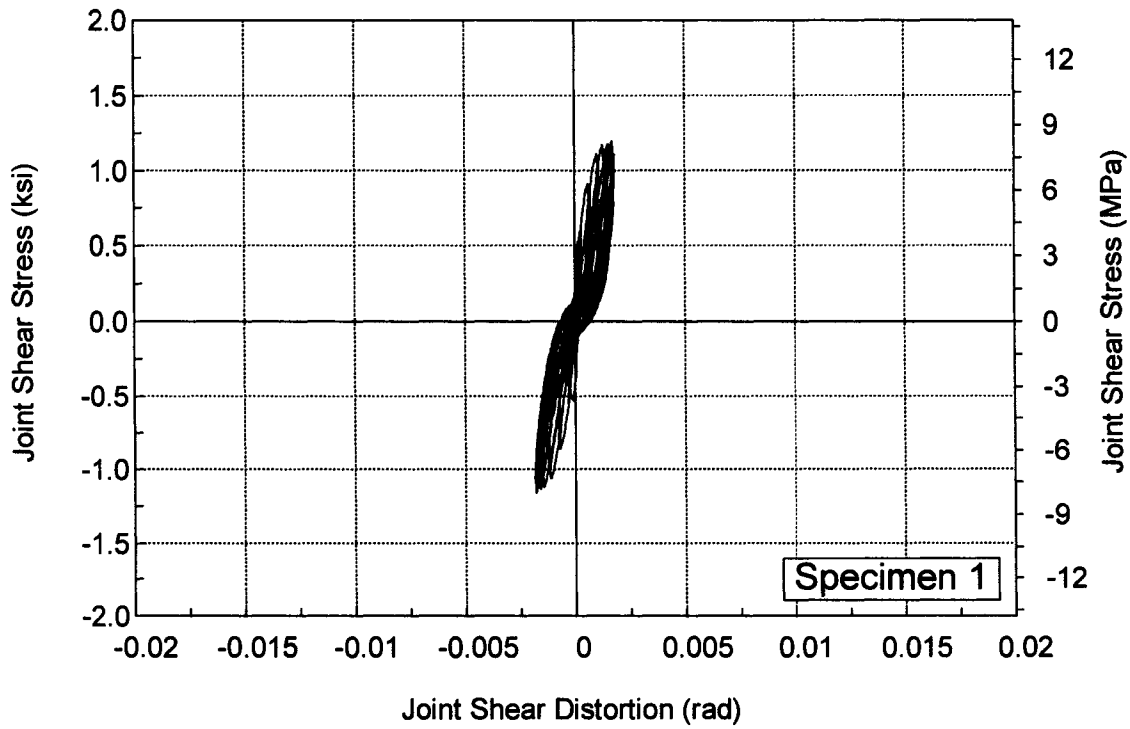

Figure 6.33 Joint shear stress versus joint distortion response for Specimen 1

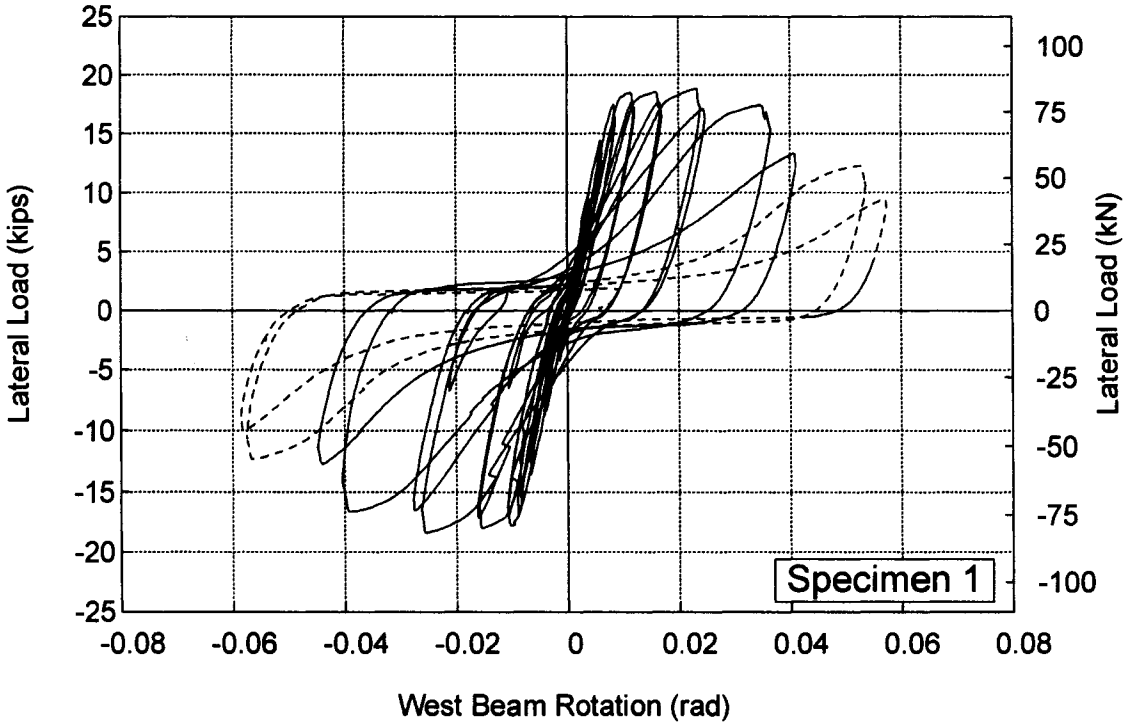

(a)

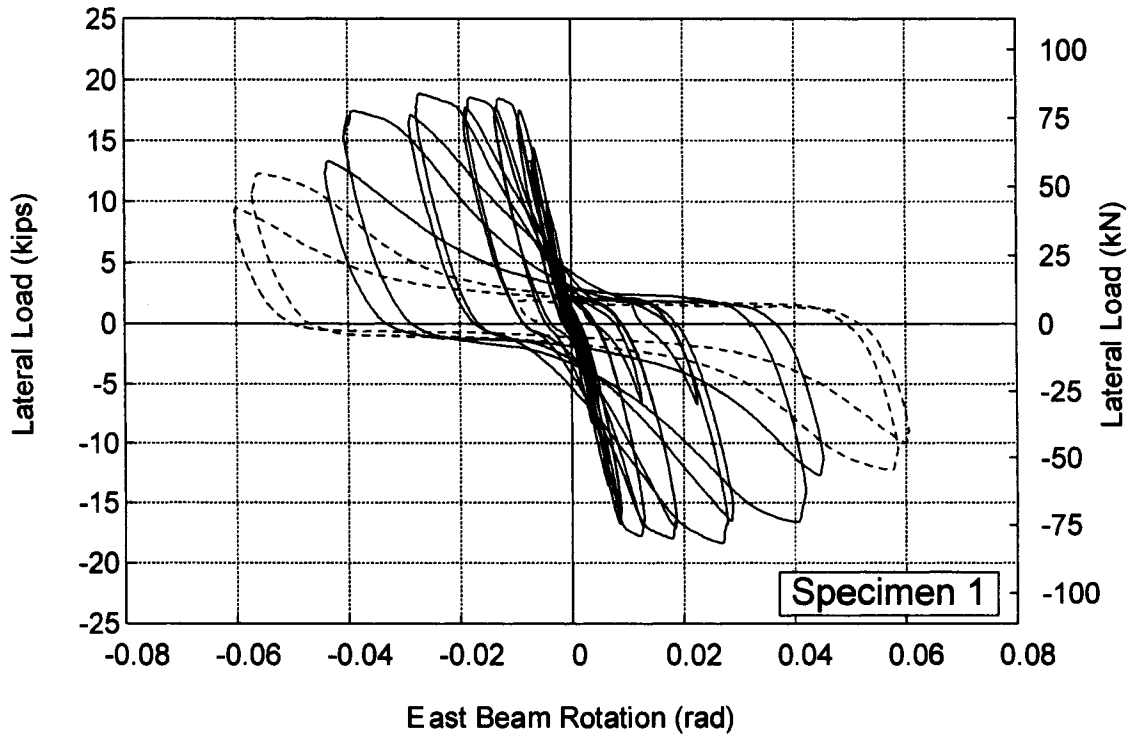

(b)

Figure 6.34 Lateral load versus beam rotation angle response for Specimen 1: (a) West beam; (b) East beam

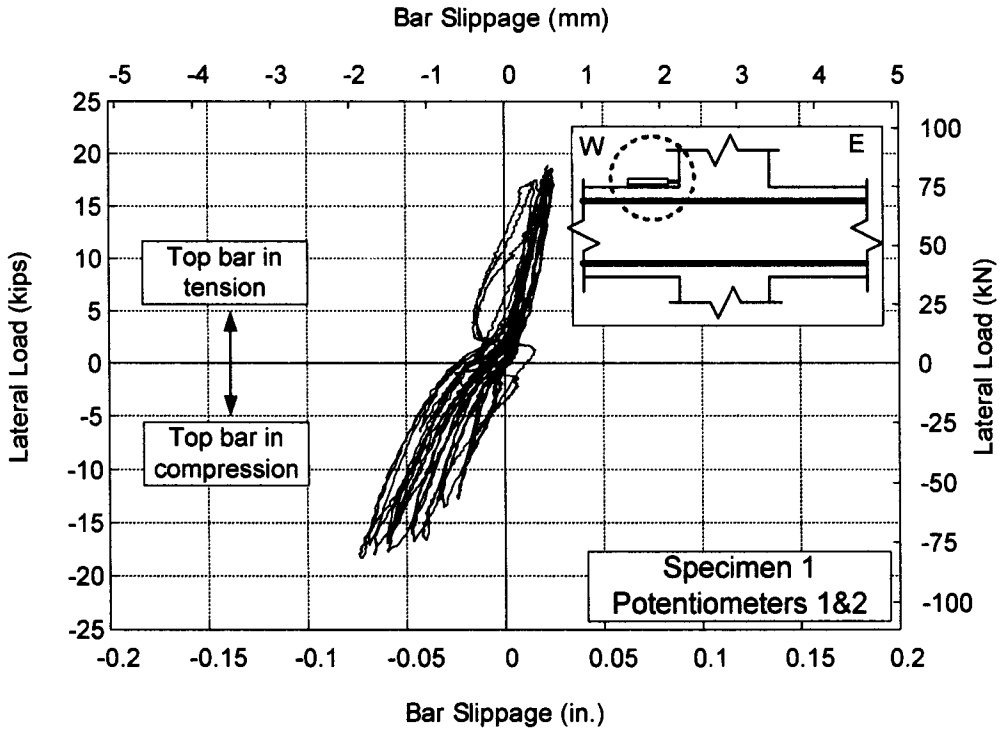

(a)

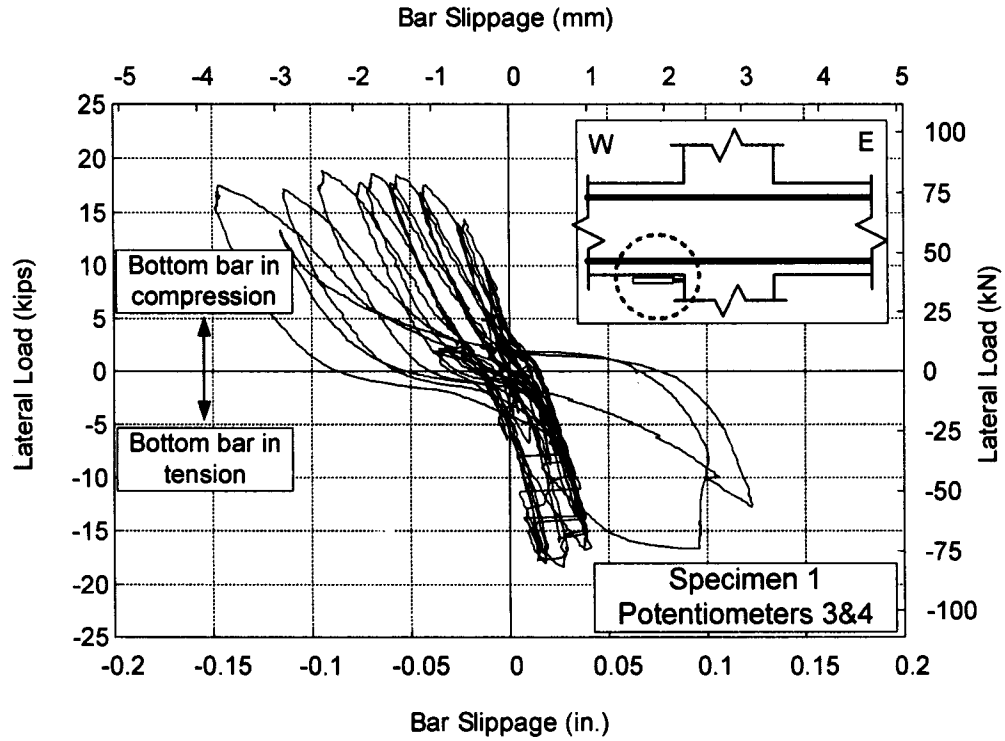

(b)

Figure 6.35 Average bar slippage measured by potentiometers up to 5% story drift in Specimen 1: (a) Top bars; (b) Bottom bars

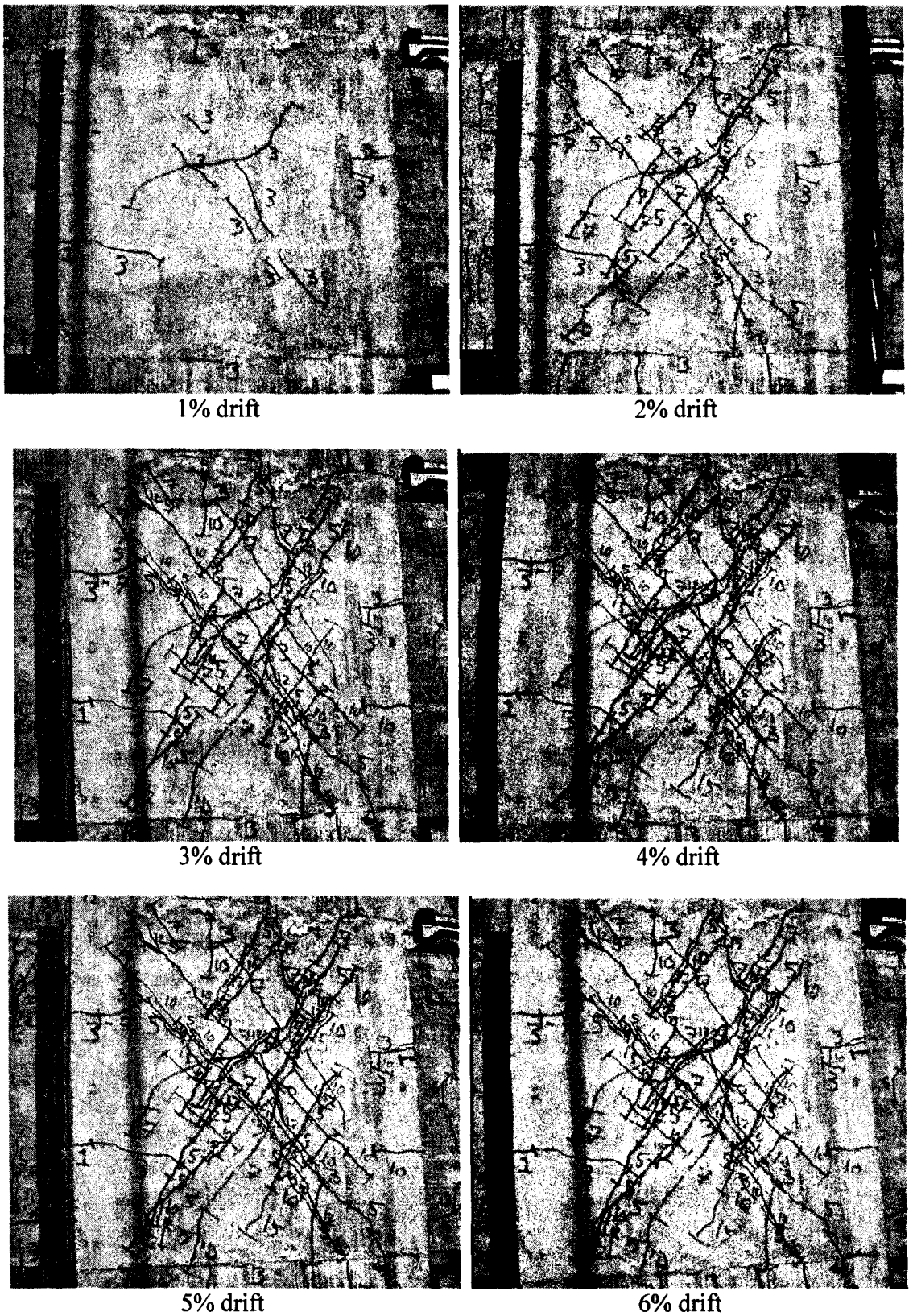

Figure 6.36 Cracking of beam- column joint at various drift levels (Specimen 1)

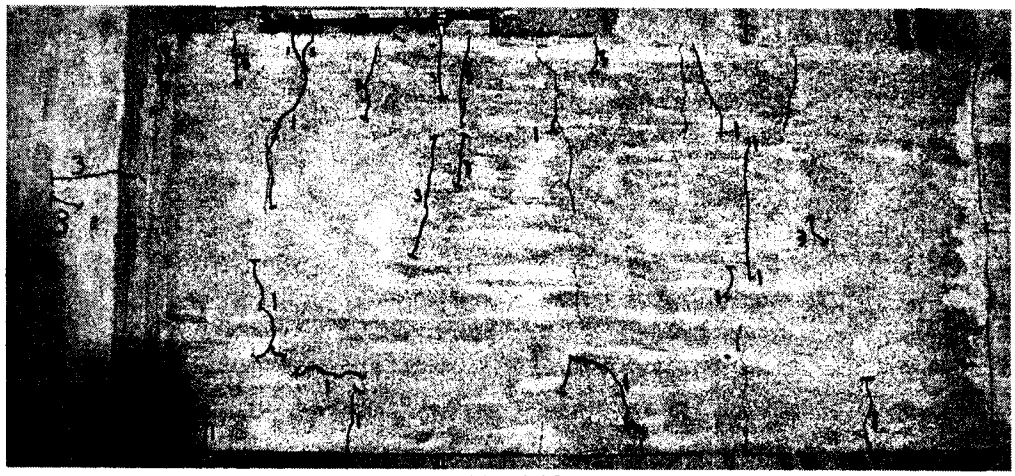

1% drift

3% drift

5% drift

Figure 6.37(a) Cracking of East beam at various drift levels (Specimen 1)

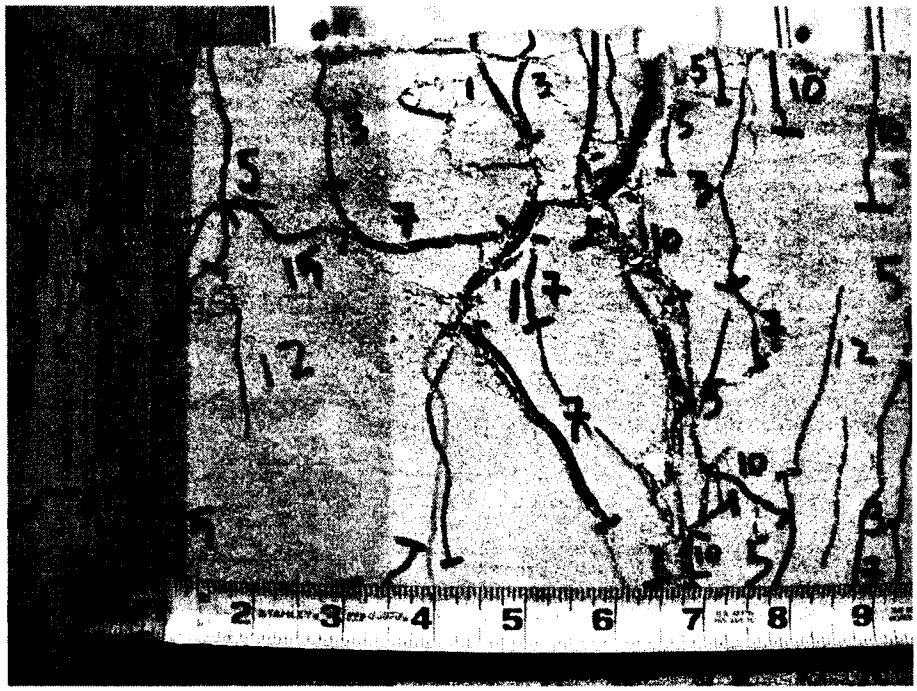

East beam

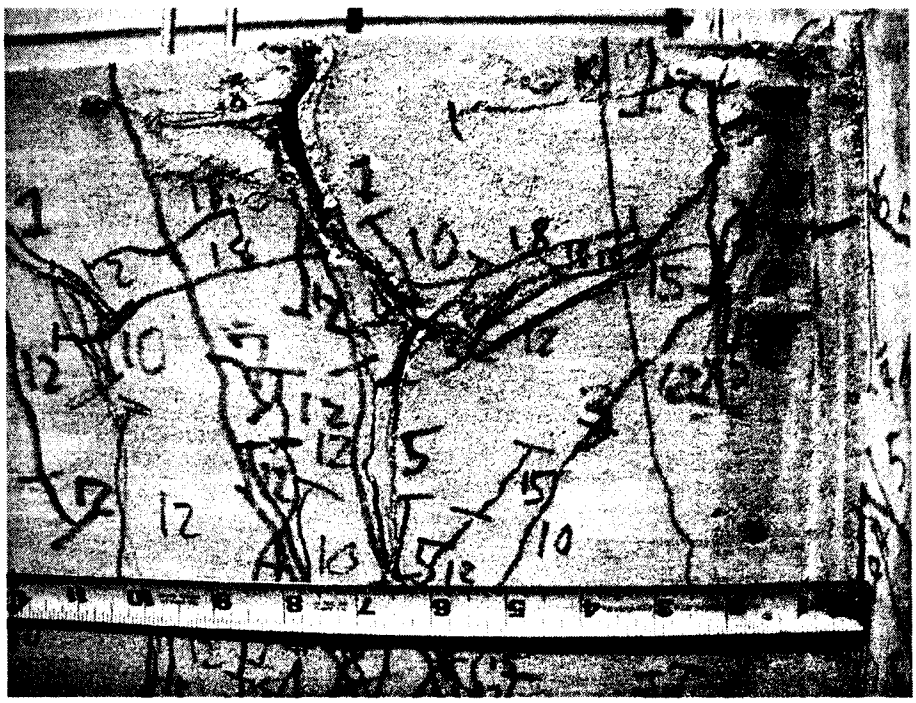

(b) West beam

Figure 6.37(b) Locations of cracks having maximum width in East and West beams (Specimen 1)

2% drift

3% drift

Figure 6.38 Cracking in the beam-column interface at various drift levels (Specimen 1)

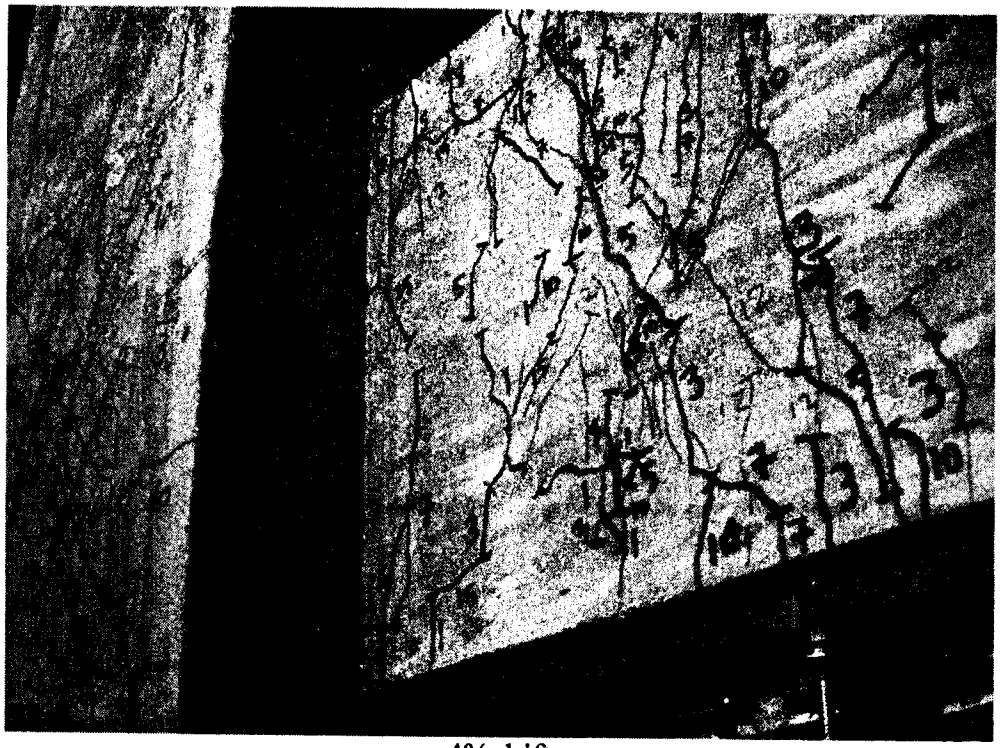

4% drift

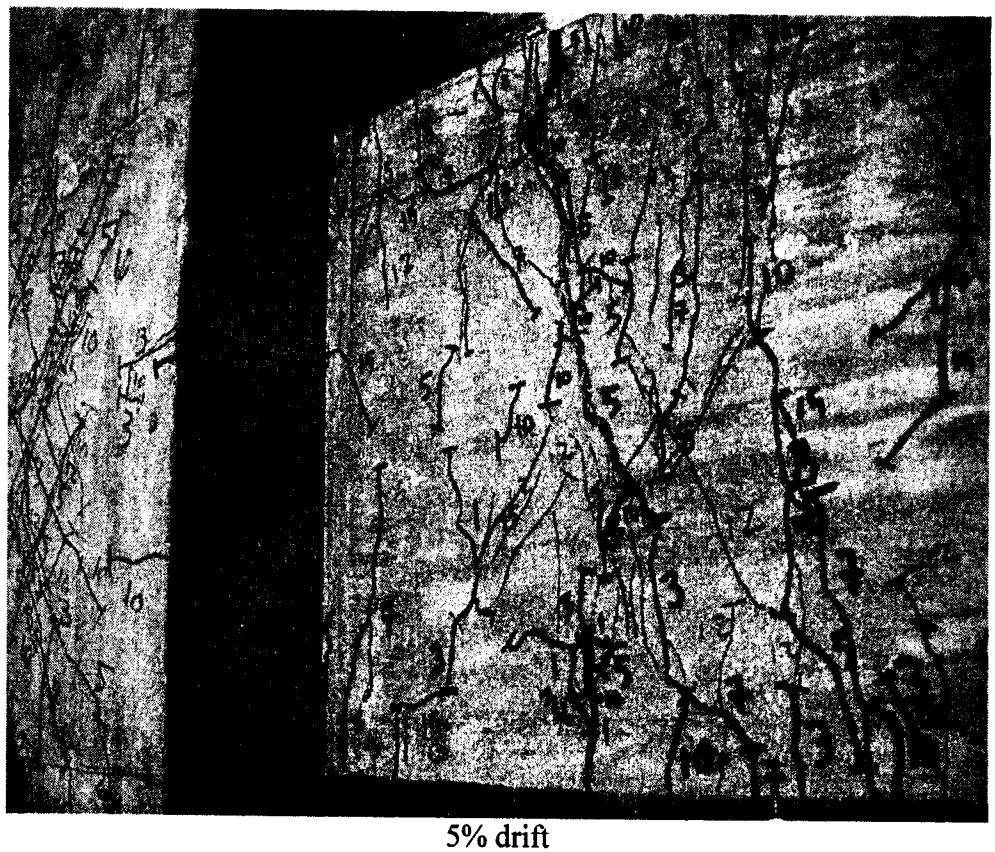

5% drift

Figure 6.38 (continued) Cracking in the beam-column interface at various drift levels (Specimen 1)

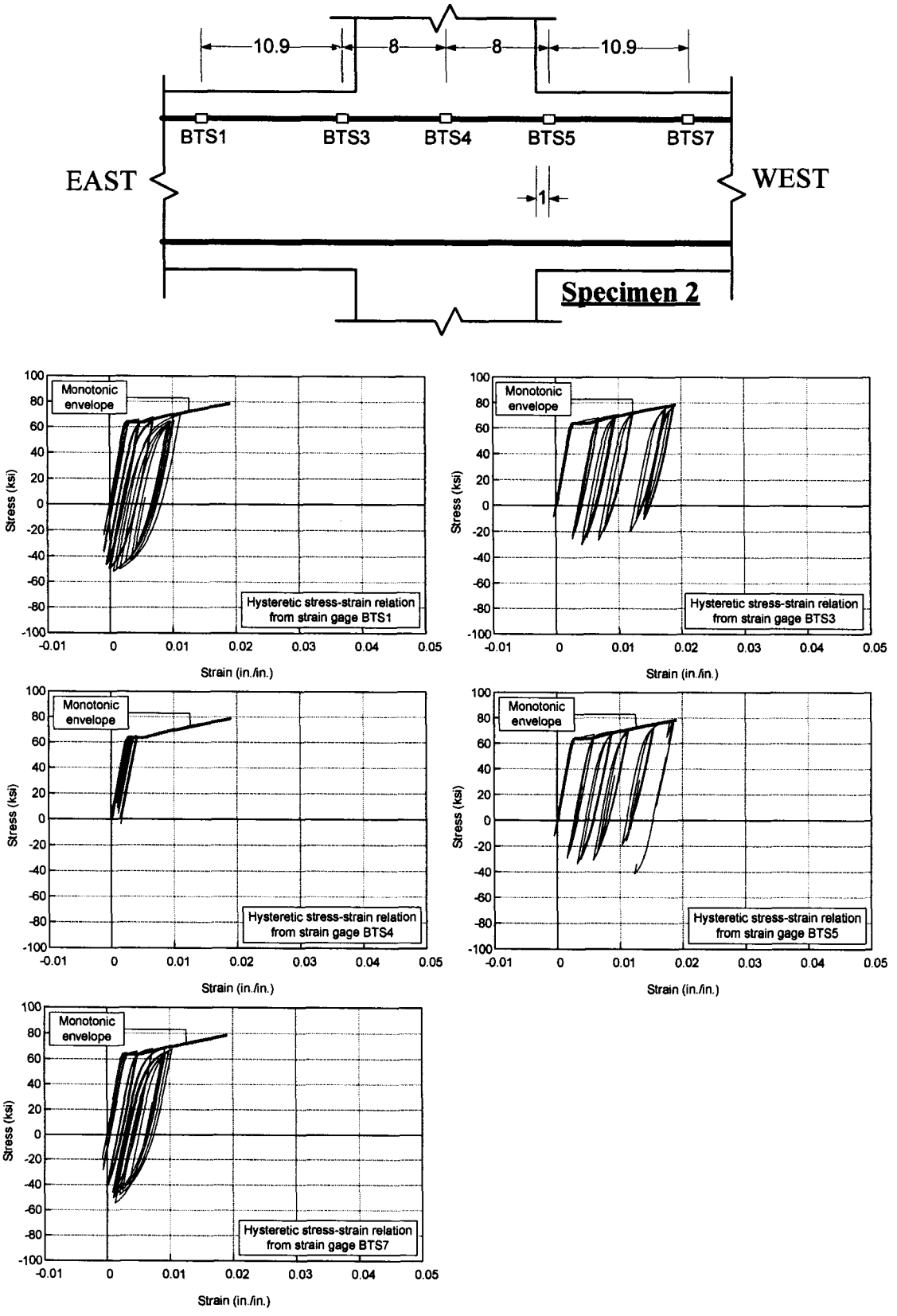

Figure 6.39 Hysteretic stress-strain responses of rebar at various locations (BTS series, Specimen 2)

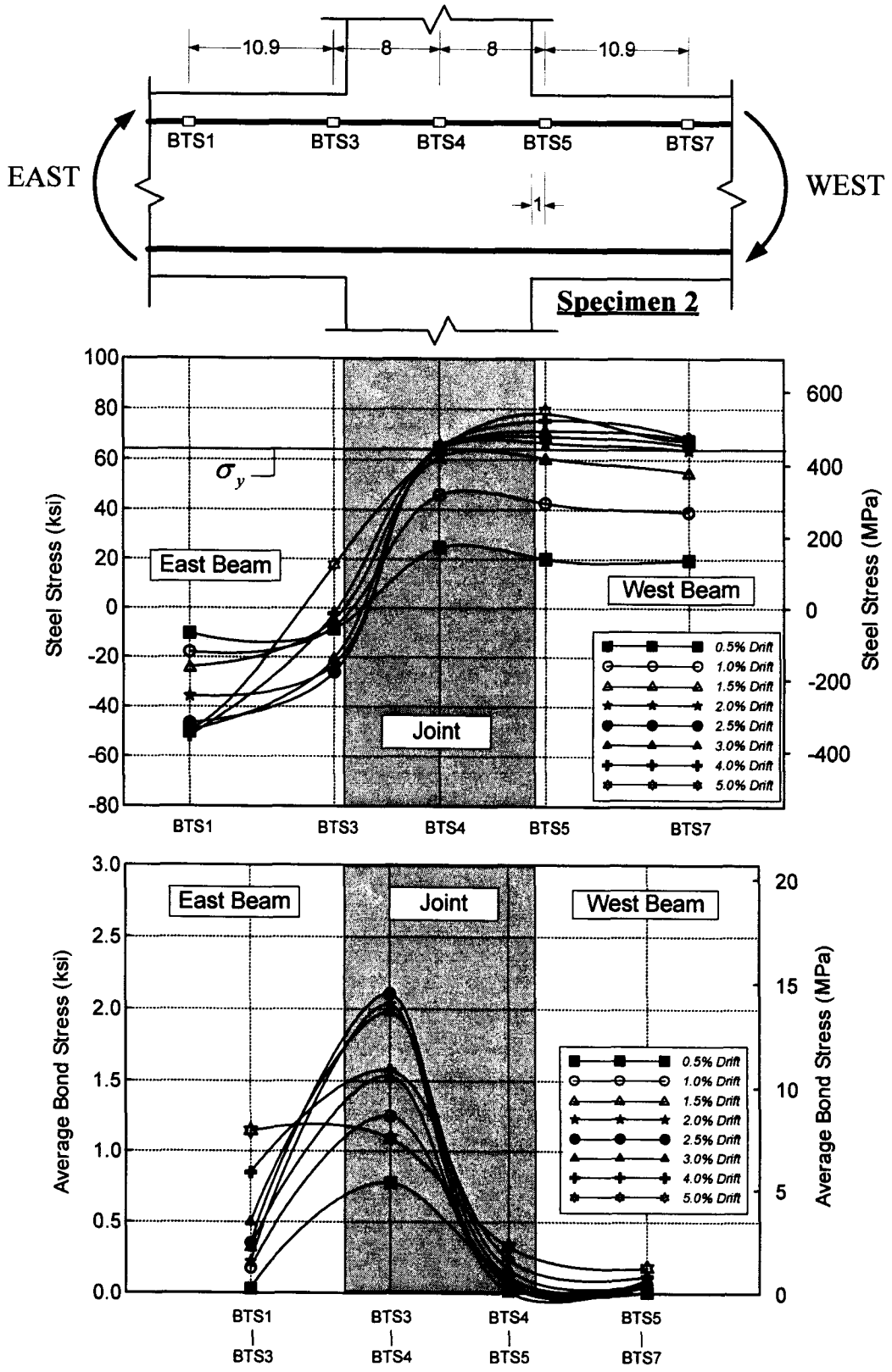

Figure 6.40 Steel stress and bond stress distributions in beam bar when specimen was pushed towards East (BTS series, Specimen 2)

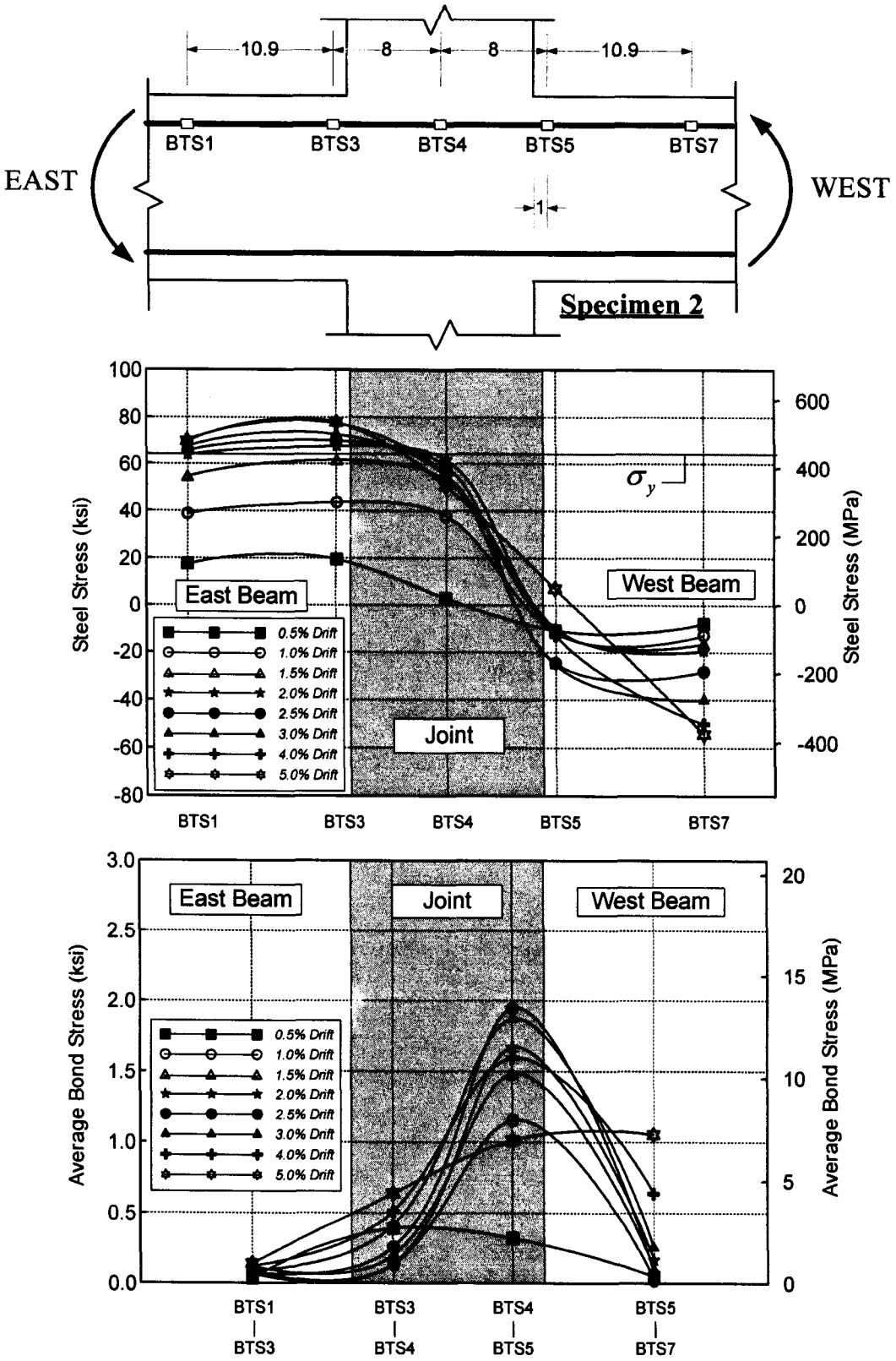

Figure 6.41 Steel stress and bond stress distributions in beam bar when specimen was pushed towards West (BTS series, Specimen 2)

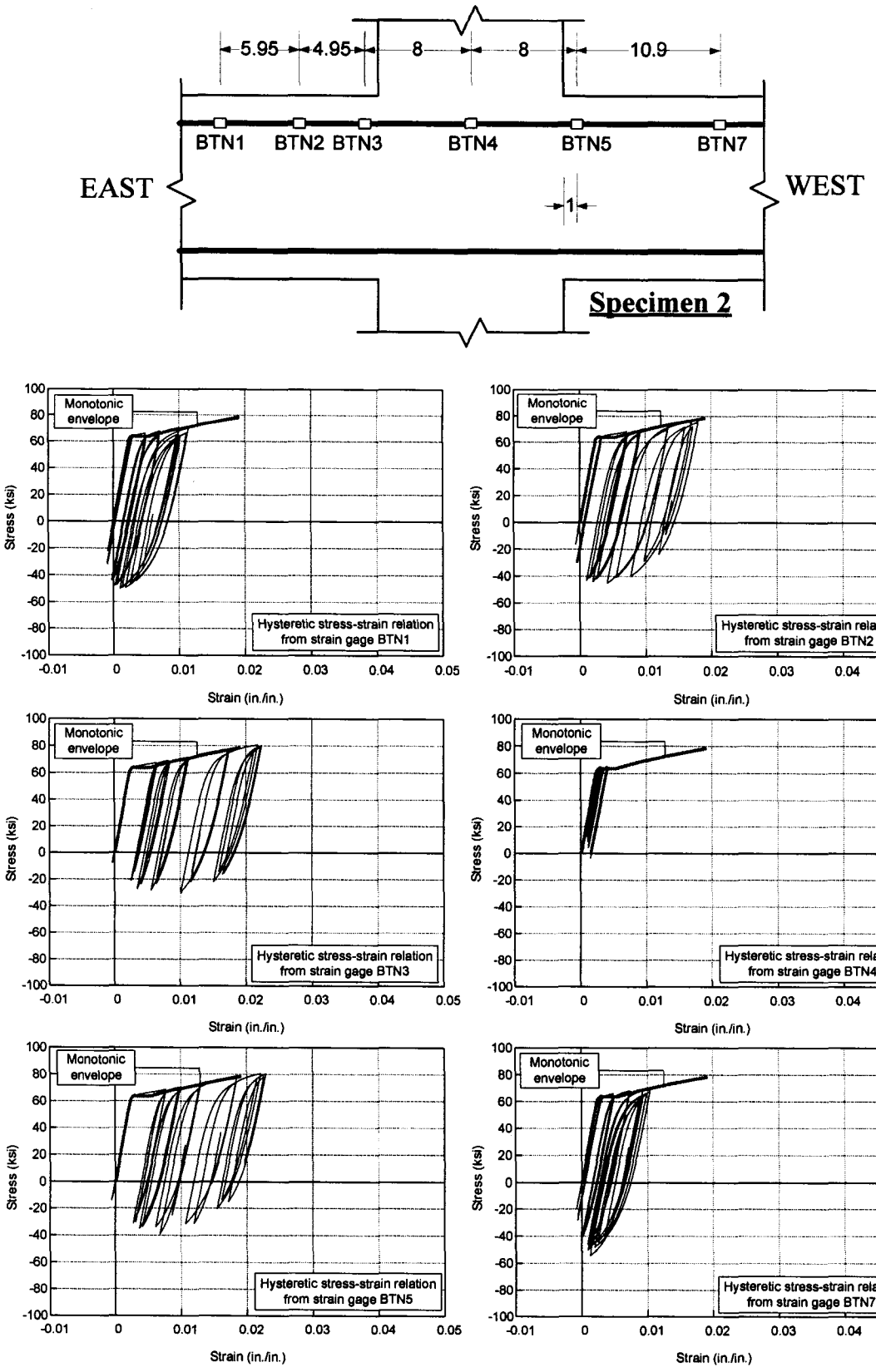

Figure 6.42 Hysteretic stress-strain responses of rebar at various locations (BTN series, Specimen 2)

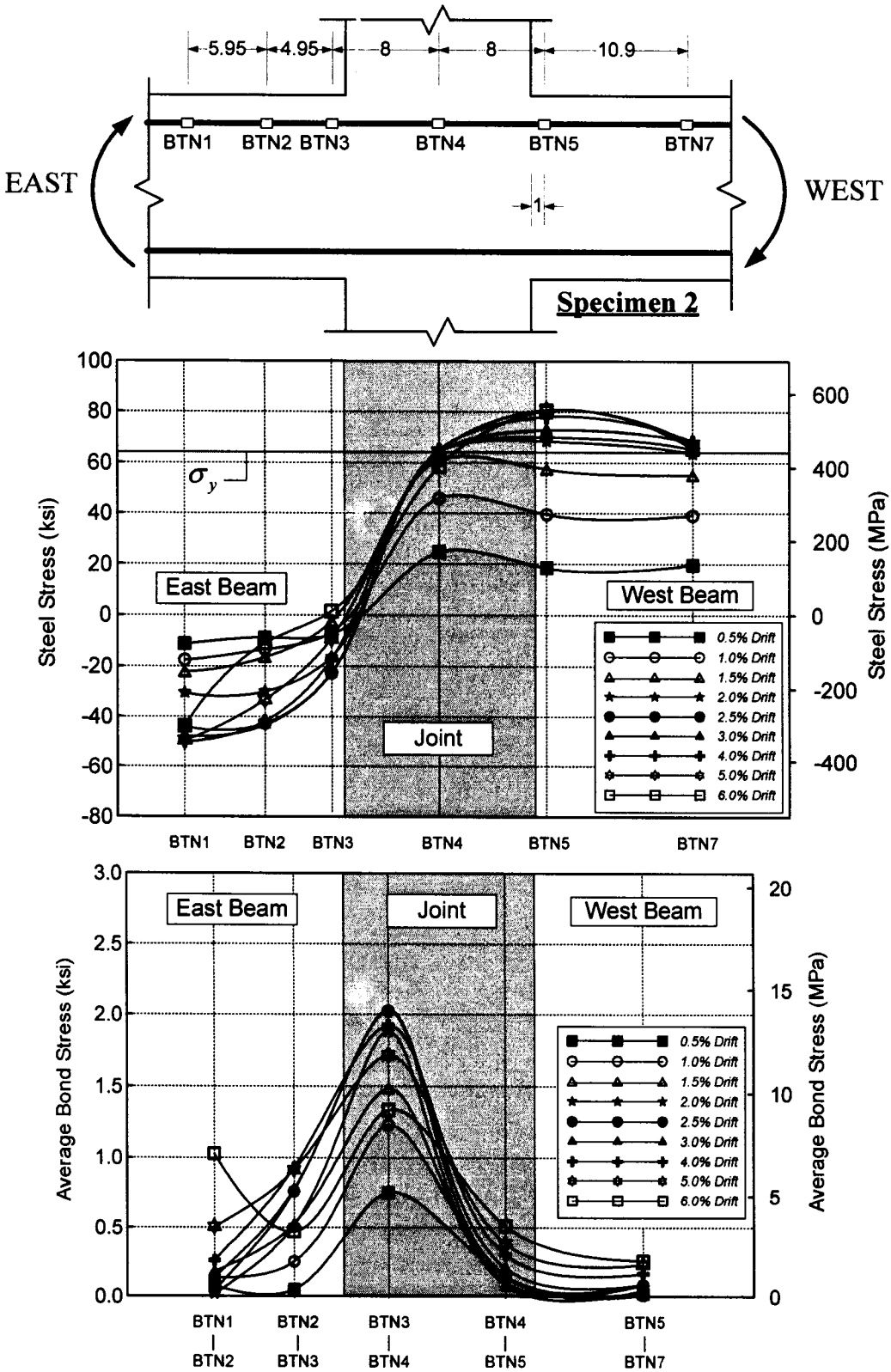

Figure 6.43 Steel stress and bond stress distributions in beam bar when specimen was pushed towards East (BTN series, Specimen 2)

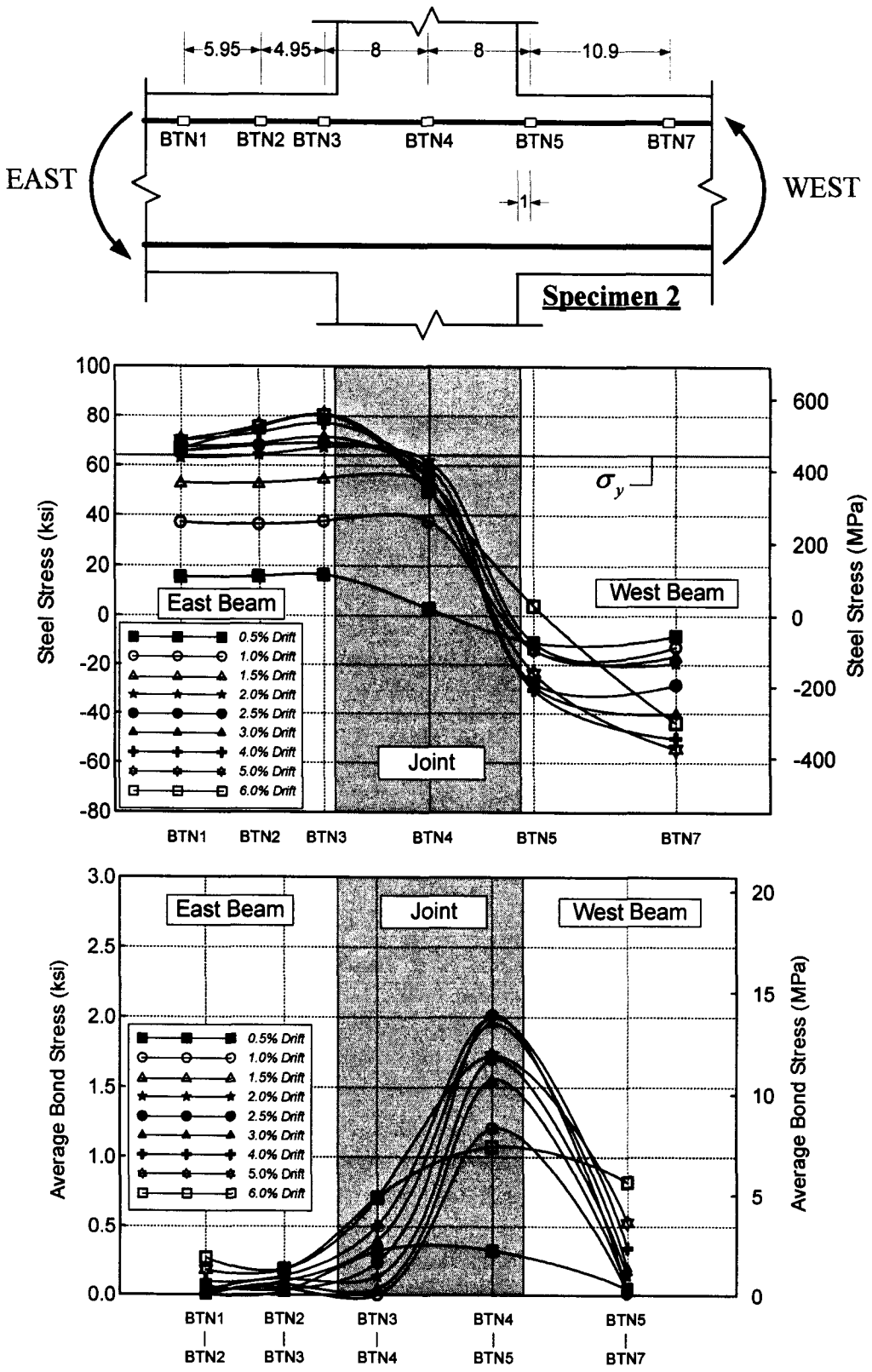

Figure 6.44 Steel stress and bond stress distributions in beam bar when specimen was pushed towards West (BTN series, Specimen 2)

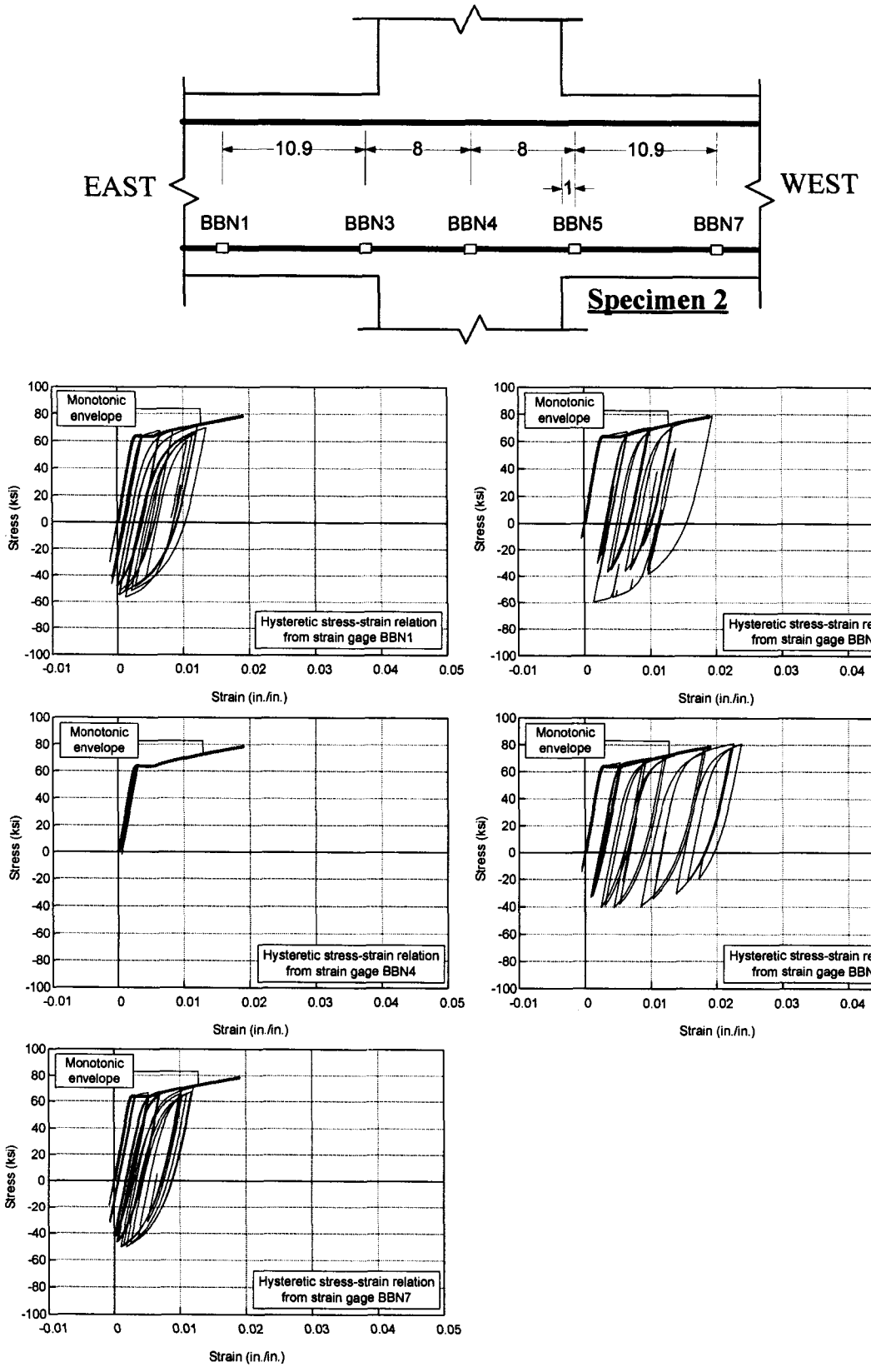

Figure 6.45 Hysteretic stress-strain responses of rebar at various locations (BBN series, Specimen 2)

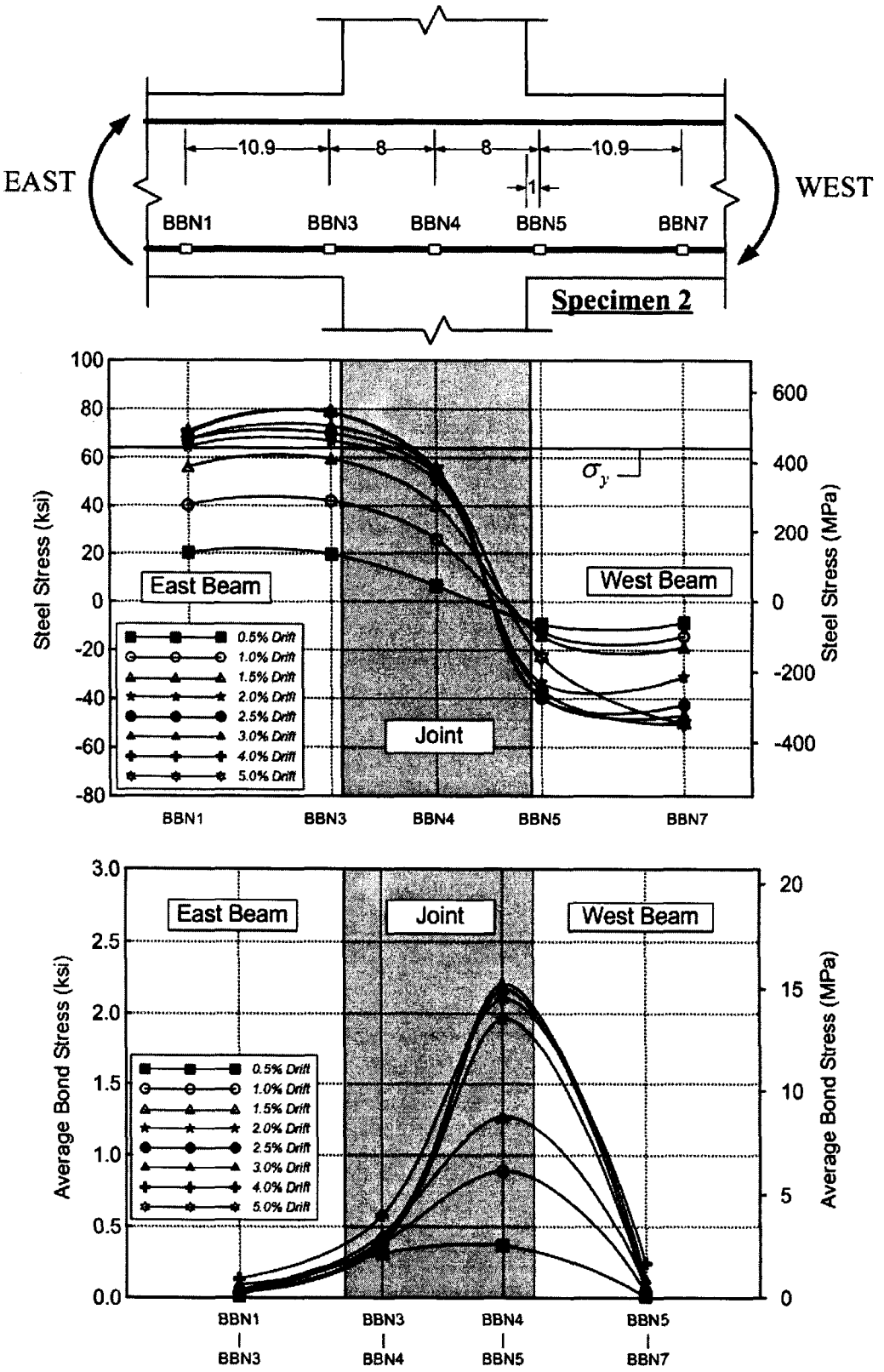

Figure 6.46 Steel stress and bond stress distributions in beam bar when specimen was pushed towards East (BBN series, Specimen 2)

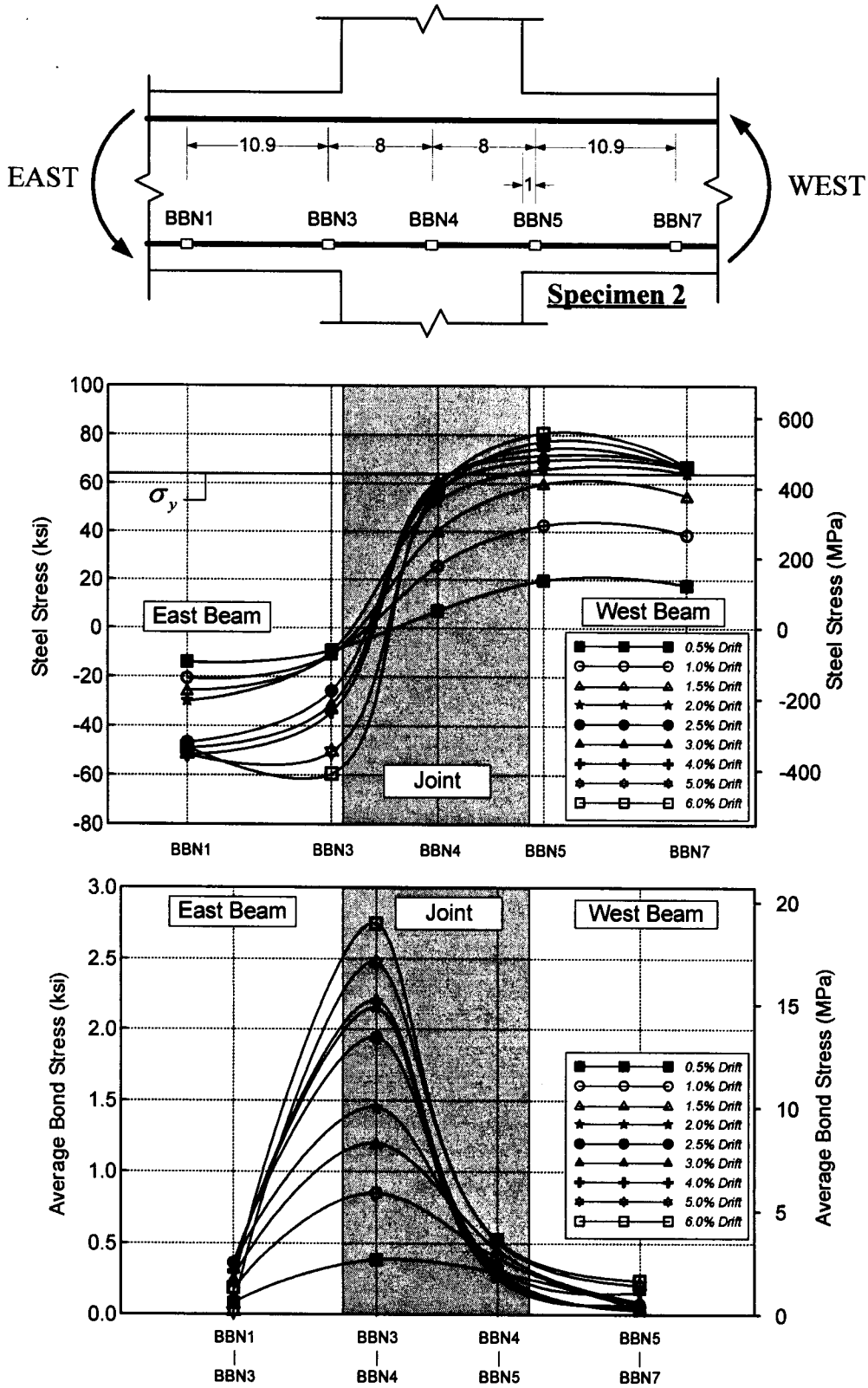

Figure 6.47 Steel stress and bond stress distributions in beam bar when specimen was pushed towards West (BBN series, Specimen 2)

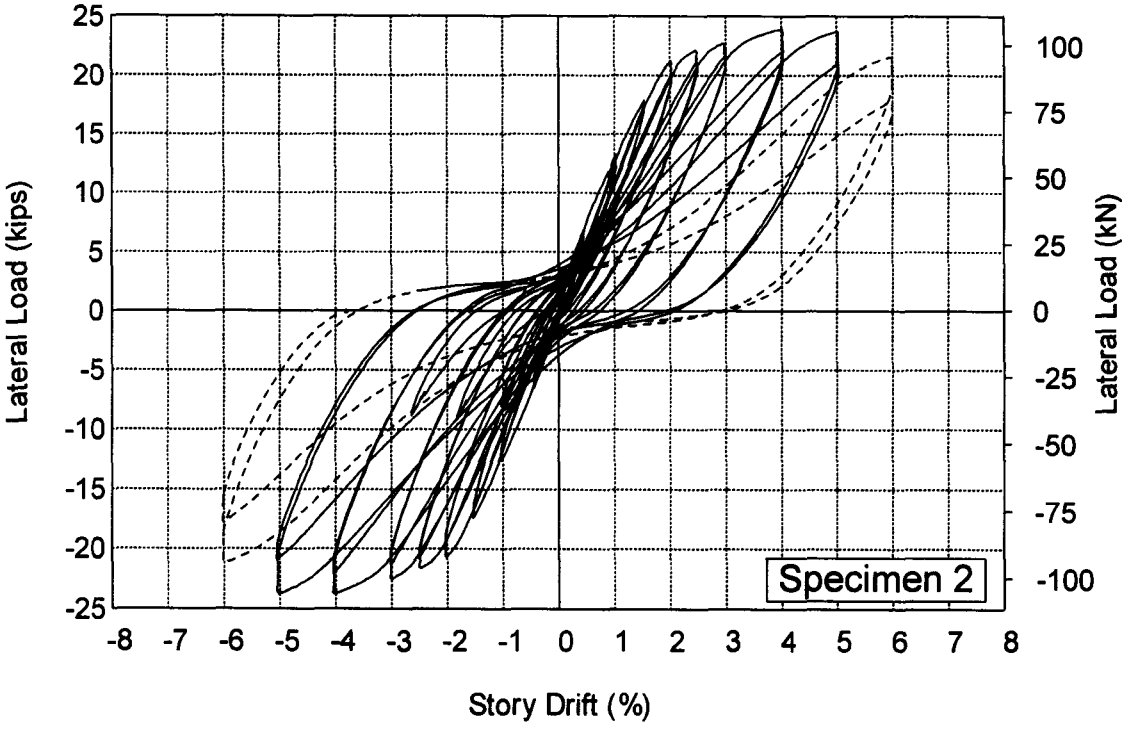

Figure 6.48 Lateral load versus drift response for Specimen 2

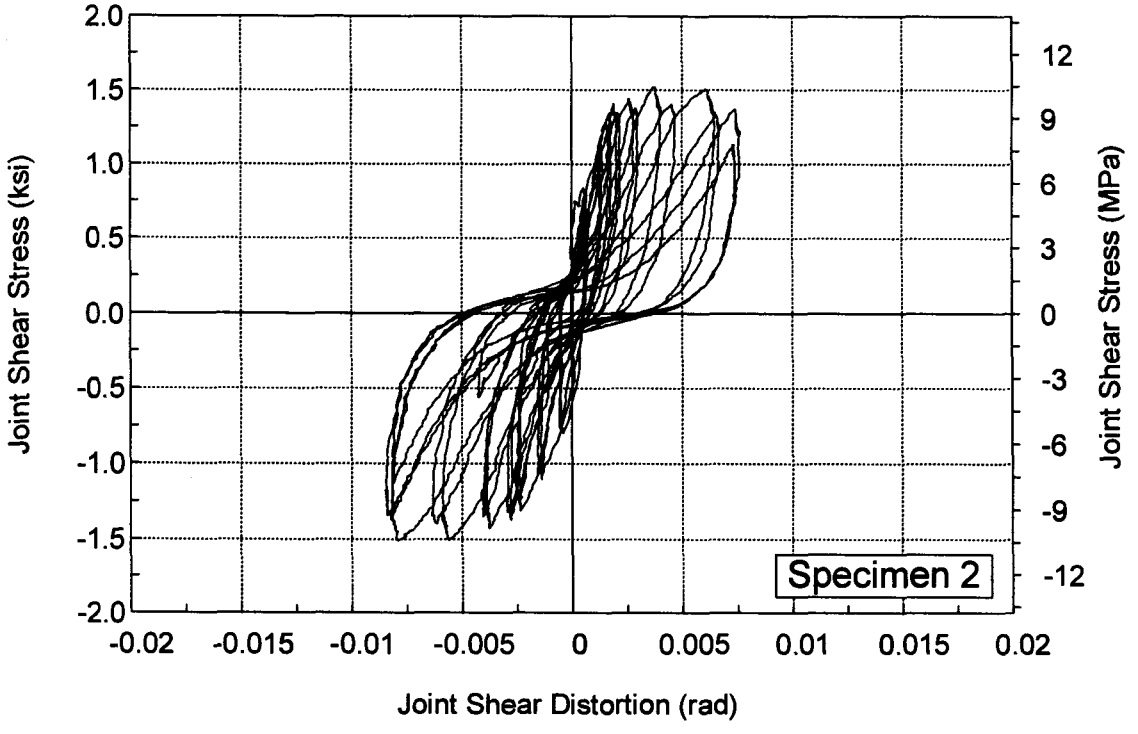

Figure 6.49 Joint shear stress versus joint distortion response for Specimen 2

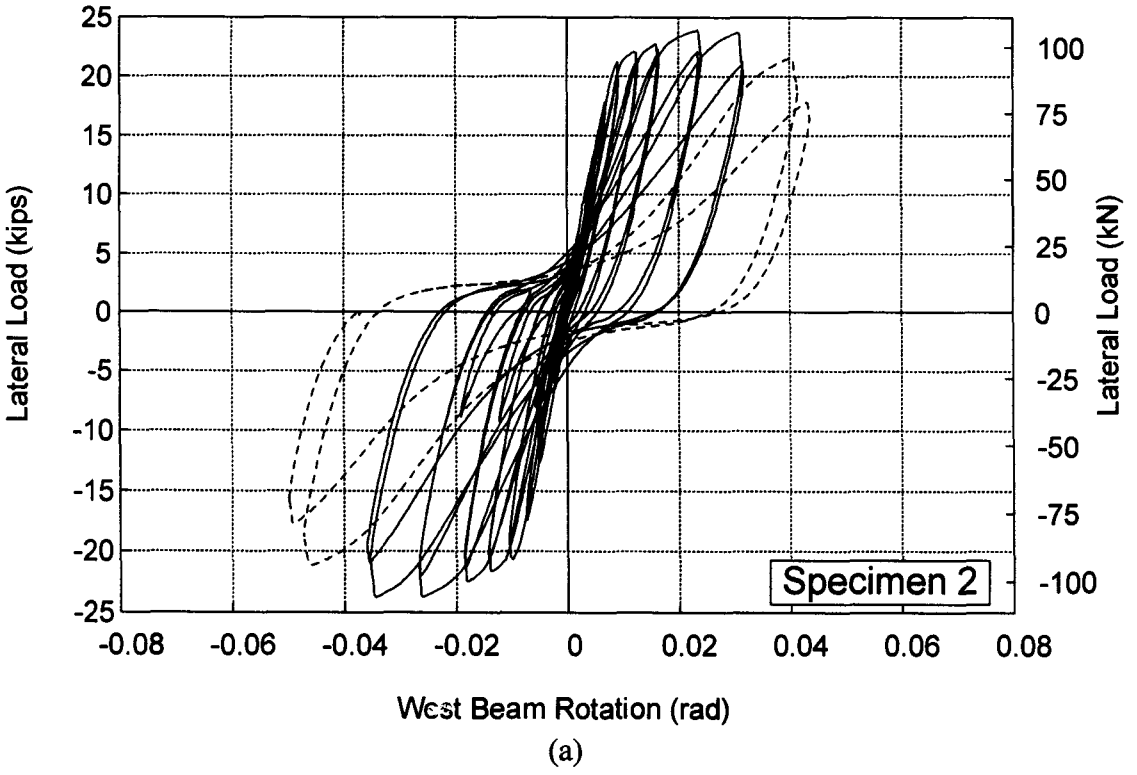

(a)

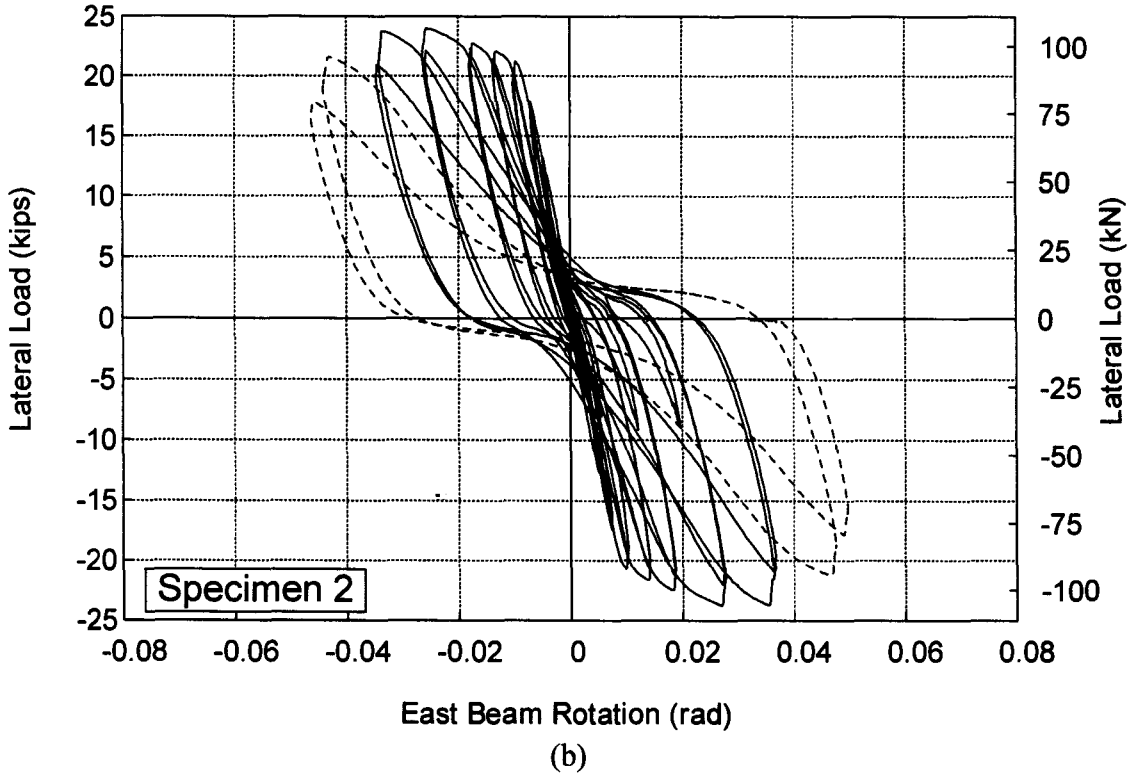

(b)

Figure 6.50 Lateral load versus beam rotation angle response for Specimen 2: (a) West beam; (b) East beam

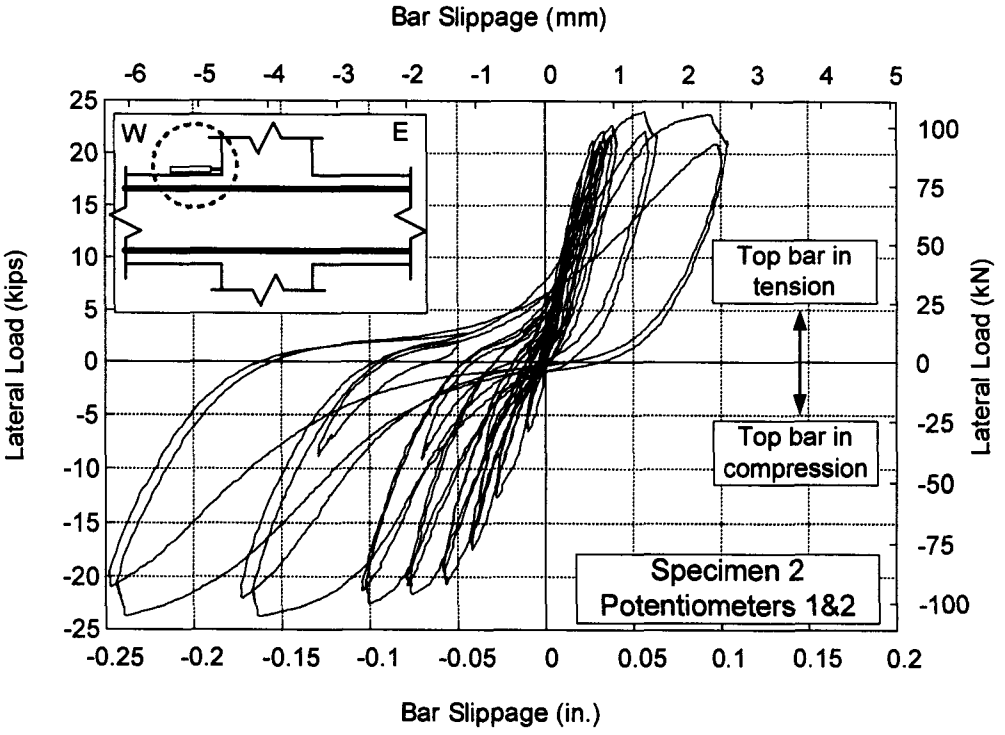

(a)

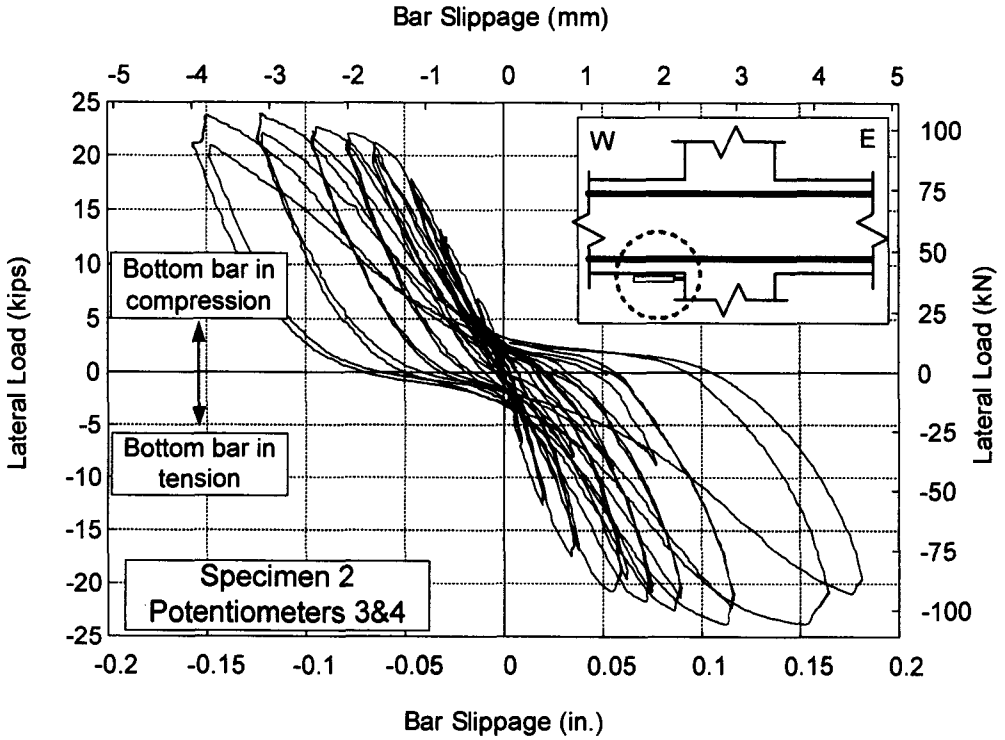

(b)

Figure 6.51 Average bar slippage measured by potentiometers up to 5% story drift in Specimen 2: (a) Top bars; (b) Bottom bars

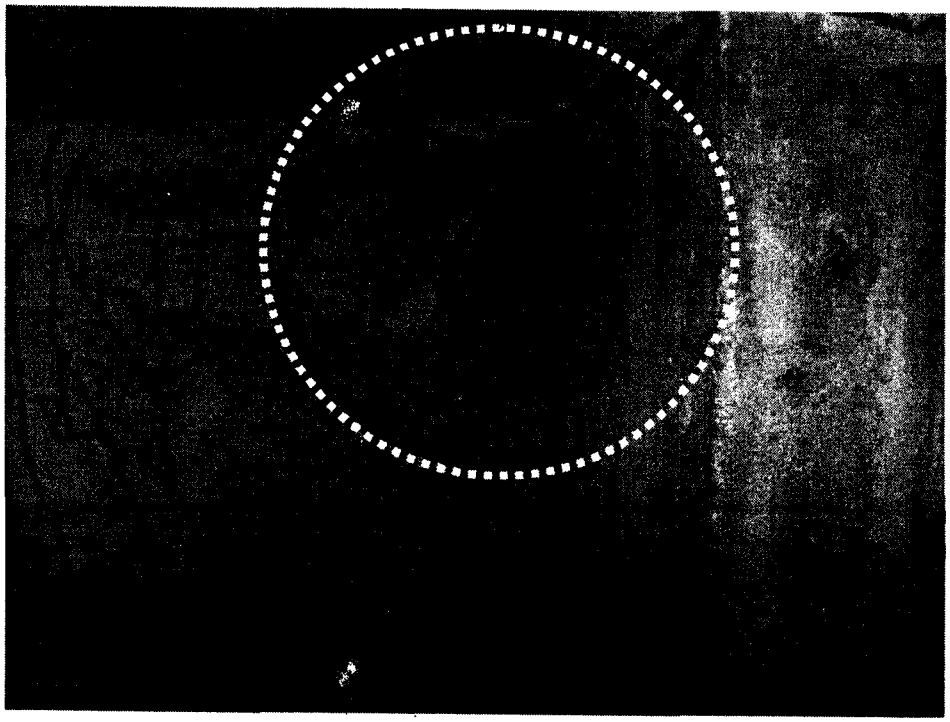

Figure 6.52 Crushed matrix at top face of west beam in the vicinity of beam-column interface

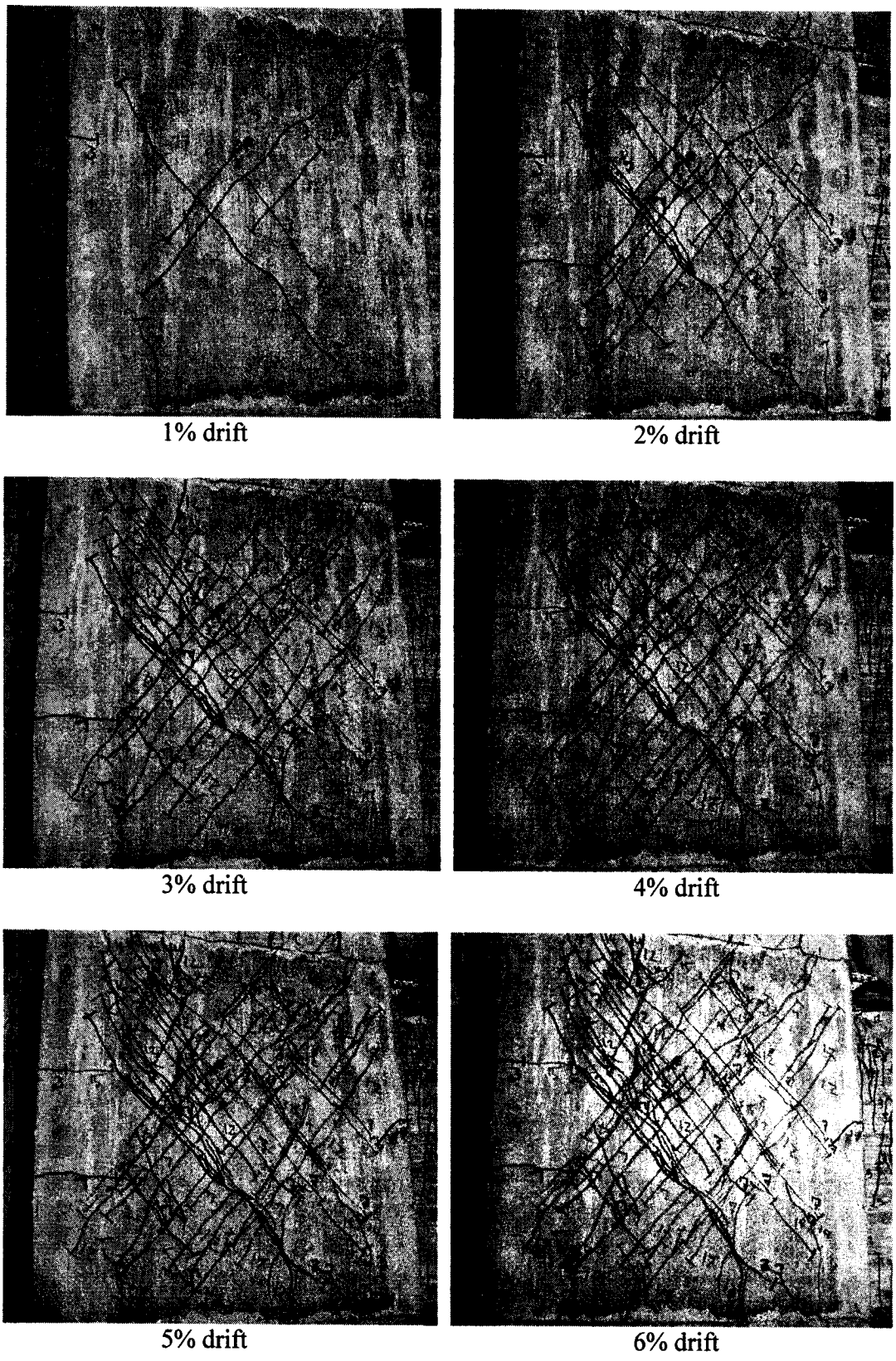

Figure 6.53 Cracking of beam- column joint at various drift levels (Specimen 2)

1% drift

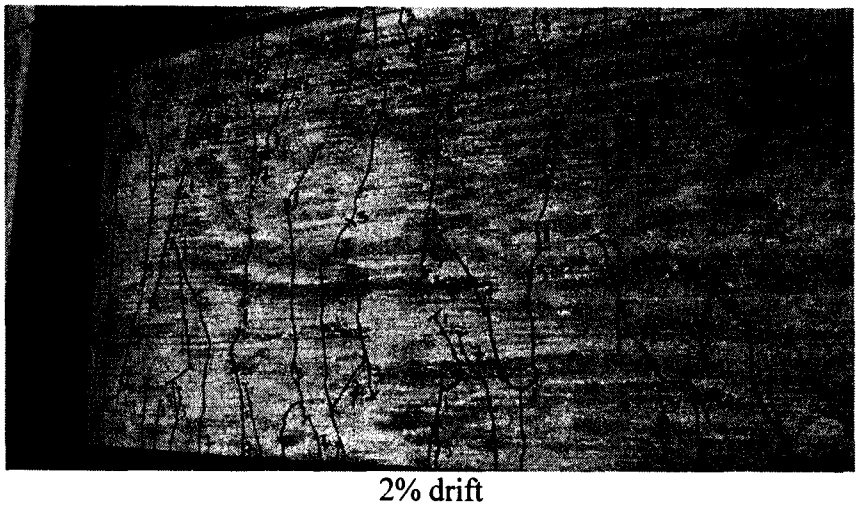

2% drift

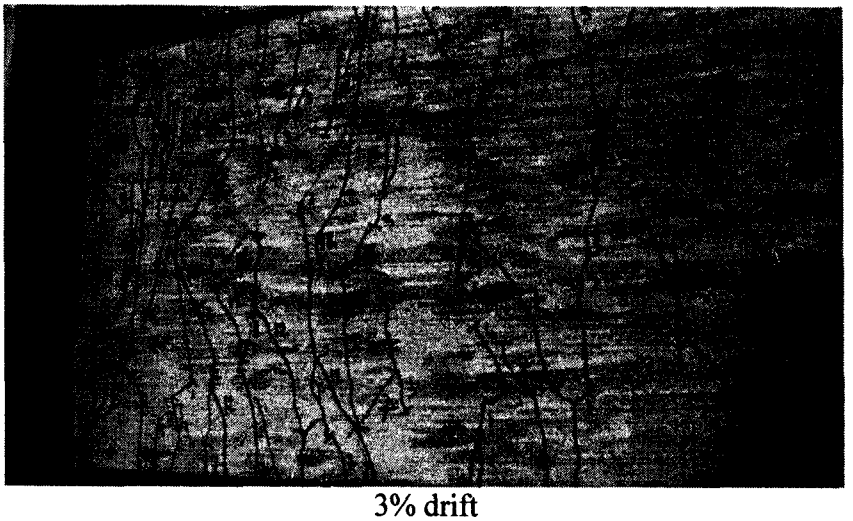

3% drift

Figure 6.54 Cracking in the West beam and beam-column interface at various drift levels (Specimen 2)

4% drift

5% drift

6% drift

Figure 6.54 (continued) Cracking in the East beam and beam-column interface at various drift levels (Specimen 2)

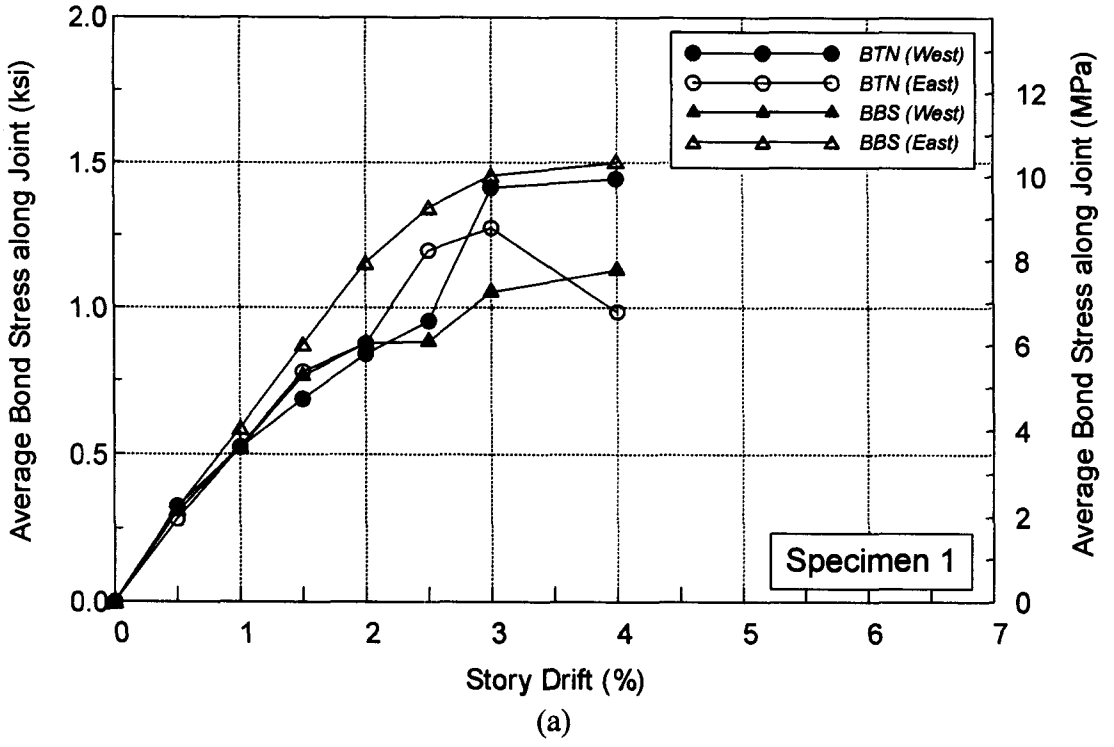

Figure 6.55 Average bond stress along beam-column joint for bars at various drift levels: (a) Specimen 1; (b) Specimen 2

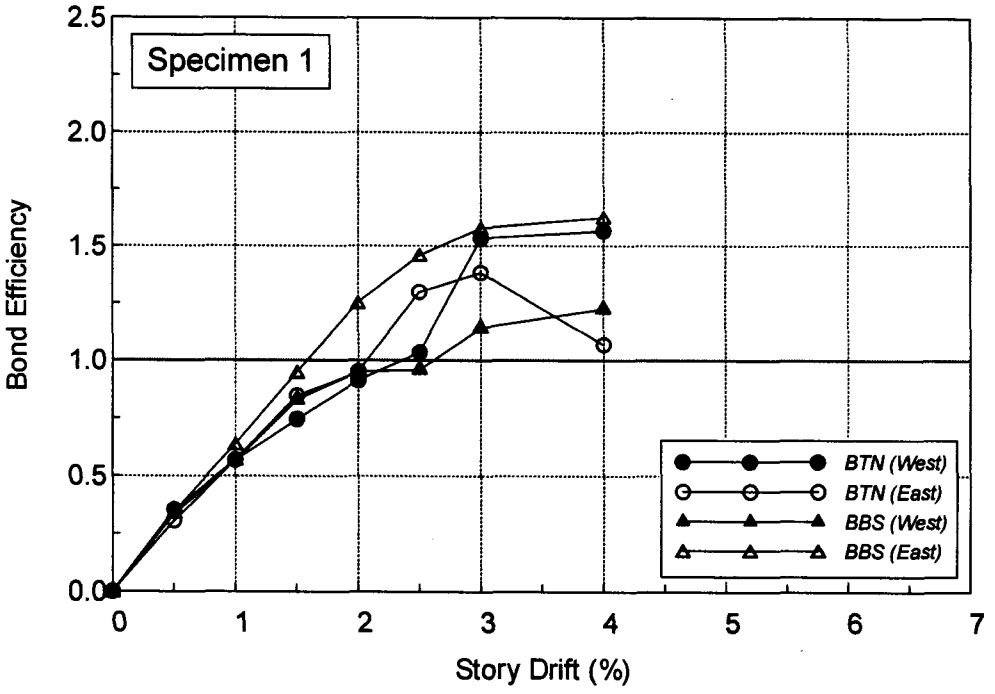

(a)

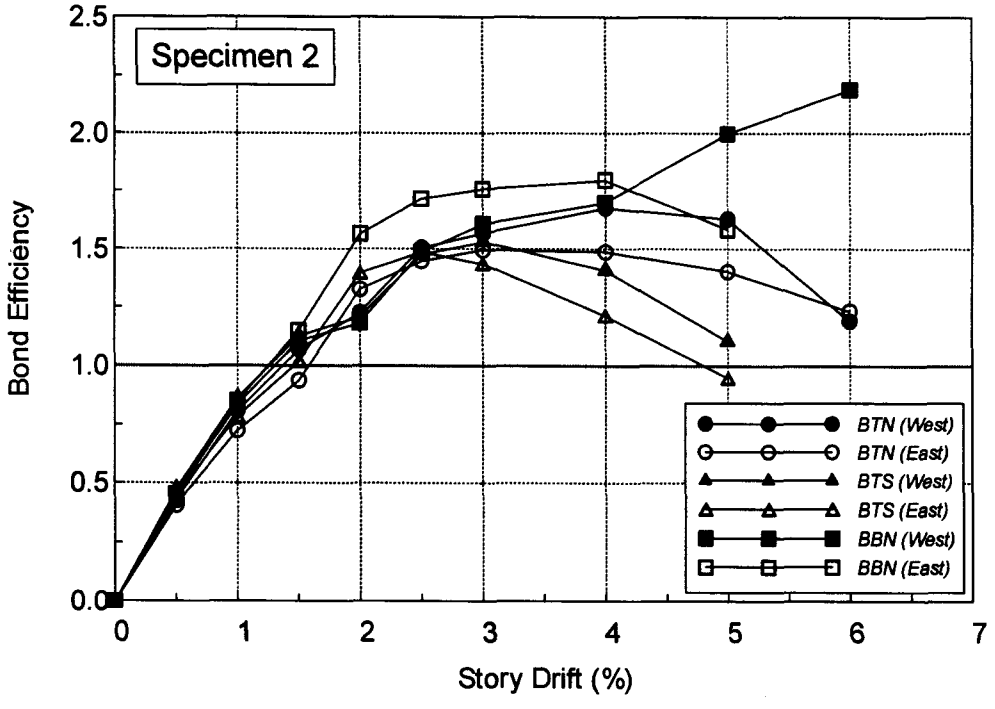

(b)

Figure 6.56 Bond efficiency of beam-column joint for bars at various drift levels: (a) Specimen 1; (b) Specimen 2

CHAPTER 7

BOND MODELING AND DESIGN RECOMMENDATIONS

7.1 Bond Modeling

Constitutive bond models can be generally grouped into two categories as illustrated in Figure 7.1. One comprises local bond stress-slip models which characterize the bond stress versus slip relationship along any typical element of a reinforcing bar or prestressing strand. This relationship is obtained through an isolated test, such as the pull-out type bond test used in this study. The other category comprises global scale bond-slip models which consider the entire member response under specific loading condition. A large scale test, such as the beam-column joint test conducted in this study (Chapter 6), can be performed to obtain the required information for such model.

The local bond stress-slip model can be used in finite element analyses as the constitutive law for a zero-thickness interface bond element (see Figure 2.5) or for the additional degree of freedom at bar element nodes to model the steel-concrete interface properties (e.g. Monti, Fillipou, and Spacone, 1997; Giard and Bastien, 2002; Tajima, Mishima, and Shirai, 2004; Lowes, Moehle, and Govindjee, 2004). In addition, the local bond stress-slip model can be applied to the analysis of reinforced concrete ties for investigating crack formation, elongation of the tie, as well as tension stiffening effects. Also, the anchorage of a reinforcing bar and corresponding steel stress versus pull-out

displacement can be studied by means of a local bond stress-slip model (CEB, 1993).

In a conventional RC beam-column joint, for example, bond deterioration is usually accelerated due to cyclic loading, which may lead to considerable reinforcing bar slippage through the joint and fixed-end rotation at beam ends. Experimental results indicate that this rotation can contribute up to 50% of the total drift in beam-column subassemblages after bar yielding occurs (Soleimani, Popov, and Bertero, 1979). As a consequence, an accurate estimation of bar slip is imperative for evaluating overall structural behavior. This can be realized by incorporating a global bond stress distribution model, in which yield penetration is inherently accounted for, into a nonlinear analysis program.

7.1.1 Local Bond Stress-Slip Model for Reinforcing Bar Embedded in HPFRCCs

Typical bond stress-slip relationships for conventional RC structures are shown in Figure 2.2 (Eligehausen et al., 1998) and Figure 2.4 (CEB, 1993), while Figure 2.7 presents a model for conventional FRC (Harajli et al., 2002). Hamza (1992) proposed a bond stress-slip model for SIFCON based on beam-type bond tests, as illustrated in Figure 7.2. The model consists of an ascending branch, a descending branch, and a residual bond resistance portion. The peak bond strength is a function of concrete cover, bar diameter, bar embedment length, and flexural strength of SIFCON matrix. An evaluation of the behavior of test specimens using a finite element analysis incorporating this model was also performed. Analysis results, such as beam deflections and steel strains, were generally consistent with the results observed from the experiments (Hamza,

1992).

There are two drawbacks, however, in the bond stress-slip model for SIFCON (Figure 7.2). First, it is limited to beam-type structures only, since the embedded length and flexural strength are two key variables. A local bond stress-slip model on a micro scale (Figure 7.1) would be more suitable for general purposes. Second, this model has no direct relationship with the fundamental characteristics of a fiber reinforced composite, such as the post-cracking tensile strength or strain. These are the fundamental characteristics of FRCCs, which distinguish themselves from the conventional concrete matrix.

The tensile stress-strain response of FRC composites can be defined as "strain-hardening" or strain-softening". For HPFRCCs, a strain-hardening type of tensile stress-strain response occurs. Minimum information on tensile strain-hardening stress-strain response of HPFRC composites that can be used for modeling or design has been suggested by Naaman and Reinhardt (2005), as illustrated in Figure 7.3. Only two points, A and B, are needed to characterize the tensile strain-hardening stress-strain response. Point A corresponds to the first percolation cracking $(\sigma_{cc}, \varepsilon_{cc})$, which is defined as a crack providing a complete separation between two parts of the tensile member. This point can be obtained either from direct tensile tests or an analytical approximation. Several methods for estimating the first percolation tensile stress and strain have been recommended by Naaman and Reinhardt (2005). After Point A, the response, usually along with multiple cracking, shows an increased tensile stress with an increase of strain

until Point B, the peak post-cracking strength point $(\sigma_{pc}, \varepsilon_{pc})$. After this point, crack localization starts and a softening tensile response occurs. Unlike Point A, Point B must be measured from direct tensile tests.

Two bond failure modes have been observed in specimens with HPFRCC materials, as discussed in Chapter 4. The separation-type failure mode characterizes a bond failure by the formation of a major crack throughout the specimen, and the bond strength drops due to opening of this crack which in turn leads to fiber pullout or break. Evident inelastic deformation along the cracked surfaces can be observed. The friction-type failure characterizes multiple cracked surfaces originating from the embedded bar. These cracks generally have much smaller width compared to that in the separation-type failure mode. The bond strength drops primarily due to shearing-off of the bar-to-matrix interface. Both types of failure modes can take place at high bond stress if an HPFRCC material is used.

In general, it was observed in this study that, 1) an HPFRCC that exhibits high tensile strength under a direct tensile test would give a high bond strength and separation-type bond failure (such as 2% Torex fiber and 11 ksi matrix strength); 2) if an HPFRCC shows moderate tensile strength but superior tensile strain before stress degradation, a high bond strength and interface-crushing-type bond failure would be obtained (such as 2% Spectra fiber and 11 ksi matrix strength; 2% Torex fiber with 7.6 ksi matrix strength).

7.1.1.1 Separation-Type Failure Mode

The bond strength for a separation-type failure can be estimated by using force equilibrium as well as the constitutive tensile stress-strain model given in Figure 7.3. The radial stress component (f_r) acts as internal burst pressure against a thick-walled cylinder having an inner diameter equal to the bar diameter (Orangun, Jirsa, and Breen, 1977), which can lead to a separation-type bond failure. In general, high strength matrix (11 ksi) specimens with Torex fibers exhibited this type of failure whereby only one through crack usually formed.

The specimen is analogous to a pressurized thick-walled cylinder which, unlike a thin-walled cylinder, has a non-uniform circumferential normal stress distribution upon internal pressure (Cook and Young, 1999) as shown in Figure 7.4. As a consequence, upon pull-out action, the maximum strain of the composite occurs at the location closest to the reinforcing steel, and gradually decreases when moving towards the edge, which agrees with the observation from the test specimen as shown in Figure 7.5. The peak bar force can be obtained through the following steps:

1) Assume the composite strain distribution is linear from a location adjacent to the reinforcing bar to the edge of the specimen, such that the stress distribution takes the same shape as the tensile stress-strain response shown in Figure 7.3.

2) Assume that failure initiates when maximum post-cracking strength $\left(\sigma_{pc}\right)$ is reached.

3) It is noted that the tensile strength shown in Figure 7.3, which is obtained from a direct tensile test, cannot be directly used due to the fiber orientation difference between 1-dimensional and 3-dimensional spaces. As shown in Figures 7.6 (a) and (b), the direct tensile specimen has random fiber distribution between 1-D and 2D (but somewhat close to 1-D) and aligned fiber distribution in the 3rd direction. For the direct tensile specimen used in this study, the fiber orientation can be conservatively taken as a 1-D distribution, especially for fibers with their length larger than the thickness of the tensile specimen (1 in.). On the other hand, the pull-out prism specimen, like the majority of structural elements, has a 3-D random fiber distribution as indicated in Figure 7.6 (c). Everything else being the same, the tensile capacity of a fiber reinforced cement composite is affected by the fiber orientation. This can be accounted for by a "bridging efficiency" factor, which defines the amount of fibers bridging across a crack with respect to fiber orientation effect. Generally, the 3-D random distribution leads to the lowest bridging efficiency due to loss of fiber bridging when oriented at high angles with respect to the tensile stress direction. It has been mathematically shown that the bridging efficiency ratio of 1-D: 2-D: 3-D fiber distribution are respectively 1, $2/\pi$, and 1/2 (Krenchell, 1964). This translates into a composite tensile capacity ratio of 1-D/3-D = 2 = η (bridging efficiency factor).

4) As shown in Figure 7.7, the cut-open specimen indicates that an inclined internal force exists in-between the steel and matrix due to the bearing action, which has also been observed in conventional reinforced concrete specimens (see Section 1.2.1). This bearing force occurs at an angle of approximately 50 degrees and is resisted by a

matrix strut. The longitudinal component and the radial component of the inclined force have the following relation (Canbay and Frosch, 2005a):

$$F_r = F_l \cdot \tan\beta = F_l \tan 50^\circ \qquad [7.1]$$

The peak force in the reinforcing bar is the summation of the longitudinal components forces from the two half portions of the specimen along its length:

$$F_s = 2F_l = 2\frac{F_r}{\tan\beta} \qquad [7.2]$$

5) Since the resultant radial force (F_r) is equal to the resultant of the composite tensile stresses on the crack surface, the peak bar force can be calculated as follows:

The resultant of the bridging forces along the crack surface is:

$$F_{bridge} = (L - d_b) l_e \cdot \left[\frac{\varepsilon_{cc} \cdot \sigma_{cc}}{2\varepsilon_{pc}} + \frac{\sigma_{cc} + \sigma_{pc}}{2} \cdot \left(1 - \frac{\varepsilon_{cc}}{\varepsilon_{pc}} \right) \right] \qquad [7.3]$$

By using the relation of $F_{bridge} = F_r$ and Equation [7.2], the peak bar force can be obtained by:

$$F_s = \frac{(L - d_b) l_e \cdot \left[(\sigma_{cc} + \sigma_{pc}) - \frac{\sigma_{cc} \cdot \sigma_{pc}}{E_c \cdot \varepsilon_{pc}} \right]}{\eta \cdot \tan\beta} \qquad [7.4]$$

where L is the length of specimen; d_b is the bar diameter; l_e is the bar embedded length; σ_{cc} is the first percolation cracking tensile strength; σ_{pc} is the peak post-cracking tensile strength and ε_{pc} is the corresponding strain. E_c ($=\sigma_{cc}/\varepsilon_{cc}$) is the elastic modulus of the composite (see Figure 7.3). Equation [7.4] assumes that the radial stress is uniform along the embedded length. Note that the bridging efficient factor in Equation [7.4], η, is used to scale down the tensile strength obtained from direct tensile test due to the fiber orientation effect (1D to 3D). The strain values (see Figure 7.3), however, are not scaled. Fiber orientation effect could have influence on the strains but this is not accounted for in this model.

Equation [7.4] was verified by the results from two No. 8 bar specimens that exhibited separation-type failure mode. The first one is the 2% square Torex fiber specimen with 11 ksi matrix strength. Its direct tensile stress-strain response is shown in Figure 7.8, together with the bi-linear tensile stress-strain model up to peak post-cracking point. The corresponding parameters are: σ_{cc} = 900 psi; σ_{pc} = 1700 psi, E_c = 1600 ksi; ε_{pc} = 0.6%; l_e = 4 in.; L = 6 in.; d_b = 1.0 in.; $\eta = 2$; $\beta = 50°$. With these values, the maximum bar force was determined from Equation [7.4] and is equal to 20.5 kips, which is close to the experimental result (21 kips, see Figure 4.22). The second example is the 2% rectangular Torex fiber specimen with 11 ksi matrix strength. Its direct tensile stress-strain response is shown in Figure 7.9, along with the bi-linear tensile stress-strain model up to peak post-cracking point. The corresponding parameters are: σ_{cc} = 850 psi; σ_{pc} = 1400 psi, E_c = 850 ksi; ε_{pc} = 0.65%; l_e = 4 in.; L = 6 in.; d_b = 1.0 in.; $\eta = 2$;

$\beta = 50°$. The obtained peak bar force is 17.1 kips, which is close to the experimental result (18.6 kips). It is noted that the composite modulus (E_c = 850 ksi) for the rectangular Torex fiber specimen should be close to that of the square Torex fiber specimen (E_c = 1600 ksi). However the value was underestimated according to the bilinear curve shown in Figure 7.9, which is generally conservative. If an modulus of 1600 ksi is used for the rectangular Torex fiber specimen, the predicted bar peak force would be 18 kips.

Equation [7.4] can be translated into a peak bond stress by dividing by $(\pi \cdot d_b \cdot l_e)$ and assuming $\beta = 50°$:

$$\tau_{\max} = \alpha \cdot \left(\frac{c}{\eta \cdot d_b}\right) \cdot \left[\left(\sigma_{cc} + \sigma_{pc}\right) - \frac{\sigma_{cc} \cdot \sigma_{pc}}{E_c \cdot \varepsilon_{pc}}\right] \qquad [7.5]$$

where α is calibration coefficient; c is the cover thickness $= (L - d_b)/2$. By using α = 0.9, the predicted peak bond stress values agree well with the experimental results, as shown in Table 7.1. Note that the above expression can also be applied to general structural elements exhibiting separation-type bond failure, such as beams (Figure 7.10). In this case the parameter c in Equation [7.5] can be taken as the smallest of the side cover, the cover of the bar (in both cases measured to the center of the bar), or one-half the center-to-center spacing of the bars, as the c_b factor in ACI Code (see Section 2.1.5).

Knowing the peak bond strength, a general bond stress-slip model with separation-type bond failure for a reinforcing bar embedded in HPFRCCs is then

proposed and is shown in Figure 7.11. The proposed model consists of a linear ascending branch and a bilinear descending branch. The expression for the average bond stress-slip relation of the ascending branch is given as follows:

$$\tau(s) = \tau_{\max} \cdot \frac{s}{s_{\max}} \text{ (psi)} \qquad [7.6]$$

The descending branch is determined by two points: $(s_{\max}, \tau_{\max})$ and (s_f, τ_f), in which $\tau_f = 0.15\tau_{\max}$ (psi); s is slip value (in.), s_f = 0.5 in., and $s_{\max} = \frac{\tau_{\max}}{3 \cdot d_b \cdot f_c'}$ (in.), where the coefficient of 3 in the denominator is empirically obtained based on test results and f_c' is the compressive strength of matrix (psi); d_b is the bar diameter (in.).

The proposed model was determined based on the following experimental observations and considerations:

1. Although prior research showed that the ascending branch can be simulated by a nonlinear curve, such as the one shown in Figure 7.2, a linear expression (Equation [7.6]) was adopted in the proposed model based on test results (Figure 7.12), for which a straight line represents reasonably well the ascending branch (No. 8 bar specimen with 2% rectangular fiber).

2. It was observed that (see Section 4.2.6), the bond modulus of reinforcing bars embedded in FRCCs is proportional to the product of matrix compressive strength

and bar diameter. As a consequence, the s_{max} value is determined using τ_{max}, f_c', and d_b.

3. The proposed model is suited for $0.2\% \leq \varepsilon_{pc} \leq 0.6\%$. The lower bound composite tensile strain (ε_{pc} =0.2%) is adopted to insure appropriate composite tensile strain-hardening behavior, while it was generally observed that composites with tensile strain capacity larger than 0.6% tended to exhibit interface-crushing-type bond failure.

4. It should be reiterated that, as pointed out in Section 4.2.5, the pull-out test employed in this study may give a lower bond strength. Comparison between SIFCON specimens using the same geometry and loading setup as the one used in this study (with 9.7% steel hooked fiber, Hota and Naaman, 1995) and beam-type specimens (5% steel hooked fiber, Hamza, 1992) shows that the bond strength in the latter was as high as 2.5 times that of the former specimens. In general, the peak bond strength given in Equation [7.5] could be regarded as lower bound value of the bond strength.

7.1.1.2 Interface-Crushing-Type Failure Mode

When the HPFRC composite exhibits multiple cracking (due to higher tensile strain capacity) leads to multiple cracked surface, the internal pressure is resisted by composite bridging tensile stress from more than one crack surfaces (see Figure 7.13 or Figure 4.14). As a result, the cracks maintain narrow and the failure mode switches from separation

type to friction (or pullout) type, and the bond strength degrades due to shearing-off of the bar-to-matrix interface; Equation [7.5], therefore, does not apply. Nevertheless, from Figure 7.13, it can be observed that the bearing and friction resistance (thus the bond resistance) improves as the clamping stress (i.e. the composite tensile stress) increases. In addition, the resistance to shearing-off of the matrix improves as the matrix compressive strength increases. Based on these two premises, the following peak bond strength is proposed for interface-crushing-type bond failure of reinforcing bars embedded in HPFRCCs:

$$\tau_{\max} = \beta \cdot \left[\frac{\sigma_{pc} \cdot (f_c')^{1/4}}{\eta \cdot d_b} \right] \qquad [7.7]$$

where β is a calibration coefficient. By using $\beta = 0.45$, predicted peak bond stress values agree well with the experimental data, as shown in Table 7.2. The $f_c'^{1/4}$ term in Equation [7.7] was determined based on the experimental observations shown in Figure 4.29, which is a lower bound value reflecting the influence of matrix strength on bond resistance. This also complies with the bond resistance (or development length) expression of ACI Committee 408 (2003) for concrete without transverse reinforcement.

Knowing the peak bond strength, a general bond stress-slip model with interface-crushing-type bond failure for reinforcing bar embedded in HPFRCCs is proposed and shown in Figure 7.14. The proposed model consists of a linear ascending branch and a bilinear descending branch. The expression of the average bond stress-slip

relation of the ascending branch has the same format as Equation [7.6].

The descending branch is determined by two points: $(s_{\max}, \tau_{\max})$ and (s_f, τ_f), in which $\tau_f = 0.3\tau_{\max}$ (psi); s is slip value (in.). $s_{\max} = \dfrac{\tau_{\max}}{3 \cdot d_b \cdot f_c'}$ (in.) and s_f = 0.5 in., where f_c' is the compressive strength of matrix (psi); d_b is the bar diameter (in.).

The proposed model was determined based on the following experimental observations and considerations:

1. As observed in Figures 4.22, 4.24, and 4.26, specimens with interface-crushing-type bond failure exhibited higher residual bond strength (τ_f), therefore a higher value is assigned in the interface-crushing-type bond stress-slip model.

2. The proposed model is suited for $\varepsilon_{pc} > 0.6\%$, in which a larger strain capacity leads to multiple cracked surface. Note HPFRC composites with ε_{pc} less than 0.6 % generally exhibit separation-type bond failure mode.

3. Note that there is no parameter representing the cover thickness in Equation [7.7]. This is mainly because that multiple cracks developed in the specimens with interface-crushing-type failure mode, thereby providing sufficient resistance against the bar bearing forces. As a consequence, the cover thickness (or bar spacing) plays lees important role in the bond strength than specimens exhibiting separation-type

bond failure.

General guidelines for bond stress-slip models under cyclic loadings are presented in Figure 7.15. Figure 7.15 (a) shows the governing envelope for reinforcing bar subjected to unidirectional type cyclic loading. The cyclic envelope value is 90% that of the monotonic envelope, which is based on the results given in Tables 4.6 and 4.7. The unloading (or reloading) branch has the same bond modulus as the monotonic bond modulus. If a reinforcing bar is subjected to fully reversed type cyclic loading, the attainable peak bond strength (Figure 7.15 (b)) is 80% of the monotonic value, as suggested by Tables 4.8 to 4.11. The monotonic bond modulus can be also used as the unloading/reloading bond modulus. The unloading-reloading paths reported by Eligehausen et al. (Eligehausen, Popov, and Bertero, 1983) or Filippou (1986) can be used as hysteretic rules for bond under fully reversed cyclic loading.

7.1.2 Local Bond Stress-Slip Model for Strand Embedded in HPFRCCs

Due to the different bond mechanism for strands in FRCCs from that of reinforcing bars, the crack width in the strand specimens with fibers is generally very small and generally less than 0.01 in. (0.25 mm), as shown in Figure 7.16 (a). As a consequence, the clamping stress is much close to the first percolation cracking strength, σ_{cc}, rather than the peak post cracking strength, σ_{pc} (Figure 7.16 (b)). Furthermore, as shown in Chapter 5, all FRCC specimens exhibited friction-type failure mode by shearing-off the strand-to-matrix interface. Based on these two observations, the following peak bond

strength is proposed for prestressing strands embedded in HPFRCCs:

$$\tau_{\max} = \gamma \cdot \left[\frac{\sigma_{cc} \cdot f_c'}{\eta \cdot d_b} \right] \qquad [7.8]$$

where γ is a calibration coefficient. The f_c' term in Equation [7.8] was determined based on the experimental observations from Figure 5.10, and is consistent with the expression of FHWA (1998). By using $\gamma = 1.5 \times 10^{-4}$, the predicted peak bond stress values have good agreement with the experimental data, as shown in Table 7.3.

A bi-linear bond stress-slip model is proposed for 0.5 in. strands embedded in HPFRCCs, which is based on the unique "ductile bond" behavior presented in Chapter 5. The proposed constitutive model is shown in Figure 7.16 (c), where the ascending branch is modeled by a straight line based on the observation from cyclic loading responses; s is slip value (in.). $s_{\max} = \tau_{\max} / 15{,}000$ (in.) and the maximum slip $s_f = 0.8$ in.

The determination of corresponding parameters in the proposed model is explained as follows:

1. The monotonic bond modulus was taken as a constant (15,000 psi/in.), which is based on the lower bound value observed from the cyclic bond responses for specimens with HPFRCC materials. No sigificant difference in the bond modulus was noticed in specimens with various matrix compressive strengths.

2. The maximum slip value, s_f, is set equal to 0.8 in. since the tests were usually stopped at a net slip approximately equal to 0.8 in.

3. Although the clamping stress used in Equation [7.8] corresponds to the first percolation cracking, it is still suggested that the composite exhibits a peak post cracking strain $\varepsilon_{pc} > 0.6\%$, in order to maintain the tensile capacity after cracking occurs. In addition, cracking resulting from other causes, such as shear, can lead to bond failure if no sufficient post-cracking tensile strain capacity is provided. This is particularly important for strands, because their bond resistance is very sensitive to the crack width. Therefore, a minimum strain capacity is necessary to ensure good bond performance.

General guidelines for bond stress-slip models under cyclic loadings are presented in Figure 7.17. Figure 7.17 (a) shows the governing envelope for a strand subjected to unidirectional loading. The cyclic envelope is 90% of the monotonic envelope, which is based on the results presented in Figures 5.15 thru 5.20. The unloading (or reloading) branch has the same bond modulus as the monotonic bond modulus. It is noted that no degradation in bond stiffness was observed up to very large slips. Unlike the monotonic or unidirectional bond stress-slip response, the backbone curve under reversed cyclic loading decreases gradually when slip increases, as shown in Figure 7.17 (b). The maximum attainable peak bond strength under fully reversed cyclic loading is 85% of the monotonic peak bond strength, which is slightly lower than that shown in Tables 5.3 and 5.4. The bond strength is 50% of the monotonic peak bond strength when s_f is reached.

In general, the monotonic bond modulus can be used for unloading/reloading bond modulus. A possible hysteretic response is also given in Figure 7.17 (b).

Figure 7.17 (c) shows a basic fully reversed cyclic bond stress-slip model which could be used for low-cycle fatigue loading, based on experimental observations as shown in Figures 5.46 thru 5.51 and Table 5.5, no bond strength and stiffness loss would result if the bond stress is less than 70% of the monotonic peak bond strength, and the slip is less than s_{max}.

7.1.3 Global Bond-Slip Model for Reinforcing Bars Embedded in HPFRCC Beam-Column Joints

7.1.3.1 Proposed Bond Stress Distribution Model

Drift control is an essential issue for structures located in zones of high seismicity. Excessive lateral displacement usually leads to severe damage not only in structural elements, but in non-structural elements such as cladding, partitions, interior veneers, and glazing systems. As a consequence, evaluation of lateral displacement should be as accurate as possible for RC frames vulnerable to earthquake excitations. Elongation and slippage of reinforcement through beam-column connections can result in fixed-end rotations at the column faces thus, additional lateral displacement. In order to investigate the bar slip effect on beam end rotations, several analytical bond models for conventional reinforced concrete beam-column joints have been developed by different researchers (e.g. Morita and Kaku, 1984; Filippou, 1986; Hawkins, Lin, and Ueda, 1987; Pochanart

and Harmon, 1989; Alsiwat and Saatcioglu,1992). Recently, bi-uniform bond stress models were proposed for use in conventional reinforced concrete beam-column joints and good agreement with experimental results was found (Lowes and Altoontash, 2003; Sezen and Moehle, 2004). Figure 7.18 illustrates the approach used by Sezen and Moehle (2004), in which the bond stress, steel stress, and steel strain distributions are schematically shown. For the steel length (l_{dy}) that remains elastic, a uniform bond stress of $12\sqrt{f_c'}$ (in units of psi) is assumed; for the yielding penetration region (l_d') the uniform bond capacity is assumed equal to $6\sqrt{f_c'}$. Zero slip is assumed at the point of zero-bar stress. The bi-linear bond stress model presumes that bond stress distribution in an RC beam-column joint is piecewise uniform and the magnitude is constant no matter how large the drift or steel strain is.

Typical steel stress and bond stress distributions for a longitudinal reinforcing bar in an HPFRCC beam-column joint are shown in Figure 7.19. It is seen that, while the steel stress distribution is close to the bi-linear model shown in Figure 7.18., the bond stress distribution is significantly different from the bi-uniform model. It is noticed that the bond stress on the tension side (West in this example) has a minimum value and it tends to be constant for all drift levels. However, the bond stress on the compression side (East) has a maximum value that changes (increases) with the increase of drift levels (as well as the steel stresses and strains). In addition, the bond stress distribution varies continuously, and may be assumed linear in between the minimum and maximum bond stresses.

Figures 7.20 (a) and (b) present the relations between the measured longitudinal

reinforcement strain at the column face (tension side) and bond stress at the compression side for all instrumented bars in Specimens 1 and 2, respectively. It can be observed that the bond stress on the compression side increases with an increase in steel strain at the beam-to-column interface. Based on test results, a bi-linear model, plotted in Figures 7.20 (c), is proposed. As shown in Figures 7.20 (a) and (b), this model represents reasonably well the bond stress-steel strain relationship. It is worth mentioning that the slopes of the steel strain at beam-to-column interface versus bond stress on the compression side of reinforcing bars may have slight change if the tensile strain-hardening ratio of the reinforcing bars is not the same as the one used in this study.

The proposed expression for maximum bond stress, τ_{max}, on the compression side is given by:

$$\tau_{max} = 120\frac{\varepsilon_s}{\varepsilon_y}\cdot\frac{(f_c')^{1/4}}{d_b} \qquad \text{when } \varepsilon_s \le \varepsilon_y \qquad [7.9]$$

$$\tau_{max} = \left[3000\left(\varepsilon_s - \varepsilon_y\right)+120\right]\cdot\frac{(f_c')^{1/4}}{d_b} \le 2500 \text{ psi} \qquad \text{when } \varepsilon_s > \varepsilon_y \qquad [7.10]$$

where f_c' is the matrix compressive strength (psi); d_b is the bar diameter (in.); ε_s is the steel tensile strain at beam ends; ε_y is the steel yield strain. An upper bound bond stress is given in Equation [7.10] for conservatism. The advantage of using steel strains as the variable in the proposed model is that the steel strain (or stress) is usually known in a

nonlinear analysis.

A linear bond stress distribution model is therefore proposed in this study for HPFRCC beam-column joint as illustrated in Figure 7.21. The minimum bond stress at the tension side, $\tau_{\min}$, is kept constant and can be calculated by:

$$\tau_{\min} = 40\frac{(f_c')^{1/4}}{d_b} \qquad [7.11]$$

In Figure 7.21, τ_d' (psi) in the linear model is the bond stress when $\varepsilon_s = \varepsilon_y$; τ_{dy} is the bond stress at zero bar tensile stress point (psi); l_d' is the development length over the inelastic portion of the bar (in.); l_{dy} is the portion of the bar with stress varying from zero to yield stress (in.); l_d is the entire tension-development length (in.).

7.1.3.2 Slip Calculation

Bar slip includes both the "physical slippage" of bar through the joint and the bar elongation. If the longitudinal bar is able to be effectively anchored in the joint without evident bond deterioration during seismic action, no appreciable physical slippage would result. This is what occurred in the HPFRCC beam-column joints as discussed in Chapter 6. Accordingly, bar slip in the connections was primarily due to the accumulated axial strain in the bar inside the beam-column joint and can be calculated by integrating the steel strains over the distance between the beam-column interface and the portion in the

bar with zero tensile stress. That is (Sezen and Moehle, 2004):

$$\text{slip} = \int_0^{l_d} \varepsilon_s dx$$

$$\text{slip} = \int_0^{l_{dy}} \varepsilon_s dx + \int_{l_{dy}}^{l_{dy}+l'_d} \varepsilon_s dx \qquad \text{when } \varepsilon_s > \varepsilon_y \qquad [7.12]$$

The above integration is actually the area under the entire strain diagram. Therefore:

$$\text{slip} = \frac{\varepsilon_s}{2} \cdot l_d \qquad \text{when } \varepsilon_s \le \varepsilon_y$$

$$\text{slip} = \frac{\varepsilon_y}{2} \cdot l_{dy} + \frac{(\varepsilon_s + \varepsilon_y)}{2} \cdot l'_d \qquad \text{when } \varepsilon_s > \varepsilon_y \qquad [7.13]$$

l'_d and l_{dy} in Equation [7.13] can be calculated from equilibrium of forces in the bar:

$$\Delta\sigma_s A_s = \int_{l'_d \text{ or } l_{dy}} \tau(x) \Sigma_o dx \qquad [7.14]$$

where $\Delta\sigma_s$ is the steel stress increment (psi) within the length of l'_d or l_{dy}; $A_s = \pi d_b^2 / 4$ is the bar cross-sectional area (in^2.); $\Sigma_o = \pi d_b$ is the bar perimeter (in.). Note the integration part in Equation [7.14] is equal to the area under bond stress distribution diagram. For example, the inelastic development length for which $\varepsilon_s > \varepsilon_y$,

l'_d, is calculated by using Equation [7.14] and Figure 7.21:

$$\left(\sigma_s - \sigma_y\right)\frac{\pi d_b^2}{4} = \pi d_b\left(\frac{\tau'_d + \tau_{\min}}{2}\right)\cdot l'_d \qquad [7.15]$$

and

$$\tau'_d = \left(\frac{\tau_{\max} - \tau_{\min}}{d_c}\right)\cdot l'_d + \tau_{\min} \qquad [7.16]$$

where σ_s is the steel stress at the beam-column interface (psi); σ_y is the yield stress of the bar (psi); d_c is the column depth (in.). l'_d can then be obtained by solving Equations [7.15] and [7.16].

Similarly, the elastic development length, l_{dy}, is calculated by solving the following two equations:

$$\sigma_y\frac{\pi d_b^2}{4} = \pi d_b\left(\frac{\tau'_d + \tau_{dy}}{2}\right)\cdot l_{dy} \qquad [7.17]$$

and

$$\tau_{dy} = \left(\frac{\tau_{\max} - \tau_{\min}}{d_c}\right)\cdot l_{dy} + \tau'_d \qquad [7.18]$$

Knowing l'_d and l_{dy}, slip can be calculated using Equation [7.13]. Beam fixed-end rotation resulting from the longitudinal bar slip is then calculated by:

$$\theta_{slip} = \frac{slip}{d-c} \qquad [7.19]$$

where d is the distance from the extreme beam compression fiber at the column face to the center of the bar (in.), and c is the neutral axis depth (in.), as shown in Figure 7.21.

7.1.3.3 Verification Example

The proposed bond stress-slip model was verified by using the test data obtained from BBN-series (Beam Bottom bar, on the North side) reinforcement in Specimen 2 (see Figures 6.45 to 6.47). The slip value was calculated when the specimen was pushed towards the west and reached 3% drift. The following data is given: $\varepsilon_s = 12{,}000 \times 10^{-6}$ (measured from Strain Gage BBN 5, see Figure 6.47); $\varepsilon_y = 2{,}520 \times 10^{-6}$; $f'_c = 6{,}200$ psi; $\sigma_y = 64$ ksi; the steel stress at the location of Strain Gage BBN 5 is: $\sigma_s = 71.7$ ksi (based on Menegotto-Pinto analysis); column depth $d_c = 14$ in. d = 11.8 in., and the neutral axis depth c is approximately 2.5 in. from nonlinear analysis. No. 6 bar diameter is 0.75 in.

Since $\varepsilon_s > \varepsilon_y$, the maximum bond stress at the compression side is calculated by Equation [7.10]:

$$\tau_{max} = \left[3000(12{,}000 - 2{,}520) \times 10^{-6} + 120\right] \cdot \frac{(6200)^{1/4}}{0.75} = 1760 \text{ psi} \qquad [7.20]$$

From Equation [7.11]:

$$\tau_{\min} = 40\frac{(6200)^{1/4}}{0.75} = 473 \text{ psi} \qquad [7.21]$$

By solving Equations [7.14] and [7.15]:

$$(71.7-64)\times 10^3 \times \frac{(0.75)}{4} = \left(\frac{\tau'_d + 473}{2}\right)\cdot l'_d \qquad [7.22]$$

and

$$\tau'_d = \left(\frac{1760-473}{14}\right)\cdot l'_d + 473 \qquad [7.23]$$

$$\Rightarrow l'_d = 2.44 \text{ in. and } \Rightarrow \tau'_d = 697 \text{ psi}$$

By solving Equations [7.17] and [7.18]:

$$64\times 10^3 \times \frac{(0.75)}{4} = \left(\frac{697+\tau_{dy}}{2}\right)\cdot l_{dy} \qquad [7.24]$$

and

$$\tau_{dy} = \left(\frac{1760-473}{14}\right)\cdot l_{dy} + 697 \qquad [7.25]$$

$$\Rightarrow l_{dy} = 10.28 \text{ in. and } \Rightarrow \tau_{dy} = 1640 \text{ psi}$$

The required anchorage (development) length is calculated by: $l_d = l'_d + l_{dy}$=2.44 in.

+ 10.28 in. = 12.72 in. $\approx 17d_b$, which is less than the column depth = 14 in. Therefore the column depth is large enough to anchor the bar when the specimen was pushed to 3% drift. The slip is then calculated using Equation [7.13]:

$$\text{slip} = \frac{2{,}520\times10^{-6}}{2}\cdot 10.28 + \frac{(12{,}000+2{,}520)\times10^{-6}}{2}\cdot 2.44 \quad [7.26]$$
$$= 0.031 \text{ in. } (0.8 \text{ mm})$$

The above value is of the same order as the measured slip during the test as shown in Figure 6.51, in which the slip value is approximately 0.08 in. (corresponding to a lateral load of 22 kips). It is noted again that the measured slip included the beam flexural deformation within a distance of 1.25 in. outside the beam-column interface (see Figure 6.20).

Beam fixed-end rotation resulting from the longitudinal bar slip is then calculated by:

$$\theta_{slip} = \frac{0.031}{11.82-2.5} = 0.33\% \text{ rad.} \quad [7.27]$$

For comparison purposes, the bi-uniform bond stress model proposed by Sezen and Moehle (2004) was used to evaluate the preceding example. The following results were obtained: the inelastic development length l'_d = 3.04 in. and the elastic development length l_{dy} = 12.7 in., which gives a total required tension-development length $l_d = l'_d + l_{dy}$ = 15.74 in. Since this length is larger than the column depth (14 in.), it

signifies that the column was not large enough to anchor the longitudinal beam bars and thus, the bar would be in tension at both column faces. Such behavior, however, was not observed in the test HPFRCC beam-column joints.

7.2 Design Recommendations

7.2.1 Development Length of Reinforcing Bar in HPFRCCs

It has been established that development (or splice) length for reinforcing bar can be significantly reduced by adding discontinuous fibers into concrete (Harajli, 1994; Hamza and Naaman, 1996). To transfer the experimental results into design application, a suitable design expression accounting for the fiber effect is essential. Harajli and Mabsout (2002) have incorporated the fiber effect into the ACI design equation for development length by expanding the transverse reinforcement index, k_{tr} (see Equation [2.18]). The revised index includes both the effects of transverse reinforcement and fiber reinforcement. They also proposed a development length expression (Equation [2.17]), which has a form similar to the ACI Committee 408 equation (Equation [2.16]). However, three problems are foreseen by expanding the k_{tr} index to incorporate the fiber effect:

1) Concerns about the increase in complexity of calculation procedures as well as in the variables in the current ACI development length expressions (ACI, 2005) have been raised (e.g. Canbay and Frosch, 2005b). In order to account for the influence of concrete cover, bar diameter, bar spacing, concrete strength, and amount of transverse reinforcement, the design equations have become considerably complicated.

Incorporating the fiber effect into the k_{tr} index, such as in Equation [2.18], would make the design expression even more complex.

2) The ACI Code requires $(c_b + k_{tr})/d_b \leq 2.5$, which gives an upper bound to the transverse reinforcement (see Equation [2.10]). Although Harajli and Mabsout (2002) have recommended raising the upper bound to 4.0 when FRC is used, the fiber effect is very likely to be ignored if a larger concrete cover or smaller bar diameter is present (thus a large c_b/d_b value). In addition, ACI Code Section 12.2.2 (ACI, 2005) offers simplified development length equations in which no $(c_b + k_{tr})/d_b$ needs to be calculated when minimum cover and minimum transverse reinforcement requirements (both are common practice) are considered. It is uncertain how the fiber effect can be taken into account under this situation.

3) The ACI development length expression was subjected to a number of changes during the last two decades. Due to its complexity, the current design equation (either the ACI 318 or ACI 408 equation) may be changed again once a better expression is proposed. It follows that a new and complicated expression accounting for the fiber effect also needs to be re-evaluated. For example, Canbay and Frosch (2005b) have proposed a simplified equation in which no k_{tr} is needed:

$$l_d = \left(0.9 \times 10^{-6} \left(\frac{f_y}{f_c'^{1/4}} \right)^2 \cdot \sqrt{d_b} \right) d_b \qquad [7.28]$$

The above equation was developed based on most common practices, such as minimum cover and spacing requirements for beams and slabs. It has been shown by Canbay and Frosch that Equation [7.28] provides excellent results by comparing with test results of 381 beam specimens. Furthermore, they pointed out that the proposed simple equation gives increased safety relative to both the ACI 318 and 408 design expressions.

Due to the aforementioned issues, a development length expression for reinforcing bars embedded in HPFRCCs is proposed in this study, based on the proposed model discussed in Section 7.1.1. It assumes that the HPFRCC completely replaces the conventional transverse reinforcement, and no k_{tr} needs to be considered:

$$l_d = \left(\frac{1}{4}\frac{f_y}{R}\right) d_b \qquad [7.29]$$

- For $0.2\% \le \varepsilon_{pc} \le 0.6\%$

$$R = 0.9\left(\frac{c}{\eta \cdot d_b}\right)\left[\left(\sigma_{cc} + \sigma_{pc}\right) - \frac{\sigma_{cc} \cdot \sigma_{pc}}{E_c \cdot \varepsilon_{pc}}\right] \qquad [7.30]$$

- For $\varepsilon_{pc} > 0.6\%$

$$R = 0.45\left[\frac{\sigma_{pc} \cdot \left(f_c'\right)^{1/4}}{\eta \cdot d_b}\right] \qquad [7.31]$$

where c can be taken as the smallest of the side cover, the cover of the bar (in both cases

measured to the center of the bar), or one-half the center-to-center spacing of the bars; d_b is the bar diameter; η is the fiber bridging efficiency; σ_{cc} is the first percolation cracking tensile strength; σ_{pc} is the peak post-cracking tensile strength and ε_{pc} is the corresponding strain. E_c is the elastic modulus of the composite; f_y is the nominal yield stress of the reinforcing bar.

For conservatism, a safety factor, such as the ACI reduction factor (ϕ), can be used in Equation [7.29]. It is noted that, conservatively, σ_{pc} can be replaced by σ_{cc} in Equations [7.30] and [7.31] if a direct tensile test is not accessible. However, this is suggested only if an "elastic-perfect-plastic" tensile stress-strain is guaranteed and σ_{cc} can be accurately estimated a priori.

7.2.2 Development Length of Strand in HPFRCCs

Although it is believed that the prestressing strand transfer length can be reduced by using HPFRCC material (see Section 5.2.2.2), only the flexural bond length for strand in HPFRCCs is proposed in this study based on the proposed model discussed in Section 7.1.2 because it resembles the test characteristics d in this study (see Section 5.2.2.1). The flexural bond length, l_f, is calculated as (the derivation of following equation is based on Section 5.2.2.1, Equation [5.4], and Equation [7.8]):

$$l_f = \frac{7}{48}\frac{(f_{ps} - f_{pe})d_b}{R} \quad [7.32]$$

$$R = 1.5\times10^{-4}\cdot\left[\frac{\sigma_{cc}\cdot f_c'}{\eta\cdot d_b}\right] \quad [7.33]$$

Minimum material requirement: $\varepsilon_{pc} > 0.6\%$ [7.34]

where f_{ps} is the nominal strength of prestressing strand; f_{pe} is the effective stress in the prestressing strand after losses.

7.2.3 Anchorage Length of Reinforcing Bar in HPFRCC Beam-Column Joints

It has been mentioned previously that the minimum anchorage length for beam bars passing through a beam-column joint required by the current ACI Code is $20d_b$. Based on the average bond stress calculation shown in Section 6.4.3, however, the required anchorage length for an HPFRCC connection would be approximately 80% of the ACI requirement, i.e., $16d_b$. As a consequence, for design purposes, a minimum anchorage length of 16 bar diameters is recommended for beam-column joints using HPFRCC materials (Parra-Montesinos, Peterfreund, and Chao, 2005). It is noted that the ACI requirements can only delay, and not prevents, bond deterioration and bar slippage. On the contrary, with suitable material design, bond deterioration and bar slippage can be prevented in HPFRCC connections for beam plastic rotations up to 4% radian

(approximately 4% story drift in the test subassemblages).

In order to apply the recommended minimum anchorage length, the following minimum material requirement is suggested: any HPFRC composite that shows a tensile pseudo strain-hardening response and a post peak tensile strain capacity $\varepsilon_{pc} > 1.0\%$. It is worth mentioning that this minimum material requirement is set based on limited results from this study, and can be relaxed if more research results are available in the future.

7.3 Conclusions

Local bond stress-slip models are proposed for reinforcing bars and prestressing strands embedded in HPFRCCs. It was found that the fundamental tensile stress-strain behavior and matrix compressive strength of an HPFRCC is directly related to the bond strength. Therefore, the bond strength can be expressed by parameters of tensile response, such as first percolation cracking stress, composite elastic modulus, peak post-cracking stress and its corresponding strain, as well as the matrix compressive strength. Design recommendations for the development length of reinforcing bars in HPFRCCs or flexural bond length of prestressing strands in HPFRCCs are given, based on the composite tensile behavior. As long as a tensile stress-strain response is known, designers can use the proposed expressions as the design parameters and do not deal with the material design (i.e, fiber types, fiber characteristics, matrix characteristics, etc.).

A global bond-slip model, specifically for reinforcing bars in HPFRCC

beam-column joints is also proposed, which can be used to predicted the required anchorage length, as well as fix-end beam rotations caused by longitudinal bar slippage.

Table 7.1 Comparison between the experimental results and the predicted values using the proposed separation-type bond model for reinforcing bar embedded in HPFRCCs

Specimen	Experimental Peak Bond Strength (psi)	Predicted Peak Bond Strength (psi)
No. 8 Bar, 2% Square Torex	1640	1591
No. 8 Bar, 2% Rectangular Torex	1490	1373
No. 5 Bar, 2% Rectangular Torex	2090	2195

Table 7.2 Comparison between the experimental results and the predicted values using the proposed friction-type bond model for reinforcing bar embedded in HPFRCCs

Specimen	Experimental Peak Bond Strength (psi)	Predicted Peak Bond Strength (psi)
No. 8 Bar, 2% Spectra $(\sigma_{pc} = 600 \text{ psi})$	1532	1382
No. 5 Bar, 2% Spectra $(\sigma_{pc} = 600 \text{ psi})$	2348	2212
No. 8 Bar, 2% Rectangular Torex $(\sigma_{pc} = 800 \text{ psi})$	1630	1680

Table 7.3 Comparison between the experimental results and the predicted values using the proposed bond model for prestressing strand embedded in HPFRCCs

Specimen	Experimental Peak Bond Strength (psi)	Predicted Peak Bond Strength (psi)
2% Spectra, 11 ksi Matrix $(\sigma_{cc} = 700 \text{ psi})$	1150	1155
2% Square Torex (30 mm), 11 ksi Matrix $(\sigma_{cc} = 900 \text{ psi})$	1500	1485
2% Rectangular Torex, 11 ksi Matrix $(\sigma_{cc} = 850 \text{ psi})$	1300	1400
2% Rectangular Torex, 7.6 ksi Matrix $(\sigma_{cc} = 800 \text{ psi})$	1000	912

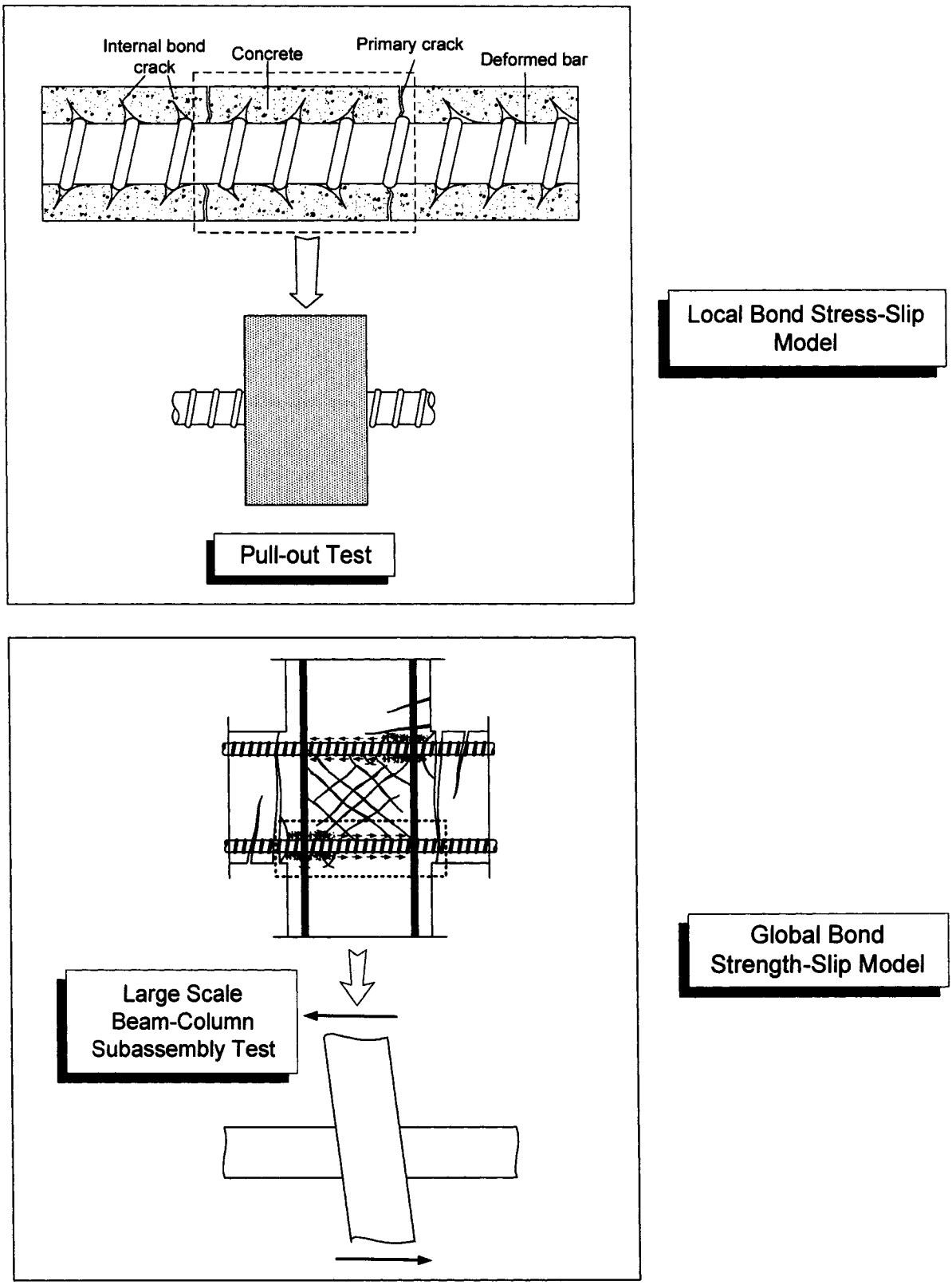

Figure 7.1 Two different bond modeling schemes

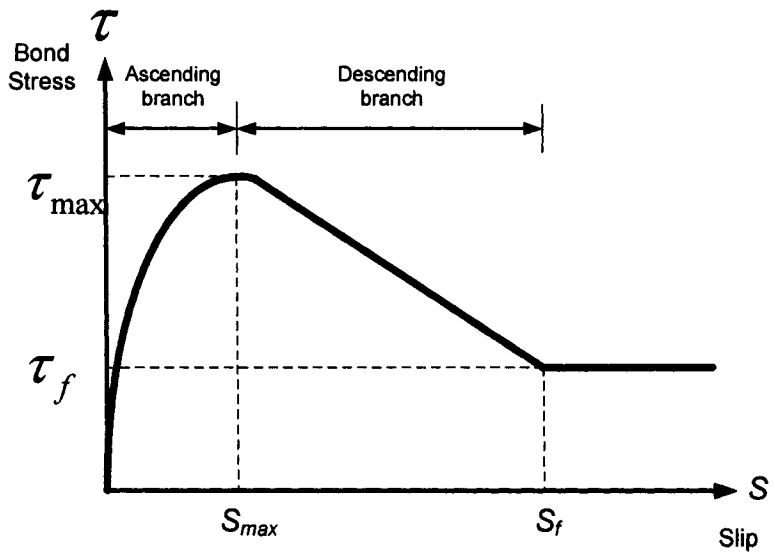

Ascending branch: $\tau(s) = \tau_{\max}\left(\frac{s}{s_{\max}}\right)^{0.5}$

Descending branch: $\tau(s) = \tau_f\left(s - s_f\right)\left(\frac{\tau_{\max} - \tau_f}{s_{\max} - s_f}\right)$

$$\tau_{\max} = \left(3.19 + 10.07\frac{c}{d_b} + 60.49\frac{d_b}{L_e}\right)\left(f_r\right)^{0.8} \text{ (psi)}$$

$\tau_f \approx 0.45\tau_{\max}$

S_{max} = 0.05 in.

S_f = 0.40 in.

Note: L_e = embedment length; c = concrete cover; d_b = bar diameter; f_r = flexural strength of SIFCON matrix

Figure 7.2 Bond stress-slip model for reinforcing bar in SIFCON (Hamza, 1992)

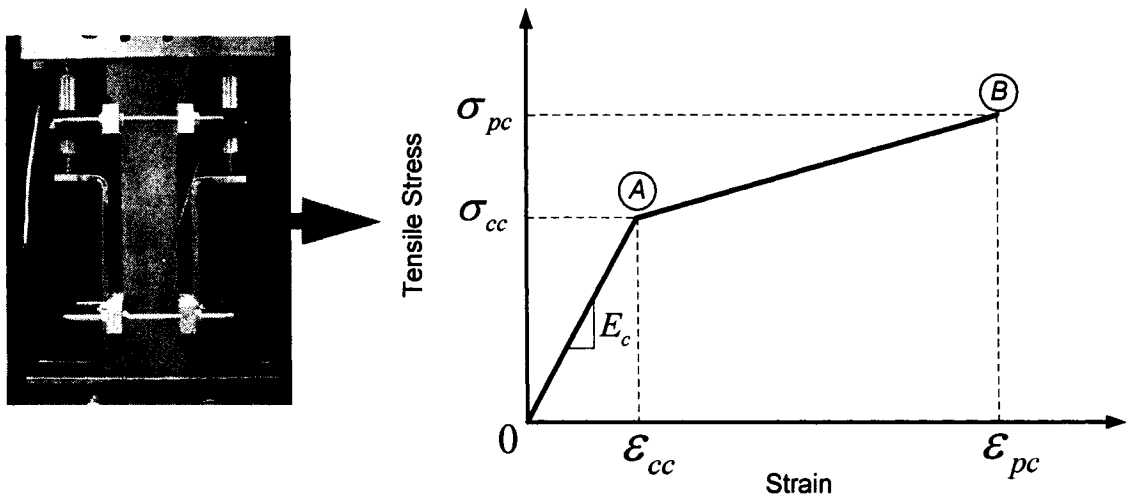

Figure 7.3 Minimum information on tensile strain-hardening stress-strain response of FRC composites needed for modeling and design (Naaman and Reinhardt, 2005)

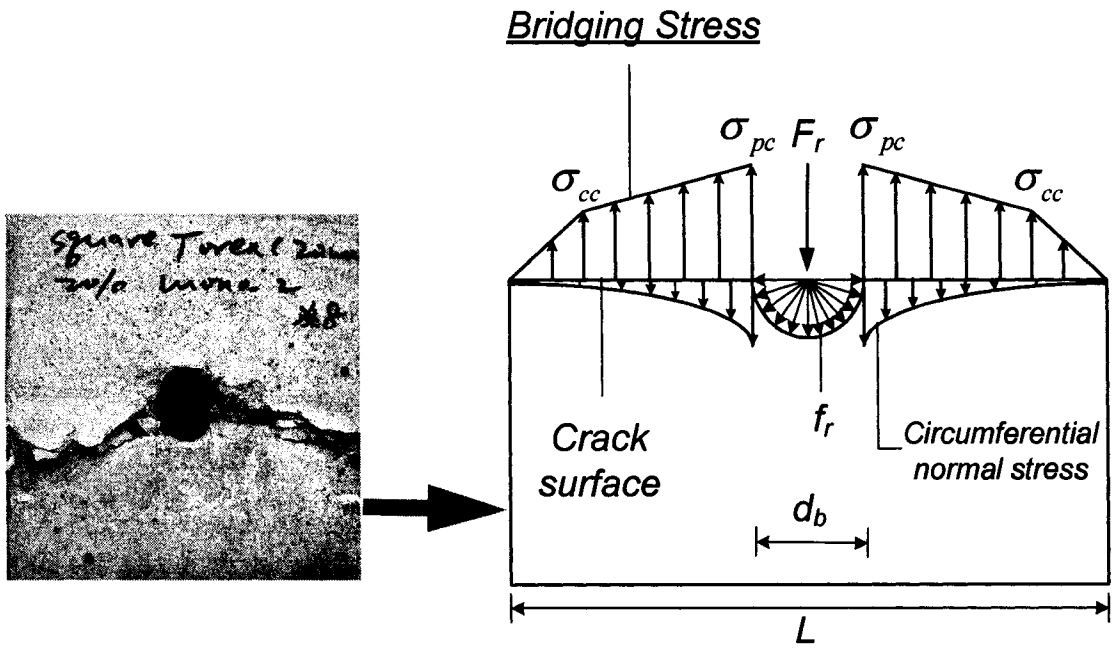

Figure 7.4 Force equilibrium in a separation-type bond failure specimen

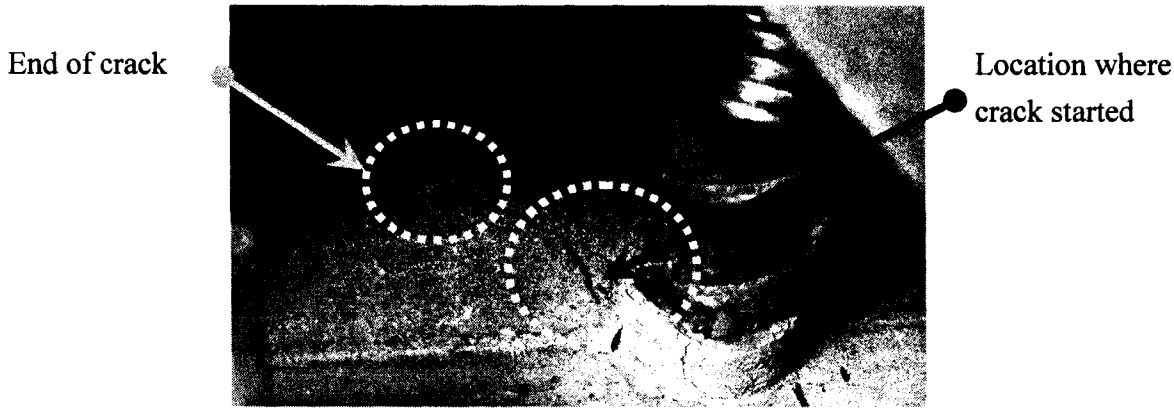

Figure 7.5 Initiation of separation crack in specimen with No. 8 bar and Torex fibers

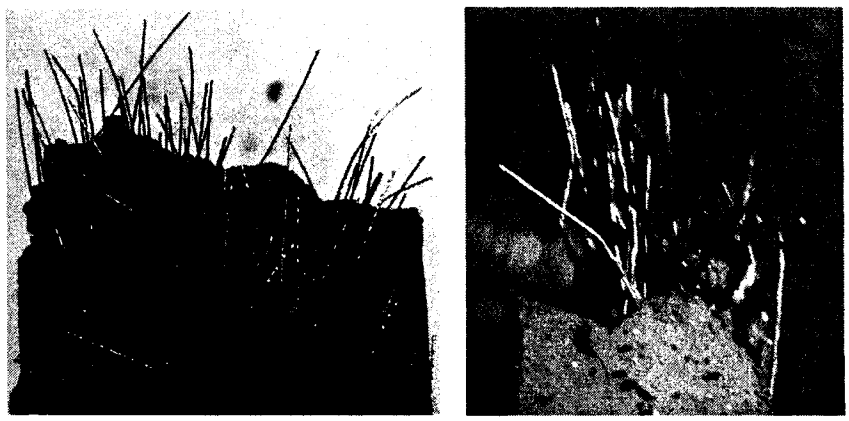

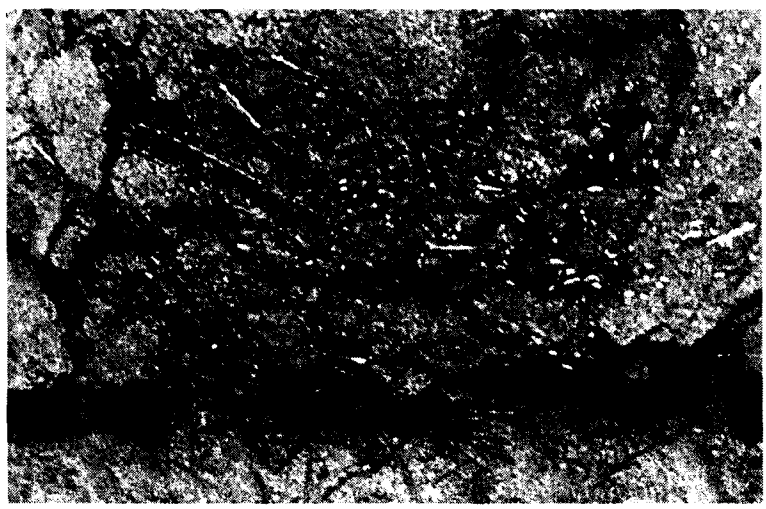

Figure 7.6 Fiber distribution in a direct tensile specimen: (a) width direction; (b) thickness direction (c) fiber distribution in a pull-out type specimen

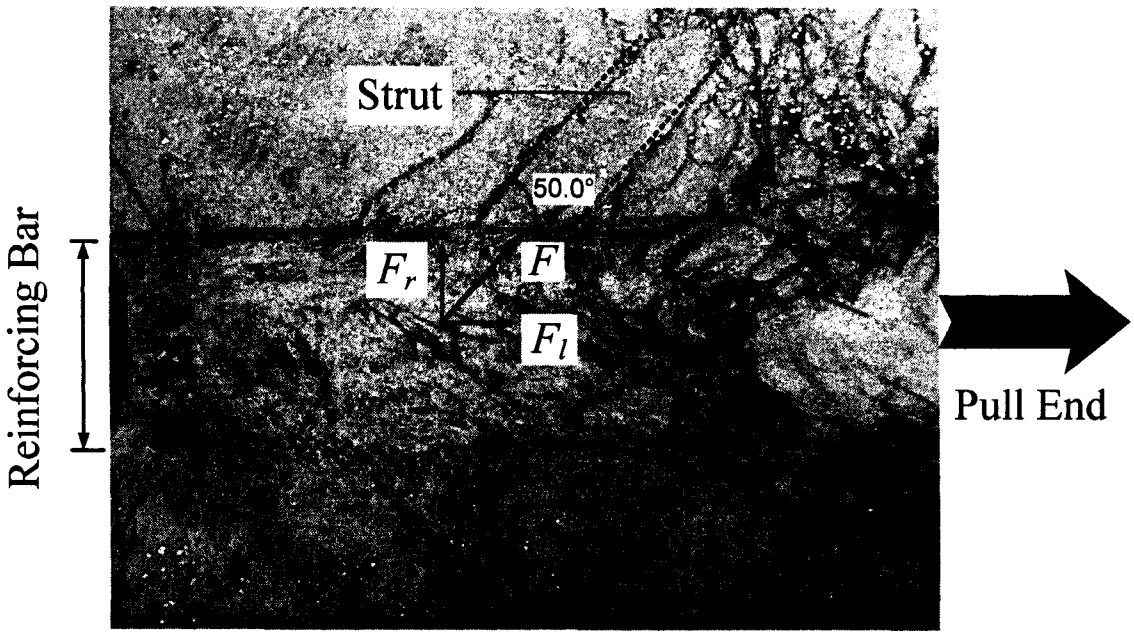

Figure 7.7 Internal inclined force and its orientation (No. 8 bar specimen with rectangular Torex fiber, matrix strength = 7.6 ksi)

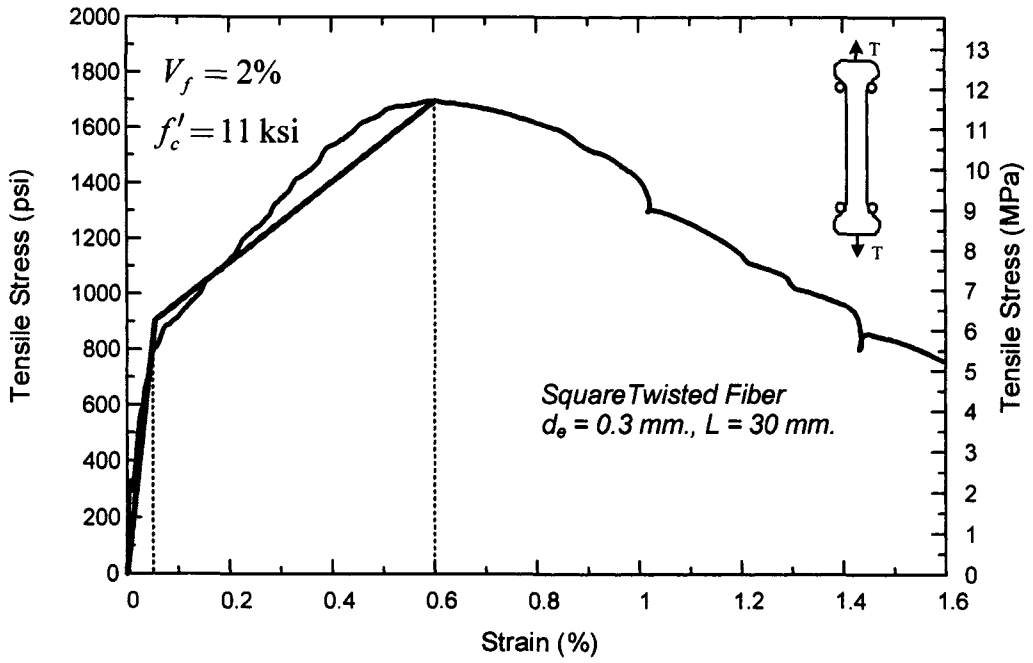

Figure 7.8 Modeling of the tensile stress-strain response for specimens with square Torex fibers

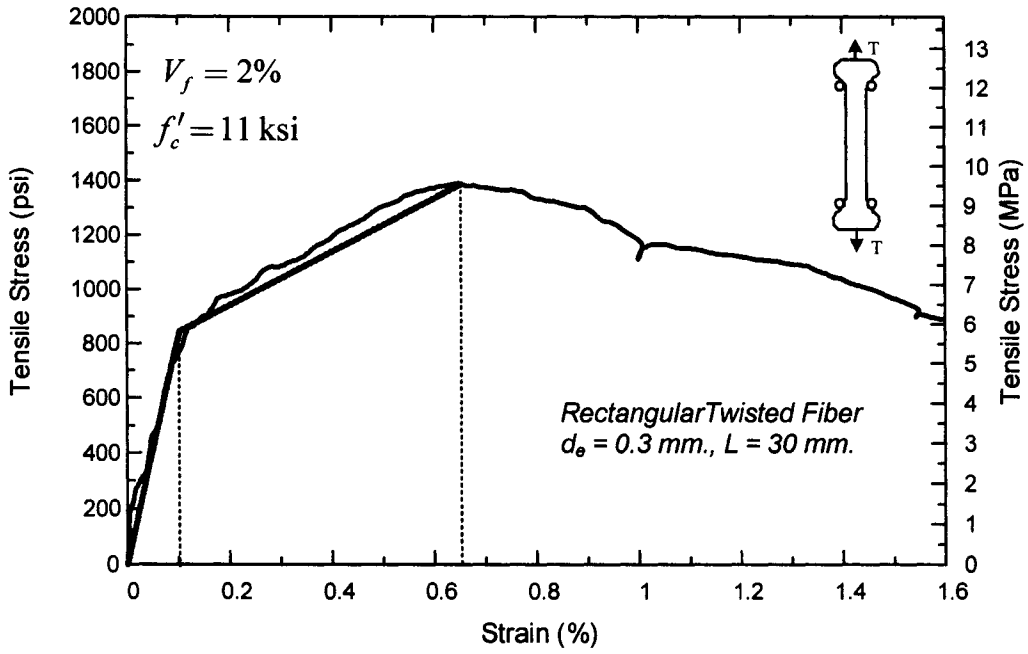

Figure 7.9 Modeling of the tensile stress-strain response for specimens with rectangular Torex fibers

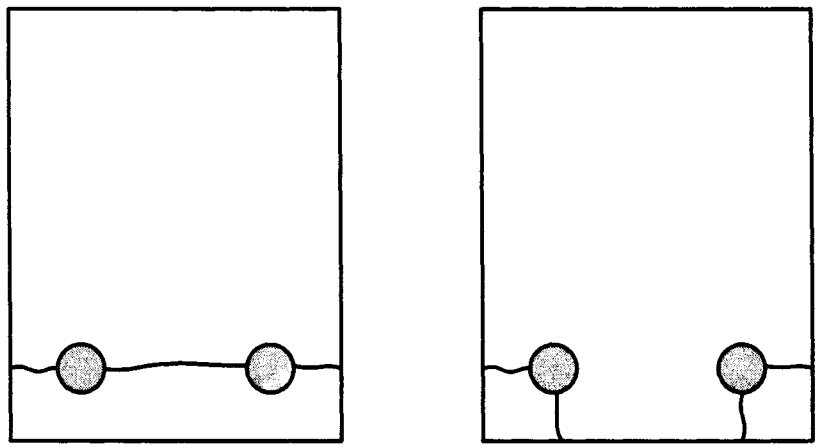

Figure 7.10 Application of proposed bond stress model to structural elements

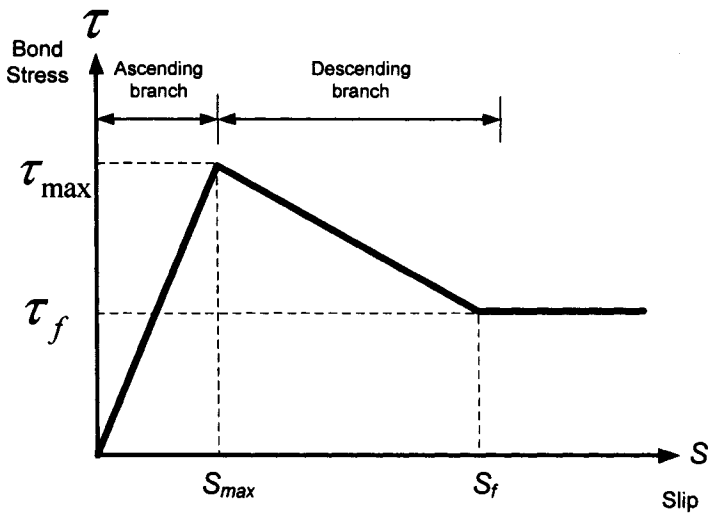

Ascending branch: $\tau(s) = \tau_{\max} \cdot \frac{s}{s_{\max}}$

$$\tau_{\max} = 0.9 \cdot \left(\frac{c}{\eta \cdot d_b}\right) \cdot \left[\left(\sigma_{cc} + \sigma_{pc}\right) - \frac{\sigma_{cc} \cdot \sigma_{pc}}{E_c \cdot \varepsilon_{pc}}\right] \text{ (psi)}$$

$$\boxed{0.2\% \le \varepsilon_{pc} \le 0.6\%}$$

$$\tau_f = 0.15\tau_{\max} \text{ (psi)}$$

$$S_{\max} = \frac{\tau_{\max}}{3 \cdot d_b \cdot f_c'}$$

$$S_f = 0.5 \text{ in.}$$

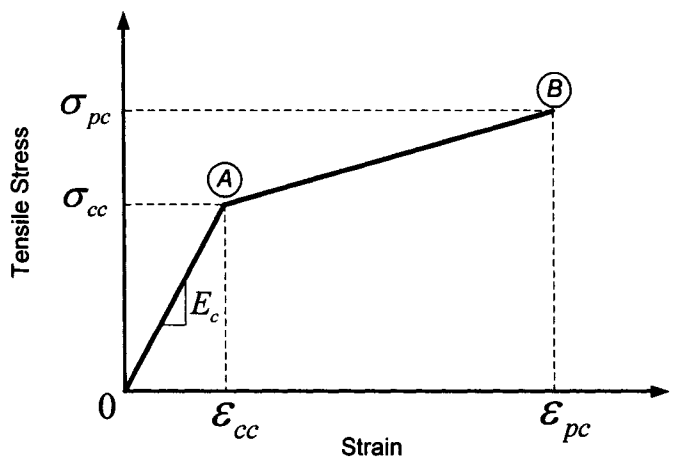

Figure 7.11 Proposed bond stress-slip model (separation-type failure) for reinforcing bar embedded in HPFRCC materials

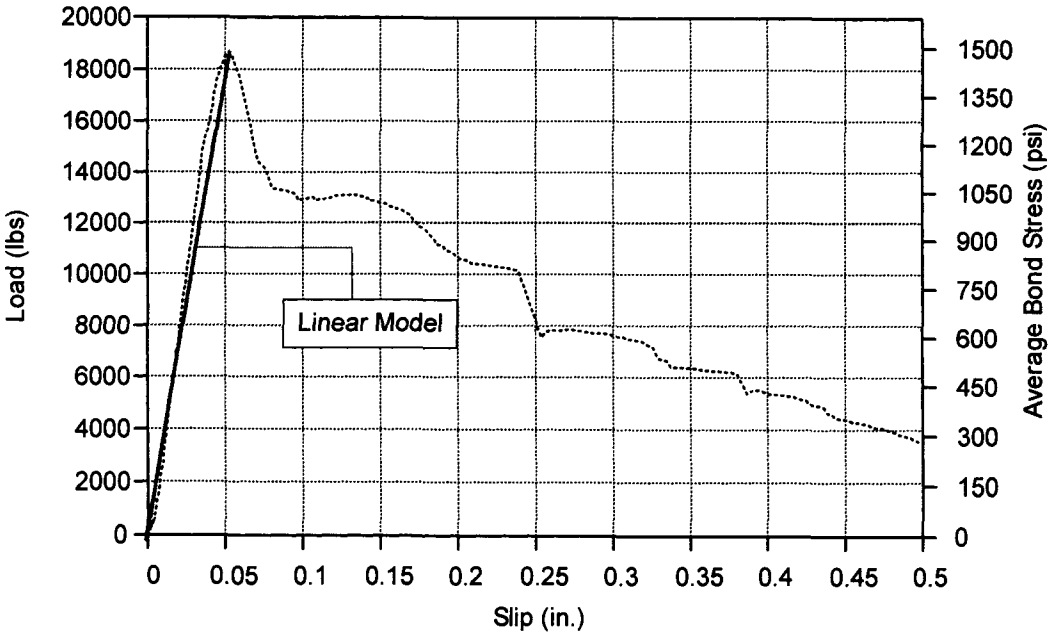

Figure 7.12 Proposed bond stress-slip model (separation-type failure) for reinforcing bar embedded

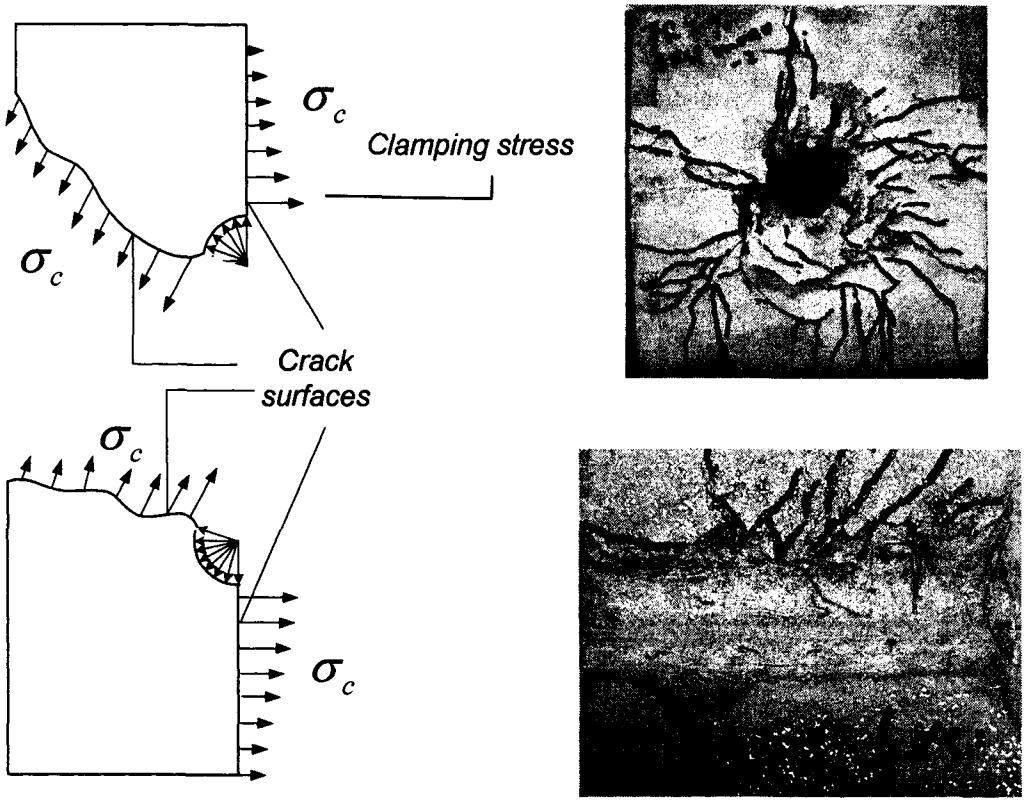

Figure 7.13 Force equilibrium in a friction-type bond failure specimen, as well as the sheared-off bar-to-matrix interface

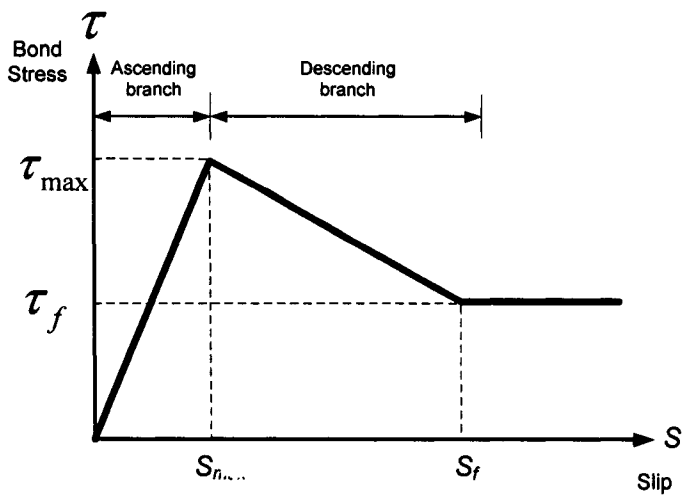

Ascending branch: $\tau(s) = \tau_{max} \cdot \frac{s}{s_{max}}$

$$\tau_{max} = 0.45 \cdot \left[\frac{\sigma_{pc} \cdot (f_c')^{1/4}}{\eta \cdot d_b} \right] \quad (psi)$$

$$\boxed{\varepsilon_{pc} > 0.6\%}$$

$$\tau_f = 0.3\tau_{max} \quad (psi)$$

$$S_{max} = \frac{\tau_{max}}{3 \cdot d_b \cdot f_c'}$$

$$S_f = 0.5 \text{ in.}$$

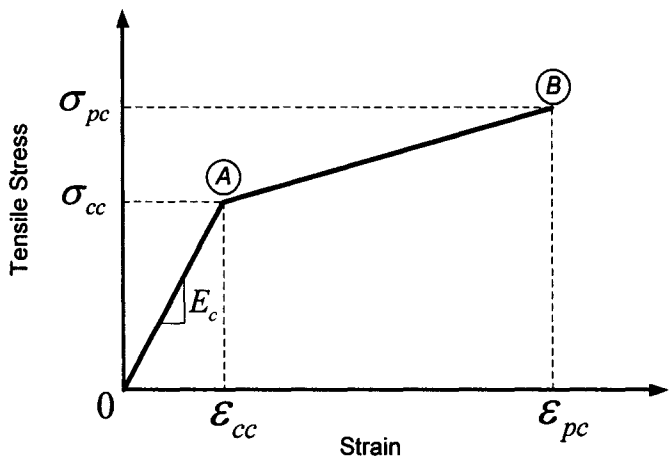

Figure 7.14 Proposed bond stress-slip model (friction-type failure) for reinforcing bar embedded in HPFRCC materials

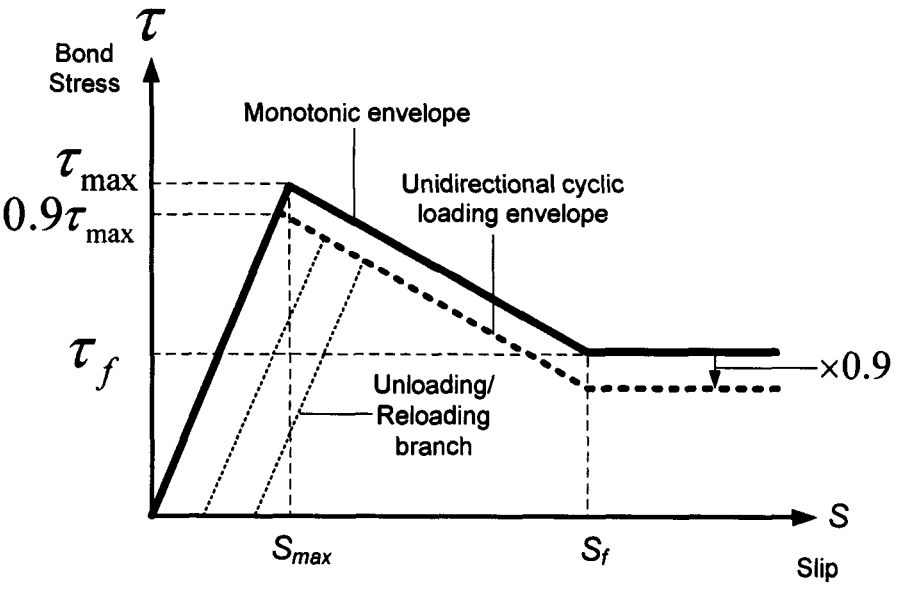

(a) Unidirectional Cyclic Loading

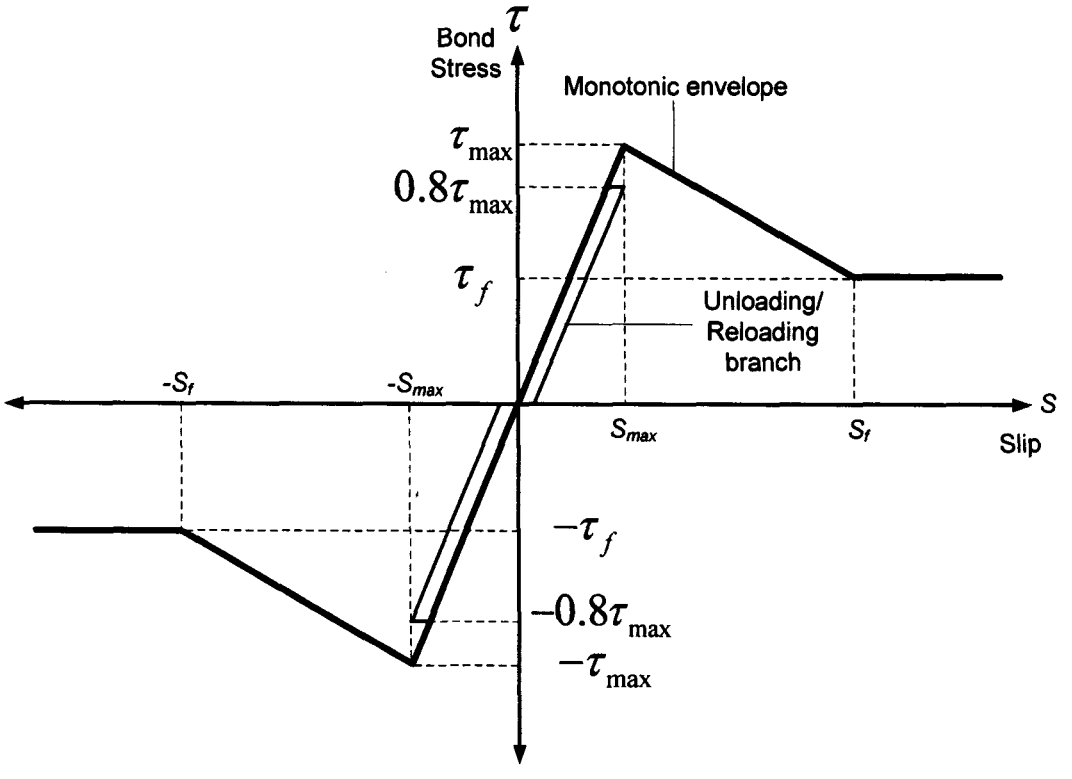

(b) Fully Reversed Cyclic Loading

Figure 7.15 General guideline of bond stress-slip model for reinforcing bar embedded in HPFRCC materials under cyclic loadings

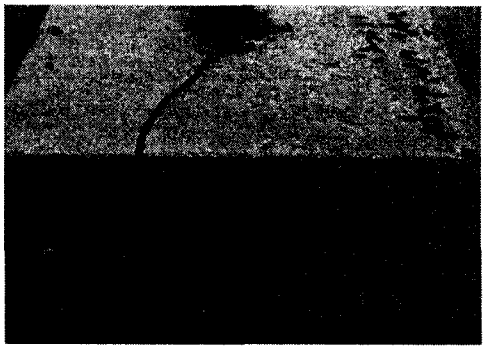

(a)

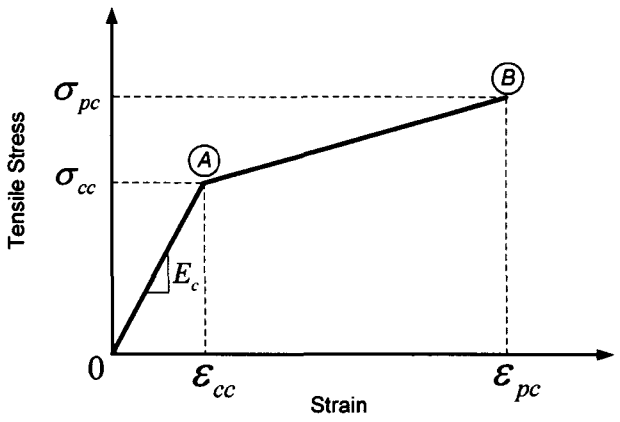

(b)

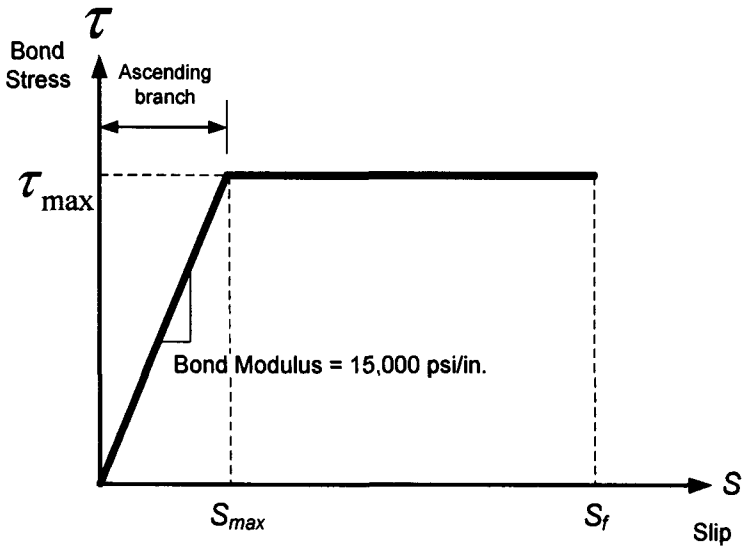

Ascending branch: $\tau(s) = \tau_{max} \cdot \frac{s}{s_{max}}$

$$\tau_{max} = 1.5 \times 10^{-4} \cdot \left[\frac{\sigma_{cc} \cdot f_c'}{\eta \cdot d_b} \right] \quad (psi)$$

$\varepsilon_{pc} \geq 0.6\%$ (in order to maintain the tensile capacity after cracking occurs)

$S_{max} = \tau_{max} / 15{,}000$

$S_f = 0.8$ in.

(c)

Figure 7.16 Proposed bond stress-slip model for 0.5 in. strand embedded in HPFRCC materials

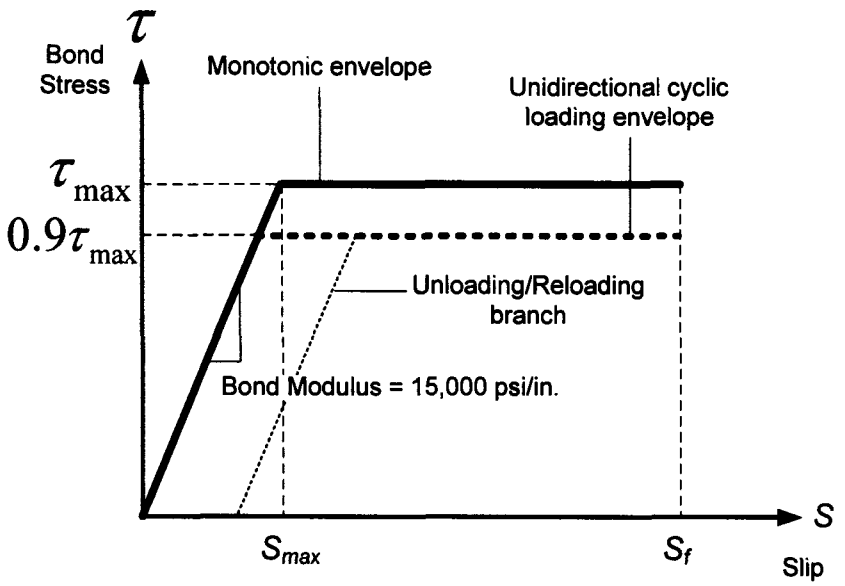

(a) Unidirectional Cyclic Loading

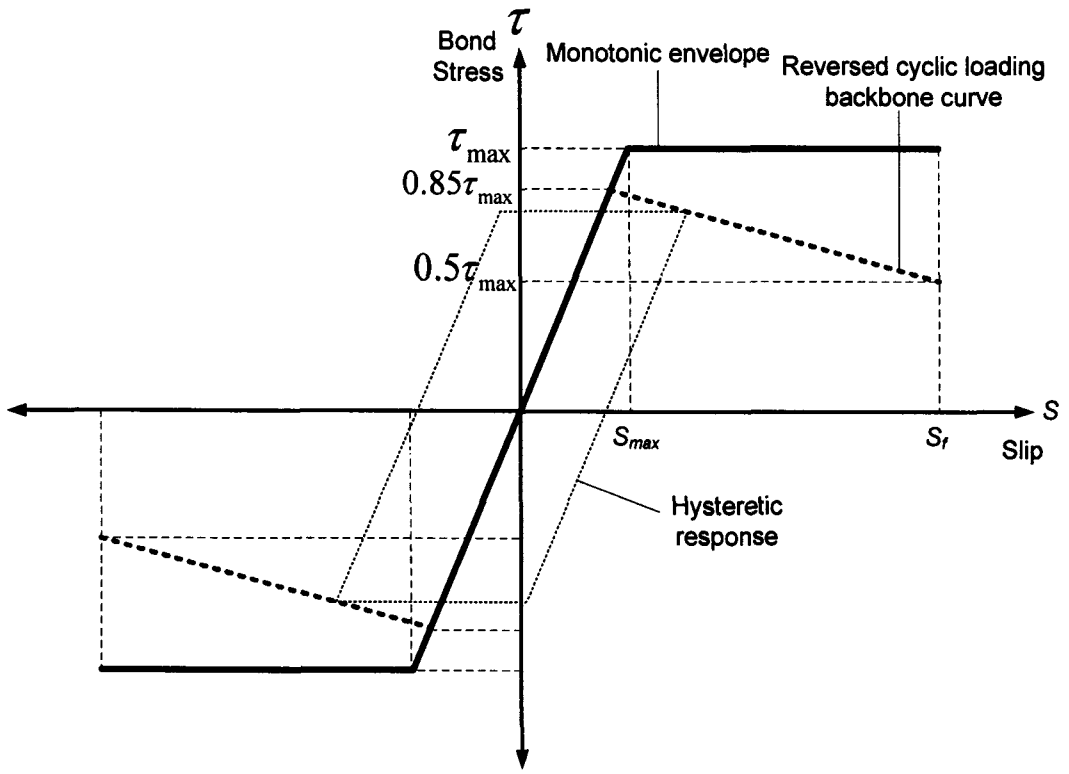

(b) Fully Reversed Cyclic Loading

Figure 7.17 General guideline of bond stress-slip model for 0.5 in. strand embedded in HPFRCC materials under cyclic loadings

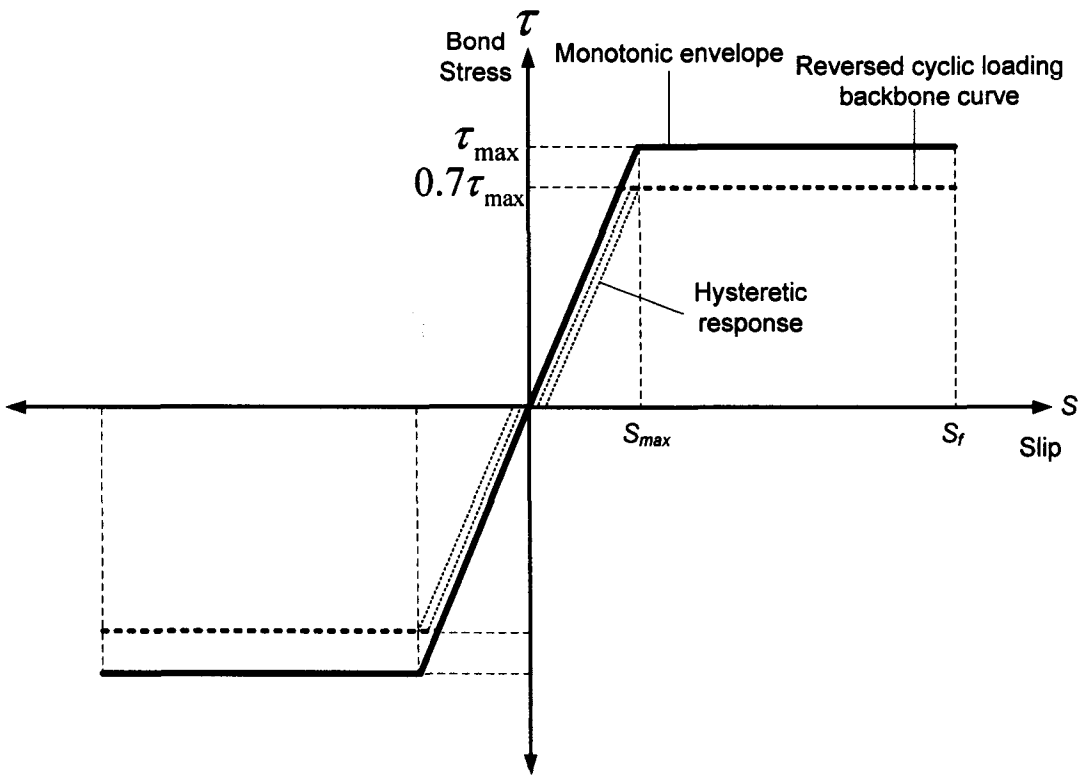

(c) Fully Reversed Cyclic Loading (Slip smaller than S_{max})

Figure 7.17 (continued) General guideline of bond stress-slip model for 0.5 in. strand embedded in HPFRCC materials under cyclic loadings

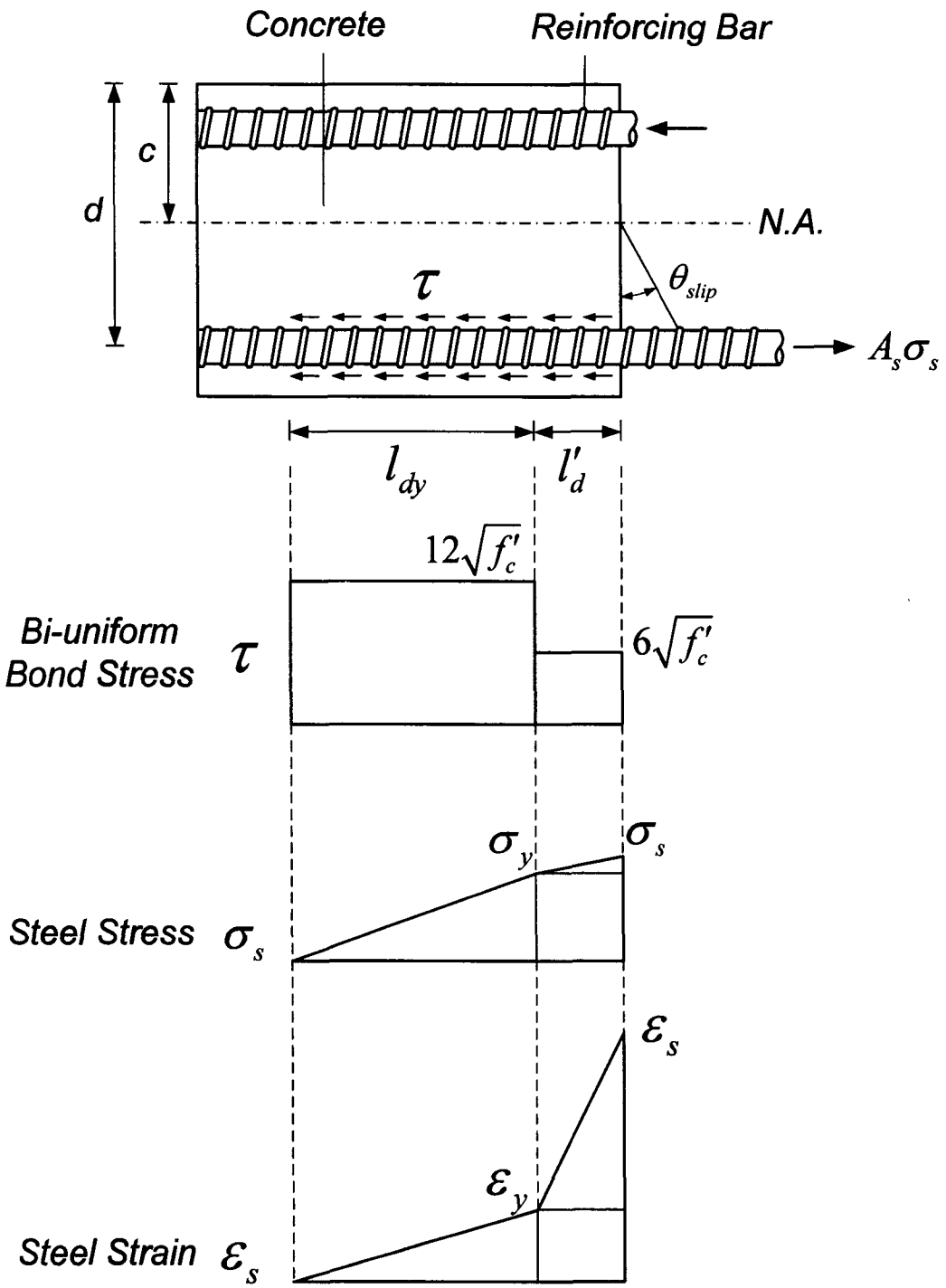

Figure 7.18 Bond strength model and corresponding reinforcing steel strain and stress distributions in conventional concrete element (Sezen and Moehle, 2004)

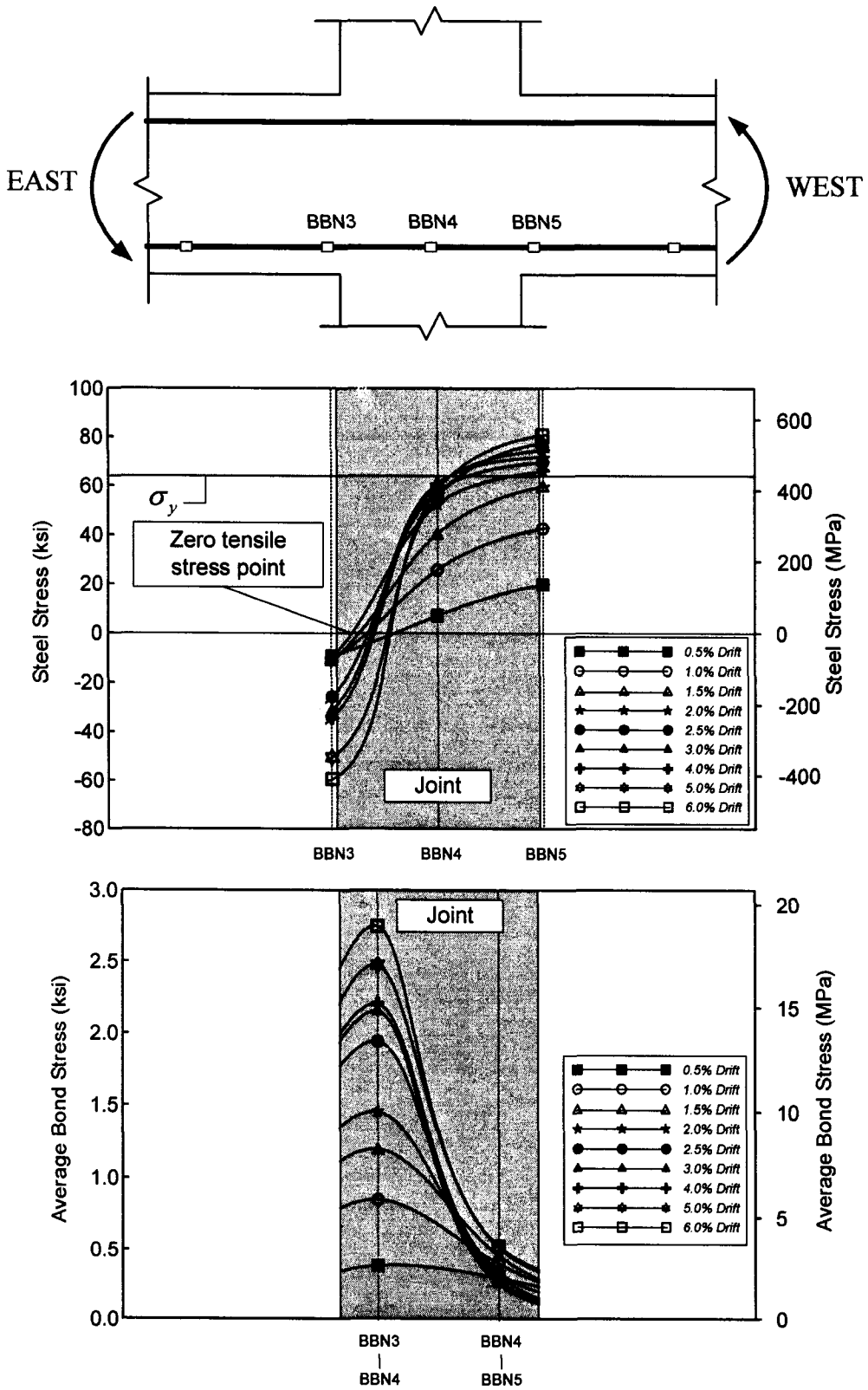

Figure 7.19 Typical steel stress and bond stress distributions in a beam-column joint with HPFRCC materials

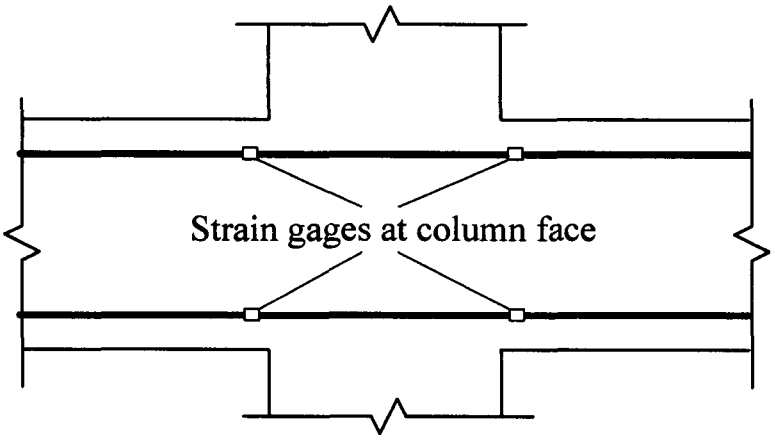

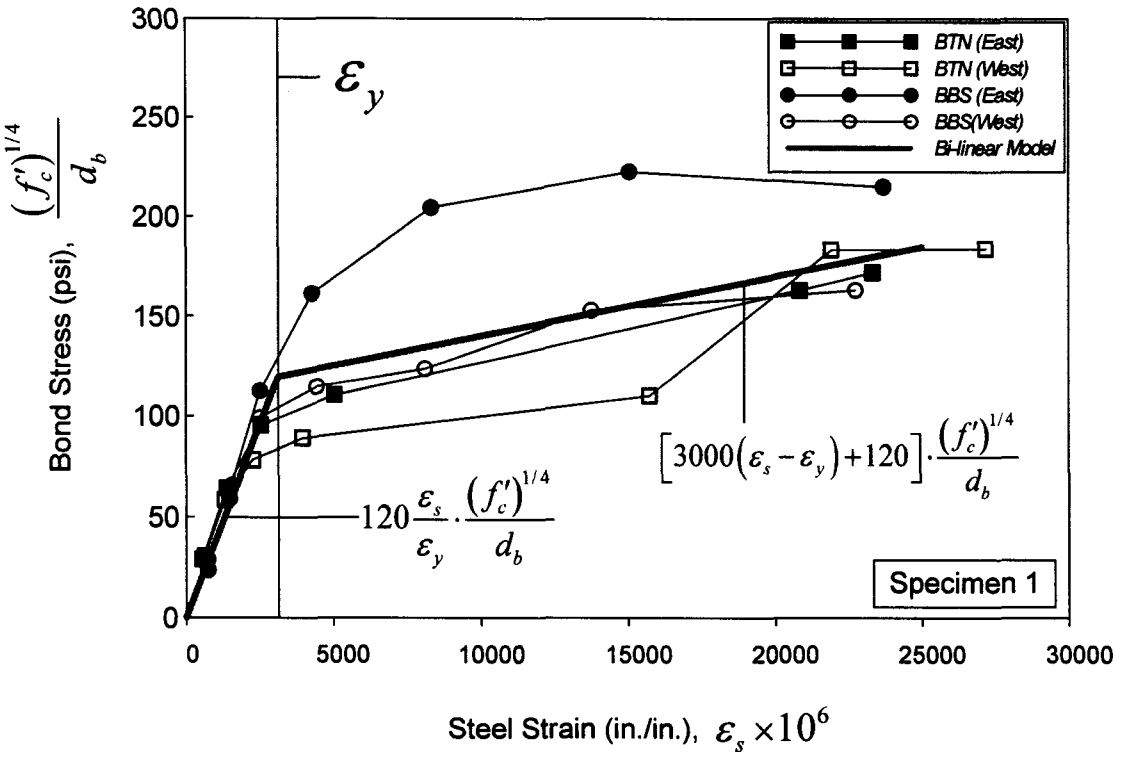

Figure 7.20 (a) Bond stress at compression side versus reinforcing bar strain (at column faces) in Specimen 1

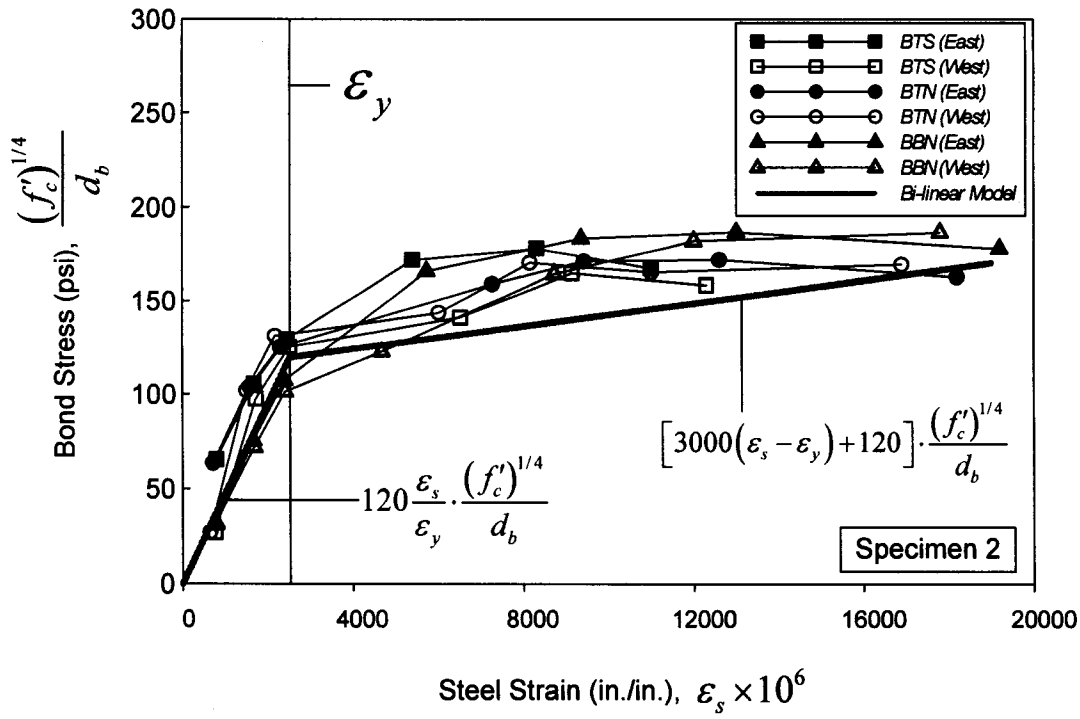

Figure 7.20 (b) Bond stress at compression side versus reinforcing bar strain (at column faces) in Specimen 2

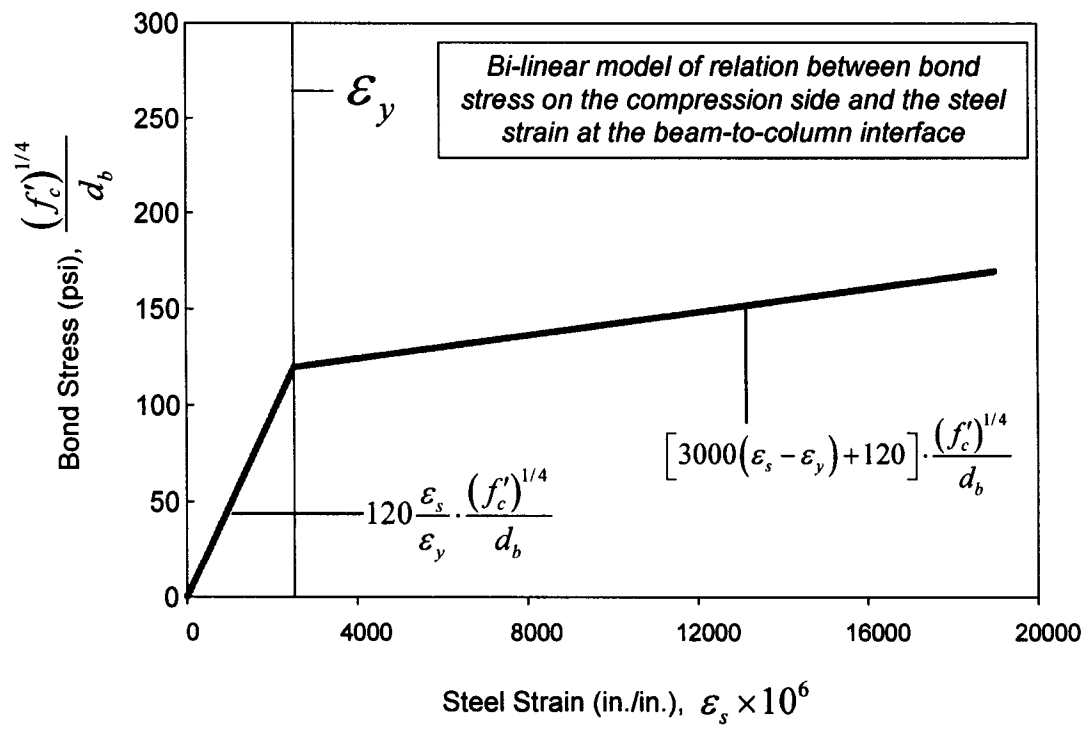

Figure 7.20 (c) Proposed bi-linear model

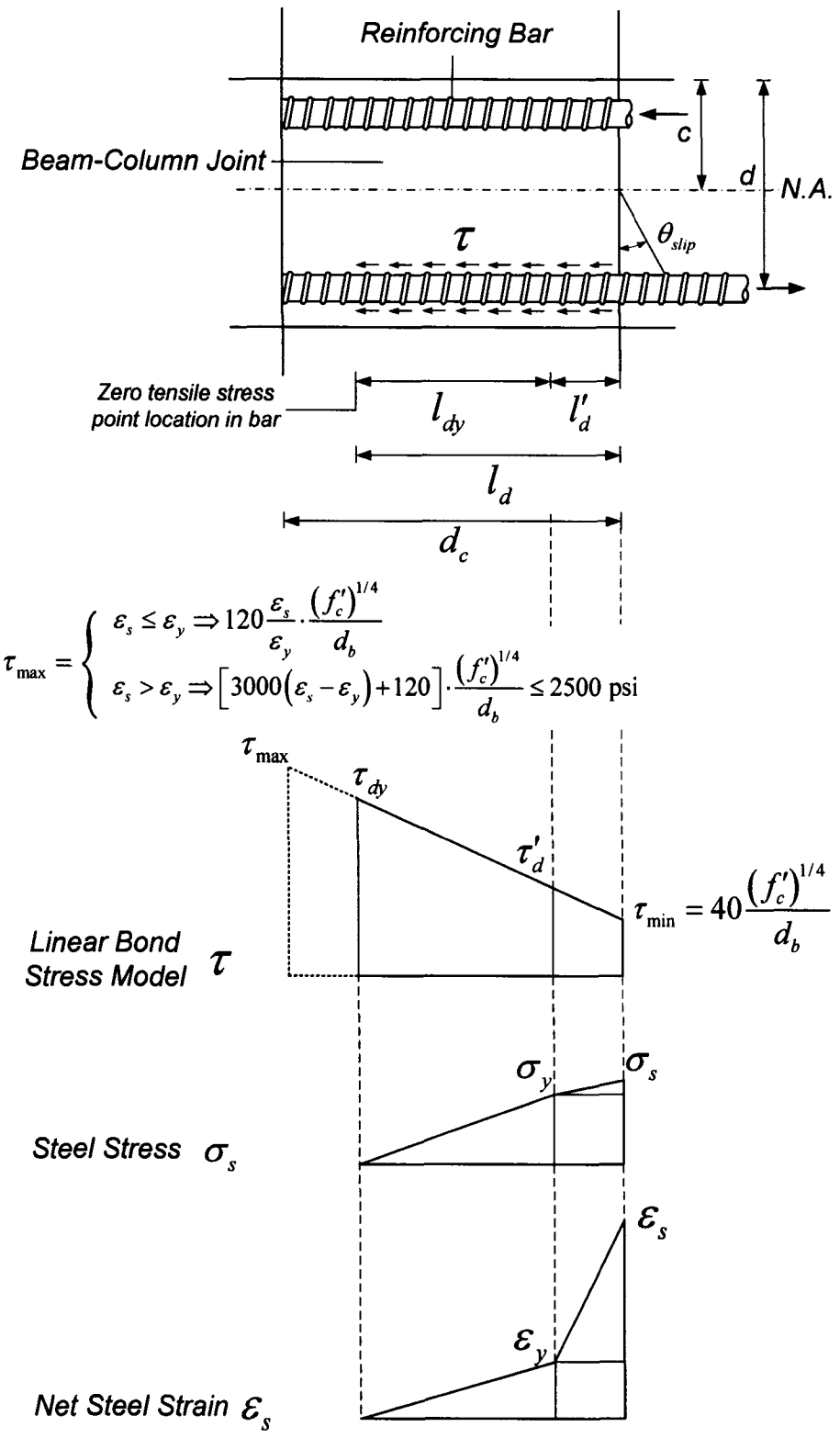

Figure 7.21 Proposed bond stress distribution model and corresponding reinforcing steel strain and stress distributions in an HPFRCC beam-column joint

CHAPTER 8

SUMMARY, CONCLUSIONS, AND FUTURE RESEARCH

8.1 Summary

8.1.1 Summary of the Research Significance and Scope

Composite action between concrete and reinforcing steel cannot occur without bond. Therefore the bond performance of reinforcing bars and/or prestressing tendons play a major role in the behavior of reinforced and prestressed concrete structural members when subjected to static and dynamic loads. Not only can poor bond lead to a loss of strength of a structural element, but it can also lead to reductions in stiffness, ductility, energy dissipation capacity and thus, safety of structural members. Besides, the development length needed for a reinforcing bar to develop its ultimate strength in a concrete element, and/or the transfer length of a prestressing strand to fully transfer the effective prestressing force to concrete by bond, also directly depend on the quality of bond.

In a concrete element with reinforcing bars, the mechanical interlock resulting from the presence of ribs creates inclined forces that lead to internal inclined cracks. These cracks reduce the bond strength, and, should their opening become too large, bond deteriorates progressively. A direct cone-shaped fracture could also result due to the

propagation of these inclined cracks. When reinforcing bars are subjected to reversed cyclic loading, the opened inclined cracks lead to significant deterioration in bond stiffness and strength when the slip is reversed in the opposite direction due to the presence of gaps between steel and concrete. The radial component of the inclined forces usually causes splitting of surrounding concrete.

In a prestressed concrete structure, such as pre-tensioned beams, swelling of the strand after release leads to the Hoyer's effect (wedge effect) which in turn gives rise to considerable radial pressure and thus, larger frictional forces against strand slip. However, when splitting cracks occur and propagate along the anchorage zone Hoyer's effect becomes less effective, leading to a reduction in frictional and mechanical bond resistance, and possibly, to bond failure.

There are a host of unfavorable conditions for bond resistance in interior beam-column joints when subjected to displacement reversals: through-cracks form at the beam-to-column interface, formation of cone-shaped fracture, yielding of the longitudinal bars penetrating into the joint, longitudinal splitting cracks along the beam bars, progressive matrix crushing and growing of splitting cracks in front of bar lugs, and extensive diagonal tensile cracking in the joint. Combination of these unfavorable conditions leads to an effective anchorage length that could be much shorter than the column width, which in turn raises the bond demand and further bond deterioration and slippage. Unfortunately, current repair techniques, such as epoxy injection, are still not able to reliably restore the destroyed bond of a beam-column joint.

It is evident, therefore, that the most important factor that influences the bond performance of reinforcing bars/prestressing strands in conventional concrete elements is the cracking of concrete; more specifically, the tensile behavior of concrete. In this regard, an emerging class of materials, High-Performance Fiber Reinforced Cement Composites (HPFRCCs), represents an attractive solution to remedy this issue. Unlike conventional concrete, whose tensile strength drops very quickly after cracks occur, HPFRC composites show no degradation in post-cracking tensile strength up to very large strains, often in excess of 0.5%. Furthermore, high performance fibers can effectively bridge the tensile cracks and constrain their development in terms of length and width, thus redistributing the internal tensile stresses and leading to the formation of multiple fine cracks. It is believed that the unique characteristics of HPFRCCs can significantly enhance the bond characteristics of reinforcing bars and prestressing strands embedded in concrete matrices. A host of additional benefits may be offered by using HPFRC composites, such as a reduction in reinforcement congestion in beam-column joints and anchorage zones of prestressed concrete beams by replacing confinement steel with fibers.

8.1.2 Summary of the Experimental Program

The experimental program consisted of two phases: 1) Pull-out type test of specimens with either reinforcing bar or prestressing strand, and 2) large scale beam-column joint test simulating the severe bond demand under earthquake-induced loading.

The first phase of the experimental program focused on pull-out type specimens that had a prismatic shape with dimensions 6 in.×6 in.×4 in. (embedment length = 4 in.). This type of test was used to investigate the bond stress versus slip relationship of the interface between reinforcement and the surrounding matrix. This relationship can be considered the "constitutive" property of the interface. It gives an entire description of the bond resistance at any given slip, thus allowing the measurement of maximum bond stress, bond modulus, average bond stress at a given slip, and shear-friction energy (thus pull-out work) absorbed up to any given slip. The following parameters were investigated:

1. Reinforcing steel bars: Deformed bars, No. 8, No. 5, and No. 4; Grade 60
2. Prestressing steel strands: 0.5 in diameter; Grade 270.
3. Fiber type: Dramix® steel Hooked fiber, PVA 13 fiber, PVA K-II fiber, Torex steel fiber (square, rectangular, and triangular (Helix®)), and Spectra® fiber.
4. Fiber volume fraction: 0% (control specimens), 1%, and 2%.
5. Confinement (for No. 8 bar specimens only): Tests using confinement in the form of spirals (2% volumetric ratio) were also conducted to provide a fair range for comparison with confined concrete.
6. Matrix compressive strength: Three strengths were tested, a normal strength of about 5.9 ksi and high strengths of 7.6 and 11 ksi.
7. Loading type for pull-out load tests: a) monotonic; b) unidirectional cyclic with displacement control; c) unidirectional cyclic with force control; d) fully reversed cyclic loading with displacement control; and e) fully reversed cyclic loading with force control.

A specific test apparatus was designed to accommodate the various types of loading conditions. The prismatic specimen was supported at its eight corners by $2 \times 1.5 \times 0.5$ in. plates. No bearing plate was used, thus, minimizing the confinement effect in the loading direction. The slip data was recorded using a pair of Linear Variable Differential Transformers (LVDTs) connected to a data acquisition system, while the applied load was monitored through a load cell. The testing machine is a closed-loop servo controlled hydraulic universal machine (INSTRON 1325) with 110 kip loading capacity.

Tests on single fiber pull-out and direct tensile tests of HPFRCCs were also performed to investigate fundamental material properties.

The following test results were investigated and evaluated:

1. Bond stress versus slip relationship; bond modulus; bond strength and corresponding slip.
2. Cracking pattern and fiber bridging effect.
3. Bond deterioration under cyclic loading; bond strength and stiffness retention capacity under low-cycle fatigue loading.
4. Bond deterioration mechanisms for reinforcing bars and prestressing strands.
5. Pull-out work and pull-out energy up to selected slip levels.
6. Development length of reinforcing bars and flexural bond length of prestressing strands.

The second phase of the experimental program focused on the evaluation of the use

of HPFRCC materials in beam-column joints. Two approximately 3/4-scale beam-column subassemblies were constructed and tested under large displacement reversals. The HPFRCC materials were placed in the beam-to-column joint and the adjacent beam regions (over two times the beam depth). Regular concrete was used in the rest portions of beams and columns. HPFRCC material employed in this phase contained 1.5% by volume of Spectra fibers. Direct tensile tests showed that this material exhibited a strain-hardening tensile behavior up to about 1% strain. The regular concrete outside the HPFRCC region was obtained from a local ready-mix concrete supplier, with a specified concrete strength of 5 ksi and a 6 in. slump. No. 6 bars (diameter = 0.75 in.) with a nominal yield strength of 60 ksi were used for both column and beam longitudinal reinforcement. Actual bar tensile strength was obtained from tensile tests conducted in a Baldwin static test frame and the corresponding yield strengths were 79.3 ksi and 64 ksi for No. 6 bars used in Specimens 1 and 2, respectively.

Design of these two beam-column subassemblies was performed according to the strong column-weak beam principle and the ratios of nominal column moment strength to ultimate beam moment strength were 2.2 and 1.6 for Specimens 1 and 2, respectively. The beam cross section was 6 in. wide and 14 in. deep, and the column cross section was 14×14 in. This gave an anchorage length equal to $18.7d_b$, which was approximately 94% of the ACI requirement ($20d_b$). In addition, no confinement steel was provided in the joint region, where large amounts of closely spaced hoops are required to ensure adequate behavior of RC joints under large shear reversals.

The following test results were investigated and evaluated:

1. Steel stress distribution and bond stress distribution in the joint region at various drift levels.
2. Average bond stress, bar slip and bond efficiency in the joint region.
3. Cracking pattern and width in the joint and beam plastic hinging regions at various drift levels.
4. Joint shear distortion.

8.1.3 Summary of the Analytical Program

The analytical work was mainly focused on the development of the following models:

1. A local bond stress-slip model. The bond stress versus slip relationship was obtained from the pull-out type bond tests conducted in this study. This model can be used in finite element analyses as the constitutive law for a zero-thickness interface bond element, or for an additional degree of freedom at bar element nodes to model the steel-concrete interface properties. In addition, the local bond stress-slip model can be applied to the analysis of reinforced concrete ties for investigating crack formation, elongation of the tie, as well as the tension stiffening effects. Also, the anchorage of a bar and its corresponding steel stress versus pull-out displacement can be studied by means of the local bond stress-slip model. Based on experimental results, local bond stress-slip models for both reinforcing bars and prestressing strands embedded in HPFRCCs under various loading conditions were proposed. Bond strength was

directly related to the tensile stress-strain behavior of HPFRCCs.

2. A global bond stress distribution model for a beam-column joint, in which the yield penetration is inherently accounted for, is essential for the evaluation of bar slippage and thus, fixed-end rotations at beam ends due to bar slip. Based on the test and analysis results, a global bond-slip model for bars passing through HPFRCC beam-column joints was proposed.

8.2 Conclusions

Conclusions on experimental and analytical results are given at the end of corresponding chapters. The most significant conclusions are listed below:

8.2.1 Bond of Reinforcing Bar

- With same reinforcement amount (volume fraction), HPFRCCs can completely replace conventional transverse reinforcement and show superior performance in terms of peak bond strength and cracking control. The ACI requirement for development length, assuming a 2% volumetric ratio of spiral reinforcement, can be reduced by 50% by using HPFRCCs without any transverse reinforcement.

- Two types of bond failure modes, separation and friction, can occur in bars embedded in HPFRCCs, generally depending on the tensile response of the fiber

cement composite. Both failure modes give bond strengths as high as 1.5 times that in the spirally reinforced specimens.

- Increasing fiber content from 1% to 2% can significantly enhance the bond performance under monotonic and cyclic loadings in terms of peak bond strength, loading cycles sustained, residual slip, and crack width.

- Specimens with twisted polygonal steel fibers (Torex fibers) showed the best bond performance under all types of loadings. Bond performance was further enhanced by tailoring the fiber geometry and matrix properties.

8.2.2 Bond of Prestressing Strand

- Preventing cracks from opening is essential for bond performance of strands because it helps to maintain the friction and mechanical interlocking between the strand and the surrounding matrix.

- HPFRCCs can effectively limit crack width, thus preventing the bond from degrading. Torex fiber specimens led to the best bond performance due to high stiffness of the fibers and their high bond with the matrix, which led to higher composite cracking strength and post-cracking stiffness before damage localization.

- The observed average bond strength of strand specimens was generally 8 to 10 times that assumed in the ACI or AASHTO Codes, and 3.5 to 4 times that assumed by

FHWA.

- Unlike specimens with reinforcing bars, specimens with prestressing strands exhibited a unique "ductile" bond stress-slip response capable of dissipating considerable energy under various types of loadings. Moreover, their maximum crack width was much smaller (usually less than 0.01 in.) than in reinforcing bar specimens.

8.2.3 Bond in HPFRCC Beam-Column Joint

- The bond performance in an HPFRCC beam-column joint is primarily affected by the yielding penetration of reinforcing bars. The multiple cracking observed in the HPFRCC joints tested did not seem to have an adverse influence on bond performance.

- A peak average bond stress of 1450 psi (10 MPa) was obtained in the tested HPFRCC beam-column joints, which could be considered a lower bound of the bond strength because no appreciable degradation of bond was observed throughout the tests. Peak bond efficiency values as high as 2.25 were calculated, which indicated excellent bond strength, even when the bars were subjected to large inelastic strains. Bond strength was maintained with no degradation up to 0.04 radian of beam plastic hinge rotation (corresponding to 4% story drift in the test specimens).

- A complete elimination of transverse reinforcement in beam-column connections is possible through the use of HPFRCC materials without compromising structural integrity and safety.

8.3 Recommendations for Future Studies

The following research work is recommended for future studies, based on the findings in this study:

1. Further research is needed to optimize matrix compressive strength and fiber properties in order to maintain both high bond strength and slip capacity.

2. Referring to previous experimental results of SIFCON specimens with pull-out type and beam-type geometries, it seems that the pullout type test would underestimate the bond strength of reinforcing bars embedded in FRC composites in a real structure. To investigate this possible phenomenon, a beam type test, with two bars spliced at midspan (constant moment region in test), is recommended.

3. The effect of different bar sizes, especially bars larger than a No. 8 bar and strands larger than a 0.5 in. seven-wire strand, should be further evaluated.

4. To investigate the possibility of shortening the transfer length in prestressed concrete elements, the testing of bonded pre-tensioned beams with HPFRCC materials is

recommended.

5. By using HPFRCC materials the flexural and shear cracking problems are able to be significantly reduced. Pre-tensioned beams using both debonded strands and HPFRCC materials are recommended to be investigated (See Section 5.7).

6. The fully reversed cyclic loading test results suggests that, potentially, prestressing strands could find applications in non-prestressed, reinforced concrete structures with HPFRCC matrices. For example, untensioned strands could be used to replace beam longitudinal reinforcing bars in a beam-column joint, along with the HPFRCC matrix placed in the joint region only. By using strands instead of reinforcing bars, a ductile bond stress versus slip behavior with less reinforcement congestion can be achieved.

7. The implementation of the proposed local and global bond stress-slip models into finite-element programs is recommended, as well as a parametric evaluation to verify their validity.

BIBLIOGRAPHY

BIBLIOGRAPHY

1. AASHTO, *Standard Specifications for Highway Bridges*, 17th Edition, American Association of State Highway and Transportation Officials, Washington, DC, 2002.

2. Abdel-Fattah, B., and Wight, J. K., "Study of Moving Beam Plastic Hinging Zones for Earthquake-Resistant Design of R/C Buildings," ACI Structural Journal, Vol. 84, No. 1, January-February, 1987, pp. 31-39.

3. Abrams D. A., "Tests of Bond Between Concrete and Steel," Bulletin No. 71, University of Illinois Engineering Experiment Station, Urbana, Illinois, 1913.

4. Abrams D. A., "Study of Bond between Concrete and Steel," Lewis Institute Bulletin 17, Chicago, Illinois, 1925.

5. Abrishami, H. H., Mitchell, D., "Simulation of Uniform Bond Stress," ACI Material Journal, V. 89, No. 2, 1992, pp. 161-168.

6. ACI Committee 318, "Building Code Requirements for Reinforced Concrete and Commentary (ACI318-05/ACI318R-05)," American Concrete Institute, Detroit. 2005.

7. ACI Committee 408, "A Guide for Determination of Bond Strength in Beam Specimens," ACI Journal, Proceedings V. 61, No.2, Feb. 1964, pp. 129-136.

8. ACI Committee 408, "Splice and Development Length of High Relative Rib Area Reinforcing Bars in Tension and Commentary," *Report ACI 408.3-01(408.3R-01)*, Farmington Hills, Michigan, 2001, 6 pp.

9. ACI Committee 408, "Bond and Development of Straight Reinforcing Bars in Tension," *Report ACI 408R-03*, Farmington Hills, Michigan, 2003, 49 pp.

10. ACI-ASCE Committee 352, "Recommendations for Design of Beam-Column Joints in Monolithic Reinforced Concrete Structures," *Report ACI 352R-02*, American Concrete Institute, Farmington Hills, MI, 2002.

11. Alsiwat, J. M., and Saatcioglu, M., "Reinforcement Anchorage Slip under Monotonic Loading," Journal of Structural Engineering, ASCE, Vol. 118, No. 9, September 1992, pp. 2421-2438.

12. ASTM A 370-03a, "Standard Test Methods and Definitions for Mechanical Testing of Steel Products," American Society for Testing and Materials, 2003.

13. ASTM C 469-94, "Standard Test Method for Static Modulus of Elasticity and Poisson's Ratio of Concrete in Compression," American Society for Testing and Materials, 1994.

14. Azizinamini, A., Chisala, M., and Ghosh, S. K., "Tension Development Length of Reinforcing Bars Embedded in High-Strength Concrete, "Engineering Structures, V. 17, No. 7, 1995, pp. 512-522.

15. Balaguru, P., Gambarova, P. G., Rosati, G. P., and Schumm, C. E., "Bond of reinforcing bars and prestressing tendons in HPFRCC matrices," High Performance Fiber Reinforced Cement Composites, HPFRCC 2, RILEM, No. 31, E & FN Spon, London, 1996. pp. 349-381.

16. Barnes, R. W., Grove, J. W., and Burns, N.H., "Experimental Assessment of Factors Affecting Transfer Length," ACI Structural Journal, Vol. 100, No. 6, November-December, 2003, pp. 740-748.

17. Burnett, E. F. P., and Marefat, M. S., "Anchorage Bond for Seven-Wire Strand," Proceedings, International Conference on Bond in Concrete, CEB, Riga, Latvia, October 15-17, 1992.

18. Canbay, E., and Frosch, J. (2005a), "Bond Strength of Lap-Spliced Bars" ACI Structural Journal, Vol. 102, No. 4, July-August, 2005, pp. 605-614.

19. Canbay, E., and Frosch, J. (2005b), "The Design of Lap-Spliced Bars: Is

Simplification Possible?" ACI Structural Journal (In review), 2005.

20. CEB, "CEB-FIP Model Code 1990," Comite Euro-International Du Beton, Thomas Telford, London, 1993.

21. CEB, "RC Elements under Cyclic Loading," Comite Euro-International Du Beton, Thomas Telford, London, 1996.

22. Chandrangsu, K., "Innovative Bridge Deck with Reduced Reinforcement and Strain-Hardening Fiber Reinforced Cementitious Composites," Ph.D. Dissertation, University of Michigan, Ann Arbor, 2003. 261 pp.

23. Chandrangsu, K. and Naaman, A. E., "Innovative Structural Elements of Super High Strength and Ductility," paper presented in PCI Annual Convention/Exhibition, October, 2005.

24. Chang, G. A., and Mander, J. B., "Seismic Energy Based Fatigue Damage Analysis of Bridge Columns" Part 1. Technical Report NCEER-94-0006, 1994.

25. Chapman, R. A., and Shah, S. P., "Early-Age Bond Strength in Reinforced Concrete," ACI Materials Journal, Vol. 84, No. 6, Nov.-Dec. 1987, pp. 501-510.

26. Clark, A. P., "Bond of Concrete Reinforcing Bars," ACI Journal, Proceedings V. 46, No.3, Nov. 1949, pp. 161-184.

27. Clark, C. R., and Johnson, D. W., "Early Loading Effects on Bond Strength," ACI Journal, Proceedings V. 86, No.6, Nov. –Dec. 1983, pp. 532-539.

28. Cook, R. D., and Young, W. C., *Advanced Mechanics of Materials*, 2nd ed. Prentice-Hall, Inc., New Jersey, 1999, 481 pp.

29. Cousins, T. E., Badeaux, M. H., and Moustafa, S., "Proposed Test for Determining Bond Characteristics of Prestressing Strand," PCI Journal, V. 37, No. 1, January-February, 1992, pp. 66-73.

30. Darwin, D., and Graham, E. K., "Effect of Deformation Height and Spacing on

Bond Strength of Reinforcing Bars," ACI Structural Journal, V. 90, No. 6, November-December, 1993, pp. 646-657.

31. Darwin, D., Tholen, M. L., Idun, E. K., and Zuo, J., "Splice Strength of High Relative Rib Area Reinforcing Bars," ACI Structural Journal, V. 93, No. 1, January-February, 1996, pp. 95-107.

32. den Uijl, J. A., "Bond Modeling of Prestressing Strand," Bond and Development of Reinforcement, SP-180, American Concrete Institute, Detroit, 1998, pp. 145-169.

33. Dorr, K., "Bond Behavior of Ribbed Reinforcement under Transverse Pressure," Proceedings IASS Symposium on Nonlinear Behavior of Reinforced Concrete Spatial Structures, Darmstadt, Germany, June 178, pp. 62-72.

34. Durrani, A. J., and Wight, J. K., "Experimental and Analytical Study of Internal Beam to Column Connections Subjected to Reversed Cyclic Loading," *Report No. UMEE 82R3*, Department of Civil and Environmental Engineering, University of Michigan, Ann Arbor, MI., 1982.

35. Ehsani, M. R., and Wight, J. K., "Behavior of External Reinforced Concrete Beam to Column Connections Subjected to Earthquake Type Loading," *Report No. UMEE 82R5*, Department of Civil and Environmental Engineering, University of Michigan, Ann Arbor, MI., 1982.

36. Eligehausen, R., Popov, E. P., and Bertero, V. V., "Local Bond Stress-Slip Relationships of Deformed Bars Under Generalized Excitations," *Report No. UCB/EERC-83/23*, Earthquake Engineering Research Center, University of California, Berkeley, Oct. 1983.

37. Eligehausen, R., Ozbolt, J., and Mayer, U., "Contribution of Concrete between Cracks at Inelastic Steel Strains and Conclusions for the Optimization of Bond," Bond and Development of Reinforcement—Special Publication 180, American Concrete Institute, 1998, pp. 45-80.

38. Engindeniz, M., Kahn, L. F., and Zureick, A. –H.," Repair and Strengthening of Reinforced Concrete Beam-Column Joints: State of the Art," ACI Structural Journal,

V. 102, No. 2, March-April 2005, pp. 1-14.

39. Ezeldin, A. S., and Balaguru, P. N., "Bond Behavior of Normal and High-Strength Fiber Reinforced Concrete," ACI Journal, Proceedings V. 86, No. 5, Nov.-Dec. 1989, pp. 514-524.

40. Ferguson, P. M., Turpin, R. D., and Thompson, J. N., "Minimum Bar Spacing as a function of Bond and Shear Strength," ACI Journal, Proceedings V. 50, No. 10, June 1954, pp. 869-888.

41. FHWA, "A New Development Length Equation for Pretensioned Strands in Bridge Beams and Piles," Publication No. FHWA-RD-98-116, Federal Highway Administration, 1998, 123pp.

42. Filippou, F. C., Popov, E. P., and Bertero, V. V., "Effects of Bond Deterioration on Hysteretic Behavior of Reinforced Concrete Joints," *Report No. UCB/EERC-83/19*, Earthquake Engineering Research Center, University of California, Berkeley, Aug. 1983.

43. Filippou, F. C., "A Simple Model for Reinforcing Bar Anchorages under Cyclic Excitations," Journal of Structural Engineering, ASCE, Vol. 112, No. 7, July 1986, pp. 1639-1659.

44. Fischer, G., and Li, V. C., " Influence of Matrix of Matrix Ductility on Tension-Stiffening Behavior of Steel Reinforced Engineered Cementitious Composites (ECC)," ACI Structural Journal, V. 99, No. 1, Jan.-Feb. 2002, pp. 104-111.

45. Giard, C., and Bastien, J., "Finite-Element Bond-Slip Model for Concrete Columns under Cyclic Loads," Journal of Structural Engineering, ASCE, Vol. 128, No. 12, December 2002, pp. 1502-1510.

46. Goto, Y., "Cracks Formed in Concrete around Deformed Tension Bars," ACI Journal, Vol. 68, No. 4, April 1971, pp. 244-251

47. Hakuto, S., Park, R., and Tanaka, H., "Effect of Deterioration of Bond of Beam Bars

Passing through Interior Beam-Column Joints on Flexural Strength and Ductility," ACI Structural Journal, Vol. 96, No. 5, September-October 1999, pp. 858-864.

48. Hamad, B. S., "Bond Strength Improvement of Reinforcing Bars with Specially Designed Rib Geometries," ACI Structural Journal, V. 92, No. 1, January-February 1995, pp. 3-13.

49. Hamza, A. M., "Bond Strength Characteristics of Deformed Reinforcing Steel Bars Embedded in SIFCON," Ph.D. Dissertation, University of Michigan, Ann Arbor, 1992. 202 pp.

50. Hamza, A. M., and Naaman, A. E., "Bond Characteristics of Deformed Reinforcing Steel Bars Embedded in SIFCON," ACI Material Journal, V. 93, No. 6, Nov.-Dec. 1996. pp.578-588,.

51. Hannant, D. J., *Fibre Cements and Fibre Concrete*, John Wiley & Sons, 1978, 234 pages

52. Hanson, N. W., and Kaar, P. H., "Flexural Bond Tests of Pretensioned Prestressed Beams," ACI Journal, Proceedings V. 55, No.7, Jan. 1959, pp. 783-802.

53. Harajli, M. H.," Development/Splice Strength of Reinforcing Bars Embedded in Plain and Fiber Reinforced Concrete," ACI Structural Journal, V. 91, No. 5, Sep.-Oct. 1994, pp. 511-520.

54. Harajli, M. H., and Mabsout, M. E., "Evaluation of Bond Strength of Steel Reinforcing Bars in Plain and Fiber-Reinforced Concrete," ACI Structural Journal, V. 99, No. 4, July-Aug. 2002, pp. 509-517.

55. Harajli, M., Hamad, B., and Karam, K., "Bond-slip Response of Reinforcing Bars Embedded in Plain and Fiber Concrete," Journal of Materials in Civil Engineering, V. 14, No. 6, November-December, 2002, pp. 503-511.

56. Harajli, M. H., Hamad, B. S., and Rteil, A. A., "Effect of Confinement on Bond Strength between Steel Bars and Concrete," ACI Structural Journal, V. 101, No. 5, September-October 2004, pp. 595-603.

57. Hawkins, N. M., Lin, I., and Ueda, T., "Anchorage of Reinforcing Bars for Seismic Forces," ACI Structural Journal, V. 84, No. 5, September-October 1987, pp. 407-418.

58. Hota, S. R., and Naaman, A. E., "Bond-Stress Slip Response of Reinforcing Bars Embedded in Fiber Reinforced Cement Composites Under Monotonic and Cyclic Loading," *Report No. UMCEE 95-15*, University of Michigan, Ann Arbor, June 1995.

59. Hota, S. R., and Naaman, A. E., "Bond-Stress Slip Response of Reinforcing Bars Embedded in FRC Matrices Under Monotonic and Cyclic Loading," ACI Structural Journal, V. 94, No. 5, Sep.-Oct. 1997, pp. 525-537.

60. Hyatt, T., "An Account of some Experiments with Portland-Cement-Concrete Combined with Iron, as a Building Material," Chiswick Press, London, 1877, 45 pp.

61. Kaar, P., LaFraugh, R., and Mass, M., "Influence of Concrete Strength on Strand Transfer Length," PCI Journal, V. 5, No. 8, Oct. 1963, pp. 47-67.

62. Kankam, C. K., "Relationship of Bond Stress, Steel Stress, and Slip in Reinforced Concrete," Journal of Structural Engineering, ASCE, Vol. 123, No. 1, Jan. 1997, pp. 79-85.

63. Kemp, E. L., "Bond in Reinforced Concrete: Behavior and Design Criteria," ACI Journal, V. 83, January-February 1986, pp. 50-57.

64. Krstulovic-Opara, N., Watson, K. A., and LaFave, J. M., "Effect of Increased Tensile Strength and Toughness on Reinforcing-Bar Bond Behavior," Cement & Concrete Composites, No. 16, pp. 129-141, 1994.

65. Krenchell, H., *Fiber Reinforcement*, Akademisk Forlag, Copenhagen, Denmark, Engl. Translation, 1964.

66. Laine, R. M., Fundamentals of Materials Science and Engineering, class note, Department of Material Science Engineering, University of Michigan, 2002.

67. Leon, R. T., "Interior Joints with Variable Anchorage Lengths" Journal of Structural Engineering, ASCE, V. 115, No. 9, Sep. 1989, pp. 2261-2275.

68. Leonhardt, F., *Prestressed Concrete—Design and Construction*, second edition, Wilhelm Ernst and Sohn, Berlin, Germany, 1964, 677 pp.

69. Li, V. C., "A Simplified Micromechanical Model of Compressive Strength of Fiber-Reinforced Cementitious Composites," Cement & Concrete Composites, V. 14, 1992, pp. 131-141.

70. Li, V. C., Wu, H. –C., and Chan, Y. –W., "Effect of Plasma Treatment of Polyethylene Fibers on Interface and Cementitious Composite Properties," Journal of the American Ceramic Society, Vol. 79, No. 3, March 1996, pp. 700-704.

71. Li, V. C., "Applicability of J-integral to Tension-Softening Materials," Journal of Engineering Mechanics, ASCE, V. 123, No. 5, May 1997, pp. 531-533.

72. Li, V. C., "Engineered Cementitious Composites (ECC)—Tailored Composites through Micromechanical Modeling," Fiber Reinforced Concrete: Present and the Future, Eds: Banthis, N., Bentur, A., and Mufti, A., Canadian Society of Civil Engineers, 1998, pp. 64-97.

73. Li, V. C., Wang, S., and Wu, C., "Tensile Strain-Hardening Behavior of Polyvinyl Alcohol Engineering Cementitious Composite (PVA-ECC)," ACI Material Journal, V. 98, No. 6, Nov.-Dec., 2001, pp. 483-492.

74. Li, V. C., Wu, C., Wang, S., Ogawa, A., and Saito, T., "Interface Tailoring for Strain-Hardening Polyvinyl Alcohol—Engineered Cementitious Composite (PVA-ECC)," ACI Material Journal, V. 99, No. 5, Sep.-Oct., 2002, pp. 463-472.

75. Lowes, L. N., and Altoontash, A., "Modeling Reinforced-Concrete Beam-Column Joints Subjected to Cyclic Loading," Journal of Structural Engineering, ASCE, Vol. 129, No. 12, December 2003, pp. 1686-1697.

76. Lowes, L. N., Moehle, J. P., and Govindjee, S., "Concrete-Steel Bond Model for Use in Finite Element Modeling of Reinforced Concrete Structures," ACI Structural

Journal, Vol. 101, No. 4, July-August 2004, pp. 510-511.

77. Maeda, M., Otani, S., and Aoyama, H., "Bond Splitting Strength in Reinforced Concrete Members," Transactions of the Japan Concrete Institute, V. 13, 1991, pp. 581-588.

78. Mains, R. M., "Measurement of the Distribution of Tensile and Bond Stresses along Reinforcing Bars," ACI Journal, Proceedings V. 48, No. 3, Nov. 1951, pp. 225-252.

79. Malvar, L. J., "Bond of Reinforcement Under Controlled Confinement" ACI Material Journal, V. 89, No. 6, pp. 593-601, 1992.

80. Mathey, R. G., and Watstein, D., "Investigation of Bond in Beam Pullout Specimens with High Yield Strength Deformed Bars," ACI Journal, Proceedings V. 57, No.9, March 1961, pp. 1071-1090.

81. Meinheit, D. F., and Jirsa, J. O., "Shear Strength of R/C Beam-Column Connections," Journal of the Structural Division, ASCE, V. 107, No. ST 11, November 1981, pp. 2227-2244.

82. Menegotto, M., and Pinto, P. E., "Method of Analysis for cyclically loaded reinforced concrete plane frames including changes in geometry and nonelastic behavior of elements under combined normal force and bending," Proceedings, IABSE Symposium on Resistance and Ultimate Deformability of Structures Acted on by Well Defined Repeated Loads, Lisbon, 1973.

83. Menzel, C. A., "Some Factors Influencing Results of Pull-out Bond Tests," ACI Journal, Proceedings V. 35, No. 3, June 1939, pp. 517-544.

84. Mindess, S., Young, J. F., and Darwin, D., *Concrete*, second edition, Prentice Hall, NJ, 2003, 644 pages

85. Mirza, S. M., and Houde, J., "Study of Bond Stress-Slip Relationships in Reinforced Concrete, "ACI Journal, Proceedings V. 76, No.1, Jan. 1979, pp. 19-46.

86. Monti, G., Fillipou, F. C., and Spacone, E., "Finite Element for Anchored Bars under

Cyclic Load Reversals," Journal of Structural Engineering, ASCE, Vol. 123, No. 5, May 1997, pp. 614-623.

87. Morita, S. and Kaku, T., "Slippage of Reinforcement in Beam-Column Joint of Reinforced Concrete Frame," Proceedings, 8th World Conference on Earthquake Engineering, San Francisco. Vol. 6. pp. 477-484, 1984.

88. Mylrea, T. D., "Bond and Anchorage," ACI Journal, Proceedings V. 44, No.2, March 1948, pp. 977-987.

89. Naaman, A.E., "A Statistical Theory of Strength for Fiber Reinforced Concrete," Ph.D. Dissertation, Massachusetts Institute if Technology, September, 1972, 196 pp.

90. Naaman, A.E., and Reinhardt, H.W., Editors, High Performance Fiber Reinforced Cement Composites, HPFRCC 2, RILEM, No. 31, E & FN Spon, London, 1996, 505 pages.

91. Naaman, A.E., and Reinhardt, H.W., "Characterization of High Performance Fiber Reinforced Cement Composites—HPFRCC," High Performance Fiber Reinforced Cement Composites, HPFRCC 2, RILEM, No. 31, E & FN Spon, London, 1996, pp. 1-24.

92. Naaman, A. E., "Fibers with Slip Hardening Bond," High Performance Fiber Reinforced Cement Composites 3 (HPFRCC 3), Proceedings of the Third International RILEM Workshop, Mainz, Germany, May 1999, Ed. H. W. Reinhardt and A. E. Naaman, RILEM Publications S.A.R.L., Cachan Cedex, France, pp. 371-385.

93. Naaman, A. E., "HPFRCCs: Properties and Applications in Repair and Rehabilitation," High-Performance Fiber-Reinforced Concrete in Infrastructural Repair and Retrofit, , ACI Special Publication 185, 2000, pp.1-16.

94. Naaman, A. E., Burns, N., French, C., Gamble, W. L., and Mattock, H., "Stresses in Unbonded Prestressing Tendons at Ultimate: Recommendation," ACI Structural Journal, Vol. 99, No. 4, July-August 2002, pp. 518-529.

95. Naaman, A.E., and Reinhardt, H.W., Editors, High Performance Fiber Reinforced Cement Composites, HPFRCC 4, RILEM Publications S.A.R.L., Proceedings PRO 6, France, 2003, 606 pages.

96. Naaman, A. E., "Strain Hardening and Deflection Hardening Fiber Reinforced Cement Composites," High Performance Fiber Reinforced Cement Composites 4 (HPFRCC 4), Proceedings of the Fourth International RILEM Workshop, Ann Arbor, U.S.A., June 2003, Ed. A. E. Naaman and H. W. Reinhardt. RILEM Publications S.A.R.L., Cachan Cedex, France, pp. 95-113.

97. Naaman, A. E., and Parra-Montesinos, G., "Bond Stress-Slip of Reinforcing Bars and Prestressing Strands in HPFRC Composites," Research Proposal submitted to National Science Foundation, 2003.

98. Naaman, A. E., *Prestressed Concrete Analysis and Design—Fundamentals*, 2nd Ed., Techno Press 3000, Ann Arbor, Michigan, 2004, 1072 pp.

99. Naaman, A. E., "Evaluation of Steel Fibers for Applications in Structural Concrete," 6th RILEM Symposium on Fiber-Reinforced Concrete (FRC), BEFIB, September 2004, Varenna, Italy, pp.359-400.

100. Naaman, A.E., and Reinhardt, H. W, "Proposed Classification of HPFRC Composites based on Their Tensile Response," Mindess Symposium, August, 2005.

101. Nilson, A. H., "Bond Stress-Slip Relations in Reinforced Concrete," Report No. 345, School of Civil and Environmental Engineering, Cornell University, Ithaca, New York, Dec. 1971, 38 pp.

102. Nilson, A. H., "Internal Measurement of Bond Slip," ACI Journal, Proceedings V. 69, No. 7, July 1972, pp. 439-441.

103. Orangun, C. O., Jirsa, J. O., and Breen, J. E., "The Strength of Anchored Bars: A reevaluation of Test Data on Development Length and Splices," Research Report No. 154-3F, Center for Highway Research, The University of Texas at Austin, Tex., Jan, 78 pp.

104. Orangun, C. O., Jirsa, J. O., and Breen, J. E., "A reevaluation of Test Data on Development Length and Splices," ACI Journal, Vol. 74, March 1977, pp. 114-122.

105. Parra-Montesinos, G., "Seismic Behavior, Strength and Retrofit of Exterior RC Column-to-steel Beam Connections," Ph.D. Dissertation, University of Michigan, Ann Arbor, 2000. 301 pp.

106. Parra-Montesinos, G., "HPFRCC in Earthquake-Resistant Structures: Current Knowledge and Future Trends," High Performance Fiber Reinforced Cement Composites 4 (HPFRCC 4), Proceedings of the Fourth International RILEM Workshop, Ann Arbor, U.S.A., June 2003, Ed. A. E. Naaman and H. W. Reinhardt. RILEM Publications S.A.R.L., Cachan Cedex, France, pp. 453-472.

107. Parra-Montesinos, G., Peterfreund, S. W., and Chao, S. -H., "Highly Damage Tolerant Beam-Column Joints Through Use of High-Performance Fiber-Reinforced Cement Composites," ACI Structural Journal, Vol. 102, No. 3, May-June 2005, pp. 487-495.

108. Parra-Montesinos, G., "High-Performance Fiber-Reinforced Cement Composites: An Alternative for Seismic Design of Structures," ACI Structural Journal, Vol. 102, No. 5, September-October 2005, pp. 668-675.

109. Paulay, T., and Priestley, M. J. N., *Seismic Design of Reinforced Concrete and Masonry Buildings*, John Wiley and Sons, Inc. 1992.

110. Paulay, T., Park, R., and Priestley, M. J. N., "Reinforced Concrete Beam-Column Joints Under Seismic Actions," ACI Journal, Vol. 75, November 1978, pp. 585-593.

111. Pochanart, S., and Harmon, T., "Bond-Slip Model for Generalized Excitations Including Fatigue," ACI Material Journal, Vol. 86, No. 5, September-October 1989, pp. 465-474.

112. Popov, E. P., "Bond and Anchorage of Reinforcing Bars Under Cyclic Loading," ACI Journal, Vol. 81, July-August 1984, pp. 340-349.

113. Rehm, G., "The Fundamental Law of Bond," RILEM Symposium on Bond and

Crack Formation in Reinforced Concrete, V. 2, Stockholm, Sweden, 1957, pp. 491-498.

114. Reinhardt, H.W., and Naaman, A.E., Editors, High Performance Fiber Reinforced Cement Composites, RILEM Publication 15, E & FN Spon, London, 1992, 565 pages.

115. Reinhardt, H.W., and Naaman, A.E., Editors, High Performance Fiber Reinforced Cement Composites, HPFRCC 3, RILEM Publications S.A.R.L., Proceedings PRO 6, France, 1999, 666 pages.

116. Rose, D. R. and Russell, B. W., "Investigation of Standardized Tests to Measure the Bond Performance of Prestressing Strand," PCI Journal, V. 42, No. 4, July-August 1997, pp. 56-80.

117. Rostásy, F. S., and Hartwich, K.,"Bond of Deformed Reinforcing Bar Embedded in Steel Fiber Reinforced Concrete," International Journal of Cement Composites and Lightweight Concrete, Vol. 10, No. 3, pp. 151-158, 1988.

118. Russell, B. W., "Design Guidelines for Transfer, Development and Debonding of Large Diameter Seven Wire Strands in Pretensioned Concrete Girders," Ph.D. Dissertation, the University of Texas at Austin, December 1992, 464 pp.

119. Russell, B. W. and Burns, N. H., "Measured Transfer Lengths of 0.5 and 0.6 in. Strands in Pretensioned Concrete," PCI Journal, V. 41, No. 5, Sep.-Oct. 1996, pp. 44-65.

120. Russell, B. W., and Paulsgrove, G. A., "NASP Strand Bond Test I & II—Pull-out Tests and Friction Bond Tests of Untensioned Strand," Fears Structural Engineering Laboratory, School of Civil Engineering and Environmental Science, University of Oklahoma, 1999.

121. Sakai, J., and Kawashima, K., "Modification of the Giuffre, Menegotto and Pinto Model for Unloading and Reloading Paths with Small Strain Variations," *Journal of Structural Mechanics and Earthquake Engineering*, JSCE, No. 738/I-64, 2003, pp. 159-169 (in Japanese),

122. Sakurada, T., Morohashi, N., and Tanaka, R., "Effect of Transverse Reinforcement on Bond Splitting Strength of Lap Splices," Transactions of the Japan concrete Institute, V. 15, 1993, pp. 573-580.

123. Sezen, H., and Moehle, J. P., "Strength and Deformation Capacity of Reinforced Concrete Columns with Limited Ductility," Proceedings, 13th World Conference on Earthquake Engineering, Vancouver, B. C., Canada, August, 2004, Paper No. 279.

124. Shah, S. P., and Rangan, V., "Fiber Reinforced Concrete Properties," ACI Journal, Proceedings, V. 68, No. 2, Feb. 1971, pp. 126-135.

125. Shahawy, M. A., Issa, M., and Batchelor, B., "Strand Transfer Lengths in Full Scale AASHTO Prestressed Concrete Girders," PCI Journal, V. 37, No. 3, May-June, 1992, pp. 84-96.

126. Soleimani, D., Popov, E. P., and Bertero, V. V., "Hysteretic Behavior of Reinforced Concrete Beam-Column Subassemblages," ACI Journal, Vol. 76, November 1979, pp. 1179-1195.

127. Specncer, R. A., Panda, A. K., and Mindess, S., "Bond of Deformed Bars in Plain and Fiber Reinforced Concrete under Reversed Cyclic Loading," The International Journal of Cement Composites, Proceedings V. 4, No. 4, Feb. 1982, pp. 3-17.

128. Stanton, J. F., and McNiven, H. D., "The Development of A Mathematical Model to Predict the Flexural Response of Reinforced Concrete Beams to Cyclic Loads, Using System Identification," *Report No. UCB/EERC-79/02*, Earthquake Engineering Research Center, University of California, Berkeley, Jan. 1979.

129. Stocker, M. F., and Sozen, M. A., "Investigation of Prestressed Reinforced Concrete for Highway Bridges, Part V: Bond Characteristics of Prestressing Strand," Engineering Experiment Station 503, The University of Illinois, 1971.

130. Sujivorakul, C., "Development of High Performance Fiber Reinforced Cement Composites Using Twisted Polygonal Steel Fibers," Ph.D. Dissertation, University of Michigan, Ann Arbor, 2002, 330 pp.

131. Swamy, R. N., "Fiber Reinforcement of Cement and Concrete," Materials and Structures Proceedings, Paris, V. 8, No. 45, 1945, pp. 235-254.

132. Swamy, R. N., and Al-Noori, K., "Bond Strength of Steel Fiber Reinforcing Concrete," Concrete Journal, Proceedings V. 8, No. 8, Aug. 1974, pp. 36-37.

133. Tajima, K., Mishima, T., and Shirai, N., "3-D Finite Element Cyclic Analysis of RC Beam/Column Joint Using Special Bond Model" Proceedings, 13th World Conference on Earthquake Engineering, Vancouver, B. C., Canada, 2004, Paper No. 446.

134. Tassios, T. P., and Bonataki, E., "Experimental Analysis of the Bond Behavior of Prestressed Tendons," Proceedings, International Conference on Bond in Concrete, CEB, Riga, Latvia, October 15-17, 1992.

135. Viawathanatepa, S., Popov, E. P., and Bertero, V. V., "Seismic Behavior of Reinforced Concrete Interior Beam-Column Subassemblages," *Report No. UCB/EERC-79/14*, Earthquake Engineering Research Center, University of California, Berkeley, June 1979.

136. Viawathanatepa, S., Popov, E. P., and Bertero, V. V., "Effects of Generalized Loadings on Bond of Reinforcing Bars Embedded in Confined Concrete Blocks," *Report No. UCB/EERC-79/22*, Earthquake Engineering Research Center, University of California, Berkeley, Aug. 1979.

137. Watstein, D., "Distribution of Bond Stress in Concrete Pull-out Specimens," ACI Journal, Proceedings V. 43, No. 9, May. 1947, pp. 1041-1053.

138. Zuo, J. and Darwin, D., "Bond Strength of High Relative Rib Area Reinforcing Bars," *SM Report No. 46*, University of Kansas Center for Research, Lawrence, Kans., 1998, 350 pp.

139. Zuo, J. and Darwin, D., "Splice Strength of Conventional and High Relative Rib Area Bars in Normal and High-Strength Concrete," ACI Structural Journal, V. 97, No. 4, July-August, 2000, pp. 630-641.